The Landscape of Relativistic Stellar Explosions

Thesis by
Anna Yen Qin Ho

In Partial Fulfillment of the Requirements for the
Degree of
Doctor of Philosophy

CALIFORNIA INSTITUTE OF TECHNOLOGY
Pasadena, California

2020
Defended July 2, 2020

Anna Yen Qin Ho
ORCID: 0000-0002-9017-3567

To my grandparents,
Ho Heng Meng, Wong Geok Kim, Robert Edward Lipsey, and Sally Irene Lipsey,
who have inspired me with their lifelong curiosity, enthusiasm, and adventurous spirit.

Before their eyes in sudden view appear
The secrets of the hoary Deep—a dark
Illimitable ocean, without bound,
Without dimension...

—*Paradise Lost*, II.890-91

He touched the brim of his hard hat and glanced back at the dome, white and round like an ancient temple, while a thought crossed his mind, by no means for the first time, that he was only paying his respects to a temple of science.

—*First Light* by Richard Preston

ACKNOWLEDGEMENTS

I could not have navigated graduate school without the support, advice, and generosity of a large number of people.

First my advisor, Shri Kulkarni. Shri set his expectations to what at first seemed like impossibly high standards, made it clear he believed I could reach those expectations through hard work, and steered me to the resources I needed to do so. I must also thank Shri for teaching me the value of a beginning-student mindset and for broadening my musical horizons, including how to listen to a song on infinite repeat.

Dan Perley, my collaborator in the trenches of ZTF fast-transient astronomy, who has been amazingly generous with his time and expertise. Dan taught me a great deal about not just gamma-ray bursts but also scientific rigor and precision.

Sterl Phinney, in front of whose chalkboard I had some of my most treasured intellectual experiences in graduate school. Thank you for sharing your library, and for reminding me to γνῶθι σεαυτόν and to σπεῦδε βραδέος.

Lynne Hillenbrand and my thesis committee: Shri, Sterl, Mansi Kasliwal, Gregg Hallinan, and Chuck Steidel. Lynne and Chuck provided a listening ear and useful perspective throughout graduate school. Gregg has been a generous and invaluable resource for making sense of radio observations. Mansi generously supported my work and my professional development through the Global Relay of Observatories Watching Transients Happen.

The astronomy faculty. It is a privilege to work in a department with wide-ranging expertise, and I benefited from discussions with Jim Fuller (pre-SN mass-loss), Vikram Ravi (synchrotron radiation and scattering), Phil Hopkins (galaxy simulations), Jonas Zmuidzinas (millimeter astronomy), and Evan Kirby (stellar evolution).

The ZTF collaboration, a wealth of technical know-how and astrophysical expertise. I would like to thank Brad Cenko and Alessandra Corsi for teaching me the ropes of X-ray and radio astronomy respectively, and Peter Nugent for his hospitality and generosity throughout my PhD. Thank you to Avishay Gal-Yam, Steve Schulze, and Eran Ofek (Weizmann), Jesper Sollerman and Ragnhild Lunnan (OKC), and Matthew Graham and Christoffer Fremling (Caltech) for generously supporting my scientific interests. Finally I would like to thank Yuhan Yao, Kishalay De, and Danny Goldstein for their friendship in the trenches of observing, data reduction, and understanding the physics of supernovae.

The staff members of observatories spanning the electromagnetic spectrum, including *Fermi*, Konus-WIND, and INTEGRAL (gamma rays), *Swift*, *Chandra*, and MAXI (X-rays), Palomar and Keck (optical), the SMA and ALMA (millimeter), the ATCA, GMRT (radio), and, especially, the National Radio Astronomy Observatory (NRAO). Thank you to the NRAO staff for hosting me during visits to Socorro and for generously answering many a helpdesk ticket.

The members of the ZTF Theory Network, particularly David Khatami and Paul Duffell, from whom I learned much about the physics of supernova ejecta-CSM interaction and jet-CSM interaction, respectively. I also benefited a great deal from the insights of Dan Kasen, Sterl Phinney, Jim Fuller, and Eliot Quataert.

Jenn Jahner and Anne Sullivan for enjoyable and stimulating reading groups and discussions on *Pearl*, *The Book of Margery Kempe*, and poetry such as *Life on Mars* by Tracy K. Smith. Thank you to Louise Hindle at the Huntington Library and Michele Judd at the Keck Institute for Space Studies for giving me the opportunity to share my scientific and literary interests with the Pasadena and Caltech communities. Finally, thank you to David Pankenier (Lehigh) for alerting me to the considerable complexities in interpreting reports of "new stars" in oracle bone inscriptions.

My middle- and high-school teachers. Chris Goff encouraged my interest in physics, and Colin McCarty and Laura Matzen gave me my first research opportunity. Richard Eisenberg taught me to teach myself, and Stephan Potchatek gave me confidence in my intellectual contributions by soliciting them at the round table.

My interest in astronomy as a profession took shape while I was an undergraduate student at MIT. I am indebted to Paul Schechter, who patiently answered my question "what is it like to be an astronomer?" and has so patiently answered so many questions in the years since. Thank you to Scott Ransom at the NRAO for providing me with a stimulating first astronomy research experience; Alan Guth, my academic advisor, for his support and encouragement; Diana Henderson and Arthur Bahr for supporting me in my development as a scholar and a citizen; Chris Peterson for helping me develop as a writer; and Richard Preston, who kindly mailed a signed book to an amazed college student. Finally, I am grateful for the mentorship and boundless hospitality of Hans-Walter Rix and Melissa Ness. Thanks to them and to the Fulbright Program, I spent a productive and enriching year at the Max Planck Institute for Astronomy in Heidelberg, Germany.

I was immensely fortunate to have such wonderful friends at Caltech. Thank you

in particular to Marta Bryan, Becky Jensen-Clem, and Alistair Hayden, the best companions and support team imaginable. I am greatly inspired by Marta's courage and conviction, Becky's humor and clarity, and Alistair's positivity and initiative. Thank you to my classmates Ivanna Escala, Kaew Tinyanont, and Yuguang Chen for their friendship and companionship over the last five years—I could not have asked for a better cohort. Thank you to Hannah Allen, Kevin Burdge, Sophia Charan, Zach Erickson, Calen Henderson, Tammy Khazaei, Heidi Klumpe, Daniel Pastor Moreno, and Florian Schaefer for supportive company and long stimulating conversations; Danny Goldstein, whose friendship made Caltech and ZTF a more enjoyable place to be; and to Yuhan Yao and Lee Rosenthal, who were technically my mentees but who I learned a great deal from as well. Thank you to my officemates Kathryn Plant, Chris Bochenek, Jake Jencson, and Nitika Yadlapalli—I can't imagine having a better work environment! Thank you to Melodie Kao for her support and advice along my astronomy journey. And finally, thank you to the astronomy department graduate-student community, who reminded me that no matter how much work you have on your plate, there is always time to be there for your friends.

An academic life entails a great deal of moving, including over oceans and across continents, and I would like to express my gratitude for the friendships that have endured many changes. Thank you first and foremost to Sophia Palenberg for helping me adjust to life in LA; to Saul Wilson and Davie Rolnick for stimulating discussions and adventures; and to Sameer Arya, Sam Bader, Monica Bonilla, Rachel Brouwer, Eric Gleiss, Daniel Levine, Cam Tenny, Sophie Weber, and Sam Young for their company and support over many years, and for helping me keep a sense of perspective during grad school.

Finally, my family. My parents William Ho and Eleanor Lipsey gave me, along with so much else, the blessings of a global perspective, steadfast support and encouragement, and the freedom to explore my interests. My sister Lisa Ho is a force and an inspiration, and has been my best friend and my first port of call for advice and companionship for as long as I can remember.

ABSTRACT

For the last half-century, relativistic outflows accompanying the final collapse of massive stars have predominantly been detected via high-energy emission (i.e., gamma-ray bursts, or GRBs). From wide-field optical and radio time-domain surveys, there have been hints of related phenomena at lower energies (e.g., X-ray flashes). For my thesis, I used the Zwicky Transient Facility to conduct the first large-scale optical survey dedicated to finding relativistic stellar explosions. I successfully detected a suite of GRB-related phenomena without relying on a GRB trigger, and followed them up with facilities across the electromagnetic spectrum including ALMA: relativistic afterglows at cosmological distances, broad-lined Ic (Ic-BL) supernovae with X-ray and radio emission, and fast-luminous transients powered by circumstellar interaction. Based on the rate of fast (intra-night) optical transients, I showed that a "clean" jet seems central to the phenomenon of collimated energetic outflows, i.e., there is no evidence for afterglow-like optical transients whose area (sky) rate greatly exceed the classical GRB rate. With a radio and millimeter-wave investigation of AT2018cow, and the discovery of a similar event in ZTF, I established a new class of engine-driven stellar explosions that arise from different progenitors to GRBs and explode embedded in dense circumstellar material. I showed that fast-luminous thermal emission can arise from late-stage eruptive mass-loss and is not necessarily linked to the presence of relativistic ejecta, complicating searches for choked jets in Ic-BL SNe. My work sets the stage for discovering and characterizing relativistic stellar explosions in large numbers during the era of ZTF Phase II, the Large Synoptic Survey Telescope (LSST), and millimeter-band facilities like ALMA and NOEMA.

PUBLISHED CONTENT AND CONTRIBUTIONS

Ho, A. Y. Q. et al. (2020a). "The Broad-lined Ic Supernova ZTF18aaqjovh (SN 2018bvw): An Optically Discovered Engine-driven Supernova Candidate with Luminous Radio Emission". In: *ApJ* 893.2, p. 132. DOI: 10.3847/1538-4357/ab7f3b. arXiv: 1912.10354 [astro-ph.HE].
A.Y.Q.H. helped acquire and reduce the follow-up observations, performed the analysis, and wrote the manuscript.

Ho, A. Y. Q. et al. (2020b). "The Koala: A Fast Blue Optical Transient with Luminous Radio Emission from a Starburst Dwarf Galaxy at z = 0.27". In: *ApJ* 895.1, p. 49. DOI: 10.3847/1538-4357/ab8bcf. arXiv: 2003.01222 [astro-ph.HE].
A.Y.Q.H. wrote the filter that led to the discovery of the event, helped acquire and reduce the follow-up observations, performed most of the analysis, and wrote most of the manuscript.

Ho, A. Y. Q. et al. (2020c). "SN2020bvc: a Broad-lined Type Ic Supernova with a Double-peaked Optical Light Curve and a Luminous X-ray and Radio Counterpart". In: *ApJ, accepted*. arXiv: 2004.10406 [astro-ph.HE].
A.Y.Q.H. conceived the idea for the project, helped acquire and reduce the follow-up observations, performed the analysis, and wrote the manuscript.

Ho, A. Y. Q. et al. (2020d). "ZTF20aajnksq (AT2020blt): A Fast Optical Transient at $z \approx 2.9$ With No Detected Gamma-Ray Burst Counterpart". In: *ApJ, submitted*. arXiv: 2006.10761 [astro-ph.HE].
A.Y.Q.H. discovered the event, helped acquire and reduce the follow-up observations, performed the analysis, and wrote the manuscript.

Ho, A. Y. Q. et al. (2019a). "AT2018cow: A Luminous Millimeter Transient". In: *The Astrophysical Journal* 871.1, p. 73. DOI: 10.3847/1538-4357/aaf473. arXiv: 1810.10880 [astro-ph.HE].
A.Y.Q.H. helped acquire and reduce the follow-up observations, performed the analysis, and wrote most of the manuscript.

Ho, A. Y. Q. et al. (2019b). "Evidence for Late-stage Eruptive Mass Loss in the Progenitor to SN2018gep, a Broad-lined Ic Supernova: Pre-explosion Emission and a Rapidly Rising Luminous Transient". In: *ApJ* 887.2, p. 169. DOI: 10.3847/1538-4357/ab55ec. arXiv: 1904.11009 [astro-ph.HE].
A.Y.Q.H. wrote the filter that led to the discovery of the event, helped acquire and reduce the follow-up observations, performed most of the analysis, and wrote most of the manuscript.

Ho, A. Y. Q. et al. (2018). "iPTF Archival Search for Fast Optical Transients". In: *ApJL* 854.1, p. L13. DOI: 10.3847/2041-8213/aaaa62. arXiv: 1712.00949 [astro-ph.HE].
A.Y.Q.H. performed the archival search and analysis, helped acquire and reduce the follow-up observations, and wrote the manuscript.

TABLE OF CONTENTS

LIST OF ILLUSTRATIONS

LIST OF TABLES

Chapter 1

INTRODUCTION AND SUMMARY

1.1 Landscape Overview

In the traditional picture of massive-star ($M \gtrsim 10\,M_{\odot}$) evolution, there is assumed to be a direct mapping between stellar mass, supernova type (and corresponding output of momentum, energy, and metals into the interstellar medium), and compact remnant (a neutron star or a black hole). This scheme is important to many areas of astrophysics: the formation of black holes, the birth of the first stars, the evolution of galaxies, and the build-up of most of the mass of the elements heavier than helium in the universe. Yet we are still ignorant of basic questions: What are the progenitors of different classes of core-collapse supernovae (Smartt, 2009)? What mechanisms explode stars as supernovae (Janka, 2012)? What are the progenitors of neutron stars and black holes (Heger et al., 2003)?

To make matters worse, massive stars shed a significant fraction of their mass through winds and violent eruptive episodes (Smith, 2014). Mass-loss is an interesting process in itself (for example, the prevalence of late-stage eruptions may result from an unrecognized form of energy transport in stars) but is a confounding factor in the mapping outlined above, both observationally (circumstellar interaction masks the nature of the underlying explosion) and theoretically (how much mass a star ejects and over what timescale plays a key role in determining its inner structure, evolutionary path, and lifetime).

For my PhD thesis, I focused on the most energetic and luminous stellar endpoints: explosions powered by a bipolar outflow from a newborn compact object, the best-studied subset being long-duration gamma-ray bursts (hereafter 'GRBs'; Kouveliotou et al. 2012; Piran 2004) which are associated with high-velocity ("broad-lined", BL) energetic (10^{52} erg) supernovae of Type Ic-BL (Woosley and Bloom, 2006).

The GRB View

Over the past half-century, thousands of GRBs have been discovered by high-energy satellites. In the traditional GRB model, a massive star that is stripped of its hydrogen and helium envelopes (Figure 1.1) collapses into a black hole or a highly magnetized

neutron star. Accretion onto the black hole or rotational spindown of the neutron star accelerates material to ultrarelativistic speeds (initial Lorentz factor $\Gamma_0 \gtrsim 100$). As illustrated in Figure 1.2, the outflow becomes narrowly collimated (opening angle $\theta_0 \approx 10°$) as it tunnels through the star, and produces an "afterglow" observable across the electromagnetic spectrum as it collides with the circumstellar medium, or CSM (Panaitescu and Kumar, 2002; van Paradijs et al., 2000). The same "central engine" that launches the jet also unbinds the stellar material in a Ic-BL SN (Barnes et al., 2018; Sobacchi et al., 2017).

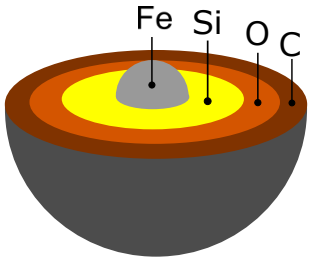

Figure 1.1: Structure of stripped-envelope SN progenitor

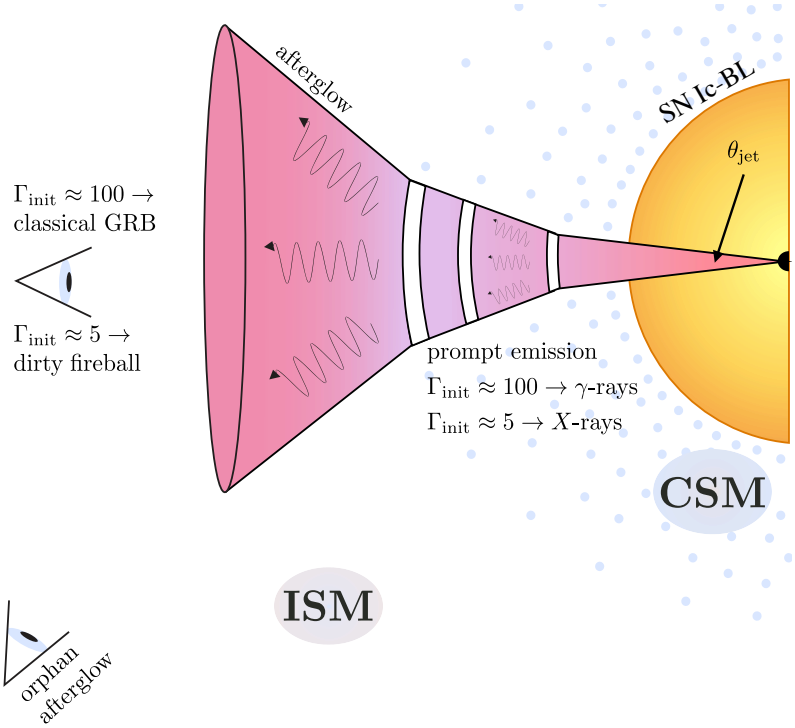

Figure 1.2: Geometry of GRBs and associated Ic-BL SNe. Classical GRBs come from on-axis jets with a large initial Lorentz factor ($\Gamma_{\rm init} \gtrsim 100$). A jet with a lower Lorentz factor ($\Gamma_{\rm init} \approx 10$) is called a dirty fireball. For clean or dirty jets, an off-axis observer will observe an orphan afterglow (an afterglow lacking prompt emission) and a Ic-BL SN.

GRBs appear to represent a rare endpoint of stellar evolution. As shown in Table 1.1, the local ($z = 0$) observed GRB rate is a factor of 10^{-5} to 10^{-7} times the local CC SN rate. Assuming that GRBs are produced exclusively by Ic-BL SN progenitors[1] the GRB beaming fraction would have to be 10^{-3} to 10^{-6} in order for all Ic-BL SNe to produce a GRB in some direction.

There are large uncertainties in the GRB beaming fraction: estimates are based on observations of breaks in afterglow light curves, and as shown in Table 1.2 beaming fraction estimates vary from 10^{-2} to 10^{-3}. More reliable estimates of the beaming fraction will be available once radio and optical surveys have the sensitivity to detect afterglow emission from large numbers of off-axis jets in the local universe. The appearance of an off-axis jet is very different from an on-axis jet. Due to relativistic beaming, there will be no bright gamma-ray emission from an off-axis jet, and the afterglow will be invisible at first. Over time, as the shock slows and the relativistic beaming cone widens to include Earth, the afterglow will become brighter (Rhoads, 1997).

So, taking into account the large uncertainties in both the local GRB rate and the GRB beaming fraction, it is clear that most CC SNe do not produce a GRB, but it is not yet clear what fraction of Ic-BL SNe produce a GRB in some direction. However, it is widely believed that most Ic-BL SNe do *not* produce a GRB, due to the non-detection of off-axis afterglows by radio follow-up observations of nearby Ic-BL SNe.

A major outstanding question is: do GRBs represent an unusual and distinct endpoint, or are they the extremum of a broad continuum of relativistic stellar explosions? It is easy to imagine variations on the traditional GRB model, since a number of stringent conditions must be met to produce a GRB. First, the jet must be nearly baryon-free—or else the available energy is insufficient to accelerate the ejecta to ultra-relativistic velocities, and gamma-ray emission will be stifled by pair-production. A jet with too many baryons ($> 10^{-4}\ M_{\odot}$) could only attain a moderate Lorentz factor ($\Gamma \sim 5$–10) and would therefore not produce *significant* gamma rays and thus not trigger Fermi/GBM or Swift/BAT (Dermer et al., 1999). This "dirty fireball" would still produce a luminous afterglow, illustrated in Figure 1.2.

[1] To date, 13 nearby GRBs have a spectroscopically confirmed Type Ic-BL SN, and a dozen more have "bumps" in the late-time light curve consistent with a nickel-powered SN (Cano et al., 2017b). However, two GRBs *lack* an accompanying SN to deep limits (Fynbo et al., 2006), and one ultra-long duration GRB had an accompanying transient that does not fit into any traditional SN spectroscopic class (Greiner et al., 2015). So, clearly GRB progenitors are diverse.

Table 1.1: Local ($z = 0$) rates of core-collapse supernovae and GRBs. Approximately 30% of CC SNe arise from a progenitor stripped of its hydrogen envelope. Among these stripped events, there are roughly equal numbers of IIb, Ib, and Ic events. Of the Ic events, $\sim$ 20% are "broad-lined" with photospheric velocities $\gtrsim$20,000 km/s. The beaming factor for LLGRBs is highly uncertain, but is probably $\sim$a few.

Class	Rate/Fraction	Ref.
SN Ia	$3.01 \pm 0.62 \times 10^{-5}\,\mathrm{yr}^{-1}\,\mathrm{Mpc}^{-3}$	[1]
CC SN	$7.05 \pm 1.57 \times 10^{-5}\,\mathrm{yr}^{-1}\,\mathrm{Mpc}^{-3}$	
... SN II	$4.47 \pm 1.39 \times 10^{-5}\,\mathrm{yr}^{-1}\,\mathrm{Mpc}^{-3}$	[1]
... SN Ibc	$2.58 \pm 0.72 \times 10^{-5}\,\mathrm{yr}^{-1}\,\mathrm{Mpc}^{-3}$	[1]
Ic-BL SN	$3.6 \pm 1.4 \times 10^{-6}\,\mathrm{yr}^{-1}\,\mathrm{Mpc}^{-3}$	
	$2.6^{+3.1}_{-2.6} \times 10^{-6}\,\mathrm{yr}^{-1}\,\mathrm{Mpc}^{-3}$	
... Frac. of Ibc SN that are Ic	0.69 ± 0.09	[2]
... Frac. of Ic SN that are Ic-BL	0.21 ± 0.05	[2]
... Frac. of CC SNe that are Ic-BL	$0.037^{+0.029}_{-0.037}$	[3]
LLGRB	$\mathcal{R}_{\rm obs} = 2.3^{+4.9}_{-1.9} \times 10^{-7}\,\mathrm{yr}^{-1}\,\mathrm{Mpc}^{-3}$	[4]
	$\mathcal{R}_{\rm obs} = 3.3^{+3.5}_{-1.8} \times 10^{-7}\,\mathrm{yr}^{-1}\,\mathrm{Mpc}^{-3}$	[5]
ℓGRB	$\mathcal{R}_{\rm obs} = 4.2^{+9.0}_{-4.0} \times 10^{-10}\,\mathrm{yr}^{-1}\,\mathrm{Mpc}^{-3}$	[6]
sGRB	$\mathcal{R}_{\rm obs} = 10^{-8}\,\mathrm{yr}^{-1}\,\mathrm{Mpc}^{-3}$	[7]
	$f_b^{-1} = 27^{+158}_{-18}$	[8]
NS-NS (GW 170817)	$1.54^{+3.20}_{-1.22} \times 10^{-6}\,\mathrm{yr}^{-1}\,\mathrm{Mpc}^{-3}$	[9]

Table 1.2: Estimates of the beaming fraction, where $f_b = 1 - \cos\theta_0$ and θ_0 is the estimated jet opening angle. The "true" GRB rate is $\mathcal{R}_{\rm obs} f_b^{-1}$.

Class	Rate/Fraction	References
ℓGRB	$\mathcal{R}_{\rm obs} = 4.2^{+9.0}_{-4.0} \times 10^{-10}\,\mathrm{yr}^{-1}\,\mathrm{Mpc}^{-3}$	[6]
	$f_b = 1.9 \pm 0.3 \times 10^{-3}$	[10]
	$f_b = 1.3 \pm 0.4 \times 10^{-2}$	[11]
	$f_b = 9.5 \pm 9.1 \times 10^{-4}$	[12]

Table 1.3: Breakdown of Ic-BL subtypes.

Class	Rate/Fraction	References
Ic-BL SN	$3.6 \pm 1.4 \times 10^{-6}\,\mathrm{yr}^{-1}\,\mathrm{Mpc}^{-3}$	Table 1
Frac. w/ opt. LC like 18gep	$\lesssim 0.1$	[13]
Frac. w/ opt. LC like 06aj	$\lesssim 0.2$	[14]
Frac. w/ strong late radio emission	≈ 0.2	[15]
Frac. w/ radio LC like 98bw	$\lesssim 0.14$	[15]

[1] Li et al. (2011), [2] Kelly and Kirshner (2012), [3] Shivvers et al. (2016), [4] Soderberg et al. (2006b), [5] Liang et al. (2007), [6] Lien et al. (2014), [7] Nakar et al. (2006), [8] Fong et al. (2015), [9] Abbott et al. (2017), [10] Frail et al. (2001), [11] Guetta et al. (2005), [12] Wang et al. (2018), [13] Ho et al. (2019d), [14] Ho et al. (2020e), [15] Corsi et al. (2016)

Second, the jet must successfully escape the star without being choked by the stellar envelope (Mészáros and Waxman, 2001). In this case, the jet energy may be transferred into a shock wave that propagates through the star and breaks out at the surface.

It is possible that dirty fireballs and choked jets have already been observed. In the local universe, a distinct population of "low-luminosity" GRBs (LLGRBs) have been identified[2], sometimes referred to as sub-energetic GRBs (Margutti et al., 2014). LLGRBs are distinguished by isotropic peak luminosities $L_{\rm iso} \approx 10^{46}$–$10^{48}\,{\rm erg\,s^{-1}}$, substantially lower than the values for cosmological GRBs ($L_{\rm iso} > 10^{49.5}\,{\rm erg\,s^{-1}}$), and a relativistic energy release that is 2-3 orders of magnitude smaller than the 10^{51} erg from GRBs with fully relativistic outflows.

Due to their lower intrinsic luminosities, LLGRBs are only discovered at low redshifts ($z \lesssim 0.1$). Thus, despite the fact that they might be 10–100 times more common than classical GRBs (Table 1.1) only seven have been discovered to date. The first LLGRB established the GRB-SN association: LLGRB 980425 and SN 1998bw at $d = 40\,{\rm Mpc}$ (Galama et al., 1998; Kulkarni et al., 1998). The second event, XRT 020903 (Bersier et al., 2006; Sakamoto et al., 2004; Soderberg et al., 2004a). The third event, LLGRB 031203/SN 2003lw (Malesani et al., 2004; Soderberg et al., 2004b; Thomsen et al., 2004; Watson et al., 2004), was discovered at $z = 0.1$ and like the other members of its class had a simple smooth gamma-ray light curve. LLGRB 060218/SN 2006aj (Mirabal et al., 2006; Pian et al., 2006; Soderberg et al., 2006a), and LLGRB 100316D/SN 2010bh (Bufano et al., 2012; Starling et al., 2011) have properties that set them apart as their own class: a long γ-ray prompt emission phase, and long-lived soft X-ray emission that might arise from continued activity of the central engine (Margutti et al., 2013; Soderberg et al., 2006a) or dust echoes (Irwin and Chevalier, 2016; Margutti et al., 2015). More recently, GRB 171205A/SN 2017iuk (D'Elia et al., 2018; Wang et al., 2018) was argued to be cocoon emission from an off-axis jet (Izzo et al., 2019) or relativistic shock breakout into dense CSM (Suzuki et al., 2019). The most recent LLGRB was LLGRB 190829A (Chand et al., 2020).

Modeling of the radio emission from LLGRBs suggests quasi-spherical ejecta coupled to mildly relativistic material, with no off-axis components. Thus, it seems that LLGRBs arise from a fundamentally different mechanism from cosmological

[2]In fact, of the thirteen nearby GRBs with a spectroscopically confirmed Ic-BL SN, half were LLGRBs.

GRBs. One suggestion is that they represent failed or choked-jet scenarios, and that the gamma rays arise from shock breakout (Bromberg et al., 2011). This is supported by the early light curve of 060218, which shows a double peak modeled as shock breakout into a dense stellar wind (Campana et al., 2006) or into an extended envelope (Margutti et al., 2015; Nakar, 2015). However, work I assisted with during my thesis suggests that observed CSM densities would be insufficient to choke an ordinary high-power GRB jet (Duffell and Ho, 2019)—perhaps instead LLGRBs are dirty fireballs, with lower-power, wider-angle jets than their "clean" counterparts.

The Ic-BL SN View

Type Ic-BL SNe are a subclass of stripped-envelope core-collapse supernovae (CC SNe) characterized by fast ejecta and large kinetic energies. While typical Type Ic SNe have photospheric velocities $v_{\rm ph} \approx 10,000\,{\rm km\,s^{-1}}$ (measured from Fe II absorption features), Type Ic-BL SNe have $v_{\rm ph} \approx 20,000\,{\rm km\,s^{-1}}$ at maximum light (Modjaz et al., 2016), resulting in very broad absorption features (see Figure 1.3). The kinetic energy release of Ic-BL SNe is typically $\sim 10^{52}$ erg (Cano, 2013; Lyman et al., 2016; Prentice et al., 2016), an order of magnitude greater than traditional CC SNe (Woosley and Janka, 2005), although this measurement is highly model-dependent.

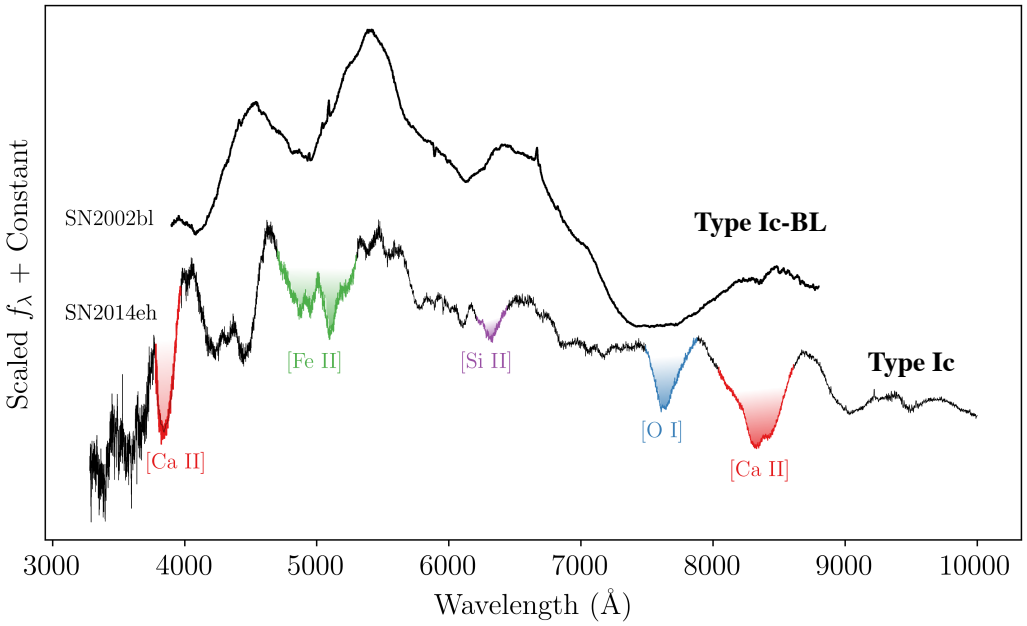

Figure 1.3: Example spectra of Type Ic and Type Ic-BL SNe near peak light. Spectra obtained from the UC Berkeley Supernova Database (Silverman et al., 2012)

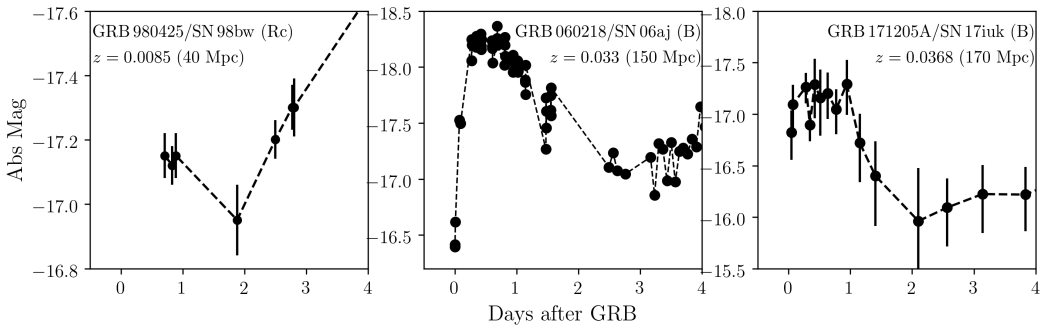

Figure 1.4: Early light curves of Ic-BL SNe with high-cadence optical observations, which in the past were most commonly obtained for events associated with GRBs.

Only $\sim$ 100 Ic-BL SNe have been classified to date, and most lack detailed observations. From well-studied events, it is clear that Ic-BL SNe are a diverse class, which I helped to elucidate in my thesis work and which I tentatively group into several subtypes (Table 1.3). Most Ic-BL SNe appear "ordinary": their optical light curves are modeled as the radioactive decay of ^{56}Ni (Taddia et al., 2019) and they lack detected radio emission (Corsi et al., 2016). However, two events show fast, luminous, and blue light curves that likely arise from shock breakout into extended CSM (Ho et al., 2019d; Whitesides et al., 2017). A subset of events have double-peaked optical light curves, and radio and X-ray emission (Ho et al., 2020e), including the Ic-BL SNe associated with LLGRBs (Figure 1.4). Some show late-rising radio and X-ray emission from circumstellar interaction (Corsi et al., 2014; Salas et al., 2013; Soderberg et al., 2005, 2006c). Finally, only a small number show evidence for relativistic ejecta.

In general, the explanation for the fast velocities and high kinetic energies in Ic-BL SNe is unknown. Due to the connection between Ic-BL SNe and GRBs (Cano et al., 2017b; Hjorth et al., 2012; Woosley and Bloom, 2006) it has been suggested and borne out in simulations (Barnes et al., 2018; Sobacchi et al., 2017) that the mechanism that produces the GRB can also produce the Ic-BL SN. However, it is not clear whether this mechanism is at work in all or just a subset of Ic-BL SNe.

Radio Unification Efforts

A major focus of scientific investigation over the past 20 years has been to unify the diverse array of phenomena laid out in the previous sections: "extreme" supernovae with successful, observed jets, mildly relativistic explosions, and ordinary (non-relativistic) supernovae. Searching for relativistic explosions via the detection of a

GRB is severely limited: dirty fireballs, choked jets, and orphan afterglows will not produce a classical high-luminosity GRB.

Prior to my thesis, the landscape of relativistic stellar explosions was explored primarily at radio wavelengths. Radio surveys uncovered events with relativistic outflows and no detected GRB, starting with SN 2009bb (Soderberg et al., 2010) at $d \approx 40$ Mpc, which had a minimum energy of 10^{49} erg coupled to relativistic ejecta. From radio observations a picture has emerged of a fixed energy budget 10^{52} erg with varying amounts of energy coupled to relativistic ejecta. Recently there has also been a promising candidate for an off-axis afterglow (Law et al., 2018).

Today, radio follow-up efforts are limited by sensitivity, and the classification rate of Ic-BL SNe has plateaued. With the commissioning of wide-field high-cadence optical surveys such as the Zwicky Transient Facility (ZTF), large fractions of the sky are being monitored at optical wavelengths on nightly or faster cadences, enabling the first systematic *optical* exploration of the landscape of relativistic stellar explosions, expected to manifest themselves as fast and luminous optical transients.

1.2 Summary of Thesis

Prior to my thesis, optical surveys demonstrated that they could discover afterglow emission without relying on a GRB trigger: iPTF14yb (Cenko et al., 2015) and ATLAS 17aeu (Bhalerao et al., 2017; Stalder et al., 2017) turned out to be afterglows to regular long GRBs[3]. PTF11agg had no detected GRB counterpart, and its nature remains uncertain because its redshift is unknown.

For my thesis, I expanded on these discoveries by conducting a search for fast-rising and luminous optical transients, summarized in Figure 1.5.

Part I of my thesis concerns cosmological afterglows. Using the ZTF high-cadence (1600 deg^2, 6×/night) and one-day cadence (3000 deg^2, 1×/night in each of g and r) surveys I found two cosmological afterglows, one of which had no detected GRB (Ho et al., 2020f) and one of which had a bright *Fermi*/LAT-associated GRB (Yao et al. in prep). Via rate estimates, I showed that the rate of afterglow-like events is not significantly higher than the rate of classical GRBs (Ho et al., 2020f), in agreement with previous results from optical (Cenko et al., 2015; Ho et al., 2018c) and X-ray (Nakar and Piran, 2003) surveys. So, if dirty fireballs exist, they are either rare or

[3]The association for ATLAS 17aeu is not fully secure because the redshift of the afterglow was not measured.

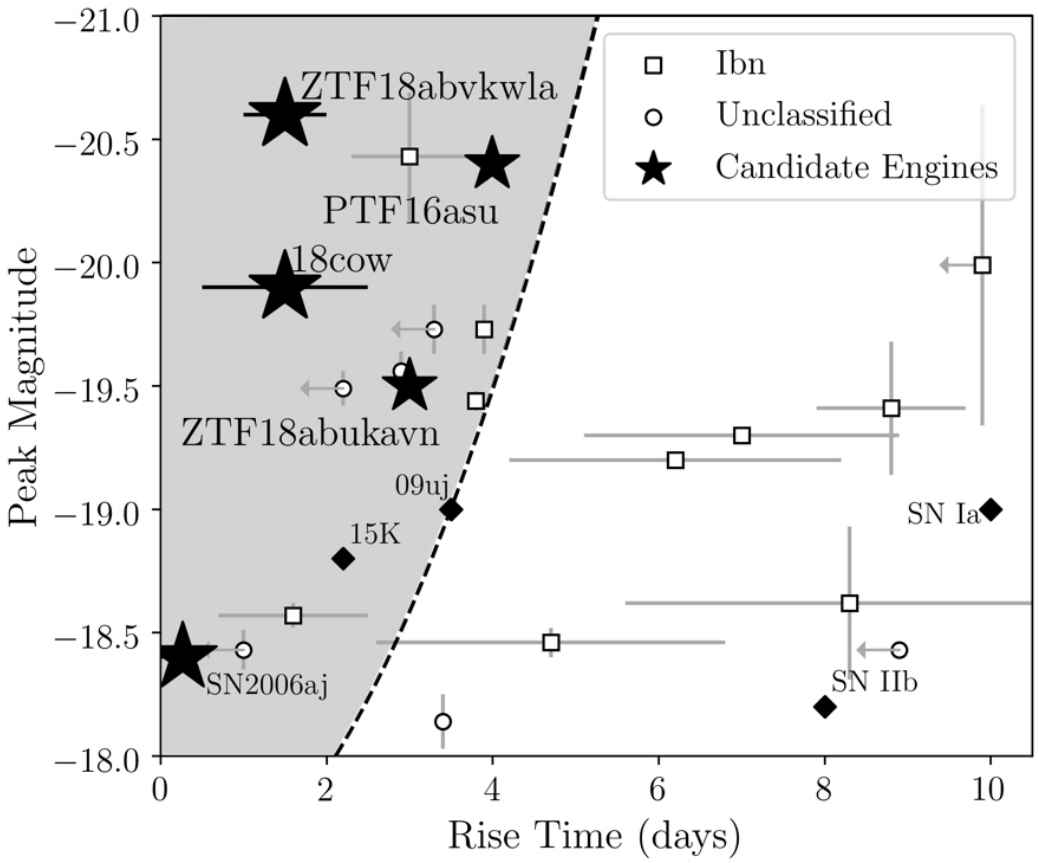

Figure 1.5: The phase-space of fast-rising and luminous transients. A significant number of the fastest and most luminous transients have turned out to be engine-driven stellar explosions, perhaps due to their fast shock velocity.

look significantly different from classical GRB afterglows; perhaps they result in wider-angle, lower-power outflows like LLGRBs.

Part II of my thesis concerns LLGRBs. LLGRBs seem to be accompanied by double-peaked Ic-BL SNe (Figure 1.4), but since high-cadence optical data was more commonly obtained for GRB-SNe, it was unclear whether this was a selection effect. Using the ZTF high-cadence survey I discovered the first optically identified double-peaked Ic-BL SN, and showed that it has radio and X-ray emission similar to LLGRB 060218/SN 2006aj (Ho et al., 2020e). I also showed that most Ic-BL SNe with high-cadence data do *not* have early peaks as luminous as that in SN 2006aj. The intriguing implication is that a double-peaked optical light curve is somehow related to the mechanism that produces the LLGRB.

Part III of my thesis concerns Ic-BL SNe more broadly. With systematic radio follow-up observations, I found one Ic-BL SN with radio emission similar to LLGRBs (Ho

et al., 2020c). I corroborated previous results showing that radio emission like SN 1998bw is rare, and that at least some Ic-BL SNe do not appear to produce a classical GRB in any direction. I delineated a class of Ic-BL SNe in dense circumstellar material (Ho et al., 2019d) and showed that CSM is an important yet neglected complication in the quest for GRB-SN unification (Duffell and Ho, 2019).

Finally, after my candidacy exam in May 2017 my thesis committee warned me that all would probably not go as planned, and that I should remain open to new avenues as they arise. Part IV of my thesis describes one such avenue: a new class of engine-driven stellar explosions (Ho et al., 2019c, 2020d), the prototype of which was AT2018cow. Together, LLGRBs and AT2018cow-like explosions are two classes of energetic explosions shocking a dense medium that at early times are most readily observed at millimeter wavelengths; these systems are a prime target for millimeter observatories such as ALMA. (Ho et al., 2019c). The presence of dense and confined circumstellar material in Ic-BL SNe and AT2018cow-like events suggests that late-stage eruptive mass-loss may be present in a greater variety of massive stars than had been previously thought.

To conclude the summary, I provide a map of a tentative GRB-SN unification scheme in Figure 1.6 and list major open questions in the field.

- What are the local rates of classical GRBs, LLGRBs, and Ic-BL SNe?
- What powers LLGRBs?
- Why do some Ic-BL SNe produce GRBs and others LLGRBs?
- What is the origin of the dense confined CSM in AT2018cow-like events and LLGRB-SNe?
- How prevalent is late-stage eruptive mass-loss in massive stars?
- If dirty fireballs are common, why don't they look like classical GRB afterglows?
- If dirty fireballs are rare, why is a "clean" jet intrinsic to phenomenon? Are LLGRBs dirty fireballs?

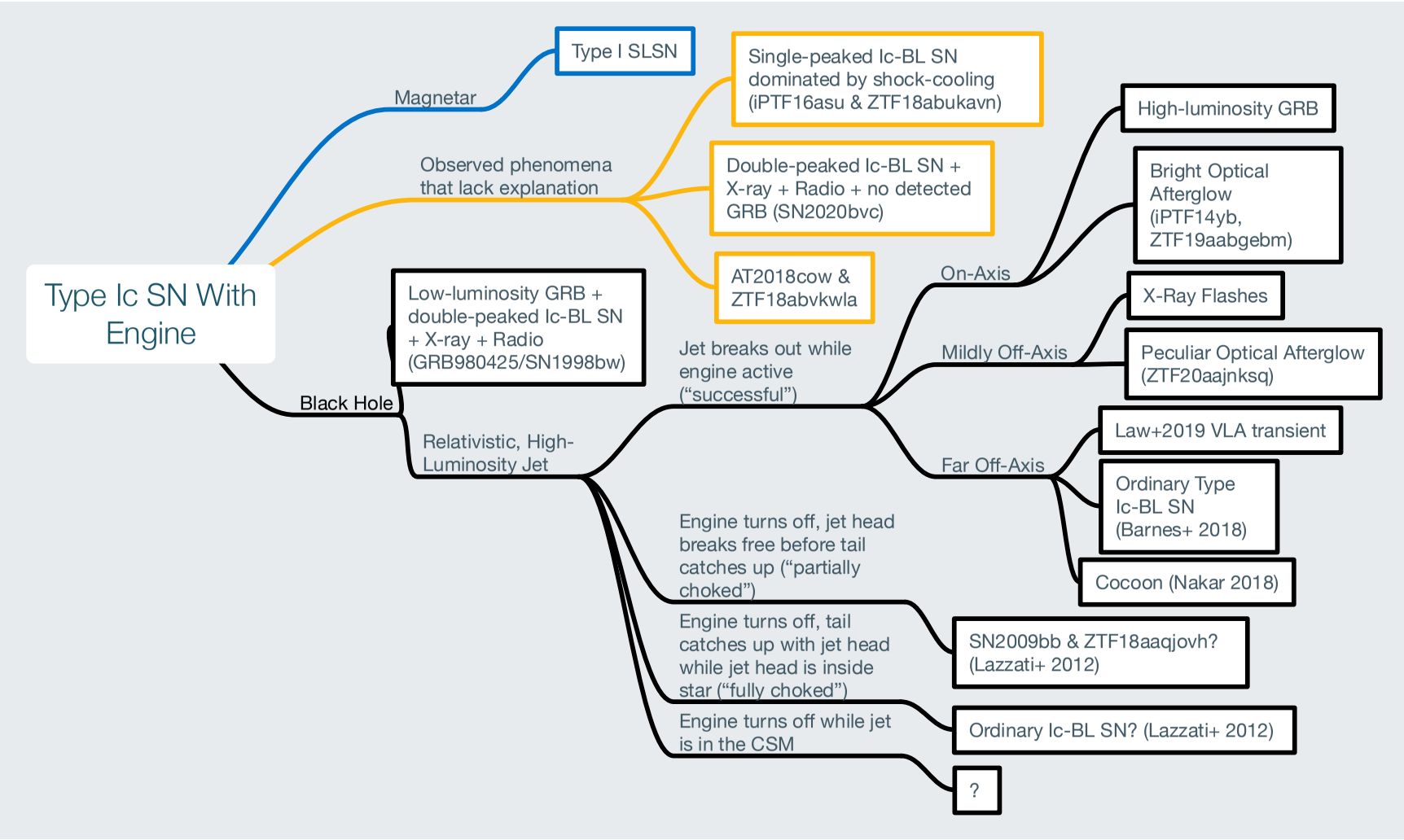

Figure 1.6: Status of GRB-SN unification efforts at the conclusion of my thesis.

Part I. Afterglows at Cosmological Distances

Your mission, should you choose/decide to accept it, is the search for dirty fireballs. *http://adsabs.harvard.edu/abs/2013ApJ...769..130C As always, should you or any of your colleagues be found making a mistake, the Secretary will disavow any knowledge of your actions. This email will self-destruct in five seconds.*

Good luck

The Secretary

—SHRI KULKARNI, 18 APRIL 2016

Chapter 2

ZTF20AAJNKSQ (AT 2020BLT): A FAST OPTICAL TRANSIENT AT $z \approx 2.9$ WITH NO DETECTED GAMMA-RAY BURST COUNTERPART

Ho, A. Y. Q. et al. (2020). "ZTF20aajnksq (AT2020blt): A Fast Optical Transient at $z \approx 2.9$ With No Detected Gamma-Ray Burst Counterpart". In: *ApJ, submitted*. arXiv: 2006.10761 [astro-ph.HE].

Anna Y. Q. Ho[1], Daniel A. Perley[2], Paz Beniamini[1], S. Bradley Cenko[3,4], S. R. Kulkarni[1], Igor Andreoni[1], Leo P. Singer[3], Mansi M. Kasliwal[1], Christoffer Fremling[1], Eric C. Bellm[5], Richard Dekany[6], Alexandre Delacroix[6], Dmitry A. Duev[1], Daniel A. Goldstein[1], V. Zach Golkhou[5,7], Ariel Goobar[8], David Hale[6], Thomas Kupfer[9], Russ R. Laher[10], Frank J. Masci[10], A. A. Miller[11,12], James D. Neill[1], Reed Riddle[6], Ben Rusholme[10], David L. Shupe[10], Roger Smith[6], Jesper Sollerman[13], Jan van Roestel[1]

[1]Cahill Center for Astronomy and Astrophysics, California Institute of Technology, Pasadena, CA 91125, USA
[2]Astrophysics Research Institute, Liverpool John Moores University, IC2, Liverpool Science Park, 146 Browlow Hill, Liverpool L3 5RF, UK
[3]Astrophysics Science Division, NASA Goddard Space Flight Center, Mail Code 661, Greenbelt, MD 20771, USA
[4]Joint Space-Science Institute, University of Maryland, College Park, MD 20742, USA
[5]DIRAC Institute, Department of Astronomy, University of Washington, 3910 15th Avenue NE, Seattle, WA 98195, USA
[6]Caltech Optical Observatories, California Institute of Technology, Pasadena, CA 91125
[7]The eScience Institute, University of Washington, Seattle, WA 98195, USA
[8]The Oskar Klein Centre & Department of Physics, Stockholm University, AlbaNova, SE-106 91 Stockholm, Sweden
[9]Kavli Institute for Theoretical Physics, University of California, Santa Barbara, CA 93106, USA
[10]IPAC, California Institute of Technology, 1200 E. California Blvd, Pasadena, CA 91125, USA
[11]Center for Interdisciplinary Exploration and Research in Astrophysics (CIERA) and Department of Physics and Astronomy, Northwestern University, 1800 Sherman Road, Evanston, IL 60201, USA
[12]The Adler Planetarium, Chicago, IL 60605, USA
[13]The Oskar Klein Centre & Department of Astronomy, Stockholm University, AlbaNova, SE-106 91 Stockholm, Sweden

Abstract

We present ZTF20aajnksq (AT 2020blt), a fast-fading ($\Delta r = 2.4$ mag in $\Delta t = 1.3$ d) red ($g - r \approx 0.6$ mag) and luminous ($M_{1626} = -25.9$ mag) optical transient at

$z = 2.9$ discovered by the Zwicky Transient Facility (ZTF). AT 2020blt shares several features in common with afterglows to long-duration gamma-ray bursts (GRBs): (1) an optical light curve well-described by a broken power-law with a break at $t_j = 1$ d (observer-frame); (2) a luminous ($L_X = 10^{46}\,\mathrm{erg\,s^{-1}}$) X-ray counterpart; and (3) luminous ($L_\nu = 4 \times 10^{31}\,\mathrm{erg\,s^{-1}\,Hz^{-1}}$ at 10 GHz) radio emission. However, no GRB was detected in the 0.74 d between the last ZTF non-detection ($r > 20.64$) and the first ZTF detection ($r = 19.57$), with an upper limit on the isotropic-equivalent gamma-ray energy release of $E_{\gamma,\mathrm{iso}} < 7 \times 10^{52}$ erg. AT 2020blt is thus the third afterglow-like transient discovered without a detected GRB counterpart (after PTF11agg and ZTF19abvizsw) and the second (after ZTF19abvizsw) with a redshift measurement. We conclude that the properties of AT 2020blt are consistent with a classical (initial Lorentz factor $\Gamma_0 \gtrsim 100$) on-axis GRB that was missed by high-energy satellites. Furthermore, by estimating the rate of transients with light curves similar to that of AT 2020blt in ZTF high-cadence data, we agree with previous results that there is no evidence for an afterglow-like phenomenon that is significantly more common than classical GRBs. We conclude by discussing the status and future of fast-transient searches in wide-field high-cadence optical surveys.

2.1 Introduction

Over the past half-century, thousands of long-duration gamma-ray bursts (GRBs; Kouveliotou et al. 2012; Mészáros 2006; Piran 2004; Zhang and Mészáros 2004) have been discovered by high-energy satellites. In the traditional GRB model, a collapsing massive star launches a collimated (opening angle $\theta_0 \approx 10^\circ$) and ultra-relativistic (initial Lorentz factor $\Gamma_0 \gg 100$) outflow (MacFadyen et al., 2001) that tunnels through the stellar material and collides with the ambient medium, producing an "afterglow" across the electromagnetic spectrum (Panaitescu and Kumar, 2002; van Paradijs et al., 2000).

Through follow-up observations of well-localized GRB triggers, hundreds of optical afterglows have been detected[1]. There are several reasons why optical surveys should also detect "orphan" afterglows, i.e., optical afterglows without associated GRBs. First, for an outflow with Lorentz factor Γ, relativistic beaming precludes the observer from seeing emission outside a cone of width $\theta = 1/\Gamma$. The outflow decelerates between the time of the GRB detection and the time of the optical afterglow detection, so the optical afterglow should be visible over a wider observing

[1] An up-to-date list is maintained at `http://www.mpe.mpg.de/\~jcg/grbgen.html`

angle than the GRB (Mészáros et al., 1998; Rhoads, 1997). Second, an outflow must entrain very little mass ($M_{\rm ej} \approx 10^{-5}\,M_{\odot}$) to produce a GRB. If GRBs represent the extreme of a continuum of baryon-loading in relativistic jets, then "dirty fireballs" should exist, which would produce an afterglow but not a GRB (Dermer et al., 1999).

To discover orphan afterglows and dirty fireballs, surveys must be able to find afterglows without relying on a GRB trigger. Independently discovering optical afterglow emission is challenging because of the need for high-cadence observations over a wide field-of-view, as well as rapid follow-up. Furthermore, there is a formidable fog of more common fast-fading transients like stellar flares (Berger et al., 2013; Ho et al., 2018c; Kulkarni and Rau, 2006; Rau et al., 2008; van Roestel et al., 2019). Of the three optically discovered afterglows in the literature, two turned out to have associated classical GRBs: iPTF14yb (Cenko et al., 2015) was the counterpart to GRB 140226A, and ATLAS17aeu (Bhalerao et al., 2017; Stalder et al., 2017) was likely the counterpart to GRB 170105A.[2]

The first optically discovered afterglow, PTF11agg (Cenko et al., 2013), had no detected GRB counterpart. The redshift was constrained to be $1 < z < 2$, and Cenko et al. (2013) argued that it could represent the first dirty fireball. It has since become clear that the rate of such events is not significantly higher than the rate of classical GRBs (Cenko et al., 2015; Ho et al., 2018c); the same conclusion was reached by Nakar and Piran (2003) based on X-ray afterglows. So, if dirty fireballs exist, they are either rare or look significantly different from classical GRB afterglows.

Making the discovery of optical afterglows *routine* is one of the primary scientific goals of the Zwicky Transient Facility (ZTF; Bellm et al. 2019b; Graham et al. 2019) high-cadence surveys (Bellm et al., 2019a). To that end, we have devised a set of filters for identifying afterglow emission in real-time, and obtaining prompt follow-up observations to measure the redshift and any accompanying X-ray and radio emission. Here we describe the first afterglow detected as part of this effort, ZTF20aajnksq (AT 2020blt) at $z \approx 2.9$. Since then, we discovered a second afterglow: ZTF20abbiixp (AT 2020kym; Ho et al. 2020b) turned out to be the afterglow to Fermi/LAT GRB 200524A (Yao et al in prep). In September 2019, ZTF also serendipitously discovered a cosmological afterglow (ZTF19abvizsw at $z = 1.26$; Burdge et al. 2019a; Ho et al. 2019a) in follow-up observations of gravitional-wave trigger S190901ap (Perley et al. in prep). Finally, ZTF detected the afterglow

[2]The association is not fully secure, because the redshift of the afterglow was not measured.

to GRB 190106A as ZTF19aabgebm; the detection was in low-cadence data and therefore the transient did not pass the fast-transient filter.

This paper is organized as follows. In §2.2 we present the discovery and follow-up observations of AT 2020blt. In §2.3 we model the outflow using the light curve and the spectral energy distribution (SED). We discuss possible interpretations in §2.4, and conclude that we cannot rule out the possibility that AT 2020blt was a classical GRB missed by high-energy detectors. We summarize and look to the future in §2.5.

2.2 Observations

ZTF Discovery

The ZTF Uniform Depth Survey (Goldstein et al. in prep) covers 2000 deg^2 twice per night in g-, r-, and i-band using the 48-inch Samuel Oschin Schmidt telescope at Palomar Observatory (P48). The ZTF observing system is described in Dekany et al. (2020). The pipeline for ZTF photometry makes use of the image subtraction algorithm of Zackay et al. (2016) and is described in Masci et al. (2019).

AT 2020blt was discovered at $r = 19.57 \pm 0.14$ mag (all magnitudes given in AB) in an image obtained on 2020 Jan 28.28[3], at the position $\alpha = 12^{\mathrm{h}}47^{\mathrm{m}}04.87^{\mathrm{s}}$, $\delta = +45^{\mathrm{d}}12^{\mathrm{m}}02.3^{\mathrm{s}}$ (J2000). One and a half hours later, the source had faded to $r = 20.01 \pm 0.16$ mag.

AT 2020blt passed a filter that searches the ZTF alert stream (Patterson et al., 2019) for young and fast transients. More specifically, the filter identifies transients that:

- have an upper limit from the previous night that is at least one magnitude fainter than the first detection,
- have no historical detections in the Catalina Real-Time Transient Survey (Djorgovski et al., 2011; Drake et al., 2009; Mahabal et al., 2011), ZTF, or the predecessor to ZTF the Palomar Transient Factory (Law et al., 2009),
- have a real-bogus score `drb` > 0.9 (Duev et al., 2019),
- have two detections separated by at least half an hour (to remove asteroids), and
- have no stellar counterpart (`sgscore` < 0.76; Tachibana and Miller 2018).

[3] All times in this paper are given in UTC.

AT 2020blt fulfilled the criteria listed above: the last upper limit from the high-cadence survey was 0.74 d prior to the first detection with an upper limit of $r > 20.73$ mag. There is no source within 15″ of the position of AT 2020blt in ZTF r-band and g-band reference images, with a 5-σ limiting magnitude in the PSF-fit reference image catalog of $r = 23.17$ mag and $g = 22.77$ mag.

Motivated by the fast rise and lack of a detected host galaxy counterpart in ZTF reference images (as expected for cosmological GRBs; the median magnitude of the TOUGH sample of 69 *Swift* GRB host galaxies (Hjorth et al., 2012) was $R = 25.52 \pm 0.23$ mag) we immediately triggered a series of follow-up observations (§2.2) which were coordinated through the GROWTH "Marshal" (Kasliwal et al., 2019). All observations will be made available on WISeREP, the Weizmann Interactive Supernova Data Repository (Yaron and Gal-Yam, 2012).

Follow-up Observations

Optical Imaging

In searches for extragalactic fast transients, the primary false positives are stellar flares in the Milky Way (Berger et al., 2013; Ho et al., 2018c; Kulkarni and Rau, 2006; Rau et al., 2008). At optical frequencies, stellar flares can be distinguished from afterglow emission by color. At peak, stellar flares have typical blackbody temperatures of $\sim 10,000$ K (Kowalski et al., 2013), so optical filters will be on the Rayleigh-Jeans tail and colors will obey $f_\nu \propto \nu^{+2}$ ($g - r = -0.17$ mag). By contrast, in optical bands synchrotron emission obeys $f_\nu \propto \nu^{-0.7}$ or steeper (Sari et al., 1998), corresponding to $g - r \gtrsim 0.24$ mag (even without extinction). To measure the color of AT 2020blt, we triggered target-of-opportunity (ToO) programs on the IO:O imager of the Liverpool Telescope[4] (LT; Steele et al. 2004) and with the Spectral Energy Distribution Machine[5] (SEDM; Blagorodnova et al. 2018; Rigault et al. 2019) on the automated 60-inch telescope at Palomar Observatory (P60; Cenko et al. 2006). LT image reduction was provided by the basic IO:O pipeline. P60 and LT image subtraction was performed following Fremling et al. (2016), using PS1 images for $griz$ and SDSS for u-band.

LT $griz$ observations on Jan 29.17 and P60 gri observations 3 hours later confirmed that AT 2020blt had red colors. Furthermore, forced photometry (Yao et al., 2019) on P48 images revealed two g-band detections that were below the 5-σ threshold

[4]PI: D. Perley
[5]PI: A. Ho

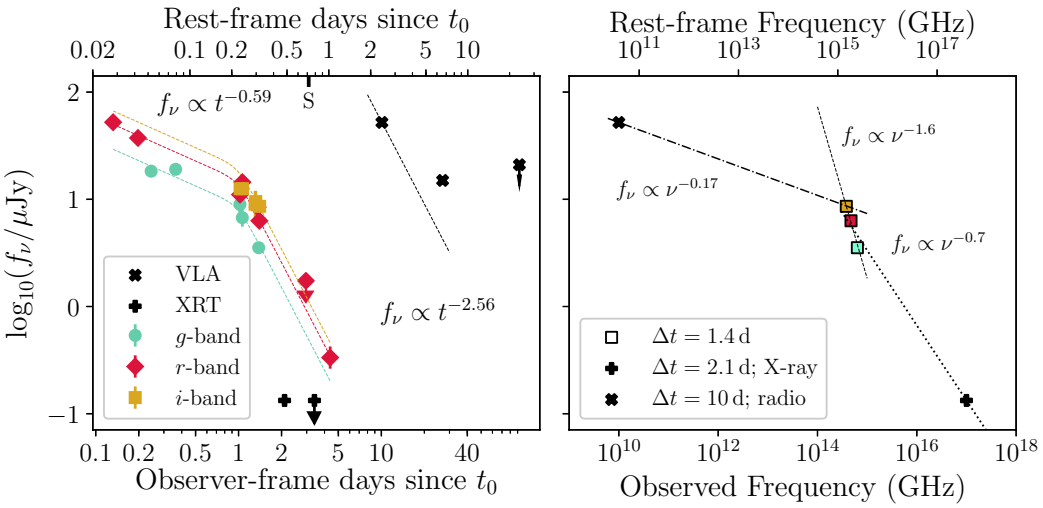

Figure 2.1: Left: The optical (colored points), X-ray (black plus), and radio (black cross) light curves of AT 2020blt, shown in observer-frame days on the bottom x-axis and rest-frame days on the top x-axis. The X-ray and radio upper limits are at 3-σ. The estimated time of first light t_0=Jan 28.15 comes from fitting a broken power-law to the optical light curve (§2.3). The fitted function is shown as dashed lines. For the radio light curve, we show a dotted line with the same temporal index as the post-break optical light curve ($t^{-2.56}$). The 'S' along the top indicates the epoch of our LRIS spectrum. Right: the spectral energy distribution of AT 2020blt.

of the nominal ZTF pipeline, which give $g - r = 0.79 \pm 0.16$ mag. Photometry was corrected for Milky Way extinction following Schlafly and Finkbeiner (2011) with $E(B-V) = A_V/R_V = 0.034$ mag, using $R_V = 3.1$ and a Fitzpatrick (1999) extinction law. The full light curve of AT 2020blt is shown in the left panel of Figure 2.1, and the photometry is listed in Table 2.1.

To monitor the light curve, we triggered a ToO program[6] with the Wafer-Scale Imager for Prime (WaSP) on the 200-inch Hale telescope at the Palomar Observatory (P200) and obtained 2×180 s exposures in each of g-, r-, and i-bands. The WaSP reductions were performed using a pipeline developed for Gattini-IR, described in De et al. (2020). The measurement established a rapid fade rate of 2.5 magnitudes in 1.25 days and confirmed the red colors ($g - r = 0.63 \pm 0.12$ mag).

For a final photometry measurement, we triggered a ToO observation with the Gemini Multi-Object Spectrograph (GMOS; Hook et al. 2004) on the Gemini-North 8-meter telescope on Mauna Kea[7]. In 8×200 s exposures on Feb 01.52,

[6]PI: I. Andreoni
[7]PI: L. Singer; Program ID GN-2019B-Q-130

Table 2.1: Summary of observations of AT 2020blt. Time given relative to t_0 as defined in §2.3. Optical magnitudes have been corrected for Milky Way extinction. P48 values were measured using forced photometry (Yao et al., 2019). X-ray uncertainties are 1-σ and upper limits are 3-σ. Radio upper limits are 3× the image RMS. Uncertainties on radio measurements are given as the quadrature sum of the image RMS and a 5% uncertainty on the flux density due to flux calibration.

Optical Photometry				
Obs. Date	Δt **(days)**	**Instrument**	**Filter**	**Mag**
Jan 28.28	0.15	P48+ZTF	r	19.60 ± 0.08
Jan 28.35	0.18	P48+ZTF	r	19.97 ± 0.08
Jan 28.39	0.19	P48+ZTF	g	20.74 ± 0.14
Jan 28.51	0.31	P48+ZTF	g	20.70 ± 0.13
Jan 29.17	0.97	LT+IO:O	g	21.52 ± 0.21
Jan 29.17	0.97	LT+IO:O	r	21.29 ± 0.18
Jan 29.17	0.97	LT+IO:O	i	21.15 ± 0.25
Jan 29.17	0.97	LT+IO:O	z	20.82 ± 0.40
Jan 29.21	1.01	LT+IO:O	g	21.83 ± 0.21
Jan 29.21	1.01	LT+IO:O	r	21.00 ± 0.16
Jan 29.21	1.01	LT+IO:O	i	21.15 ± 0.27
Jan 29.45	1.25	P48+ZTF	i	21.52 ± 0.32
Jan 29.47	1.27	P48+ZTF	i	21.45 ± 0.25
Jan 29.51	1.31	P48+ZTF	r	21.58 ± 0.26
Jan 29.53	1.33	P200+WaSP	g	22.53 ± 0.10
Jan 29.55	1.35	P200+WaSP	r	21.90 ± 0.07
Jan 29.55	1.35	P200+WaSP	i	21.56 ± 0.05
Feb 01.53	4.33	Gemini-N+GMOS	r	25.09 ± 0.26
Optical Spectrum with LRIS on Keck-I				
Obs. Date	Δt **(days)**	**Observing Setup**		**Exposure Time**
Jan 30.64	2.44	1" slit, 400/3400 grism, 400/8500 grating, D560 dichroic		900 s
0.3–10 keV X-ray Observations with *Swift*/XRT				
Obs. Date	Δt **(days)**	**Count Rate**	**Flux**	
Jan 29.70	2.1	$(3.96^{+1.30}_{-1.08}) \times 10^{-3}$ s^{-1}	$1.33^{+0.44}_{-0.36} \times 10^{-13}$ erg s^{-1} cm^{-2}	
Jan 31.04	3.4	$< 3.95 \times 10^{-3}$ s^{-1}	$< 1.33 \times 10^{-13}$ erg s^{-1} cm^{-2}	
VLA Radio Observations at 10 GHz				
Obs. Date	Δt	**Flux Density**	**Flux at 10 GHz**	
Feb 07.24	9.96	$52.1 \pm 6.5\,\mu$Jy	$(5.21 \pm 0.65) \times 10^{-18}$ erg s^{-1} cm^{-2}	
Feb 23.54	26.34	$< 15\,\mu$Jy	$< 1.5 \times 10^{-18}$ erg s^{-1} cm^{-2}	
Apr 29.98	92.78	$< 21\,\mu$Jy	$< 2.1 \times 10^{-18}$ erg s^{-1} cm^{-2}	

calibrating against PS1 DR1 (Chambers et al., 2016), we detected the source at $r = 25.20 \pm 0.05$ (Singer et al., 2020). Data were reduced using DRAGONS (Data Reduction for Astronomy from Gemini Observatory North and South), a Python-based reduction package provided by the Gemini Observatory. In §2.3 we model the full optical light curve of AT 2020blt and compare it to GRB afterglows in the literature.

Optical Spectroscopy

We triggered ToO observations[8] using the Low Resolution Imaging Spectrometer (LRIS; Oke et al. 1995) on the Keck I 10-m telescope. The observation details are

[8]PI: M. Kasliwal

listed in Table 2.1. The spectrum was reduced with `LPipe` (Perley, 2019) and is shown in Figure 2.2. The spectrum showed features consistent with the Lyman break (rest-frame 912 Å) and Lyman-α absorption (rest-frame 1216 Å) at $z = 2.90^{+0.05}_{-0.04}$ (luminosity distance 25 Gpc[9]), although the S/N is low due to the short exposure time and the fact that the observation started close to morning twilight. The redshift sets the rest-frame UV magnitude at the time of discovery as $M_{1626} = -25.91$ mag, assuming a distance modulus of 46.99 mag and a central wavelength of the ZTF r-band filter of 6340 Å. We searched for narrow lines consistent with $z = 2.9$ with no convincing detections.

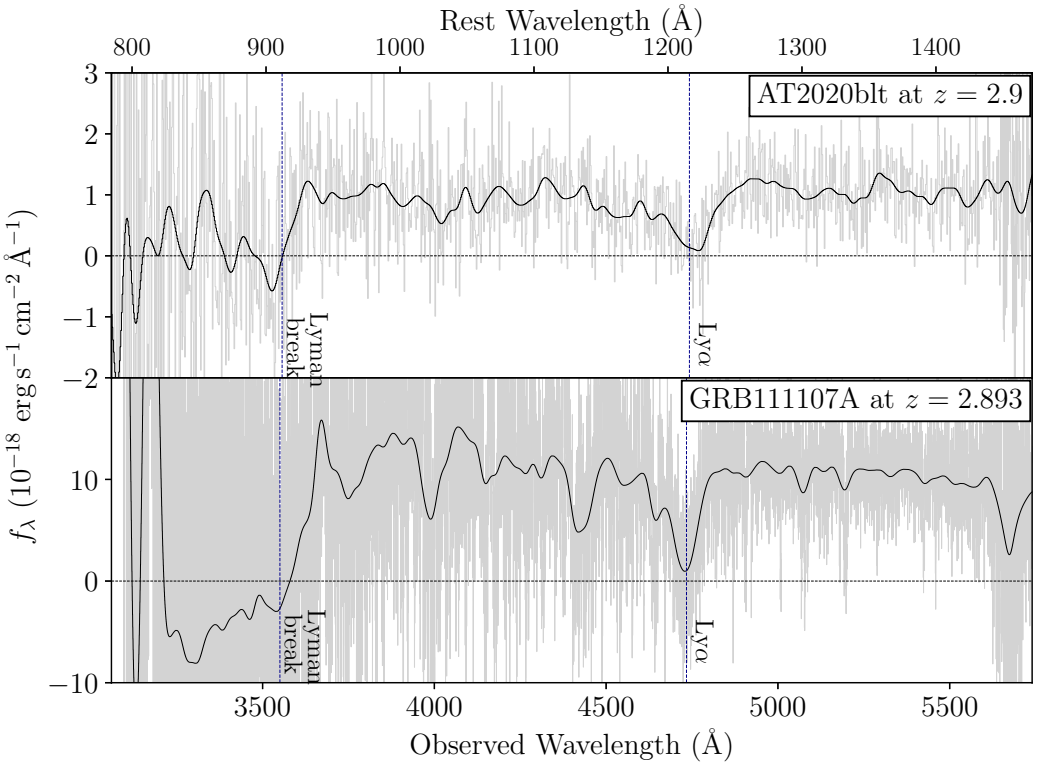

Figure 2.2: Spectrum of AT 2020blt at $\Delta t = 2.4$ d (top panel) with a spectrum of a GRB at a similar redshift in the literature for comparison (bottom panel). The spectrum of AT 2020blt was obtained with the blue arm of LRIS; there was negligible signal in the red arm. The spectrum of GRB 111107A is from Selsing et al. (2019). In each panel, the full spectrum is shown in grey and a smoothed spectrum is overplotted in black. The Lyman-α and Lyman break absorption features are marked with vertical dashed lines. We show $f_\lambda = 0$ with a horizontal dotted line.

[9] ΛCDM cosmology of Planck Collaboration et al. (2016) used throughout.

X-ray Observations

We triggered ToO observations[10] with the X-Ray Telescope (XRT; Burrows et al. 2005) on board the Neil Gehrels *Swift* observatory (Gehrels et al., 2004). We obtained two epochs of 4 ks exposures and reduced the data using the online tool[11] developed by the *Swift* team (Evans et al., 2009). In the first epoch (Jan 29.70; $\Delta t = 2.1$ d) a source was detected at the position of AT 2020blt with a 0.3–10 keV count rate of $(3.96^{+1.30}_{-1.08}) \times 10^{-3}$ s^{-1}. Assuming a neutral hydrogen column density $n_H = 1.69 \times 10^{20}$ cm^{-2} and a photon index $\Gamma = 2$ the unabsorbed flux density is $2.1^{+1.6}_{-1.2} \times 10^{-13}$ erg s^{-1} cm^{-2}. The source was not detected in the second epoch (Jan 31.04; $\Delta t = 3.4$ d) with a 3-σ upper limit of $< 4.57 \times 10^{-3}$ s^{-1}. We used `webpimms`[12] with $\Gamma = 2$ and the same value of n_H from the first observation to convert the upper limit on the count rate to an upper limit on the flux density of $< 1.57 \times 10^{-13}$ erg s^{-1} cm^{-2}. A log of our X-ray observations is provided in Table 2.1, and we model the X-ray to radio SED in §2.3.

Radio Observations

On Feb 03 we triggered our ToO program on the Karl G. Jansky Very Large Array (VLA; Perley et al. 2011) for fast-rising and luminous transients[13]. We obtained an X-band observation on Feb 7.24 ($\Delta t = 9.96$) in C configuration, using 3C286 as the bandpass and flux density calibrator and J1219+4829 as the phase calibrator. We calibrated the data using the automated pipeline available in the Common Astronomy Software Applications (CASA; McMullin et al. 2007), and performed additional flagging manually before imaging. Imaging was performed using the CLEAN algorithm (Högbom, 1974) implemented in CASA. The cell size was 1/10 of the synthesized beamwidth, and the field size was the smallest magic number (10×2^n) larger than the number of cells needed to cover the primary beam. A source was detected at the position of AT 2020blt with a flux density of 47 ± 5 μJy. In the next X-band image (Feb 24; $\Delta t \approx 27$ d) the source was not detected with an RMS of 5 μJy. In the final observation (Apr 29; $\Delta t \approx 92$ d) the source was not detected with an RMS of 7 μJy. A log of our radio observations is provided in Table 2.1. In §2.3 we model the X-ray to radio SED and in §2.3 we put the radio luminosity in the context of GRB afterglows.

[10] PI: A. Ho, Target ID 13197

[11] `https://www.swift.ac.uk/user_objects/`

[12] `https://heasarc.gsfc.nasa.gov/cgi-bin/Tools/w3pimms/w3pimms.pl`

[13] VLA/20A-374; PI: A. Ho

Search for Associated GRB

The third Interplanetary Network (IPN[14]) consists of six spacecraft that provide all-sky full-time monitoring for high-energy bursts. The most sensitive detectors in the IPN are the *Swift* Burst Alert Telescope (BAT; Barthelmy et al. 2005) the *Fermi* Gamma-ray Burst Monitor (GBM; Meegan et al. 2009), and the Konus instrument on the WIND spacecraft (Aptekar et al., 1995).

We searched the *Fermi* GBM Burst Catalog[15], the *Fermi*-GBM Subthreshold Trigger list[16] (with reliability flag not equal to 2), the *Swift* GRB Archive[17], and the Gamma-Ray Coordinates Network archives[18] for an associated GRB between the last ZTF non-detection (Jan 27.54) and the first ZTF detection (Jan 28.28). There were no GRBs coincident with the position and time of AT 2020blt.[19]

The position of AT 2020blt was visible[20] to GBM only 65% of the time: 27% of the time it was occulted by the Earth, and 8% of the time GBM was not observing due to a South Atlantic Anomaly passage. By contrast, Konus-WIND is in interplanetary space, not Earth orbit, and therefore had complete coverage. Konus-WIND found no detection with a 90% confidence upper limit on the peak flux of $1.7 \times 10^{-7}\,\mathrm{erg\,cm^{-2}\,s^{-1}}$ for a typical long-GRB spectrum[21] (Ridnaia et al., 2020). At the distance of AT 2020blt, this corresponds to an upper limit on the isotropic gamma-ray luminosity of $L_{\gamma,\mathrm{iso}} < 1.3 \times 10^{52}\,\mathrm{erg\,s^{-1}}$.

Overall, the IPN detects bursts with a 50–300 keV fluence of 1–3$\times 10^{-6}\,\mathrm{erg\,cm^{-2}}$ at 50% efficiency. Following Cenko et al. (2013) we take $10^{-6}\,\mathrm{erg\,cm^{-2}}$ as a nominal fluence threshold and obtain a limit on the isotropic gamma-ray energy release of $E_{\gamma,\mathrm{iso}} < 7 \times 10^{52}$ erg. We put the limit on $E_{\gamma,\mathrm{iso}}$ in the context of classical GRBs in §2.3.

2.3 Comparison to GRB Afterglows

AT 2020blt shares a number of features in common with classical GRBs in the literature. The redshift is typical of GRBs detected by *Swift* (Gehrels et al., 2009) and the absorption features seen in the spectrum are often seen in afterglows at

[14] `http://ssl.berkeley.edu/ipn3/index.html`

[15] `https://heasarc.gsfc.nasa.gov/W3Browse/fermi/fermigbrst.html`

[16] `https://gcn.gsfc.nasa.gov/fermi\_gbm\_subthresh\_archive.html`

[17] `https://swift.gsfc.nasa.gov/archive/grb\_table/`

[18] `https://gcn.gsfc.nasa.gov/gcn3\_archive.html`

[19] AT 2020blt was originally in the localization map of GRB 200128A because Earth occultation had not been taken into consideration (Hamburg and Fermi-GBM Team, 2020).

[20] Search conducted using `https://github.com/annayqho/HE_Burst_Search`

[21] 20–1500 keV, 2.944 s scale, Band spectrum with $\alpha = 1, \beta = 2.5, E_p = 300$ keV

these distances (Fynbo et al., 2009; Selsing et al., 2019). Given the low S/N of our spectrum we are not able to detect common metal lines at this redshift (e.g. C IV, Si IV) and we do not attempt to use the Ly-α absorption feature to measure the host hydrogen column density.

In Figure 2.3 we compare the X-ray, optical and radio luminosity of AT 2020blt to GRB afterglows (Chandra and Frail, 2012; Nysewander et al., 2009), and show that a classical GRB cannot be ruled out based on the limit from *Konus-Wind* (in general, at cosmological redshifts *Konus-Wind* only detects the brightest GRBs). In the following sections we discuss the optical light curve and SED in more detail.

Optical Light Curve

As shown in Figure 2.1, the light curve of AT 2020blt has a clear break well-described by a broken power law. Optical afterglows with "classical" breaks like this were commonly observed prior to the *Swift* era (Harrison et al., 2001; Klose et al., 2004; Kulkarni et al., 1999; Zeh et al., 2006), so it was a surprise when relatively few such breaks were detected in the X-ray afterglows of *Swift* GRBs (Gehrels et al., 2009). Suggestions for why breaks are rarely detected include that observations do not extend long enough after the burst time (Dai et al., 2008), that the breaks are present in the data but missed in fitting (Curran et al., 2008), that bursts are viewed from a range of viewing angles (Zhang et al., 2015), and that *Swift* GRBs are on average more distant (Gehrels et al., 2009) and less energetic (Kocevski and Butler, 2008). Furthermore, in X-ray as well as optical bands, the search for breaks can be complicated by the presence of flares or rebrightening episodes (e.g. Kann et al. 2010).

To make a direct comparison to afterglows in the literature with breaks (Kann et al., 2010; Wang et al., 2018; Zeh et al., 2006) we fit the light curve using a conventional smooth broken power law, modifying it to take into account the fact that we do not know the burst time t_0:

$$m(t) = -2.5 \log_{10} \Bigg(10^{-0.4 m_c} \left[\frac{(t - t_0)}{t_b}^{\alpha_1 n} + \frac{(t - t_0)}{t_b}^{\alpha_2 n} \right] \Bigg)^{-1/n} . \tag{2.1}$$

In Equation 2.1, $m(t)$ is the apparent magnitude as a function of time, n parameterizes the smoothness of the break (where $n = \infty$ is a sharp break), α_1 is the power-law

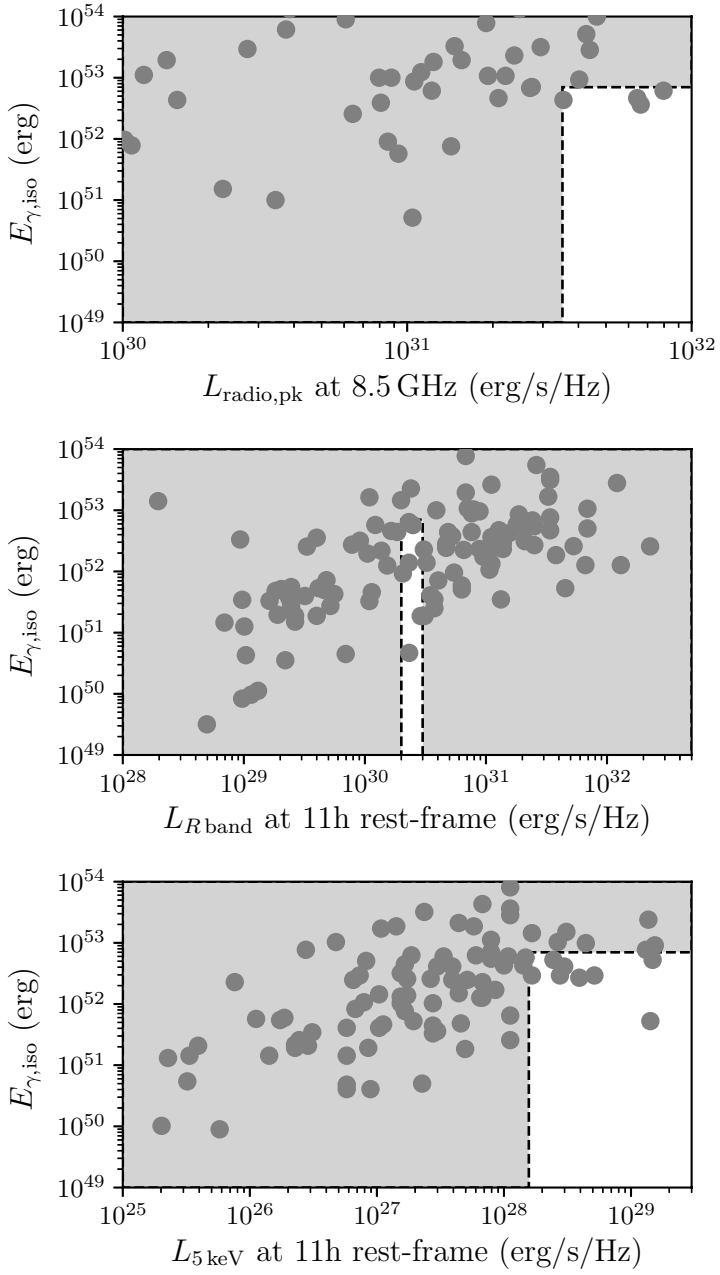

Figure 2.3: Optical, X-ray, and radio afterglow luminosity of classical GRB afterglows in the literature, compared to the isotropic gamma-ray energy release $E_{\gamma,\mathrm{iso}}$ (grey circles). The optical and X-ray afterglow values were taken from Figure 5 and Figure 6 of Nysewander et al. (2009), and the radio afterglow values were taken from Figure 20 of Chandra and Frail (2012). The region shaded in grey indicates the phase-space ruled out for AT 2020blt based on an upper limit on $E_{\gamma,\mathrm{iso}}$ from *Konus-Wind*. We cannot rule out the possibility that AT 2020blt was a classical GRB afterglow missed by high-energy detectors.

index before the break, α_2 is the power-law index after the break, t_b is the time of the break, and m_c is the magnitude at the time of the break assuming $n = \infty$. Note that the original equation also includes terms for the underlying supernova and the host galaxy, which we take to be zero—a reasonable assumption given that we do not observe any flattening in the optical light curve.

First we fit Equation 2.1 to the r-band light curve, because it has the most extensive temporal coverage and we cannot necessarily assume constant colors across the optical light curve. Using the Levenberg-Marquardt algorithm implemented in `scipy` we find $m_c = 20.99 \pm 5.01$, $t_0 = 2458876.69 \pm 0.42$, $t_b = 1.00 \pm 1.84$ d, $\alpha_1 = 0.52 \pm 2.81$, $\alpha_2 = 2.59 \pm 0.26$, and a smoothing parameter that is very poorly constrained (large error bars). The fit has a reduced $\chi^2/\nu = 3.6/\nu$ where $\nu = 1$ is the number of degrees of freedom (number of data points minus number of fitted parameters).

In §2.2 we show that constant colors are a reasonable assumption at optical frequencies. So, to obtain more precise parameters we fit Equation 2.1 to the g-, r-, and i-band light curves simultaneously, assuming constant $g - r$ and $r - i$ offsets. The result is $m_c = 20.95 \pm 0.84$, $t_0 = 2458876.65 \pm 0.18$, $t_b = 1.00 \pm 0.43$ d, $\alpha_1 = 0.59 \pm 0.68$, and $\alpha_2 = 2.56 \pm 0.28$ (the smoothing parameter is still poorly constrained; $n = 5.54 \pm 14.2$). Note that we cannot assume a single spectral index across the optical band because the g-band flux is attenuated by the Ly-α absorption feature and the Lyman forest. The fit has a reduced $\chi^2/\nu = 11.8/\nu = 1.32$ where $\nu = 9$ is the number of degrees of freedom. Throughout the paper, we use the parameters resulting from the multi-band fit, which results in a best-fit light curve shown in the left panel of Figure 2.1.

The best-fit t_0 is Jan 28.15 ± 0.18, 3.1 hours before the first detection and 14.6 hours after the last non-detection. The best-fit $t_j = 1.00 \pm 0.43$ d after t_0 (observer-frame) is typical of optical afterglows with breaks (e.g. Kann et al. 2010; Wang et al. 2018; Zeh et al. 2006). In Figure 2.4 we show the resulting value of $\Delta\alpha = 1.97 \pm 0.74$ compared to the distribution in Zeh et al. (2006) and Kann et al. (2010). The value of $\Delta\alpha$ appears to be large compared to afterglows in the literature, but given the uncertainties we cannot conclude that it is truly unusual.

The origin of breaks in afterglow light curves is still debated. A leading hypothesis is that a break results from a collimated jet (Rhoads, 1997; Sari et al., 1999). The traditional argument is that while $\Gamma(t) \gg \theta^{-1}$, the emission cannot be distinguished from an isotropic outflow, because relativistic beaming confines the viewing angle to

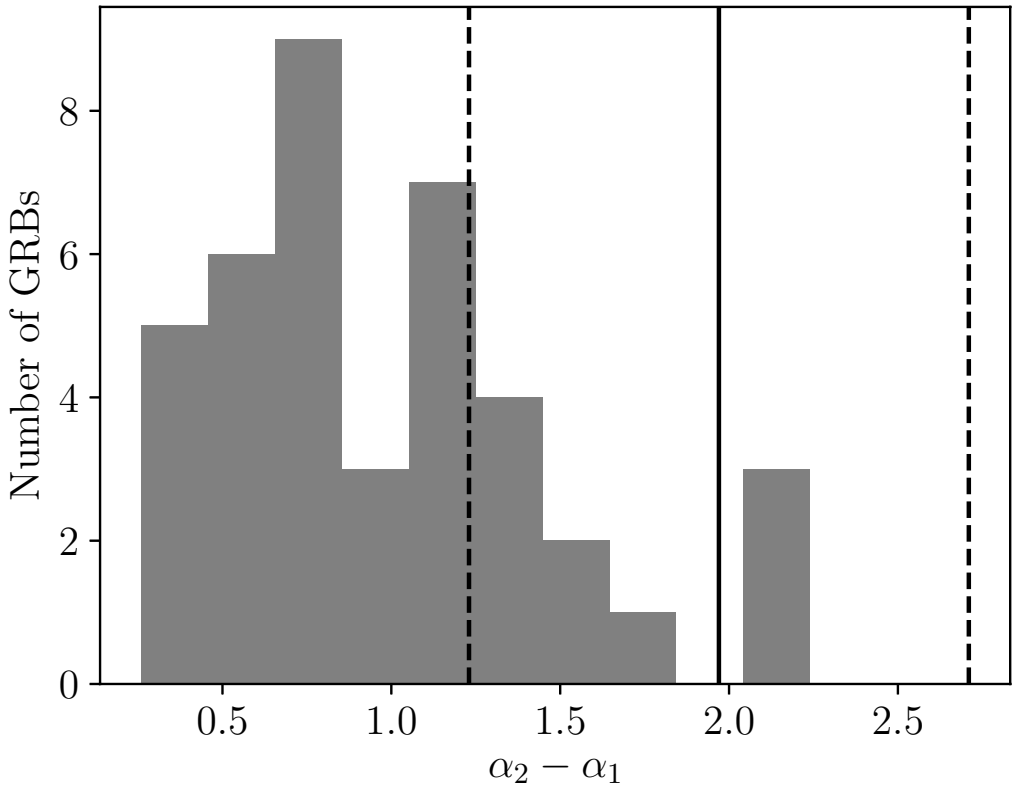

Figure 2.4: The difference between the post-break and pre-break temporal index, compared to a sample of GRBs with jet breaks from the literature (Kann et al., 2010; Zeh et al., 2006). The solid vertical line is the best-fit value of $\alpha_2 - \alpha_1$ from §2.3. The dashed vertical lines represent the error bars on the best-fit value.

a small region that is expanding too quickly to interact sideways. As $\Gamma(t)$ decreases to $\Gamma(t) \sim \theta^{-1}$, two effects become important: the jet begins expanding sideways (Rhoads, 1997), and the edge of the jet becomes visible (Mészáros and Rees, 1999). However, "textbook" achromatic breaks are rarely observed, and simulations suggest that breaks can be chromatic (van Eerten et al., 2011) and that sideways expansion can take place significantly later than when the edge of the jet becomes visible (Granot and Piran, 2012; Panaitescu et al., 1998).

If the break in the light curve of AT 2020blt is a jet break—and we caution that it is rare to see breaks that actually behave in the way one would expect for jet breaks, e.g. Liang et al. (2008)—we can use the timing of the break to estimate the opening angle of the jet θ_0. For a constant-density ISM we have from Sari et al. (1999) that

$$t_{\rm jet} \approx 6.2 (E_{52}/n_1)^{1/3} (\theta_0/0.1)^{8/3} \,{\rm hr}, \tag{2.2}$$

where E_{52} is the kinetic energy release of the explosion in units of 10^{52} erg, θ_0 is in radians, and n_1 is the ambient density in units $1\,\mathrm{cm}^{-3}$. Using our rest-frame value $t_{\rm jet} = 0.26 \pm 0.11$ d (6.24 ± 2.64 hr) we have

$$1.0 \pm 0.4 = (E_{52}/n_1)^{1/3} (\theta_0/0.1)^{8/3}\,\mathrm{hr}. \tag{2.3}$$

We do not have an independent constraint on E_{52} and n_1, but the E_{52}/n_1 term has a much weaker dependence than the opening angle term. Taking (E_{52}/n_1) to be unity, we find an opening angle of $\theta_0 = 0.10 \pm 0.07 = 5.7 \pm 4.0$ degrees, typical of opening angles inferred from optical jet breaks (Panaitescu and Kumar, 2001; Wang et al., 2018; Zeh et al., 2006).

If the break is due to the material spreading sideways, then the temporal index after the break is $F_\nu(t) \propto t^{-p}$ (Sari et al., 1999) where p is the power-law index of the electron energy distribution. Using the value of α_2 above we have $p = \alpha_2 = 2.9 \pm 0.4$, which is large but consistent with values expected for shock acceleration (Jones and Ellison, 1991) given the uncertainties, and furthermore is within the normal range of values inferred from optical afterglows in the literature (Wang et al., 2018).

If the steepening is due solely to detecting the edge of the jet, the expected post-break slope[22] is the slope of a spherically expanding outflow ($t^{-3(p-1)/4}$; Sari et al. 1999) with two additional powers of $\Gamma \propto t^{-3/8}$. The resulting temporal slope is $F_\nu(t) \propto t^{-3p/4}$, so $3p/4 = \alpha_2 = 2.9 \pm 0.4$. The value of $p = 3.9 \pm 0.5$ is larger than what is predicted for shock acceleration (Jones and Ellison, 1991) so in what follows we assume $p = 2.9 \pm 0.4$.

Spectral Energy Distribution

The spectrum of an afterglow is determined by the kinetic energy of the explosion, the ambient density, and the fraction of the energy in magnetic fields ϵ_B and relativistic electrons ϵ_e (Sari et al., 1998). The spectrum is characterized by several break frequencies: the cooling frequency ν_c, the characteristic frequency ν_m, and the self-absorption frequency ν_a. The spectral index in any region of the spectrum therefore depends on physical properties of the explosion and on the position of the observing frequency relative to the break frequencies.

In §2.3 we found $p = 2.9 \pm 0.4$ based on the post-break light curve power-law index. Because the g-band measurement is attenuated by Lyman-α and Lyman forest

[22]Here we assume that the optical frequency ν is in the regime $\nu_m < \nu < \nu_c$, motivated in §2.3 and §2.3.

absorption, we use the $r-i$ color from the WASP observation ($r-i = 0.34\pm0.09$ mag) to estimate that the optical spectral index $\beta_{\rm opt} = 1.5 \pm 0.4$. Such a steep spectral index is only ever observed as a result of absorption (Cenko et al., 2009; Greiner et al., 2011): at this redshift even i-band is well into the far-ultraviolet, so it takes relatively little extinction to significantly alter the flux and color. If $\beta_{\rm opt}$ were the "true" (unextincted) spectral index, that would indicate that the cooling frequency ν_c lies below the optical bands (Sari et al., 1999). Taking $\nu_c < 10^{14}$ Hz at $t_d \approx 0.5$ d we have, following Sari et al. (1998)

$$26 > \epsilon_B^{-3/2} E_{52}^{-1/2} n_1^{-1}. \tag{2.4}$$

Using $\epsilon_B < 3 \times 10^{-4}$ and $E_{52} = 1$ (§2.3) we find a very large CSM density of $n > 7 \times 10^3\,{\rm cm}^{-3}$. Furthermore, as shown in the right panel of Figure 2.1, the optical to X-ray spectral index is $\beta_{{\rm opt},X} \approx 0.7$, inconsistent with $\beta_{\rm opt}$. It seems natural that the optical spectral index is steepened by dust attenuation, and $\beta_{{\rm opt},X}$ is the "true" spectral index.

The value of $\beta_{{\rm opt},X}$ is consistent with $(p-1)/2$ but not with $p/2$, so the cooling frequency ν_c lies above the X-ray band (Sari et al., 1999). For adiabatic evolution we have (Sari et al., 1998)

$$\nu_c = 2.7 \times 10^{12} \epsilon_B^{-3/2} E_{52}^{-1/2} n_1^{-1} t_d^{-1/2}\,{\rm Hz}, \tag{2.5}$$

where t_d is the time (in days) after the explosion. Taking $\nu_c > 10^{18}$ Hz and $t_d = 0.5$ d (time of the X-ray observation; rest-frame), we have

$$2.6 \times 10^5 < \epsilon_B^{-3/2} E_{52}^{-1/2} n_1^{-1}. \tag{2.6}$$

Using $\epsilon_B < 3 \times 10^{-4}$ and $E_{52} = 1$ (§2.3) we find $n < 0.7\,{\rm cm}^{-3}$, which is typical for GRBs (Chandra and Frail, 2012; Panaitescu and Kumar, 2001).

Radio Light Curve

In §2.3 we showed that the optical light curve of AT 2020blt is fairly typical for classical GRBs. However, In the radio light curve of AT 2020blt (left panel of Figure 2.1) we detect a decay steeper than $F_\nu \propto t^{-2.3}$, which is unusual for GRBs with detected radio afterglows in general (Chandra and Frail, 2012), including PTF11agg (Cenko et al., 2013).

Early fast-evolving emission in GRB radio afterglow light curves can arise from reverse shocks or diffractive scintillation in the interstellar medium (Alexander et al., 2017, 2019; Laskar et al., 2013; Laskar et al., 2016, 2018; Perley et al., 2014). To determine whether scintillation could be the origin in this case, we use the NE2001 model of the ISM (Cordes and Lazio, 2002). For context, scintillation results from small-scale inhomogeneities in the ISM, which change the phase of an incoming wavefront. As the Earth moves, the line of sight to a background source changes, so the net effect is an observed change in flux. The effect is greatest for sources observed at a frequency $\nu_{\rm obs}$ that is close to the transition frequency ν_0, which separates strong scattering ($\nu_{\rm obs} < \nu_0$) from weak scattering ($\nu_{\rm obs} > \nu_0$).

Using the NE2001 map, we determine that the line-of-sight towards AT 2020blt has a transition frequency $\nu_0 = 7.12\,$GHz, which is close to our observing frequency. Furthermore, we can estimate the timescale for flux changes. Using $D = 100\,$pc as the characteristic scale height of the ISM, and $\lambda = 3\,$cm as our observing wavelength, the Fresnel length is $r_f = \sqrt{\lambda D} \approx 10^{10}\,$cm. Assuming that Earth moves at $v = 30{\rm km\,s^{-1}}$, we obtain $t \sim r_f/v \approx 1\,$hr. In conclusion, the flux could easily change by an order of magnitude due to scintillation over the large time window (16 d) between our observations. Note that the timescale is close to our time on-source ($\sim 30\,$minutes), so there could be some damping of the scintillation over the course of our observation. However, the signal-to-noise of the data is not high enough for us to search for scintillation within the observation.

If, on the other hand, the rapid change in flux is due to a truly steep power-law decay in the radio emission, there would be implications for the ambient density and the value of ϵ_B. In particular, the characteristic frequency ν_m must lie below the radio band. For adiabatic evolution we have (Sari et al., 1998)

$$\nu_m = 5.7 \times 10^{14} \epsilon_B^{1/2} \epsilon_e^2 E_{52}^{1/2} t_d^{-3/2}\,{\rm Hz}. \tag{2.7}$$

Requiring $\nu_m < 10\,$GHz (39 GHz rest-frame) at $t_d = 2\,$d (time of the radio detection; rest-frame) and adopting $\epsilon_e = 0.1$ (Beniamini and van der Horst, 2017; Kumar and Zhang, 2015) we find

$$0.02 > \epsilon_B^{1/2} E_{52}^{1/2}. \tag{2.8}$$

Assuming $E_{52} = 1$, we find $\epsilon_B < 3 \times 10^{-4}$, which is also typical for GRBs based on high-energy and optical afterglow modeling (Beniamini and van der Horst, 2017;

Kumar and Zhang, 2015). So, although an early steep-decaying radio light curve is unusual for GRBs with detailed raido observations, we have no reason to believe that the radio behavior of AT 2020blt is unusual for the population of GRBs as a whole.

2.4 Interpretation

In §2.3 we found that the optical and radio light curve of AT 2020blt is similar to that of classical GRB afterglows. The fact that we observed an achromatic steepening suggests that there was a jet break, which requires that our observing angle was within the jet opening angle.

Three possibilities remain for the origin of AT 2020blt. The first (and simplest) possibility is that AT 2020blt was a classical GRB viewed directly on-axis ($\theta_{\rm obs} < \theta_0$) for which the high-energy emission was simply missed by GRB satellites. As discussed in §2.3, the on-axis scenario is entirely possible. With an eye to the future, when larger samples of optical afterglows will be available (including some with more stringent limits on associated GRB emission), we consider two additional possibilities: that AT 2020blt is a classical GRB observed slightly off-axis $\theta_{\rm obs} \gtrsim \theta_0$ (§2.4) and that AT 2020blt is a dirty fireball (§2.4).

A Slightly Off-Axis GRB

Here we consider the possibility that AT 2020blt was a classical GRB viewed slightly outside the jet opening angle. Beniamini and Nakar (2019) argued that the vast majority of GRBs observed so far must have been observed close to or within the jet core, implying that GRB emission is not produced efficiently away from the core. So, as discussed in §2.1, there is a natural expectation for X-ray and optical afterglows without detected GRB emission (Mészáros and Rees, 1997; Nakar and Piran, 2003; Rhoads, 1997). The slightly off-axis model has been invoked to explain low-luminosity GRBs or X-ray flashes (Ramirez-Ruiz et al., 2005) as well as plateaus observed in X-ray afterglow light curves (Beniamini et al., 2020b; Eichler and Granot, 2006).

One signature of a slightly off-axis afterglow could be an early shallow decay and a large value of $\Delta\alpha$ (Beniamini et al., 2020a; Ryan et al., 2019). This can be understood as follows. In on-axis events, the early stage of the light curve is set by two competing effects: the shock is decelerating, but the beaming cone is widening to include more material. In a slightly off-axis event, there is a third effect, which is that the beaming cone widens to include material of increasing energy per solid

angle—hence a shallower decay.

A larger number of events would help to test this hypothesis: the luminosity function of the early afterglow should be different from the luminosity function of directly on-axis afterglows, and the distribution of limits on $E_{\rm iso}$ would eventually make it unlikely that the afterglows are drawn from the same population as classical GRBs. With more events, we could hope to make the first measurement of the optical beaming factor in GRB afterglows (Nakar and Piran, 2003).

A Dirty Fireball

Here we consider the possibility that AT 2020blt was a "dirty fireball," i.e., a jet with lower Lorentz factor ($\Gamma \sim 10$) that did not produce any GRB emission, as proposed for PTF11agg (Cenko et al., 2013). The basis for the dirty fireball argument for PTF11agg was the rate: at the time, it seemed that the rate of PTF11agg-like events may have been significantly higher than the rate of classical GRBs (Cenko et al., 2013), although this was later shown to not be the case (Cenko et al., 2015; Ho et al., 2018c). Taking a similar approach to Cenko et al. (2015) and Ho et al. (2018c), we searched high-cadence (6×/night) ZTF survey data (Bellm et al., 2019a) from 2018 March 1 to 2020 May 12 to estimate the areal exposure in which an event like AT 2020blt would have passed our filter.

We folded the light curve of AT 2020blt through all r-band exposures in the ZTF high-cadence fields, varying the burst time by 0.01 d intervals, to see over what duration the transient would have had two r-band detections above the limiting magnitude, with a first detection over one magnitude brighter than the last non-detection. We found a total exposure of 855 field-nights. We assume a 100% detection efficiency, so our result is somewhat of a lower limit, particularly at these fainter magnitudes; the efficiency as a function of limiting magnitude has not yet been characterized for ZTF. The 92 high-cadence survey fields included in our search have a combined footprint of 3307 deg^2 after removing the overlap between fields. So, we estimate the all-sky rate of transients similar to AT 2020blt to be

$$\begin{aligned}\mathcal{R} &\equiv \frac{N_{\rm rel}}{A_{\rm eff}} \\ &= \frac{1}{30,734\,\mathrm{deg}^2\,\mathrm{d}} \times \frac{365.25\,\mathrm{d}}{\mathrm{year}} \times \frac{41,253\,\mathrm{deg}^2}{\mathrm{sky}} \\ &= 490\,\mathrm{yr}^{-1}\end{aligned} \tag{2.9}$$

with a 68% confidence interval from Poisson statistics of 85–1611 yr^{-1}. For comparison, the all-sky rate of *Swift* GRBs out to $z = 3$ has been estimated to be 1455^{+80}_{-112} yr^{-1} (Lien et al., 2014). The *Swift* GRB rate is larger than the rate of optical afterglows, since only a subset of GRBs show bright optical afterglow emission (Cenko et al., 2009). So, within the uncertainties, the rate of optical afterglows in ZTF is compatible with the GRB rate. We therefore concur with the conclusion in Cenko et al. (2015) and Ho et al. (2018c) that there is no evidence for an afterglow-like phenomenon that is significantly more common than classical GRBs.

Of course, this assumes that a dirty fireball would look like a classical optical afterglow. We caution, however, that the light curve of a dirty fireball should take longer to rise to peak. The rise time of an afterglow is the time it takes the shock to sweep up material of mass $1/\Gamma_0$ times the ejecta mass (the "deceleration" time). For a uniform-density medium, the expression (observer-frame) is

$$t_{\mathrm{dec}} = 30\, E_{53}^{1/3} n^{-1/3} \Gamma_{0,2.5}^{-8/3} \ \mathrm{sec}\,. \tag{2.10}$$

So, an outflow with $\Gamma_0 = 100$ will have an afterglow that rises to peak in 300 s, but an outflow with $\Gamma_0 = 10$ will have an afterglow that rises to peak in 1.2 d. We have no evidence for such a long rise time in AT 2020blt; the last non-detection was 0.74 d prior to the first detection. A slower-rising event might not pass our fast-transient filter (§2.2) so the limit we set on the rate would not be correct, i.e., the rate could be larger.

2.5 Summary and Conclusions

To summarize, we used a filter for extragalactic fast transients together with fast-turnaround follow-up observations to discover a cosmological afterglow ($z \approx 2.9$) in ZTF high-cadence data. Our search strategy (§2.2) is to find fast-appearing transients with no host galaxy and red colors, inconsistent with the thermal emission expected for the foreground fog of stellar flares. Additional photometry obtained within 24 hours confirmed rapid fading, and a spectrum obtained within three days established the cosmological origin (§2.2). AT 2020blt is one of only a few optical afterglows discovered independently of a high-energy trigger, and one of only two events with both a redshift measurement and no detected GRB.

One lesson from our work is that for a single event, it is very difficult to rule out a classical GRB missed by high-energy detectors. The most sensitive detectors have

the smallest probability of observing the field over the relevant time interval, given the typical cadence of optical observations.

We consider what might be possible with a large sample of events. From existing survey data, it is already clear that the rate of afterglow-like events cannot be significantly higher than the rates of classical GRBs (§2.4). Dirty fireballs could have a significantly longer duration (§2.4), in which case they would not pass our fast-transient filter and the rate could be significantly higher than the limits set by intra-night fast-transient searches. The appearance of slightly off-axis events (§2.4) depends on the structure of the jet, currently unknown, but the luminosity function should be different (with lower overall luminosity) than that of classical GRBs.

Perhaps the strategy of searching for intra-night transients is too restrictive, given the likelihood that dirty fireballs would be longer-duration transients and the uncertainty in the appearance of a slightly off-axis jet. A more agnostic strategy could be to search for relativistic explosions on the basis of luminosity. If dirty fireballs have an intrinsically lower redshift distribution, then their host galaxies are more likely to be detected; in fact, of the three afterglows with ZTF detections, two (ZTF19aabgebm and ZTF19abvizsw) have detected host galaxies in the Legacy Survey DR8 (Dey et al., 2019) with high photometric redshifts. In a search for luminous transients, interlopers like superluminous supernovae could be easily ruled out by light-curve duration. A search for luminous transients using host-galaxy photometric and spectroscopic catalogs during ZTF Phase II could help set the stage for a similar search strategy during LSST.

A.Y.Q.H. would like to thank Udi Nakar for pointing out that dirty fireballs will have a longer rise time than clean fireballs, and Chris Bochenek and Vikram Ravi for useful discussions regarding scintillation of radio point sources. She would also like to thank Steve Schulze, Eran Ofek, Avishay Gal-Yam, and David Kaplan for their detailed reading of the manuscript.

A.Y.Q.H. and K.D. were supported by the GROWTH project funded by the National Science Foundation under PIRE Grant No. 1545949. A. A. Miller is funded by the Large Synoptic Survey Telescope Corporation, the Brinson Foundation, and the Moore Foundation in support of the LSSTC Data Science Fellowship Program; he also receives support as a CIERA Fellow by the CIERA Postdoctoral Fellowship Program (Center for Interdisciplinary Exploration and Research in Astrophysics, Northwestern University). C.F. gratefully acknowledges support of his research by the Heising-Simons Foundation (#2018-0907). A. Goobar acknowledges support

from the K & A Wallenberg Foundation, the Swedish Research Council (VR), and the GREAT research environment grant 2016-06012.

Based on observations obtained with the Samuel Oschin Telescope 48-inch and the 60-inch Telescope at the Palomar Observatory as part of the Zwicky Transient Facility project. ZTF is supported by the National Science Foundation under Grant No. AST-1440341 and a collaboration including Caltech, IPAC, the Weizmann Institute for Science, the Oskar Klein Center at Stockholm University, the University of Maryland, the University of Washington, Deutsches Elektronen-Synchrotron and Humboldt University, Los Alamos National Laboratories, the TANGO Consortium of Taiwan, the University of Wisconsin at Milwaukee, and Lawrence Berkeley National Laboratories. Operations are conducted by COO, IPAC, and UW. SED Machine is based upon work supported by the National Science Foundation under Grant No. 1106171. This work made use of data supplied by the UK Swift Science Data Centre at the University of Leicester. Based on observations obtained at the international Gemini Observatory, a program of NSF's OIR Lab, which is managed by the Association of Universities for Research in Astronomy (AURA) under a cooperative agreement with the National Science Foundation. on behalf of the Gemini Observatory partnership: the National Science Foundation (United States), National Research Council (Canada), Agencia Nacional de Investigación y Desarrollo (Chile), Ministerio de Ciencia, Tecnología e Innovación (Argentina), Ministério da Ciência, Tecnologia, Inovações e Comunicações (Brazil), and Korea Astronomy and Space Science Institute (Republic of Korea). Gemini data were processed using the Gemini IRAF package and DRAGONS (Data Reduction for Astronomy from Gemini Observatory North and South). The Liverpool Telescope is operated on the island of La Palma by Liverpool John Moores University in the Spanish Observatorio del Roque de los Muchachos of the Instituto de Astrofisica de Canarias with financial support from the UK Science and Technology Facilities Council.

Chapter 3

IPTF ARCHIVAL SEARCH FOR FAST OPTICAL TRANSIENTS

Ho, A. Y. Q. et al. (2018). "iPTF Archival Search for Fast Optical Transients". In: *ApJL* 854.1, p. L13. DOI: 10.3847/2041-8213/aaaa62. arXiv: 1712.00949 [astro-ph.HE].

Anna Y. Q. Ho[1], S. R. Kulkarni[1], Peter E. Nugent[2], Weijie Zhao[3], Florin Rusu[3], S. Bradley Cenko[4,5], Vikram Ravi[1], Mansi M. Kasliwal[1], Daniel A. Perley[6], Scott M. Adams[1], Eric C. Bellm[7], Patrick Brady[8], Christoffer Fremling[1], Avishay Gal-Yam[9], David Alexander Kann[10], David Kaplan[8], Russ R. Laher[11], Frank Masci[11], Eran O. Ofek[9], Jesper Sollerman[12], Alex Urban[13]

[1]Cahill Center for Astronomy and Astrophysics, California Institute of Technology, Pasadena, CA 91125, USA
[2]Lawrence Berkeley National Laboratory, 1 Cyclotron Road, Berkeley, CA, 94720, USA
[3]University of California Merced, 5200 Lake Rd, Merced, CA 95340
[4]Astrophysics Science Division, NASA Goddard Space Flight Center, Mail Code 661, Greenbelt, MD 20771, USA
[5]Joint Space-Science Institute, University of Maryland, College Park, MD 20742, USA
[6]Astrophysics Research Institute, Liverpool John Moores University, IC2, Liverpool Science Park, 146 Browlow Hill, Liverpool L3 5RF, UK
[7]University of Washington Astronomy Dept., Box 351580, Seattle, WA 98195, USA
[8]Department of Physics, University of Wisconsin-Milwaukee, Milwaukee, WI 53201, USA
[9]Benoziyo Center for Astrophysics, Weizmann Institute of Science, 76100 Rehovot, Israel
[10]Instituto de Astrofísica de Andalucía (IAA-CSIC), Glorieta de la Astronomía s/n, 18008 Granada, Spain
[11]Infrared Processing and Analysis Center, California Institute of Technology, Pasadena, CA 91125, U.S.A.
[12]Department of Astronomy and The Oskar Klein Centre, AlbaNova University Center, Stockholm University, SE-106 91 Stockholm, Sweden
[13]LIGO Laboratory, California Institute of Technology, Pasadena, CA 91125, U.S.A.

Abstract

There has been speculation of a class of relativistic explosions with an initial Lorentz factor $\Gamma_{\rm init}$ smaller than that of classical Gamma-Ray Bursts (GRBs). These "dirty fireballs" would lack prompt GRB emission but could be pursued via their optical afterglow, appearing as transients that fade overnight. Here we report a search for such transients (transients that fade by 5-σ in magnitude overnight) in four years of archival photometric data from the intermediate Palomar Transient Factory (iPTF). Our search criteria yielded 50 candidates. Of these, two were afterglows to GRBs that had been found in dedicated follow-up observations to triggers from the

Fermi GRB Monitor (GBM). Another (iPTF14yb; Cenko et al. 2015) was a GRB afterglow discovered serendipitously. Eight were spurious artifacts of reference image subtraction and one was an asteroid. The remaining 38 candidates have red stellar counterparts in external catalogs. The photometric and spectroscopic properties of the counterparts identify these transients as strong flares from M dwarfs of spectral type M3-M7 at distances of $d \approx 0.15$–2.1 kpc; three counterparts were already spectroscopically classified as late-type M stars. With iPTF14yb as the only confirmed relativistic outflow discovered independently of a high-energy trigger, we constrain the all-sky rate of transients that peak at $m = 18$ and fade by $\Delta m = 2$ mag in $\Delta t = 3$ hr to be $680\,\mathrm{yr}^{-1}$ with a 68% confidence interval of 119–$2236\,\mathrm{yr}^{-1}$. This implies that the rate of visible dirty fireballs is at most comparable to that of the known population of long-duration GRBs.

3.1 Introduction

The focus of this letter is fast (significant fading in $\lesssim 1$ night) optical transients. The sky is poorly characterized on these timescales, in part because a short cadence comes at the cost of a decrease in sky coverage. These difficulties are exacerbated by the need for rapid follow-up. By contrast, novae and supernovae (SNe) evolve on timescales of days to weeks. It is therefore not surprising that they are the best-characterized classes of transients in the optical sky.

The dominant population of fast optical transients (FOTs) is flares from Galactic low-mass main sequence stars, particularly M dwarfs (e.g., Berger et al. 2013; Kulkarni and Rau 2006; Rau et al. 2008). These flares are thought to arise from magnetic reconnection events in convective envelopes. Behind this foreground of stellar flares is a population of extragalactic relativistic explosions: the optical afterglows to gamma-ray bursts (GRBs).[1] GRBs can be explained by the "collapsar" model: a star of mass $M > 30\,M_\odot$ collapses to form a black hole, and the resulting accretion disk powers a jet (Piran, 2004). The burst of γ rays arises from within the jet, while the optical afterglow is synchrotron emission from the jet shocking the circumstellar medium.

Searching for optical or radio afterglows could yield relativistic explosions that are related to GRBs but lack high-energy emission. One example is the hypothesized

[1] In this paper we focus on transients related to long duration GRBs because, due to their higher energetics and larger volumetric rates, these events dominate the observed population of relativistic explosions. However, short GRB afterglows also produce fast optical transients that could conceivably pass our selection criteria.

class of “dirty fireballs” (Dermer et al., 1999): explosions with a lower $\Gamma_{\rm init}$ than those of classical GRBs but with similar $E_{\rm iso}$ (energy released per unit solid angle). Classical GRBs are “clean" in the sense that they have a very low baryon loading fraction, which enables matter to be accelerated to hyper-relativistic (initial Lorentz factor, $\Gamma_{\rm init} \gtrsim 100$) speeds. The primary motivation to consider dirty fireballs is the absence of a compelling reason for all relativistic explosions to have the requisite low baryon loading. The prompt emission from a dirty fireball would peak at energies below the range of γ-ray detectors. However, like a classical GRB, a dirty fireball would produce a rapidly fading (on-axis) optical afterglow and long-lived radio emission (Rhoads, 2003).

Another class of optical afterglows that would lack prompt high-energy emission are off-axis (“orphan”) afterglows (Rhoads, 1997). Unlike for classical (on-axis, $\theta_{\rm obs} \lesssim 1/\Gamma_{\rm init}$) GRBs, an observer to an off-axis burst would not see the prompt high-energy emission, nor the initial afterglow. However, as the jet slows down it also expands sideways and as a result the afterglow becomes visible to an off-axis observer. While classical GRBs can be seen across the Universe due to relativistic beaming and Doppler boosting, orphan afterglows would be seen to shorter distances. However, the larger opening angle means that the solid angle of visibility is significantly larger than that of on-axis bursts (Ghirlanda et al., 2015; Nakar et al., 2002).

Wide-field optical surveys have already demonstrated the technical capability to find optical afterglows independently of a GRB trigger. For example, iPTF14yb (Cenko et al., 2015) and ATLAS17aeu (Bhalerao et al., 2017; Stalder et al., 2017) were optical afterglows to GRBs identified via fading broadband afterglow emission; in both cases, only later was the “parent" GRB identified (*ibid*). Then there is the curious PTF11agg (Cenko et al., 2013), which had no identified high-energy counterpart but had other characteristic features of a GRB afterglow: a rapidly-fading optical source, a long-lived scintillating radio counterpart, and coincidence with a dwarf galaxy with an estimated redshift of $0.5 \lesssim z \lesssim 3.0$.

In this *Letter*, we report a search for fast optical transients in the *intermediate* Palomar Transient Factory (iPTF). This is similar to the search by Berger et al. (2013) for “fast optical transients" (defined as transients on timescales of 0.5 hr to 1 day) in 1.5 years of data from the PanSTARRS-1 Medium Deep Survey (PS1/MDS). Relative to our search PS-1 is deeper (10σ of 22.5 mag in the equivalent of g and r bands). They found 19 transients; of these, eight were most reasonably explained as main-belt asteroids at their turning points, and the remaining eleven were identified with

quiescent M-dwarf counterparts. This work emphasized the importance of avoiding low ecliptic latitudes for future searches and highlighted the significant foreground of M-dwarf flares.

By focusing on fast transients, our search is sensitive to on-axis sources (dirty fireballs) and not off-axis events (orphan afterglows). The latter will be investigated in subsequent work, in which we search for transients that evolve rapidly on a timescale of days, like those in Drout et al. (2014) and Yang et al. (2017). §3.2 describes the survey, data, and search procedure, and §3.3 outlines the properties of the iPTF FOTs. In §3.4 we use the results of our search to constrain the rate of extragalactic FOTs. We conclude with a view to the upcoming Zwicky Transient Facility (ZTF; Bellm and Kulkarni 2017).

3.2 Data and Candidate Selection

The intermediate Palomar Transient Factory (iPTF) ran from 1 January 2013 to 2 March 2017 as the successor to the Palomar Transient Factory (PTF; Law et al. 2009). iPTF used a camera with a 7.26 $\deg^2$ field-of-view on the 48-inch Samuel Oschin Schmidt Telescope at Palomar Observatory (P48) and a real-time image subtraction pipeline (Cao et al., 2016) that was run at the National Energy Research Scientific Computing Center (NERSC) to search for transient and variable activity in the night sky. The iPTF transient surveys generally emphasized higher-cadence observations than the PTF surveys, making them well-suited for searches for fast-fading events.

The full set of candidates were saved in a database at NERSC, and the subset that passed human inspection were saved in the iPTF database at Caltech. Light curves could also be obtained using the PTF IPAC/iPTF Discovery Engine (PTFIDE) tool (Masci et al., 2017), although PTFIDE has only been run on a small subset of the iPTF database due to computational expense.

Significant improvements to the image differencing pipeline (see Section 3.2) were made on 1 February 2013. We therefore selected this as the start date for our search. We then performed our search in four steps, listed below. The motivation for (a) and (c) is that the afterglows discovered by optical surveys thus far manifest themselves as sources that fade overnight: iPTF14yb faded by ~ 0.7 mag/hr, ATLAS17aeu faded by ~ 0.7 mag/hr, and PTF11agg faded by ~ 0.2 mag/hr. With an initial magnitude of $r = 18$ mag, all three of these sources would become undetectable by iPTF (typical limiting mag $r \sim 20.5$ mag) within a night (14 hours, or 0.6 days). We chose to search for sources that have at least one pair of fading detections in order

to accommodate the diversity of observed afterglow light curve shapes (e.g., Kann et al. 2010).

1. Query the NERSC database for candidates that have two detections[2] with magnitudes m_1, m_2 separated by Δt. This pair must satisfy the following criteria:

   a) Fading ($m_2 > m_1$) within $\Delta t < 1$ night (0.6 day)

   b) Real-bogus (RB[3]) score ≥ 0.3

   c) All detections confined to 1 night (0.6 day) [4]

   d) All detections spatially coincident to within 1.5″

   e) No bad image or bad subtraction flags (`image_id` > -1, `sub_flag` $\neq 0$)

2. Save all candidates from (1) to the iPTF database of named transients at Caltech. Many of these candidates were not in the iPTF database because they were not saved by human scanners (for example, because they fell below the RB threshold used during the survey).

3. Search the iPTF database (existing named transients as well as the ones added in step [2]) for candidates exhibiting afterglow behavior: significant fading, $m_2 > m_1$ at 5-σ.

4. For all candidates in (3), generate forced PSF photometry on the difference image using PTFIDE to confirm the significance of the fading.

Of the 14,961 sources with a pair of detections separated by $\Delta t < 0.6$ days, there were 1,371 sources with no detections outside this window. Of these non-repeating sources, there were 680 sources that were fading. Of these 680 sources, there were 50 that had significant (5-σ) fading.

Of the candidates, one has two detections arising from two separate asteroids[5] and eight are artifacts of image subtraction identified in visual inspection. Note that the rate of false positives is what one would expect from the raw classifier performance (Bloom et al., 2012). Removing the asteroids and artifacts, we have

[2] If there are > 2 detections, there must exist a pair of detections satisfying (a) and (b)

[3] Brink et al. (2013)

[4] This eliminates periodic or repeating sources like AGN and variable stars.

[5] `https://www.minorplanetcenter.net/cgi-bin/checkmp.cgi`

41 candidates. In Figure 3.1 we show the $\Delta t = t_{\rm end} - t_{\rm start}$ and $\Delta m = m_{\rm end} - m_{\rm start}$ for these 41 candidates. For reference, we show PTF11agg as well as a sample of GRB afterglows from the literature (Kann et al., 2010) sampled between three hours and nine hours after peak. iPTF14cva and iPTF14cyb were afterglows discovered by PTF in searches of the *Fermi* GBM error regions (Singer et al., 2015); they correspond to the events GRB 140620A (Kasliwal et al., 2014) and GRB 140623A (von Kienlin, 2014) respectively. Note that there were six more afterglows detected by iPTF in following up *Fermi* GBM triggers (Singer et al., 2015) but these did not pass the search criteria because they were detected late after the trigger time and thus were not fading significantly (all below 5-σ).

The remaining 38 have red stellar hosts in external catalogs and can thus be identified as M-dwarf flares; we spectroscopically confirm these and discuss their properties in Section 3.3. Fortunately, all of the M dwarfs in our sample have red counterparts in external catalogs (described in Section 3.3) whereas none of the afterglows have detectable hosts. Indeed, of the 16 M-dwarf flares that were saved to the iPTF database during the survey (that is, prior to our search) 12 had red stellar counterparts in SDSS. The transients were thus readily classified as M-dwarf flares, although one was assigned for spectroscopic follow-up due to being faint ($r = 23.4$ mag).

3.3 Properties of the iPTF M-dwarf Flares

Figure 3.2 shows the light curves of all 38 M-dwarf flares, superimposed with the two afterglows discovered in survey mode (as opposed to in follow-up to GRBs). The positions and classifications can be found in Table 3.2 and the spectra can be found in Figure 3.6 and Figure 3.6.

For each candidate, a counterpart was present in the Panoramic Survey Telescope and Rapid Response System (PanSTARRS; Chambers et al. 2016). For most (31 of 38) candidates, a counterpart was detected in WISE (Wright et al., 2010). PanSTARRS host IDs and peak flare magnitudes are listed in Table 3.1, and a color-magnitude diagram based on PanSTARRS i and WISE W1 magnitudes is shown in Figure 3.3.

Of the 38 M dwarfs, three had spectra from the Sloan Digital Sky Survey (Albareti et al., 2017). For eight of the sources that were accessible in the night sky while this work was conducted, we obtained host spectra using the Double Spectrograph on the 200-inch Hale telescope at Palomar and the Low Resolution Imaging Spectrometer (LRIS) on Keck.

In Table 3.1 we present derived properties of the flare stars. Note that this is not

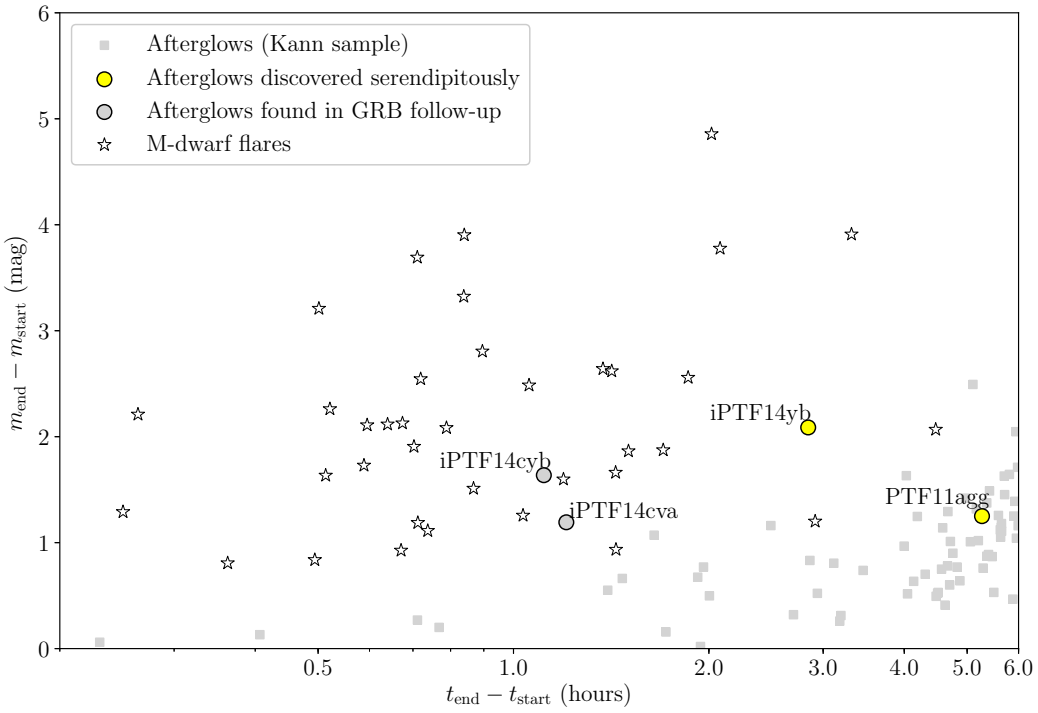

Figure 3.1: The $(\Delta t, \Delta m)$ for the 41 candidates that show significant (5-σ) intra-night fading (asteroids and artifacts of bad subtractions have been removed). The grey unlabeled points are a sample of GRB afterglows from Kann et al. (2010). For candidates with > 2 points in their light curves, we show the change in magnitude from the first observation after 3 hours to the last observation before 9 hours (times measured since the burst): $\Delta t = t_{\rm end} - t_{\rm start}$ and $\Delta m = m_{\rm end} - m_{\rm start}$. M-dwarf flares typically fade faster and are detected in PanSTARRS (see Table 3.1) with a characteristic red color. Thus, in our sample, filtering out sources with red hosts exclusively identifies iPTF14yb, the GRB discovered serendipitously by iPTF, as well as two afterglows found in follow-up to Fermi GRB triggers. PTF11agg is shown for reference. There is one M-dwarf with a Δt below the lower limit on the plot.

a complete sample of flaring M dwarfs in iPTF, because many were filtered out by the criterion of no prior of subsequent activity (criterion [c] in Section 3.2). To determine spectral type, we fit the spectra using the PyHammer software package (Kesseli et al., 2017). When a spectrum was not available, we used the quiescent PanSTARRS colors and the relations in West et al. (2011) and Berger et al. (2013).

To estimate absolute magnitude, we used the relation between SDSS $r - z$ and M_r in Bochanski et al. (2011). More precisely, we interpolated between the values in Table 5 of that paper, assuming that the stars are active and have subsolar metallicity.

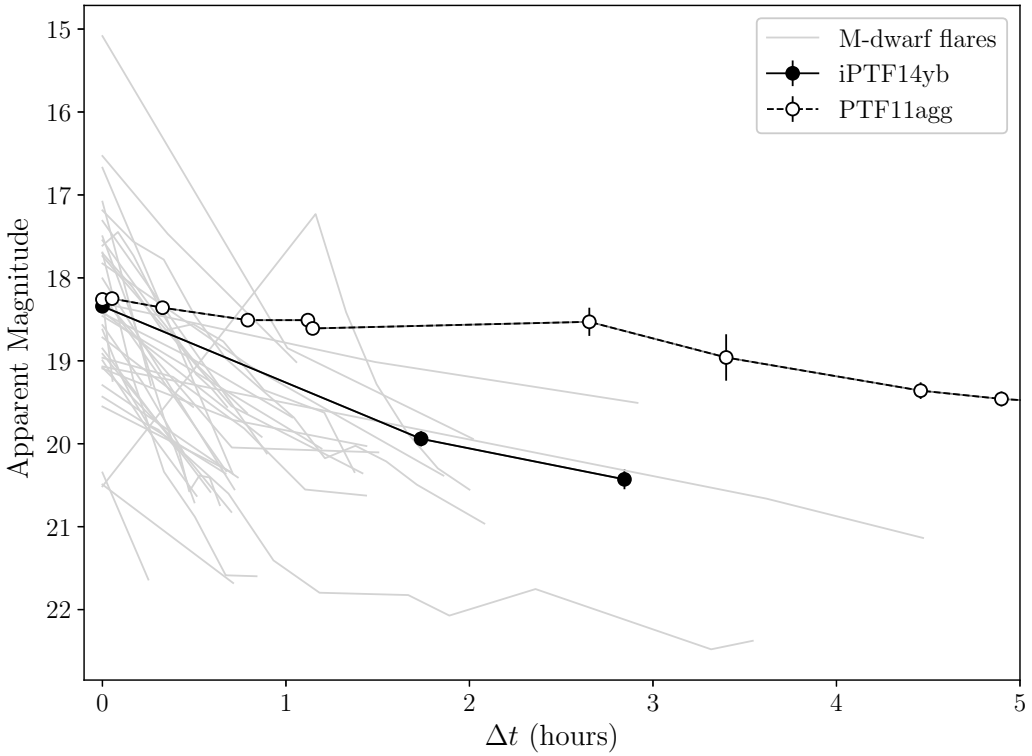

Figure 3.2: r-band light curves for the 38 M-dwarf flares in our sample (grey, background) overlaid with light curves of iPTF14yb and PTF11agg

Because some sources are outside the SDSS footprint, we used the $r - z$ color from PanSTARRS instead. Using the sample in our work and in Berger et al. (2013), we find that in this magnitude range (r =16-22 mag) the $r - z$ colors are equal to within 0.1 mag between SDSS and PanSTARRS.

Note that the values in Table 3.1 are subject to large uncertainties. In general, M-dwarf classifications are only reliable to within one spectral type. Taking into account uncertainties in color, metallicity, and in the interpolation tables in Bochanski et al. (2011), the uncertainty on absolute magnitude M_r is roughly 25%. This translates into a factor of 3-4 uncertainty in distance d, a factor of 3-4 uncertainty in absolute height above the Galactic plane $|z|$, and an order of magnitude uncertainty in the peak luminosity of the flare $L_{\rm peak,flare}$. The u-band magnitude enhancement Δu is robust to uncertainties in spectral type to within 10% and the percentile values are robust to uncertainties in spectral type to within 1%.

The fraction of active stars and the flare rate have been found to increase with later spectral type (Kowalski et al., 2009; West et al., 2011), so it is not surprising that

Table 3.1: Host and flare properties of 38 iPTF FOTs classified as M-dwarf flares. iPTF mags with a † are in g-band, otherwise r-band. In the Notes section, K means a spectrum was obtained with LRIS on Keck, P means that a spectrum was obtained with the Double Spectrograph on the Palomar 200-inch telescope, S means that an SDSS spectrum was already available. Positions and spectra can be found in the supplementary material. As described in the text, M-dwarf classifications are only reliable to within one spectral type. Other uncertainties are roughly 25% in absolute magnitude M_r, a factor of 3-4 in distance d and absolute height above the Galactic plane $|z|$, an order of magnitude in the peak luminosity of the flare $L_{\rm peak,flare}$, 10% in the u-magnitude enhancement Δu, and 1% in the percentile of Δu.

iPTF ID	PS1 ID (PSO)	$m_{{\rm flare},iPTF}$	Sp. Type	M	d	$\|z\|$	$L_{\rm peak,flare}$	Δu	Percentile	Notes
13agt	J170326.056+233048.207	20.8 ± 0.2	M6	14.0	790	8.0	5.6e+30	4.4	0.99	
13asy	J122714.515+170827.218	20.4 ± 0.1	M5	12.0	810	19.0	8.8e+30	3.6	0.97	
13bde	J163025.023+394425.607	20.1 ± 0.09	M4	11.0	980	13.0	1.7e+31	4.4	0.99	
13bku	J132710.975+121305.263	20.1 ± 0.1	M5	10.0	2100	46.0	8e+31	4.1	0.98	
13dqr	J022241.723+251722.567	21.1 ± 0.2	M5	13.0	730	7.4	3.6e+30	4.6	0.99	
13gt	J133612.438+322415.839	20.03 ± 0.08	M5	11.0	1000	24.0	1.9e+31	3.4	0.97	
13nn	J074457.731+522431.570	21.7 ± 0.2	M5	11.0	1400	13.0	8.7e+30	3.7	0.97	
14q	J075205.876+464103.422	$22.5 \pm 0.2^{\dagger}$	M3	9.7	1800	16.0	8.1e+30	6.0	1.0	
15bgf	J204038.050+394012.906	20.3 ± 0.1	M4	11.0	1200	0.46	1.9e+31	4.6	0.99	
15bm	J075629.265+195502.966	20.6 ± 0.1	M7	14.0	350	2.4	1.4e+30	5.8	1.0	
15dto	J002938.210+034148.808	$20.4 \pm 0.2^{\dagger}$	M5	12.0	560	10.0	5.7e+30	3.0	0.92	K
15ell	J034044.994+181735.258	19.56 ± 0.09	M5	12.0	1100	9.5	3.4e+31	4.6	0.99	K
16bse	J204045.160+411809.265	20.7 ± 0.2	M4	11.0	590	0.062	3.4e+30	4.6	0.99	P
16bxw	J002145.452+005843.242	19.5 ± 0.2	M6	12.0	180	3.4	9.9e+29	3.7	0.97	S,P
16ccd	J025954.415+602506.863	19.89 ± 0.08	M5	12.0	740	0.32	1.2e+31	3.3	0.94	K
17ady	J141130.672+304100.846	21.6 ± 0.1	M7	14.0	150	3.3	9.9e+28	3.8	0.97	
17ahn	J164144.856+403623.379	20.3 ± 0.1	M5	10.0	1900	24.0	4.2e+31	5.0	0.99	K
17alz	J022942.051+191822.355	20.6 ± 0.1	M6	11.0	480	5.5	4e+30	5.3	0.99	P
17amj	J012608.197+353352.587	20.12 ± 0.09	M5	11.0	950	7.7	1.9e+31	4.0	0.98	K
17bub	J054206.049+700935.192	19.92 ± 0.09	M4	11.0	430	2.6	5.5e+30	3.3	0.94	
17eur	J080132.966+180821.586	19.56 ± 0.08	M3	9.6	640	4.5	4.5e+30	4.2	0.98	
17hce	J020737.876+135531.430	20.63 ± 0.09	M5	12.0	540	7.4	4.1e+30	5.1	0.99	
17hhv	J072756.444+180748.975	20.3 ± 0.2	M4	11.0	280	1.4	3e+30	4.4	0.99	
17hmf	J093025.725+114653.074	19.3 ± 0.1	M4	11.0	500	6.2	2e+30	6.3	1.0	
17hmz	J080557.336+154053.582	21.0 ± 0.2	M5	13.0	240	1.7	6.8e+29	4.2	0.99	
17ipt	J133442.745+055903.060	20.6 ± 0.2	M5	12.0	190	3.9	4.1e+29	4.1	0.98	
17iwk	J153313.078+571537.332	20.6 ± 0.1	M4	10.0	360	5.4	1.8e+30	5.1	0.99	
17jlt	J151344.316+200736.440	20.4 ± 0.1	M5	12.0	480	8.2	6.2e+30	4.6	0.99	
17jq	J032221.653+264423.619	19.63 ± 0.09	M5	12.0	470	3.6	5.8e+30	3.8	0.97	
17jqb	J150608.089+134859.802	19.7 ± 0.1	M5	13.0	620	11.0	8.2e+30	4.8	0.99	
17jvl	J114254.502+275546.738	19.9 ± 0.1	M4	11.0	190	4.4	1.4e+30	4.7	0.99	
17knl	J083105.765+160952.079	19.29 ± 0.07	M4	10.0	680	6.0	2.2e+31	5.0	0.99	
17mlj	J074900.627+210136.013	19.0 ± 0.2	M4	11.0	220	1.5	1e+30	7.4	1.0	
17py	J162922.139+335645.582	19.9 ± 0.2	M7	14.0	370	4.9	5.5e+30	3.5	0.97	
17qfn	J103422.298+091040.949	19.24 ± 0.06	M4	11.0	610	9.9	3.8e+30	5.7	1.0	
17rzn	J084115.859+181628.242	20.7 ± 0.1	M6	14.0	280	2.8	3.5e+29	6.4	1.0	S
17yz	J104639.306+323916.760	21.6 ± 0.2	M6	14.0	200	3.8	5.6e+29	6.2	1.0	S
17ze	J131505.985+430400.947	20.4 ± 0.1	M5	12.0	290	6.6	1.2e+30	5.1	0.99	

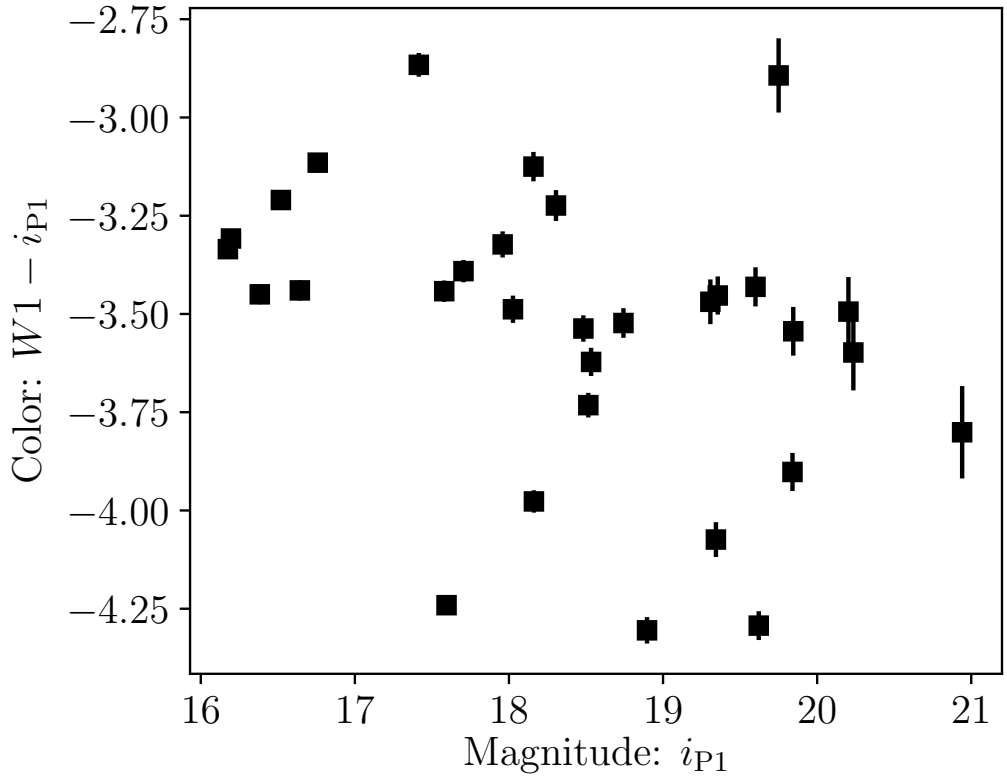

Figure 3.3: A color-magnitude diagram for 31 of the 38 M dwarfs in our sample using PanSTARRS i for the magnitude and WISE $W1$ − PanSTARRS i for the color. All of the M-dwarfs have red counterparts in PanSTARRS, and most (31) have detected counterparts in WISE.

most of the stars in our sample are spectral type M5 or M6. Furthermore, these stars are all located at small vertical distances from the Galactic plane, consistent with the finding in Kowalski et al. (2009) that flare rate decreases strongly with distance from the plane (stars lying close to the plane are younger, which may be associated with stronger activity).

Next, we compare the flare amplitudes to the sample in Kowalski et al. (2009) and list the percentile in the last column of Table 3.1. Kowalski et al. (2009) measure flare luminosities in u band[6]. To estimate the Δu of the flares in our sample, we convert Δr or Δg to Δu using the model in Davenport et al. (2012). The flares in our sample are large compared to those from most active stars of this spectral type. This is because of our selection criteria: the typical uncertainty on an iPTF magnitude

[6]M-dwarf flares are typically studied in the u band because this holds the greatest contrast between the blue flare and red host.

is ~ 0.1, so a 5-σ change in magnitude is typically $\Delta r > 0.5$ or $\Delta g > 0.5$. A magnitude change of $\Delta r > 0.5$ corresponds to $\Delta u > 3$ in the Davenport et al. (2012) model, which is already at the 92nd percentile of the distribution in Kowalski et al. (2009).

3.4 Rate of Relativistic Fast Optical Transients in iPTF

With iPTF14yb remaining the only confirmed afterglow in iPTF discovered independently of a high-energy trigger, we can constrain the rate of transients that exhibit the same fading behavior (peak at $m = 18$, fade by $\Delta m = 2$ mag in $\Delta t = 3$ hr). With our selection criteria and observations from 1 February 2013 through 2 March 2017, we follow a similar procedure to that in Section 5 of Cenko et al. (2015). We take all of the iPTF observations over this four-year period. We insert the light curve of iPTF14yb (for simplicity) stepping through a range of burst times. Using the limiting magnitude of the exposure and the brightness of the source at the time of observation, we determine whether the event would have been detected using our search criteria, i.e., two detections with a 5-σ difference in magnitude.

This gives a total areal exposure of $\mathrm{A_{eff}} = 22,146\,\mathrm{deg^2}$ days. So, we constrain the all-sky rate of on-axis relativistic transients similar to iPTF14yb to be

$$\mathcal{R} \equiv \frac{N_{\mathrm{rel}}}{\mathrm{A_{eff}}} = \frac{1}{22,146\,\mathrm{deg^2\,d}} \times \frac{365.25\,\mathrm{d}}{\mathrm{yr}} \times \frac{41,253\,\mathrm{deg^2}}{\mathrm{sky}} = 680\,\mathrm{yr^{-1}} \tag{3.1}$$

with a 68% confidence interval from Poisson statistics of 119–2236 $\mathrm{yr^{-1}}$. The expected rate of classical optical afterglows that can be detected by (i)PTF is two-thirds of the rate of on-axis *Swift* GRBs, or $\mathcal{R} = 970^{+53}_{-74}\,\mathrm{yr^{-1}}$ (Cenko et al., 2015). Thus, our search sets a limit on the relative rate of visible dirty fireballs to classical on-axis afterglows and suggests that it is at most comparable.

We now estimate the volumetric rate of transients with these characteristics (peak at $m = 18$, fade by $\Delta m = 2$ mag in $\Delta t = 3$ hr). iPTF14yb was observed at redshift $z = 1.9733 \pm 0.0003$ with spectral index $\beta = 1.3 \pm 0.1$ and apparent magnitude $m_{\mathrm{p}} = 18.16 \pm 0.03$ in its first discovery image. Applying a standard K-correction (Hogg et al., 2002), this corresponds to an absolute magnitude $M_{\mathrm{p}} = -27.5 \pm 0.1$ in the r-band some $\sim$300 s after the initial outburst, which is fairly typical of the afterglows of *Swift* long GRBs (Cenko et al., 2009). Assuming iPTF14yb represents a population of standard candles (which is not really the case; see Kann et al. 2010) an identical explosion would appear with magnitude $m \approx 21$ if it occurred at redshift

$z \approx 3$; thus we infer a volumetric rate of 0.395 Gpc^{-3} yr^{-1} with a 1σ credible interval of (0.022–0.708) Gpc^{-3} yr^{-1} . This is roughly consistent with 1/3–2/3 the rate of long-duration *Swift* GRBs in the local universe (1.3 Gpc^{-3} yr^{-1}; Wanderman and Piran 2010) without accounting for beaming. A more detailed analysis of this volumetric rate is forthcoming (Urban et al., in prep.).

3.5 Conclusions

The Zwicky Transient Facility (ZTF; Bellm and Kulkarni 2017) has just achieved first light, and with its 47 deg^2 field of view and faster readout will represent on average a 12-fold increase in volumetric survey speed over PTF. Thus, in one routine semester of ZTF, we will be able to reproduce the coverage of iPTF, setting very strong limits on the rates of extragalactic fast optical transients, or potentially providing the first confirmed detection of afterglows lacking prompt high-energy emission.

So far, it seems that M-dwarf flares are the only astrophysical contaminant in searching for afterglows via rapidly-fading emission. In particular, our selection criteria identify flares from late-type M-dwarfs in the top decile of flare amplitude. Such events are rare due to the intrinsic faintness of late-type M dwarfs and the anti-correlation of flare frequency with flare energy (e.g., Davenport 2016). Wide-area, high-cadence surveys like PTF and ZTF are thus well-suited for identifying the most extreme examples of flaring activity (so-called “hyperflares"), aiding studies of chromospheric activity and stellar dynamos.

That said, the cadence of these wide-field surveys (PTF, ZTF, LSST) is not well-suited for constraining detailed physics of flares. Instead, the cadence is more suited to flare population statistics. The spatial distribution of these extreme examples of flaring activity is interesting because flares are typically an indicator of stellar youth. The same ZTF data (and other such surveys) can be used to measure rotation rates and therefore estimate stellar ages (gyrochronology). Therefore, properly modeling the transient contribution for flares could result in a relation between activity and rotation period for these stars. The latter is usually taken as a proxy for age.

It is a pleasure to thank Yi Cao, Jim Davenport, Adam Miller, Yuguang Chen, Harish Vendantham, Lynne Hillenbrand, and Trevor David for helpful discussions and assistance. We are grateful to the anonymous referee for constructive feedback that improved the quality of the paper. A.Y.Q.H. was supported by a National Science Foundation Graduate Research Fellowship under Grant No. DGE-1144469. DAK acknowledges support from from the Spanish research project AYA 2014-58381-P

and the Juan de la Cierva Incorporacíon fellowship IJCI-2015-261. This work was supported by the GROWTH project funded by the National Science Foundation under PIRE Grant No 1545949. The Intermediate Palomar Transient Factory project is a scientific collaboration among the California Institute of Technology, Los Alamos National Laboratory, the University of Wisconsin, Milwaukee, the Oskar Klein Center, the Weizmann Institute of Science, the TANGO Program of the University System of Taiwan, and the Kavli Institute for the Physics and Mathematics of the Universe. This research made use of Astropy, a community-developed core Python package for Astronomy (Astropy Collaboration et al., 2013).

3.6 Appendix

Table 3.2: Table of iPTF Fast Optical Transients

PTF ID	RA	Dec	UT Date	Classification
13agt	17:03:26.07	+23:30:48.0	2013-04-04	M-dwarf
13asy	12:27:14.53	+17:08:27.2	2013-05-04	M-dwarf
13bde	16:30:25.03	+39:44:25.5	2013-05-15	M-dwarf
13bku	13:27:11.00	+12:13:05.2	2013-06-01	M-dwarf
13dqr	02:22:41.74	+25:17:22.6	2013-10-04	M-dwarf
13gt	13:36:12.43	+32:24:15.8	2013-02-18	M-dwarf
13nn	07:44:57.71	+52:24:31.4	2013-03-06	M-dwarf
13qz	12:02:07.82	+01:22:50.8	2013-03-13	Bad Subtraction
14cva	18:47:29.00	+49:43:51.7	2014-06-20	Afterglow
14cyb	15:01:53.41	+81:11:29.0	2014-06-23	Afterglow
14q	07:52:05.86	+46:41:03.2	2014-01-03	M-dwarf
14ts	10:05:47.69	+10:25:52.2	2014-02-22	Rock
14yb	14:45:58.01	+14:59:35.3	2014-02-26	Afterglow
15bgf	20:40:38.04	+39:40:12.7	2015-06-12	M-dwarf
15bm	07:56:29.27	+19:55:02.9	2015-01-18	M-dwarf
15dto	00:29:38.21	+03:41:48.9	2015-11-09	M-dwarf
15ell	03:40:45.01	+18:17:35.2	2015-11-20	M-dwarf
16bse	20:40:45.14	+41:18:08.9	2016-07-11	M-dwarf
16bxw	00:21:45.47	-00:58:43.1	2013-10-01	M-dwarf
16ccd	02:59:54.41	+60:25:06.7	2016-11-23	M-dwarf
16hdn	00:58:13.16	+06:24:00.9	2016-10-13	Bad Subtraction
17ady	14:11:30.65	+30:41:00.7	2013-03-15	M-dwarf
17ahn	16:41:44.86	+40:36:23.0	2013-05-21	M-dwarf
17alz	02:29:42.04	+19:18:22.5	2013-09-04	M-dwarf
17amj	01:26:08.20	+35:33:52.6	2013-09-07	M-dwarf
17bub	05:42:06.04	+70:09:35.1	2017-03-02	M-dwarf
17eur	08:01:32.94	+18:08:21.3	2014-01-07	M-dwarf
17hce	02:07:37.89	+13:55:31.5	2014-11-17	M-dwarf
17hhv	07:27:56.48	+18:07:49.0	2015-01-15	M-dwarf
17hmf	09:30:25.74	+11:46:53.1	2015-02-21	M-dwarf
17hmz	08:05:57.36	+15:40:54.2	2015-03-10	M-dwarf
17ipt	13:34:42.67	+05:59:02.4	2013-03-14	M-dwarf
17iwk	15:33:13.10	+57:15:36.8	2013-04-22	M-dwarf
17jlt	15:13:44.32	+20:07:36.6	2013-03-15	M-dwarf
17jq	03:22:21.67	+26:44:23.2	2014-02-11	M-dwarf
17jqb	15:06:08.11	+13:48:59.9	2013-03-15	M-dwarf
17jvl	11:42:54.48	+27:55:46.7	2013-03-14	M-dwarf
17knl	08:31:05.76	+16:09:51.7	2014-05-19	M-dwarf
17mlj	07:49:00.62	+21:01:35.7	2014-01-20	M-dwarf
17py	16:29:22.15	+33:56:45.5	2013-03-14	M-dwarf
17qfn	10:34:22.32	+09:10:40.9	2015-02-26	M-dwarf
17rzn	08:41:15.87	+18:16:28.0	2015-01-19	M-dwarf
17tq	04:57:50.59	+00:27:30.8	2013-12-14	Bad Subtraction
17ufp	08:01:27.39	+18:08:07.0	2015-01-19	Bad Subtraction
17uo	07:18:12.25	+64:21:19.6	2014-01-18	Bad Subtraction
17whs	01:54:27.77	+20:29:35.9	2013-10-05	Bad Subtraction
17wok	05:15:28.12	+01:30:47.1	2013-12-14	Bad Subtraction
17wsv	08:09:42.13	+19:45:05.3	2015-01-19	Bad Subtraction
17yz	10:46:39.27	+32:39:16.4	2013-03-11	M-dwarf
17ze	13:15:06.05	+43:04:01.5	2013-03-12	M-dwarf

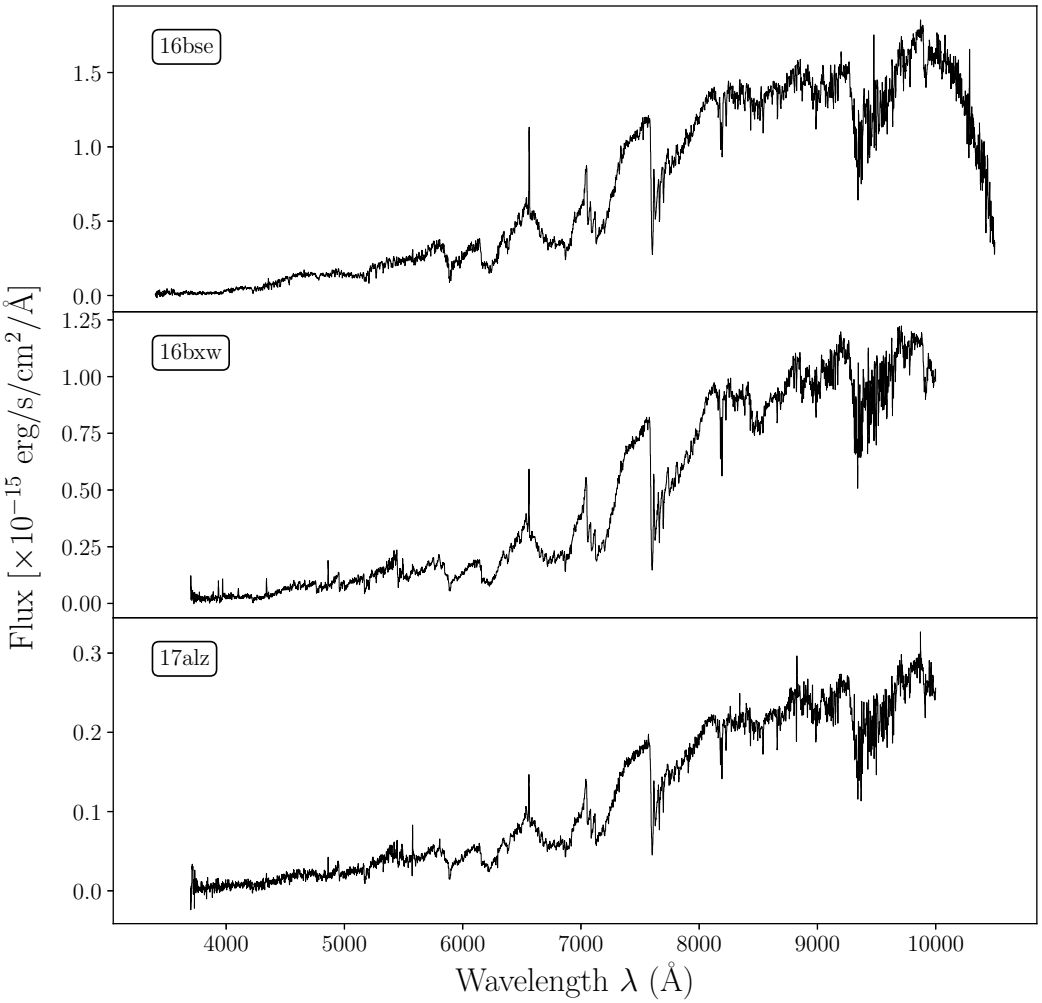

Figure 3.4: DBSP spectra of three of the M dwarfs in our sample

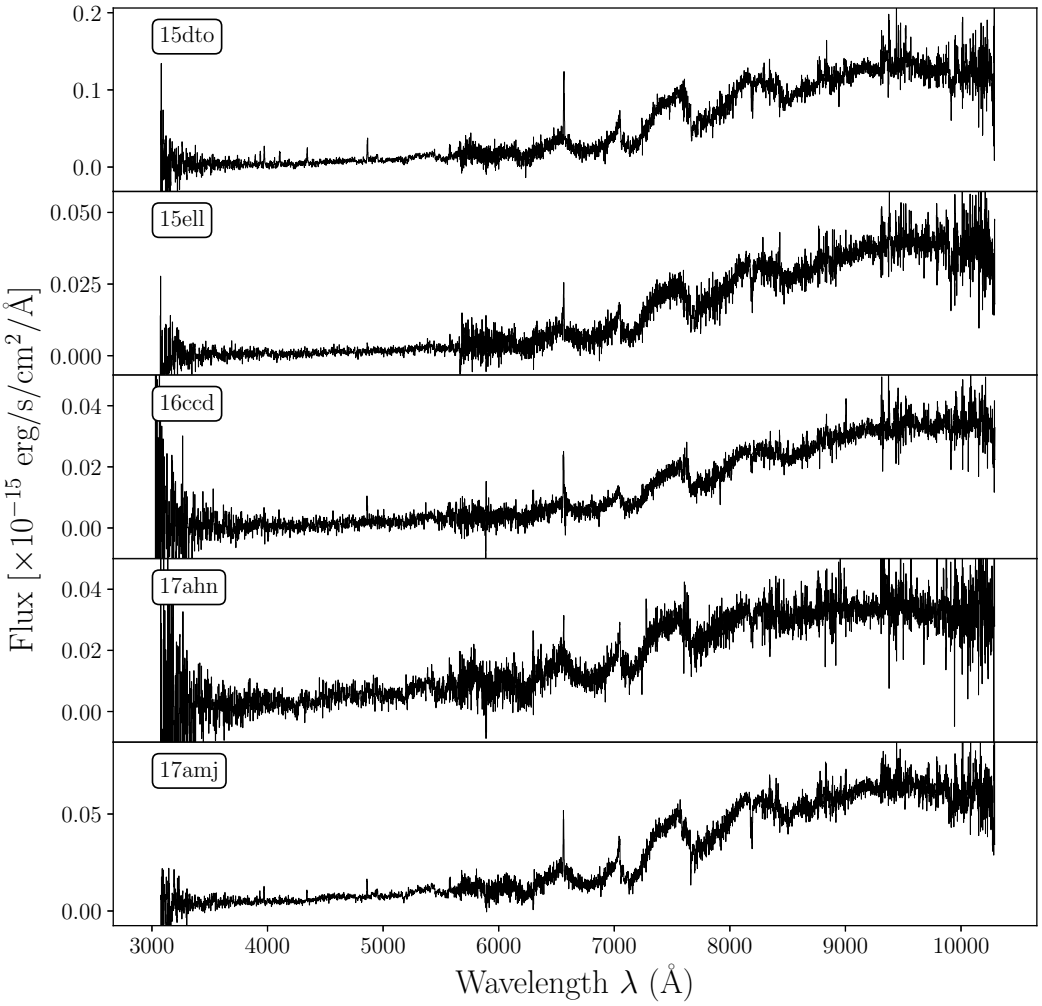

Figure 3.5: LRIS spectra of five of the M dwarfs in our sample

Part II. Low-Luminosity Gamma-Ray Bursts

...the hour will come
When all these splendours bursting on my sight
Shall stand unveil'd

—"A SUMMER EVENING'S MEDITATION"
ANNA LAETITIA BARBAULD (1743–1825)

Chapter 4

SN 2020BVC: A BROAD-LINED TYPE IC SUPERNOVA WITH A DOUBLE-PEAKED OPTICAL LIGHT CURVE AND A LUMINOUS X-RAY AND RADIO COUNTERPART

Ho, A. Y. Q. et al. (2020). "SN2020bvc: a Broad-lined Type Ic Supernova with a Double-peaked Optical Light Curve and a Luminous X-ray and Radio Counterpart". In: *ApJ, accepted*. arXiv: 2004.10406 [astro-ph.HE].

Anna Y. Q. Ho[1], S. R. Kulkarni[1], Daniel A. Perley[2], S. Bradley Cenko[3,4], Alessandra Corsi[5], Steve Schulze[6], Ragnhild Lunnan[7], Jesper Sollerman[7], Avishay Gal-Yam[6], Shreya Anand[8], Cristina Barbarino[7], Eric C. Bellm[9], Rachel J. Bruch[6], Eric Burns[10,11], Kishalay De[1], Richard Dekany[12], Alexandre Delacroix[12], Dmitry A. Duev[1], Dmitry D. Frederiks[7], Christoffer Fremling[1], Daniel A. Goldstein[1], V. Zach Golkhou[9,13,14], Matthew J. Graham[1], David Hale[12], Mansi M. Kasliwal[1], Thomas Kupfer[15], Russ R. Laher[16], Julia Martikainen[17,18], Frank J. Masci[16], James D. Neill[1], Anna Ridnaia[7], Ben Rusholme[16], Volodymyr Savchenko[19], David L. Shupe[16], Maayane T. Soumagnac[6,20], Nora L. Strotjohann[6], Dmitry S. Svinkin[21], Kirsty Taggart[2], Leonardo Tartaglia[7], Lin Yan[12], Jeffry Zolkower[12]

[1]Cahill Center for Astronomy and Astrophysics, California Institute of Technology, Pasadena, CA 91125, USA
[2]Astrophysics Research Institute, Liverpool John Moores University, IC2, Liverpool Science Park, 146 Browlow Hill, Liverpool L3 5RF, UK
[3]Astrophysics Science Division, NASA Goddard Space Flight Center, Mail Code 661, Greenbelt, MD 20771, USA
[4]Joint Space-Science Institute, University of Maryland, College Park, MD 20742, USA
[5]Department of Physics and Astronomy, Texas Tech University, Box 1051, Lubbock, TX 79409-1051, USA
[6]Department of Particle Physics and Astrophysics, Weizmann Institute of Science, 234 Herzl St, 76100 Rehovot, Israel
[7]The Oskar Klein Centre & Department of Astronomy, Stockholm University, AlbaNova, SE-106 91 Stockholm, Sweden
[8]Division of Physics, Mathematics, and Astronomy, California Institute of Technology, Pasadena, CA 91125, USA
[9]DIRAC Institute, Department of Astronomy, University of Washington, 3910 15th Avenue NE, Seattle, WA 98195, USA
[10]NASA Postdoctoral Program Fellow, Goddard Space Flight Center, Greenbelt, MD 20771, USA
[11]Department of Physics & Astronomy, Louisiana State University, Baton Rouge, LA 70803, USA
[12]Caltech Optical Observatories, California Institute of Technology, Pasadena, CA 91125
[13]The eScience Institute, University of Washington, Seattle, WA 98195, USA
[14]Moore-Sloan, WRF Innovation in Data Science, and DIRAC Fellow
[15]Kavli Institute for Theoretical Physics, University of California, Santa Barbara, CA 93106, USA

[16]IPAC, California Institute of Technology, 1200 E. California Blvd, Pasadena, CA 91125, USA
[17]Department of Physics, University of Helsinki, P.O. box 64, FI-00014, Finland
[18]Nordic Optical Telescope, Roque de Los Muchachos Observatory, Rambla José Ana Fernández Pérez 7, 38711 Breña Baja, La Palma, Canarias, Spain
[19]ISDC, Department of Astronomy, University of Geneva, Chemin d'Ecogia, 16 CH-1290 Versoix, Switzerland
[20]Lawrence Berkeley National Laboratory, 1 Cyclotron Road, Berkeley, CA 94720, USA
[21]Ioffe Institute, Politekhnicheskaya 26, St. Petersburg 194021, Russia

Abstract

We present optical, radio, and X-ray observations of SN 2020bvc (=ASASSN20bs; ZTF20aalxlis), a nearby ($z = 0.0252$; $d = 114$ Mpc) broad-lined (BL) Type Ic supernova (SN) and the first double-peaked Ic-BL discovered without a gamma-ray burst (GRB) trigger. Our observations show that SN 2020bvc shares several properties in common with the Ic-BL SN 2006aj, which was associated with the low-luminosity gamma-ray burst (LLGRB) 060218. First, the 10 GHz radio luminosity ($L_{\rm radio} \approx 10^{37}$ erg s^{-1}) is brighter than ordinary core-collapse SNe but fainter than LLGRB-SNe such as SN 1998bw (associated with LLGRB 980425). We model our VLA observations (spanning 13–43 d) as synchrotron emission from a mildly relativistic ($v \gtrsim 0.3c$) forward shock. Second, with *Swift* and *Chandra* we detect X-ray emission ($L_X \approx 10^{41}$ erg s^{-1}) that is not naturally explained as inverse Compton emission or as part of the same synchrotron spectrum as the radio emission. Third, high-cadence (6×/night) data from the Zwicky Transient Facility (ZTF) shows a double-peaked optical light curve, the first peak from shock-cooling of extended low-mass material (mass $M_e < 10^{-2}\,M_\odot$ at radius $R_e > 10^{12}$ cm) and the second peak from the radioactive decay of ^{56}Ni. SN 2020bvc is the first double-peaked Ic-BL SN discovered without a GRB trigger, so it is noteworthy that it shows X-ray and radio emission similar to LLGRB-SNe. For four of the five other nearby ($z \lesssim 0.05$) Ic-BL SNe with ZTF high-cadence data, we rule out a first peak like that seen in SN 2006aj and SN 2020bvc, i.e., that lasts ≈ 1 d and reaches a peak luminosity $M \approx -18$. X-ray and radio follow-up observations of Ic-BL SNe with well-sampled early optical light curves will establish whether double-peaked optical light curves are indeed predictive of LLGRB-like X-ray and radio emission.

4.1 Introduction

It is well-established that most long-duration gamma-ray bursts (GRBs) arise from massive-star explosions (see Woosley and Bloom (2006) for a detailed review, and Hjorth et al. (2012) and Cano et al. (2017b) for recent updates). The traditional

model (reviewed in Piran 2004) is that a massive star, stripped of its hydrogen and helium envelopes, collapses and forms a black hole or neutron star. Through rotational spindown or accretion, the newborn compact object launches an outflow that tunnels through the star, breaks out from the surface as a narrowly collimated jet, and appears as a GRB when viewed on-axis from Earth. The jet shocks the circumburst medium, producing a long-lived "afterglow" across the electromagnetic spectrum. The same "central engine" that launches the GRB also unbinds the stellar material in a supernova (SN) that has a greater kinetic energy (10^{52} erg) and photospheric velocity ($\gtrsim 20,000\,\mathrm{km\,s^{-1}}$) than ordinary core-collapse SNe do (Barnes et al., 2018; Sobacchi et al., 2017). These high-velocity, high-energy SNe were originally called "hypernovae" (e.g. Iwamoto et al. 1998) but a more common term today is "broad-lined Type Ic" (Ic-BL) SNe (Gal-Yam, 2017).

Thousands of GRBs have been discovered, with hundreds of afterglows and a dozen Ic-BL SNe (GRB-SNe) identified in follow-up observations. Half of known GRB-SNe are associated with *low-luminosity* GRBs (LLGRBs), defined as having an isotropic gamma-ray luminosity of $L_{\gamma,\mathrm{iso}} < 10^{48.5}\,\mathrm{erg\,s^{-1}}$ rather than the $L_{\gamma,\mathrm{iso}} > 10^{49.5}\,\mathrm{erg\,s^{-1}}$ of cosmological GRBs (Cano et al., 2017b; Hjorth, 2013). Although LLGRBs are 10–100 times more common than cosmological GRBs (Liang et al., 2007; Soderberg et al., 2006b), the discovery rate by GRB detectors is much lower (one every few years) due to the small volume in which they can be detected. So, the sample size remains small, and the connection between classical GRBs, LLGRBs, and Ic-BL SNe remains unknown.

To make progress on understanding the GRB-LLGRB-SN connection, wide-field high-cadence optical surveys can be used in conjunction with radio and X-ray follow-up observations to discover GRB-related phenomena without relying on a GRB trigger (e.g. Cenko et al. 2013; Corsi et al. 2017; Margutti et al. 2014; Soderberg et al. 2010). To this end, for the past two years we have been conducting a systematic search for engine-driven explosions using the (6×/night) and nightly cadence (2×/night) surveys of the Zwicky Transient Facility (ZTF; Bellm et al. 2019b; Graham et al. 2019), which have a combined area of 5000 $\mathrm{deg^2}$ (Bellm et al., 2019a).

Here we present the most recent event detected as part of the ZTF engine-driven SN program: SN 2020bvc (=ASASSN-20bs) was first reported to the Transient Name Server (TNS[1]) by the All-Sky Automated Survey for SuperNovae (Shappee et al.,

[1] `https://wis-tns.weizmann.ac.il/`

2014), and the discovery announcement noted the rapid rise and likely CC SN origin (Stanek, 2020). It was also reported by ATLAS (Tonry et al., 2018) as ATLAS20feh (on Feb 05.61). The first detection of SN 2020bvc was in ZTF high-cadence data on Feb 04.34. We classified the event as a Type Ic-BL SN (Perley et al., 2020), and the high-cadence data showed a double-peaked light curve. Recognizing the similarity to the Ic-BL SN 2006aj associated with LLGRB 060218 (Ferrero et al., 2006; Mirabal et al., 2006; Pian et al., 2006; Soderberg et al., 2006b; Sollerman et al., 2006), we triggered X-ray (Ho et al., 2020a) and radio (Ho, 2020) follow-up observations.

This paper is structured as follows. We present our observations of SN 2020bvc in §4.2. In §4.3 we measure basic light-curve properties and the blackbody evolution. In §4.4 we discuss the evolution of the optical spectra. In §4.5 we show that the optical light curve can be explained as a combination of shock-cooling emission from extended low-mass material ($M_e < 10^{-2}\,M_\odot$ at $R_e > 10^{12}$ cm) and radioactive decay of ^{56}Ni. In §4.6 we model the forward shock, and show that the radio emission can be explained with velocities that are only mildly relativistic. In §4.7 we show ZTF light curves of five other nearby ($z < 0.05$) Ic-BL SNe in the high-cadence surveys, and rule out a luminous first peak like that seen in SN 2006aj and SN 2020bvc for four events. We conclude in §4.8 by summarizing the properties of SN 2020bvc and discussing its implications for the GRB-LLGRB-SN connection.

4.2 Observations

ZTF Detection and Classification

SN 2020bvc was first detected on 2020 Feb 04.34[2] at $i = 17.48 \pm 0.05$ mag[3] at $\alpha = 14^{\rm h}33^{\rm m}57\farcs01$, $\delta = +40^{\rm d}14^{\rm m}37\farcs5$ (J2000), as part of the ZTF Uniform Depth Survey[4] (Goldstein et al. in prep) with the 48-inch Samuel Oschin Schmidt telescope at Palomar Observatory (P48). The ZTF observing system is described in Dekany et al. (2020). The identification of SN 2020bvc made use of machine learning-based real-bogus classifiers (Duev et al., 2019; Mahabal et al., 2019) and a star-galaxy separator (Tachibana and Miller, 2018).

The last non-detection by ZTF was 1.78 d prior ($r > 20.67$ mag), with more recent limits from ATLAS (0.67 d, $o > 19.4$ mag) and ASAS-SN (0.74 d, $g > 18.6$ mag). Throughout the paper, we use the time of the ATLAS non-detection (Feb 03.67) as

[2] All times given in UTC

[3] All magnitudes given in AB

[4] 45 fields (2000 deg^2) twice per night in each of g-, r-, and i-band

our reference epoch t_0. Our estimate of the "epoch of first light" t_0 is supported by aligning the light curves of SN 2020bvc and SN 2006aj, discussed in §4.3.

Two hours after the first detection, we obtained a spectrum using the Spectral Energy Distribution Machine (SEDM; Blagorodnova et al. 2018; Rigault et al. 2019), a low-resolution spectrograph on the automated 60-inch telescope at Palomar Observatory (P60; Cenko et al. 2006). The spectrum is dominated by a thermal continuum, with hydrogen emission lines from the host galaxy and possible weak absorption features that we discuss in §4.4. On Feb 08.24, a spectrum we obtained using the Spectrograph for the Rapid Acquisition of Transients (SPRAT; Piascik et al. 2014) on the Liverpool Telescope (LT; Steele et al. 2004) showed features consistent with a Type Ic-BL SN (Perley et al., 2020). We discuss the spectroscopic evolution of SN 2020bvc in §4.4. Follow-up observations were coordinated through the GROWTH Marshal (Kasliwal et al., 2019), and the optical photometry and spectroscopy will be made public through WISeREP, the Weizmann Interactive Supernova Data Repository (Yaron and Gal-Yam, 2012).

Host Galaxy

The position of SN 2020bvc is 13″ (7.2 kpc[5]) from the center of UGC 09379 (z = 0.025201 ± 0.000021 from NED[6]), which also hosted PTF13ast (Gal-Yam et al., 2014). UGC 09379 is a massive galaxy: Chang et al., 2015 estimate a stellar mass $\log_{10}(M/M_\odot) = 10.28^{+0.01}_{-0.16}$ while the NASA-SDSS Atlas value (Blanton et al. 2011) is $\log_{10}(M/M_\odot) = 10.26$, comparable to the Milky Way and other large spirals. The stellar mass of UGC 09379 is larger than that of all known GRB-SN host galaxies (Hjorth et al., 2012; Taggart and Perley, 2019) and similar only to the host galaxy of LLGRB 171205A/SN 2017iuk (D'Elia et al., 2018; Izzo et al., 2019; Wang et al., 2018), which had $\log_{10}(M/M_\odot) = 10.1 \pm 0.1$ (Perley and Taggart, 2017). The stellar mass of UGC 09379 is also larger than that of most Ic-BL SN host galaxies (Modjaz et al., 2020), with the exception of SN 2002ap[7] and SN 1997ef[8].

As shown in Figure 4.1, SN 2020bvc is 1.46 ± 0.34″ (804 ± 187 pc) from a bright H II region. We leave a detailed analysis of the SN site to future work, but note that two nearby LLGRB-SNe, LLGRB 980425/SN 1998bw (Galama et al., 1998; Kulkarni et al., 1998) and LLGRB 020903 (Bersier et al., 2006; Sakamoto et al.,

[5] ΛCDM cosmology of Planck Collaboration et al. (2016) used throughout.

[6] `ned.ipac.caltech.edu`

[7] M74: $\log_{10}(M/M_\odot) = 11.52^{+0.05}_{-0.05}$ (Kelly and Kirshner, 2012)

[8] UGC 4107: $\log_{10}(M/M_\odot) = 10.55^{+0.07}_{-0.56}$ (Kelly and Kirshner, 2012)

2004; Soderberg et al., 2004a), were located 800 pc and 460 pc, respectively, from similar bright compact regions in the outskirts of their host galaxies (Hammer et al., 2006; Sollerman et al., 2005). Because these events took place outside the nearest massive-star cluster, it has been argued that the progenitors were Wolf-Rayet stars ejected from the cluster (Cantiello et al., 2007; Eldridge et al., 2011; Hammer et al., 2006; van den Heuvel and Portegies Zwart, 2013). We also note that the metallicity of the SN site is quite low (we infer 12+log[O/H] = 8.2 from the underlying nebular emission in our March 22nd LRIS spectrum using the N2 diagnostic from Pettini and Pagel 2004), making the appearance of a SN of this type in such a massive galaxy less surprising. This metallicity estimate is consistent with the measurement of Izzo et al. (2020).

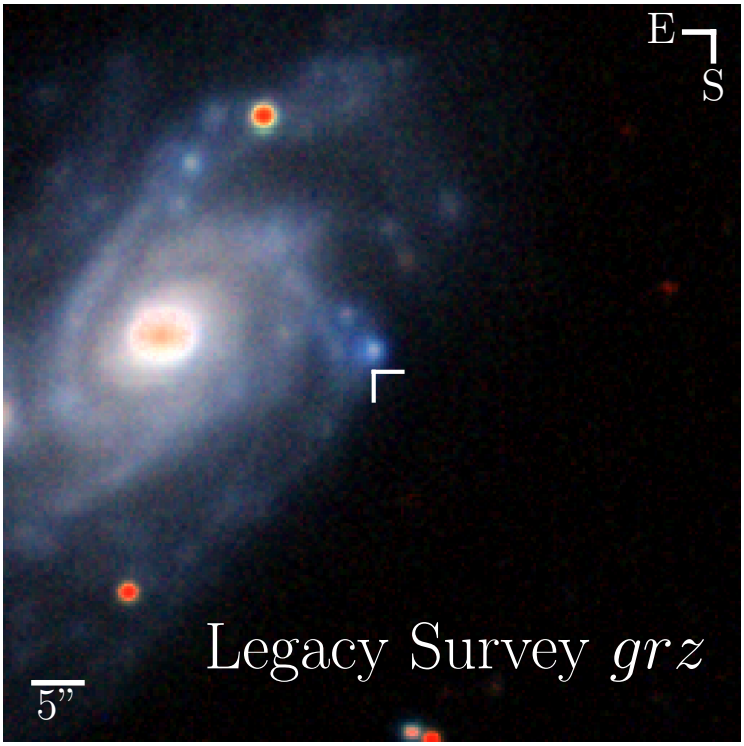

Figure 4.1: The position of SN 2020bvc (white crosshairs) in its host galaxy UGC 09379. *g*-, *r*-, and *z*-band images from the DESI Legacy Survey (Dey et al., 2019) were combined using the prescription in Lupton et al. (2004).

Optical Photometry

As shown in Figure 4.2, SN 2020bvc was observed almost nightly in *gri* by the P48 for the first month post-explosion. We obtained additional *ugriz* and *gri* photometry

using the IO:O on LT and the SEDM on the P60, respectively. The pipeline for P48 photometry is described in Masci et al. (2019), and makes use of the the image subtraction method of Zackay et al. (2016). LT image reduction was provided by the basic IO:O pipeline. P60 and LT image subtraction were performed following Fremling et al. (2016), using PS1 images for $griz$ and SDSS for u-band. Values were corrected for Milky Way extinction following Schlafly and Finkbeiner (2011) with $E(B-V) = A_V/R_V = 0.034$ mag, using $R_V = 3.1$ and a Fitzpatrick (1999) extinction law. The full set of photometry is provided in Table 4.6 in Appendix 4.9, and plotted in Figure 4.3.

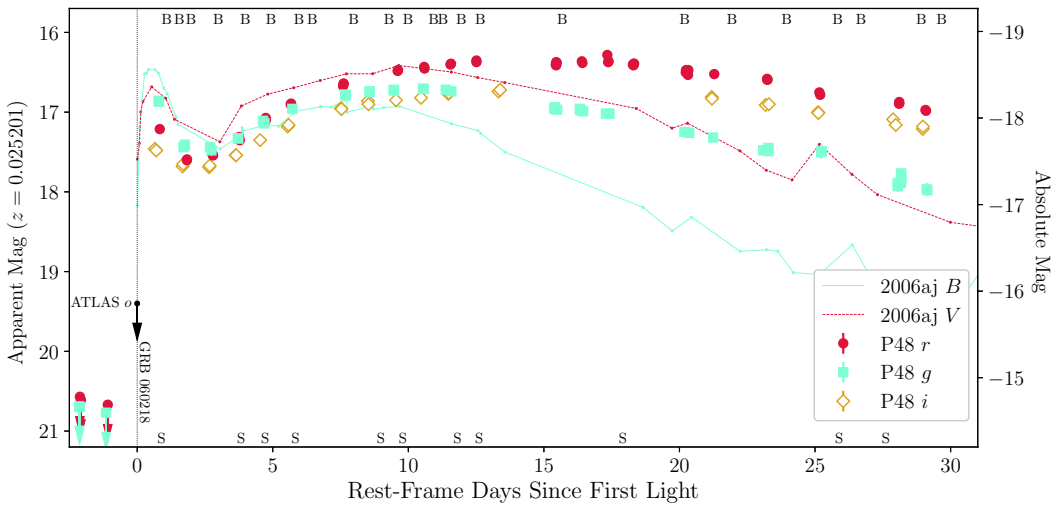

Figure 4.2: g-, r-, and i-band light curves of SN 2020bvc from the ZTF Uniform Depth Survey (ZUDS), and an upper limit from ATLAS. Measurements have been corrected for Milky Way extinction. Epochs of follow-up spectroscopy are indicated with an 'S' along the bottom of the figure. Epochs of blackbody fits (Section 4.3) are indicated with 'B' along the top of the figure. For comparison, we show B and V-band light curves of SN 2006aj ($z = 0.033$) transformed to the redshift of SN 2020bvc ($z = 0.025201$). The SN 2006aj light curve was taken from the Open Supernova Catalog and corrected for Milky Way extinction; the data is originally from Modjaz et al. (2006), Bianco et al. (2014), and Brown et al. (2014). We indicate the relative time of LLGRB 060218 compared to the light curve of SN 2006aj.

Spectroscopy

We obtained 13 ground-based optical spectra using the SEDM, the Andalusia Faint Object Spectrograph and Camera (ALFOSC[9]) on the Nordic Optical Telescope (NOT; Djupvik and Andersen 2010), the Double Beam Spectrograph (DBSP; Oke

[9]http://www.not.iac.es/instruments/alfosc/

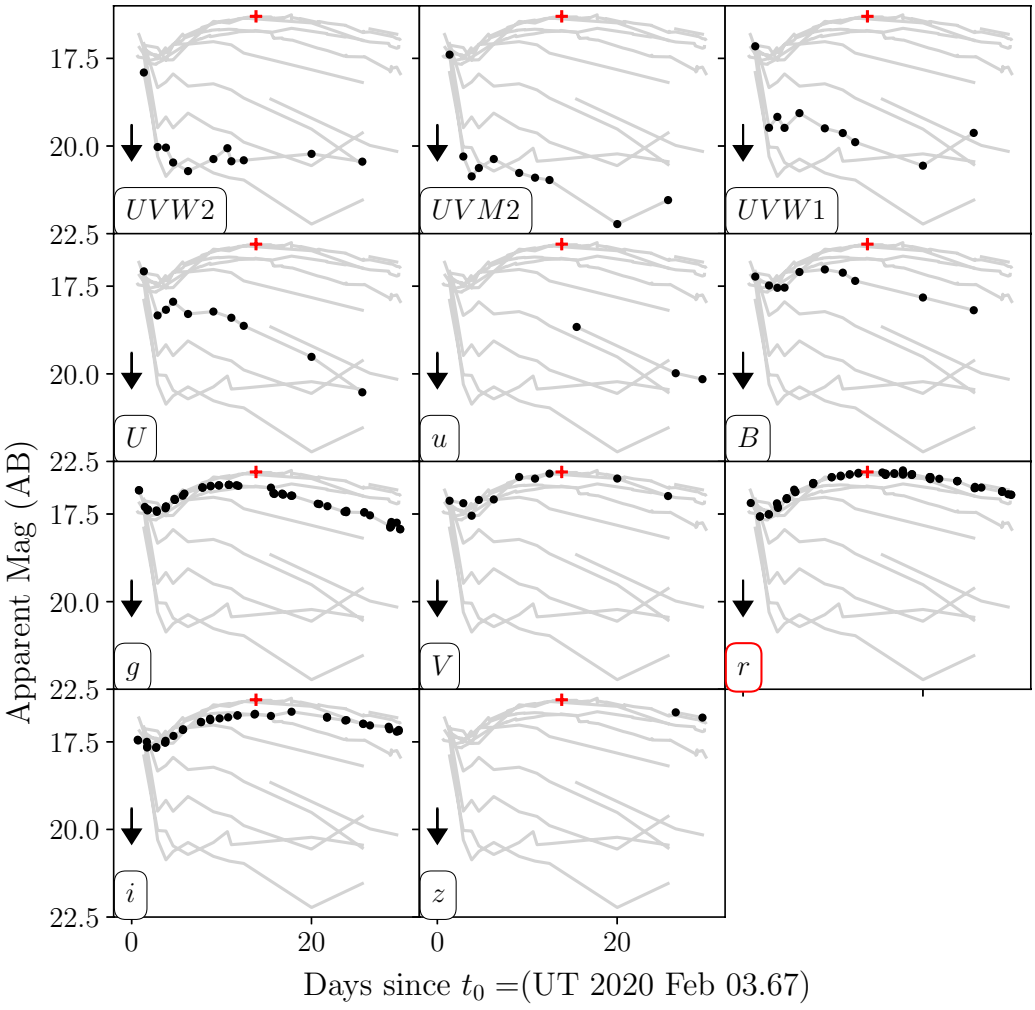

Figure 4.3: UV and optical light curves of SN 2020bvc from *Swift* and ground-based facilities. The arrow marks the last upper limit, which was in ATLAS o-band. The red cross marks the peak of the r-band light curve. The full set of lightcurves are shown as grey lines in the background, and each panel highlights an individual filter in black.

and Gunn 1982) on the 200-inch Hale telescope at Palomar Observatory, SPRAT on LT, and the Low Resolution Imaging Spectrometer (LRIS; Oke et al. 1995) on the Keck I 10-m telescope. The SEDM pipeline is described in Rigault et al. (2019), the SPRAT pipeline is based on the FrodoSpec pipeline (Barnsley et al., 2012), the P200/DBSP pipeline is described in Bellm and Sesar (2016), and the Keck/LRIS pipeline `Lpipe` is described in Perley (2019).

Epochs of spectroscopic observations are marked with 'S' in Figure 4.2, and observation details are provided in Table 4.1. The spectral sequence is shown in Figure 4.4, and discussed in more detail in §4.4. Both raw and smoothed versions of the spectra will be made available on WISeREP.

Table 4.1: Spectroscopic observations of SN 2020bvc. Epochs given since t_0 as defined in §4.2. Velocities are derived from Fe II absorption features as described in §4.4.

Date UTC	Δt (d)	Tel.+Instr.	Exp. Time (s)	$v_{\rm ph}$ (10^4 km s^{-1})
Feb 04.43	0.76	P60+SEDM	1800	–
Feb 07.36	3.7	P60+SEDM	1800	5.1 ± 0.1
Feb 08.25	4.6	LT+SPRAT	600	2.58 ± 0.51
Feb 09.36	5.7	P60+SEDM	1800	–
Feb 12.51	8.8	P200+DBSP	600	1.83 ± 0.32
Feb 13.33	9.7	P60+SEDM	1800	–
Feb 15.33	11.7	P60+SEDM	1800	–
Feb 16.14	12.5	NOT+ALFOSC	1200	1.90 ± 0.25
Feb 21.43	17.7	P60+SEDM	1800	–
Feb 29.42	25.8	P60+SEDM	1800	–
Mar 02.14	27.5	NOT+ALFOSC	1200	–
Mar 17.19	42.6	LT+SPRAT	900	1.72 ± 0.32
Mar 22.50	47.9	Keck1+LRIS	300	1.79 ± 0.39

UV and X-ray Observations

We obtained ten observations of SN 2020bvc[10] with the UV/optical (UVOT; Roming et al. 2005) and X-Ray Telescope (XRT; Burrows et al. 2005) on board the Neil Gehrels *Swift* observatory (Gehrels et al., 2004) under a target-of-opportunity program (PI: Schulze). The first observation was on Feb 05.02 (Δt = 1.35). We also obtained two 10 ks observations with the *Chandra* X-ray Observatory under Director's Discretionary Time (PI A. Ho), one epoch on Feb 16[11] (Δt = 13.2) and one

[10]The target name was PTF13ast, a previous SN hosted by UGC 09379.

[11]ObsId 23171

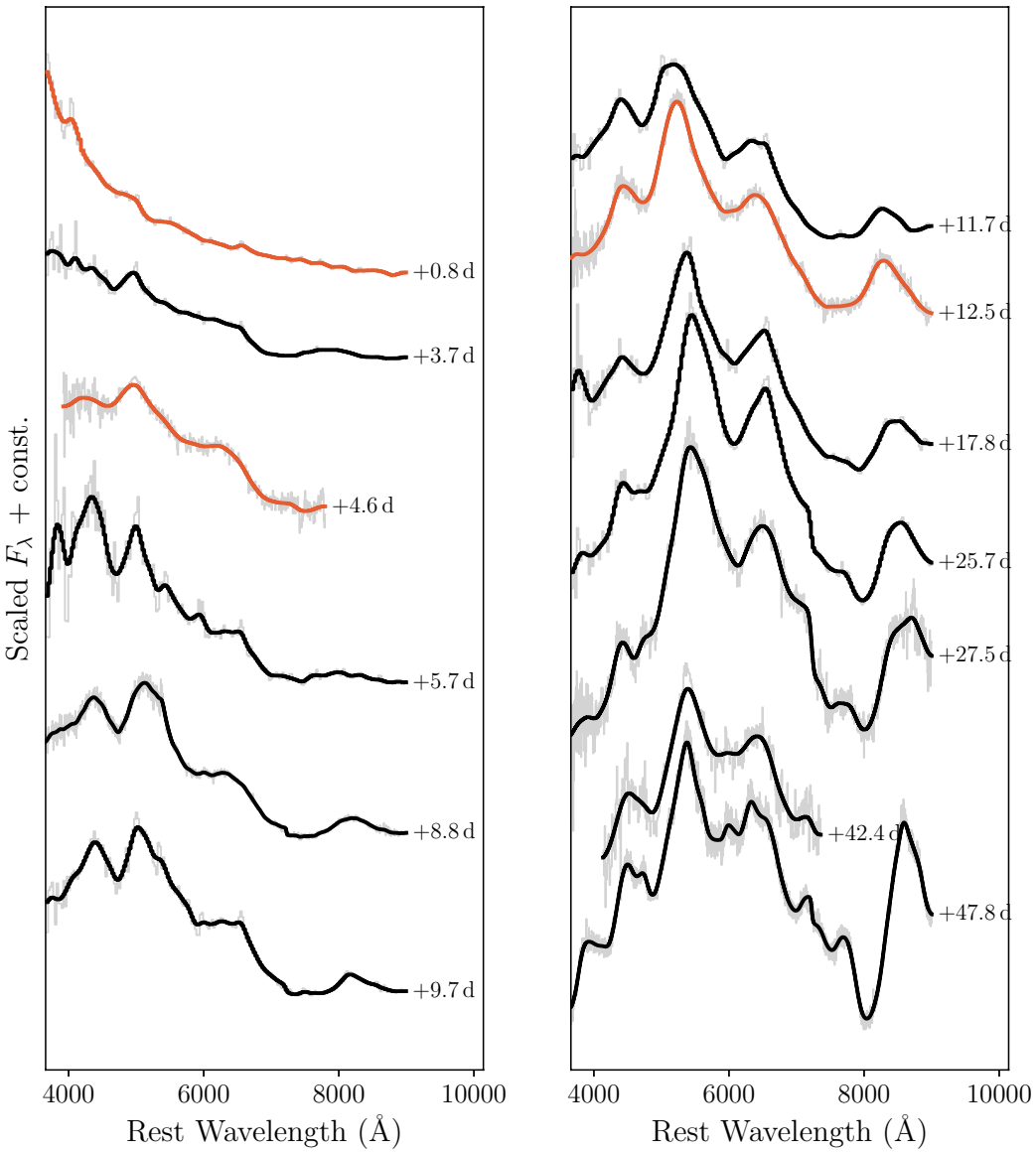

Figure 4.4: Optical spectra of SN 2020bvc. Phase is relative to t_0, defined in §4.2 as the time of last non-detection by ATLAS. The first spectrum is dominated by a blue continuum. By $\Delta t = 5.7$ d the spectrum strongly resembled a Ic-BL SN. The raw spectrum is shown in light grey, and a smoothed spectrum (with host emission lines removed) is overlaid in black. Spectra highlighted in orange are plotted compared to LLGRB-SNe at similar phases in Figure 4.10.

epoch on Feb 29[12] ($\Delta t = 25.4$).

UVOT photometry was performed using the task `UVOTsource` in HEASoft[13] version

[12] ObsId 23172

[13] `http://heasarc.gsfc.nasa.gov/ftools`

6.25 (Blackburn et al., 1999), with a 3″-radius aperture. For host subtraction, a template was constructed from data prior to 2014 Dec 09. Host-subtracted, Milky Way extinction-corrected values are provided in Table 4.6 in Appendix 4.9. XRT data were reduced using the online tool[14] from the *Swift* team (Evans et al., 2007, 2009), with default values except for centroiding, which was turned off, and the binning method, which was set to by observation. *Chandra* data were reduced using the Chandra Interactive Analysis of Observations (CIAO) software package (v4.12; Fruscione et al. 2006).

Stacking the first 2.2 ks of XRT observations (four nightly 0.6 ks exposures) we detected 4 counts with an expected background of 0.16 counts. The resulting count rate is $(2.9^{+3.3}_{-1.9}) \times 10^{-3}$ s^{-1} (90% confidence interval). To convert count rate to flux, we used a hydrogen column density $n_H = 9.90 \times 10^{19}$cm^{-2} (HI4PI Collaboration et al., 2016) and a photon power-law index of $\Gamma = 2$. The resulting unabsorbed 0.3–10 keV flux is $(9.3^{+10.6}_{-6.1}) \times 10^{-14}$ erg s^{-1} cm^{-2}, and the luminosity is $(1.4^{+1.7}_{-0.9}) \times 10^{41}$ erg s^{-1}. From prior *Swift* observations of the position of SN 2020bvc, we measured a 90% upper limit of $< 7.8 \times 10^{-4}$ s^{-1}, suggesting that the emission is not from the host. We note that there is a discrepancy between our *Swift* measurements and those in Izzo et al. (2020), who find a significantly higher XRT flux value.

In the first epoch of our *Chandra* observations, a total of eight counts were detected in a 1″-radius region centered on the source. To measure the background, we set an annulus around the source with an inner radius of 3″ and an outer radius of 10″. The average background was 0.21 arcsec^{-2}, so the expected number of background counts within the source region is 0.65. The 90% confidence interval for the number of detected counts from the source is 3.67–13.16 (Kraft et al., 1991), so we conclude that the detection is significant.

We used CIAO to convert the count rate from the first observation ($(5.9^{+5.1}_{-3.3}) \times 10^{-4}$ s^{-1}) to flux, assuming the same photon index and n_H value as for the *Swift* observations, finding an unabsorbed 0.5–7 keV flux of $(7.2^{+6.3}_{-3.9}) \times 10^{-15}$ erg s^{-1} cm^{-2}. In the second epoch, seven counts were detected, with a count rate of $(5.9^{+5.1}_{-3.2}) \times 10^{-4}$ s^{-1} and an unabsorbed 0.5–7 keV flux of $(7.2^{+6.2}_{-4.0}) \times 10^{-15}$ erg s^{-1} cm^{-2}. The corresponding luminosity is $(1.1^{+1.0}_{-0.6}) \times 10^{40}$ erg s^{-1} in each epoch. In §4.6 we compare the X-ray light curve to that of other Ic-BL SNe. Again, we note a discrepancy with the measurements of Izzo et al. (2020), who find a significantly higher flux value than we do (as shown in their Fig. 2).

[14] https://www.swift.ac.uk/user_objects/

Submillimeter and Radio Observations

As listed in Table 4.2, we obtained eight observations of SN 2020bvc[15] with the Karl G. Jansky Very Large Array (VLA; Perley et al. 2011), while the array was in C configuration. 3C286 was used as the flux density and bandpass calibrator and J1417+4607 as the complex gain calibrator. Data were calibrated using the automated pipeline available in the Common Astronomy Software Applications (CASA; McMullin et al. 2007), with additional flagging performed manually, and imaged[16] using the CLEAN algorithm (Högbom, 1974).

Table 4.2: Submillimeter- and centimeter-wavelength radio observations of SN 2020bvc. The 230 GHz measurement was obtained using the Submillimeter Array (upper limit given as 1σ RMS) and the lower-frequency measurements were obtained using the Very Large Array.

Start Date UTC	Time on-source hr	Δt days	ν GHz	Flux Density (μJy)
Feb 09.42	4.7	5.8	230	< 250
Feb 16.67	0.4	13.0	10	63 ± 6
Feb 20.64	0.4	17.0	6	83 ± 6
Feb 27.64	0.4	24.0	3	111 ± 10
Mar 02.63	0.4	28.0	15	33 ± 4
Mar 09.60	0.4	35.0	10	50 ± 5
Mar 13.59	0.4	39.0	3	106 ± 10
Mar 17.33	0.4	42.7	6	63 ± 6

Motivated by the detection of LLGRB 980425/SN 1998bw (Galama et al., 1998) at 2 mm (Kulkarni et al., 1998) and of LLGRB 171205A/SN 2017iuk at 3 mm and 1 mm (Perley et al., 2017), we also observed[17] SN 2020bvc with the Submillimeter Array (Ho et al., 2004), which was in its compact configuration.[18] The phase and amplitude gain calibrators were J1419+383 and J1310+323, the passband calibrator was 3C84, and the flux calibrator was Uranus. Data were calibrated using the SMA MIR IDL package and imaged using MIRIAD (Sault et al., 1995).

No source was detected by the SMA, with a spectral channel-averaged 1σ RMS of 0.25 mJy. A source was detected at the position of SN 2020bvc in all epochs of VLA

[15]Program VLA/20A-374; PI A. Ho

[16]Cell size was 1/10 of the synthesized beamwidth, field size was the smallest magic number (10×2^n) larger than the number of cells needed to cover the primary beam.

[17]Program 2019B-S026; PI A. Ho

[18]RxA and RxB receivers were tuned to a local-oscillator frequency of 223.556 GHz, providing 16 GHz of overlapping bandwidth: 211.56 GHz–219.56 GHz in the lower side-band and 227.56–235.56 GHz in the upper side-band with a spectral resolution of 140.0 kHz per channel.

observations, and no sources were detected elsewhere in the host galaxy. Using the task `imfit`, we confirm that the radio source is a point source at all frequencies, and that the centroid is at the position of the optical transient. In Figure 4.5 we show the centroid of the radio emission and the position of the optical transient, and that both are offset from the nearby H II region.

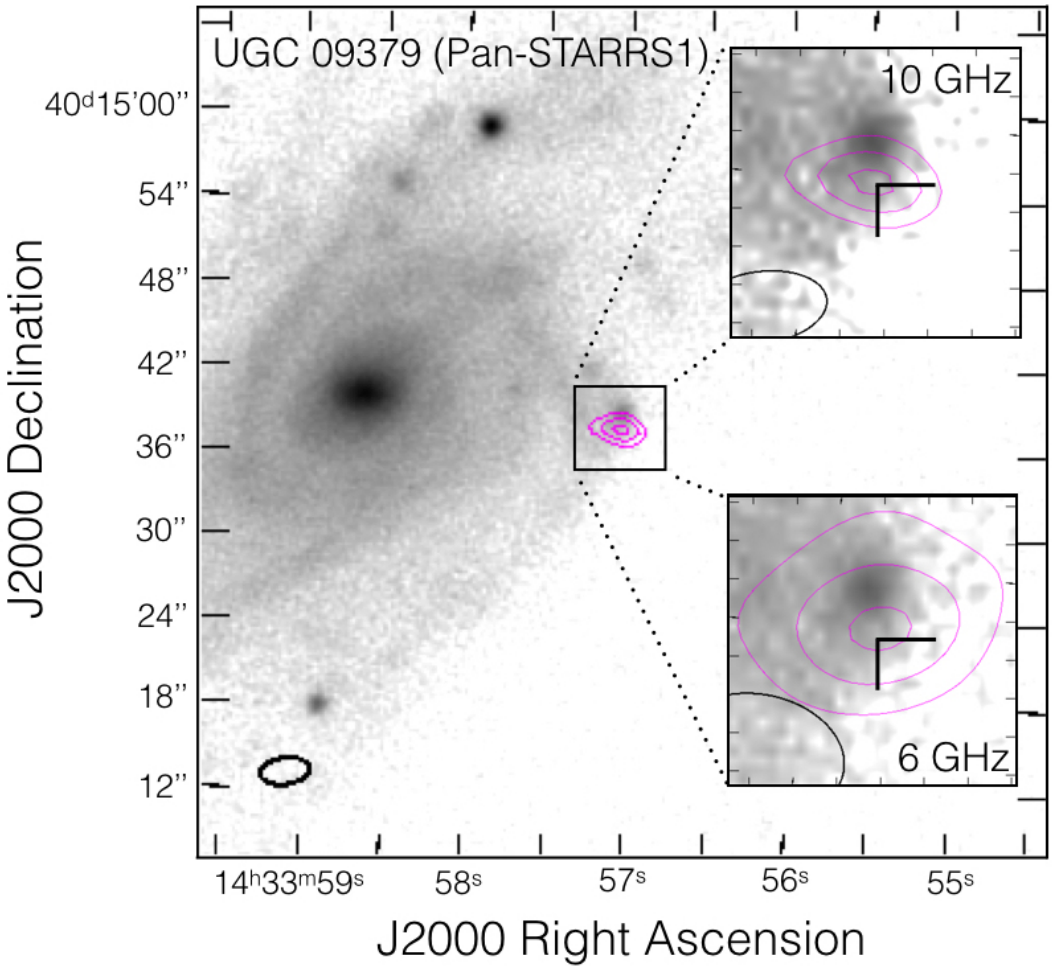

Figure 4.5: Image of the 10GHz and 6 GHz VLA observations of SN2020bvc. The background image of UGC 09379 is from Pan-STARRS1 (Chambers et al., 2016; Flewelling et al., 2016). The radio data is overlaid as contours and the size of the synthesized beam is shown as an ellipse on the bottom left. The position of the optical transient is shown as cross-hairs in the zoom-in panels.

In the first observation ($\Delta t = 13$ d) the 10 GHz peak flux density was $63 \pm 6\,\mu$Jy, corresponding to a luminosity of 1.0×10^{27} erg s^{-1} Hz^{-1} (Ho, 2020). The source was brighter at lower frequencies, and there is marginal (2σ) evidence for fading at 6 GHz ($F_\nu \propto t^{-0.23\pm0.15}$) and 10 GHz ($F_\nu \propto t^{-0.25\pm0.16}$), but no evidence for fading

at 3 GHz. The radio SED is shown in Figure 4.6. In §4.6 we compare the 10 GHz light curve to that of other Ic-BL SNe and use the SED to model the forward shock.

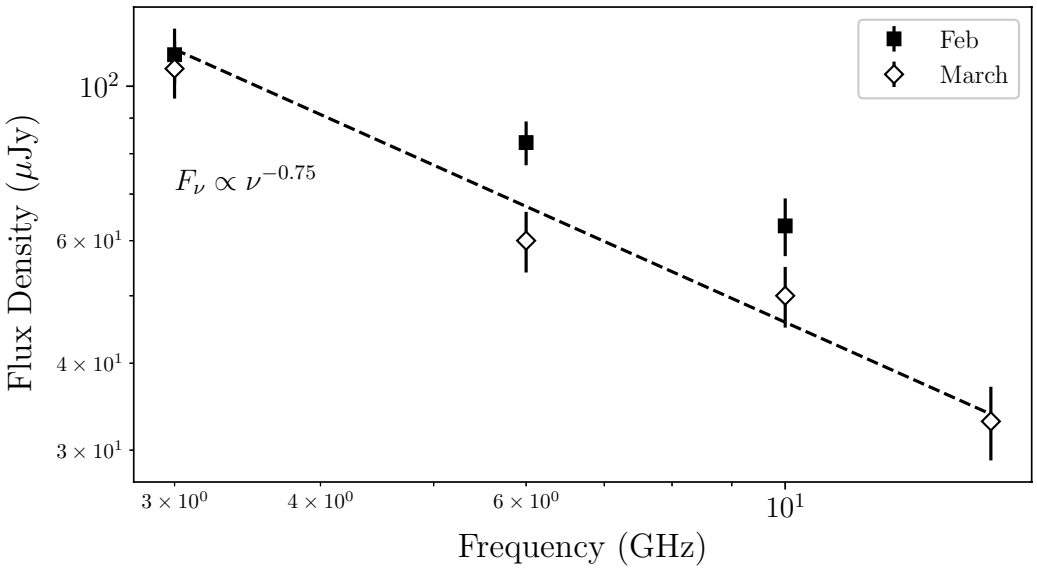

Figure 4.6: Radio SED of SN 2020bvc from VLA observations spanning two months post-explosion.

Search for a Gamma-ray Burst

The third Interplanetary Network (IPN[19]) consists of six spacecraft that provide all-sky full-time monitoring for high-energy bursts. The most sensitive detectors in the IPN are the *Swift* Burst Alert Telescope (BAT; Barthelmy et al. 2005) the *Fermi* Gamma-ray Burst Monitor (GBM; Meegan et al. 2009), and the Konus instrument on the WIND spacecraft (Aptekar et al., 1995).

We searched the *Fermi* GBM Burst Catalog[20] (Gruber et al., 2014; Narayana Bhat et al., 2016; von Kienlin, 2014), the *Fermi*-GBM Subthreshold Trigger list[21] (with reliability flag `!=2`), the *Swift* GRB Archive[22], the IPN master list[23], and the Gamma-Ray Coordinates Network archives[24] for a GRB between the last ZTF non-detection (Feb 02.56) and the first ZTF detection (Feb 04.34). The only bursts consistent with the position of SN 2020bvc were detected by Konus-WIND, but likely arose from

[19] `http://ssl.berkeley.edu/ipn3/index.html`
[20] `https://heasarc.gsfc.nasa.gov/W3Browse/fermi/fermigbrst.html`
[21] `https://gcn.gsfc.nasa.gov/fermi\_gbm\_subthresh\_archive.html`
[22] `https://swift.gsfc.nasa.gov/archive/grb\_table/`
[23] `http://ipn3.ssl.berkeley.edu/masterli.txt`
[24] `https://gcn.gsfc.nasa.gov/gcn3\_archive.html`

an X-ray binary system that was active at the time. We conclude that SN 2020bvc had no detected GRB counterpart.

Given the lack of a detected GRB, we can use the sensitivity of the IPN spacecraft to set a limit on the isotropic-equivalent gamma-ray luminosity $L_{\gamma,\mathrm{iso}}$ of any counterpart. During the time interval of interest (16 h) the position of SN 2020bvc was within the coded field-of-view of the BAT for only 5.25 hours[25]. So, we cannot set a useful limit using BAT.

Fermi/GBM had much better coverage[26], with the position of SN 2020bvc visible most of the time (12.7 h). *Fermi*/GBM is in a low-Earth ($\sim$ 1.5 hr) orbit, and the position was occulted by the Earth for ten minutes per orbit, although in six out of ten of these occultations the position was visible to *Swift*/BAT. During the interval of interest *Fermi* went through five South Atlantic Anomaly passages ranging from 10–30 min in duration. Since SN 2020bvc was visible to GBM most of the time, it is worthwhile to use the GBM sensitivity to place a limit on an accompanying GRB. For a long and soft template[27] the GBM sensitivity is a few $\times 10^{-8}$ erg s^{-1} cm^{-2} (see the discussion in §2.7 of Ho et al. 2019d), so the isotropic equivalent luminosity $L_{\gamma,\mathrm{iso}} \lesssim$ few $\times\, 10^{46}$ erg s^{-1}.

We obtain our most conservative lower limit on accompanying GRB emission using Konus-WIND, which had continuous visibility of the SN 2020bvc position due to its position beyond low-Earth orbit. Assuming a Band spectral model with $\alpha = -1$, $\beta = -2.5$, and $E_{\mathrm{pk}} = 50$–500 keV, the limiting 20–1500 keV peak energy flux for a 2.944 s timescale is 1–2$\times 10^{47}$ erg s^{-1}, corresponding to an upper limit on the peak isotropic-equivalent gamma-ray luminosity of 1.7–3.4$\times 10^{47}$ erg s^{-1}.

For reference, classical GRBs have $L_{\gamma,\mathrm{iso}} > 10^{49.5}$ erg s^{-1} (Cano et al., 2017b). LLGRBs have $L_{\gamma,\mathrm{iso}} < 10^{48.5}$ erg s^{-1}: LLGRB 060218 had $L_{\gamma,\mathrm{iso}} = 2.6\times 10^{46}$ erg s^{-1} (Cano et al., 2017b). However, GBM would be unlikely to detect a GRB like LLGRB 060218 accompanying SN 2006aj because of the low peak energy $E_{\mathrm{pk}} \sim$ 5 keV and long duration $T_{90} \sim 2100$ s (Cano et al., 2017b). Weak signals longer than 100 s look like background evolution to GBM because the detector background can change significantly over 100–200 s. Therefore, although a classical GRB is clearly ruled out (both by the lack of GRB and the lack of strong afterglow emission) we

[25] Search conducted using `https://github.com/lanl/swiftbat\_python`.

[26] Search conducted using `https://github.com/annayqho/HE\_Burst\_Search`

[27] a smoothly broken power law with low-energy index -1.9 and high-energy index -2.7, and $E_{\mathrm{pk}} = 70$ keV

cannot rule out the possibility that SN 2020bvc had prompt emission identical to an LLGRB like 060218.

4.3 Light Curve Analysis

Comparisons to Other Ic-BL SNe

The P48 light curve of SN 2020bvc is shown in Figure 4.2, aligned with the light curve of SN 2006aj. The relative time of LLGRB 060218 is close to the time of the ATLAS non-detection, supporting our choice of the ATLAS non-detection as our estimated epoch of first light t_0. In both SN 2006aj and SN 2020bvc, the first peak fades on the timescale of one day, followed by the rise of the main peak of the light curve. In §4.5 we model the first peak as arising from shock-cooling of extended low-mass material and discuss the implication of the fact that SN 2006aj and SN 2020bvc have similar first peaks.

The second peak has a rise time from first light of 13–15 d in r-band ($M_{r,\mathrm{pk}} = -18.7$) and 10–12 d in g-band ($M_{g,\mathrm{pk}} = -18.3$). In Figure 4.7 we compare the light curve to several LLGRB-SNe. The timescale of the second peak is most similar to that of SN 1998bw in r-band and most similar to SN 2006aj and SN 2017iuk in g-band. The peak luminosity is intermediate to SN 2006aj and SN 1998bw. We discuss the implications in §4.3, when we use the light curve of the main peak to measure properties of the explosion such as the nickel mass, ejecta mass, and kinetic energy.

Blackbody Fits

We fit blackbody functions to the photometry of SN 2020bvc in order to measure the evolution of the bolometric luminosity L_{bol}, photospheric radius R_{ph}, and effective temperature T_{eff}. First we manually selected 23 time bins as close as possible to epochs with observations in multiple filters. We binned the P48 light curve such that observations in a single band clustered within a few hours were averaged together. For each time bin, we constructed an SED by linearly interpolating the UV and optical light curves shown in Figure 4.3. For each SED, we used the nonlinear least squares routine of `curve_fit` in `scipy` (Virtanen et al., 2020) to fit a blackbody. To estimate uncertainties, we performed a Monte Carlo simulation with 600 realizations of the data. The size of the error bar on each point is a 30% fractional systematic uncertainty, chosen to obtain a combined $\chi^2/\mathrm{dof} \approx 1$ across all epochs.

The fits are shown in Figure 4.8. The best-fit parameters are listed in Table 4.3 and plotted in Figure 4.9. L_{bol} peaks after $\Delta t \approx 12$–14 d at $L_{\mathrm{bol,pk}} = 4 \times 10^{42}\,\mathrm{erg\,s^{-1}}$, and R_{ph} increases by $v_{\mathrm{ph}} \approx 0.06\,c$, which is consistent with the 18,000 $\mathrm{km\,s^{-1}}$ that

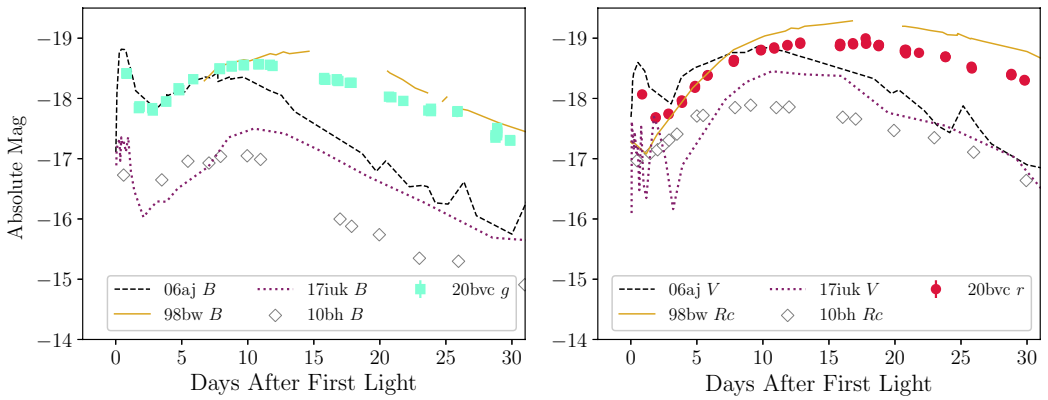

Figure 4.7: Comparison of the light curve of SN 2020bvc to nearby LLGRB-SNe, shifted to a common redshift. The SN 1998bw light curve was taken from Table 2 of Clocchiatti et al. (2011), which uses data from Galama et al. (1998) and Sollerman et al. (2002), and corrected for Milky Way extinction. The SN 2006aj light curve was taken from the Open SN catalog and corrected for MW extinction, with original data from Modjaz et al. (2006), Bianco et al. (2014), and Brown et al. (2014). The SN 2010bh data were taken as-is from Cano et al. (2011). The SN 2017iuk data were taken from D'Elia et al. (2018) and corrected for MW extinction.

we measure from the spectra in §4.4. Using trapezoidal integration we find a total radiated energy $E_{\rm rad} = 7.1 \times 10^{48}$ erg.

In the top panel of Figure 4.9 we show the evolution of $L_{\rm bol}$ compared to nearby LLGRB-SNe. For the second (main) peak, we chose bolometric light curves constructed using similar filters: UBVRI for SN 2006aj and SN 1998bw, and BVRI for SN 2010bh (Cano, 2013). We could not find a similar bolometric light curve for SN 2017iuk, so we used $L_{\rm bol}$ from the spectral modeling of Izzo et al. (2019) and caution that this is not a direct comparison. For SN 2006aj we used an early measurement of the bolometric luminosity from the UVOT data (Campana et al., 2006). SN 2020bvc and SN 2017iuk have a similarly fast-declining first peak; early detailed UV observations were not obtained for SN 1998bw and SN 2010bh. Overall, SN 1998bw is the most luminous LLGRB-SN, followed by SN 2006aj and SN 2020bvc, which are similar to one another. SN 2010bh is significantly less luminous. We revisit these comparisons when we calculate the explosion parameters of SN 2020bvc in §4.5.

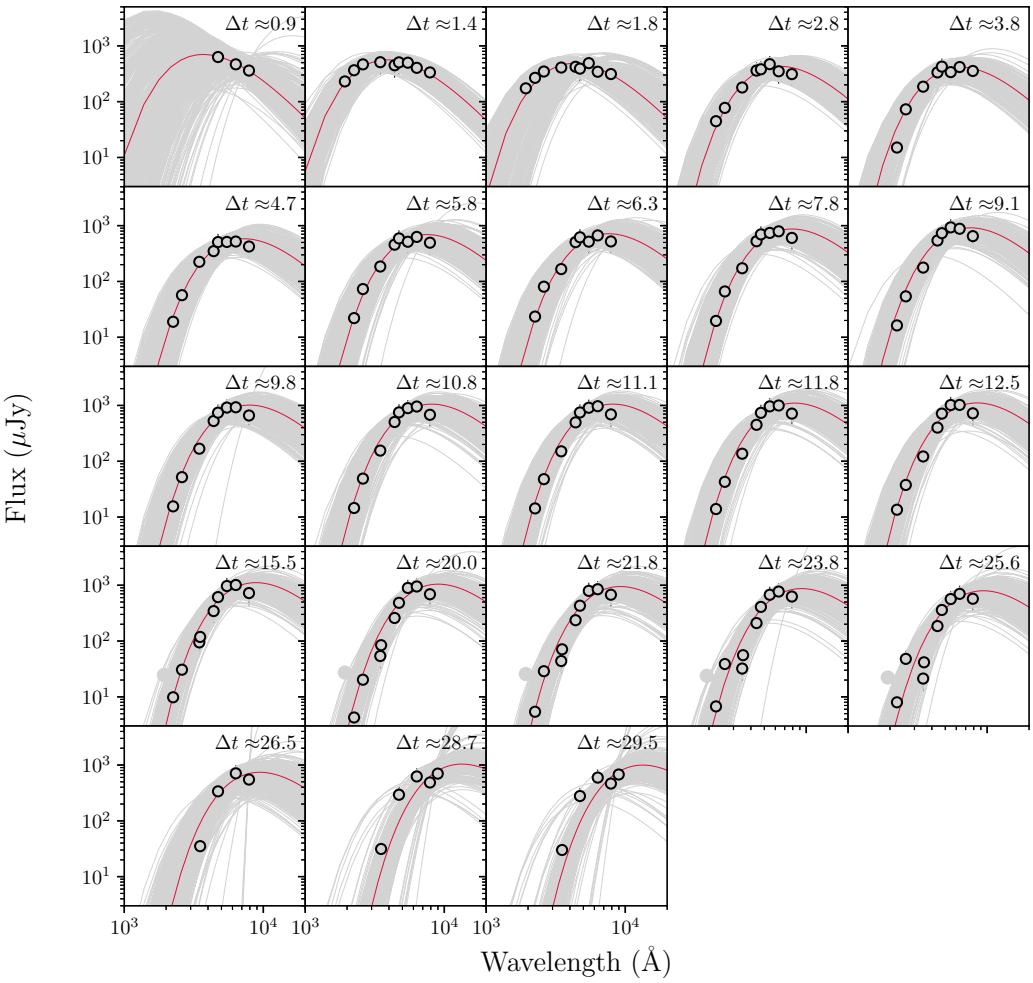

Figure 4.8: Blackbody fits to optical and *Swift*/UVOT photometry of SN 2020bvc. Photometry has been interpolated onto common epochs as described in §4.3. Fit was run through a Monte Carlo with 600 realizations of the data. Individual fits are shown as thin grey lines; dispersion corresponds to overall uncertainties in the fits.

4.4 Spectroscopic Properties

Spectroscopic Evolution and Comparisons

As outlined in §4.2, we obtained 13 spectra of SN 2020bvc in the 50 days following discovery, shown in Figure 4.4. Here we discuss the spectroscopic evolution in more detail and compare it to LLGRB-SNe.

The first spectrum (Δt = 0.7 d) is shown in the top panel of Figure 4.10, together with two blackbody fits. The spectrum is best described by a blackbody with $L_{\rm bol} = (5.62 \pm 0.25) \times 10^{42}\,{\rm erg\,s^{-1}}$, $T_{\rm eff} = (13.21 \pm 0.27) \times 10^{3}\,{\rm K}$, and $R_{\rm ph} = (5.09 \pm 0.10) \times 10^{14}\,{\rm cm}$. Here we are reporting statistical errors on the fit, but

Table 4.3: Blackbody evolution of SN 2020bvc. The first epoch is from fitting the optical spectrum (§4.4). The remaining epochs are from fitting multi-band photometry (§4.3).

Δt (d)	$L_{\rm bol}$ (10^{42} erg s^{-1})	$T_{\rm eff}$ (10^3 K)	$R_{\rm ph}$ (10^{14} cm)
0.67	5.6 ± 0.3	13.2 ± 0.3	5.1 ± 0.1
0.9	$5.4^{+6.2}_{-2.7}$	$13.3^{+4.6}_{-3.8}$	$5.0^{+2.0}_{-1.2}$
1.4	$3.8^{+0.7}_{-0.4}$	$12.2^{+1.2}_{-1.2}$	$4.9^{+0.9}_{-0.7}$
1.8	$3.1^{+0.5}_{-0.9}$	$11.3^{+1.4}_{-2.3}$	$5.1^{+2.1}_{-0.9}$
2.8	$1.8^{+0.2}_{-0.3}$	$7.6^{+1.0}_{-1.2}$	$8.9^{+2.9}_{-1.9}$
3.8	$1.8^{+0.2}_{-0.2}$	$7.4^{+0.9}_{-0.6}$	$9.1^{+1.8}_{-1.7}$
4.7	$2.1^{+0.3}_{-0.2}$	$6.8^{+1.3}_{-0.9}$	$11.7^{+4.6}_{-3.5}$
5.8	$2.4^{+0.3}_{-0.3}$	$6.6^{+1.1}_{-1.0}$	$13.6^{+5.8}_{-3.8}$
6.3	$2.5^{+0.3}_{-0.3}$	$6.5^{+1.1}_{-1.1}$	$14.5^{+6.6}_{-4.2}$
7.8	$3.0^{+0.4}_{-0.4}$	$6.3^{+0.7}_{-1.0}$	$16.3^{+7.1}_{-3.0}$
9.1	$3.3^{+0.4}_{-0.5}$	$6.4^{+0.7}_{-0.5}$	$16.6^{+3.8}_{-3.9}$
9.8	$3.4^{+0.4}_{-0.4}$	$6.1^{+0.6}_{-0.9}$	$18.7^{+6.5}_{-3.6}$
10.8	$3.4^{+0.4}_{-0.4}$	$5.9^{+0.6}_{-0.9}$	$19.9^{+6.5}_{-3.9}$
11.1	$3.5^{+0.4}_{-0.4}$	$5.9^{+0.8}_{-0.8}$	$20.5^{+6.1}_{-4.7}$
11.8	$3.5^{+0.4}_{-0.5}$	$5.7^{+0.7}_{-0.7}$	$21.6^{+5.4}_{-4.5}$
12.5	$3.6^{+0.4}_{-0.6}$	$5.6^{+0.6}_{-0.6}$	$22.2^{+5.3}_{-3.7}$
15.5	$3.4^{+0.5}_{-0.5}$	$5.4^{+0.6}_{-0.5}$	$23.2^{+5.0}_{-4.6}$
20.0	$3.1^{+0.4}_{-0.5}$	$5.3^{+0.4}_{-0.4}$	$23.3^{+4.6}_{-4.1}$
21.8	$2.8^{+0.4}_{-0.5}$	$5.2^{+0.4}_{-0.3}$	$23.5^{+3.7}_{-4.3}$
23.8	$2.6^{+0.4}_{-0.5}$	$5.2^{+0.5}_{-0.3}$	$22.4^{+3.8}_{-4.4}$
25.6	$2.3^{+0.3}_{-0.4}$	$5.1^{+0.4}_{-0.3}$	$21.6^{+3.6}_{-3.9}$
26.5	$2.2^{+0.4}_{-0.4}$	$5.1^{+0.6}_{-0.3}$	$21.2^{+4.6}_{-5.0}$
28.7	$2.1^{+0.3}_{-0.3}$	$3.6^{+0.2}_{-0.2}$	$40.7^{+7.3}_{-4.1}$
29.5	$2.0^{+0.4}_{-0.3}$	$3.6^{+0.2}_{-0.2}$	$40.6^{+6.9}_{-4.9}$

there is also considerable systematic uncertainty due to being on the Rayleigh-Jeans tail. We repeated the fit fixing $T_{\rm eff} = 20,000$ K, and found $R = 3.4 \times 10^{14}$ cm and $L = 1.3 \times 10^{43}$ erg s^{-1}. Assuming that the value of $R_{\rm ph} \approx 5 \times 10^{14}$ cm at $\Delta t = 0.7$ d is much larger than the value of $R_{\rm ph}$ at t_0, we can estimate that the mean velocity until 0.7 d is 5×10^{14} cm/0.7 d = 0.3 c. Taking the last ZTF non-detection as t_0, the mean velocity is reduced to 5×10^{14} cm/1.8 d = 0.1 c.

For comparison, in the top panel of Figure 4.10 we show a higher-resolution spectrum obtained at $\Delta t = 1.9$ and presented in Izzo et al. (2020). We mark the Fe II and Ca II at $v_{\rm exp} = 70,000$ km s^{-1} that Izzo et al. (2020) identified in their analysis, which are not clearly distinguishable in the SEDM spectrum. We also show early spectra

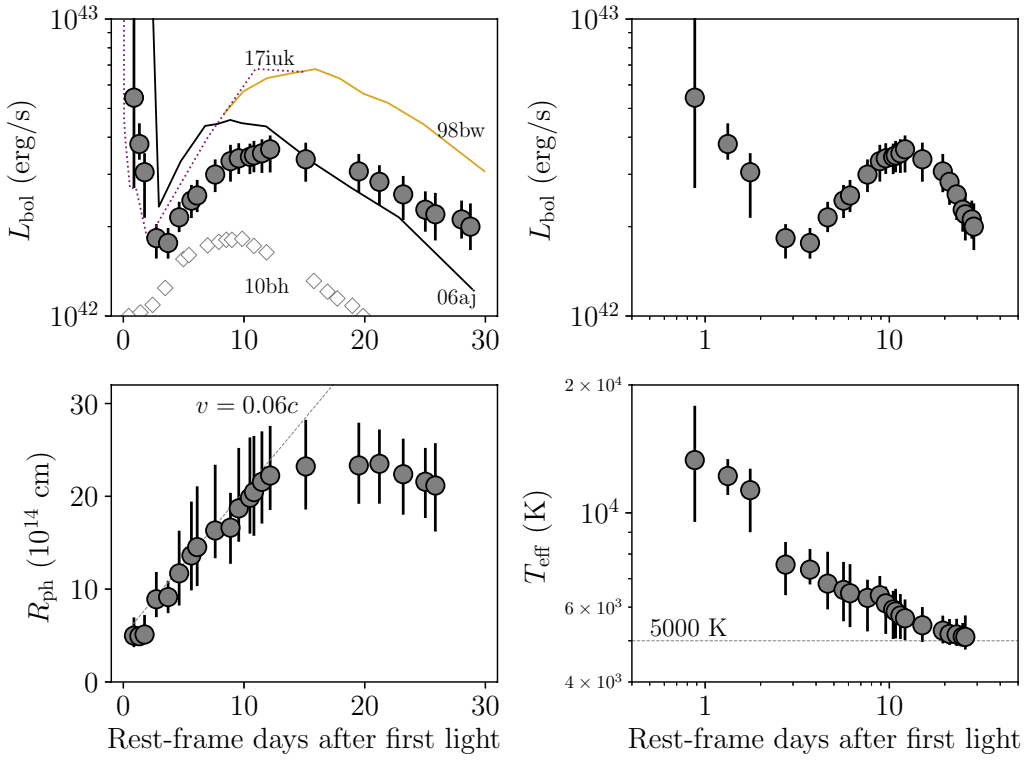

Figure 4.9: Blackbody evolution of SN 2020bvc. Top panel: bolometric light curve compared to LLGRB-SNe: SN 2006aj and SN 1998bw (UBVRI; Cano 2013), SN 2010bh (BVRI; Cano 2013), SN 2017iuk (spectral modeling; Izzo et al. 2019). We add early $L_{\rm bol}$ measurements of SN 2006aj from Campana et al. (2006). Second panel: bolometric light curve in log-log space. Third panel: photospheric radius, with a dotted line indicating $v = 18,000\,{\rm km\,s^{-1}}$. Bottom panel: effective temperature, with a horizontal line marking 5000 K, the recombination temperature of carbon and oxygen.

of LLGRB-SNe: a spectrum of LLGRB 171205A/SN 2017iuk at $\Delta t = 1.5$ hr from Izzo et al. (2019) and a spectrum of LLGRB 060218/SN 2006aj at $\Delta t = 2.6$ d from Fatkhullin et al. (2006). Both spectra are dominated by continuum, with a broad absorption feature near 5900 Å that is not clearly seen in the early spectrum of SN 2020bvc.

The next spectrum of SN 2020bvc was obtained at $\Delta t = 3.7$ d, which we show in the middle panel of Figure 4.10. A broad absorption feature is present at 7300 Å, which in Figure 4.4 appears to shift redward with time. For comparison, and to assist with identification of this feature, we compare the spectrum to two LLGRB-SN spectra obtained at a similar epoch, LLGRB 060218/SN 2006aj (Fatkhullin et al., 2006) and LLGRB 171205A/SN 2017iuk (Izzo et al., 2019). The spectrum of

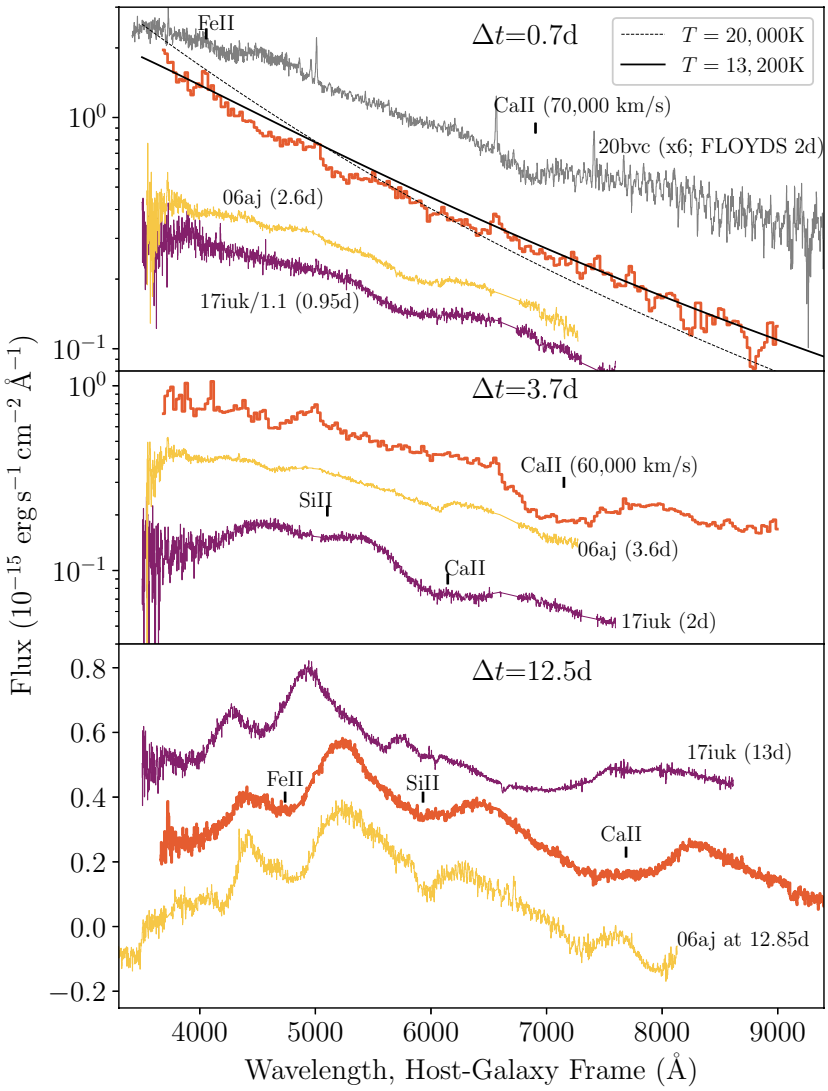

Figure 4.10: Spectra of SN 2020bvc compared to spectra of two LLGRB-SNe, SN 2017iuk (Izzo et al., 2019) and SN 2006aj (Fatkhullin et al., 2006; Modjaz et al., 2006), at similar epochs. In the top panel, we show the blackbody fits described in §4.4, and the spectrum of SN 2020bvc at $\Delta t = 1.9$ d (Hiramatsu et al., 2020) obtained by the FLOYDS-N instrument on Faulkes Telescope North (Brown et al., 2013). The identification of Fe II and Ca II at 70,000 km s^{-1} is from Izzo et al. (2020).

SN 2020bvc most closely resembles that of SN 2017iuk. We show two features in the SN 2017iuk spectrum identified by Izzo et al. (2019), Ca II and Si II at very high velocities (105,000 km s^{-1} for Ca II). Based on the similarity between the spectra, we also attribute the broad absorption feature to Ca II. To measure the expansion velocity we measure the minimum of the absorption trough, finding $v_{\rm exp} = 60,000\,{\rm km\,s^{-1}}$ (based on the Gaussian center) and a full-width at half-maximum (FWHM) of $0.16\,c$, or 48,000 km s^{-1}. The spectrum of SN 2006aj shows hints of broad absorption features at similar wavelengths, but the lack of coverage on the red side makes it difficult to confirm the Ca II absorption.

After 3.7 d, the spectra of SN 2020bvc can be readily classified as Type Ic-BL. A spectrum of SN 2020bvc near peak optical light ($\Delta t = 13$ d) is shown in the bottom panel of Figure 4.10 compared to SN 2006aj and SN 2017iuk at a similar epoch. The Si II and Ca II absorption lines are clearly broader in the spectrum of SN 2020bvc than in the spectrum of SN 2006aj, although the centroids are at a similar wavelength, suggesting that the expansion velocities are similar. The absorption lines are at a higher expansion velocity in the spectrum of SN 2017iuk than in the spectrum of SN 2020bvc, although they do not appear broader.

Velocity Estimates from Fe II Features

For each spectrum after $\Delta t = 5$ d, we used publicly available code[28] from Modjaz et al. (2016) to measure the absorption (blueshift) velocities of the blended Fe II features at $\lambda\lambda$4924,5018,5169, which are a proxy for photospheric velocity. The resulting velocities are listed in Table 4.1. Note that the fit did not converge for the NOT spectrum on Mar 02.14, and that we were unable to obtain satisfactory fits for the SEDM spectra.

In Figure 4.11 we compare the velocity evolution of SN 2020bvc to that of nearby LLGRB-SNe. Only SN 2017iuk and SN 2020bvc have spectral velocity estimates at early times, and both exhibit a steep drop during the transition from the first to the second optical peak. During the second peak, the velocities of all but SN 2010bh are similar to the velocities of Ic-BL SNe associated with GRBs, which are systematically higher than the velocities of Ic-BL SNe lacking associated GRBs (Modjaz et al., 2016).

[28] https://github.com/nyusngroup/SESNspectraLib

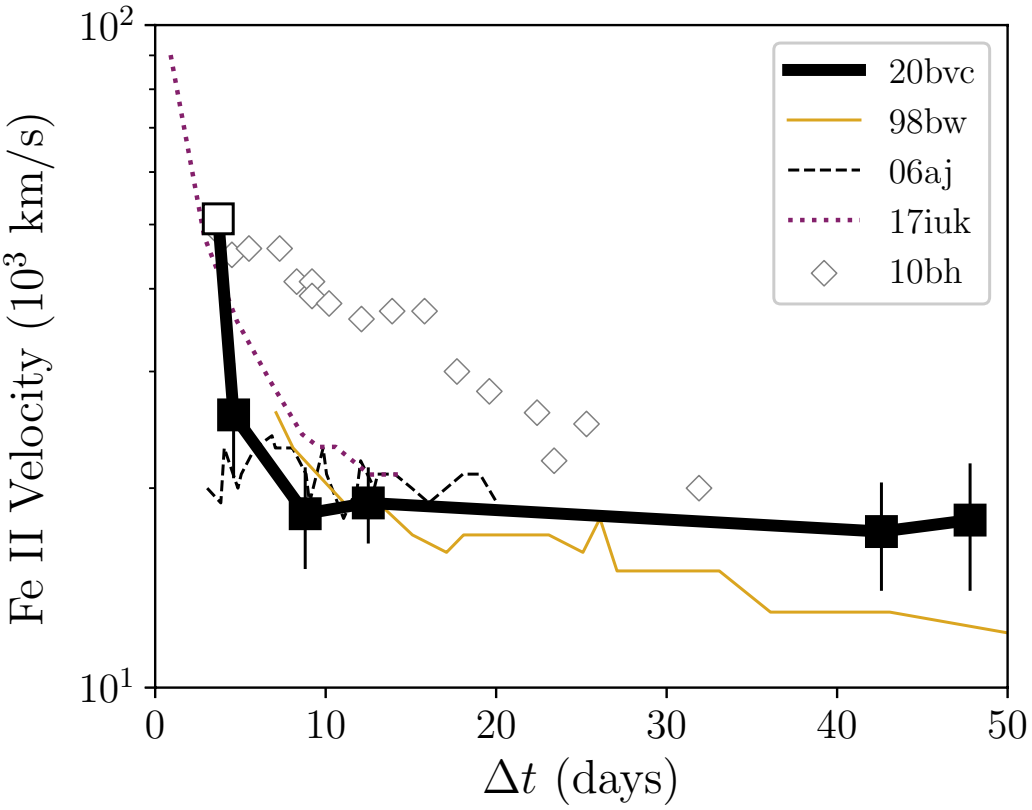

Figure 4.11: Velocity of SN 2020bvc (black) compared to LLGRB-SNe. Open symbol corresponds to Ca II velocity measured from absorption-line minimum, and closed symbols correspond to velocities measured by fitting the Fe II absorption complex. Velocities come from Izzo et al. (2019) for SN 2017iuk and Modjaz et al. (2016) for all other SNe. Modjaz et al. (2016) reports velocities from the peak of the optical light curve, so we shifted to time since GRB using Galama et al. (1998) for SN 1998bw, Campana et al. (2006) for SN 2006aj, and Bufano et al. (2012) for SN 2010bh.

4.5 Modeling the Light Curve

Double-peaked optical light curves have been observed in all types of stripped-envelope SNe: Type Ic-BL (with SN 2006aj as the prime example), Type Ic (De et al., 2018; Taddia et al., 2016), Type Ib (Chevalier and Fransson, 2008; Mazzali et al., 2008; Modjaz et al., 2009), and Type IIb (Arcavi et al., 2011; Bersten et al., 2018; Bersten et al., 2012; Fremling et al., 2019b). The leading explanation for double-peaked light curves in these systems is that the progenitor has as non-standard structure, with a compact core of mass M_c and low-mass material with $M_e \ll M_c$ extending out to a large radius R_e (Bersten et al., 2012; Nakar and Piro, 2014; Piro, 2015), although Sapir and Waxman (2017) have argued that a non-standard envelope

structure is not required.

After core-collapse, a shockwave runs through the thin outer layer, and in its wake the layer cools (the "post-shock cooling" or "cooling-envelope" phase), producing a short-duration first peak. The remnant is heated from within by the radioactive decay of ^{56}Ni to ^{56}Co, which dominates the light curve after a few days, producing the second peak.

In Type IIb SNe, the extended material is thought to be the stellar envelope. By contrast, Type Ic-BL SNe such as SN 2006aj and SN 2020bvc are thought to arise from compact stars, so the envelope is more likely to be extended material that was ejected in a mass-loss episode (Smith, 2014). It is unknown why Ic-BL progenitors would undergo late-stage eruptive mass-loss; possibilities include binary interaction (Chevalier, 2012) and gravity waves excited by late-stage convection in the core (Quataert and Shiode, 2012).

Motivated by the similarity between SN 2006aj and SN 2020bvc, we assume that the light curve of SN 2020bvc is also powered by these two components, and calculate the properties of the explosion and the extended material.

Nickel Decay

We use the luminosity and width of the second peak of the SN 2020bvc light curve to estimate the nickel mass $M_{\rm Ni}$ and the ejecta mass $M_{\rm ej}$, by fitting an Arnett model (Arnett, 1982). Building on the Arnett model, Valenti et al. (2008) give an analytic formula for $L_{\rm bol}(t)$ as a function of $M_{\rm Ni}$ and a width parameter τ_m, which assumes complete trapping of gamma-rays (not significant in the regime we deal with here). Fitting the Valenti et al. (2008) light curve to the bolometric light curve from 4.3, we obtain $M_{\rm Ni} = 0.13 \pm 0.01$ and $\tau_m = 8.9 \pm 0.4$. The fit is shown in Figure 4.12.

The value of $M_{\rm Ni}$ we obtain for SN 2020bvc is similar to literature estimates for SN 2006aj ($M_{\rm Ni} = 0.20 \pm 0.10\,M_\odot$; Cano et al. 2017b) and smaller than the nickel mass of SN 1998bw (0.3–0.6 $M_\odot$; Cano et al. 2017b), which is consistent with the relative luminosity of the bolometric light curves (Figure 4.9).

Next, we solve for $M_{\rm ej}$ and the explosion energy E_k using Equations (2) and (3) in Lyman et al. (2016). Taking the opacity $\kappa = 0.1\,{\rm cm^2\,g^{-1}}$ (close to the value found from spectral modeling of Ic-BL SNe near peak; Mazzali et al. 2000) and $v_{\rm ph} = 18,000\,{\rm km\,s^{-1}}$, we find $M_{\rm ej} = 2.2 \pm 0.4\,M_\odot$, where the uncertainty is dominated by the 20% uncertainty on $v_{\rm ph}$. The resulting kinetic energy is $E_K = 0.5\,M_{\rm ej}\,v_{\rm ph}^2 =\approx$

$7.1 \pm 2.8 \times 10^{51}$ erg. The explosion parameters for SN 2020bvc are summarized in Table 4.4.

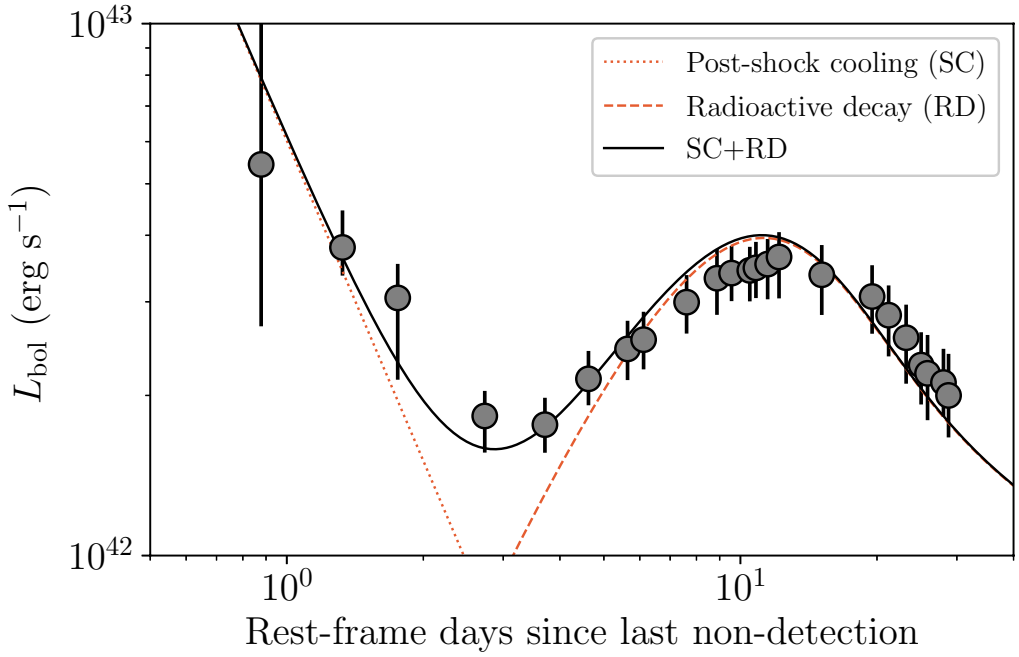

Figure 4.12: Bolometric luminosity evolution of SN 2020bvc. The shock-cooling model from §4.5 is shown as a dotted orange line. The radioactive decay model from §4.5 is shown as a dashed line. The black line is the sum of the two models.

Table 4.4: Explosion properties of SN 2020bvc

Parameter	Value
E_k (10^{51} erg)	7.1 ± 2.8
$M_{\rm ej}$ ($M_\odot$)	2.2 ± 0.4
$M_{\rm Ni}$ ($M_\odot$)	0.13 ± 0.01
M_e ($M_\odot$)	< 0.01
R_e (cm)	$> 10^{12}$

Shock cooling

The mass M_e and radius R_e of the material surrounding the progenitor can be estimated using the timescale and luminosity of the first peak. In §4.4 we measured a lower limit on the peak bolometric luminosity $L_{\rm bol} > 5.62 \times 10^{42}\,{\rm erg\,s^{-1}}$, with an upper limit on the time to peak of 0.7 d. From our calculation in Appendix 4.9, we obtain an upper limit on $M_e < 10^{-2}\,M_\odot$ and a lower limit on $R_e > 10^{12}$cm. In Figure 4.12 we show that the bolometric light curve is well described by the

sum of the shock cooling model from Appendix 4.9 with $R_e = 4 \times 10^{12}$ cm and $M_e = 10^{-2}\,M_\odot$, and a ^{56}Ni-powered light curve with the properties calculated in §4.5. The shock-cooling light curve only describes the decline after peak; we do not attempt to model the rise. The properties of the ambient material are summarized in Table 4.4.

The values of M_e and R_e we measured for SN 2020bvc are consistent with what was inferred for SN 2006aj, which had much more detailed early UV and optical data: $M_e = 4 \times 10^{-3}\,M_\odot$ and $R_e = 9 \times 10^{12}$ cm (Irwin and Chevalier, 2016). A similar low-mass shell was inferred for the Ic-BL SN 2018gep (Ho et al., 2019d): in that case, the shell ($M_e = 0.02\,M_\odot$) was at a larger radius ($R_e = 3 \times 10^{14}$ cm), which prolonged the shock-interaction peak and blended it with the ^{56}Ni-powered peak. A similarly low-mass, large-radius shell may also explain the luminous light curve of the Ic-BL SN iPTF16asu (Whitesides et al., 2017). With these four events, we may be seeing a continuum in shell properties around Ic-BL SNe, resulting from different mass-loss behavior shortly prior to core-collapse (Smith, 2014).

4.6 Modeling the Fast Ejecta

One of the key features of LLGRB 060218 / SN 2006aj was radio and X-ray emission that peaked earlier and was more luminous than that of ordinary CC SNe. Here we compare the early (1–50 d) radio and X-ray properties of SN 2020bvc to that of SN 2006aj and other LLGRB-SNe.

Radio Emission

We have several reasons to believe that the radio emission is dominated by the transient rather than by the host galaxy. First, the flux density is observed to decline at 6 GHz and 10 GHz, albeit marginally. Second, in §4.2 we found that the source is unresolved (i.e., a point source) at all frequencies. Third, at all frequencies the centroid of the radio source is consistent with the position of the optical transient, and there is no other radio source detected in the vicinity of the galaxy. (There is a nearby H II region, but this would produce free-free emission and therefore a flat spectral index, which is inconsistent with our observations.) Late-time radio observations will be used to be secure, and to subtract any host contribution.

If the emission at 3 GHz were entirely from the underlying host-galaxy region (the synthesized beamwidth at this frequency is $7''$) the flux density at this frequency can be used to estimate a star-formation rate of $0.2\,M_\odot\,\mathrm{yr}^{-1}$ using the prescription in (Greiner et al., 2016; Murphy et al., 2011):

$$\left(\frac{\mathrm{SFR_{Radio}}}{M_\odot\,\mathrm{yr}^{-1}}\right) = 0.059\left(\frac{F_\nu}{\mu\mathrm{Jy}}\right)(1+z)^{-(\alpha+1)} \times \left(\frac{D_L}{\mathrm{Gpc}}\right)^2\left(\frac{\nu}{\mathrm{GHz}}\right)^{-\alpha}, \tag{4.1}$$

where we use $F_\nu = 120\,\mu$Jy, $\nu = 3$ GHz, and $\alpha = -0.9$ for $F_\nu \propto \nu^\alpha$.

For now, we assume that the radio emission is primarily from the transient. In Figure 4.13 we show the 10 GHz radio light curve of SN 2020bvc. The luminosity is similar to that of SN 2006aj and SN 2010bh, and significantly fainter than that of SN 2017iuk, SN 1998bw. In Ho et al. (2019c) we found that the radio luminosity is directly proportional to U/R, the (thermalized) energy of the blastwave divided by the shock radius. So, the lower radio luminosity of SN 2006aj and SN 2020bvc could correspond to a lower explosion energy. This is consistent with the finding in §4.5 that SN 2006aj and SN 2020bvc have a similar kinetic energy, which is significantly smaller than the kinetic energy of SN 1998bw and SN 2017iuk.

From the radio SED, we estimate that the peak frequency is < 3 GHz at $\Delta t = 24$ d, with a peak flux density $> 113\,\mu$Jy. We use these values and the framework described in Chevalier (1998) to estimate properties of the forward shock and ambient medium. We list the results in Table 4.5, discuss the implications here, and provide the calculation in Appendix 4.9. In Figure 4.14 we show the peak frequency and time compared to the peak luminosity, with lines indicating how these values correspond to ambient density (mass-loss rate) and energy.

Table 4.5: Properties of the forward shock in SN 2020bvc derived from radio and X-ray observations at $\Delta t = 24$ d

Parameter	Value
$\nu_a = \nu_p$ (GHz)	< 3
$F_{\nu,p}$ (μJy)	> 110
R (cm)	$> 1.7 \times 10^{16}$
v/c	> 0.3
B (G)	< 0.34
U (erg)	1.5×10^{47}
n_e (cm^{-3})	160
ν_c (Hz)	1.4×10^{13}

First, we find a forward shock radius of 1.7×10^{16} cm, implying a mean velocity up to 24 d of ($\Gamma\beta > 0.28$). As shown in Figure 4.14, the lower limit on the velocity we

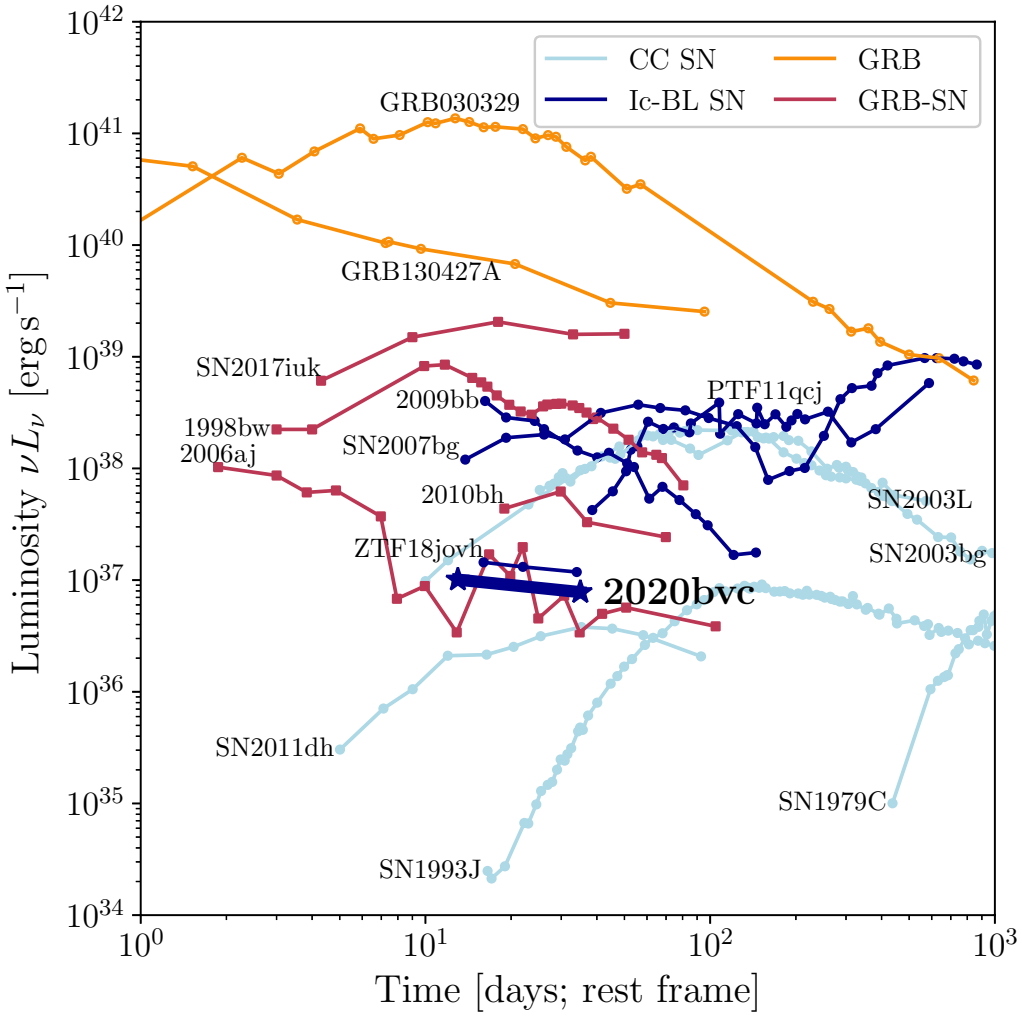

Figure 4.13: 10 GHz radio light curve of SN 2020bvc (points) compared to low-luminosity GRBs and relativistic Ic-BL SNe. Light curve of GRB 130427A is the 6.8 GHz light curve from Perley et al. (2014). Data point for SN 2017iuk is at 6 GHz (Laskar et al., 2017). SN 2006aj data is at 8.5 GHz from Soderberg et al. (2006b). ZTF18aaqjovh data is from Ho et al. (2020c). SN 2010bh light curve is at 5.4 GHz from Margutti et al. (2014). PTF 11qcj light curve is at 5 GHz from Corsi et al. (2014). All other sources are as described in Appendix C of Ho et al. (2019c).

infer is similar to the mildly relativistic velocities inferred for some LLGRB-SNe, in particular SN 2010bh. It is also possible that the velocity approaches the relativistic speeds inferred for SN 2006aj and SN 1998bw.

Second, we find a lower limit on the energy thermalized by the shock of 1.3×10^{47} erg. As shown in Figure 4.14, SN 2020bvc appears to have an energy most similar to that of SN 2006aj and a radio-loud Ic-BL SN recently discovered in ZTF (Ho et al.,

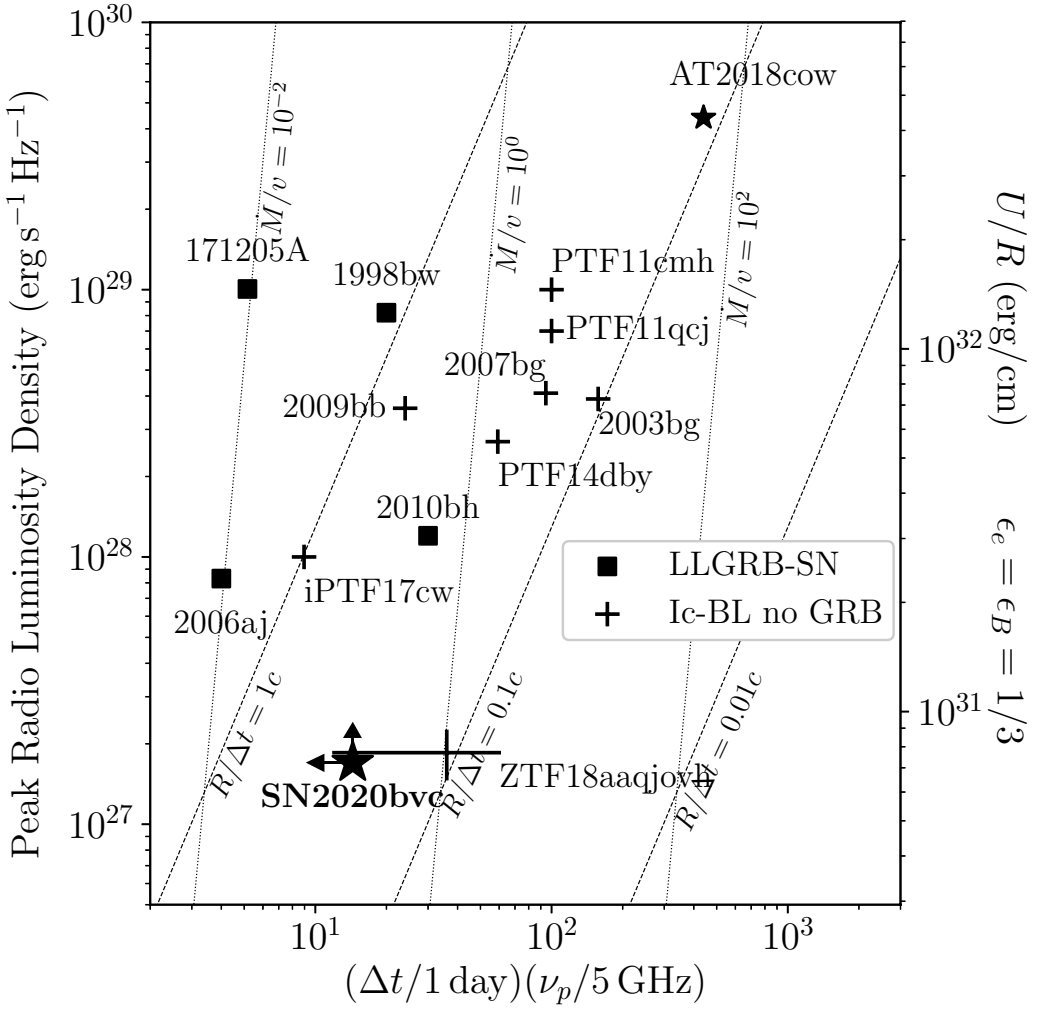

Figure 4.14: Luminosity and peak frequency of the radio light curve of SN 2020bvc compared to LLGRBs and energetic SNe. Lines of constant mass-loss rate (scaled to wind velocity) are shown in units of $10^{-4}\,M_\odot\,\mathrm{yr}^{-1}/1000\,\mathrm{km\,s}^{-1}$. Data for PTF14dby are from 7.4 GHz light curve in Corsi et al. (2016). Data for PTF11cmh and PTF11qcj are from 5 GHz light curve in Corsi et al. (2016). Data for iPTF17cw are from the 2.8 GHz light curve in Corsi et al. (2017). Data for ZTF18aaqjovh are from Ho et al. (2020c). For details on all other sources, see caption to Figure 5 and Appendix C in Ho et al. (2019c).

2020c).

Third, we find an ambient density of $n_e = 160\,\mathrm{cm}^{-3}$, which we show in Figure 4.14 as a mass-loss rate of $\sim 10^{-5}\,M_\odot\,\mathrm{yr}^{-1}$, assuming a wind velocity $v_w = 1000\,\mathrm{km\,s}^{-1}$. As shown in the figure, this mass-loss rate is within an order of magnitude of LLGRB-SNe, including SN 2006aj, SN 1998bw, and SN 2010bh.

Fourth, we find that the cooling frequency is $\nu_c = 1.0 \times 10^{13}$ Hz, below the X-ray band. We discuss the implications in §4.2.

Finally, we address the model proposed in Izzo et al. (2020), that SN 2020bvc represents a GRB jet with energy 2×10^{51} erg viewed at an angle of 23 degrees ($\theta_{\rm obs} = 0.4$), propagating into a power-law density profile $R^{-1.5}$. The authors argue that this event has similar early optical behavior to LLGRB 171205A / SN 2017iuk and that the X-ray emission is consistent with the predicted light curve from Granot et al. (2018). We point out that the same model predicts an 8.5 GHz radio light curve that exceeds 10^{30} erg s^{-1} Hz^{-1} over the period of our VLA observations, several orders of magnitude more luminous than our measurements. An off-axis jet cannot be entirely ruled out; future radio observations will be needed to determine whether a highly off-axis jet could be present. However, for now we find that no off-axis jet is required to explain the 1–50 d radio light curve, as was the case for SN 2006aj (Soderberg et al., 2006b). To our knowledge only one radio data point has been published for SN 2017iuk, and the radio emission compared to off-axis models was not discussed in Izzo et al. (2019).

In conclusion, the radio properties of SN 2020bvc are similar to what has been observed for LLGRB-SNe. Although we do not have evidence for relativistic ejecta or a GRB, the radio light curve is unlike what has been seen for "ordinary" core-collapse SNe, suggesting that SN 2020bvc is related to the LLGRB phenomenon, i.e., an LLGRB-like event discovered optically.

X-ray Emission

In this section we compare the X-ray light curve, and the X-ray to radio SED, of SN 2020bvc to that of SN 2006aj and other LLGRBs in the literature.

The X-ray light curve of LLGRB 060218 / SN 2006aj had two components: the prompt emission itself, which lasted until 10^4 s (often called a GRB, but given the low peak energy is also called an X-Ray Flash or XRF) and an afterglow that decayed as $t^{-\alpha}$ where $\alpha = 1.2 \pm 0.1$ until 10^6 s (Campana et al., 2006; Soderberg et al., 2006b). The 0.3–10 keV luminosity was 8×10^{41} erg s^{-1} at three days post-explosion (Campana et al., 2006). In Figure 4.15 we show the 0.3–10 keV light curve of SN 2020bvc compared to that of SN 2006aj and nearby LLGRB-SNe. We find that the X-ray luminosity is within an order of magnitude of SN 2006aj, as well as SN 1998bw and SN 2010bh.

Next we consider the radio to X-ray spectral index. At $\Delta t = 13$ d the radio to X-ray

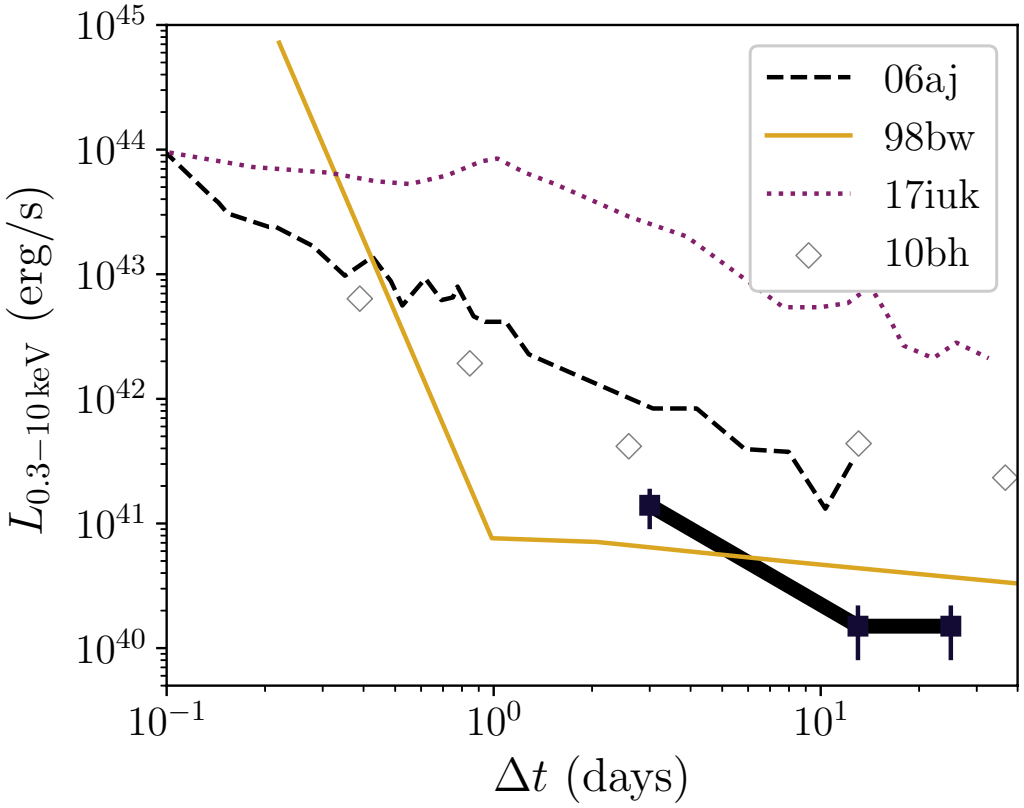

Figure 4.15: The 0.3–10 keV X-ray light curve of SN 2020bvc (black connected squares) compared to that of nearby Ic-BL SNe associated with LLGRBs. Data on GRB-SNe taken from Campana et al. (2006), Corsi et al. (2017), and D'Elia et al. (2018).

spectral index of SN 2020bvc is $\beta_{RX} = 0.5$, where $F_\nu \propto \nu^{-\beta}$. Given that the cooling frequency lies below the X-ray band (§4.6) the value of β_{RX} is too shallow for the X-rays to be an extension of the radio synchrotron spectrum. The same was true of SN 2006aj, which had a very similar value of $\beta_{RX} = 0.5$ (Fan et al., 2006; Irwin and Chevalier, 2016; Soderberg et al., 2006b).

Furthermore, for the X-rays to be an extension of the synchrotron spectrum we would require $\nu_c > 10^{17}$ Hz at $t \approx 30$ d and therefore $B < 0.01$ G, which is over an order of magnitude smaller than the value of B measured in any known SN (Chevalier, 1998; Chevalier and Fransson, 2006; Corsi et al., 2016). This is another argument for why the X-rays are unlikely to arise from the same synchrotron spectrum as the radio emission.

Finally, from the ratio of the optical to radio luminosity, we can estimate the expected contribution of X-rays from inverse Compton scattering. We find (Appendix 4.9) that

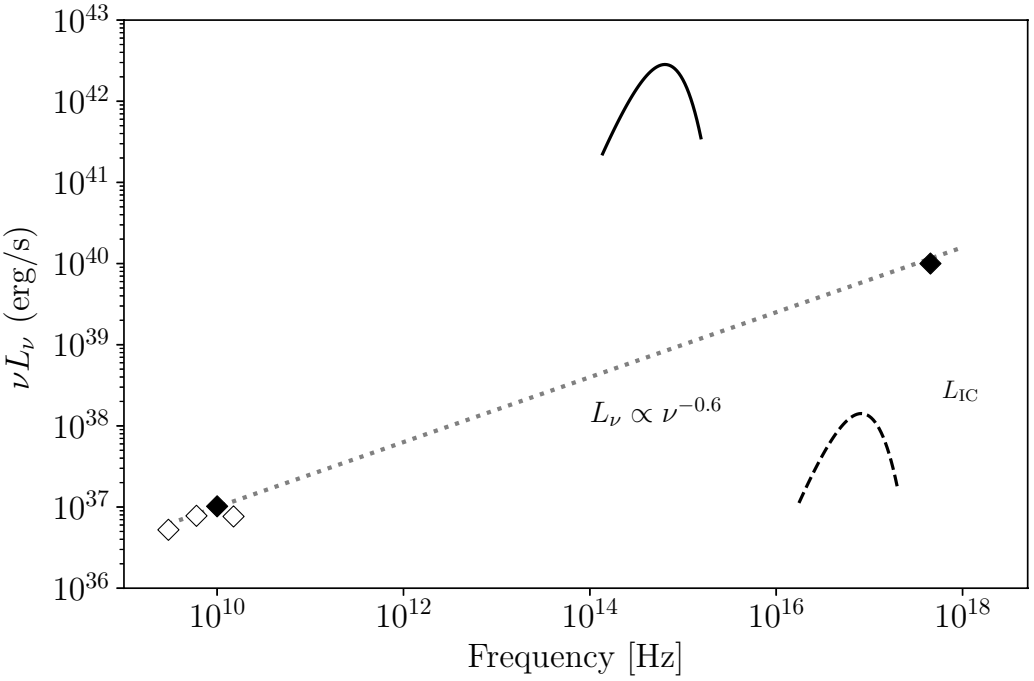

Figure 4.16: The SED from radio to X-rays at $\Delta t = 13$ d. The empty diamonds are VLA data points from 17–28 d. The solid line is the blackbody fit to the optical SED. The dotted line shows an extrapolation of $L_\nu \propto \nu^{-(p-1)/2}$ where $p = 2.2$, and the dashed curve shows the predicted emission from inverse Compton scattering (calculated in Appendix 4.9).

the contribution is not sufficient to explain the X-ray luminosity that we observe, which again was also the case in SN 2006aj. The X-ray "excess" observed in SN 2006aj has been attributed to the long-lived activity of a central engine (Fan et al., 2006; Soderberg et al., 2006b) and to dust scattering (Irwin and Chevalier, 2016; Margutti et al., 2015). On the other hand, Waxman et al. (2007) argued that the long-lived X-ray emission could be explained naturally in a model of mildly relativistic shock breakout into a wind, and that it was the radio emission that required a separate component. The data we have are less detailed than that obtained for SN 2006aj, and so are not useful in distinguishing between these different possibilities.

4.7 Early ZTF Light Curves of Nearby Ic-BL SNe

As discussed in §4.5, the timescale and luminosity of the shock-cooling peak is most sensitive to the shell properties (mass, radius) and the shock velocity. By contrast, the timescale and luminosity of the radioactively-powered peak is set by the nickel mass, the ejecta mass, and the explosion energy. So it is not obvious

that the properties of the second peak (which are heterogeneous; Taddia et al. 2019) should be correlated with the properties of the first peak.

In Figure 4.17 we show early (< 4 d) light curves of five nearby ($z \lesssim 0.05$) Ic-BL SNe observed as part of ZTF's high-cadence surveys, which were spectroscopically classified as part of the ZTF flux-limited (Fremling et al., 2019c) and volume-limited (De et al., 2020) experiments. The light curves shown are from forced photometry on P48 images (Yao et al., 2019), and epochs of spectroscopy are marked with 'S.' For the two most luminous events, we show the light curve of SN 2006aj for comparison. We can rule out a first peak like that of SN 2006aj (duration ≈ 1 d, peak luminosity ≈ -18) for all events except one (ZTF19ablesob). Note that the faintest LLGRB-SN, SN 2010bh, peaked at $M = -17$ mag: with the ZTF flux-limited survey we would be over 90% complete for such events out to $z = 0.03$. SN 2020bvc peaked brighter than $M = -18.5$, so the flux-limited survey would be over 90% complete for such events out to $z = 0.06$.

Our high-cadence optical observations provide the first evidence that Ic-BL SNe like LLGRB 060218/SN 2006aj are not the norm. Radio follow-up observations have only been sensitive enough to show that events like LLGRB 980425/SN 1998bw are uncommon (Corsi et al., 2016), and in most cases have been unable to rule out emission like that seen in SN 2006aj and SN 2020bvc.

There are many degeneracies that complicate the interpretation of Figure 4.17. Rise time and peak luminosity are sensitive to the velocity of the shock. The shock velocity when it breaks out of the star is sensitive to the outer density gradient in the stellar envelope and the energy of the explosion. Even if all Ic-BL progenitors were identical, there could be a strong dependence with observing angle. Ic-BL SNe are expected to be asymmetric and bipolar, so the ejecta directed along the poles will move faster than along the equator. Thus, an event viewed along the poles could have a much brighter shock-interaction peak.

Even assuming identical and spherically symmetric explosions for the Ic-BL SNe, there could be wide diversity in properties of the ambient material, i.e., mass, radius, and geometry. The CSM itself could be asymmetric (e.g. a disk rather than a spherical wind) introducing even more complicated viewing-angle effects. Finally, as we discussed in our analysis of another fast-rising luminous Ic-BL SN, SN 2018gep (Ho et al., 2019d), it can be difficult to know when it is appropriate to model such emission as arising from shock breakout in low-mass, large-radius material, and when it is appropriate to model such emission as arising from post-

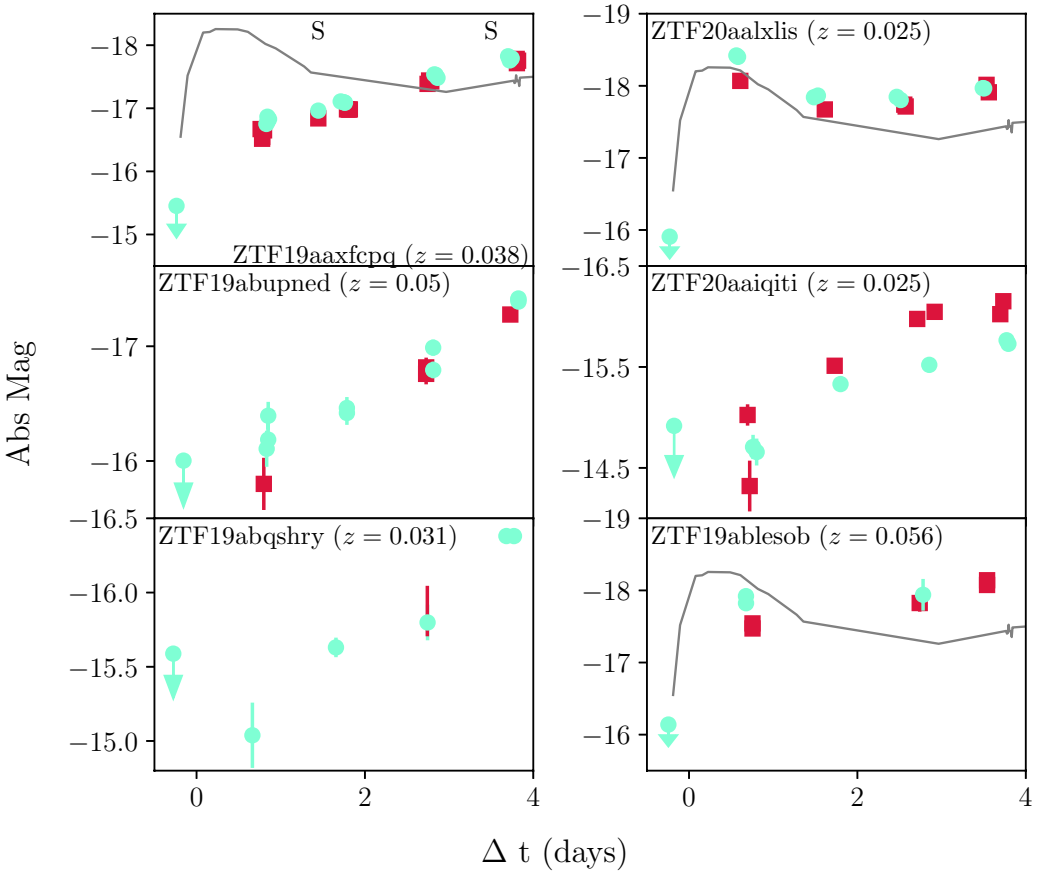

Figure 4.17: Early ($\Delta t \lesssim 4$ d) light curves of nearby Ic-BL SNe observed as part of ZTF's high-cadence surveys, from forced photometry on P48 images (Yao et al., 2019). The *B*-band light curve of SN 2006aj is shown as a grey line for comparison. Epochs of follow-up spectroscopy are marked with 'S' along the top of the panel.

shock cooling in higher-mass, smaller-radius material (e.g. Nakar and Piro 2014; Piro 2015). In short, it is extremely difficult at present to explain why we see such diversity in the early light curves of Ic-BL SNe. A model grid of different explosion and CSM properties, with resulting light curves, is in preparation (Khatami et al. in prep) and will be useful in understanding what configurations are ruled out or allowed for each of the objects in Figure 4.17.

4.8 Summary and Discussion

We presented optical, X-ray, and radio observations of SN 2020bvc, which shares key characteristics with the Ic-BL SN 2006aj associated with LLGRB 060218. Both events had:

- A double-peaked optical light curve. The first peak is fast (≈ 1 d), luminous ($M = -18$), and blue ($g-r \approx -0.3$ mag), and can be modeled as shock-cooling emission from low-mass ($M_e < 10^{-2}\,M_\odot$) extended ($R_e > 10^{12}$ cm) material;
- Radio emission (10^{37} erg s^{-1} at 10 GHz) from a mildly relativistic ($v > 0.3c$) forward shock, much fainter than that observed in LLGRB-SNe such as SN 1998bw and SN 2017iuk; and
- X-ray emission of a similar luminosity (10^{41} erg s^{-1}) that likely requires a separate emission component from that producing the radio emission.

When our paper was nearly complete, Izzo et al. (2020) presented an interpretation of SN 2020bvc as a classical high-energy (2×10^{51} erg) GRB viewed 23 degrees off-axis on the basis of (1) the fast expansion velocities ($v_{\rm exp} \approx 70,000$ km s^{-1}) measured from the early optical spectra, similar to those observed in the Ic-BL SN 2017iuk accompanying LLGRB 171205A, (2) the X-ray light curve, and (3) the double-peaked UVOT light curve, where the first peak was argued to arise from the cocoon expanding and cooling after breaking out of the progenitor star. In our work we found that from the perspective of the radio observations obtained so far (1–50 d post-discovery), no off-axis jet is required. In particular, the faint radio light curve is not consistent with the model in Granot et al. (2018) invoked by Izzo et al. (2020) to explain the X-ray data.

Instead, the simplest explanation from our data is that SN 2020bvc is a similar event to LLGRB 060218/SN 2006aj. LLGRB 060218/SN 2006aj has been extensively modeled and a summary of leading interpretations can be found in Irwin and Chevalier (2016). Here we outline the different models, then discuss how high-cadence optical surveys, together with early spectroscopy and X-ray and radio follow-up observations, can help distinguish between them.

(a) *Mildly relativistic shock breakout into a wind.* Campana et al. (2006) and Waxman et al. (2007) proposed that this single mechanism was responsible for the LLGRB, the shock-cooling emission, and the X-ray afterglow, in which case all three would be isotropic (a different low-energy component would be needed for the radio emission).

(b) *Choked jet.* Nakar (2015) expanded on the model above by suggesting that the shock breakout is powered by an energetic GRB-like jet that is choked

in extended low-mass material surrounding the progenitor star. Again, all emission components would be expected to be isotropic.

(c) *On-axis low-power jet.* Irwin and Chevalier (2016) proposed that the LLGRB and the shock-cooling emission are decoupled: the LLGRB was produced by a successful collimated low-power jet, and the shock-cooling emission by spherical SN ejecta. In that case, the LLGRB would only be observable within a small viewing angle, while the shock-cooling emission would be isotropic.

In all cases, the optical shock-cooling emission is expected to be isotropic, but in §4.7 we found that a number of Ic-BL lack luminous early peaks. If X-ray and radio observations of such events reveal LLGRB-like X-ray and radio emission, this would argue against a single mechanism for the shock-cooling emission and the afterglow. If, on the other hand, a double-peaked optical light curve is predictive of LLGRB-like X-ray and radio emission, and single-peaked events lack such emission, that would support models in which these components are produced by the same mechanism. Another test is the relative rates: if the LLGRB is only observable within a small viewing angle, the rate of double-peaked Ic-BL SNe should significantly exceed the rate of LLGRBs.

The key argument that LLGRB 171205A / SN 2017iuk arose from a jet was the presence of iron-peak elements in the early spectra, thought to have been transported to the surface by the jet (Izzo et al., 2019). SN 2017iuk was discovered via a GRB trigger, but with SN 2020bvc we have demonstrated that high-cadence optical surveys can enable similarly early spectroscopic observations. So, it should be possible to search for these cocoon signatures for a larger sample of events, without relying on the detection of an LLGRB. For events with detected cocoon emission, the long-term radio light curve is crucial for distinguishing between off-axis jets and choked jets.

We point out that based on estimated rates of GRBs and LLGRBs, the rate of off-axis GRBs in the local universe ($z < 0.05$) is only one order of magnitude smaller than the rate of LLGRBs (Liang et al., 2007; Soderberg et al., 2006b), which are detected routinely (if infrequently–see the discussion below regarding why). The estimated rate of on-axis GRBs at $z = 0$ is $0.42^{+0.90}_{-0.40}$ yr^{-1} Gpc^{-3}, as measured from the *Swift* sample of classical GRBs (Lien et al., 2014). Taking a beaming fraction of 0.01 (Guetta et al., 2005) the expectation is for two (and up to six) GRBs in the local universe per year. Recently, Law et al. (2018) identified a candidate off-axis GRB

afterglow in data from the VLA Sky Survey. Their estimate of the rate of events similar to this off-axis candidate is consistent with the expected off-axis GRB rate in the local universe.

Unfortunately, bursts like LLGRB 060218 are difficult to detect with ongoing GRB satellites, which are tuned to finding cosmological GRBs. First, the low luminosity ($L_{\rm iso} = 2.6\times10^{46}$ erg s^{-1}) means that an LLGRB like 060218 can only be detected in the nearby universe. Second, the long timescale ($T_{90} = 2100$ s) makes it difficult to detect the event above the background evolution of wide-field detectors. Third, the low peak energy ($E_{\rm pk} = 5$ keV) means that the burst is at the bottom of the energy range for sensitive wide-field detectors like *Fermi*/GBM and the Interplanetary Network (Hurley et al., 2010). Finally, the fact that a burst like 060218 would only be detected in the local universe means that the number N detectable above a flux threshold S goes as $\log(N > S) \propto S^{-3/2}$: the number detected is very sensitive to the threshold used. Going forward, it would be useful to have a wide-field mission optimized for the detection of low-luminosity, long-duration bursts that peak in the soft X-ray band.

Due to the low LLGRB discovery rate and the small sample size, the LLGRB rate is highly uncertain; it is currently roughly consistent with the rate of Ic-BL SNe (Kelly and Kirshner, 2012; Li et al., 2011). An outstanding question is therefore whether all Ic-BL SNe harbor an LLGRB. The effort to answer this question has been led by radio follow-up observations: by following up dozens of Ic-BL SNe found in wide-field optical surveys, Corsi et al. (2016) limited the fraction harboring SN 1998bw-like radio emission to $\lesssim 14\%$ (Corsi et al., 2016). However, as shown in Figure 4.13, SN 1998bw was the most radio-luminous LLGRB-SN. Radio observations have generally not been sensitive enough to rule out a radio counterpart like that accompanying SN 2006aj.

High-cadence optical surveys provide a novel opportunity to measure the rate of Ic-BL SNe that are similar to SN 2006aj. Optical shock-cooling emission is expected to be isotropic, and should not depend on the explosion properties that determine the second peak (ejecta mass, nickel mass). From the events in ZTF with early high-cadence light curves, it appears that SN 2006aj-like events are uncommon, but more events will be needed to measure a robust rate.

It is a pleasure to thank the anonymous referee for detailed feedback that greatly improved the clarify and thoroughness of the paper.

A.Y.Q.H. was supported by the GROWTH project funded by the National Science Foundation under PIRE Grant No. 1545949, as well as by the Heising-Simons Foundation. She would like to thank A. Jaodand and M. Brightman for their assistance with the *Chandra* data reduction and D. Dong for his help with imaging VLA data. She would also like to thank D. Khatami and D. Kasen for useful discussions regarding shock-cooling emission, and E. Ofek for his detailed reading of the manuscript.

R.L. is supported by a Marie Skłodowska-Curie Individual Fellowship within the Horizon 2020 European Union (EU) Framework Programme for Research and Innovation (H2020-MSCA-IF-2017-794467). AGY's research is supported by the EU via ERC grant No. 725161, the ISF GW excellence center, an IMOS space infrastructure grant and BSF/Transformative and GIF grants, as well as The Benoziyo Endowment Fund for the Advancement of Science, the Deloro Institute for Advanced Research in Space and Optics, The Veronika A. Rabl Physics Discretionary Fund, Paul and Tina Gardner, Yeda-Sela and the WIS-CIT joint research grant; AGY is the recipient of the Helen and Martin Kimmel Award for Innovative Investigation. C. F. gratefully acknowledges support of his research by the Heising-Simons Foundation (#2018-0907).

Based on observations obtained with the Samuel Oschin Telescope 48-inch and the 60-inch Telescope at the Palomar Observatory as part of the Zwicky Transient Facility project. ZTF is supported by the National Science Foundation under Grant No. AST-1440341 and a collaboration including Caltech, IPAC, the Weizmann Institute for Science, the Oskar Klein Center at Stockholm University, the University of Maryland, the University of Washington, Deutsches Elektronen-Synchrotron and Humboldt University, Los Alamos National Laboratories, the TANGO Consortium of Taiwan, the University of Wisconsin at Milwaukee, and Lawrence Berkeley National Laboratories. Operations are conducted by COO, IPAC, and UW. The scientific results reported in this article are based on observations made by the Chandra X-ray Observatory. This research has made use of software provided by the Chandra X-ray Center (CXC) in the application packages CIAO and Sherpa. This work made use of data supplied by the UK Swift Science Data Centre at the University of Leicester. SED Machine is based upon work supported by the National Science Foundation under Grant No. 1106171. The Submillimeter Array is a joint project between the Smithsonian Astrophysical Observatory and the Academia Sinica Institute of Astronomy and Astrophysics and is funded by the Smithsonian Institution

and the Academia Sinica. The Liverpool Telescope is operated on the island of La Palma by Liverpool John Moores University in the Spanish Observatorio del Roque de los Muchachos of the Instituto de Astrofisica de Canarias with financial support from the UK Science and Technology Facilities Council. Based on observations made with the Nordic Optical Telescope, operated by the Nordic Optical Telescope Scientific Association at the Observatorio del Roque de los Muchachos, La Palma, Spain, of the Instituto de Astrofisica de Canarias.

This work made use of the data products generated by the NYU SN group, and released under DOI:10.5281/zenodo.58767, available at `https://github.com/nyusngroup/SESNspectraLib`.

Funding for the Sloan Digital Sky Survey IV has been provided by the Alfred P. Sloan Foundation, the U.S. Department of Energy Office of Science, and the Participating Institutions. SDSS-IV acknowledges support and resources from the Center for High-Performance Computing at the University of Utah. The SDSS web site is www.sdss.org.

SDSS-IV is managed by the Astrophysical Research Consortium for the Participating Institutions of the SDSS Collaboration including the Brazilian Participation Group, the Carnegie Institution for Science, Carnegie Mellon University, the Chilean Participation Group, the French Participation Group, Harvard-Smithsonian Center for Astrophysics, Instituto de Astrofísica de Canarias, The Johns Hopkins University, Kavli Institute for the Physics and Mathematics of the Universe (IPMU) / University of Tokyo, the Korean Participation Group, Lawrence Berkeley National Laboratory, Leibniz Institut für Astrophysik Potsdam (AIP), Max-Planck-Institut für Astronomie (MPIA Heidelberg), Max-Planck-Institut für Astrophysik (MPA Garching), Max-Planck-Institut für Extraterrestrische Physik (MPE), National Astronomical Observatories of China, New Mexico State University, New York University, University of Notre Dame, Observatário Nacional / MCTI, The Ohio State University, Pennsylvania State University, Shanghai Astronomical Observatory, United Kingdom Participation Group, Universidad Nacional Autónoma de México, University of Arizona, University of Colorado Boulder, University of Oxford, University of Portsmouth, University of Utah, University of Virginia, University of Washington, University of Wisconsin, Vanderbilt University, and Yale University.

4.9 Appendix

Photometry Table

Table 4.6: UVOIR photometry for SN 2020bvc, corrected for Milky Way extinction. Epochs given in observer-frame since t_0 (defined in §4.2)

Date (MJD)	Δt (d)	Inst.	Filt.	Mag (AB)
58883.3406	0.67	P48+ZTF	i	17.44 ± 0.05
58883.3901	0.72	P48+ZTF	i	17.46 ± 0.04
58883.4763	0.81	P48+ZTF	g	16.82 ± 0.04
58883.4966	0.83	P48+ZTF	g	16.83 ± 0.05
58883.524	0.85	P48+ZTF	r	17.19 ± 0.04
58884.0245	1.35	Swift+UVOT	$UVW1$	17.15 ± 0.01
58884.0253	1.36	Swift+UVOT	U	17.08 ± 0.01
58884.0257	1.36	Swift+UVOT	B	17.23 ± 0.01
58884.0268	1.36	Swift+UVOT	$UVW2$	17.90 ± 0.01
58884.028	1.36	Swift+UVOT	V	17.12 ± 0.01
58884.0297	1.36	Swift+UVOT	$UVM2$	17.39 ± 0.01
58884.1362	1.47	LT+IOO	g	17.30 ± 0.01
58884.3634	1.69	P60+SEDM	i	17.50 ± 0.03
58884.3889	1.72	P48+ZTF	i	17.66 ± 0.05
58884.4109	1.74	P48+ZTF	i	17.63 ± 0.04
58884.4212	1.75	P48+ZTF	g	17.40 ± 0.06
58884.469	1.8	P48+ZTF	g	17.38 ± 0.05
58884.4754	1.81	P48+ZTF	g	17.37 ± 0.05
58884.5473	1.88	P48+ZTF	r	17.58 ± 0.06
58884.5533	1.88	P48+ZTF	r	17.57 ± 0.04
58885.3891	2.72	P48+ZTF	i	17.67 ± 0.06
58885.4111	2.74	P48+ZTF	i	17.65 ± 0.04
58885.429	2.76	P48+ZTF	g	17.40 ± 0.05
58885.4774	2.81	P48+ZTF	g	17.44 ± 0.07
58885.5211	2.85	P48+ZTF	r	17.51 ± 0.04
58885.538	2.87	P48+ZTF	r	17.52 ± 0.05
58885.5533	2.88	Swift+UVOT	$UVW1$	19.48 ± 0.01
58885.554	2.88	Swift+UVOT	U	18.33 ± 0.01
58885.5543	2.88	Swift+UVOT	B	17.48 ± 0.01
58885.5553	2.89	Swift+UVOT	$UVW2$	20.03 ± 0.01
58885.5563	2.89	Swift+UVOT	V	17.19 ± 0.01

58885.5577	2.89	Swift+UVOT	$UVM2$	20.30 ± 0.01
58886.3926	3.72	P48+ZTF	i	17.52 ± 0.04
58886.4112	3.74	P48+ZTF	i	17.52 ± 0.03
58886.4337	3.76	P60+SEDM	r	17.20 ± 0.01
58886.4354	3.77	P60+SEDM	g	17.34 ± 0.02
58886.437	3.77	P60+SEDM	i	17.47 ± 0.01
58886.4768	3.81	P48+ZTF	g	17.29 ± 0.04
58886.4809	3.81	Swift+UVOT	$UVW1$	19.17 ± 0.01
58886.4816	3.81	Swift+UVOT	U	18.17 ± 0.01
58886.4819	3.81	Swift+UVOT	B	17.55 ± 0.01
58886.4829	3.81	Swift+UVOT	$UVW2$	20.05 ± 0.01
58886.4839	3.81	Swift+UVOT	V	17.55 ± 0.01
58886.4854	3.82	Swift+UVOT	$UVM2$	20.87 ± 0.01
58886.4941	3.82	P48+ZTF	g	17.29 ± 0.05
58886.5229	3.85	P48+ZTF	r	17.29 ± 0.05
58886.5506	3.88	P48+ZTF	r	17.33 ± 0.04
58887.2802	4.61	Swift+UVOT	$UVW1$	19.48 ± 0.01
58887.2808	4.61	Swift+UVOT	U	17.94 ± 0.01
58887.2812	4.61	Swift+UVOT	B	17.54 ± 0.01
58887.2821	4.61	Swift+UVOT	$UVW2$	20.47 ± 0.01
58887.2829	4.61	Swift+UVOT	V	17.10 ± 0.01
58887.2842	4.61	Swift+UVOT	$UVM2$	20.63 ± 0.01
58887.3208	4.65	P48+ZTF	i	17.33 ± 0.05
58887.429	4.76	P48+ZTF	g	17.07 ± 0.04
58887.468	4.8	P48+ZTF	g	17.10 ± 0.05
58887.4751	4.81	P48+ZTF	g	17.10 ± 0.05
58887.5039	4.83	P48+ZTF	r	17.07 ± 0.05
58887.5305	4.86	P48+ZTF	r	17.08 ± 0.05
58887.5314	4.86	P48+ZTF	r	17.05 ± 0.04
58888.3553	5.69	P60+SEDM	r	16.81 ± 0.02
58888.357	5.69	P60+SEDM	g	16.98 ± 0.03
58888.36	5.69	P48+ZTF	i	17.16 ± 0.04
58888.3928	5.72	P48+ZTF	i	17.14 ± 0.05
58888.4746	5.8	P48+ZTF	r	16.88 ± 0.04
58888.4892	5.82	P48+ZTF	r	16.87 ± 0.05
58888.5373	5.87	P48+ZTF	g	16.92 ± 0.05

58888.9397	6.27	Swift+UVOT	$UVW1$	19.06 ± 0.01
58888.9404	6.27	Swift+UVOT	U	18.29 ± 0.01
58888.9408	6.27	Swift+UVOT	B	17.09 ± 0.01
58888.9418	6.27	Swift+UVOT	$UVW2$	20.72 ± 0.01
58888.9428	6.27	Swift+UVOT	V	17.08 ± 0.01
58888.9444	6.27	Swift+UVOT	$UVM2$	20.37 ± 0.01
58890.3717	7.7	P48+ZTF	i	16.93 ± 0.03
58890.3941	7.72	P48+ZTF	i	16.94 ± 0.03
58890.4565	7.79	P48+ZTF	r	16.65 ± 0.04
58890.4747	7.8	P48+ZTF	r	16.62 ± 0.06
58890.4756	7.81	P48+ZTF	r	16.62 ± 0.04
58890.5276	7.86	P48+ZTF	g	16.74 ± 0.05
58890.5588	7.89	P48+ZTF	g	16.75 ± 0.05
58890.5597	7.89	P48+ZTF	g	16.75 ± 0.05
58891.3937	8.72	P48+ZTF	i	16.84 ± 0.03
58891.4157	8.75	P48+ZTF	i	16.88 ± 0.03
58891.4552	8.79	P48+ZTF	g	16.71 ± 0.04
58891.4626	8.79	P48+ZTF	g	16.70 ± 0.04
58891.7595	9.09	Swift+UVOT	$UVW1$	19.49 ± 0.01
58891.7608	9.09	Swift+UVOT	U	18.22 ± 0.01
58891.7615	9.09	Swift+UVOT	B	17.02 ± 0.01
58891.7634	9.09	Swift+UVOT	$UVW2$	20.37 ± 0.01
58891.7654	9.1	Swift+UVOT	V	16.44 ± 0.01
58891.7683	9.1	Swift+UVOT	$UVM2$	20.77 ± 0.01
58892.3651	9.7	P48+ZTF	g	16.68 ± 0.05
58892.3832	9.71	P48+ZTF	g	16.69 ± 0.04
58892.4559	9.79	P48+ZTF	i	16.83 ± 0.03
58892.5181	9.85	P48+ZTF	r	16.46 ± 0.04
58892.534	9.86	P48+ZTF	r	16.45 ± 0.04
58893.3186	10.65	Swift+UVOT	$UVW2$	20.06 ± 0.01
58893.4023	10.73	P48+ZTF	i	16.80 ± 0.03
58893.4715	10.8	P48+ZTF	g	16.67 ± 0.04
58893.4965	10.83	P48+ZTF	g	16.67 ± 0.04
58893.4974	10.83	P48+ZTF	g	16.67 ± 0.04
58893.521	10.85	P48+ZTF	r	16.41 ± 0.04
58893.53	10.86	Swift+UVOT	V	16.49 ± 0.01

58893.5325	10.86	Swift+UVOT	$UVM2$	20.90 ± 0.01
58893.5338	10.86	P48+ZTF	r	16.43 ± 0.03
58893.7579	11.09	Swift+UVOT	$UVW1$	19.63 ± 0.01
58893.759	11.09	Swift+UVOT	U	18.40 ± 0.01
58893.7595	11.09	Swift+UVOT	B	17.11 ± 0.01
58893.7604	11.09	Swift+UVOT	$UVW2$	20.43 ± 0.01
58894.3388	11.67	P48+ZTF	g	16.68 ± 0.04
58894.4351	11.77	P48+ZTF	i	16.75 ± 0.03
58894.4554	11.79	P48+ZTF	i	16.74 ± 0.03
58894.5153	11.85	P48+ZTF	r	16.38 ± 0.04
58894.535	11.87	P48+ZTF	r	16.37 ± 0.04
58894.5468	11.88	P48+ZTF	g	16.70 ± 0.03
58895.137	12.47	Swift+UVOT	$UVW1$	19.89 ± 0.01
58895.1377	12.47	Swift+UVOT	U	18.63 ± 0.01
58895.138	12.47	Swift+UVOT	B	17.35 ± 0.01
58895.1391	12.47	Swift+UVOT	$UVW2$	20.41 ± 0.01
58895.14	12.47	Swift+UVOT	V	16.35 ± 0.01
58895.1417	12.47	Swift+UVOT	$UVM2$	20.97 ± 0.01
58895.4968	12.83	P48+ZTF	r	16.35 ± 0.03
58895.4972	12.83	P48+ZTF	r	16.33 ± 0.04
58896.3318	13.66	P48+ZTF	i	16.72 ± 0.03
58896.3934	13.72	P48+ZTF	i	16.70 ± 0.03
58898.1568	15.49	LT+IOO	r	16.32 ± 0.02
58898.1576	15.49	LT+IOO	i	16.76 ± 0.02
58898.1585	15.49	LT+IOO	g	16.75 ± 0.02
58898.1593	15.49	LT+IOO	u	18.66 ± 0.04
58898.445	15.77	P48+ZTF	g	16.92 ± 0.04
58898.4558	15.79	P48+ZTF	g	16.90 ± 0.03
58898.4955	15.83	P48+ZTF	r	16.38 ± 0.03
58898.5119	15.84	P48+ZTF	r	16.39 ± 0.04
58898.5128	15.84	P48+ZTF	r	16.35 ± 0.04
58898.5335	15.86	P48+ZTF	r	16.36 ± 0.03
58898.5463	15.88	P48+ZTF	g	16.93 ± 0.04
58899.4051	16.74	P48+ZTF	g	16.92 ± 0.04
58899.4351	16.77	P48+ZTF	g	16.94 ± 0.04
58899.4828	16.81	P48+ZTF	r	16.34 ± 0.04

58899.5057	16.84	P48+ZTF	r	16.36 ± 0.03
58899.5302	16.86	P48+ZTF	g	16.95 ± 0.05
58900.3929	17.72	P48+ZTF	g	16.98 ± 0.05
58900.4467	17.78	P48+ZTF	r	16.26 ± 0.04
58900.4499	17.78	P60+SEDM	r	16.38 ± 0.01
58900.4516	17.78	P60+SEDM	g	16.98 ± 0.02
58900.4532	17.78	P60+SEDM	i	16.64 ± 0.02
58900.4787	17.81	P48+ZTF	r	16.35 ± 0.03
58900.4938	17.82	P48+ZTF	r	16.34 ± 0.04
58900.5289	17.86	P48+ZTF	g	16.98 ± 0.07
58901.4137	18.74	P48+ZTF	r	16.38 ± 0.03
58901.4335	18.76	P48+ZTF	r	16.39 ± 0.03
58901.4546	18.78	P48+ZTF	r	16.37 ± 0.03
58901.4546	18.78	P48+ZTF	r	16.37 ± 0.03
58902.6701	20.0	Swift+UVOT	$UVW1$	20.56 ± 0.01
58902.6715	20.0	Swift+UVOT	U	19.52 ± 0.01
58902.6725	20.0	Swift+UVOT	B	17.82 ± 0.01
58902.6748	20.0	Swift+UVOT	$UVW2$	20.22 ± 0.01
58902.6772	20.01	Swift+UVOT	V	16.49 ± 0.01
58902.6791	20.01	Swift+UVOT	$UVM2$	22.23 ± 0.01
58903.36	20.69	P48+ZTF	g	17.21 ± 0.06
58903.412	20.74	P48+ZTF	r	16.48 ± 0.03
58903.4217	20.75	P48+ZTF	r	16.45 ± 0.03
58903.4571	20.79	P48+ZTF	r	16.48 ± 0.03
58903.4605	20.79	P48+ZTF	r	16.46 ± 0.05
58903.4953	20.83	P48+ZTF	r	16.47 ± 0.03
58903.4962	20.83	P48+ZTF	r	16.51 ± 0.04
58903.5079	20.84	P48+ZTF	r	16.45 ± 0.04
58903.5409	20.87	P48+ZTF	g	17.22 ± 0.05
58904.3954	21.73	P48+ZTF	i	16.79 ± 0.03
58904.4029	21.73	P48+ZTF	i	16.81 ± 0.02
58904.4461	21.78	P48+ZTF	g	17.28 ± 0.05
58904.489	21.82	P48+ZTF	r	16.50 ± 0.03
58906.3392	23.67	P48+ZTF	g	17.44 ± 0.05
58906.4339	23.76	P48+ZTF	i	16.89 ± 0.02
58906.4868	23.82	P48+ZTF	r	16.56 ± 0.04

58906.4878	23.82	P48+ZTF	r	16.57 ± 0.03
58906.5057	23.84	P48+ZTF	r	16.57 ± 0.03
58906.5381	23.87	P48+ZTF	g	17.41 ± 0.05
58906.539	23.87	P48+ZTF	g	17.45 ± 0.06
58906.5551	23.89	P48+ZTF	i	16.88 ± 0.04
58908.3226	25.65	Swift+UVOT	$UVW1$	19.63 ± 0.01
58908.3236	25.65	Swift+UVOT	U	20.53 ± 0.01
58908.3243	25.65	Swift+UVOT	B	18.19 ± 0.01
58908.3259	25.66	Swift+UVOT	$UVW2$	20.45 ± 0.01
58908.3275	25.66	Swift+UVOT	V	16.99 ± 0.01
58908.3288	25.66	Swift+UVOT	$UVM2$	21.54 ± 0.01
58908.4122	25.74	P48+ZTF	i	16.98 ± 0.03
58908.4158	25.75	P60+SEDM	r	16.77 ± 0.02
58908.4258	25.76	P48+ZTF	i	16.99 ± 0.03
58908.4624	25.79	P48+ZTF	r	16.73 ± 0.04
58908.4949	25.82	P48+ZTF	r	16.76 ± 0.04
58908.5315	25.86	P48+ZTF	g	17.46 ± 0.09
58908.5565	25.89	P48+ZTF	g	17.45 ± 0.05
58909.175	26.5	LT+IOO	r	16.75 ± 0.02
58909.1758	26.51	LT+IOO	i	17.03 ± 0.02
58909.1766	26.51	LT+IOO	g	17.54 ± 0.02
58909.1775	26.51	LT+IOO	u	19.98 ± 0.07
58909.1789	26.51	LT+IOO	z	16.66 ± 0.01
58911.2535	28.58	P48+ZTF	i	17.07 ± 0.05
58911.3516	28.68	P48+ZTF	i	17.14 ± 0.03
58911.4256	28.76	P48+ZTF	g	17.85 ± 0.06
58911.4265	28.76	P48+ZTF	g	17.89 ± 0.07
58911.4766	28.81	P48+ZTF	r	16.87 ± 0.04
58911.4826	28.81	P48+ZTF	r	16.87 ± 0.04
58911.4836	28.81	P48+ZTF	r	16.85 ± 0.04
58911.551	28.88	P48+ZTF	g	17.85 ± 0.07
58911.5515	28.88	P48+ZTF	g	17.81 ± 0.08
58911.5533	28.88	P48+ZTF	g	17.73 ± 0.07
58911.5538	28.88	P48+ZTF	g	17.79 ± 0.06
58912.1515	29.48	LT+IOO	r	16.94 ± 0.02
58912.1523	29.48	LT+IOO	i	17.21 ± 0.02

58912.1532	29.48	LT+IOO	g	17.75 ± 0.01
58912.154	29.48	LT+IOO	u	20.15 ± 0.10
58912.1554	29.49	LT+IOO	z	16.81 ± 0.02
58912.3746	29.7	P48+ZTF	i	17.19 ± 0.03
58912.3792	29.71	P48+ZTF	i	17.16 ± 0.04
58912.4747	29.8	P48+ZTF	r	16.95 ± 0.04
58912.4973	29.83	P48+ZTF	r	16.96 ± 0.04
58912.5209	29.85	P48+ZTF	g	17.93 ± 0.08
58912.5468	29.88	P48+ZTF	g	17.94 ± 0.07

Details: mass and radius of the extended material

This calculation closely follows that of Kasen (2017) and Nakar and Piro (2014).

Assume that the layer undergoing shock cooling has mass M_e and radius R_e. Photons diffuse from this layer on a timescale $t_{\rm diff} \sim \tau R_e/c$. The layer itself is moving at a characteristic velocity v_e: the timescale of expanding is $t_{\rm exp} \sim R_e/v_e$.The bulk of photons emerge from the layer where $\tau R_e/c \sim R_e/c$, or $\tau \sim c/v_e$.

At a given radius, the optical depth τ drops due to expansion: $\tau \sim \kappa\rho R$ where $\rho \sim M_e/(4\pi R^3/3)$. The radius increases as $R \sim v_e t$, so we find that $\tau \sim 3\kappa M_e/(4\pi(v_e t)^2)$. Setting this equal to c/v_e,

$$t \sim \left(\frac{3}{4\pi}\frac{\kappa M_e}{v_e c}\right)^{1/2}. \tag{4.2}$$

For SN2020bvc, we have an upper limit on the time to peak of $t_p \lesssim 1$ d. From the spectra, we estimate $v_e \sim 0.1c$. We take $\kappa = 0.2\,{\rm cm^{-2}\,g^{-1}}$ for a hydrogen-poor gas. Altogether, we find $M_e \sim 10^{-2}\,M_\odot$. Note that this is an upper limit, because the rise time was likely much faster than what we could measure. So, we conclude that $M_e < 10^{-2}\,M_\odot$.

Next we estimate R_e. We assume that the shock deposits energy $E_{\rm dep}$in to the layer. Then the layer cools from expansion, $E_{\rm cool} \sim E_{\rm dep}(R_e/v_e t)$. The luminosity from cooling is $L_{\rm cool} \sim E_{\rm cool}/t_{\rm cool} \sim E_{\rm dep}R_0/v_e t^2$.

Assuming that the deposited energy is half the kinetic energy $E_{\rm KE}$ of the shock, $E_{\rm dep} \sim E_{\rm KE}/2 = \pi R_e^2 dR\rho v_s^2$, where dR and ρ are the width and density of the layer.

Taking $dR \approx R_e$ and $\rho \sim M_e/(4\pi R_e^2 dR)$ we find $E_{\rm dep} \sim v_e^2 M_e/4$. So, our expression for the luminosity is

$$L_{\rm cool} \sim \frac{v_e R_e M_e}{4t^2}. \tag{4.3}$$

Taking $M_e < 10^{-2}\,M_\odot$, $t < 1\,$d, $v_e = 0.1c$, and $L > 10^{43}\,{\rm erg\,s^{-1}}$, we find $R_e > 10^{12}\,$cm. We can only measure a lower limit on the radius because the true peak luminosity is likely much higher than what we can measure.

Details: properties of the forward shock

The framework described in Chevalier (1998) assumes that the radio emission arises from a population of relativistic electrons with Lorentz factors that follow a power law of index p down to a cutoff γ_m,

$$\frac{dN(\gamma_e)}{d\gamma_e} \propto \gamma_e^{-p}, \gamma \geq \gamma_m, \tag{4.4}$$

where $2.3 \lesssim p \lesssim 3$ (Jones and Ellison, 1991; Pelletier et al., 2017). The expression for the typical electron Lorentz factor γ_m is

$$\gamma_m - 1 \approx \epsilon_e \frac{m_p v^2}{m_e c^2}, \tag{4.5}$$

where ϵ_e is the fraction of energy in relativitic electrons, m_p is the proton mass, v is the shock velocity, m_e is the electron mass, and c is the speed of light.

The resulting spectrum is a broken power law where $\nu^{5/2}$ at $\nu < \nu_a$ and $\nu^{-(p-1)/2}$ at $\nu > \nu_a$, and ν_a is called the self-absorption frequency (Rybicki and Lightman, 1986). By observing the peak frequency ν_p and peak flux F_p and assuming that $\nu_p = \nu_a$, we can estimate the outer shock radius R_p and magnetic field strength B_p. We take $p = 3$ (the results do not depend strongly on the value of p), a filling factor $f = 0.5$, and assume equipartition ($\alpha = \epsilon_e/\epsilon_B = 1$, where ϵ_e/ϵ_B is the ratio of the energy density in relativistic electrons to the energy density in magnetic fields).

Assuming that the radio emission is dominated by the transient, we have an upper limit on the peak frequency of $\nu_p < 3\,$GHz and a lower limit on the peak flux density of $F_p > 113\,\mu$Jy at $\Delta t = 24\,$d. We use Equations (13) and (14) of Chevalier (1998) (C98) to solve for R and B, and find $R > 1.7 \times 10^{16}\,$cm, $B < 0.34\,$G, and a mean shock velocity up to 13 d of $v > 0.3c$. Expressions for the total energy

thermalized by the shock U and the ambient density n_e are given in Ho et al. (2019c) (H19), following the same framework as in C98. Using Equation (12) in H19 and taking $\epsilon_B = 1/3$ we find $U = 1.3 \times 10^{47}$ erg. Using Equation (16) in H19 we find $n_e \approx 160\,\mathrm{cm}^{-3}$, which corresponds to a mass-loss rate (Equation (23) of H19) of

$$\frac{\dot{M}}{v_w}\left(\frac{1000\,\mathrm{km\,s^{-1}}}{10^{-4}\,M_\odot\,\mathrm{yr}^{-1}}\right) = 0.2, \tag{4.6}$$

where v_w is the wind velocity.

The cooling frequency is defined as

$$\nu_c = \gamma_c^2 \nu_g, \tag{4.7}$$

where

$$\gamma_c = \frac{6\pi m_e c}{\sigma_T B^2 t} \tag{4.8}$$

and

$$\nu_g = \frac{q_e B}{2\pi m_e c}. \tag{4.9}$$

Combining Equations 4.7, 4.8, and 4.9, we have

$$\nu_c = \frac{18\pi m_e c q_e}{\sigma_T^2 B^3 t^2} \approx 1.0 \times 10^{13}\,\mathrm{GHz}. \tag{4.10}$$

Finally, we find that the bulk of the electrons have Lorentz factor $\gamma_m = 22$.

Inverse Compton Scattering

The luminosity from inverse Compton scattering of optical photons from the relativistic electrons is

$$\frac{L_{\mathrm{IC}}}{L_{\mathrm{syn}}} = \frac{u_{ph}}{u_B}, \tag{4.11}$$

where u_{ph} is the photon energy density (which we measure from our UVOIR observations) and u_B is the magnetic energy density (which we measure from our

radio observations; Rybicki and Lightman 1986). Taking $R_{\rm ph} = 2 \times 10^{14}\,{\rm cm}$ and $L_{\rm bol} > 2 \times 10^{42}\,{\rm erg\,s^{-1}}$ we have

$$u_{ph} = \frac{L_{\rm bol}}{4\pi R^3/3} > 0.07\,{\rm erg\,cm^{-3}}. \tag{4.12}$$

Using $B < 0.34\,{\rm G}$ we have

$$u_B = \frac{B^2}{8\pi} < 0.005\,{\rm erg\,cm^{-3}}. \tag{4.13}$$

So, the dominant cooling mechanism is inverse Compton scattering rather than synchrotron radiation, and $L_{\rm IC}$ is an order of magnitude greater than $L_{\rm syn}$ (the radio luminosity). Photons emitted at frequency ν_0 that are upscattered by electrons at γ_m will emerge with an average frequency $\nu_{\rm IC}$ where

$$\langle \nu_{\rm IC} \rangle = \frac{4}{3}\gamma_m^2 \nu_0. \tag{4.14}$$

Part III. Ic-BL Supernovae

*Jingde reign period, third year, [=AD 1006–1007], there was a huge (*ju*) star seen in the sky in the west of* Di *(lunar lodge). Its bright rays were like a golden disc. No-one could determine its significance. Zhou Keming, the chief official of the Spring Agency reported that according to the (star manuals)* Tianwen Lu *and the* Jingzhou Zhan*, the star was a* Zhoubo*. Its form was like the half Moon and it had pointed rays. It was so brilliant (*huang huang*) that one could really see things clearly (*ran ke yi jian wu*) (by its light.)*

—THE *WENXIAN TONGKAO*
Translation from Stephenson and Green (2002)

Chapter 5

THE BROAD-LINED IC SUPERNOVA ZTF18AAQJOVH (SN 2018BVW): AN OPTICALLY DISCOVERED ENGINE-DRIVEN SUPERNOVA CANDIDATE WITH LUMINOUS RADIO EMISSION

Ho, A. Y. Q. et al. (2020). "The Broad-lined Ic Supernova ZTF18aaqjovh (SN 2018bvw): An Optically Discovered Engine-driven Supernova Candidate with Luminous Radio Emission". In: *ApJ* 893.2, p. 132. DOI: 10.3847/1538-4357/ab7f3b. arXiv: 1912.10354 [astro-ph.HE].

Anna Y. Q. Ho[1], Alessandra Corsi[2], S. Bradley Cenko[3,4], Francesco Taddia[5], S. R. Kulkarni[1], Scott M. Adams[1], Kishalay De [1], Richard Dekany [6], Dmitry D. Frederiks [7], Christoffer Fremling[1], V. Zach Golkhou[8,9,10], Thomas Kupfer[11], Russ R. Laher[12], Ashish Mahabal[1,13], Frank Masci[12], Adam A. Miller[14,15], James D. Neill[6], Daniel Reiley[6], Reed Riddle[6], Anna Ridnaia[7], Ben Rusholme[12], Yashvi Sharma[1], Jesper Sollerman[5], Maayane T. Soumagnac[16,17], Dmitry S. Svinkin[7], David L. Shupe[12],

[1]Cahill Center for Astronomy and Astrophysics, California Institute of Technology, Pasadena, CA 91125, USA [2]Department of Physics and Astronomy, Texas Tech University, Box 1051, Lubbock, TX 79409-1051, USA [3]Astrophysics Science Division, NASA Goddard Space Flight Center, Mail Code 661, Greenbelt, MD 20771, USA [4]Joint Space-Science Institute, University of Maryland, College Park, MD 20742, USA [5]Department of Astronomy and The Oskar Klein Centre, AlbaNova University Center, Stockholm University, SE-106 91 Stockholm, Sweden [6]Caltech Optical Observatories, California Institute of Technology, Pasadena, CA, USA [7]Ioffe Institute, Politekhnicheskaya 26, St. Petersburg 194021, Russia [8]DIRAC Institute, Department of Astronomy, University of Washington, 3910 15th Avenue NE, Seattle, WA 98195, USA [9]The eScience Institute, University of Washington, Seattle, WA 98195, USA [10]Moore-Sloan, WRF Innovation in Data Science, and DIRAC Fellow [11]Kavli Institute for Theoretical Physics, University of California, Santa Barbara, CA 93106, USA [12]IPAC, California Institute of Technology, 1200 E. California Blvd, Pasadena, CA 91125, USA [13]Center for Data Driven Discovery, California Institute of Technology, Pasadena, CA 91125, USA [14]Center for Interdisciplinary Exploration and Research in Astrophysics (CIERA) and Department of Physics and Astronomy, Northwestern University, 2145 Sheridan Road, Evanston, IL 60208, USA [15]The Adler Planetarium, Chicago, IL 60605, USA [16]Lawrence Berkeley National Laboratory, 1 Cyclotron Road, Berkeley, CA 94720, USA [17]Department of Particle Physics and Astrophysics, Weizmann Institute of Science, Rehovot 76100, Israel

Abstract

We present ZTF18aaqjovh (SN 2018bvw), a high-velocity ("broad-lined") stripped-envelope (Type Ic) supernova (Ic-BL SN) discovered in the Zwicky Transient Facility one-day cadence survey. ZTF18aaqjovh shares a number of features in common with engine-driven explosions: the photospheric velocity and the shape of the optical light curve are very similar to that of the Type Ic-BL SN 1998bw, which was associated with a low-luminosity gamma-ray burst (LLGRB) and had relativistic ejecta. However, the radio luminosity of ZTF18aaqjovh is almost two orders of magnitude fainter than that of ZTF18aaqjovh at the same velocity phase, and the shock velocity is at most mildly relativistic ($v = 0.06$–$0.4c$). A search of high-energy catalogs reveals no compelling GRB counterpart to ZTF18aaqjovh, and the limit on the prompt GRB luminosity of $L_{\gamma,\mathrm{iso}} \approx 1.6 \times 10^{48}\,\mathrm{erg\,s^{-1}}$ excludes a classical GRB but not an LLGRB. Altogether, ZTF18aaqjovh represents another transition event between engine-driven SNe associated with GRBs and "ordinary" Ic-BL SNe.

5.1 Introduction

Broad-lined Type Ic supernovae (Ic-BL SNe) are a subclass of stripped-envelope core-collapse supernovae (CC SNe) characterized by fast ejecta and large kinetic energies. While typical Type Ic SNe have photospheric velocities $v_{\mathrm{ph}} \approx 10,000\,\mathrm{km\,s^{-1}}$ (measured from Fe II absorption features), Type Ic-BL SNe have $v_{\mathrm{ph}} \approx 20,000\,\mathrm{km\,s^{-1}}$ at maximum light (Modjaz et al., 2016). The kinetic energy release of Ic-BL SNe is typically $\sim 10^{52}$ erg (Cano, 2013; Lyman et al., 2016; Prentice et al., 2016), an order of magnitude greater than traditional CC SNe (Woosley and Janka, 2005), although this measurement is highly model-dependent.

A clue to the high energies and fast velocities present in Ic-BL SNe is their connection to long-duration gamma-ray bursts, reviewed in Cano et al. (2017b), Hjorth et al. (2012), and Woosley and Bloom (2006). The association began with the coincident discovery of GRB 980425 and SN 1998bw at $d = 40\,\mathrm{Mpc}$ (Galama et al., 1998; Kulkarni et al., 1998). However, GRB 980425 was different from typical GRBs: it was under-luminous in γ-rays ($L_{\gamma,\mathrm{iso}} \sim 5 \times 10^{46}\,\mathrm{erg\,s^{-1}}$ compared to typical values of 10^{51}–$10^{53}\,\mathrm{erg\,s^{-1}}$) and sub-energetic, with an isotropic equivalent energy four orders of magnitude smaller than that of typical GRBs. Thus, it took the discovery of the cosmological GRB 030329 ($z = 0.1685$) in association with SN 2003dh (Hjorth et al., 2003; Stanek et al., 2003) to solidify the relationship between GRBs and SNe.

Since then, ~ 20 SNe accompanying GRBs have been spectroscopically confirmed.

All show broad Type Ic-BL features near maximum light, with two exceptions: SN 2011kl had a relatively featureless spectrum, and SN 2013ez more closely resembled a Type Ic (Cano et al., 2017b). The GRB-SN association has led to the suggestion GRBs and Ic-BL SNe are powered by a single central engine (Barnes et al., 2018; Lazzati et al., 2012; Sobacchi et al., 2017). However, a systematic search for radio emission from Ic-BL SNe constrained the fraction harboring a relativistic outflow as bright as that of SN 1998bw to be at most 30–40% (Corsi et al., 2016).

Complicating matters, additional underluminous GRBs have been discovered since GRB 980425 and are collectively referred to as low-luminosity GRBs (LLGRBs). LLGRBs are distinguished by isotropic peak luminosities $L_{\rm iso} \approx 10^{46}$–$10^{48}\,{\rm erg\,s^{-1}}$ and a relativistic energy release that is 2–3 orders of magnitude smaller than the 10^{51} erg from GRBs with fully relativistic outflows (Cano et al., 2017b). Due to their lower intrinsic luminosities, LLGRBs are discovered at low redshifts ($z \lesssim 0.1$). Thus, despite the fact that their measured rates might be 10–100 larger than that classical GRBs (Pian et al., 2006; Soderberg et al., 2006b), only seven have been discovered: LLGRB 980425/SN 1998bw, XRF 020903 (Bersier et al., 2006; Sakamoto et al., 2004; Soderberg et al., 2004a), LLGRB 031203/SN 2003lw (Malesani et al., 2004; Soderberg et al., 2004b; Thomsen et al., 2004; Watson et al., 2004), LLGRB 060218/SN 2006aj (Mirabal et al., 2006; Pian et al., 2006; Soderberg et al., 2006b), LLGRB 100316D/SN 2010bh (Bufano et al., 2012; Starling et al., 2011), LLGRB 171205A/SN 2017iuk (D'Elia et al., 2018; Wang et al., 2018), and most recently LLGRB 190829A (Chand et al., 2020). LLGRB 060218 and LLGRB 100316D have their own distinct properties: a long γ-ray prompt emission phase, and long-lived soft X-ray emission that might arise from continued activity of the central engine (Margutti et al., 2013).

Modeling of the radio emission from LLGRBs suggests quasi-spherical ejecta coupled to mildly relativistic material, with no off-axis components (Kulkarni et al., 1998; Margutti et al., 2013; Pian et al., 2006; Soderberg et al., 2006b). Thus, it seems that LLGRBs arise from a fundamentally different mechanism to cosmological GRBs. One suggestion is that they represent failed or choked-jet events, and that the gamma rays arise from shock breakout (Bromberg et al., 2011). This is supported by the early light curve of the LLGRB 060218, whose double peak in ultraviolet and optical filters has been modeled as shock breakout into a dense stellar wind (Campana et al., 2006) or into an extended envelope (Margutti et al., 2015; Nakar, 2015).

A major focus of scientific investigation over the past 20 years has been to unify this diverse array of phenomena: "extreme" SNe with successful, observed jets (classical GRBs), mildly relativistic explosions (LLGRBs or radio-emitting SNe), and ordinary (non-relativistic) SNe. The traditional avenue to discovering central engines—the detection of a GRB—is severely limited because a number of conditions must be met for a central engine to produce a GRB. First, the jet must be nearly baryon-free—or else the available energy is insufficient to accelerate the ejecta to ultra-relativistic velocities, and gamma-ray emission will be stifled by pair-production (Piran, 2004). Next, the jet must successfully escape the star without being choked by the stellar envelope (MacFadyen et al., 2001). Finally, the jet must be directed at Earth.

Today, wide-field optical time-domain surveys have the field-of-view and cadence to discover engine-driven explosions without relying on a high-energy trigger (e.g. Corsi et al. 2017). Radio observations are central to this effort, because they trace the fastest-moving ejecta. The Zwicky Transient Facility (ZTF; Bellm et al. 2019b; Graham et al. 2019) is conducting several different surveys (Bellm et al., 2019a) using a custom mosaic camera (Dekany et al., 2016) on the 48-inch Samuel Oschin Telescope (P48) at Palomar Observatory. ZTF discovers one Ic-BL SN per month, and we are conducting a follow-up campaign of a subset of these events with the Very Large Array (VLA). Here, we present our first detection of radio emission from the Ic-BL ZTF18aaqjovh (SN 2018bvw). In Section 5.2 we describe our optical, radio, and X-ray observations, as well as our search for contemporaneous gamma-ray emission. In Section 3 we constrain the physical properties of the explosion (energy, velocity, ejecta mass). We present our conclusions in Section 4.

Throughout the paper we use the ΛCDM cosmology from Planck Collaboration et al. (2016).

5.2 Observations

Zwicky Transient Facility Discovery

ZTF images are processed and reference-subtracted by the IPAC ZTF pipeline (Masci et al., 2019) using the method described in Zackay et al. (2016), and every 5-σ point-source detection is saved as an "alert." Alerts are distributed in Apache Avro format (Patterson et al., 2019) and can be filtered based on a machine learning real-bogus metric (Duev et al., 2019; Mahabal et al., 2019), host characteristics (including a

star-galaxy classifier; Tachibana and Miller 2018[1]), and light-curve properties. The ZTF collaboration uses a web-based system called the GROWTH marshal (Kasliwal et al., 2019) to identify, monitor, and coordinate follow-up observations for transients of interest.

ZTF18aaqjovh was discovered in an image obtained on 2018 May 5 UT as part of the ZTF one-day cadence survey, which covers 3000 deg^2 in two visits (one g, one r) per night (Bellm et al., 2019a). The alert passed two filters, as part of two systematic surveys being conducted by ZTF: a filter for transients in the local universe that cross-matches sources with a catalog of nearby galaxies (Cook et al., 2019), and a filter for bright transients (Fremling et al., 2019c). Because it passed these filters, the source was reported to the Transient Name Server (TNS[2]; Fremling 2018) and received the designation SN 2018bvw. After being reported, it was spectroscopically classified (Section 5.2; Fremling et al. 2019a).

The discovery magnitude was $r = 18.65 \pm 0.02$ mag, where the error bar is a 1-σ estimate of the background RMS, derived using a pixel-uncertainty map created for the difference image (Masci et al., 2019). The source position was measured to be $\alpha = 11^{\rm h}52^{\rm m}43.62^{\rm s}$, $\delta = +25^{\rm d}40^{\rm m}30.1^{\rm s}$ (J2000). The position is 4.71″ from SDSS J115244.11+254027.1, a star-forming galaxy at $z = 0.05403 \pm 0.00001$ (248.85 Mpc; Alam et al. 2015). The transient position with respect to the host galaxy is shown in Figure 5.1, with the host galaxy image constructed from SDSS g, r, and i-band cutouts using the method in Lupton et al. (2004). At this distance, the projected offset between ZTF18aaqjovh and the center of the host corresponds to $d = 5.68$ kpc. This offset is larger than the typical offset of Ic-BL SNe accompanied by GRBs, which is $1.54^{+3.13}_{-1.28}$ kpc (1-σ confidence), and more consistent with the offsets of Ic-BL SNe without detected GRBs, measured to be $\left(3.08^{+2.98}_{-2.35}\right)$ kpc (Japelj et al., 2018).

The full light curve, corrected for Milky Way extinction, is provided in Table 5.1 and shown in Figure 5.2. The P48 measurements come from forced photometry (Yao et al., 2019). The g-band reference image was constructed from data taken between 2018 April 22 and 2018 May 16, so we had to subtract a baseline flux to account for SN light in the reference. To calculate the baseline flux, we measured the mean flux of photometry in images where the SN light was not present: a set of

[1]In this context TM18 define star as an unresolved point source and galaxy as an extended unresolved source

[2]https://wis-tns.weizmann.ac.il

images at $\Delta t \approx -50$d and a set of images at $\Delta t \approx 400$ d. We confirmed that this baseline level was consistent, i.e., that by 400 d the SN light had returned to a level consistent with the pre-explosion level.

We obtained two epochs of photometry from the Spectral Energy Distribution Machine (SEDM; Blagorodnova et al. 2018; Rigault et al. 2019) mounted on the automated 60-inch telescope at Palomar (P60; Cenko et al. 2006). Digital image subtraction and photometry for the SEDM was performed using the Fremling Automated Pipeline (`FPipe`; Fremling et al. 2016). `Fpipe` performs calibration and host subtraction against SDSS reference images and catalogs (Ahn et al., 2014).

The peak r-band absolute magnitude is typical of Ic-BL light curves compiled from untargeted surveys (Taddia et al., 2019), and the light curve of ZTF18aaqjovh is very similar in shape to the light curve of SN 1998bw (Figure 5.2). Assuming that the time from explosion to peak is the same in ZTF18aaqjovh as in SN 1998bw, we can estimate that the explosion time t_0 is about the time of the last non-detection, 2018 April 25 UT. The optical spectra of ZTF18aaqjovh (Section 5.2) suggest that this t_0 is accurate to within a few days: the spectrum of ZTF18aaqjovh on May 9 was most similar to that of SN 1998bw at 16 d post-explosion. With this t_0, the first detection of ZTF18aaqjovh by ZTF was at $\Delta t = 10$ days. Throughout the paper, we use this definition of t_0 and report all times Δt with respect to this reference point.

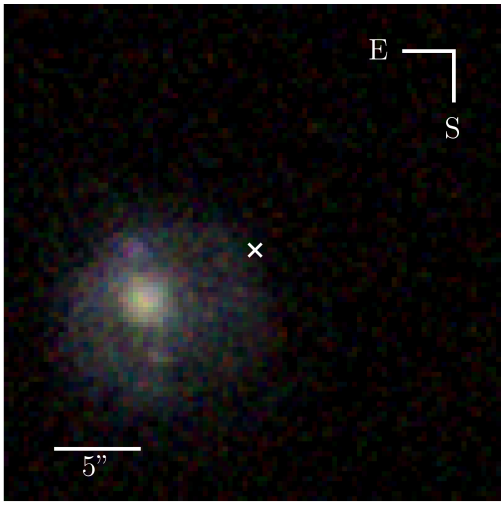

Figure 5.1: Image of the host galaxy of ZTF18aaqjovh (SN 2018bvw), constructed from g, r, and i-band SDSS cutouts. The position of ZTF18aaqjovh is shown with a white cross, 4.71″ from the center of the galaxy, or 5.68 kpc assuming $d = 249$ Mpc.

Table 5.1: Optical light curve of ZTF18aaqjovh from forced photometry on P48 images (Yao et al., 2019). Values have been corrected for Milky Way extinction. Phase is relative to t_0 defined in Section 5.2.

Date (MJD)	Δt	Instrument	Filter	AB Mag	Error in AB Mag
58243.170324	9.99	P48	r	18.59	0.03
58244.170880	10.99	P48	r	18.47	0.02
58245.171447	12.00	P48	r	18.32	0.02
58245.172384	12.00	P48	r	18.31	0.02
58246.233762	13.06	P48	r	18.32	0.03
58247.234363	14.06	P48	r	18.28	0.02
58247.358800	14.18	P60	r	18.30	0.04
58248.235324	15.06	P48	r	18.21	0.02
58248.236250	15.06	P48	r	18.17	0.02
58248.335300	15.16	P60	r	18.21	0.03
58249.234444	16.06	P48	r	18.23	0.03
58250.234803	17.06	P48	r	18.17	0.03
58254.191401	21.02	P48	r	18.31	0.02
58254.192338	21.02	P48	r	18.26	0.02
58255.238356	22.06	P48	r	18.32	0.02
58256.217651	23.04	P48	g	19.02	0.05
58256.218113	23.04	P48	g	18.98	0.05
58256.218565	23.04	P48	g	19.06	0.06
58256.219028	23.04	P48	g	19.05	0.05
58256.219479	23.04	P48	g	19.05	0.04
58256.219942	23.04	P48	g	19.02	0.03
58256.220393	23.04	P48	g	19.03	0.02
58256.220845	23.04	P48	g	19.07	0.03
58256.221308	23.05	P48	g	19.11	0.02
58256.221759	23.05	P48	g	19.05	0.02
58256.222222	23.05	P48	g	19.04	0.03
58256.222674	23.05	P48	g	19.04	0.03
58256.223125	23.05	P48	g	19.04	0.03
58256.223588	23.05	P48	g	19.12	0.03
58256.244317	23.07	P48	r	18.40	0.03
58256.278032	23.10	P48	r	18.43	0.02

58257.232951	24.06	P48	r	18.42	0.03
58257.233877	24.06	P48	r	18.41	0.03
58258.168634	24.99	P48	g	19.32	0.04
58262.202593	29.03	P48	r	18.72	0.04
58262.220127	29.04	P48	g	19.53	0.08
58262.252870	29.08	P48	r	18.64	0.05
58263.235185	30.06	P48	r	18.74	0.03
58263.259248	30.08	P48	g	19.81	0.11
58266.250648	33.07	P48	r	19.02	0.07
58266.251562	33.08	P48	r	19.08	0.07
58267.185671	34.01	P48	g	20.08	0.29
58267.290174	34.11	P48	r	18.91	0.07
58268.167917	34.99	P48	g	20.13	0.24
58269.185035	36.01	P48	r	19.20	0.07
58269.185972	36.01	P48	r	19.08	0.06
58270.173681	37.00	P48	r	19.28	0.05
58272.184954	39.01	P48	r	19.37	0.04
58272.185880	39.01	P48	r	19.26	0.04
58274.198912	41.02	P48	r	19.45	0.05
58276.198576	43.02	P48	r	19.67	0.05
58276.199502	43.02	P48	r	19.50	0.05
58276.213970	43.04	P48	g	20.51	0.11
58276.214907	43.04	P48	g	20.56	0.11
58277.193495	44.02	P48	g	20.75	0.15
58277.243113	44.07	P48	r	19.51	0.06
58278.194016	45.02	P48	g	20.32	0.13
58278.237199	45.06	P48	r	19.62	0.07
58279.171516	46.00	P48	r	19.63	0.08
58279.187500	46.01	P48	r	19.63	0.06
58279.207593	46.03	P48	g	20.63	0.13
58279.208530	46.03	P48	g	20.60	0.12
58280.174988	47.00	P48	r	19.63	0.09
58280.227755	47.05	P48	g	20.85	0.15
58281.194468	48.02	P48	r	19.76	0.07
58281.237141	48.06	P48	g	20.65	0.14
58282.193773	49.02	P48	r	19.77	0.07

58282.194699	49.02	P48	r	19.82	0.07
58282.243113	49.07	P48	g	20.51	0.14
58282.244039	49.07	P48	g	20.58	0.15
58283.215544	50.04	P48	r	19.81	0.07
58283.237836	50.06	P48	g	20.45	0.13
58284.203982	51.03	P48	r	19.80	0.08
58284.214236	51.04	P48	g	20.83	0.17

Spectral Classification

A log of our spectroscopic follow-up observations of ZTF18aaqjovh is provided in Table 5.2.

On 9 May 2018 UT we obtained a spectrum of ZTF18aaqjovh using the SEDM and compared it to a set of spectral templates from the publicly-available Supernova Identification code (SNID; Blondin and Tonry 2007). The best match was to a spectrum of SN 1998bw taken at 16 days post-explosion. As shown in Figure 5.2, a comparison with the light curve of SN 1998bw suggests that these two spectra were obtained at comparable phases. So, we classified ZTF18aaqjovh as Type Ic-BL.

On 14 May 2018 UT, we observed ZTF18aaqjovh using the Low Resolution Imaging Spectrometer (Oke et al., 1995) on the Keck I 10-m telescope. The spectrum was reduced and extracted using `LPipe` (Perley, 2019). The next day, we observed the source using the Andalusia Faint Object Spectrograph and Camera (ALFOSC[3]) on the Nordic Optical Telescope (NOT; Djupvik and Andersen 2010). The NOT spectrum was reduced in a standard way, including wavelength calibration against an arc lamp, and flux calibration using a spectrophotometric standard star. We obtained another spectrum on 8 June 2018 UT using the Double Beam Spectrograph (DBSP; Oke and Gunn 1982) on the 200-inch Hale telescope at Palomar Observatory. The DBSP spectrum was reduced using a PyRAF-based pipeline (Bellm and Sesar, 2016). We obtained a final spectrum one month later using LRIS.

The spectral sequence obtained via our follow-up for ZTF18aaqjovh is shown in Figure 5.3, compared to spectra of SN 1998bw at similar phases post-explosion. We used our spectra to estimate the photospheric velocity of ZTF18aaqjovh as a function of time. In typical Ic SNe, photospheric velocity is measured using the

[3]http://www.not.iac.es/instruments/alfosc/

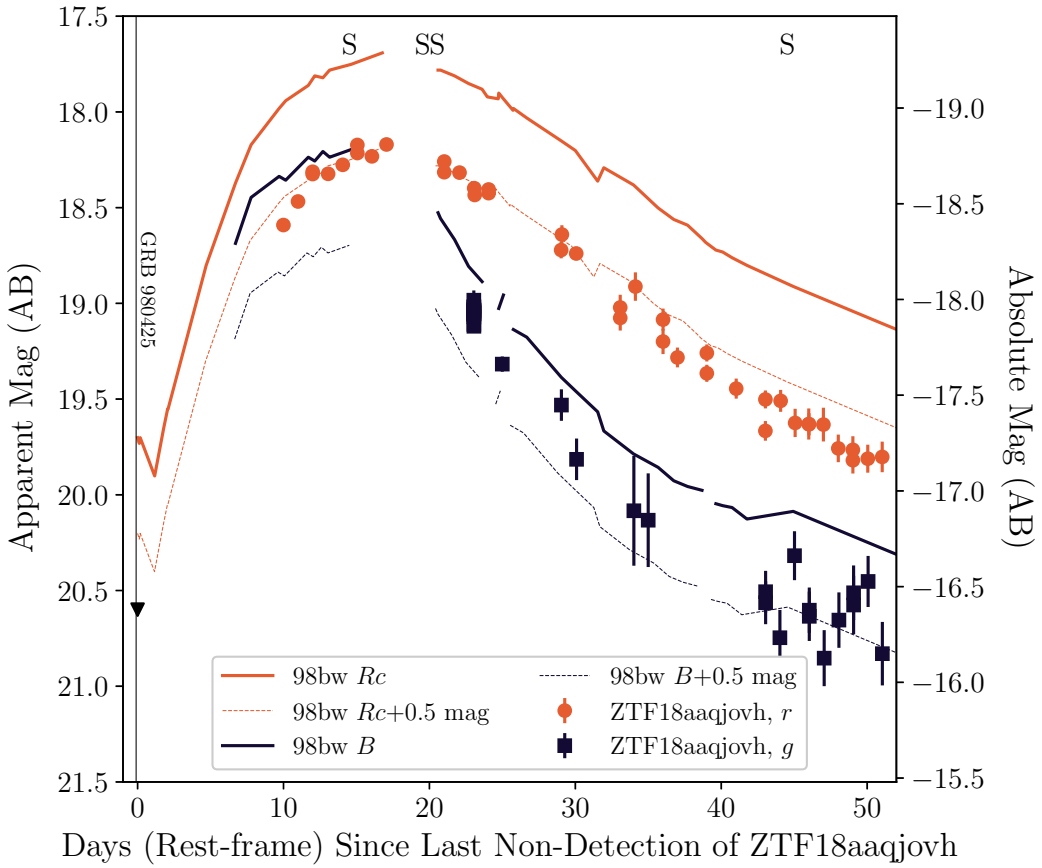

Figure 5.2: The optical light curve of ZTF18aaqjovh, corrected for Milky Way extinction, with P48 r-band in orange circles and P48 g-band in black squares. The light curve of SN 1998bw from Table 2 of Clocchiatti et al. (2011) is shown for comparison as thick black (B-band) and thick orange (Rc-band) lines, shifted to the redshift of ZTF18aaqjovh and also corrected for Milky Way extinction. The same SN 1998bw light curves are shifted by 0.4 mag for closer comparison and are shown as thin dotted lines. The vertical line on the left-hand side indicates the relative time of the GRB 980425, the low-luminosity gamma-ray burst associated with SN 1998bw. The epochs of optical spectra of ZTF18aaqjovh are marked with 'S' along the top of the figure.

width of the Fe II λ5169 line (e.g., Branch et al. 2002). However, due to the high velocities in Ic-BL SNe, the Fe II λ5169 line is blended with the nearby Fe II $\lambda\lambda$4924,5018 lines. So, to perform our velocity measurements, we use the publicly available code[4] based on the method in Modjaz et al. (2016), which convolves a Ic spectrum with Gaussian functions of varying widths until a best match is reached. For the SEDM measurements, we subtracted the contribution to the velocity from

[4]https://github.com/nyusngroup/SESNspectraLib

the resolution of the spectrograph, assuming that $\Delta v^2_{\rm obs} = \Delta v^2_{\rm real} + \Delta v^2_{\rm inst}$ and that $\Delta v_{\rm inst} = 3000\,{\rm km\,s^{-1}}$. The resulting velocities are listed in Table 5.2, and we show the velocity evolution compared to other Ic-BL SNe in Figure 5.4.

Table 5.2: Spectroscopic observations of ZTF18aaqjovh

Date (MJD)	Δt (d)	Tel.+Instr.	Exp. Time (s)	$v_{\rm ph}$ ($10^4\,{\rm km\,s^{-1}}$)
58247.359	14	P60+SEDM	1800	2.12 ± 0.46
58252.322	19	Keck1+LRIS	920	1.74 ± 0.28
58253.977	20	NOT+ALFOSC	2400	1.84 ± 0.54
58277.253	44	P200+DBSP	2700	1.12 ± 0.33
58338.249	105	Keck1+LRIS	1720	N/A

Radio Observations

Upon classifying ZTF18aaqjovh as a Type Ic-BL SN (Section 5.2) we triggered the NSF's Karl G. Jansky Very Large Array (VLA; Perley et al. 2011) for radio follow-up observations under the program VLA/18A-176 (PI: A. Corsi). A log of our observations is provided in Table 5.3.

We observed the field of ZTF18aaqjovh with the VLA over several epochs using the S, C, and Ku bands. We used J1150+2417 as our complex gain calibrator, and 3C286 as our flux density and bandpass calibrator. Data were calibrated using the VLA calibration pipeline available in the Common Astronomy Software Applications (CASA; McMullin et al. 2007). After calibration, we inspected the data manually for further flagging. Images of the field were created using the CLEAN algorithm (Högbom, 1974) available in CASA.

In our VLA images, we found a radio point source consistent with the optical position of ZTF18aaqjovh. Although the radio emission from this source remained fairly constant during the three epochs of our monitoring in C-band (see Table 5.3), its transient nature was confirmed by a non-detection about 280 days after the SN optical discovery. The radio peak flux densities are reported in Table 5.3. Flux density errors are calculated as the quadrature sum of the image RMS and a fractional 5% absolute flux calibration error.

The radio light curve of ZTF18aaqjovh is shown in Figure 5.5, compared to several

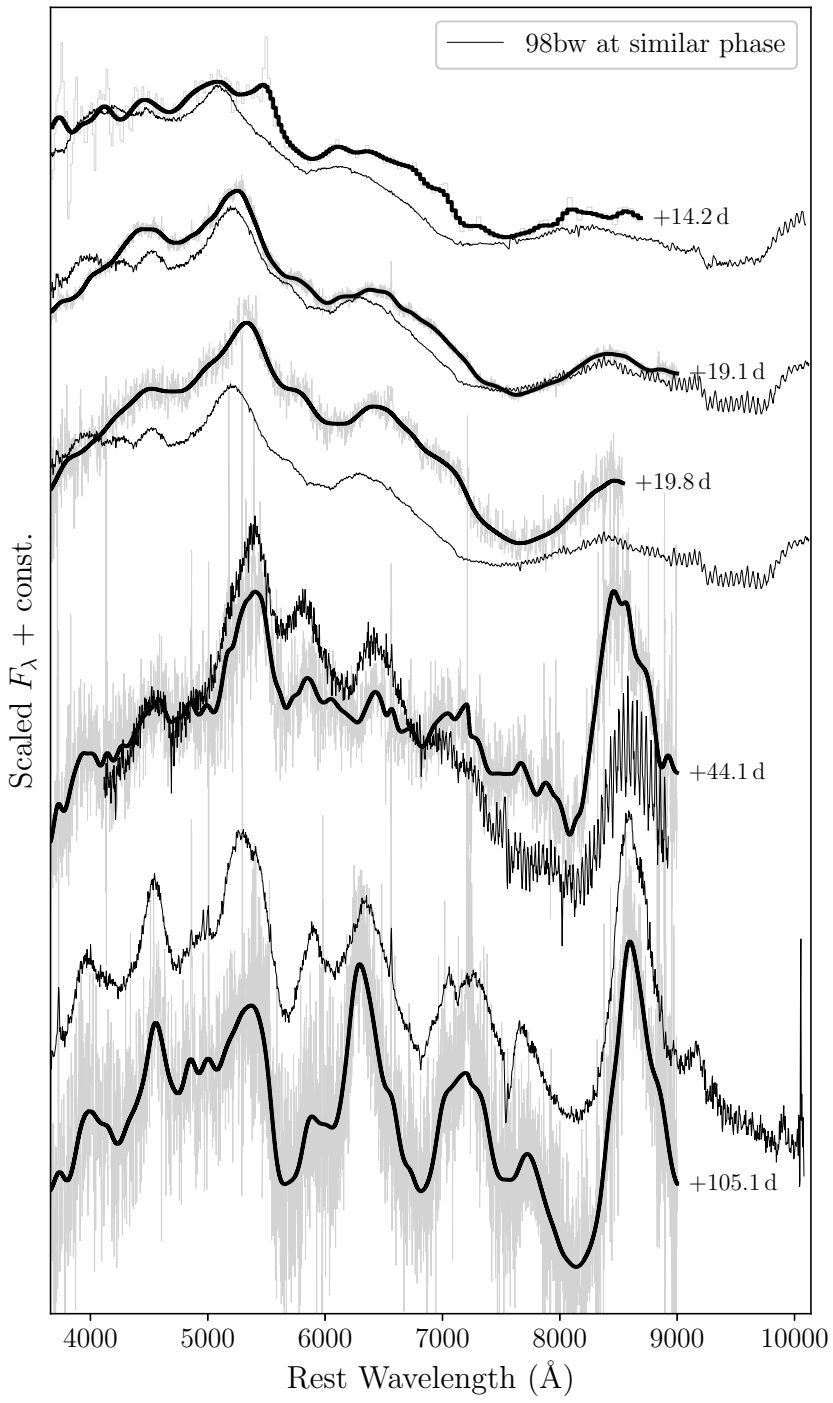

Figure 5.3: Optical spectra of ZTF18aaqjovh. Full spectra are shown in light grey and smoothed spectra are shown in thick black lines. For comparison, we show spectra of SN 1998bw at similar phases as thin black lines. The SN 1998bw spectra were taken from the Open Supernova Catalog (https://sne.space/) and are originally from Patat et al. (2001).

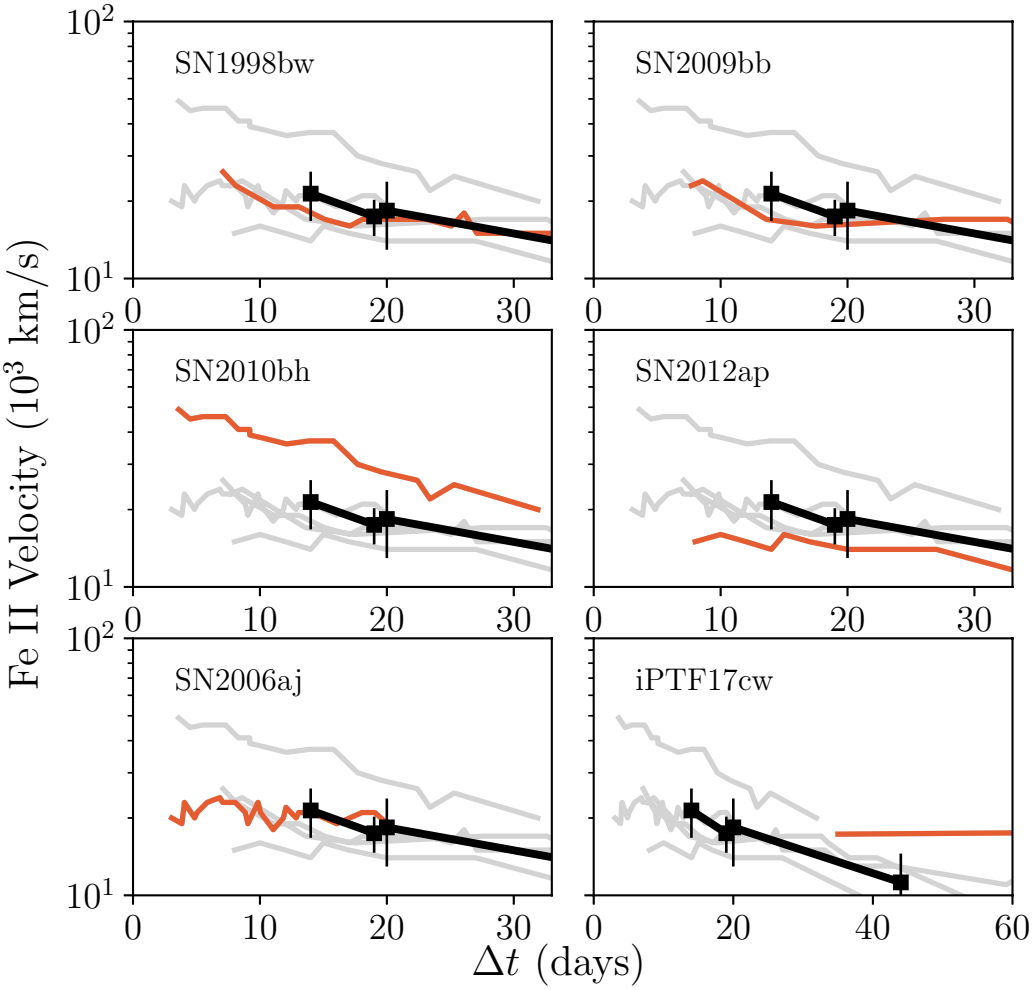

Figure 5.4: Evolution of the photospheric velocity of ZTF18aaqjovh over time as measured from Fe II absorption features in the Ic-BL spectra. For comparison, we show the velocity evolution of several LLGRB-SNe (SN 1998bw / GRB 908425, SN 2010bh / GRB 100316D, SN 2006aj / GRB 060218) and radio-loud relativistic SNe lacking a coincident GRB detection (SN 2009bb, SN 2012ap, iPTF 17cw). Each panel shows measurements for ZTF18aaqjovh as black squares, the population of comparison events as light grey lines in the background, and one comparison SN highlighted in orange. Data were taken from Modjaz et al. (2016) and explosion times were estimated from Bufano et al. (2012), Campana et al. (2006), Galama et al. (1998), Milisavljevic et al. (2015), and Soderberg et al. (2010), and Corsi et al. (2014).

other Ic-BL SNe. At the distance of ZTF18aaqjovh, the 6 GHz radio luminosity density at $\Delta t \approx 20$ d since explosion is 2×10^{27} erg s^{-1} Hz^{-1}. This is over an order of magnitude fainter than SN 1998bw at a similar epoch, and most similar to the luminosity of iPTF17cw at similar frequencies.

Table 5.3: Radio flux density measurements of ZTF18aaqjovh

Start Date UT	Time on-source hr	Δt days	$S_{3\,\mathrm{GHz}}$ (μJy)	$S_{6\,\mathrm{GHz}}$ (μJy)	$S_{15\,\mathrm{GHz}}$ (μJy)	Array config.
11 May 2018	0.67	16	–	32.5 ± 7.1	–	A
16 May 2018	0.67	21	26.0 ± 6.9	–	15.1 ± 5.2	A
17 May 2018	0.67	22	–	29.6 ± 5.3	–	A
29 May 2018	0.67	34	–	26.6 ± 5.4	–	A
31 May 2018	1.5	36	34.6 ± 4.8	–	–	A
26 Jan 2019	1.5	276	–	$\lesssim 15$	–	C

X-ray Observations

A log of our X-ray observations is provided in Table 5.4.

On 31 May 2018 UT we obtained a 2.5 ks *Swift*/XRT target-of-opportunity observation of ZTF18aaqjovh. We built the XRT light curve using the online generator (Evans et al., 2009). On the web form[5], we used the default values except for `Try to centroid?` which was set to `No`. The source was not detected with a 3-σ upper limit of 7.2×10^{-3} cps. To convert the upper limit from count rate to flux, we assumed a Galactic neutral hydrogen column density[6] of $n_H = 1.37 \times 10^{20}$ cm^{-2} and a power-law spectrum $f \propto E^{-\Gamma}$ where f is flux (photons cm^{-2} s^{-1}), E is energy, and $\Gamma = 2$ is the photon index. This gives an unabsorbed upper-limit on the 0.3–10 keV flux of 2.3×10^{-13} erg cm^{-2} s^{-1}, corresponding to a luminosity of 1.7×10^{42} erg s^{-1}.

We also obtained two epochs of observations of ZTF18aaqjovh with the Advanced CCD Imaging Spectrometer (ACIS; Garmire et al. 2003) on the *Chandra* X-ray Observatory via our approved program (No. 19500451, PI: Corsi). The first epoch began at 11:07 on 28 May 2018 UT ($\Delta t \approx 33$ d) under ObsId 20315 (integration time 9.93 ks), and the second began at 11:10 on 24 July 2018 UT ($\Delta t \approx 90$ d) under ObsId 20316. No X-ray emission was detected at the location of ZTF18aaqjovh in either epoch, with a 90% upper limit on the 0.5–7.0 keV count rate of 2.52×10^{-4} ct s^{-1} and 2.32×10^{-4} ct s^{-1}, respectively. For the same Galactic n_H and power-law source model that we used in the *Swift* data, we obtain an upper limit on the unabsorbed 0.3–

[5] https://www.swift.ac.uk/user_objects/

[6] https://heasarc.gsfc.nasa.gov/cgi-bin/Tools/w3nh/w3nh.pl

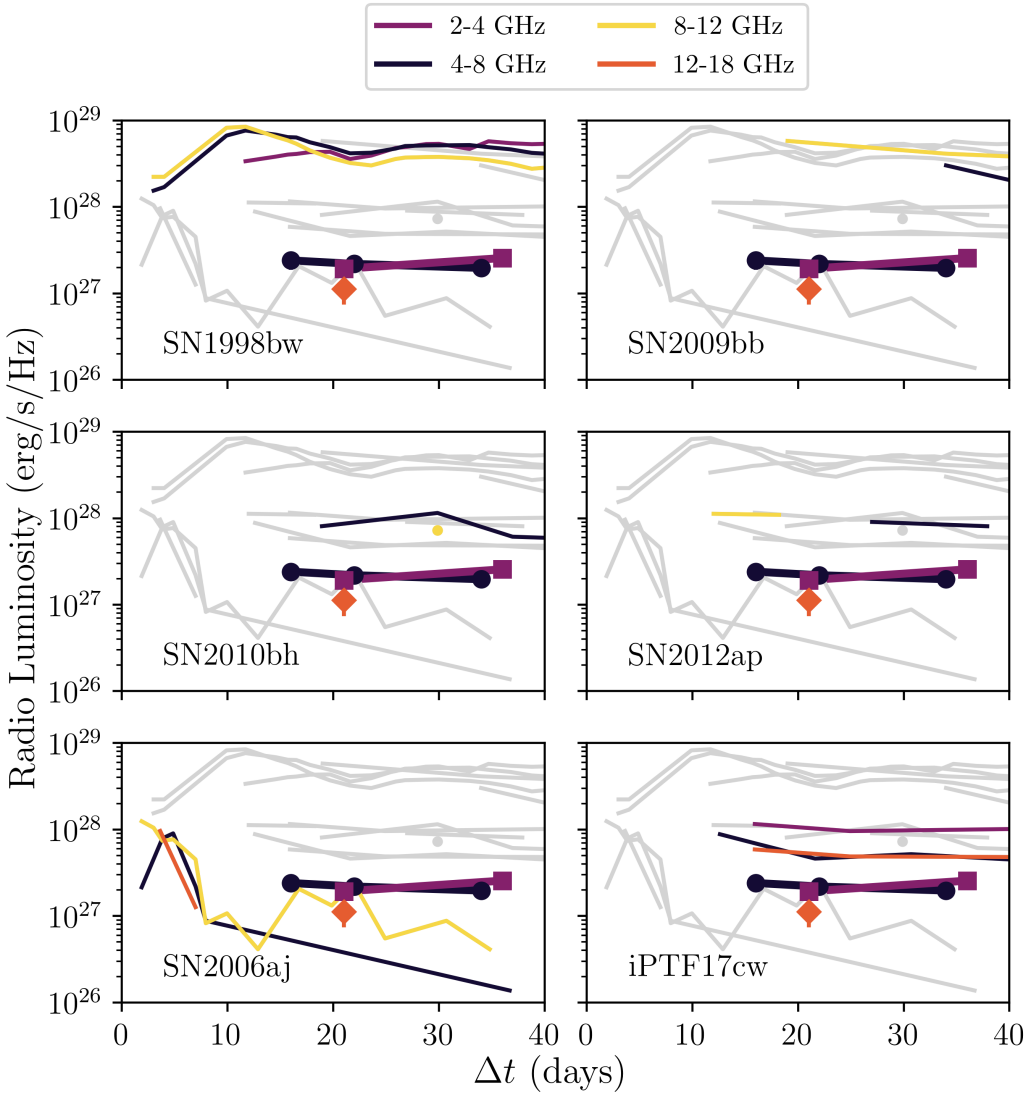

Figure 5.5: Radio light curve of ZTF18aaqjovh compared with LLGRB-SNe (SN 1998bw / GRB 980425, SN 2010bh / GRB 100316D, SN 2006aj / GRB 060218) and relativistic SNe (SN 2009bb, SN 2012ap, iPTF17cw). Each panel shows observations of ZTF18aaqjovh (connected symbols), the population of comparison events as light grey lines in the background, and one SN highlighted as colored lines for comparison. Note that ZTF18aaqjovh lacks data in the 8–12 GHz range. Data were taken from Chakraborti et al. (2015), Corsi et al. (2017), Kulkarni et al. (1998), Margutti et al. (2014), and Soderberg et al. (2006b, 2010).

10 keV flux of 3.4×10^{-15} erg s^{-1} cm^{-2} in the first epoch and 3.1×10^{-15} erg s^{-1} cm^{-2} in the second epoch. At the distance of ZTF18aaqjovh, these correspond to upper limits on the X-ray luminosity of 2.5×10^{40} erg s^{-1} and 2.3×10^{40} erg s^{-1}. These upper limits are compared with the X-ray luminosity of radio-loud Ic-BL SNe in Figure 5.6.

Table 5.4: X-ray observations of ZTF18aaqjovh

Start Date (UT)	Δt (d)	Instr.	Int. (ks)	Flux (erg s^{-1} cm^{-2})
2018-05-28 11:07:06	33	*Chandra*/ACIS	9.93	$< 3.4 \times 10^{-15}$
2018-05-31 00:33:57	36	*Swift*/XRT	2.5	$< 2.3 \times 10^{-13}$
2018-07-24 11:10:42	90	*Chandra*/ACIS	9.93	$< 3.1 \times 10^{-15}$

Search for Gamma-Rays

We searched for any gamma-ray burst (GRB) coincident with the position and estimated time of first light of ZTF18aaqjovh. As shown in Figure 5.2 and discussed in more detail in Section 5.3, we can use the relative time between GRB 980425 and the r-band peak of SN 1998bw to estimate the time of a GRB associated with ZTF18aaqjovh. If this relative time is the same between the two SNe, then the associated GRB would have been approximately at the time of the last non-detection ($t_0 \approx$ 2018 April 25 UT), ten days prior to the first detection on 2018 May 5 UT.

To be conservative, we set our search window to be $t_0 \pm 10$ d. In Table 5.5 we list all 20 GRBs detected in this window. Of the 20, all but one are ruled out based on the position of the SN. The only possible counterpart is a GRB on 2018 May 3 03:41:01 ($\Delta t = 8$) detected by *Konus-Wind* while *Fermi*/GBM was offline. The duration of this burst was 35 s. Modeling the spectrum with a cutoff power law model with $E_p = 107^{+64}_{-25}$ keV and 20–1500 keV fluence 2×10^{-6} erg cm^{-2} we obtain an $L_{\rm iso} = 8 \times 10^{47}$ erg s^{-1}, which is typical of LLGRBs (Cano et al., 2017b).

Table 5.5: Gamma-ray bursts within 10 days of the estimated time of first light of ZTF18aaqjovh

Date (UT)	Name	Δt (d)	Instr.[a]	Pos.[b]	Verdict[c]
20180416	180416D	-9	KAI	N	N(a)
20180416	180416A	-9	KGI	113.65, +49.120	N(b)
20180416	180416B	-9	KGAC	354.233, +78.433	N(b)
20180417		-8	K	S	N(c)

20180420		-5	KG	93.510, -28.320	N(b)
20180420		-5	KGI	83.230, -25.250	N(b)
20180421		-4	K	N	N(c)
20180423		-2	KGI	208.680, +9.840	N(b)
20180425	180425A	0	KS	64.452, -32.952	N(b)
20180426		1	KGI	251.240, +81.390	N(b)
20180426		1	KG	202.410, +58.170	N(b)
20180426		1	K	N	N(c)
20180426		1	K	S	N(b)
20180427	180427A	2	KGI	283.330, +70.300	N(b)
20180428		3	KGI	92.120, +54.780	N(b)
20180428		3	K	N	N(c)
20180429		4	KI	S	N(b)
20180503		8	K	N	Y
20180504		9	KGI	220.230, +38.720	N(b)
20180504	180504A	9	KSI	331.144, -14.658	N(b)

[a]K: *Konus-Wind*, A: Astrosat, I: *INTEGRAL* SPI-ACS, G: *Fermi*/GBM, S: *Swift*/BAT.
[b]N and S: position is localized to the Northern and Southern ecliptic hemispheres, respectively
[c]N:association ruled out because SN position (a) Earth-occulted for Astrosat and GBM,
(b) inconsistent with the localized burst position, (c) visible to GBM but not detected.
Y: association is possible.

However, due to the coarse localization and the implication that the light curve of ZTF18aaqjovh increased to peak brightness much more steeply than the light curve of SN 1998bw, we consider the association with the GRB on May 3 unlikely. Assuming it is not related, we can set a limit on the fluence and corresponding isotropic equivalent energy of a prompt burst associated with ZTF18aaqjovh. The Interplanetary Network (IPN) has essentially a 100% duty cycle across the sky, and detects GRBs with $E_{\rm pk} > 20\,$keV down to $6 \times 10^{-7}\,{\rm erg\,cm^{-2}}$ at 50% efficiency (Hurley et al., 2010, 2016). Using *Konus-Wind* waiting mode data near t_0 and assuming a typical GRB spectrum (a Band function with $\alpha = -1, \beta = -2.5$, and $E_p = 300\,$keV; Band et al. 1993; Preece et al. 2000), we estimate a peak limiting flux of $2.1 \times 10^{-7}\,{\rm erg\,cm^{-2}\,s^{-1}}$ (20–1500 keV, 2.944 s scale). At the distance of ZTF18aaqjovh, this corresponds to an upper limit on a GRB peak luminosity of $L_{\rm iso} \approx 1.6 \times 10^{48}\,{\rm erg\,s^{-1}}$, two orders of magnitude less luminous than classical GRBs but similar to LLGRBs (Cano et al., 2017b). We note that the IPN would not be sensitive to LLGRBs such as LLGRB 060218 associated with SN 2006aj (Cano et al., 2017b) because of their soft spectra ($E_{\rm pk} < 20\,$keV for 060218).

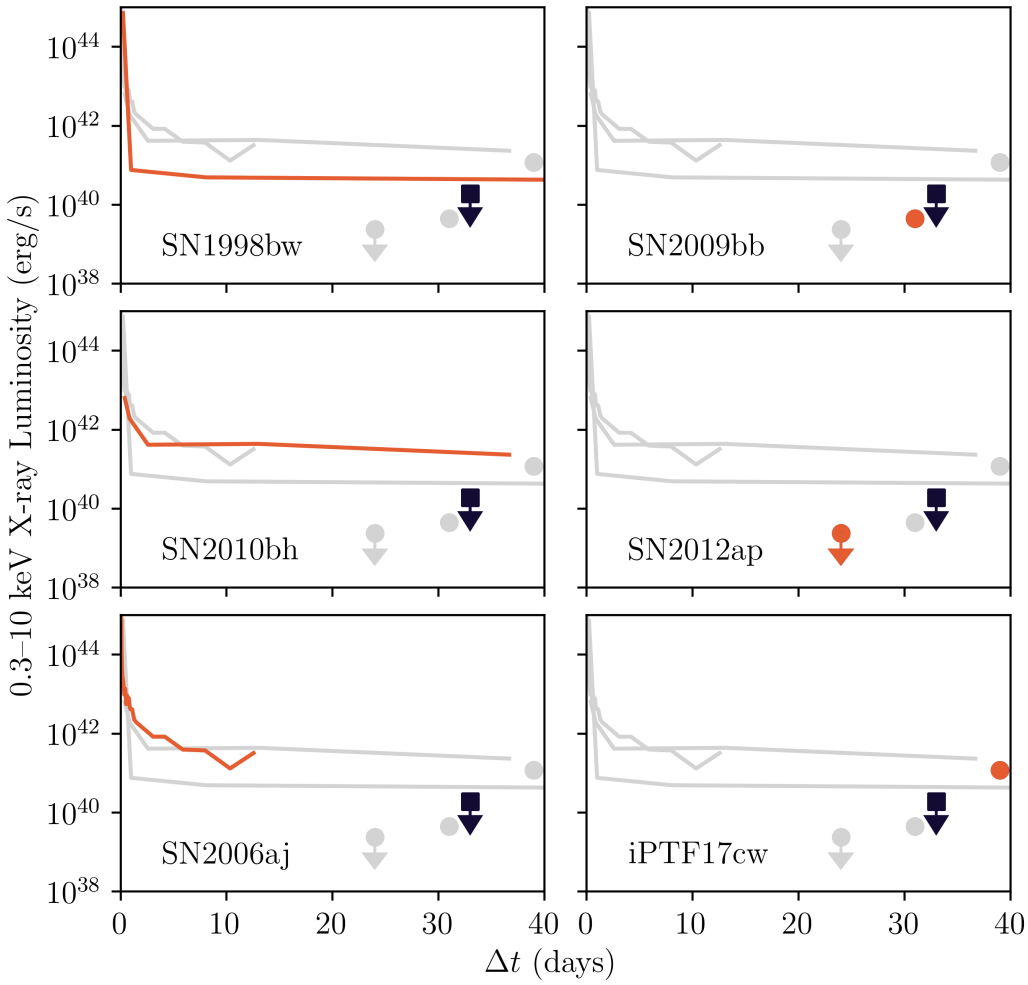

Figure 5.6: Upper limit on the X-ray luminosity of ZTF18aaqjovh from our first *Chandra* observation (black square) compared to the X-ray luminosity at similar epochs of LLGRBs (SN 1998bw, SN 2010bh, SN 2006aj) and Ic-BL SNe with relativistic outflows discovered independently of a γ-ray trigger (iPTF17cw, SN 2009bb, SN 2012ap). Each panel shows the full set of comparison events in light grey, with one event highlighted in orange. Data were taken from Campana et al. (2006), Corsi et al. (2017), and Margutti et al. (2014).

5.3 Analysis and Discussion

Modeling the Optical Light Curve

As shown in Figure 5.2, the r-band light curve of ZTF18aaqjovh declines slightly faster than the light curve of SN 1998bw, and is 0.4 mag fainter. For a SN with an optical light curve powered by radioactive decay, the "stretch" (width) of the light curve scales with the kinetic energy and ejecta mass as (Lyman et al., 2016; Valenti et al., 2008)

$$\tau_m \propto \left(\frac{{M_{\rm ej}}^3}{E_k}\right)^{1/4}, \tag{5.1}$$

where τ_m is the width of the light curve, $M_{\rm ej}$ is the ejecta mass, and E_k is the kinetic energy of the explosion. The degeneracy between $M_{\rm ej}$ and E_k is broken by the photospheric velocity (see Eq. 2 in Lyman et al., 2016):

$$v_{\rm ph}^2 = \frac{5}{3}\frac{2E_k}{M_{\rm ej}}. \tag{5.2}$$

As shown in Figure 5.2 and Figure 5.4, ZTF18aaqjovh has a photospheric velocity close to that of SN 1998bw, and its light curve is narrower. So, we expect the ejecta mass and kinetic energy of ZTF18aaqjovh to be slightly smaller to that of SN 1998bw, which had $M_{\rm ej} \approx 4.4^{+1.2}_{-0.8}\,M_\odot$ and $E_k \approx 9.9^{+3.8}_{-2.2} \times 10^{51}$ erg, respectively (Lyman et al., 2016), values typical of Ic-BL SNe from untargeted surveys (Taddia et al., 2019).

Finally, assuming that the dominant powering mechanism for the optical light curve is radioactive decay, we have the following energy deposition rate from ^{56}Ni (Kasen, 2017):

$$L_{^{56}\rm Ni}(t) = 2 \times 10^{43} \left(\frac{M_{\rm Ni}}{M_\odot}\right) \left[3.9e^{-t/\tau_{\rm Ni}} + 0.678\left(e^{-t/\tau_{\rm Co}} - e^{-t/\tau_{\rm Ni}}\right)\right] {\rm erg\,s^{-1}}, \tag{5.3}$$

where the decay lifetimes of ^{56}Ni and ^{56}Co are $\tau_{\rm Ni} = 8.8\,$d and $\tau_{\rm Co} = 113.6\,$d, respectively. Arnett's law (Arnett, 1982) states that the instantaneous energy deposition rate is equal to the SN luminosity at peak. Under this assumption, the peak luminosity is simply equal to $L_{^{56}\rm Ni}$ at that time, so is directly proportional to $M_{\rm Ni}$.

Taking $L \approx \nu L_\nu \approx 6.9 \times 10^{42}\,{\rm erg\,s^{-1}}$ at peak light ($t \approx 15\,$d) we find that $M_{\rm Ni} \approx 0.3\,M_\odot$. For reference, the nickel mass of SN 1998bw has been estimated to be $M_{\rm Ni} \approx 0.54^{+0.08}_{-0.07}\,M_\odot$ (Lyman et al., 2016). These values are typical for GRB-SNe (Cano et al., 2017b) and for Ic-BL SNe in general (Taddia et al., 2019).

Properties of the Fastest (Radio-emitting) Ejecta

As shown in Figure 5.5, the radio luminosity of ZTF18aaqjovh is between that of SN 2006aj and that of iPTF17cw. Due to the faintness of the SN it is unfortunately difficult to measure the true rate of change of the flux, but the slow temporal

evolution of the 3-6 GHz flux during the first four epochs of observation (Δt = 16 d to Δt = 36 d) may imply that the synchrotron self-absorption (SSA) frequency is passing through these frequencies at this time. This is supported by the 3–15 GHz observations at Δt = 21 − 22 d, which suggest that the SSA peak is below 15 GHz and close to 3–6 GHz. Altogether, we conclude that the SSA peak is 3–15 GHz at $\Delta t \approx 20$ d, and that the peak flux is 20–30 μJy.

With these estimates of the SSA peak frequency and peak flux, we use the framework laid out in Chevalier (1998) to estimate the shock energy U (the amount that has been converted into pressure by the ambient medium), the ambient density, and the mean shock velocity at $\Delta t \sim 20$ d. The assumption is that the synchrotron spectrum arises from a population of relativistic electrons with a power-law number distribution in Lorentz factor γ_e and some minimum Lorentz factor γ_m:

$$\frac{dN(\gamma_e)}{d\gamma_e} \propto \gamma_e^{-p}, \gamma_e \geq \gamma_m. \tag{5.4}$$

For typical radio SNe, $2.5 < p < 3$ (Jones and Ellison, 1991). Here we assume $p \approx 3$, as in Chevalier (1998). Under this assumption, expressions for the shock radius and magnetic field strength are given in Equations 13 and 14 of Chevalier (1998). The magnetic field strength can then be used to estimate the magnetic energy density, assuming that equal amounts of energy are partitioned into electrons, magnetic fields, and protons (Soderberg et al., 2010).

These relations between observables and physical properties are summarized in Figure 5.7, adapted from Ho et al. (2019c). The mean velocity of the shock we derive for ZTF18aaqjovh is $v = 0.06$–$0.4c$. So, the outflow associated with ZTF18aaqjovh could have been as fast as that observed in the GRB-associated SN 2010bh. The implied mass-loss rate is $0.1\text{–}3 \times 10^{-4} (v_w / 1000\,\mathrm{km\,s^{-1}})\ M_\odot\ \mathrm{yr}^{-1}$, which could be as high as that of the strongly CSM-interacting SN PTF 11qcj (Corsi et al., 2014).

Modeling the Radio to X-ray SED

In SN explosions, the shockwave that accelerates electrons into a power-law distribution and produces synchrotron radiation, detected as radio emission, can also produce X-rays (Chevalier and Fransson, 2006) via several mechanisms. X-rays can have the same origin as the radio emission (lying along the same synchrotron spectrum). However, X-rays can also arise from inverse Compton scattering of the optical photons by the electrons producing the radio emission (Chevalier and

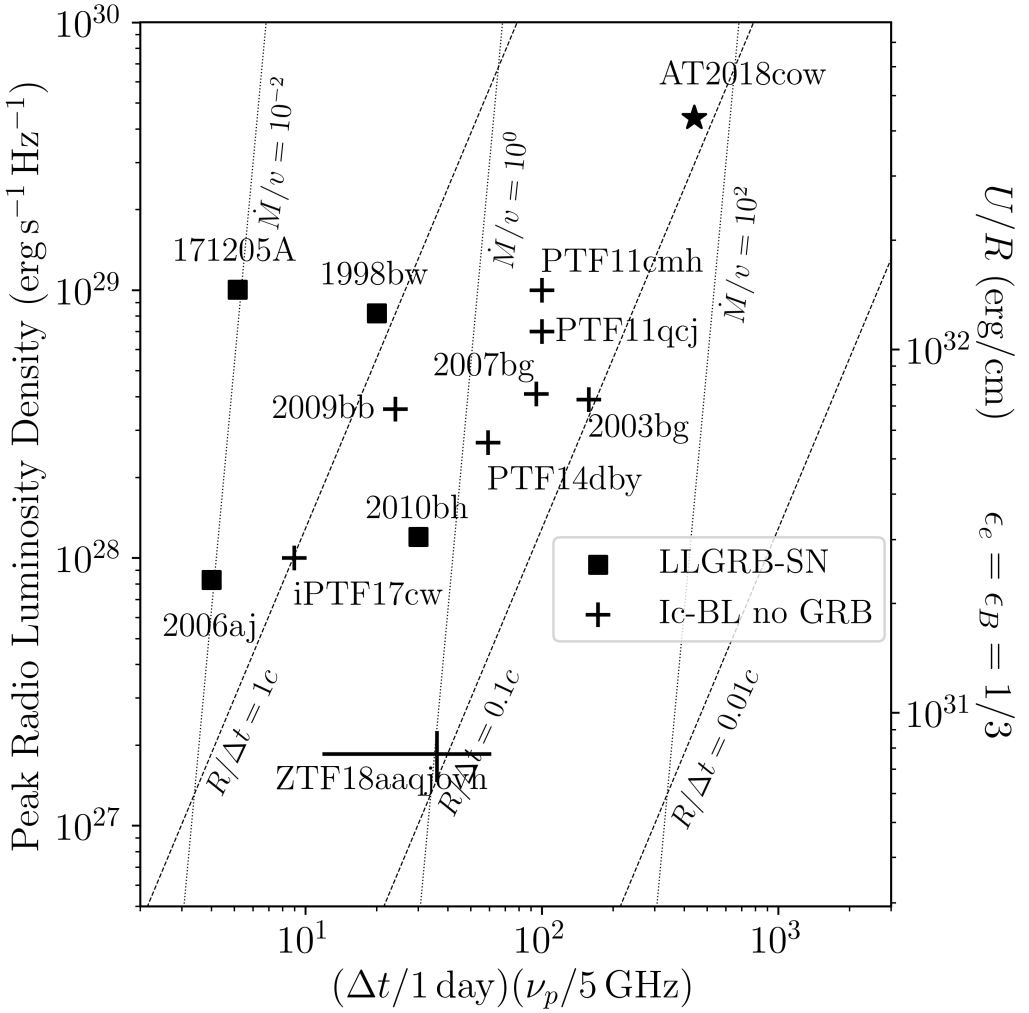

Figure 5.7: The peak radio luminosity of ZTF18aaqjovh compared to other energetic stellar explosions, cf. Chevalier (1998), Ho et al. (2019c), and Soderberg et al. (2010). In Ho et al. (2019c) we showed that the peak luminosity is directly proportional to U/R, the energy swept up per unit radius; we display this value on the right-hand side. Error bars reflect the estimated SSA peak (20–30 μJy, 3–15 GHz) at $\Delta t \approx 20$ d. Lines of constant velocity are shown, as well as lines of constant mass-loss rate (scaled to wind velocity) in units of $10^{-4}\,M_\odot \mathrm{yr}^{-1}/1000\,\mathrm{km\,s}^{-1}$. The radio luminosity for GRB 171205A was taken from VLA observations reported by Laskar et al. (2017) but we note that this is a lower limit in luminosity and in peak frequency because the source was heavily self-absorbed at this epoch. The radio luminosity for other sources is from, or derived using data from, Corsi et al. (2014, 2017), Kulkarni et al. (1998), Margutti et al. (2013), Salas et al. (2013), and Soderberg et al. (2005, 2006b, 2010).

Fransson, 2006, 2017). For a number of Ic-BL SNe, it seems that the simple syn-

chrotron scenario is insufficient to explain the radio and X-ray observations — in other words, there is an excess of X-ray emission (Corsi et al., 2014; Margutti et al., 2013; Soderberg et al., 2006b).

As described in Section 5.2, we do not detect X-ray emission from ZTF18aaqjovh, corresponding to upper limits of $L_X < 3.4 \times 10^{40}\,\mathrm{erg\,s^{-1}}$ at $\Delta t \sim 33$ d and $L_X < 3.1 \times 10^{40}\,\mathrm{erg\,s^{-1}}$ at $\Delta t \sim 90$ d. At $\Delta t \sim 33$ d, this is smaller than the luminosity of X-ray emission associated with iPTF17cw, SN 1998bw (GRB 980425), and SN 2010bh (GRB 031203) at a similar epoch. The 0.3–10 keV luminosity of SN 2010bh at $\Delta t = 38$ d was $2.4 \times 10^{41}\,\mathrm{erg\,s^{-1}}$ (Margutti et al., 2014), which was already the least X-ray luminous LLGRB at this phase (second only to GRB 980425). Due to a lack of data later than 10 d we cannot rule out a luminosity similar to SN 2006aj, SN 2009bb, and SN 2012ap (Margutti et al., 2014).

Figure 5.8 shows the radio luminosity and X-ray upper limit at $\Delta t \approx 33$ days, from our observations of ZTF18aaqjovh with the VLA and *Chandra* on 2018 May 28–29 UT. The spectral index is constrained to be $\beta < -0.6$ where $L_\nu \propto \nu^\beta$. A common optically thin spectral index for radio SNe is $\beta \sim -0.5$ to -1 (Chevalier, 1998) where $F_\nu \propto \nu^\beta$. Above the cooling frequency, this steepens to $\beta \sim -1$ or $\beta \sim -1.5$. Thus we cannot conclude whether there is X-ray emission from an extension of the synchrotron spectrum, or whether there is an excess from some other mechanism such as cosmic ray-dominated shocks (Chevalier and Fransson, 2006), which has been observed in a number of engine-driven SNe including iPTF17cw ($\beta = -0.6$; Corsi et al. 2017), GRB 060218 ($\beta = -0.5$; Soderberg et al. 2006b), and GRB 100316D ($\beta < -0.6$; Margutti et al. 2014).

Gamma-Ray Burst

In Section 5.2 we searched for coincident GRBs and found one possible counterpart, although the association is highly unlikely due to the close proximity of the burst time with the first detection of the light curve.

Here we work under the hypothesis that ZTF18aaqjovh was associated with a GRB that we missed, and attempt to derive possible constraints on the γ-ray emission based on the SN properties. From four GRB-SNe, Li (2006) found the following relation between the peak spectral energy of the GRB and the peak bolometric luminosity of the associated SN:

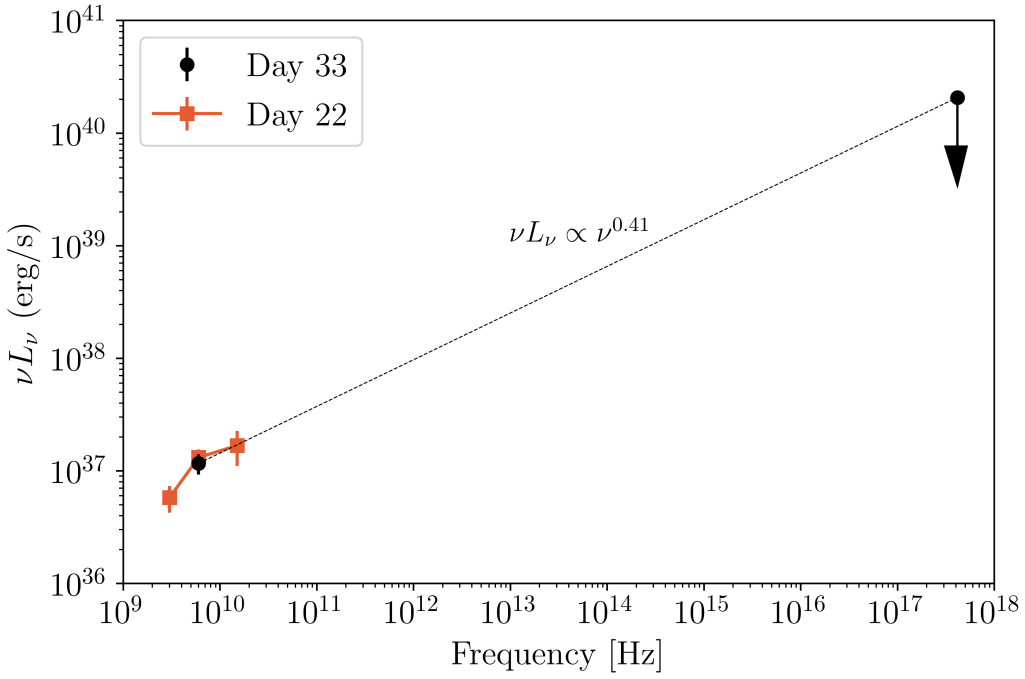

Figure 5.8: The radio luminosity and upper limit on X-ray luminosity of ZTF18aaqjovh at $\Delta t \approx 33$ d. From these measurements, we constrain the spectral index from the radio to X-ray frequencies to be $\beta < -0.6$ where $L_\nu \propto \nu^\beta$.

$$E_{\gamma,\mathrm{peak}} = 90.2\,\mathrm{keV}\left(\frac{L_{\mathrm{SN,peak}}}{10^{43}\,\mathrm{erg\,s^{-1}}}\right)^{4.97}. \tag{5.5}$$

From the peak of the r-band light curve of ZTF18aaqjovh, we can estimate $L_{\mathrm{SN,peak}} \approx \nu f_\nu \approx 1.7 \times 10^9\,L_\odot$, which gives $E_{\gamma,\mathrm{peak}} \approx 15$ keV. Using the so-called Amati relationship between a GRB peak energy and its isotropic equivalent energy (Amati, 2006; Li, 2006):

$$E_{\gamma,\mathrm{peak}} = 97\,\mathrm{keV}\left(\frac{E_{\gamma,\mathrm{iso}}}{10^{52}\,\mathrm{erg\,s^{-1}}}\right)^{0.49}, \tag{5.6}$$

we find an expected $E_{\mathrm{iso}} \approx 2 \times 10^{50}$ erg for a potential GRB associated with ZTF18aaqjovh. These values of $E_{\gamma,\mathrm{peak}}$ and E_{iso} are similar to what has been measured for LLGRBs (Cano et al., 2017b), and would not have been detectable by the IPN.

5.4 Summary and Conclusions

We presented optical, X-ray, and radio observations of ZTF18aaqjovh, a Ic-BL SN discovered by ZTF as part of our campaign with the VLA to search for engine-driven explosions. ZTF18aaqjovh shares a number of features in common with relativistic SNe: an optical light curve similar to SN 1998bw and early-peaking radio emission similar to iPTF17cw. The limits on X-ray and gamma-ray emission rule out a classical GRB but cannot rule out an LLGRB. Due to the low signal-to-noise of our measurements, we can only constrain the velocity of the forward shock to be 0.06–0.4c. Thus, this is at most a mildly relativistic explosion, and we have no definitive evidence of a long-lived central engine.

From radio follow-up observations of Ic-BL SNe discovered by PTF and now ZTF, it has become clear that emission as luminous as that accompanying SN 1998bw is rare. Without a GRB trigger it is challenging to discover explosions similar to SN 2006aj, which had a low-frequency radio light curve that peaked within the first five days and faded more quickly than the light curve of SN 1998bw. In the case of ZTF18aaqjovh, X-ray observations within the first ten days may have enabled us to detect an X-ray light curve like that accompanying SN 2006aj, but we were unable to observe with *Swift* due to the proximity of ZTF18aaqjovh to the Sun at the time.

At present, Ic-BL SNe are discovered and classified via brute-force spectroscopy, so unless they are very nearby they are typically not recognized until a week after explosion. It would be useful to develop strategies for discovering Ic-BL SNe earlier in their evolution, perhaps based on the properties of their host environment, or—in higher-cadence surveys—from the presence of an early (< 1 d) peak in the optical light curve, like that seen in SN 2006aj and SN 1998bw. These could perhaps be distinguished from double-peaked light curves of other SN progenitors (e.g. Fremling et al. 2019b) by the luminosity of this first peak, if the redshift to the SN is known.

When the paper has been accepted for publication the data will be made publicly available via WISeREP, an interactive repository of supernova data (Yaron and Gal-Yam, 2012). The code to produce the figures in this paper has been released under `10.5281/zenodo.3634931`.

We would like to thank the anonymous referee for taking the time to do a thorough reading of the manuscript, and for providing detailed and useful comments. A.Y.Q.H. thanks Kevin Hurley for maintaining the IPN master burst list (`ssl.berkeley.edu/ipn3/masterli.html`) that was used to compile Table 6, and

Daniel Goldstein and Yuhan Yao (Caltech) for useful discussions regarding ZTF photometry.

Based on observations obtained with the Samuel Oschin Telescope 48-inch and the 60-inch Telescope at the Palomar Observatory as part of the Zwicky Transient Facility project. ZTF is supported by the National Science Foundation under Grant No. AST-1440341 and a collaboration including Caltech, IPAC, the Weizmann Institute for Science, the Oskar Klein Center at Stockholm University, the University of Maryland, the University of Washington, Deutsches Elektronen-Synchrotron and Humboldt University, Los Alamos National Laboratories, the TANGO Consortium of Taiwan, the University of Wisconsin at Milwaukee, and Lawrence Berkeley National Laboratories. Operations are conducted by COO, IPAC, and UW. This work made use of data supplied by the UK Swift Science Data Centre at the University of Leicester. This work made use of the data products generated by the NYU SN group, and released under DOI:10.5281/zenodo.58767, available at `https://github.com/nyusngroup/SESNspectraLib`. SED Machine is based upon work supported by the National Science Foundation under Grant No. 1106171. The ZTF forced-photometry service was funded under the Heising-Simons Foundation grant #12540303 (PI: Graham). Partially based on observations made with the Nordic Optical Telescope, operated by the Nordic Optical Telescope Scientific Association at the Observatorio del Roque de los Muchachos, La Palma, Spain, of the Instituto de Astrofisica de Canarias. The data presented here were obtained in part with ALFOSC, which is provided by the Instituto de Astrofisica de Andalucia (IAA) under a joint agreement with the University of Copenhagen and NOTSA. The National Radio Astronomy Observatory is a facility of the National Science Foundation operated under cooperative agreement by Associated Universities, Inc.

A.Y.Q.H. is supported by a National Science Foundation Graduate Research Fellowship under Grant No. DGE-1144469. A.C. acknowledges support from the National Science Foundation CAREER award #1455090. A.C. and A.Y.Q.H. acknowledge support from the Chandra GI award #19500451. This work was partially supported by the GROWTH project funded by the National Science Foundation under PIRE Grant No. 1545949. A.A.M. is funded by the Large Synoptic Survey Telescope Corporation, the Brinson Foundation, and the Moore Foundation in support of the LSSTC Data Science Fellowship Program; he also receives support as a CIERA Fellow by the CIERA Postdoctoral Fellowship Program (Center for Interdisciplinary Exploration and Research in Astrophysics, Northwestern University). CF gratefully

acknowledges support of his research by the Heising-Simons Foundation (#2018-0907)

Chapter 6

EVIDENCE FOR LATE-STAGE ERUPTIVE MASS LOSS IN THE PROGENITOR TO SN 2018GEP, A BROAD-LINED IC SUPERNOVA: PRE-EXPLOSION EMISSION AND A RAPIDLY RISING LUMINOUS TRANSIENT

Ho, A. Y. Q. et al. (2019). "Evidence for Late-stage Eruptive Mass Loss in the Progenitor to SN2018gep, a Broad-lined Ic Supernova: Pre-explosion Emission and a Rapidly Rising Luminous Transient". In: *ApJ* 887.2, p. 169. DOI: 10.3847/1538-4357/ab55ec. arXiv: 1904.11009 [astro-ph.HE].

Anna Y. Q. Ho[1], Daniel A. Goldstein[1], Steve Schulze[2], David K. Khatami[3], Daniel A. Perley[4] Mattias Ergon[5] , Avishay Gal-Yam[2] , Alessandra Corsi[6], Igor Andreoni[1] , Cristina Barbarino[5] , Eric C. Bellm[7], Nadia Blagorodnova[8], Joe S. Bright[9] , E. Burns[10] , S. Bradley Cenko[11, 12] , Virginia Cunningham[13] , Kishalay De[1], Richard Dekany[14] , Alison Dugas[1] , Rob P. Fender[9] , Claes Fransson[5] , Christoffer Fremling[15], Adam Goldstein[16] , Matthew J. Graham[15] , David Hale[14] , Assaf Horesh[17] , Tiara Hung[18] , Mansi M. Kasliwal[1], N. Paul M. Kuin[19] , S. R. Kulkarni[1] , Thomas Kupfer[20] , Ragnhild Lunnan[5] , Frank J. Masci[21], Chow-Choong Ngeow[22] , Peter E. Nugent[23] , Eran O. Ofek[2] , Maria T. Patterson[7] , Glen Petitpas[24], Ben Rusholme[21] , Hanna Sai[25] , Itai Sfaradi[17] , David L. Shupe[21] , Jesper Sollerman[5] , Maayane T. Soumagnac[2], Yutaro Tachibana[26] , Francesco Taddia[5] , Richard Walters[1], Xiaofeng Wang[25], Yuhan Yao[1], Xinhan Zhang[25]

[1]Cahill Center for Astrophysics, California Institute of Technology, MC 249-17, 1200 E California Boulevard, Pasadena, CA, 91125, USA

[2]Department of Particle Physics and Astrophysics, Weizmann Institute of Science, 234 Herzl St, 76100 Rehovot, Israel

[3]Department of Astronomy, University of California, Berkeley, CA, 94720

[4]Astrophysics Research Institute, Liverpool John Moores University, IC2, Liverpool Science Park, 146 Brownlow Hill, Liverpool L3 5RF,UK

[5]The Oskar Klein Centre & Department of Astronomy, Stockholm University, AlbaNova, SE-106 91 Stockholm, Sweden

[6]Department of Physics and Astronomy, Texas Tech University, Box 1051, Lubbock, TX 79409-1051, USA

[7]DIRAC Institute, Department of Astronomy, University of Washington, 3910 15th Avenue NE, Seattle, WA 98195, USA

[8]Department of Astrophysics/IMAPP, Radboud University, Nijmegen, The Netherlands

[9]Department of Physics, University of Oxford, Denys Wilkinson Building, Keble Road, Oxford OX1 3RH, UK

[10]NASA Postdoctoral Program Fellow, Goddard Space Flight Center, Greenbelt, MD 20771, USA

[11]Astrophysics Science Division, NASA Goddard Space Flight Center, Mail Code 661, Greenbelt, MD 20771, USA
[12]Joint Space-Science Institute, University of Maryland, College Park, MD 20742, USA
[13]Astronomy Department, University of Maryland, College Park, MD 20742, USA
[14]Caltech Optical Observatories, California Institute of Technology, MC 11-17, 1200 E. California Blvd., Pasadena, CA 91125 USA
[15]Division of Physics, Mathematics and Astronomy, California Institute of Technology, Pasadena, CA 91125, USA
[16]Science and Technology Institute, Universities Space Research Association, Huntsville, AL 35805, USA
[17]Racah Institute of Physics, Hebrew University, Jerusalem 91904, Israel
[18]Department of Astronomy and Astrophysics, University of California, Santa Cruz, CA 95064, USA
[19]Mullard Space Science Laboratory, University College London, Holmbury St. Mary, Dorking, Surrey RH5 6NT, UK
[20]Kavli Institute for Theoretical Physics, University of California, Santa Barbara, CA 93106, USA
[21]IPAC, California Institute of Technology, 1200 E. California Blvd, Pasadena, CA 91125, USA
[22]Graduate Institute of Astronomy, National Central University, 32001, Taiwan
[23]Lawrence Berkeley National Laboratory, 1 Cyclotron Road, Berkeley, CA, 94720, USA
[24]Harvard-Smithsonian Center for Astrophysics, 60 Garden Street, Cambridge, MA 02138, USA
[25]Physics Department/Tsinghua Center for Astrophysics, Tsinghua University; Beijing, 100084, China
[26]Department of Physics, Tokyo Institute of Technology, 2-12-1 Ookayama, Meguro-ku, Tokyo 152-8551, Japan

Abstract

We present detailed observations of ZTF18abukavn (SN 2018gep), discovered in high-cadence data from the Zwicky Transient Facility as a rapidly rising (1.4 ± 0.1 mag/hr) and luminous ($M_{g,\rm peak} = -20$ mag) transient. It is spectroscopically classified as a broad-lined stripped-envelope supernova (Ic-BL SN). The high peak luminosity ($L_{\rm bol} \gtrsim 3{\times}10^{44}\,{\rm erg\,s^{-1}}$), the short rise time ($t_{\rm rise} = 3$ d in g-band), and the blue colors at peak ($g-r \sim -0.4$) all resemble the high-redshift Ic-BL iPTF16asu, as well as several other unclassified fast transients. The early discovery of SN 2018gep (within an hour of shock breakout) enabled an intensive spectroscopic campaign, including the highest-temperature ($T_{\rm eff} \gtrsim 40,000$K) spectra of a stripped-envelope SN. A retrospective search revealed luminous ($M_g \sim M_r \approx -14$ mag) emission in the days to weeks before explosion, the first definitive detection of precursor emission for a Ic-BL. We find a limit on the isotropic gamma-ray energy release $E_{\gamma,\rm iso} < 4.9 \times 10^{48}$ erg, a limit on X-ray emission $L_{\rm X} < 10^{40}\,{\rm erg\,s^{-1}}$, and a limit on radio emission $\nu L_\nu \lesssim 10^{37}\,{\rm erg\,s^{-1}}$. Taken together, we find that the early (< 10 d) data are best explained by shock breakout in a massive shell of dense circumstellar material ($0.02\,M_\odot$) at large radii (3×10^{14} cm) that was ejected in eruptive pre-explosion mass-loss episodes. The late-time (> 10 d) light curve requires an additional energy source, which could be the radioactive decay of Ni-56.

6.1 Introduction

Recent discoveries by optical time-domain surveys challenge our understanding of how energy is deposited and transported in stellar explosions (Kasen, 2017). For example, over 50 transients have been discovered with rise times and peak luminosities too rapid and too high, respectively, to be explained by radioactive decay (Arcavi et al., 2016; Drout et al., 2014; Poznanski et al., 2010; Pursiainen et al., 2018; Rest et al., 2018; Shivvers et al., 2016; Tanaka et al., 2016). Possible powering mechanisms include interaction with extended circumstellar material (CSM; Chevalier and Irwin 2011), and energy injection from a long-lived central engine (Kasen and Bildsten, 2010; Kasen et al., 2016; Woosley, 2010). These models have been difficult to test because the majority of fast-luminous transients have been discovered *post facto* and located at cosmological distances ($z \sim 0.1$).

The discovery of iPTF16asu (Wang et al., 2019; Whitesides et al., 2017) in the intermediate Palomar Transient Factory (iPTF; Law et al. 2009) showed that at least some of these fast-luminous transients are energetic (10^{52} erg) high-velocity ("broad-lined"; $v \gtrsim 20,000\,\mathrm{km\,s^{-1}}$) stripped-envelope (Ic) supernovae (Ic-BL SNe). The light curve of iPTF16asu was unusual among Ic-BL SNe in being inconsistent with ^{56}Ni-decay (Cano, 2013; Taddia et al., 2019). Suggested power sources include energy injection by a magnetar, ejecta-CSM interaction, cooling-envelope emission, and an engine-driven explosion similar to low-luminosity gamma-ray bursts — or some combination thereof. Unfortunately, the high redshift ($z = 0.187$) precluded a definitive conclusion.

Today, optical surveys such as ATLAS (Tonry et al., 2018) and the Zwicky Transient Facility (ZTF; Bellm et al. 2019b; Graham et al. 2019) have the areal coverage to discover rare transients *nearby*, as well as the cadence to discover transients when they are young (< 1 d). For example, the recent discovery of AT2018cow at 60 Mpc (Prentice et al., 2018; Smartt et al., 2018) represented an unprecedented opportunity to study a fast-luminous optical transient up close, in detail, and in real-time. Despite an intense multiwavelength observing campaign, the nature of AT2018cow remains unknown—possibilities include an engine-powered stellar explosion (Ho et al., 2019c; Margutti et al., 2019; Perley et al., 2019; Prentice et al., 2018), the tidal disruption of a white dwarf by an intermediate-mass black hole (Kuin et al., 2019; Perley et al., 2019), and an electron capture SN (Lyutikov and Toonen, 2019). Regardless of the origin, it is clear that the explosion took place within dense material (Ho et al., 2019c; Margutti et al., 2019; Perley et al., 2019) confined to $\lesssim 10^{16}$ cm

(Ho et al., 2019c).

Here we present SN 2018gep, discovered as a rapidly rising ($1.4 \pm 0.1\,\mathrm{mag\,hr^{-1}}$) and luminous ($M_{g,\mathrm{peak}} = -20$) transient in high-cadence data from ZTF (Ho et al., 2018b). The high inferred velocities ($> 20,000\,\mathrm{km\,s^{-1}}$), the spectroscopic evolution from a blue continuum to a Ic-BL SN (Costantin et al., 2018), the rapid rise ($t_{\mathrm{rise}} = 3\,\mathrm{d}$ in g-band) to high peak luminosity ($L_{\mathrm{bol}} \gtrsim 3 \times 10^{44}\,\mathrm{erg\,s^{-1}}$) all suggest that SN 2018gep is a low-redshift ($z = 0.03154$) analog to iPTF16asu. The early discovery enabled an intensive follow-up campaign within the first day of the explosion, including the highest-temperature ($T_{\mathrm{eff}} \gtrsim 40,000\,\mathrm{K}$) spectra of a stripped-envelope SN to-date. A retrospective search in ZTF data revealed the first definitive detection of pre-explosion activity in a Ic-BL.

The structure of the paper is as follows. We present our radio through X-ray data in Section 6.2. In Section 6.3 we outline basic properties of the explosion and its host galaxy. In Section 6.4 we attribute the power source for the light curve to shock breakout in extended CSM. In Section 6.5 we compare SN 2018gep to unidentified fast-luminous transients at high redshift. Finally, in Section 6.6 we summarize our findings and look to the future. Throughout the paper, absolute times are reported in UTC and relative times are reported with respect to t_0, which is defined in Section 6.2. We assume a standard ΛCDM cosmology (Planck Collaboration et al., 2016).

6.2 Observations

Zwicky Transient Facility Discovery

ZTF observing time is divided between several different surveys, conducted using a custom mosaic camera (Dekany et al., 2016) on the 48-inch Samuel Oschin Telescope (P48) at Palomar Observatory. See Bellm et al. (2019b) for an overview of the observing system, Bellm et al. (2019a) for a description of the surveys and scheduler, and Masci et al. (2019) for details of the image processing system.

Every 5-σ point-source detection is saved as an "alert." Alerts are distributed in avro format (Patterson et al., 2019) and can be filtered based on a machine learning-based real-bogus metric (Duev et al., 2019; Mahabal et al., 2019), light-curve properties, and host characteristics (including a star-galaxy classifier; Tachibana and Miller (2018)). The ZTF collaboration uses a web-based system called the GROWTH marshal (Kasliwal et al., 2019) to identify and keep track of transients of interest.

ZTF18abukavn was discovered in an image obtained at 2018-09-09 03:55:18 (start

of exposure) as part of the ZTF extragalactic high-cadence partnership survey, which covers 1725 deg^2 in six visits ($3g$, $3r$) per night (Bellm et al., 2019a). The discovery magnitude was $r = 20.5 \pm 0.3$ mag, and the source position was measured to be $\alpha = 16^{\mathrm{h}}43^{\mathrm{m}}48.22^{\mathrm{s}}$, $\delta = +41^{\mathrm{d}}02^{\mathrm{m}}43.4^{\mathrm{s}}$ (J2000), coincident with a compact galaxy (Figure 6.1) at $z = 0.03154$ or $d \approx 143$ Mpc. As described in Section 6.2, the redshift was unknown at the time of discovery; we measured it from narrow galaxy emission lines in our follow-up spectra. The host redshift along with key observational properties of the transient are listed in Table 6.1.

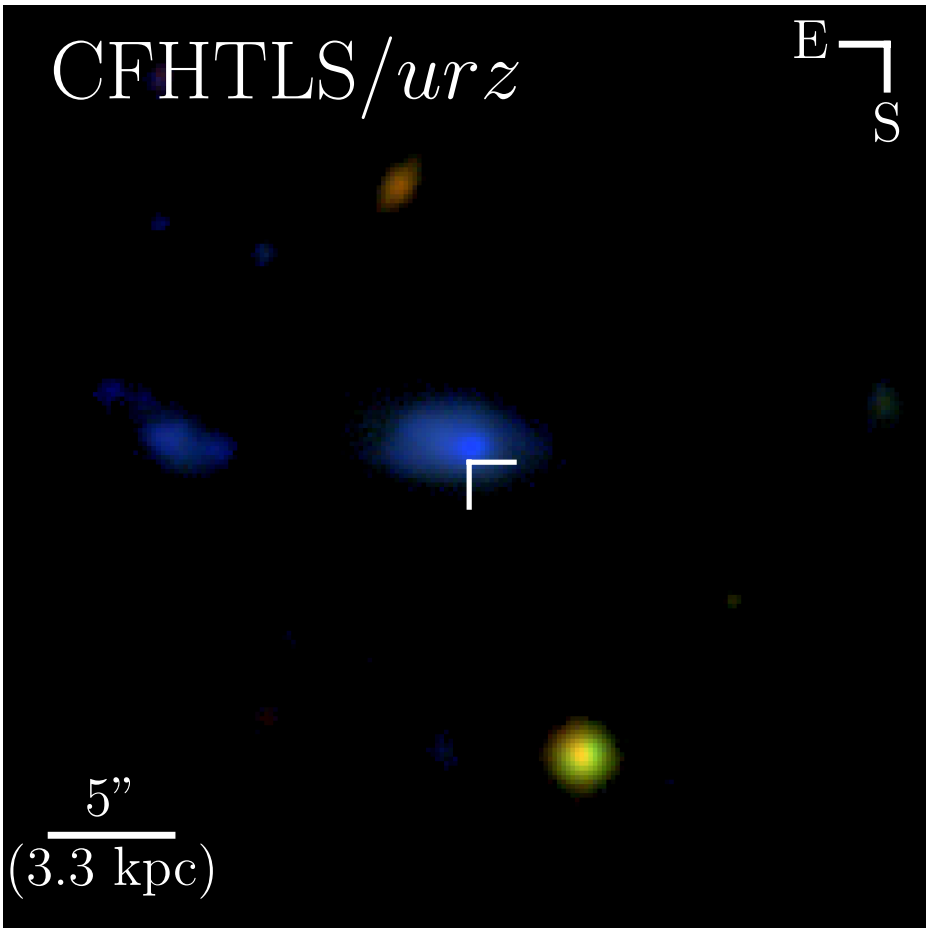

Figure 6.1: The position of SN 2018gep (white crosshairs) in its host galaxy. Images from the Canada-France-Hawaii Telescope Legacy Survey (2004–2012), combined using the prescription in Lupton et al. (2004).

As shown in Figure 6.2, the source brightened by over two magnitudes within the first three hours. These early detections passed a filter written in the GROWTH

Table 6.1: Key observational properties of SN 2018gep and its host galaxy

Parameter	Value	Notes
z	0.03154	From narrow host emission lines
$L_{\rm peak}$	$\gtrsim 3 \times 10^{43}$ erg	Peak UVOIR bolometric luminosity
$t_{\rm rise}$	0.5–3 d	Time from t_0 to $L_{\rm peak}$
$E_{\rm rad}$	10^{50} erg	UVOIR output, Δt = 0.5–40 d
$M_{r,\rm prog}$	−15	Peak luminosity of pre-explosion emission
$E_{\gamma,\rm iso}$	$< 4.9 \times 10^{48}$ erg	Limit on prompt gamma-ray emission from *Fermi*/GBM
L_X	$< 2.5 \times 10^{41}$ erg s^{-1}	X-ray upper limit from *Swift*/XRT at Δt = 0.4–14 d
	$< 10^{40}$ erg s^{-1}	X-ray upper limit from *Chandra* at Δt = 15 and Δt = 70 d
νL_ν	$\approx 10^{37}$ erg s^{-1}	9 GHz radio luminosity from VLA at Δt = 5 and Δt = 16
$M_{*,\rm host}$	$1.3 \times 10^8\ M_\odot$	Host stellar mass
SFR$_{\rm host}$	0.12 $M_\odot$ yr^{-1}	Host star-formation rate
Host metallicity	1/5 solar	Oxygen abundance on O3N2 scale

marshal that was designed to find young SNe. We announced the discovery and fast rise via the Astronomer's Telegram (Ho et al., 2018b), and reported the object to the IAU Transient Server (TNS[1]), where it received the designation SN 2018gep.

We triggered ultraviolet (UV) and optical observations with the UV/Optical Telescope (UVOT; Roming et al. 2005) aboard the *Neil Gehrels Swift Observatory* (Gehrels et al., 2004), and observations began 10.2 hours after the ZTF discovery (Schulze et al., 2018). A search of IceCube data found no temporally coincident high-energy neutrinos (Blaufuss, 2018).

Over the first two days, the source brightened by two additional magnitudes. A linear fit to the early g-band photometry gives a rise of 1.4 ± 0.1 mag hr^{-1}. This rise rate is second only to the IIb SN 16gkg (Bersten et al., 2018) but several orders of magnitude more luminous at discovery ($M_{g,\rm disc} \approx -17$ mag).

To establish a reference epoch, we fit a second-order polynomial to the first three days of the g-band light curve in flux space, and define t_0 as the time at which the flux is zero. This gives t_0 as being 25 ± 2 minutes prior to the first detection, or $t_0 \approx$ UTC 2018-09-09 03:30. The physical interpretation of t_0 is not straightforward, since the light curve flattens out at early times (see Figures 6.2 and 6.3). We proceed using t_0 as a reference epoch but caution against assigning it physical meaning.

Photometry

From $\Delta t \approx 1$ d to $\Delta t \approx 60$ d, we conducted a photometric follow-up campaign at UV and optical wavelengths using *Swift*/UVOT, the Spectral Energy Distribution Machine (SEDM; Blagorodnova et al. 2018) mounted on the automated 60-inch

[1] `https://wis-tns.weizmann.ac.il`

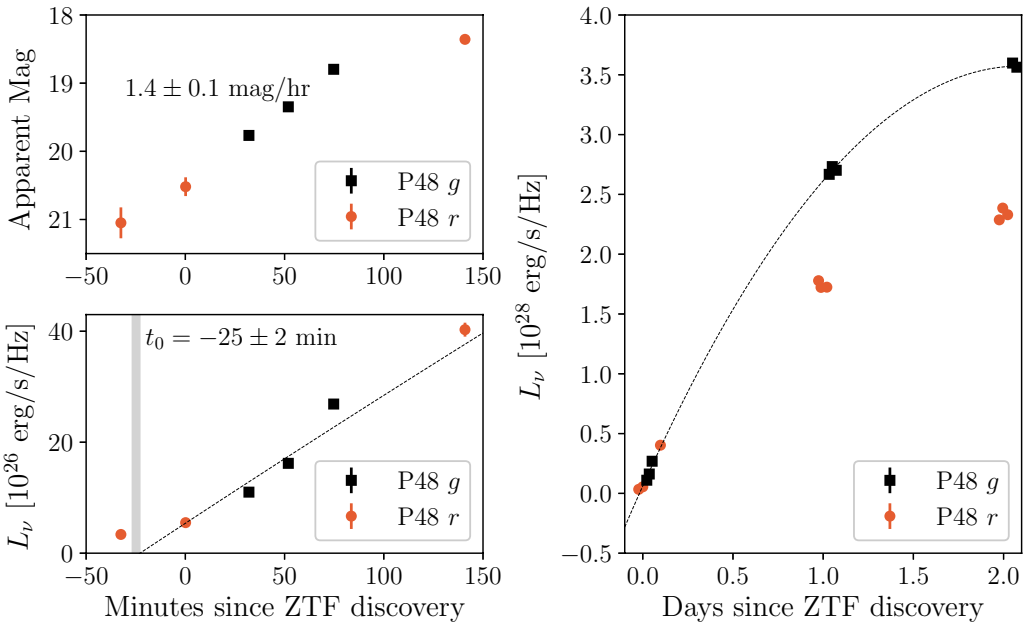

Figure 6.2: The rapid rise in the first few minutes and first few days after the ZTF discovery of SN 2018gep. We also show an r-band point from prior to discovery that was found in retrospect by lowering the detection threshold from 5-σ to 3-σ. Top left: the rise in magnitudes gives an almost unprecedented rate of 1.4 ± 0.1 mag hr^{-1}. Bottom left: the rise in flux space together with the quadratic fit and definition of t_0. Right: the rise in flux space showing the quadratic fit.

telescope at Palomar (P60; Cenko et al. 2006), the optical imager (IO:O) on the Liverpool Telescope (LT; Steele et al. 2004), and the Lulin 1-m Telescope (LOT).

Basic reductions for the LT IO:O imaging were performed by the LT pipeline[2]. Digital image subtraction and photometry for the SEDM, LT and LOT imaging was performed using the Fremling Automated Pipeline (`FPipe`; Fremling et al. 2016). `Fpipe` performs calibration and host subtraction against Sloan Digital Sky Survey reference images and catalogs (SDSS; Ahn et al. 2014). SEDM spectra were reduced using `pysedm` (Rigault et al., 2019).

The UVOT data were retrieved from the NASA *Swift* Data Archive[3] and reduced using standard software distributed with HEAsoft version 6.19[4]. Photometry was measured using UVOTMAGHIST with a 3″ circular aperture. To remove the host contribution, we obtained a final epoch in all broad-band filters on 18 October 2018

[2] `https://telescope.livjm.ac.uk/TelInst/Pipelines/\#ioo`
[3] `https://heasarc.gsfc.nasa.gov/cgi-bin/W3Browse/swift.pl`
[4] `https://heasarc.nasa.gov/lheasoft/`

and built a host template using UVOTIMSUM and UVOTSOURCE with the same aperture used for the transient.

Figure 6.3 shows the full set of light curves, with a cross denoting the peak of the r-band light curve for reference. The position of the cross is simply the time and magnitude of our brightest r-band measurement, which is a good estimate given our cadence. The photometry is listed in Table 6.5 in Appendix 6.7. Note that despite the steep SED at early times, the K-correction is minimal. We estimate that the effect is roughly 0.03 mag, which is well within our uncertainties. In Figure 6.4 we compare the rise time and peak absolute magnitude to other rapidly evolving transients from the literature.

Spectroscopy

The first spectrum was taken 0.7 d after discovery by the Spectrograph for the Rapid Acquisition of Transients (SPRAT; Piascik et al. 2014) on the Liverpool Telescope (LT). The spectrum showed a blue continuum with narrow galaxy emission lines, establishing this as a luminous transient ($M_{\mathrm{g,peak}} = -19.7$). Twenty-three optical spectra were obtained from $\Delta t = 0.7$–61.1 d, using SPRAT, the Andalusia Faint Object Spectrograph and Camera (ALFOSC) on the Nordic Optical Telescope (NOT), the Double Spectrograph (DBSP; Oke and Gunn 1982) on the 200-inch Hale telescope at Palomar Observatory, the Low Resolution Imaging Spectrometer (LRIS; Oke et al. 1995) on the Keck I 10-m telescope, and the Xinglong 2.16-m telescope (XLT+BFOSC) of NAOC, China (Wang et al., 2019). As discussed in Section 6.3, the early $\Delta t < 5$ d spectra show broad absorption features that evolve redward with time, which we attribute to carbon and oxygen. By $\Delta t \sim 8$ d, the spectrum resembles a stripped-envelope SN, and the usual broad features of a Ic-BL emerge (Costantin et al., 2018).

We use the automated LT pipeline reduction and extraction for the LT spectra. LRIS spectra were reduced and extracted using `Lpipe` (Perley, 2019). The NOT spectrum was obtained at parallactic angle using a $1''$ slit, and was reduced in a standard way, including wavelength calibration against an arc lamp, and flux calibration using a spectrophotometric standard star. The XLT+BFOSC spectra were reduced using the standard IRAF routines, including corrections for bias, flat field, and removal of cosmic rays. The Fe/Ar and Fe/Ne arc lamp spectra obtained during the observation night are used to calibrate the wavelength of the spectra, and the standard stars observed on the same night at similar airmasses as the supernova

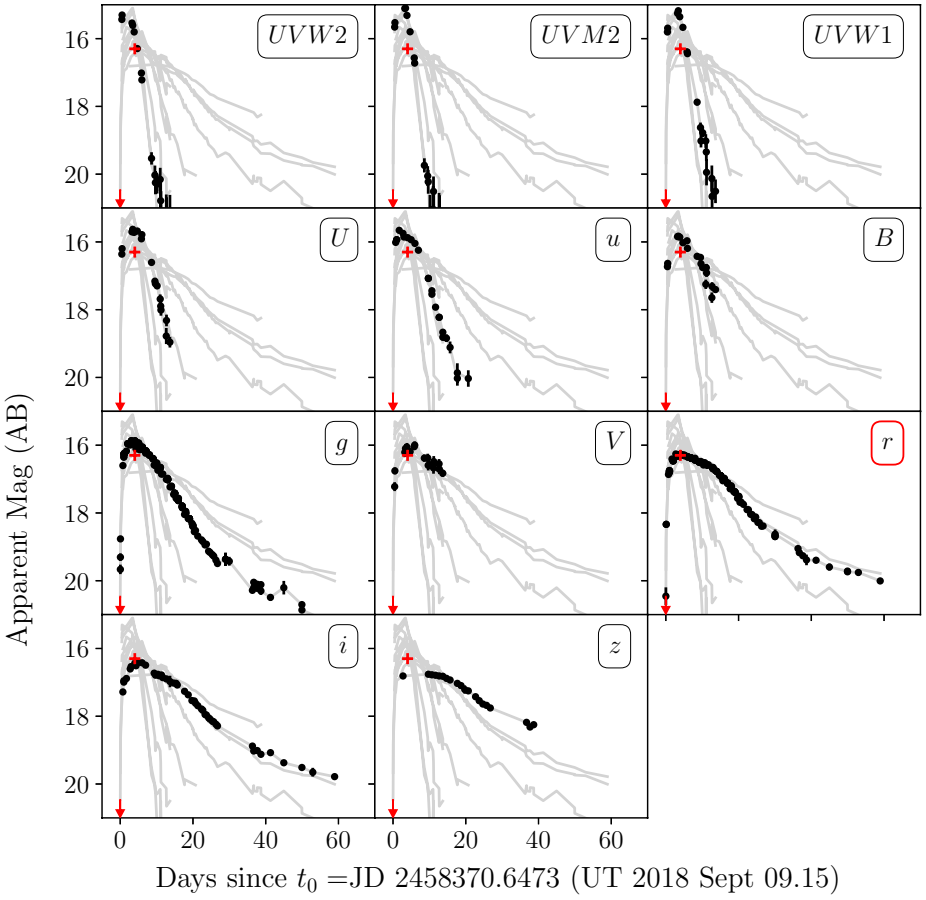

Figure 6.3: UV and optical light curves from *Swift* and ground-based facilities. The arrow marks the last non-detection, which was in r-band. The red cross marks the peak of the r-band light curve, which is 16.3 mag at $\Delta t = 4$ d. The full set of light curves are shown as grey lines in the background, and each panel highlights an individual filter in black. We correct for Galactic extinction using the attenuation curve from Fitzpatrick (1999) and $E_{B-V} = A_V/R_V = 0.01$ for $R_V = 3.1$ and $A_V = 0.029$ (Schlafly and Finkbeiner, 2011).

were used to calibrate the flux of spectra. The spectra were further corrected for continuum atmospheric extinction during flux calibration, using mean extinction curves obtained at Xinglong Observatory. Furthermore, telluric lines were removed from the data.

Swift obtained three UV-grism spectra between 2018-09-15 3:29 and 6:58 UTC ($\Delta t \approx 6.4$ d) for a total exposure time of 3918 s. The data were processed using the

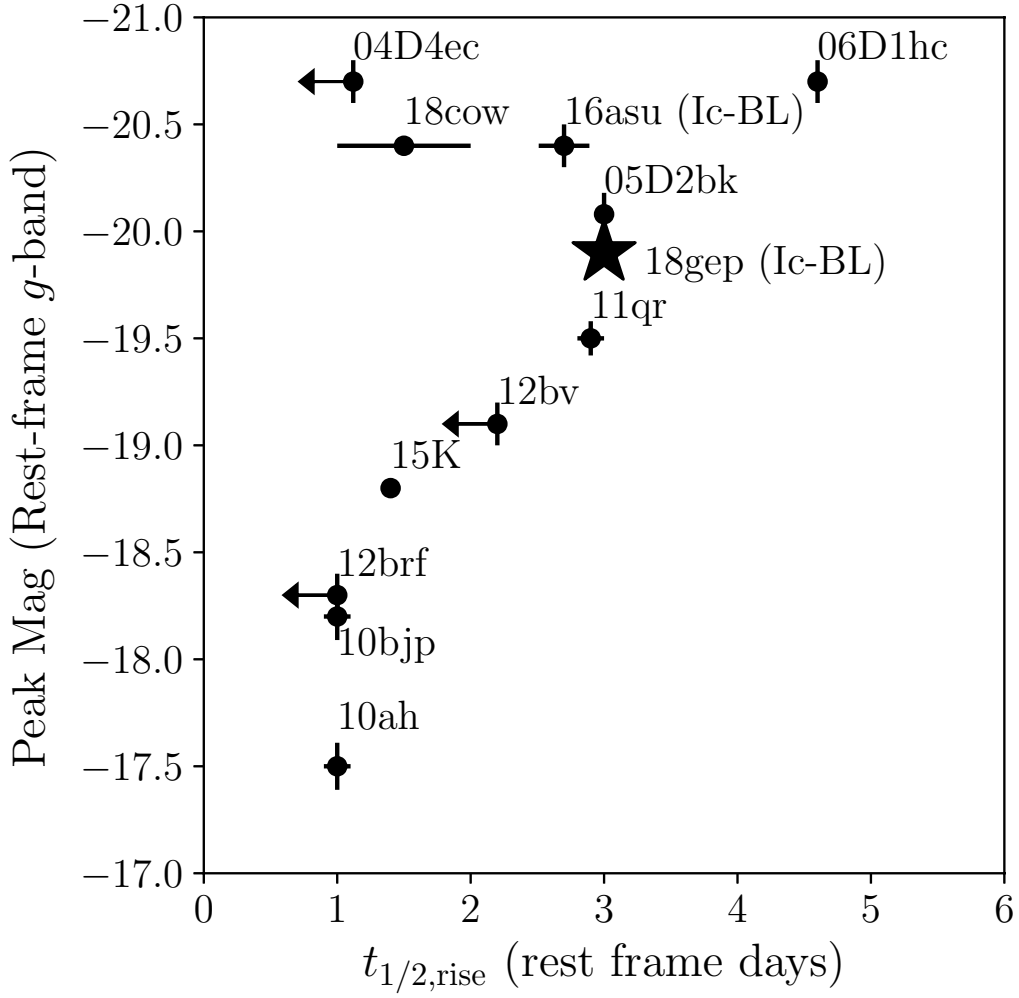

Figure 6.4: The rise time and peak absolute magnitude of SN 2018gep, iPTF16asu (a high-redshift analog), and unclassified fast-luminous transients from Drout et al. (2014), Arcavi et al. (2016), Rest et al. (2018), and Perley et al., 2019. When possible, we report measurements in rest-frame g-band, and define "rise time" as time from half-max to max. For iPTF16asu, we use the quadratic fit to the early g-band light curve from Whitesides et al. (2017) as well as their reported peak magnitude, but caution that this is rest-frame r-band. For KSN2015K, there are only observations in the *Kepler* white filter (Rest et al., 2018).

calibration and software described by Kuin et al. (2015). During the observation, the source spectrum was centered on the detector, which is the default location for *Swift*/UVOT observations. Because of this, there is second-order contamination from a nearby star, which was reduced by using a narrow extraction width (1.3″ instead of 2.5″). The contamination renders the spectrum unreliable at wavelengths

longer than 4100 Å, but is negligible in the range 2850–4100 Å due to absorption from the ISM. Below 2200 Å, the spectrum overlaps with the spectrum from another star in the field of view.

The resulting spectrum (Figure 6.5) shows a single broad feature between 2200 Å and 3000 Å (rest frame). One possibility is that this is a blend of the UV features seen in SLSNe. Line identifications for these features vary in the SLSN literature, but are typically blends of Ti III, Si III, C II, C III, and Mg II (Howell et al., 2013; Mazzali et al., 2016; Quimby et al., 2011; Yan et al., 2017).

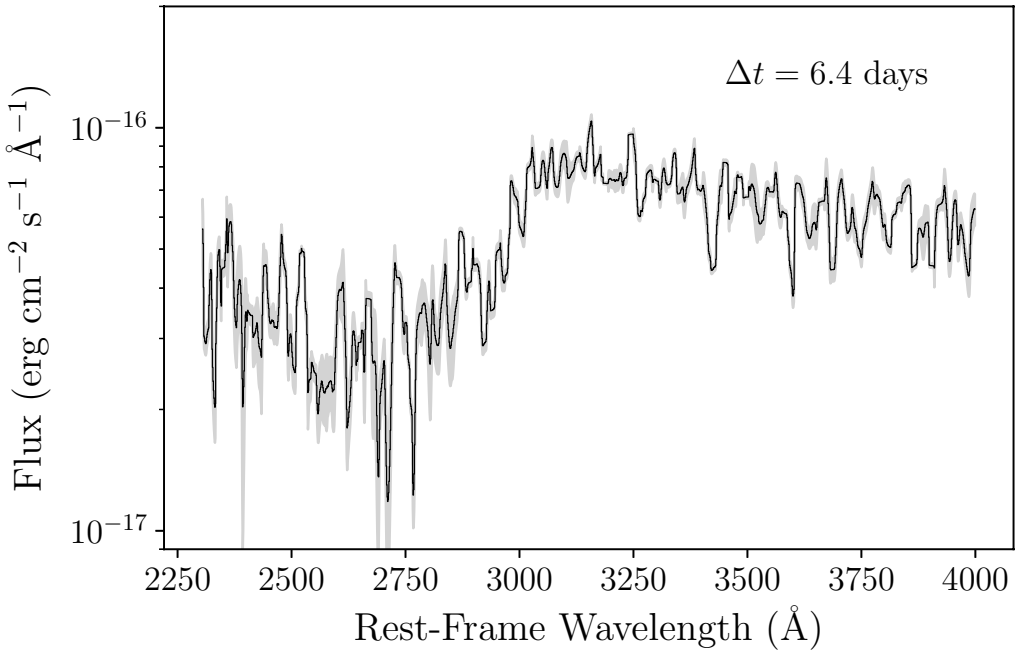

Figure 6.5: *Swift*/UVOT grism spectrum shifted to the rest frame. Black line shows the data binned such that each bin size is 10 Å. Light grey represents 1-σ uncertainties after binning. The spectrum has been scaled to match the UVOT *u*-band flux at this epoch (integrated from 3000 Å to 3900 Å), which was determined by interpolating the *Swift u*-band light curve.

The spectral log and a figure showing all the spectra are presented in Appendix 6.7. In Section 6.3 we compare the early spectra to spectra at similar epochs in the literature. We model one of the early spectra, which shows a "W" feature that has been seen in superluminous supernovae (SLSNe), to measure the density, density profile, and element composition of the ejecta. From the Ic-BL spectra, we measure the velocity evolution of the photosphere.

Search for Pre-discovery Emission

The nominal ZTF pipeline only generates detections above a 5-σ threshold. To extend the light curve further back in time, we performed forced photometry at the position of SN 2018gep on single-epoch difference images from the IPAC ZTF difference imaging pipeline. The ZTF forced photometry PSF-fitting code will be described in detail in a separate paper (Yao, Y. et al. in preparation). As shown in Figure 6.2, forced photometry uncovered an earlier 3-σ r-band detection.

Next, we searched for even fainter detections by constructing deeper reference images than those used by the nominal pipeline, and subtracting them from 1-to-3 day stacks of ZTF science images. The reference images were generated by performing an inverse-variance weighted coaddition of 298 R-band and 69 g-band images from PTF/iPTF taken between 2009 and 2016 using the `CLIPPED` combine strategy in `SWarp` (Bertin, 2010; Gruen et al., 2014). PTF/iPTF images were used instead of ZTF images to build references as they were obtained years prior to the transient, and thus less likely to contain any transient flux. No cross-instrument corrections were applied to the references prior to subtraction. Pronounced regions of negative flux on the PTF/iPTF references caused by crosstalk from bright stars were masked out manually.

We stacked ZTF science images obtained between 2018 Feb 22 and 2018 Aug 31 in a rolling window (segregated by filter) with a width of 3 days and a period of 1 day, also using the `CLIPPED` technique in `SWarp`. Images taken between 2018 Sep 01 and t_0 were stacked in a window with a width of 1 day and a period of 1 day. Subtractions were obtained using the `HOTPANTS` (Becker, 2015) implementation of the Alard and Lupton (1998) PSF matching algorithm. Many of the ZTF science images during this period were obtained under exceptional conditions, and the seeing on the ZTF science coadds was often significantly better than the seeing on the PTF/iPTF references. To correct for this effect, ZTF science coadds were convolved with their own point spread functions (PSFs), extracted using `PSFEx`, prior to subtraction. During subtraction, PSF matching and convolution were performed on the template and the resulting subtractions were normalized to the photometric system of the science images. We show two example subtractions in Figure 6.6.

Using these newly constructed deep subtractions, PSF photometry was performed at the location of SN 2018gep using the PSF of the science images. To estimate the uncertainty on the flux measurements made on these subtractions, we employed a Monte Carlo technique, in which thousands of PSF fluxes were measured at

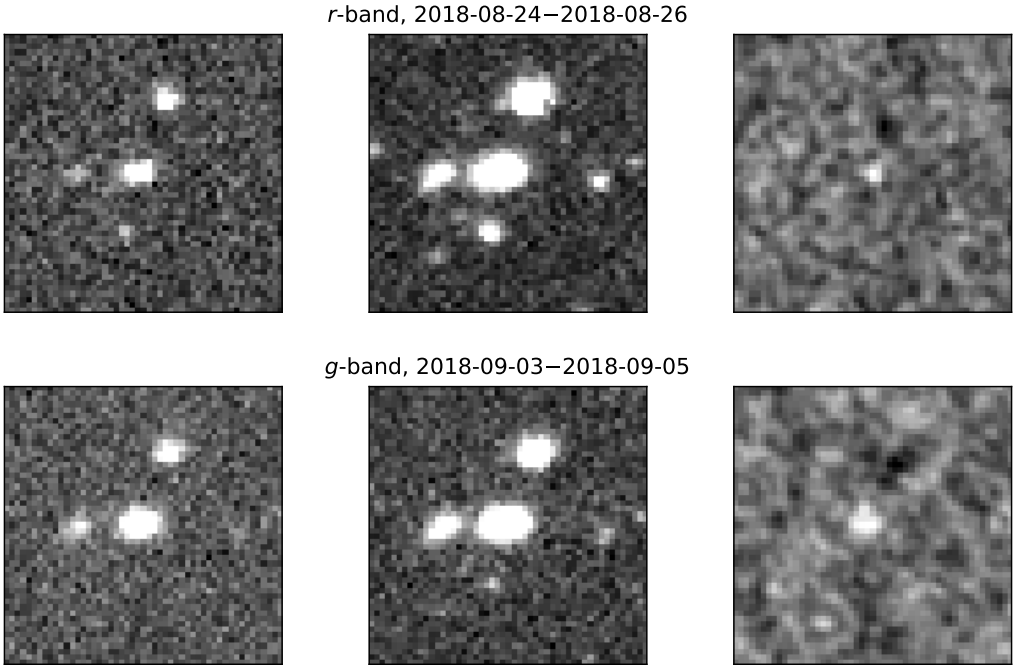

Figure 6.6: Sample pre-explosion subtractions of deep PTF/iPTF references from ZTF science images stacked in 3-day bins (see Section 6.2). Each cutout is centered on the location of SN 2018gep. The subtractions show clear emission at the location of the SN in both g and r-bands days to weeks before the discovery of the SN in ZTF.

random locations on the image, and the PSF-flux uncertainty was taken to be the 1σ dispersion in these measurements. We loaded this photometry into a local instance of SkyPortal (van der Walt et al., 2019), an open-source web application that interactively displays astronomical datasets for annotation, analysis, and discovery.

We detected significant flux excesses at the location of SN 2018gep in both g and r bands in the weeks preceding t_0 (i.e., its first detection in single-epoch ZTF subtractions). The effective dates of these extended pre-discovery detections are determined by taking an inverse-flux variance weighted average of the input image dates. The detections in the week leading up to explosion are $m_g \sim m_r \approx 22$, which is approximately the magnitude limit of the coadd subtractions. However, in an r-band stack of images from August 24–26 (inclusive), we detect emission at $m_r \sim 21.5$ at 5σ above the background.

Assuming that the rapid rise we detected was close to the time of explosion, this is the first definitive detection of pre-explosion emission in a Ic-BL SN. There was a

tentative detection in another source, PTF 11qcj (Corsi et al., 2014), 1.5 and 2.5 years prior to the SN. In Section 6.4 we discuss possible mechanisms for this emission, and conclude that it is likely related to a period of eruptive mass-loss immediately prior to the explosion. We note that it is unlikely that this variability arises from AGN activity, due to the properties of the host galaxy (Section 6.3).

With forced photometry and faint detections from stacked images and deep references, we can construct a light curve that extends weeks prior to the rapid rise in the light curve, shown in Figure 6.7.

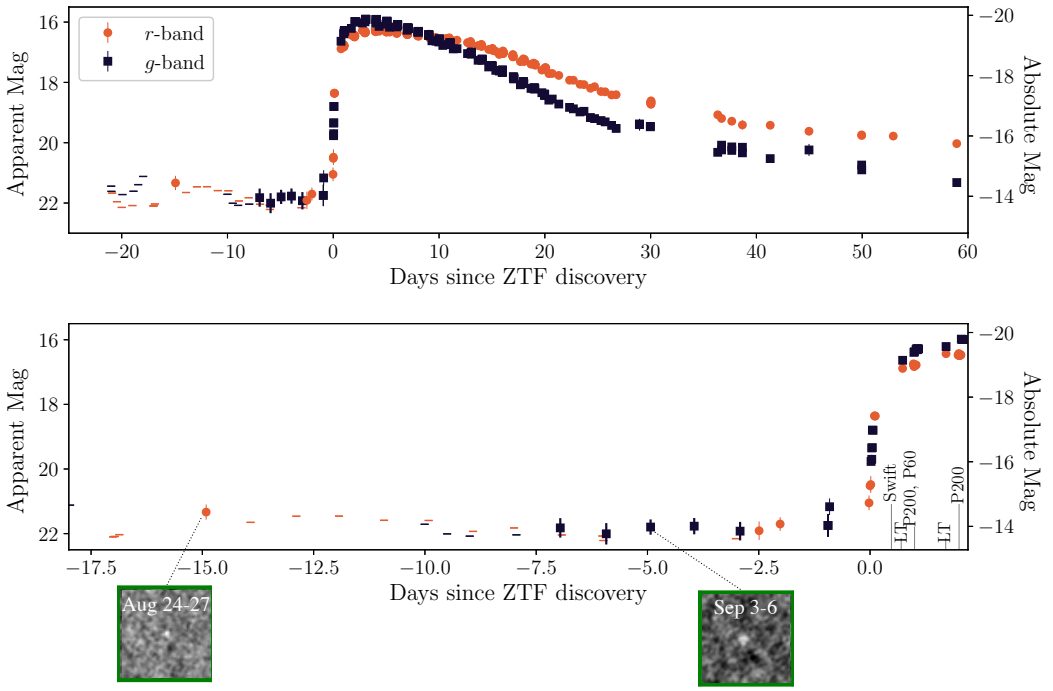

Figure 6.7: Full r and g-band light curves of SN 2018gep. 3-σ upper limits are shown as horizontal lines. Points at $t < 0$ are from 3-day stacks of ZTF/P48 data as described in Section 6.2. Sample subtractions from two of these stacks are shown in the bottom row.

Radio Follow-up

We observed the field of SN 2018gep with the Karl G. Jansky Very Large Array (VLA) on three epochs: on 2018 September 14 UT under the Program ID VLA/18A-242 (PI: D. Perley; Ho et al. 2018a), and on 2018 September 25 and 2018 November 23 UT under the Program ID VLA/18A-176 (PI: A. Corsi). We used 3C286 for flux

calibration, and J1640+3946 for gain calibration. The observations were carried out in X- and Ku-band (nominal central frequencies of 9 GHz and 14 GHz, respectively) with a nominal bandwidth of 2 GHz. The data were calibrated using the automated VLA calibration pipeline available in the CASA package (McMullin et al., 2007) then inspected for further flagging. The CLEAN procedure (Högbom, 1974) was used to form images in interactive mode. The image rms and the radio flux at the location of SN 2018gep were measured using `imstat` in CASA. Specifically, we report the maximum flux within pixels contained in a circular region centered on the optical position of SN 2018gep with radius comparable to the FWHM of the VLA synthesized beam at the appropriate frequency. The source was detected in the first two epochs, but not in the third (see Table 6.2). As we discuss in Section 6.4, the first two epochs were conducted in a different array configuration than the third epoch, and may have had a contribution from host galaxy light.

We also obtained three epochs of observations with the AMI large array (AMI-LA; Hickish et al. 2018; Zwart et al. 2008), on UT 2018 Sept 12, 2018 Sept 23, and 2018 Oct 20. AMI-LA is a radio interferometer comprised of eight, 12.8 m diameter that extends from 18 m up to 110 m in length and operates with a 5 GHz bandwidth around a central frequency of 15.5 GHz.

We used a custom AMI data reduction software package `reduce_dc` (e.g. Perrott et al. 2013) to perform initial data reduction, flagging, and calibration of phase and flux. Phase calibration was conducted using short interleaved observations of J1646+4059, and for absolute flux calibration we used 3C286. Additional flagging and imaging were performed using CASA. All three observations resulted in null-detections with 3-σ upper limits of $\approx 120\,\mu$Jy in the first two observations, and a 3-σ upper limit of $\approx 120\,\mu$Jy in the last observation.

Finally, we observed at higher frequencies using the Submillimeter Array (SMA; Ho et al. 2004) on UT 2018 Sep 15 under its target-of-opportunity program. The project ID was 2018A-S068. Observations were performed in the sub-compact configuration using seven antennas. The observations were performed using RxA and RxB receivers tuned to LO frequencies of 225.55 GHz and 233.55 GHz respectively, providing 32 GHz of continuous bandwidth ranging from 213.55 GHz to 245.55 GHz with a spectral resolution of 140.0 kHz per channel. The atmospheric opacity was around 0.16-0.19 with system temperatures around 100-200 K. The nearby quasars 1635+381 and 3C345 were used as the primary phase and amplitude gain calibrators with absolute flux calibration performed by comparison to Neptune.

Passband calibration was derived using 3C454.3. Data calibration was performed using the MIR IDL package for the SMA, with subsequent analysis performed in MIRIAD (Sault et al., 1995). For the flux measurements, all spectral channels were averaged together into a single continuum channel and an rms of 0.6 mJy was achieved after 75 minutes on-source.

The full set of radio and sub-millimeter measurements are listed in Table 6.2.

Table 6.2: Radio flux density measurements for SN 2018gep. For VLA measurements, the quoted errors are calculated as the quadrature sums of the image rms, plus a 5% nominal absolute flux calibration uncertainty. When the peak flux density within the circular region is less than three times the RMS, we report an upper limit equal to three times the RMS of the image. For AMI measurements, non-detections are reported as 3-σ upper limits. For SMA measurements, non-detections are reported as a 1-σ upper limit.

Start Time (UTC)	Δt (d)	Inst.	ν (GHz)	f_ν (μJy)	L_ν (erg s^{-1} Hz^{-1})	$\theta_{\rm FWHM}$ $''$	Int. time (hr)
2018-09-12 17:54	3.6	AMI	15	< 120	$< 2.9 \times 10^{27}$	43.53×30.85	4
2018-09-23 15:35	14.5	AMI	15	< 120	$< 2.9 \times 10^{27}$	39.3×29.29	4
2018-10-20 14:01	41.4	AMI	15	< 120	$< 2.9 \times 10^{27}$	43.53×30.85	4
2018-09-15 02:33	6.0	SMA	230	< 590	$< 1.4 \times 10^{28}$	4.828×3.920	1.25
2018-09-14 01:14	4.9	VLA	9.7	34 ± 4	8.3×10^{26}	7.06×5.92	0.5
2018-09-25 00:40	15.9	VLA	9	24.4 ± 6.8	6.0×10^{26}	7.91×6.89	0.7
2018-09-25 00:40	15.9	VLA	14	26.8 ± 6.8	6.6×10^{26}	4.73×4.26	0.5
2018-11-23 13:30	75.4	VLA	9	< 16	$< 3.9 \times 10^{26}$	3.52×2.08	0.65
2018-11-23 13:30	75.4	VLA	14	< 17	$< 4.2 \times 10^{26}$	2.77×1.32	0.65

X-ray Follow-up

We observed the position of SN 2018gep with *Swift*/XRT from $\Delta t \approx 0.4$–14 d. The source was not detected in any epoch. To measure upper limits, we used web-based tools developed by the *Swift*-XRT team (Evans et al., 2009). For the first epoch, the 3-σ upper limit was 0.003 ct/s. To convert the upper limit from count rate to flux, we assumed[5] a Galactic neutral hydrogen column density of 1.3×10^{20} cm^{-2}, and a power-law spectrum with photon index $\Gamma = 2$. This gives[6] an unabsorbed 0.3–10 keV flux of $< 9.9 \times 10^{-14}$ erg cm^{-2} s^{-1}, and $L_X < 2.5 \times 10^{41}$ erg s^{-1}.

We obtained two epochs of observations with the Advanced CCD Imaging Spectrometer (ACIS; Garmire et al. 2003) on the *Chandra* X-ray Observatory via our approved program (Proposal No. 19500451; PI: Corsi). The first epoch began at 9:25 UTC on 10 October 2018 ($\Delta t \approx 15$ d) under ObsId 20319 (integration time 12.2 ks), and the second began at 21:31 UTC on 4 December 2018 ($\Delta t \approx 70$ d)

[5] `https://heasarc.gsfc.nasa.gov/cgi-bin/Tools/w3nh/w3nh.pl`

[6] `https://heasarc.gsfc.nasa.gov/cgi-bin/Tools/w3pimms/w3pimms.pl`

under ObsId 20320 (integration time 12.1 ks). No X-ray emission is detected at the location of SN 2018gep in either epoch, with 90% upper limits on the 0.5–7.0 keV count rate of $\approx 2.7 \times 10^{-4}$ ct s^{-1}. Using the same values of hydrogen column density and power-law photon index as in our XRT measurements, we find upper limits on the unabsorbed 0.5–7 keV X-ray flux of $< 3.2 \times 10^{-15}$ erg cm^{-2} s^{-1}, or (for a direct comparison to the XRT band) a 0.3–10 keV X-ray flux of $< 4.2 \times 10^{-15}$ erg cm^{-2} s^{-1}. This corresponds to a 0.3–10 keV luminosity upper limit of $L_X < 1.0 \times 10^{40}$ erg s^{-1}.

Search for Prompt Gamma-ray Emission

We created a tool to search for prompt gamma-ray emission (GRBs) from *Fermi*-GBM (Gruber et al., 2014; Narayana Bhat et al., 2016; von Kienlin, 2014), the *Swift* Burst Alert Telescope (BAT; Barthelmy et al. 2005), and the IPN, which we have made available online[7]. We did not find any GRB consistent with the position and t_0 of SN 2018gep.

Our tool also determines whether a given position was visible to BAT and GBM at a given time, using the spacecraft pointing history. We use existing code[8] to determine the BAT history. We find that the position of SN 2018gep was in the BAT field-of-view from UTC 03:13:40 to 03:30:38, before *Swift* slewed to another location.

We also find that at t_0 SN 2018gep was visible to the *Fermi* Gamma-Ray Burst Monitor (GBM; Meegan et al. 2009). We ran a targeted GRB search in 10–1000 keV *Fermi*/GBM data from three hours prior to t_0 to half an hour after t_0. We use the soft template, which is a smoothly broken power law with low-energy index -1.9 and high-energy index -2.7, and an SED peak at 70 keV. The search methodology (and parameters of the other templates) are described in Blackburn et al. (2015) and Goldstein et al. (2016). No signals with a consistent location were found. For the 100 s integration time, the fluence upper limit is 2×10^{-6} erg cm^{-2}. This limit corresponds to a 10–1000 keV isotropic energy release of $E_{\gamma,\mathrm{iso}} < 4.9 \times 10^{48}$ erg. Limits for different spectral templates and integration times are shown in Figure 6.8.

Host Galaxy Data

We measure line fluxes using the Keck optical spectrum obtained at $\Delta t \approx 61$ d (Figure 6.26). We model the local continuum with a low-order polynomial and each emission line by a Gaussian profile of FHWM ~ 5.3 Å. This is appropriate if Balmer

[7] `https://github.com/annayqho/HE\_Burst\_Search`

[8] `https://github.com/lanl/swiftbat\_python`

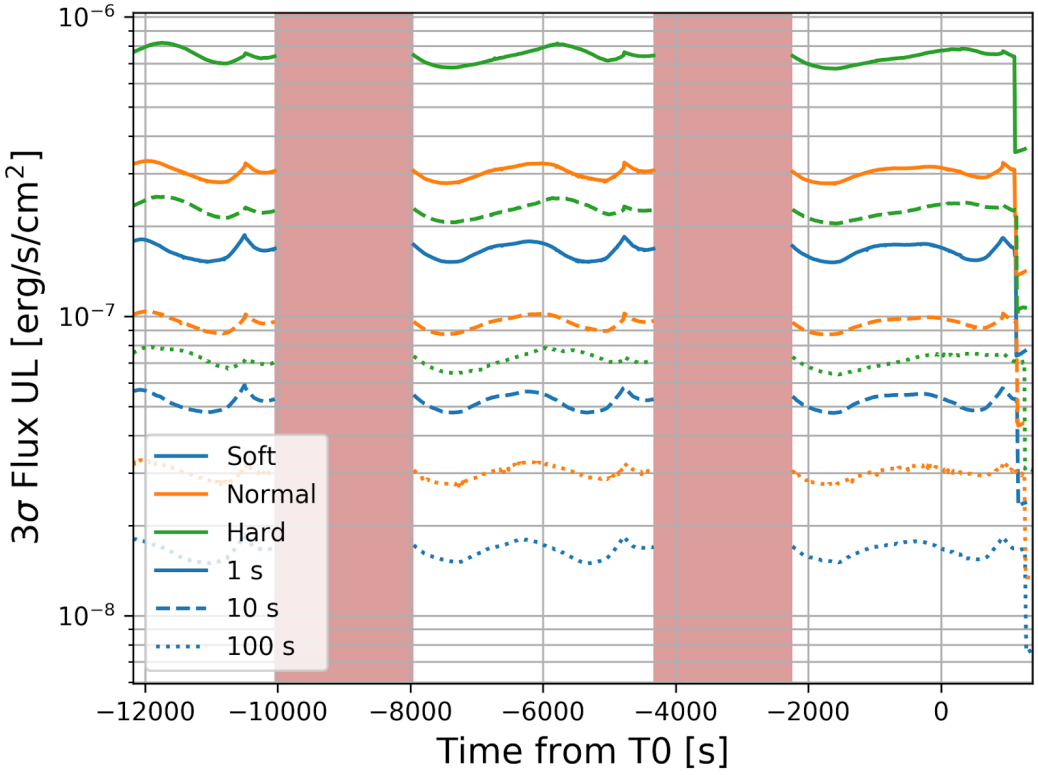

Figure 6.8: 3-σ upper limits from GBM GRB search, which we performed for three hours prior to t_0. The red vertical bars indicate epochs when GBM was not taking data due to passing through the South Atlantic Anomaly. The time of t_0 was estimated from a fit to the early data (Figure 6.7), and is 26 ± 5 minutes prior to the first detection.

absorption is negligible, which is generally the case for starburst galaxies. For the host of SN 2018gep, the Balmer decrement between Hβ, Hγ, and Hδ does not show any excess with respect to the expected values in Osterbrock and Ferland (2006). The resulting line fluxes are listed in Table 6.7.

We retrieved archival images of the host galaxy from *Galaxy Evolution Explorer* (*GALEX*) Data Release (DR) 8/9 (Martin et al., 2005), Sloan Digital Sky Survey (SDSS) DR9 (Ahn et al., 2012), Panoramic Survey Telescope And Rapid Response System (PanSTARRS, PS1) DR1 (Chambers et al., 2016), Two-Micron All Sky Survey (2MASS; Skrutskie et al., 2006), and *Wide-Field Infrared Survey Explorer* (WISE; Wright et al., 2010). We also used UVOT photometry from *Swift*, and NIR photometry from the Canada-France-Hawaii Telescope Legacy Survey (CFHTLS; Hudelot et al., 2012).

The images are characterized by different pixel scales (e.g., SDSS 0.″40/px, GALEX

1.″/px) and different point spread functions (e.g., SDSS/PS1 1–2″, WISE/W2 6.″5). To obtain accurate photometry, we use the matched-aperture photometry software package Lambda Adaptive Multi-Band Deblending Algorithm in R (LAMBDAR; Wright et al., 2016) that is based a photometry software package developed by Bourne et al. (2012). To measure the total flux of the host galaxy, we defined an elliptical aperture that encircles the entire galaxy in the SDSS/r'-band image. This aperture was then convolved in LAMBDAR with the point-spread function of a given image that we specified directly (*GALEX* and WISE data) or that we approximated by a two-dimensional Gaussian (2MASS, SDSS and PS1 images). After instrumental magnitudes were measured, we calibrated the photometry against instrument-specific zeropoints (*GALEX*, SDSS and PS1 data), or as in the case of 2MASS and WISE images against a local sequence of stars from the 2MASS Point Source Catalogue and the AllWISE catalogue. The photometry from the UVOT images were extracted with the command uvotsource in HEAsoft and a circular aperture with a radius of 8″. The photometry of the CFHT/WIRCAM data was done performed the software tool presented in Schulze et al. (2018)[9]. To convert the 2MASS, UVOT, WIRCAM and WISE photometry to the AB system, we applied the offsets reported in Blanton and Roweis (2007), Breeveld et al. (2011) and Cutri et al. (2013). The resulting photometry is summarized in Table 6.8.

6.3 Basic Properties of the Explosion and its Host Galaxy

The observations we presented in Section 6.2 constitute some of the most detailed early-time observations of a stripped-envelope SN to date. In this section we use this data to derive basic properties of the explosion: the evolution of bolometric luminosity, radius, and effective temperature over time (Section 6.3), the velocity evolution of the photosphere and the density and composition of the ejecta as measured from the spectra (Section 6.3), and the mass, metallicity, and SFR of the host galaxy (Section 6.3). These properties are summarized in Table 6.1.

Physical Evolution from Blackbody Fits

By interpolating the UVOT and ground-based photometry, we construct multi-band SEDs and fit a Planck function on each epoch, to measure the evolution of luminosity, radius, and effective temperature. To estimate the uncertainties, we perform a Monte Carlo simulation with 600 trials, each time adding noise corresponding to a 15% systematic uncertainty on each data point, motivated by the need to obtain a

[9] https://github.com/steveschulze/aperture_photometry

combined χ^2/dof ~ 1 across all epochs. The uncertainties for each parameter are taken as the 16-to-84 percentile range from this simulation. The SED fits are shown in Appendix 6.7, and the resulting evolution in bolometric luminosity, photospheric radius, and effective temperature is listed in Table 6.3. We plot the physical evolution in Figure 6.9, with a comparison to iPTF16asu and AT2018cow.

The bolometric luminosity peaks between $\Delta t = 0.5$ d and $\Delta t = 3$ d, at $> 3 \times 10^{44}$ erg s^{-1}. In Figure 6.10 we compare this peak luminosity and time to peak luminosity with several classes of stellar explosions. As in iPTF16asu, the bolometric luminosity falls as an exponential at late times ($t > 10$ d). The total integrated UV and optical ($\approx$ 2000–9000Å) blackbody energy output from $\Delta t = 0.5$–40 d is $\sim 10^{50}$ erg, similar to that of iPTF16asu.

The earliest photospheric radius we measure is ~ 20 AU, at $\Delta t = 0.05$ d. Until $\Delta t \approx 17$ d the radius expands over time with a very large inferred velocity of $v \approx 0.1c$. After that, it remains flat, and even appears to recede. This possible recession corresponds to a flattening in the temperature at ~ 5000 K, which is the recombination temperature of carbon and oxygen. This effect was not seen in iPTF16asu, which remained hotter (and more luminous) for longer. Finally, the effective temperature rises before falling as $\sim t^{-1}$. We interpret these properties in the context of shock-cooling emission in Section 6.4.

Spectral Evolution and Velocity Measurements

Comparisons to Early Spectra in the Literature

We obtained nine spectra of SN 2018gep in the first five days after discovery. These early spectra are shown in Figure 6.11, when the effective temperature declined from 50,000 K to 20,000 K. In Figure 6.12 we show selected spectra compared to other early SN spectra in the literature. To our knowledge, our early spectra have no analogs in the literature, in that there has never been a spectrum of a stripped-envelope SN at such a high temperature (excluding spectra during the afterglow phase of GRBs).[10] Two of the earliest spectra in the literature, one at $\Delta t = 2$ d for Type Ic SN PTF10vgv (Corsi et al., 2012) and one at $\Delta t = 3$ d for Type Ic SN PTF12gzk (Ben-Ami et al., 2012) are redder and exhibit more features than the spectrum of SN 2018gep. We show the comparison in Figure 6.12.

At $\Delta t \approx 4$ d, a "W" feature emerges in the rest-frame wavelength range 3800–

[10]There is however a spectrum of a Type II SN at a comparable temperature: iPTF13dqy was $\sim 50,000$ K at the time of the first spectrum (Yaron et al., 2017).

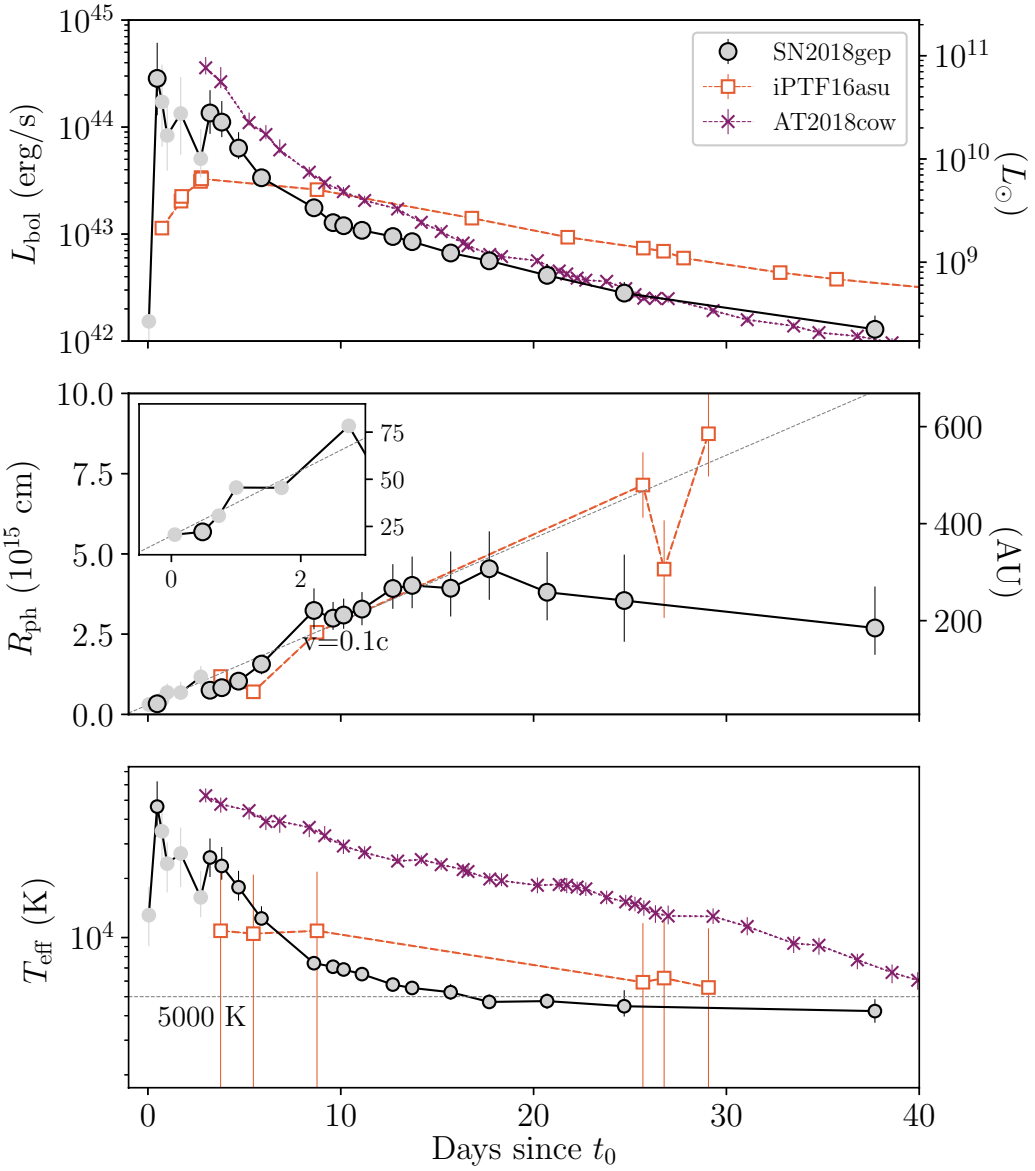

Figure 6.9: Evolution of blackbody properties (luminosity, radius, temperature) over time compared to the Ic-BL SN iPTF16asu and the luminous fast-rising optical transient AT2018cow. The light gray circles are derived from optical data only. The outlined circles are derived from UV and optical data. Middle panel: dotted line shows $v = 0.1c$. Note that $R \neq 0$ at t_0, and instead $R(t = 0) = 3 \times 10^{14}$ cm. Due to the scaling of our plot we do not show the radius evolution of AT2018cow, which drops from $8{\times}10^{14}$ cm to 10^{14} cm on this timescale. Bottom panel: dotted horizontal line shows 5000 K, the recombination temperature for carbon and oxygen. Once this temperature is reached, the photosphere flattens out (and potentially begins to recede).

Table 6.3: Physical evolution of SN 2018gep from blackbody fits.

Δt	$L(10^{10}L_\odot)$	R (AU)	T (kK)
0.05	$0.04^{+0.04}_{-0.02}$	21^{+14}_{-6}	13^{+5}_{-4}
0.48	$7.4^{+8.6}_{-4.1}$	22^{+7}_{-5}	46^{+16}_{-13}
0.73	$4.5^{+5.5}_{-2.8}$	31^{+11}_{-6}	35^{+12}_{-11}
1.0	$2.2^{+2.1}_{-1.2}$	46^{+18}_{-9}	24^{+6}_{-6}
1.7	$3.5^{+4.2}_{-2.1}$	46^{+22}_{-10}	27^{+9}_{-8}
2.7	$1.3^{+1.2}_{-0.4}$	78^{+22}_{-20}	16^{+5}_{-3}
3.2	$3.5^{+2.2}_{-1.3}$	50^{+14}_{-8}	26^{+6}_{-5}
3.8	$2.9^{+1.7}_{-0.8}$	56^{+11}_{-11}	23^{+5}_{-3}
4.7	$1.7^{+0.7}_{-0.3}$	69^{+16}_{-14}	18^{+3}_{-2}
5.9	$0.88^{+0.17}_{-0.08}$	100^{+14}_{-21}	13^{+1}_{-0}
8.6	$0.46^{+0.08}_{-0.06}$	220^{+46}_{-39}	$7.4^{+0.6}_{-0.5}$
9.6	$0.33^{+0.04}_{-0.03}$	200^{+33}_{-24}	$7.1^{+0.4}_{-0.4}$
10.0	$0.31^{+0.04}_{-0.03}$	210^{+34}_{-28}	$6.9^{+0.4}_{-0.4}$
11.0	$0.28^{+0.04}_{-0.03}$	220^{+35}_{-33}	$6.5^{+0.4}_{-0.3}$
13.0	$0.25^{+0.04}_{-0.03}$	260^{+50}_{-42}	$5.8^{+0.3}_{-0.3}$
14.0	$0.22^{+0.04}_{-0.03}$	270^{+60}_{-47}	$5.5^{+0.4}_{-0.3}$
16.0	$0.17^{+0.04}_{-0.03}$	260^{+76}_{-58}	$5.3^{+0.5}_{-0.5}$
18.0	$0.15^{+0.04}_{-0.02}$	300^{+77}_{-64}	$4.7^{+0.4}_{-0.4}$
21.0	$0.11^{+0.03}_{-0.02}$	250^{+83}_{-58}	$4.7^{+0.4}_{-0.4}$
25.0	$0.073^{+0.02}_{-0.013}$	240^{+95}_{-85}	$4.5^{+0.9}_{-0.5}$
38.0	$0.034^{+0.012}_{-0.007}$	180^{+86}_{-55}	$4.2^{+0.6}_{-0.5}$

4350 Å. In the second-from-bottom panel of Figure 6.12 we make a comparison to "W" features seen in SN 2008D (e.g. Modjaz et al. 2009), which was a Type Ib SN associated with an X-ray flash (Mazzali et al., 2008), and in a typical pre-max stripped-envelope superluminous supernova (Type I SLSN; Gal-Yam 2019; Moriya et al. 2018). The absorption lines are broadened much more than in PTF12dam (Nicholl et al., 2013) and probably more than in SN2008D as well. Finally, SN 2018gep cooled more slowly than SN 2008D: only after 4.25 days did it reach the temperature that SN 2008D reached after < 2 days.

Origin of the "W" Feature

The lack of comparison data at such early epochs (high temperatures) motivated us to model one of the early spectra, in order to determine the composition and density profile of the ejecta. We used the spectral synthesis code JEKYLL (Ergon et al., 2018), configured to run in steady-state using a full NLTE-solution. An inner blackbody boundary was placed at an high continuum optical depth (~50), and the

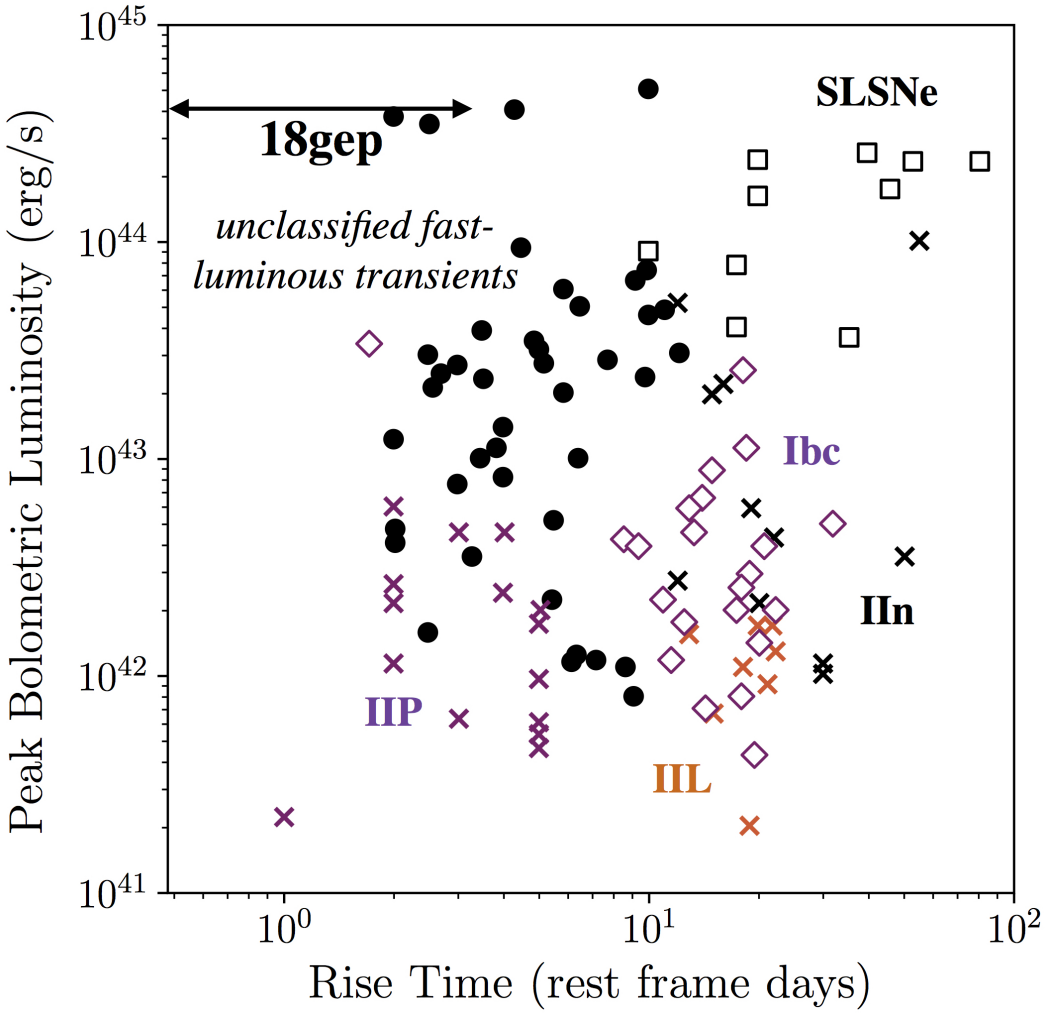

Figure 6.10: Rise to peak bolometric luminosity compared to other classes of transients. Modified from Figure 1 in Margutti et al. (2019).

temperature at this boundary was iteratively determined to reproduce the observed luminosity. The atomic data used is based on what was specified in Ergon et al. (2018), but has been extended as described in Appendix 6.7. We explored models with C/O (mass fractions: 0.23/0.65) and O/Ne/Mg (mass fractions: 0.68/0.22/0.07) compositions taken from a model by Woosley and Heger (2007)[11] and a power-law density profile, where the density at the inner border was adjusted to fit the observed line velocities. Except for the density at the inner border, various power-law indices were also explored, but in the end an index of -9 worked out best.

Figures 6.13 and 6.14 show the model with the best overall agreement with the

[11] The model was divided into compositional zones by Jerkstrand et al. (2015) and a detailed specification of the C/O and O/Ne/Mg zones is given in Table D.2 therein.

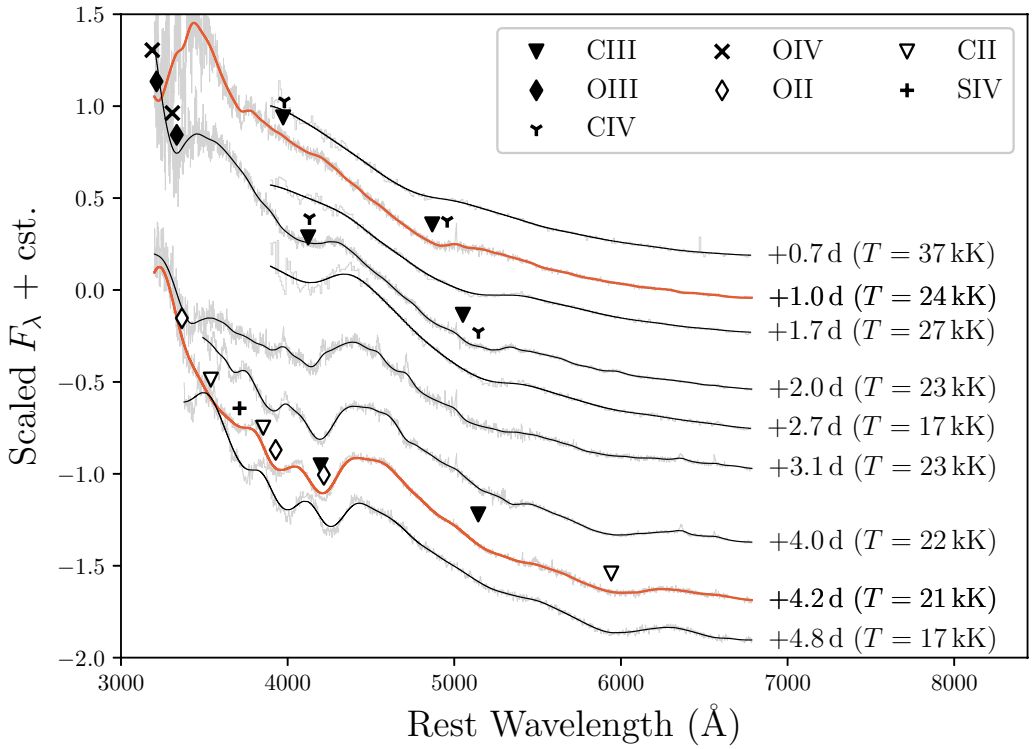

Figure 6.11: Spectra of SN 2018gep taken in the first five days. Broad absorption features are consistent with ionized carbon and oxygen, which evolve redward with time. Spectra highlighted in orange are shown compared to other early SN spectra in Figure 6.12.

spectra and the SED (as listed in Table 6.6 the spectrum was obtained at high airmass, making it difficult to correct for telluric features). The model has a C/O composition, an inner border at 22,000 km s^{-1} (corresponding to an optical depth of ~50), a density of 4×10^{-12} g cm^{-3} at this border and a density profile with a power-law index of −9. In Figure 6.13 we show that the model does a good job of reproducing both the spectrum and the SED of SN 2018gep. In particular, it is interesting to note that the "W" feature seem to arise naturally in C/O material at the observed conditions. A similar conclusion was reached by Dessart (2019), whose magnetar-powered SLSN-I models, calculated using the NLTE code CMFGEN, show the "W" feature even when non-thermal processes where not included in the calculation (as in our case).

In the model, the "W" feature mainly arises from the O II 2p^2(3P)3s 4P ↔ 2p^2(3P)3p 4D° (4639–4676 Å), O II 2p^2(3P)3s 4P ↔ 2p^2(3P)3p 2D (4649 Å) and O II 2p^2(3P)3s 4P ↔ 2p^2(3P)3p 4P° (4317–4357 Å) transitions. The departure from LTE is modest

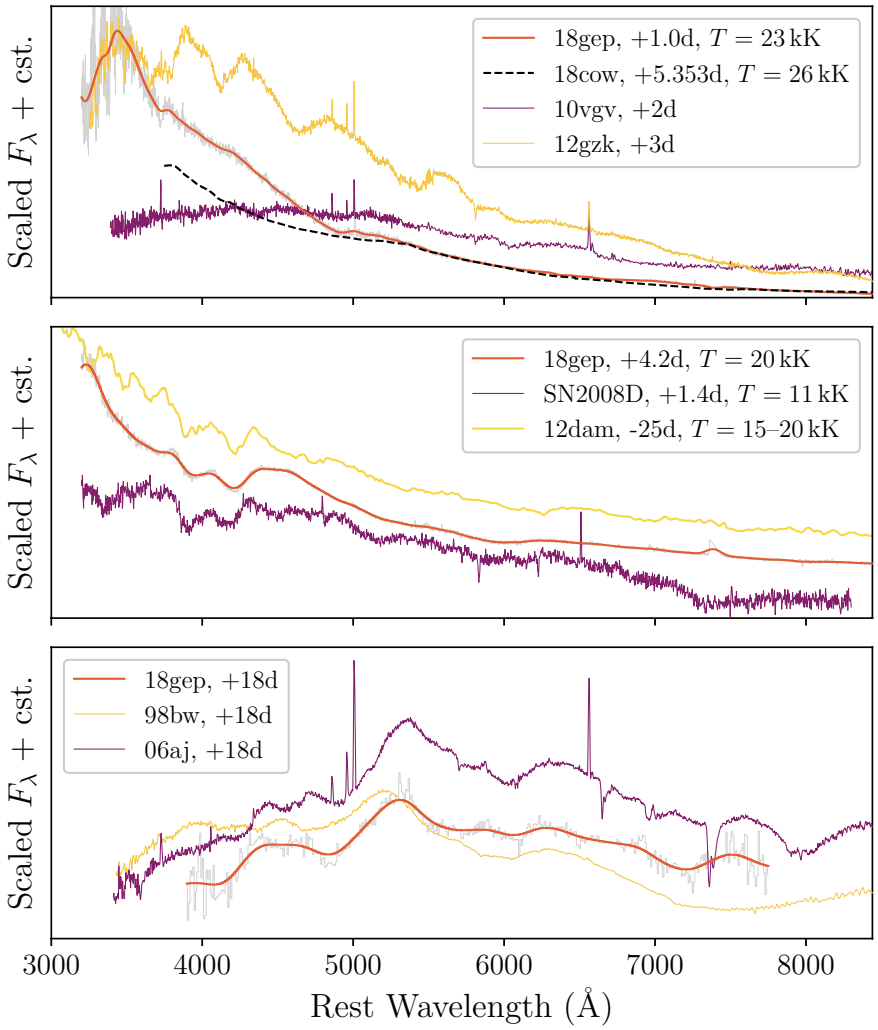

Figure 6.12: Top panel: an early spectrum of 18gep compared to spectra from other stellar explosions at a comparable phase. Middle panel: The spectrum at $\Delta t = 4.2$ d shows a "W" feature, which we compare to similar "W" features seen in an early spectrum of SN2008D from Modjaz et al., 2009, and a typical pre-max spectrum of a SLSN-I (PTF12dam, from Nicholl et al. 2013). We boost the SLSN spectrum by an additional expansion velocity of $\sim 15000\,\mathrm{km\,s^{-1}}$, and apply reddening of $E(B-V) = 0.63$ to SN 2008D. Weak features in the red are also similar to what are seen in PTF12dam, and are consistent with arising from CII and CIII lines, following the analysis of Gal-Yam, 2019. The lack of narrow carbon features as well as the smooth spectrum below 3700 Å suggest a large velocity dispersion leading to significant line broadening, compared to the intrinsically narrow features observed in SLSNe-I (Gal-Yam, 2019; Quimby et al., 2018). Bottom panel: a spectrum of 18gep when it resembled an ordinary Ic-BL SN, compared to spectra at similar phases of Ic-BL SNe accompanying GRBs.

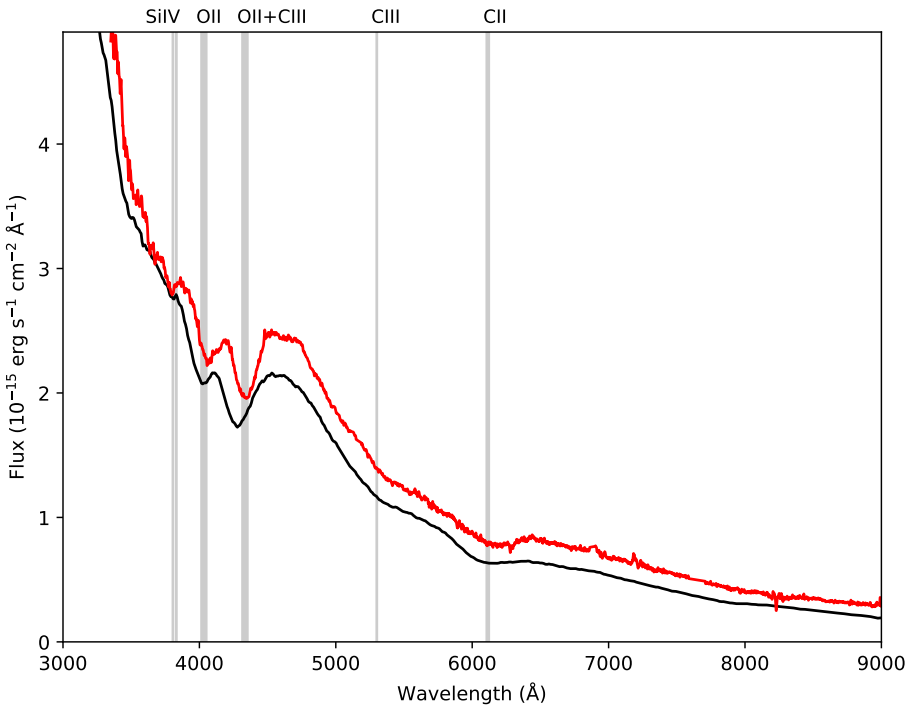

Figure 6.13: Observed spectrum (red) at 4.2 d, compared to our model spectrum (black) from the spectral synthesis code JEKYLL configured to run in steady-state using a full NLTE solution. The model has a C/O composition, an inner border at 22,000 km s^{-1}, a density of 4×10^{-12} g cm^{-3}, and a density profile with a power-law index of -9. The absolute (but not relative) flux of the spectrum was calibrated using the interpolated P48 g and r magnitudes. We also show the O II, C II, C III, and Si IV lines discussed in the text shifted to the velocity of the model photosphere.

in the line-forming region, and the departure coefficients for the O II states are small. The spectrum redward of the "W" feature is shaped by carbon lines, and the features near 5700 and 6500 Å arise from the C II 3s 2S ↔ 3p 2P° (6578,6583 Å) and C III 2s3p 1P° ↔ 2s3d 1D (5696 Å) transitions, respectively. In the model, the C II feature is too weak, suggesting that the ionization level is too high in the model. There is also a contribution from the C III 2s3s 3S ↔ 2s3p 3P° (4647–4651 Å) transition to the red part of the "W" feature, which could potentially be what is seen in the spectra from earlier epochs. In addition, there is a contribution from Si IV 4s 2S ↔ 4p 2P° (4090, 4117 Å) near the blue side of the "W" feature, which produce a distinct feature in models with lower velocities and which could explain the observed feature on the blue side of the "W" feature.

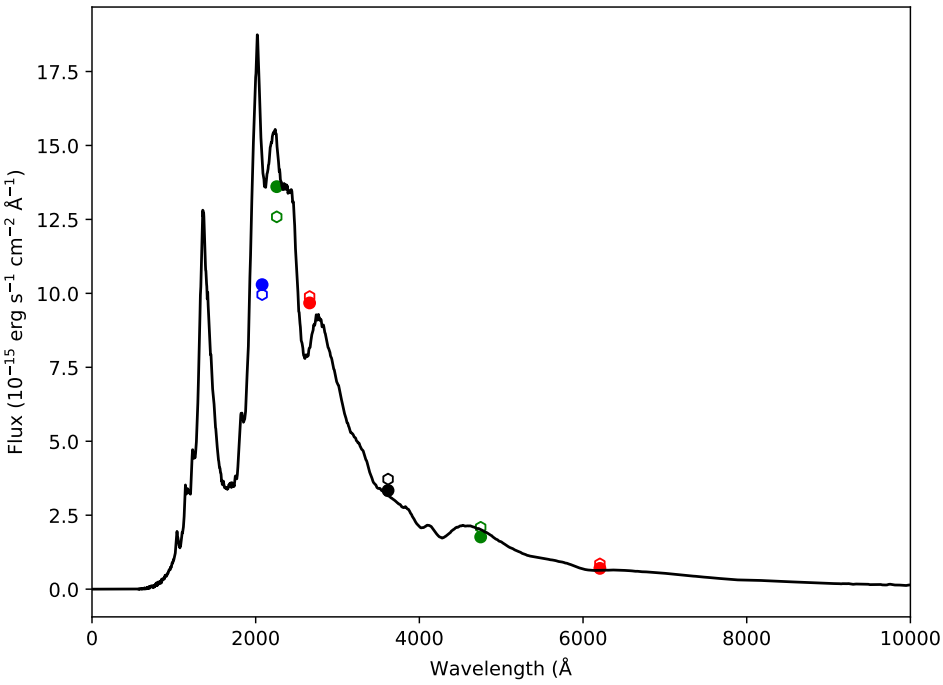

Figure 6.14: Comparison of model (filled circles) and observed (unfilled circles) mean fluxes through the *Swift* UVW1 (blue), UVM2 (green), UVW2 (red), and the SDSS u (black), g (green), and r (red) filters. We also show the model spectrum in black.

In spite of the overall good agreement, there are also some differences between the model and the observations. In particular the model spectrum is bluer and the velocities are higher. These two quantities are in tension and a better fit to one of them would result in a worse fit to the other. As mentioned above, the ionization level might be too high in the model, which suggests that the temperature might be too high as well. It should be noted that adding host extinction (which is assumed to be zero) or reducing the distance (within the error bars) would help in making the model redder (in the observer frame), and the latter would also help in reducing the temperature. The (modest) differences between the model and the observations could also be related to physics not included in the model, like a non-homologous velocity field, departures from spherical asymmetry, and clumping.

The total luminosity of the model is 6.2×10^{43} erg s^{-1}, the photosphere is located at $\sim$33,000 km s^{-1} and the temperature at the photosphere is $\sim$17,500 K, which is consistent with the values estimated from the blackbody fits (although the blackbody

radius and temperature fits refer to the thermalization layer). As mentioned, we have also tried models with a O/Ne/Mg composition. However, these models failed to reproduce the carbon lines redwards of the "W" feature. We therefore conclude that the (outer) ejecta probably has a C/O-like composition, and that this composition in combination with a standard power-law density profile reproduce the spectrum of SN 2018gep at the observed conditions (luminosity and velocity) 4.2 days after explosion.

In our model, the broad feature seen in our *Swift* UVOT grism spectrum is dominated by the strong Mg II (2796,2803 Å) resonance line. However, a direct comparison is not reliable because the ionization is probably lower at this epoch than what we consider for our model.

Photospheric Velocity from Ic-BL Spectra

At $\Delta t \gtrsim 7.8$ d, the spectra of SN 2018gep qualitatively resemble those of a stripped-envelope SN. We measure velocities using the method in Modjaz et al. (2016), which accommodates blending of the Fe IIλ5169 line (which has been shown to be a good tracer of photospheric velocity; Branch et al. 2002) with the nearby Fe II$\lambda\lambda$4924,5018 lines.

At earlier times, when the spectra do not resemble typical Ic-BL SNe, we use our line identifications of ionized C and O to measure velocities. As shown in Figure 6.15, the velocity evolution we measure is comparable to that seen in Ic-BL SNe associated with GRBs (more precisely, low-luminosity GRBs; LLGRBs) which are systematically higher than those of Ic-BL SNe lacking GRBs (Modjaz et al., 2016). However, as discussed in Section 6.2, no GRB was detected.

Properties of the Host Galaxy

We infer a star-formation rate of $0.09 \pm 0.01\ M_\odot\ \mathrm{yr}^{-1}$ from the Hα emission line using the Kennicutt (1998) relation converted to use a Chabrier initial mass function (Chabrier, 2003; Madau and Dickinson, 2014). We note that this is a lower limit as the slit of the Keck observation did not enclose the entire galaxy. We estimate a correction factor of 2–3: the slit diameter in the Keck spectra was 1.0", and the extraction radius was $\sim 1.75''$ in the February observation and $\sim 1.21''$ in the March observation. The host diameter is roughly 4".

We derive an electron temperature of $13,100^{+900}_{-1000}$ K from the flux ratio between [O III]λ4641 and [O III]λ5007, using the software package PyNeb version 1.1.7

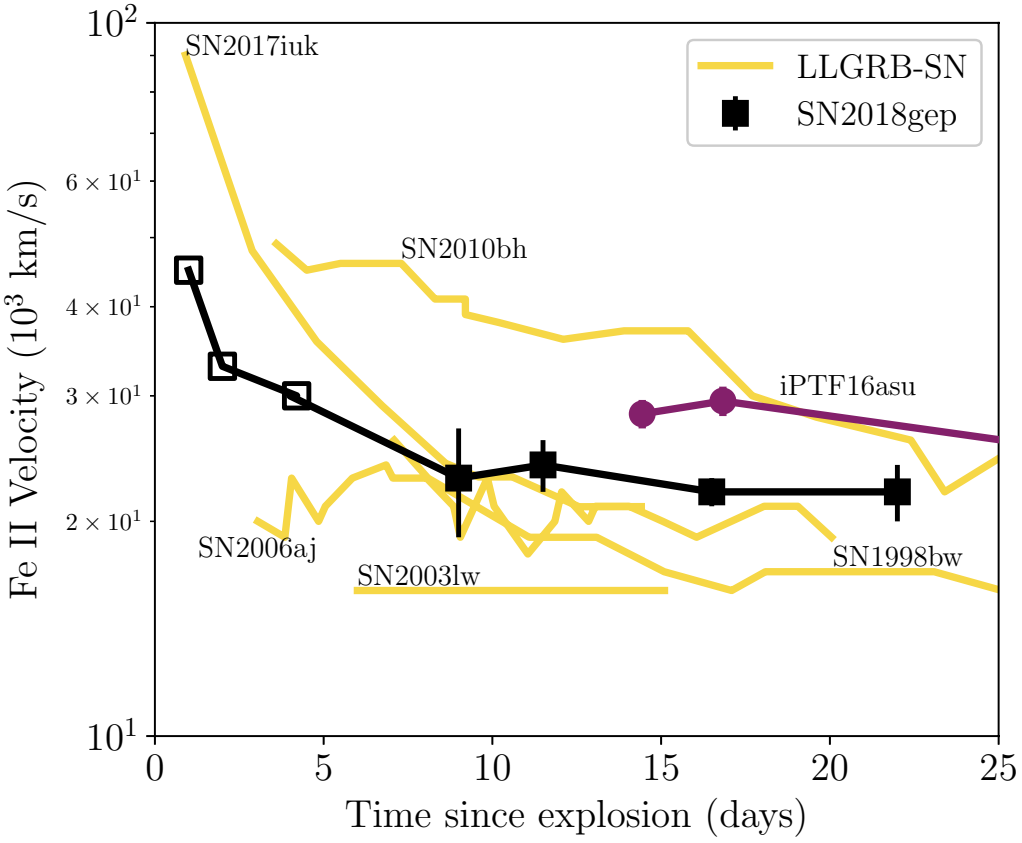

Figure 6.15: Velocity evolution over time as measured from spectral absorption features. Open symbols for SN 2018gep come from C/O velocities measured from line minima. Closed symbols come from the Fe II feature in the Ic-BL spectra. The velocities are comparable to those measured for Ic-BL SNe associated with low-luminosity GRBs (LLGRBs). The velocity evolution for SN2017iuk is taken from Izzo et al. (2019). Velocities for iPTF16asu are taken from Whitesides et al. (2017). Velocities for the other Ic-BL SNe are taken from Modjaz et al. (2016) and shifted from V-band max using data from Galama et al. (1998), Campana et al. (2006), Malesani et al. (2004), and Bufano et al. (2012).

(Luridiana et al., 2015). In combination with the [O II]$\lambda\lambda$3226,3729, [O III]λ4364, [O III]λ4960, [O III]λ5008, and Hβ flux measurements, we infer a total oxygen abundance of $8.01^{+0.10}_{-0.09}$ (statistical error; using Eqs. 3 and 5 in Izotov et al. 2006). Assuming a solar abundance of 8.69 (Asplund et al., 2009), the metallicity of the host is $\sim$ 20% solar.

We also compute the oxygen abundance using the strong-line metallicity indicator O3N2 (Pettini and Pagel, 2004) with the updated calibration reported in Marino et al.

(2013). The oxygen abundance in the O3N2 scale is 8.05 ± 0.01 (stat) ± 0.10 (sys).[12]

We also estimate mass and star-formation rate by modeling the host SED; see Appendix 6.7 for a table of measurements, and details on where we obtained them. We use the software package LePhare version 2.2 (Arnouts et al., 1999; Ilbert et al., 2006). We generated 3.9×10^6 templates based on the Bruzual and Charlot (2003) stellar population-synthesis models with the Chabrier initial mass function (IMF; Chabrier, 2003). The star formation history (SFH) was approximated by a declining exponential function of the form $\exp(-t/\tau)$, where t is the age of the stellar population and τ the e-folding time-scale of the SFH (varied in nine steps between 0.1 and 30 Gyr). These templates were attenuated with the Calzetti attenuation curve (Calzetti et al., 2000) varied in 22 steps from $E(B-V) = 0$ to 1 mag .

The SED (Figure 6.16) is well characterized by a galaxy mass of $\log(M/M_\odot) = 8.11^{+0.07}_{-0.08}$ and an attenuation-corrected star-formation rate of $0.12^{+0.08}_{-0.05}\, M_\odot\, \mathrm{yr}^{-1}$. The derived star-formation rate is comparable to measurement inferred from Hα. The attenuation of the SED is marginal, with $E(B-V)_{\mathrm{star}} = 0.05$, and consistent with the negligible Balmer decrement 6.2.

Figure 6.17 shows that the host galaxy of SN 2018gep is even more low-mass and metal-poor than the typical host galaxies of Ic-BL SNe, which are low-mass and metal-poor compared to the overall core collapse SN population to begin with. The figure uses data for 28 Ic-BL SNe from PTF and iPTF (Modjaz et al., 2020; Taddia et al., 2019) and a sample of 11 long-duration GRBs (including LLGRBs, all at $z < 0.3$). We measured the emission lines from the spectra presented in Taddia et al. (2019) and used line measurements reported in Modjaz et al. (2020) for objects with missing line fluxes. The photometry was taken from Schulze, S. et al. (in preparation). Photometry and spectroscopy were taken from a variety of sources[13]. The oxygen abundances were measured in the O3N2 scale like for SN 2018gep and their SEDs were modelled with the same set of galaxy templates. For reference, the mass and SFR of the host of AT2018cow was $1.4 \times 10^9\, M_\odot$ and $0.22\, M_\odot\, \mathrm{yr}^{-1}$, respectively (Perley et al., 2019). The mass and SFR of the host of iPTF16asu was

[12]Note the oxygen abundance of SN 2018gep's host lies outside of the domain calibrated by Marino et al. (2013). However, we will use the measurement from the O3N2 indicator only to put the host in context of other galaxy samples that are on average more metal-enriched.

[13]Gorosabel et al. (2005), Bersier et al. (2006), Margutti et al. (2007), Ovaldsen et al. (2007) Kocevski et al. (2007), Thöne et al. (2008), Michałowski et al. (2009), Han et al. (2010), Levesque et al. (2010), Starling et al. (2011), Hjorth et al. (2012), Thöne et al. (2014), Schulze et al. (2014), Krühler et al. (2015), Stanway et al. (2015), Toy et al. (2016), Izzo et al. (2017), and Cano et al. (2017a)

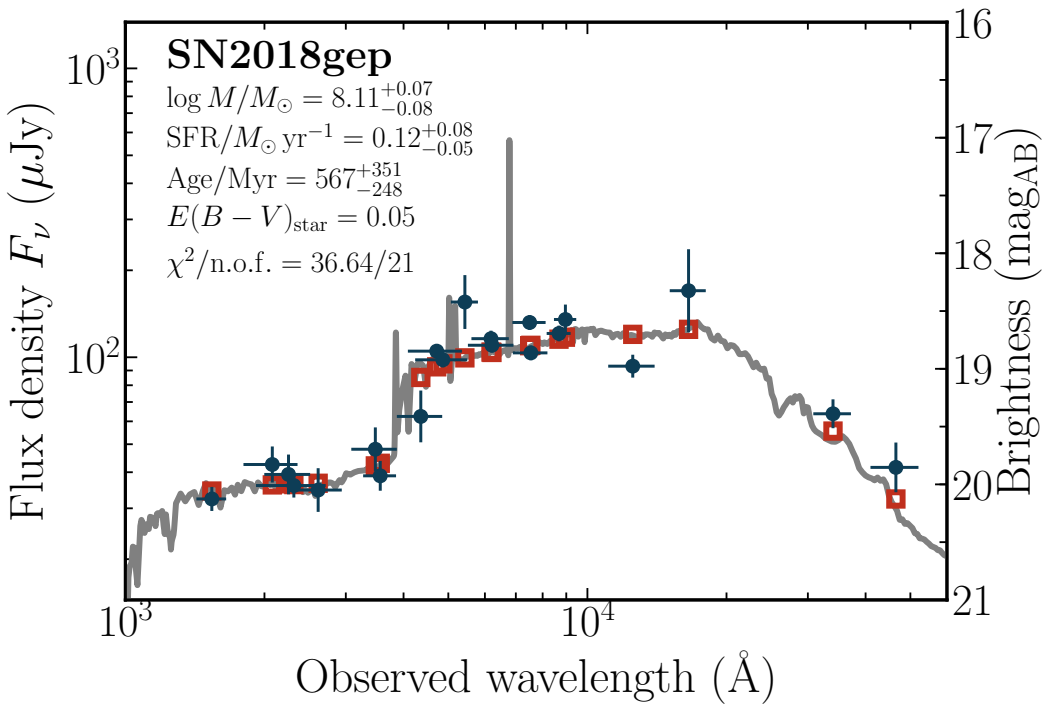

Figure 6.16: The spectral energy distribution of the host galaxy of SN 2018gep from 1,000 to 60,000 Å and the best fit (solid line) in the observer frame. Filled data points represent photometric measurements. The error bars in the 'x' direction indicate the full-width half maximum of each filter response function. The open data points signify the model-predicted magnitudes. The quoted values of the host properties represent the median values and the corresponding 1-σ errors.

$4.6^{+6.5}_{-2.3} \times 10^8\ M_\odot$ and $0.7\ M_\odot$ yr^{-1}, respectively (Whitesides et al., 2017).

6.4 Interpretation

In Sections 6.2 and 6.3, we presented our observations and basic inferred properties of SN 2018gep and its host galaxy. Now we consider what we can learn about the progenitor, beginning with the power source for the light curve.

Radioactive Decay

The majority of stripped-envelope SNe have light curves powered by the radioactive decay of ^{56}Ni. As discussed in Kasen (2017), this mechanism can be ruled out for light curves that rise rapidly to a high peak luminosity, because this would require the unphysical condition of a nickel mass that exceeds the total ejecta mass. With a peak luminosity exceeding 10^{44} erg s^{-1} and a rise to peak of a few days, SN 2018gep clearly falls into the disallowed region (see Figure 1 in Kasen 2017). Thus, we rule

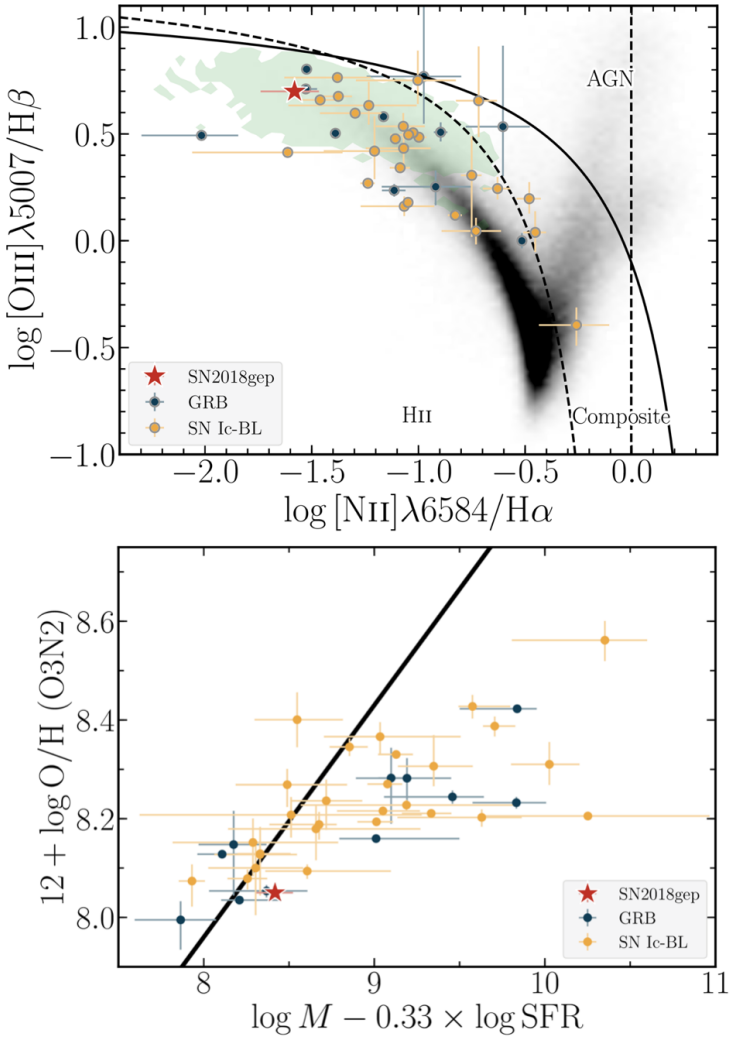

Figure 6.17: Top: BPT diagram. The host of SN 2018gep is a low-metallicity galaxy with an intense ionizing radiation field (green shaded region indicates extreme emission line galaxies). The majority of Ic-BL SNe and long-duration GRBs are found in more metal enriched galaxies (parameterized by [N II]/Hα), and galaxies with less intense radiation fields (parameterized by [O III]/Hα). Field galaxies from SDSS DR15 are shown as a background density distribution. The thick solid line separates star formation- and AGN-dominated galaxies (Kewley et al., 2001). The thick dashed lines encircle the region of composite galaxies (Kauffmann et al., 2003). Bottom: The mass-metallicity-star-formation-rate plane. The bulk of the the SN-Ic-BL and GRB host populations are found in hosts that are more metal enriched. For reference, the host of AT2018cow had $\log M - 0.33 \times \log \mathrm{SFR} \approx 9.4$. The black line is the fundamental metallicity relation in Mannucci et al. (2010).

out radioactive decay as the mechanism powering the peak of the light curve.

We now consider whether radioactive decay could dominate the light curve at late times ($t \gg t_{\rm peak}$). The left panel of Figure 6.18 shows the bolometric light curve of SN 2018gep compared to several other Ic-BL SNe from the literature (Cano, 2013), whose light curves are thought to be dominated by the radioactive decay of ^{56}Ni (although see Moriya et al. (2017) for another possible interpretation). The luminosity of SN 2018gep at $t \sim 20$ d is about half that of SN1998bw, and double that of SN2010bh and SN2006aj. By modeling the light curves of the three Ic-BL SNe shown, Cano (2013) infers nickel masses of 0.42 $M_\odot$, 0.12 $M_\odot$, and 0.21 $M_\odot$, respectively. On this scale, SN 2018gep has $M_{\rm Ni} \sim 0.1$–$0.2\,M_\odot$.

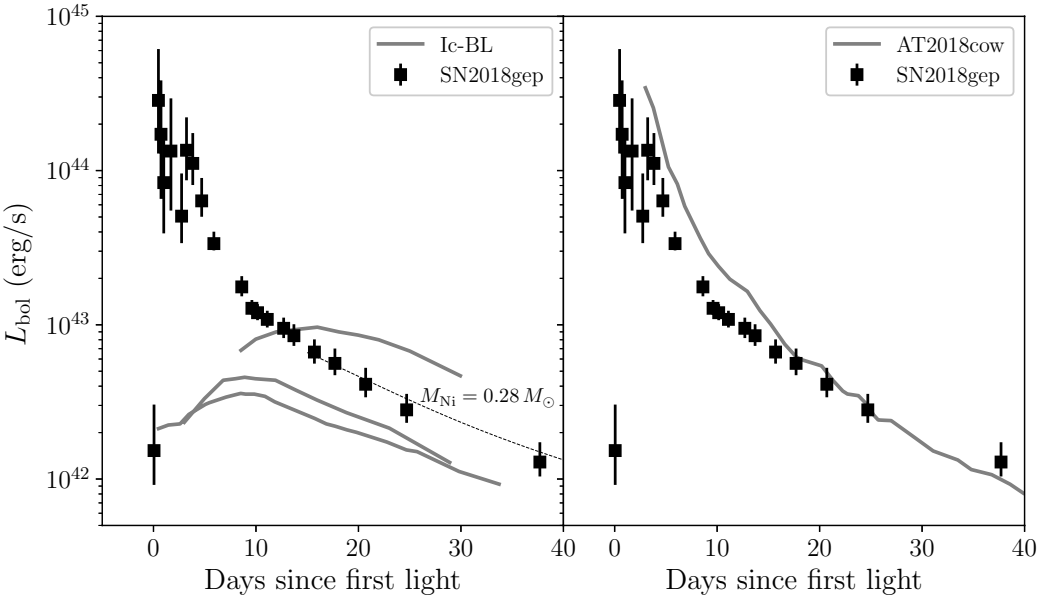

Figure 6.18: The bolometric light curve of SN 2018gep compared to (left) other Ic-BL SNe from the literature (Cano, 2013) and (right) to AT2018cow (Perley et al., 2019). The dotted line shows the expected contribution from the radioactive decay of ^{56}Ni, for a gamma-ray escape time of 30 d and $M_{\rm Ni}$=0.28 $M_\odot$. In order of decreasing $L_{\rm bol}$, the three Ic-BL SNe are SN1998bw, SN2010bh, and SN2006aj.

The right panel of Figure 6.18 shows the light curve of SN 2018gep compared to that of AT2018cow (Perley et al., 2019). To estimate the nickel mass of AT2018cow, Perley et al. (2019) compared the bolometric luminosity at $t \sim 20$ d to that of SN2002ap (whose nickel mass was derived via late-time nebular spectroscopy; Foley et al. 2003) and found $M_{\rm Ni} < 0.05\,M_\odot$. On this scale, we would expect $M_{\rm Ni} \lesssim 0.05\,M_\odot$ for SN 2018gep as well.

Finally, Katz et al. (2013) and Wygoda et al. (2019) present an analytical technique for testing whether a light curve is powered by radioactive decay. At late times, the bolometric luminosity is equal to the rate of energy deposition by radioactive decay $Q(t)$, because the diffusion time is much shorter than the dynamical time: $L_{\rm bol}(t) = Q(t)$. At any given time, the energy deposition rate $Q(t)$ is

$$Q(t) = Q_\gamma(t) \left(1 - e^{-(t_0/t)^2}\right) + Q_{\rm pos}(t), \tag{6.1}$$

where $Q_\gamma(t)$ is the energy release rate of gamma-rays and t_0 is the time at which the ejecta becomes optically thin to gamma rays. The expression for $Q_\gamma(t)$ is

$$\frac{Q_\gamma(t)}{10^{43}\,{\rm erg\,s^{-1}}} = \frac{M_{\rm Ni}}{M_\odot}\left(6.45e^{-t/8.76\,{\rm d}} + 1.38e^{-t/111.4\,{\rm d}}\right). \tag{6.2}$$

$Q_{\rm pos}(t)$ is the energy deposition rate of positron kinetic energy, and the expression is

$$\frac{Q_{\rm pos}(t)}{10^{41}\,{\rm erg\,s^{-1}}} = 4.64\frac{M_{\rm Ni}}{M_\odot}\left(-e^{-t/8.76\,{\rm d}} + e^{-t/111.4\,{\rm d}}\right). \tag{6.3}$$

The dotted line in Figure 6.18 shows a model track with $M_{\rm Ni} = 0.28\,M_\odot$ and $t_0 = 30\,{\rm d}$. Lower nickel masses produce tracks that are too low to reproduce the data, and larger values of t_0 produce tracks that drop off too rapidly. Thus on this scale it seems that $M_{\rm Ni} \sim 0.3\,M_\odot$, similar to other Ic-BL SNe (Lyman et al., 2016).

We can also try to solve directly for t_0 and $M_{\rm Ni}$ using the technique for Ia SNe in Wygoda et al. (2019). The first step is to solve for t_0 using Equation 6.1 and a second equation resulting from the fact that the expansion is adiabatic,

$$\int_0^t Q(t')\,t'\,dt' = \int_0^t L_{\rm bol}(t')\,t'\,dt'. \tag{6.4}$$

The ratio of Equation 6.1 to Equation 6.4 removes the dependence on $M_{\rm Ni}$, and enables t_0 to be measured. However, as shown in Figure 6.19, the data have not yet converged to model tracks, so we cannot apply this method.

Interaction with Extended Material

One way to power a rapid and luminous light curve is to deposit energy into circumstellar material (CSM) at large radii (Nakar and Piro, 2014; Nakar and Sari, 2010;

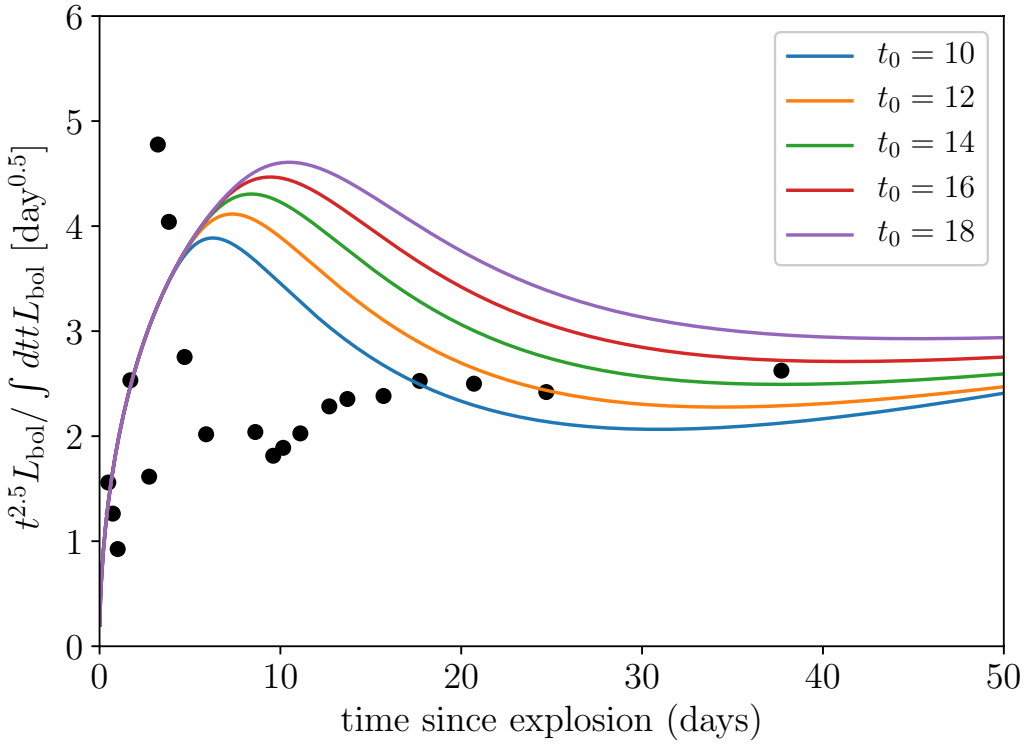

Figure 6.19: To test whether a light curve is powered by radioactive decay, the ratio of the bolometric luminosity to the time-weighted integrated bolometric luminosity should converge to model tracks, as described in Katz et al. (2013) and Wygoda et al. (2019). This enables a direct measurement of the gamma-ray escape time t_0 and the nickel mass $M_{\rm Ni}$. However, our data have not converged to these tracks, suggesting that either radioactive decay is not dominant, or that we are not yet in a phase where we can perform this measurement.

Piro, 2015). Since this is a Ic-BL SN, we expect the progenitor to be stripped of its envelope and therefore compact ($R \sim 0.5\,R_\odot \sim 10^{10}$ cm; Groh et al. 2013), although there have never been any direct progenitor detections for a Ic-BL SN.

With this expectation, extended material at larger radii would have to arise from mass-loss. This would not be surprising, as massive stars are known to shed a significant fraction of their mass in winds and eruptive episodes; see Smith (2014) for a review.

First we perform an order-of-magnitude calculation to see whether the rise time and peak luminosity could be explained by a model in which shock interaction powers the light curve ("wind shock breakout"). Assuming that the progenitor ejected material with a velocity v_w at a time t prior to explosion, the radius of this material

at any given time is

$$\begin{aligned} R_{\rm sh} &= R_* + v_{\rm w} t \\ &\approx (8.64 \times 10^{12}\,{\rm cm}) \left(\frac{v_w}{1000\,{\rm km\,s^{-1}}}\right) \left(\frac{t}{\rm d}\right). \end{aligned} \tag{6.5}$$

For material ejected 15 days prior to explosion, traveling at $1000\,{\rm km\,s^{-1}}$, the radius would be $R_{\rm CSM} \sim 10^{14}\,{\rm cm}$ at the time of explosion. The shock crossing timescale is $t_{\rm cross}$:

$$t_{\rm cross} \sim R_{\rm CSM}/v_s \approx (0.4\,{\rm d}) \left(\frac{R}{10^{14}\,{\rm cm}}\right) \left(\frac{v_s}{0.1c}\right)^{-1}, \tag{6.6}$$

where v_s is the velocity of the shock. The shock heats the CSM with an energy density that is roughly half of the kinetic energy of the shock, so $e_s \sim (1/2)(\rho v_s^2/2)$. The luminosity is the total energy deposited divided by $t_{\rm cross}$,

$$\begin{aligned} L_{\rm BO} &\sim \frac{E_{\rm BO}}{t_{\rm cross}} \sim \frac{v_s^3}{4}\frac{dM}{dR} \\ &= (8 \times 10^{44}\,{\rm erg\,s^{-1}}) \left(\frac{v_s}{0.1c}\right)^3 \left(\frac{dM}{M_\odot}\right) \left(\frac{dR}{10^{14}\,{\rm cm}}\right)^{-1} \end{aligned} \tag{6.7}$$

assuming a constant density. Thus, for shock velocities on the order of the observed photospheric radius expansion ($0.1c$), and a CSM radius on the order of the first photospheric radius that we measure ($3 \times 10^{14}\,{\rm cm}$), it is easy to explain the rise time and peak luminosity that we observe.

To test whether shock breakout (and subsequent post-shock cooling) can explain the evolution of the physical properties we measured in Section 6.3, we ran one-dimensional numerical radiation hydrodynamics simulations of a SN running into a circumstellar shell with CASTRO (Almgren et al., 2010; Zhang et al., 2011). We assume spherical symmetry and solve the coupled equations of radiation hydrodynamics using a grey flux-limited non-equilibrium diffusion approximation. The setup is similar to the models presented in Rest et al. (2018) but with parameters modified to fit SN 2018gep.

The ejecta is assumed to be homologously expanding, characterized by a broken power-law density profile, an ejecta mass $M_{\rm ej}$, and energy $E_{\rm ej}$. The ejecta density

profile has an inner power-law index of $n = 0$ (that is, $\rho(r) \propto r^{-n}$) then steepens to an index $n = 10$, as is appropriate for core-collapse SN explosions (Matzner and McKee, 1999). The circumstellar shell is assumed to be uniform in density with radius $R_{\rm CSM}$ and mass $M_{\rm CSM}$. We adopt a uniform opacity of $\kappa = 0.2$ cm^2 g^{-1}, which is characteristic of hydrogen-poor electron scattering.

The best-fit model, shown in Figure 6.20, used the following parameters: $M_{\rm ej} = 8\,M_\odot$, $E_{\rm ej} = 2 \times 10^{52}$ erg, $M_{\rm CSM} = 0.02\,M_\odot$, and $R_{\rm CSM} = 3 \times 10^{14}$ cm. The inferred kinetic energy is consistent with typical values measured for Ic-BL SNe (e.g. Cano et al. 2017b; Taddia et al. 2019), and $R_{\rm CSM}$ is similar in value to the first photospheric radius we measure (at $\Delta t = 0.05$ d; see Figure 6.9).

The inferred values presented here are likely uncertain to within a factor of a few, given the degeneracies of the rise time and peak luminosity with the CSM mass and radius. Qualitatively, a larger CSM radius will result in a higher peak luminosity and longer rise time. The peak luminosity is relatively independent of the CSM mass, which instead affects the photospheric velocity and temperature (i.e., a larger CSM mass slows down the post-interaction velocity to a greater extent and increases the shock-heated temperature). A full discussion of the dependencies of the light curve and photospheric properties on the CSM parameters will be presented in an upcoming work (Khatami, D. et al., in preparation).

In this framework, the shockwave sweeps through the CSM prior to peak luminosity, so that at maximum luminosity the outer parts of the CSM have been swept into a dense shell moving at SN-like velocities ($v_{\rm post-shock} \approx 3v_s/4$). This scenario was laid out in Chevalier and Irwin (2011) and discussed in Kasen (2017). This explains the high velocities we measure at early times and the absence of narrow emission features in our spectra. For another discussion of the absence of narrow emission lines due to an abrupt cutoff in CSM density, see Moriya and Tominaga (2012). Following Chevalier and Irwin (2011), the rapid rise corresponds to shock breakout from the CSM, and begins at a time $R_{\rm CSM}/v_{\rm sh}$ after the explosion, where $v_{\rm sh}$ is the velocity of the shock. The time to peak luminosity (1.2 d) is longer than this delay time by a factor (R_w/R_d). Given the best-fit $R_w = 3 \times 10^{14}$ cm, and assuming $R_d \sim R_w$, we find $v_{\rm sh} = 0.1c$, and an explosion time ~ 1 d prior to t_0. This model also predicts an increasing temperature while the shock breaks out (i.e., during the rise to peak bolometric luminosity).

Other Ic SNe have shown early evidence for interaction in their light curves, but in other cases the emission has been attributed to post-shock cooling in expanding

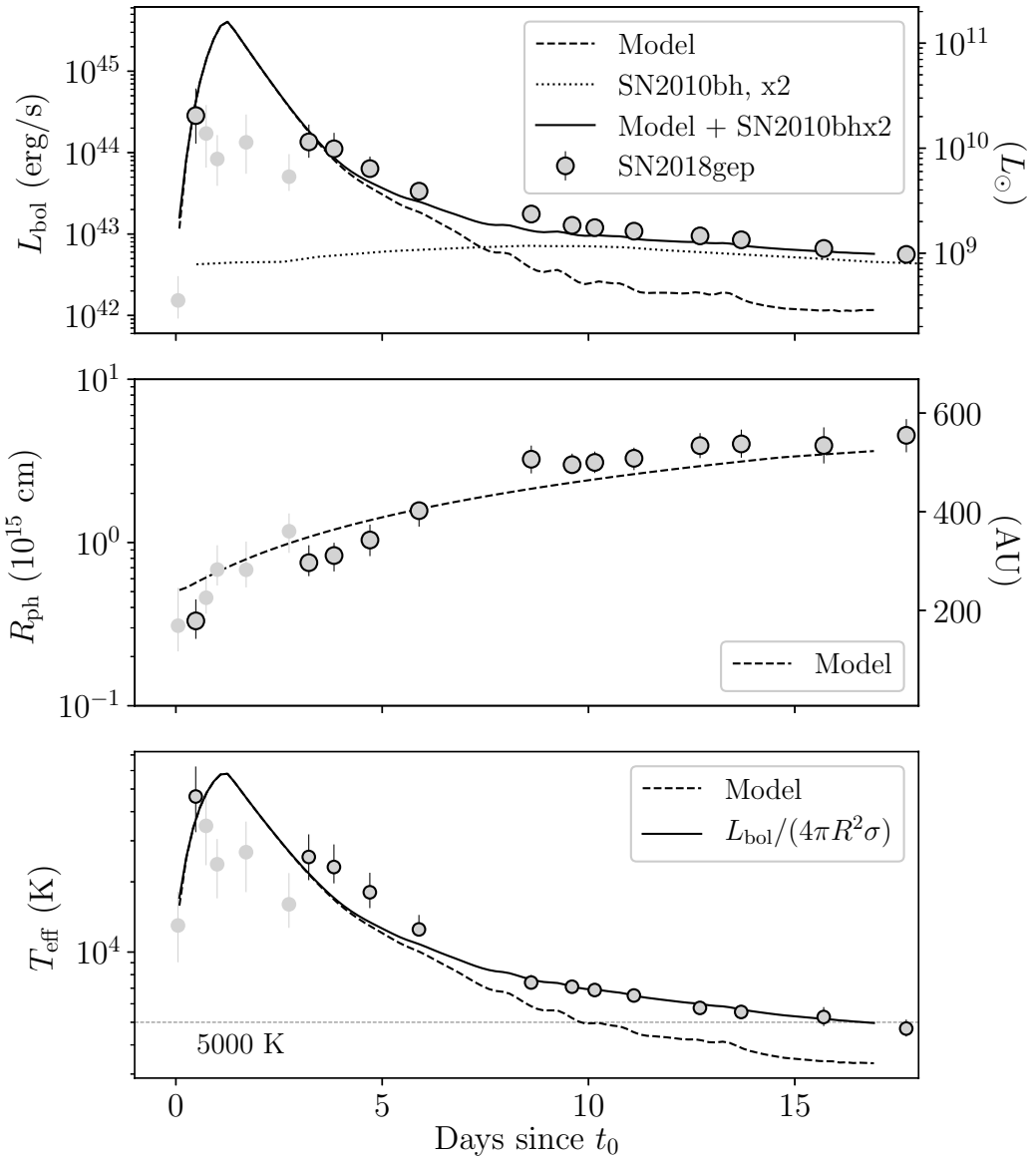

Figure 6.20: Best-fit CSM interaction model with the light curve of the Ic-BL SN 2010bh (Cano, 2013) scaled up by a factor of two. The model parameters are $M_{\rm ej} = 8\,M_\odot$, $E_{\rm ej} = 2 \times 10^{52}$ erg, $M_{\rm CSM} = 0.02\,M_\odot$, and $R_{\rm CSM} = 3 \times 10^{14}$ cm. As in Figure 6.9, the outlined circles are derived from UV and optical data, while the light grey circles are derived from optical data only.

material rather than shock breakout itself. For example, the first peak observed in iPTF14gqr (De et al., 2018) was short-lived ($\lesssim 2$ d) and attributed to shock-cooling emission from material stripped by a compact companion. iPTF14gqr is different in a number of ways from SN 2018gep: the spectra showed high-ionization emission lines, including He II, and the explosion had a much smaller kinetic

energy ($E_K \approx 10^{50}$ erg) and smaller velocities (10,000 km s^{-1}). The main peak in iPTF16asu was also modeled as shock-cooling emission rather than shock breakout (Whitesides et al., 2017).

Under the assumption that the light curve represented post-shock cooling emission, De et al. (2018) and Whitesides et al. (2017) both used one-zone analytic models from Piro (2015) to estimate the properties of the explosion and the CSM. This approximation assumes that the emitting region is a uniformly heated expanding sphere. In iPTF14gqr the inferred properties of the extended material were $M_e \sim 8 \times 10^{-3}\, M_\odot$ at $R_e \sim 3 \times 10^{13}$ cm. In iPTF16asu the inferred properties of the extended material were $M_e \sim 0.45\, M_\odot$ at $R_e \sim 1.7 \times 10^{12}$ cm. The fit also required a more energetic explosion than iPTF14gqr (4×10^{51} erg). By applying the same framework to the decline of the bolometric light curve of SN 2018gep, we arrive at similar values to those inferred for iPTF16asu, as shown in Figure 6.21.

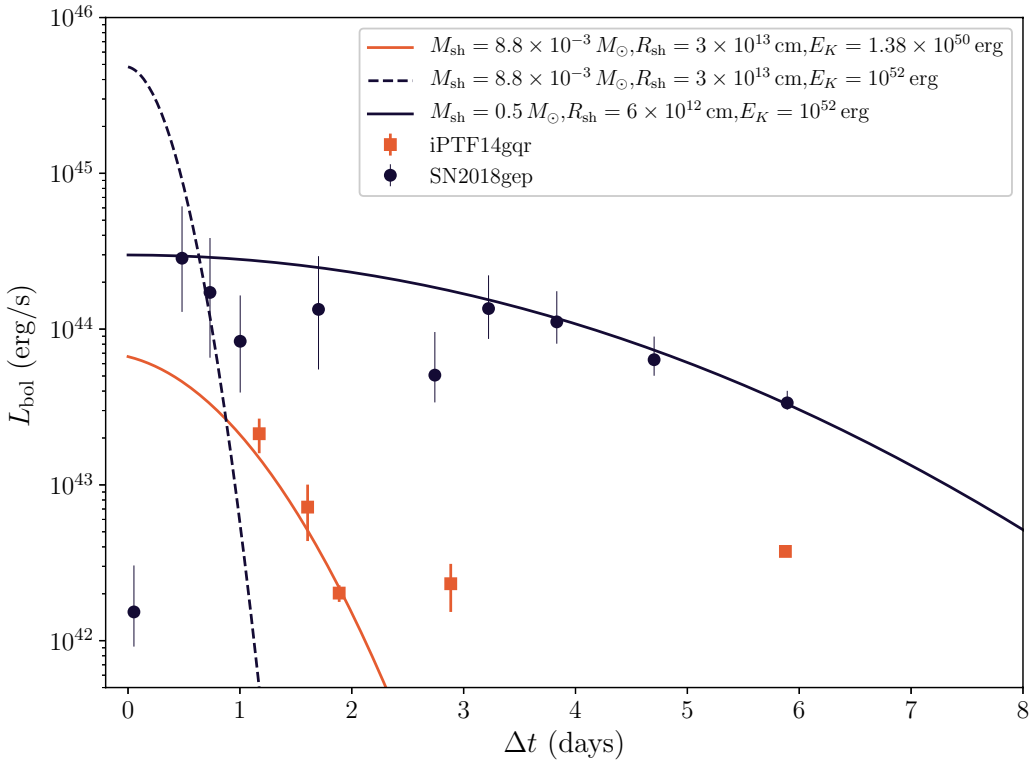

Figure 6.21: Estimated CSM and explosion properties using models from Piro (2015). The shell mass is much larger than the one in iPTF14gqr, which is the reason for the more extended shock-cooling peak.

We model the main peak of SN 2018gep as shock breakout rather than post-shock cooling emission. Our motivation for this choice is that the timescale over which

we detect the precursor emission is more consistent with a large radius and lower shell mass. From the shell mass and radius, we can also estimate the mass-loss rate immediately prior to explosion,

$$\frac{\dot{M}}{M_\odot\,\mathrm{yr}^{-1}} \approx 32 \left(\frac{M_{\rm sh}}{M_\odot}\right) \left(\frac{v_w}{1000\mathrm{km\,s}^{-1}}\right) \left(\frac{R_{\rm sh}}{10^{14}\mathrm{cm}}\right)^{-1}. \tag{6.8}$$

For our best-fit parameters $M_{\rm sh} = 0.02\,M_\odot$ and $R_{\rm sh} = 3 \times 10^{14}\,\mathrm{cm}$, and taking $v_w = 1000\,\mathrm{km\,s}^{-1}$, we find $\dot{M} \approx 0.6\,M_\odot\,\mathrm{yr}^{-1}$, 4–6 orders of magnitude higher than what is typically expected for Ic-BL SNe (Smith, 2014).

In the shock breakout model, the shock sweeps through confined CSM and passes into lower-density material. Thus, it is not surprising that we do not observe the X-ray or radio emission that would indicate interaction with high-density material. From our VLA observations of SN 2018gep, the radio flux marginally decreased from $\Delta t = 5\,\mathrm{d}$ to $\Delta t = 75\,\mathrm{d}$. This could be astrophysical, but could also be instrumental (change in beamsize due to change in VLA configuration). Using the relation of Murphy et al. (2011), the estimated contribution from the host galaxy (for a SFR of $0.12^{+0.08}_{-0.05}\,M_\odot\,\mathrm{yr}^{-1}$; see Section 6.3) is

$$\begin{aligned}\left(\frac{L_{1.4\,\mathrm{GHz}}}{\mathrm{erg\,s}^{-1}\,\mathrm{Hz}^{-1}}\right) &\approx 1.57 \times 10^{28} \left(\frac{\mathrm{SFR_{radio}}}{M_\odot\,\mathrm{yr}^{-1}}\right) \\ &\approx 1.9 \times 10^{27}\,\mathrm{erg\,s}^{-1}\,\mathrm{Hz}^{-1}.\end{aligned} \tag{6.9}$$

Taking a spectral index of -0.7 (a synchrotron spectrum), the expected 9 GHz luminosity would be between $3.0 \times 10^{26}\,\mathrm{erg\,s}^{-1}\,\mathrm{Hz}^{-1}$ and $8.6 \times 10^{26}\,\mathrm{erg\,s}^{-1}\,\mathrm{Hz}^{-1}$. From Table 6.2, the measured spectral luminosity is $8.3 \times 10^{26}\,\mathrm{erg\,s}^{-1}\,\mathrm{Hz}^{-1}$ (at 10 GHz) in the first epoch, and $6 \times 10^{26}\,\mathrm{erg\,s}^{-1}\,\mathrm{Hz}^{-1}$ (at 9 GHz) in the second epoch. The slit covering fraction of our LRIS observations is again relevant here; as discussed in Section 6.3, the true SFR is likely a factor of a few higher than what we inferred from modeling the galaxy SED. So, it is plausible that the first two radio detections are entirely due to the host galaxy.

In the third epoch, the luminosity is (at 9 GHz) is $< 3.9 \times 10^{26}\,\mathrm{erg\,s}^{-1}\,\mathrm{Hz}^{-1}$, although the difference from the first two epochs may be due to the different array configuration. Taking the peak of the 9–10 GHz light curve to be $8.3 \times 10^{26}\,\mathrm{erg\,s}^{-1}\,\mathrm{Hz}^{-1}$ at $\Delta t \approx 5\,\mathrm{d}$, Figure 6.22 shows that SN 2018gep would be an order of magnitude

less luminous in radio emission than any other Ic-BL SN. If the luminosity truly decreased, then the implied mass-loss rate is $\dot{M} \sim 3 \times 10^{-6}$, consistent with the idea that the shock has passed from confined CSM into much lower-density material.

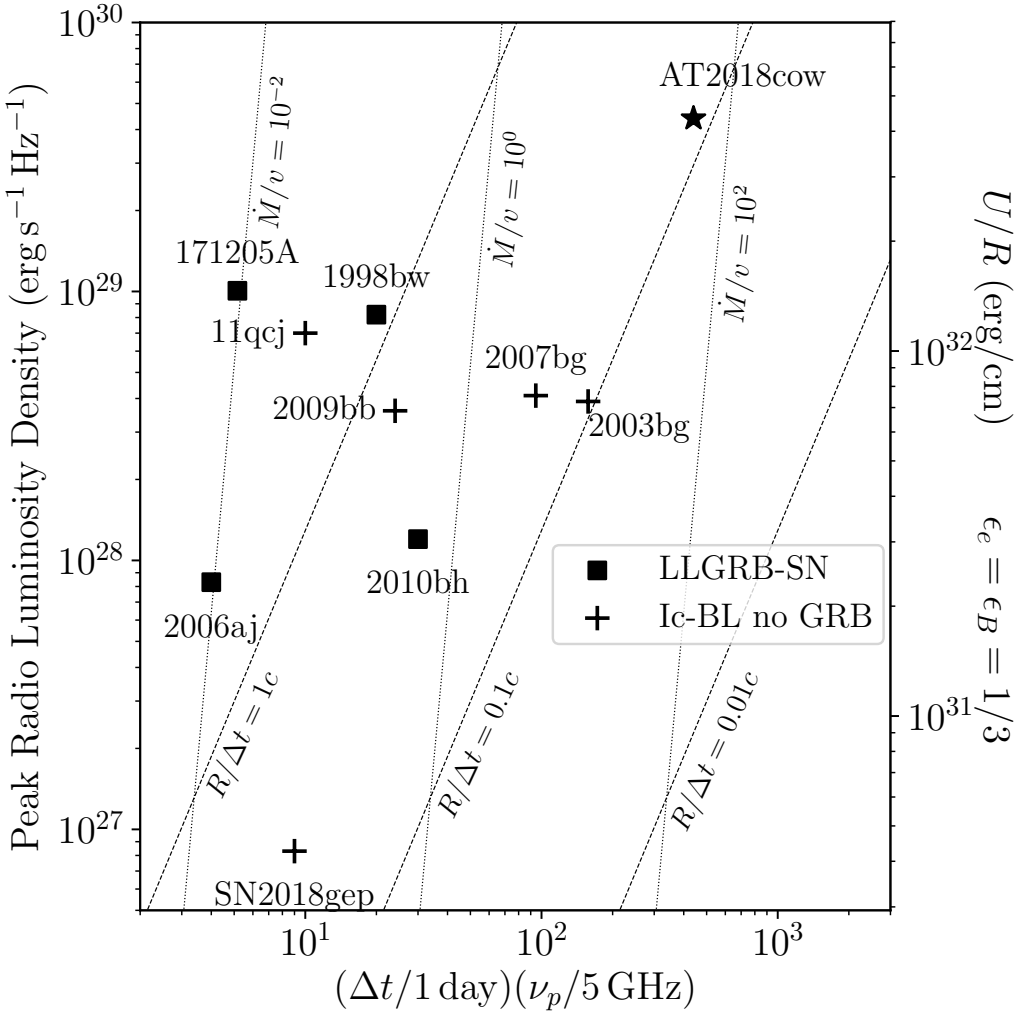

Figure 6.22: The radio luminosity of SN 2018gep compared to AT2018cow and radio-loud Ic-BL SNe (assuming $\epsilon_e = \epsilon_B = 1/3$, cf. Chevalier 1998; Ho et al. 2019c; Soderberg et al. 2010). Lines of constant mass-loss rate (scaled to wind velocity) are shown in units of $10^{-4}\,M_\odot\,\mathrm{yr}^{-1}/1000\,\mathrm{km\,s}^{-1}$. The radio luminosity for GRB 171205A was taken from VLA observations reported by Laskar et al. (2017), but we note that this is a lower limit in luminosity and in peak frequency because the source was heavily self-absorbed at this epoch.

If the emission is constant and due entirely to the host galaxy, the point shown in Figure 6.22 is an upper limit in luminosity. Assuming that the peak of the SED of any radio emission from the SN is not substantially different from the frequencies we

measure (i.e., that the spectrum is not self-absorbed at these frequencies), we have a limit on the 9 GHz radio luminosity of $L_p \lesssim 10^{27}$ erg s^{-1} Hz^{-1} at $\Delta t \approx 5$–15 d.

The shell mass and radius also give an estimate of the optical depth: $\tau \approx \kappa M/r^2 \approx 100 >> 1$, which means that the shell would be optically thick. The lack of detected X-ray emission is consistent with the expectation that any X-ray photons produced in the collision would be thermalized by the shell and reradiated as blackbody emission.

Finally, assuming that the rapid rise to peak is indeed caused by shock breakout, we examine whether our model is consistent with our detections in the weeks prior to explosion. Material ejected 10 days prior to the explosion at the escape velocity of a Wolf-Rayet star ($v_{\rm esc} \sim 1000$ km s^{-1}) would lie at $R \sim 10^{14}$ cm, which is consistent with our model. Assuming that the emission mechanism is internal shocks between shells of ejected material traveling at different velocities, we can estimate the amount of mass required:

$$\frac{1}{2}\epsilon M v^2 = L\tau, \tag{6.10}$$

where $v \approx 1000$ km s^{-1}, $\epsilon \approx 0.5$ is the efficiency of thermalizing the kinetic energy of the shells, M is the shell mass, $L \approx 10^{39}$ erg s^{-1} is the luminosity we observe, and $\tau \approx 10$ d is the timescale over which we observe the emission. We find $M \approx 0.02\,M_\odot$, again consistent with our model.

We conclude that the data are consistent with a scenario in which a compact Ic-BL progenitor underwent a period of eruptive mass-loss shortly prior to explosion. In the terminal explosion, the light curve was initially dominated by shock breakout through (and post-shock cooling of) this recently-ejected material.

Finally, we return to the question of the emission detected in the first few minutes, which showed an inflection point prior to the rapid rise to peak (Figure 6.2). Given the pre-explosion activity and inference of CSM interaction, it is not surprising that the rise is not well-modeled by a simple quadratic function. One possibility is that we are seeing ejecta already heated from earlier precursor activity. Another possibility is that we are seeing the effects of a finite light travel time. For a sphere of $R \sim 3 \times 10^{14}$ cm, the light crossing time is ~ 20 minutes. The slower rising phase could represent the time for photons to reach us across the extent of the emitting sphere.

In Table 6.4, we summarize the key properties inferred from Section 6.4.

Table 6.4: Key model properties of SN 2018gep

Parameter	Value	Notes
$t_{\rm rise}$	1.2 d	
$E_{\rm SN}$	2×10^{52} erg	
$M_{\rm ej}$	$8\,M_\odot$	
$M_{\rm CSM}$	$0.02\,M_\odot$	
$R_{\rm CSM}$	3×10^{14} cm	
$\dot{M}$	$0.6\,M_\odot\,{\rm yr}^{-1}$	Assuming $v_w = 1000\,{\rm km\,s^{-1}}$
$M_{\rm Ni}$	< 0.2–$0.3\,M_\odot$	

6.5 Comparison to Unclassified Rapidly Evolving Transients at High Redshift

In terms of the timescale of its light curve evolution, SN 2018gep is similar to AT2018cow in fulfilling the criteria that optical surveys use to identify rapidly evolving transients (e.g. Drout et al. 2014; Pursiainen et al. 2018; Tanaka et al. 2016). However, there are a number of ways in which SN 2018gep is more of a "typical" member of these populations than AT2018cow. In particular, SN 2018gep has an expanding photospheric radius and declining effective temperature. By contrast, one of the challenges in explaining AT2018cow as a stellar explosion was its nearly constant temperature (persistent blue color) and *declining* photospheric radius. In Figure 6.23 we show these two different kinds of evolution as very different tracks in color-magnitude space. We also show a late-time point for KSN2015K (Rest et al., 2018), which shows blue colors even after the transient had faded to half-max. The mass-loss rate inferred for Rest et al. (2018) was $2 \times 10^{-3}\,M_\odot\,{\rm yr}^{-1}$.

Of the PS-1 events, most appear to expand, cool, and redden with time (Drout et al., 2014). That said, there are few co-eval data points in multiple filters, even in the gold sample transients. The transients are also faint; all but one lie at $z > 0.1$. Of the DES sample, most also show evidence for declining temperatures and increasing radii, although three show evidence of a constant temperature and decreasing radius: 15X3mxf, 16X1eho, and 15C3opk. The peak bolometric luminosities for these three transients are reported as 3×10^{43} erg s^{-1}, 9×10^{43} erg s^{-1}, and 5×10^{43} erg s^{-1}, respectively (Pursiainen et al., 2018).

To estimate a rate of Ic-BL SNe that have a light curve powered by shock breakout, we used the sample of 25 nearby ($z < 0.1$) Ic-BL SNe from PTF (Taddia et al., 2019), because these were found in an untargeted survey. Of these, we could not draw a conclusion about eight (either because the peak was not resolved or there was

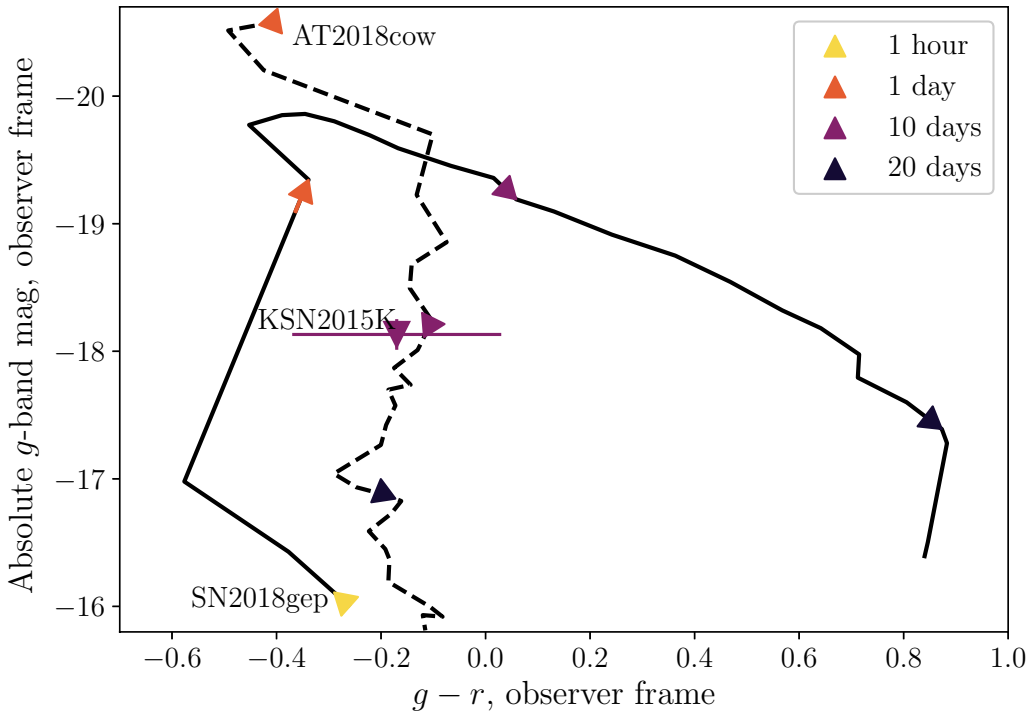

Figure 6.23: A "color-magnitude" diagram of AT2018cow and SN 2018gep, showing the evolution of color with time from first light (t_0). Like AT2018cow, the fast transient KSN2015K stayed persistently blue even after it had faded to half-maximum. SN 2018gep has more typical SN evolution, reddening with time (cooling in temperature).

no multi-color photometry available around peak, or both). The remaining clearly lacked the rise time or blue colors of SN 2018gep. Furthermore, SN 2018gep is unique among the sample of 12 nearby ($z < 0.1$) Ic-BL SNe from ZTF discovered so far, which will be presented in a separate publication. From this, we estimate that the rate of Ic-BL SNe with a main peak dominated by shock breakout is no more than 10% of the rate of Ic-BL SNe.

6.6 Summary and Future Work

In this paper, we presented an unprecedented dataset that connects late-stage eruptive mass loss in a stripped massive star to its subsequent explosion as a rapidly rising luminous transient. Here we summarize our key findings:

1. High-cadence dual-band observations with ZTF (six observations in 3 hours) captured a rapid rise (1.4 ± 0.1 mag/hr) to peak luminosity, and a corre-

sponding increase in temperature. This rise rate is second only to that of SN 2016gkg (Bersten et al., 2018), which was attributed to shock breakout in extended material surrounding a Type IIb progenitor. However, the signal in SN 2018gep is two magnitudes more luminous.

2. A retrospective search in ZTF data revealed clear detections of precursor emission in the days and months leading up to the terminal explosion. The luminosity of these detections ($M = -14$) and evidence for variability suggests that they arise from eruptive mass-loss, rather than the luminosity of a quiescent progenitor. This is the first definitive pre-explosion detection of a Ic-BL SN to date.

3. The bolometric light curve peaks after a few days at $> 3 \times 10^{44}\,\mathrm{erg\,s^{-1}}$. At late times, a power-law and an exponential decay are both acceptable fits to the data.

4. The temperature rises to 50,000 K in the first day, then declines as t^{-1} then flattens at 5000 K, which we attribute to recombination of carbon and oxygen.

5. The photosphere expands at $v = 0.1c$, and flattens once recombination sets in.

6. We obtained nine spectra in the first five days of the explosion, as the effective temperature declined from 50,000 K to 20,000 K. To our knowledge, these represent the earliest-ever spectra of a stripped-envelope SN, in terms of temperature evolution.

7. The early spectra exhibit a "W" feature similar to what has been seen in stripped-envelope superluminous SNe. From a NLTE spectral synthesis model, we find that this can be reproduced with a carbon and oxygen composition.

8. The velocities inferred from the spectra are among the highest observed for stripped-envelope SNe, and are most similar to the velocities of Ic-BL SNe accompanied by GRBs.

9. The host galaxy has a star-formation rate of $0.12\,M_\odot\,\mathrm{yr^{-1}}$, and a lower mass and lower metallicity than galaxies hosting GRB-SNe, which are low-mass and low-metallicity compared to the overall core collapse SN population.

10. The early light curve is best-described by shock breakout in extended but confined CSM, with $M = 0.02\,M_\odot$ at $R = 3 \times 10^{14}$ cm. The implied mass-loss

rate is $0.6\,M_{\odot}\,\mathrm{yr}^{-1}$ in the days leading up to the explosion, consistent with our detections of precursor emission. After the initial breakout, the shock runs through CSM of much lower density, hence the lack of narrow emission features and lack of strong radio and X-ray emission.

11. Although SN 2018gep is similar to AT2018cow in terms of its bolometric light curve, it has a very different color evolution. In this sense, the "rapidly evolving transients" in the PS-1 and DES samples are more similar to SN 2018gep than to AT2018cow.

12. The late-time light curve seems to require an energy deposition mechanism distinct from shock-interaction. Radioactive decay is one possibility, but further monitoring is needed to test this.

The code used to produce the results described in this paper was written in Python and is available online in an open-source repository[14]. When the paper has been accepted for publication, the data will be made publicly available via WISeREP, an interactive repository of supernova data (Yaron and Gal-Yam, 2012).

The authors would like to thank the anonymous referee whose comments improved the flow, precision, and clarify of the paper. It is a pleasure to thank Tony Piro, Dan Kasen, E. Sterl Phinney, Eliot Quataert, Maryam Modjaz, Jim Fuller, Lars Bildsten, Udi Nakar, Paul Duffell, and Luc Dessart for helpful discussions. A.Y.Q.H. is particularly grateful to Tony Piro and the community at Carnegie Observatories for their hospitality on Tuesdays during the period in which this work was performed. Thank you to the staff at the SMA, AMI, the VLA, *Swift*, and Chandra for rapidly scheduling and executing the observations. Thank you to David Palmer (LANL) for his assistance in searching the pointing data for *Swift*/BAT. Thank you to Michael J. Koss (Eureka Scientific Int), Andrew Drake (Caltech), Scott Adams (Caltech), Matt Hankins (Caltech), Kevin Burdge (Caltech), and Kirsty Taggart (LJMU) for assisting with optical spectroscopic observations. Thank you to Erik Petigura and David Hogg for their advice on figure aesthetics. Thank you to David Alexander Kann (IAA-CSIC) and Nhan Nguyen (Bonn) for pointing out errors in early versions of the paper posted to the arXiv. D.A.G. thanks Stéfan van der Walt and Ari Crellin-Quick for assistance with skyportal, which enabled the search for pre-explosion emission.

[14] `https://github.com/annayqho/SN2018gep`

A.Y.Q.H. is supported by a National Science Foundation Graduate Research Fellowship under Grant No. DGE-1144469. This work was supported by the GROWTH project funded by the National Science Foundation under PIRE Grant No. 1545949. A.G.-Y. is supported by the EU via ERC grant No. 725161, the ISF, the BSF Transformative program and by a Kimmel award. Y.T. studied as a GROWTH intern at Caltech during the summer and fall of 2017. C.C.N. thanks the funding from MOST grant 104-2923-M-008 -004-MY5. R.L. is supported by a Marie Skłodowska-Curie Individual Fellowship within the Horizon 2020 European Union (EU) Framework Programme for Research and Innovation (H2020-MSCA-IF-2017-794467). A.H. acknowledges support by the I-Core Program of the Planning and Budgeting Committee and the Israel Science Foundation, and support by the ISF grant 647/18. This research was supported by a Grant from the GIF, the German-Israeli Foundation for Scientific Research and Development. This research was funded in part by the Gordon and Betty Moore Foundation through Grant GBMF5076, and a grant from the Heising-Simons Foundation. A.C. acknowledges support from the NSF CAREER award N. 1455090 and from the NASA/Chandra GI award N. GO8-19055A. Research support to I.A. is provided by the GROWTH project, funded by the National Science Foundation under Grant No 1545949.

Based on observations obtained with the Samuel Oschin Telescope 48-inch and the 60-inch Telescope at the Palomar Observatory as part of the Zwicky Transient Facility project. Major funding has been provided by the U.S National Science Foundation under Grant No. AST-1440341 and by the ZTF partner institutions: the California Institute of Technology, the Oskar Klein Centre, the Weizmann Institute of Science, the University of Maryland, the University of Washington, Deutsches Elektronen-Synchrotron, the University of Wisconsin-Milwaukee, and the TANGO Program of the University System of Taiwan. Partially based on observations made with the Nordic Optical Telescope, operated by the Nordic Optical Telescope Scientific Association at the Observatorio del Roque de los Muchachos, La Palma, Spain, of the Instituto de Astrofisica de Canarias. The Liverpool Telescope is operated by Liverpool John Moores University with financial support from the UK Science and Technology Facilities Council. LT is located on the island of La Palma, in the Spanish Observatorio del Roque de los Muchachos of the Instituto de Astrofisica de Canarias. The scientific results reported in this article are based in part on observations made by the Chandra X-ray Observatory. The data presented here were obtained in part with ALFOSC, which is provided by the Instituto de Astrofisica de Andalucia (IAA) under a joint agreement with the University of Copenhagen

and NOTSA. The Submillimeter Array is a joint project between the Smithsonian Astrophysical Observatory and the Academia Sinica Institute of Astronomy and Astrophysics and is funded by the Smithsonian Institution and the Academia Sinica. We acknowledge the support of the staff of the Xinglong 2.16-m telescope. This work is supported by the National Natural Science Foundation of China (NSFC grants 11325313 and 11633002), and the National Program on Key Research and Development Project (grant no. 2016YFA0400803). SED Machine is based upon work supported by the National Science Foundation under Grant No. 1106171. This publication has made use of data collected at Lulin Observatory, partly supported by MoST grant 105-2112-M-008-024-MY3. The JEKYLL simulations were performed on resources provided by the Swedish National Infrastructure for Computing (SNIC) at Parallelldatorcentrum (PDC).

6.7 Appendix

Here we provide supplementary figures and tables. In Appendix 6.7 we provide the full set of optical and UV photometry and the blackbody fits to this photometry. In Appendix 6.7 we provide the log of optical and UV spectroscopic observations, as well as a figure showing all of our optical spectra. In Appendix 6.7 we include more details about the atomic data used for our spectral modeling. In Appendix 6.7 we show the spectrum, line-flux measurements, and photometry that was used to derive properties of the host galaxy.

UV and Optical Photometry

Here we provide our optical and UV photometry (Table 6.5) and the blackbody fits to this photometry used to derive the photospheric evolution (Figure 6.24).

Table 6.5: Optical and ultraviolet photometry for SN 2018gep

Date (JD)	Δt	Instrument	Filter	AB Mag	Error in AB Mag
2458370.6634	0.02	P48+ZTF	r	20.48	0.26
2458370.6856	0.04	P48+ZTF	g	19.70	0.14
2458370.6994	0.05	P48+ZTF	g	19.34	0.11
2458370.7153	0.07	P48+ZTF	g	18.80	0.08
2458370.7612	0.11	P48+ZTF	r	18.36	0.08
2458370.7612	0.11	P48+ZTF	r	18.36	0.08
2458371.6295	0.98	P60+SEDM	r	16.78	0.01
2458371.6323	0.99	P60+SEDM	g	16.39	0.02
2458371.6351	0.99	P60+SEDM	i	17.01	0.01

2458371.6369	0.99	P48+ZTF	r	16.83	0.03
2458371.6378	0.99	P48+ZTF	r	16.81	0.04
2458371.6378	0.99	P48+ZTF	r	16.81	0.04
2458371.6392	0.99	P60+SEDM	u	15.98	0.02
2458371.642	0.99	P60+SEDM	r	16.77	0.01
2458371.6448	1.0	P60+SEDM	g	16.37	0.02
2458371.6476	1.0	P60+SEDM	i	16.97	0.01
2458371.6514	1.0	P48+ZTF	r	16.80	0.03
2458371.6517	1.0	P60+SEDM	u	15.98	0.02
2458371.6838	1.04	P48+ZTF	r	16.78	0.04
2458371.6959	1.05	P48+ZTF	g	16.31	0.02
2458371.6968	1.05	P48+ZTF	g	16.29	0.03
2458371.6968	1.05	P48+ZTF	g	16.29	0.03
2458371.7138	1.07	P48+ZTF	g	16.29	0.03
2458371.7138	1.07	P48+ZTF	g	16.29	0.03
2458371.7359	1.09	P48+ZTF	g	16.28	0.03
2458372.6396	1.99	P48+ZTF	r	16.48	0.04
2458372.6396	1.99	P48+ZTF	r	16.48	0.04
2458372.6586	2.01	P48+ZTF	r	16.49	0.06
2458372.6586	2.01	P48+ZTF	r	16.49	0.06
2458372.6861	2.04	P48+ZTF	r	16.47	0.04
2458372.6861	2.04	P48+ZTF	r	16.47	0.04
2458372.7134	2.07	P48+ZTF	g	15.99	0.03
2458372.7371	2.09	P48+ZTF	g	15.99	0.02
2458372.7371	2.09	P48+ZTF	g	15.99	0.02
2458373.6276	2.98	P48+ZTF	r	16.36	0.03
2458373.6447	3.0	P60+SEDM	r	16.32	0.01
2458373.6464	3.0	P60+SEDM	g	15.99	0.01
2458373.6481	3.0	P60+SEDM	i	16.55	0.01
2458373.6498	3.0	P60+SEDM	u	15.90	0.02
2458373.6627	3.02	P48+ZTF	r	16.35	0.03
2458373.6627	3.02	P48+ZTF	r	16.35	0.03
2458373.685	3.04	P48+ZTF	r	16.34	0.03
2458373.685	3.04	P48+ZTF	r	16.34	0.03
2458373.6984	3.05	P48+ZTF	g	15.91	0.02
2458373.7189	3.07	P48+ZTF	g	15.90	0.03

2458373.736	3.09	P48+ZTF	g	15.91	0.02
2458374.6316	3.98	P48+ZTF	r	16.30	0.04
2458374.6316	3.98	P48+ZTF	r	16.30	0.04
2458374.6429	4.0	P48+ZTF	r	16.32	0.03
2458374.6495	4.0	P48+ZTF	r	16.30	0.03
2458374.6551	4.01	P60+SEDM	r	16.29	0.01
2458374.6569	4.01	P60+SEDM	g	16.03	0.01
2458374.6586	4.01	P60+SEDM	i	16.45	0.01
2458374.6603	4.01	P60+SEDM	u	15.92	0.03
2458374.6845	4.04	P48+ZTF	r	16.29	0.04
2458374.6845	4.04	P48+ZTF	r	16.29	0.04
2458374.6994	4.05	P48+ZTF	g	15.91	0.03
2458374.6994	4.05	P48+ZTF	g	15.91	0.03
2458374.7041	4.06	P48+ZTF	g	15.93	0.02
2458374.7264	4.08	P48+ZTF	g	15.92	0.03
2458374.7428	4.1	P48+ZTF	g	15.91	0.03
2458374.7428	4.1	P48+ZTF	g	15.91	0.03
2458375.6247	4.98	P60+SEDM	r	16.31	0.01
2458375.6265	4.98	P60+SEDM	g	16.07	0.01
2458375.6282	4.98	P60+SEDM	i	16.43	0.01
2458375.6299	4.98	P60+SEDM	u	15.98	0.03
2458375.6757	5.03	P48+ZTF	r	16.33	0.04
2458375.6757	5.03	P48+ZTF	r	16.33	0.04
2458375.7144	5.07	P48+ZTF	g	15.97	0.04
2458375.7144	5.07	P48+ZTF	g	15.97	0.04
2458375.7381	5.09	P48+ZTF	g	15.99	0.03
2458376.62	5.97	P48+ZTF	r	16.37	0.04
2458376.6623	6.02	P60+SEDM	r	16.37	0.01
2458376.6626	6.02	P48+ZTF	r	16.37	0.04
2458376.664	6.02	P60+SEDM	g	16.16	0.02
2458376.6657	6.02	P60+SEDM	i	16.44	0.01
2458376.6674	6.02	P60+SEDM	u	16.09	0.03
2458376.6739	6.03	P48+ZTF	r	16.36	0.04
2458376.7272	6.08	P48+ZTF	g	16.10	0.03
2458376.7272	6.08	P48+ZTF	g	16.10	0.03
2458376.7423	6.1	P48+ZTF	g	16.09	0.03

2458376.7423	6.1	P48+ZTF	g	16.09	0.03
2458377.6186	6.97	P60+SEDM	r	16.40	0.01
2458377.6204	6.97	P60+SEDM	g	16.27	0.02
2458377.6221	6.97	P60+SEDM	i	16.51	0.01
2458377.6238	6.98	P60+SEDM	u	16.29	0.01
2458377.6301	6.98	P48+ZTF	r	16.41	0.03
2458377.6301	6.98	P48+ZTF	r	16.41	0.03
2458377.6513	7.0	P48+ZTF	r	16.41	0.03
2458377.6639	7.02	P48+ZTF	r	16.40	0.03
2458377.6639	7.02	P48+ZTF	r	16.40	0.03
2458377.6761	7.03	P48+ZTF	r	16.41	0.03
2458377.6761	7.03	P48+ZTF	r	16.41	0.03
2458377.6935	7.05	P48+ZTF	g	16.21	0.03
2458377.7038	7.06	P48+ZTF	g	16.20	0.03
2458377.7165	7.07	P48+ZTF	g	16.20	0.04
2458377.7165	7.07	P48+ZTF	g	16.20	0.04
2458377.7458	7.1	P48+ZTF	g	16.22	0.03
2458377.7458	7.1	P48+ZTF	g	16.22	0.03
2458378.6164	7.97	P48+ZTF	r	16.45	0.04
2458378.6437	8.0	P48+ZTF	r	16.46	0.05
2458378.665	8.02	P48+ZTF	g	16.33	0.03
2458378.665	8.02	P48+ZTF	g	16.33	0.03
2458378.6844	8.04	P48+ZTF	g	16.32	0.03
2458378.693	8.05	P60+SEDM	r	16.41	0.01
2458378.7039	8.06	P48+ZTF	g	16.32	0.03
2458378.7158	8.07	P48+ZTF	r	16.47	0.03
2458379.6623	9.02	P48+ZTF	g	16.44	0.04
2458379.6823	9.04	P48+ZTF	g	16.43	0.03
2458379.6823	9.04	P48+ZTF	g	16.43	0.03
2458379.6977	9.05	P48+ZTF	g	16.44	0.03
2458379.7176	9.07	P48+ZTF	r	16.51	0.04
2458379.7409	9.09	P48+ZTF	r	16.52	0.04
2458379.7577	9.11	P48+ZTF	r	16.52	0.03
2458380.6214	9.97	P48+ZTF	g	16.63	0.04
2458380.6251	9.98	P48+ZTF	g	16.66	0.04
2458380.6778	10.03	P48+ZTF	g	16.56	0.03

2458380.6778	10.03	P48+ZTF	g	16.56	0.03
2458381.6238	10.98	P48+ZTF	r	16.58	0.04
2458381.6289	10.98	P48+ZTF	r	16.59	0.04
2458381.659	11.01	P48+ZTF	r	16.59	0.04
2458381.6837	11.04	P48+ZTF	g	16.69	0.04
2458381.7053	11.06	P48+ZTF	g	16.69	0.05
2458381.7122	11.06	P48+ZTF	g	16.71	0.04
2458383.6141	12.97	P48+ZTF	r	16.72	0.05
2458383.6141	12.97	P48+ZTF	r	16.72	0.05
2458383.6342	12.99	P48+ZTF	r	16.68	0.03
2458383.6555	13.01	P48+ZTF	r	16.70	0.04
2458383.6829	13.04	P48+ZTF	g	17.05	0.06
2458383.6829	13.04	P48+ZTF	g	17.05	0.06
2458383.6838	13.04	P48+ZTF	g	17.05	0.04
2458383.6838	13.04	P48+ZTF	g	17.05	0.04
2458383.705	13.06	P48+ZTF	g	17.01	0.05
2458383.7143	13.07	P48+ZTF	g	17.05	0.05
2458383.7143	13.07	P48+ZTF	g	17.05	0.05
2458384.6451	14.0	P48+ZTF	r	16.80	0.05
2458384.6525	14.01	P48+ZTF	r	16.80	0.05
2458384.6741	14.03	P48+ZTF	r	16.80	0.04
2458384.717	14.07	P48+ZTF	g	17.26	0.06
2458384.717	14.07	P48+ZTF	g	17.26	0.06
2458384.7384	14.09	P48+ZTF	g	17.24	0.05
2458385.6151	14.97	P48+ZTF	g	17.45	0.05
2458385.633	14.99	P48+ZTF	g	17.45	0.04
2458385.633	14.99	P48+ZTF	g	17.45	0.04
2458385.6622	15.01	P48+ZTF	g	17.46	0.05
2458385.6622	15.01	P48+ZTF	g	17.46	0.05
2458385.6844	15.04	P48+ZTF	r	16.92	0.04
2458385.6844	15.04	P48+ZTF	r	16.92	0.04
2458385.6919	15.04	P48+ZTF	r	16.92	0.04
2458385.6919	15.04	P48+ZTF	r	16.92	0.04
2458385.7117	15.06	P48+ZTF	r	16.93	0.04
2458385.7117	15.06	P48+ZTF	r	16.93	0.04
2458386.6167	15.97	P48+ZTF	g	17.62	0.07

2458386.6242	15.98	P48+ZTF	g	17.67	0.06
2458386.6242	15.98	P48+ZTF	g	17.67	0.06
2458386.6404	15.99	P48+ZTF	g	17.65	0.06
2458386.6546	16.01	P48+ZTF	g	17.60	0.06
2458386.6994	16.05	P48+ZTF	r	17.02	0.05
2458386.6994	16.05	P48+ZTF	r	17.02	0.04
2458386.7013	16.05	P48+ZTF	r	17.04	0.05
2458386.7158	16.07	P48+ZTF	r	17.04	0.04
2458386.7377	16.09	P48+ZTF	r	17.00	0.05
2458387.6227	16.98	P48+ZTF	r	17.14	0.04
2458387.6227	16.98	P48+ZTF	r	17.14	0.04
2458387.6399	16.99	P48+ZTF	r	17.14	0.05
2458387.6541	17.01	P48+ZTF	r	17.15	0.04
2458387.6541	17.01	P48+ZTF	r	17.15	0.04
2458387.6822	17.03	P48+ZTF	g	17.85	0.08
2458387.6822	17.03	P48+ZTF	g	17.85	0.08
2458387.7041	17.06	P48+ZTF	g	17.83	0.10
2458387.7041	17.06	P48+ZTF	g	17.83	0.10
2458387.7232	17.08	P48+ZTF	g	17.88	0.09
2458387.7232	17.08	P48+ZTF	g	17.88	0.09
2458388.6124	17.97	P60+SEDM	r	17.22	0.02
2458388.6154	17.97	P48+ZTF	g	18.04	0.06
2458388.6154	17.97	P48+ZTF	g	18.04	0.06
2458388.6396	17.99	P48+ZTF	g	17.99	0.07
2458388.6396	17.99	P48+ZTF	g	17.99	0.07
2458388.6542	18.01	P48+ZTF	g	18.04	0.06
2458388.6542	18.01	P48+ZTF	g	18.04	0.06
2458388.6834	18.04	P48+ZTF	r	17.30	0.06
2458388.6936	18.05	P48+ZTF	r	17.30	0.05
2458388.7203	18.07	P48+ZTF	r	17.25	0.06
2458389.6156	18.97	P48+ZTF	r	17.39	0.06
2458389.6227	18.98	P48+ZTF	r	17.40	0.05
2458389.6317	18.98	P48+ZTF	g	18.20	0.06
2458389.6317	18.98	P48+ZTF	g	18.20	0.06
2458389.6416	18.99	P48+ZTF	g	18.20	0.06
2458389.6416	18.99	P48+ZTF	g	18.20	0.06

2458389.6804	19.03	P48+ZTF	g	18.21	0.08
2458389.6804	19.03	P48+ZTF	g	18.21	0.08
2458389.6947	19.05	P48+ZTF	g	18.21	0.09
2458389.6947	19.05	P48+ZTF	g	18.21	0.09
2458389.7166	19.07	P48+ZTF	r	17.41	0.05
2458389.7476	19.1	P48+ZTF	r	17.43	0.04
2458390.6228	19.98	P48+ZTF	g	18.43	0.06
2458390.6228	19.98	P48+ZTF	g	18.43	0.06
2458390.6326	19.99	P48+ZTF	g	18.40	0.06
2458390.6326	19.99	P48+ZTF	g	18.40	0.06
2458390.6797	20.03	P48+ZTF	r	17.55	0.04
2458390.7209	20.07	P48+ZTF	r	17.56	0.07
2458390.7347	20.09	P48+ZTF	r	17.53	0.05
2458399.5989	28.95	P48+ZTF	g	19.40	0.19
2458399.5989	28.95	P48+ZTF	g	19.40	0.19
2458400.6307	29.98	P48+ZTF	g	19.46	0.13
2458400.6638	30.02	P48+ZTF	r	18.68	0.11
2458400.6756	30.03	P48+ZTF	r	18.72	0.10
2458400.6756	30.03	P48+ZTF	r	18.72	0.10
2458400.6987	30.05	P48+ZTF	r	18.65	0.14
2458415.6169	44.97	P60+SEDM	r	19.62	0.10
2458415.6196	44.97	P60+SEDM	g	20.24	0.20
2458415.6223	44.98	P60+SEDM	i	19.39	0.06
2458420.593	49.95	P60+SEDM	r	19.74	0.03
2458420.5958	49.95	P60+SEDM	g	20.74	0.06
2458420.5984	49.95	P60+SEDM	i	19.53	0.03
2458420.6011	49.95	P60+SEDM	r	19.76	0.04
2458420.6038	49.96	P60+SEDM	g	20.90	0.08
2458423.584	52.94	P60+SEDM	r	19.78	0.10
2458423.5894	52.94	P60+SEDM	i	19.67	0.13
2458429.5848	58.94	P60+SEDM	r	20.03	0.06
2458429.5875	58.94	P60+SEDM	g	21.32	0.11
2458429.5902	58.94	P60+SEDM	i	19.80	0.04
2458371.3802	0.73	LT	u	16.06	0.01
2458372.3561	1.71	LT	u	15.70	0.01
2458373.3944	2.75	LT	u	15.79	0.01

2458380.3607	9.71	LT	u	17.12	0.02
2458380.3612	9.71	LT	u	17.12	0.02
2458381.3403	10.69	LT	u	17.49	0.03
2458381.3409	10.69	LT	u	17.59	0.04
2458382.3451	11.7	LT	u	17.97	0.04
2458383.3399	12.69	LT	u	18.27	0.06
2458383.3404	12.69	LT	u	18.27	0.06
2458384.34	13.69	LT	u	18.71	0.08
2458384.3405	13.69	LT	u	18.86	0.10
2458385.339	14.69	LT	u	18.89	0.11
2458386.3369	15.69	LT	u	19.16	0.17
2458388.3375	17.69	LT	u	20.07	0.22
2458388.338	17.69	LT	u	19.91	0.28
2458391.3458	20.7	LT	u	20.08	0.24
2458371.3794	0.73	LT	g	16.64	0.01
2458372.3554	1.71	LT	g	16.21	0.01
2458373.3951	2.75	LT	g	16.03	0.01
2458380.3599	9.71	LT	g	16.63	0.01
2458381.3396	10.69	LT	g	16.74	0.01
2458382.3438	11.7	LT	g	16.88	0.01
2458383.3391	12.69	LT	g	17.04	0.01
2458384.3392	13.69	LT	g	17.27	0.01
2458385.3377	14.69	LT	g	17.49	0.01
2458386.3362	15.69	LT	g	17.62	0.05
2458388.3367	17.69	LT	g	18.08	0.01
2458389.3394	18.69	LT	g	18.20	0.01
2458390.367	19.72	LT	g	18.34	0.06
2458391.3445	20.7	LT	g	18.55	0.01
2458393.3452	22.7	LT	g	18.88	0.02
2458394.3463	23.7	LT	g	18.96	0.01
2458395.3462	24.7	LT	g	19.20	0.03
2458396.3496	25.7	LT	g	19.31	0.03
2458397.3884	26.74	LT	g	19.53	0.04
2458407.3531	36.71	LT	g	20.08	0.06
2458407.3537	36.71	LT	g	20.24	0.07
2458408.3179	37.67	LT	g	20.26	0.10

2458408.3186	37.67	LT	g	20.14	0.07
2458409.3255	38.68	LT	g	20.15	0.09
2458409.3262	38.68	LT	g	20.34	0.12
2458371.3787	0.73	LT	r	16.89	0.01
2458372.3546	1.71	LT	r	16.43	0.01
2458373.3958	2.75	LT	r	16.28	0.01
2458380.3592	9.71	LT	r	16.51	0.01
2458381.3389	10.69	LT	r	16.54	0.01
2458382.3431	11.7	LT	r	16.60	0.01
2458383.3384	12.69	LT	r	16.68	0.01
2458384.3385	13.69	LT	r	16.78	0.01
2458385.337	14.69	LT	r	16.91	0.01
2458386.3354	15.69	LT	r	17.07	0.01
2458388.336	17.69	LT	r	17.31	0.01
2458389.3387	18.69	LT	r	17.40	0.01
2458390.3663	19.72	LT	r	17.59	0.04
2458391.3438	20.7	LT	r	17.70	0.01
2458393.3444	22.7	LT	r	17.93	0.01
2458394.3456	23.7	LT	r	18.07	0.01
2458395.3455	24.7	LT	r	18.14	0.02
2458396.3489	25.7	LT	r	18.31	0.02
2458397.3877	26.74	LT	r	18.41	0.02
2458407.3524	36.71	LT	r	19.20	0.03
2458408.317	37.67	LT	r	19.29	0.04
2458409.3246	38.68	LT	r	19.41	0.16
2458371.378	0.73	LT	i	17.30	0.01
2458372.3539	1.71	LT	i	16.90	0.01
2458373.3965	2.75	LT	i	16.62	0.01
2458380.3585	9.71	LT	i	16.81	0.01
2458381.3381	10.69	LT	i	16.82	0.01
2458382.3424	11.7	LT	i	16.88	0.01
2458383.3377	12.69	LT	i	16.92	0.01
2458384.3378	13.69	LT	i	16.99	0.17
2458385.3363	14.69	LT	i	17.04	0.01
2458386.3347	15.69	LT	i	17.10	0.01
2458388.3353	17.69	LT	i	17.28	0.01

2458389.338	18.69	LT	i	17.39	0.01
2458390.3656	19.72	LT	i	17.56	0.04
2458391.3431	20.7	LT	i	17.63	0.01
2458393.3437	22.7	LT	i	17.84	0.01
2458394.3449	23.7	LT	i	17.98	0.01
2458395.3448	24.7	LT	i	18.10	0.04
2458396.3481	25.7	LT	i	18.18	0.01
2458397.3869	26.74	LT	i	18.30	0.02
2458407.3517	36.7	LT	i	19.04	0.03
2458408.3162	37.67	LT	i	19.03	0.07
2458409.3238	38.68	LT	i	19.14	0.07
2458373.3972	2.75	LT	z	16.82	0.01
2458380.3577	9.71	LT	z	16.77	0.01
2458381.3374	10.69	LT	z	16.79	0.01
2458382.3416	11.69	LT	z	16.80	0.01
2458383.3369	12.69	LT	z	16.82	0.01
2458384.337	13.69	LT	z	16.83	0.01
2458385.3355	14.69	LT	z	16.89	0.01
2458386.334	15.69	LT	z	16.94	0.01
2458388.3345	17.69	LT	z	17.04	0.01
2458389.3372	18.69	LT	z	17.11	0.02
2458390.3648	19.72	LT	z	17.23	0.12
2458391.3423	20.7	LT	z	17.26	0.01
2458393.343	22.7	LT	z	17.44	0.01
2458394.3441	23.7	LT	z	17.55	0.02
2458395.344	24.7	LT	z	17.65	0.05
2458396.3474	25.7	LT	z	17.69	0.02
2458397.3862	26.74	LT	z	17.77	0.03
2458407.3509	36.7	LT	z	18.19	0.03
2458408.3155	37.67	LT	z	18.33	0.06
2458409.3231	38.68	LT	z	18.26	0.07
2458374.9769	4.33	LOT	g	16.14	0.01
2458375.9702	5.32	LOT	g	16.17	0.01
2458379.9736	9.33	LOT	g	16.62	0.01
2458381.0023	10.36	LOT	g	16.77	0.01
2458381.9909	11.34	LOT	g	16.89	0.01

2458386.0102	15.36	LOT	g	17.60	0.01
2458391.0243	20.38	LOT	g	18.59	0.01
2458391.9648	21.32	LOT	g	18.72	0.01
2458392.9823	22.34	LOT	g	18.83	0.01
2458393.9679	23.32	LOT	g	18.98	0.01
2458394.9508	24.3	LOT	g	19.16	0.02
2458395.9525	25.31	LOT	g	19.26	0.01
2458396.9584	26.31	LOT	g	19.43	0.02
2458406.9893	36.34	LOT	g	20.32	0.07
2458411.95	41.3	LOT	g	20.53	0.10
2458374.9847	4.34	LOT	i	16.53	0.01
2458379.9812	9.33	LOT	i	16.75	0.01
2458381.01	10.36	LOT	i	16.78	0.01
2458381.9986	11.35	LOT	i	16.80	0.01
2458386.018	15.37	LOT	i	17.05	0.01
2458391.0321	20.38	LOT	i	17.57	0.01
2458391.9726	21.33	LOT	i	17.71	0.01
2458392.9901	22.34	LOT	i	17.80	0.01
2458393.9756	23.33	LOT	i	17.97	0.01
2458394.9692	24.32	LOT	i	18.07	0.01
2458395.9603	25.31	LOT	i	18.16	0.01
2458396.978	26.33	LOT	i	18.25	0.01
2458406.9971	36.35	LOT	i	18.90	0.03
2458411.9578	41.31	LOT	i	19.09	0.04
2458374.9807	4.33	LOT	r	16.30	0.01
2458375.974	5.33	LOT	r	16.33	0.01
2458379.9774	9.33	LOT	r	16.54	0.01
2458381.0061	10.36	LOT	r	16.61	0.01
2458381.9947	11.35	LOT	r	16.62	0.01
2458386.014	15.37	LOT	r	16.97	0.01
2458391.0282	20.38	LOT	r	17.71	0.01
2458391.9686	21.32	LOT	r	17.77	0.01
2458392.9862	22.34	LOT	r	17.93	0.01
2458393.9717	23.32	LOT	r	18.06	0.01
2458394.9653	24.32	LOT	r	18.19	0.01
2458395.9564	25.31	LOT	r	18.30	0.01

2458396.9623	26.31	LOT	r	18.42	0.01
2458406.9932	36.35	LOT	r	19.07	0.02
2458411.9538	41.31	LOT	r	19.42	0.03
2458371.0917	0.44	UVOT	B	16.77	0.06
2458371.1601	0.51	UVOT	B	16.67	0.06
2458373.8837	3.24	UVOT	B	15.88	0.07
2458374.0828	3.44	UVOT	B	15.87	0.08
2458374.481	3.83	UVOT	B	15.90	0.07
2458375.3416	4.69	UVOT	B	16.06	0.06
2458376.48	5.83	UVOT	B	16.00	0.06
2458376.599	5.95	UVOT	B	16.23	0.07
2458379.2575	8.61	UVOT	B	16.46	0.07
2458380.184	9.54	UVOT	B	16.50	0.08
2458380.3172	9.67	UVOT	B	16.68	0.09
2458380.7873	10.14	UVOT	B	16.80	0.07
2458381.6447	11.0	UVOT	B	17.29	0.14
2458381.7774	11.13	UVOT	B	16.80	0.11
2458381.8438	11.2	UVOT	B	16.95	0.12
2458383.3045	12.66	UVOT	B	17.68	0.15
2458383.3705	12.72	UVOT	B	17.35	0.13
2458384.3114	13.66	UVOT	B	17.44	0.08
2458371.0908	0.44	UVOT	U	16.41	0.06
2458371.1591	0.51	UVOT	U	16.24	0.05
2458373.8834	3.24	UVOT	U	15.75	0.07
2458374.0825	3.44	UVOT	U	15.68	0.07
2458374.4806	3.83	UVOT	U	15.76	0.07
2458375.3411	4.69	UVOT	U	15.72	0.06
2458376.4794	5.83	UVOT	U	15.95	0.06
2458376.5986	5.95	UVOT	U	15.83	0.06
2458379.2569	8.61	UVOT	U	16.65	0.07
2458380.1836	9.54	UVOT	U	17.21	0.10
2458380.3168	9.67	UVOT	U	17.28	0.10
2458380.7866	10.14	UVOT	U	17.34	0.08
2458381.6444	11.0	UVOT	U	17.73	0.14
2458381.7771	11.13	UVOT	U	17.94	0.15
2458381.8435	11.2	UVOT	U	18.06	0.17

2458383.3041	12.66	UVOT	U	18.82	0.24
2458383.37	12.72	UVOT	U	18.36	0.17
2458384.3105	13.66	UVOT	U	19.01	0.16
2458371.1013	0.45	UVOT	UVM2	15.74	0.05
2458371.1669	0.52	UVOT	UVM2	15.61	0.05
2458373.8864	3.24	UVOT	UVM2	15.19	0.05
2458374.0856	3.44	UVOT	UVM2	15.19	0.05
2458374.4841	3.84	UVOT	UVM2	15.40	0.05
2458375.3466	4.7	UVOT	UVM2	15.88	0.05
2458376.4854	5.84	UVOT	UVM2	16.66	0.06
2458376.6032	5.96	UVOT	UVM2	16.81	0.06
2458379.2631	8.62	UVOT	UVM2	19.83	0.21
2458380.1881	9.54	UVOT	UVM2	20.14	0.29
2458380.3209	9.67	UVOT	UVM2	20.31	0.35
2458380.7945	10.15	UVOT	UVM2	21.34	0.64
2458381.648	11.0	UVOT	UVM2	21.12	0.67
2458381.7807	11.13	UVOT	UVM2	20.60	0.44
2458381.8472	11.2	UVOT	UVM2	21.87	1.23
2458383.3088	12.66	UVOT	UVM2	21.45	0.81
2458383.3752	12.73	UVOT	UVM2	22.09	1.38
2458384.3213	13.67	UVOT	UVM2	26.70	76.24
2458371.0893	0.44	UVOT	UVW1	15.86	0.05
2458371.1577	0.51	UVOT	UVW1	15.75	0.05
2458373.8829	3.24	UVOT	UVW1	15.32	0.06
2458374.082	3.43	UVOT	UVW1	15.24	0.05
2458374.4801	3.83	UVOT	UVW1	15.42	0.05
2458375.3402	4.69	UVOT	UVW1	15.73	0.05
2458376.4784	5.83	UVOT	UVW1	16.45	0.06
2458376.5979	5.95	UVOT	UVW1	16.50	0.06
2458379.2558	8.61	UVOT	UVW1	17.94	0.09
2458380.1828	9.54	UVOT	UVW1	18.69	0.15
2458380.3161	9.67	UVOT	UVW1	19.08	0.19
2458380.7853	10.14	UVOT	UVW1	18.84	0.13
2458381.6437	11.0	UVOT	UVW1	19.08	0.20
2458381.7765	11.13	UVOT	UVW1	19.41	0.26
2458381.8429	11.2	UVOT	UVW1	20.01	0.39

2458383.3033	12.66	UVOT	UVW1	20.19	0.38
2458383.3692	12.72	UVOT	UVW1	20.72	0.57
2458384.3086	13.66	UVOT	UVW1	20.57	0.35
2458371.0941	0.45	UVOT	UVW2	15.51	0.06
2458371.1625	0.52	UVOT	UVW2	15.38	0.06
2458373.8845	3.24	UVOT	UVW2	15.62	0.06
2458374.0835	3.44	UVOT	UVW2	15.68	0.06
2458374.4818	3.83	UVOT	UVW2	15.88	0.06
2458375.343	4.7	UVOT	UVW2	16.37	0.06
2458376.4815	5.83	UVOT	UVW2	17.09	0.07
2458376.6002	5.95	UVOT	UVW2	17.29	0.08
2458379.2591	8.61	UVOT	UVW2	19.61	0.18
2458380.1852	9.54	UVOT	UVW2	20.11	0.28
2458380.3183	9.67	UVOT	UVW2	20.33	0.34
2458380.7894	10.14	UVOT	UVW2	20.37	0.28
2458381.6457	11.0	UVOT	UVW2	20.23	0.34
2458381.7783	11.13	UVOT	UVW2	20.86	0.56
2458381.8447	11.2	UVOT	UVW2	21.58	1.00
2458383.3057	12.66	UVOT	UVW2	21.53	0.85
2458383.3718	12.72	UVOT	UVW2	21.77	1.00
2458384.3142	13.67	UVOT	UVW2	21.17	0.48
2458371.0965	0.45	UVOT	V	17.25	0.13
2458371.1649	0.52	UVOT	V	16.79	0.10
2458373.8852	3.24	UVOT	V	16.24	0.14
2458374.0843	3.44	UVOT	V	16.13	0.13
2458374.4827	3.84	UVOT	V	16.08	0.12
2458375.3444	4.7	UVOT	V	16.22	0.10
2458376.483	5.84	UVOT	V	16.07	0.09
2458376.6013	5.95	UVOT	V	16.03	0.11
2458379.2607	8.61	UVOT	V	16.41	0.11
2458380.1863	9.54	UVOT	V	16.41	0.13
2458380.3193	9.67	UVOT	V	16.62	0.15
2458380.7914	10.14	UVOT	V	16.62	0.11
2458381.6466	11.0	UVOT	V	16.61	0.16
2458381.7793	11.13	UVOT	V	16.70	0.17
2458381.8456	11.2	UVOT	V	16.51	0.16

2458383.3069	12.66	UVOT	V	16.58	0.14
2458383.3731	12.73	UVOT	V	16.74	0.15
2458384.317	13.67	UVOT	V	16.86	0.11

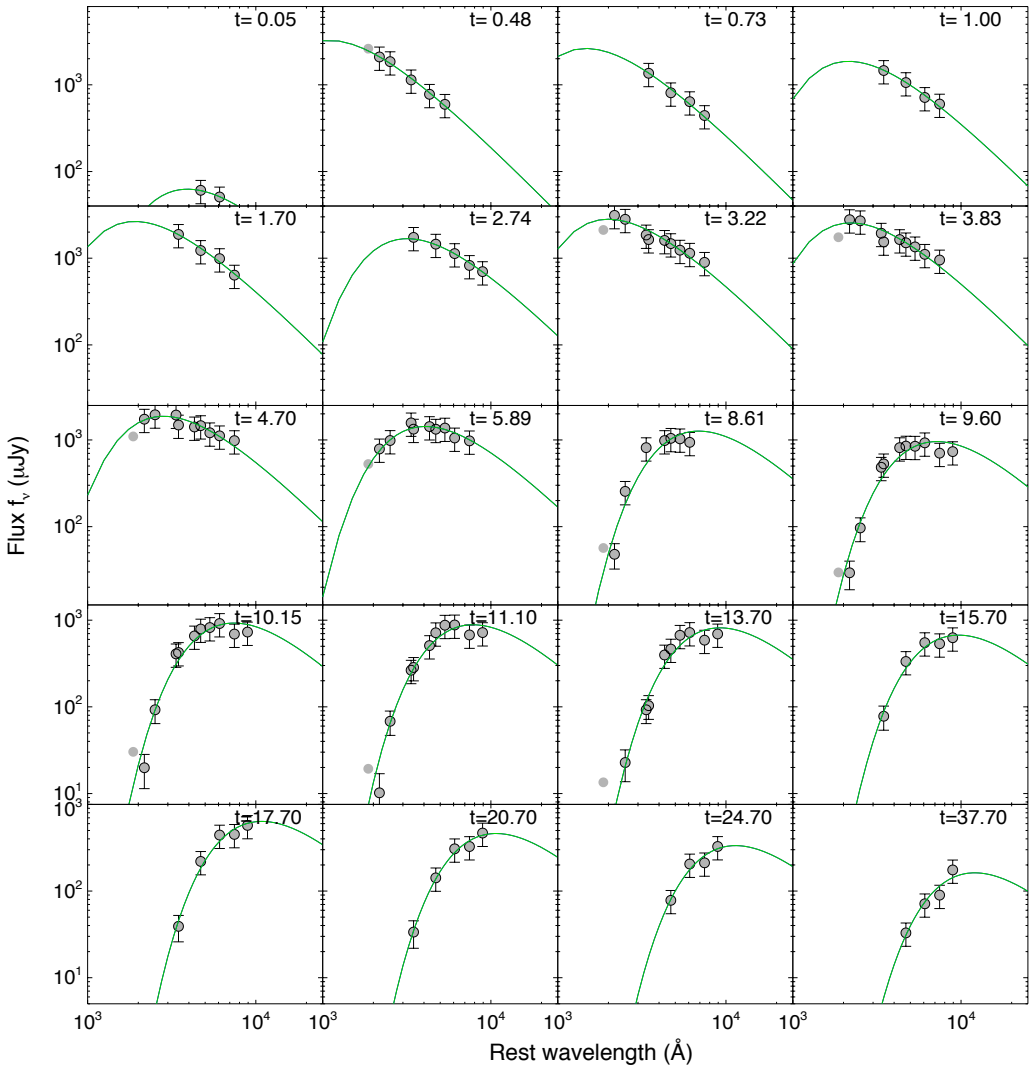

Figure 6.24: Blackbody fits to *Swift*/UVOT and optical photometry for SN 2018gep. Since the UVOT and ground-based observations were taken at slightly different epochs, we interpolated the data in time using UVOT epochs at early times and LT epochs at later times.

UV and Optical Spectroscopy

The observation log of our UV and optical spectra is provided in Table 6.6. A plot showing the full sequence of optical spectra is shown in Figure 6.25.

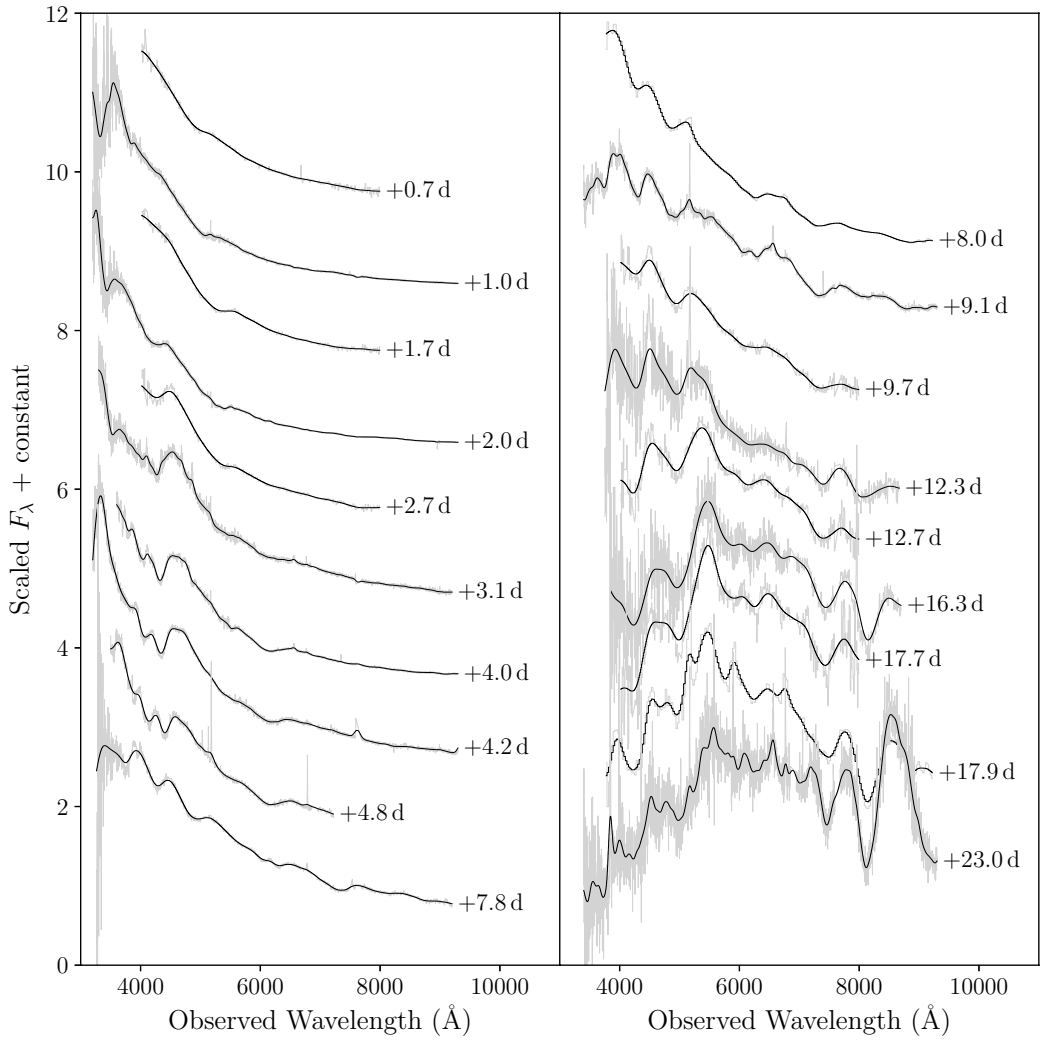

Figure 6.25: Ground-based optical spectra of SN 2018gep. The light grey represents the observed spectrum, interpolating over host emission lines and telluric features. The black line is a Gaussian-smoothed version of the spectrum, using a Gaussian width that is several times the width of a galaxy emission line at that resolution. For more details on the smoothing procedure, see Section 2.1 of Ho et al. (2017).

Atomic Data for Spectral Modeling

The atomic data used for the spectral modelling in Section 6.3 is the same as described in Appendix A.4 of Ergon et al. (2018), but with the following modifications. The stage II-IV ions where (whenever possible) updated to include at least 50 levels

Table 6.6: Log of SN 2018gep optical spectra

Start Time (UTC)	Δt	Instrument	Exp. Time (s)	Airmass
2018 Sep 09 20:30:01	0.7	LT+SPRAT	1200	1.107
2018 Sep 10 04:28:51	1.0	P200+DBSP	600	1.283
2018 Sep 10 21:03:42	1.7	LT+SPRAT	900	1.182
2018 Sep 11 04:59:19	2.0	P200+DBSP	600	1.419
2018 Sep 11 20:22:35	2.7	LT+SPRAT	900	1.107
2018 Sep 12 06:09:59	3.1	P200+DBSP		
2018 Sep 13 03:52:58	4.0	P200+DBSP	300	1.209
2018 Sep 13 09:17:25	4.2	Keck1+LRIS	300	3.483
2018 Sep 14 02:44:24.24	4.8	DCT+Deveny+LMI	300	1.11
2018 Sep 17 04:38:40	8.0	P60+SEDM	1440	1.435
2018 Sep 17 20:40:25.750	8.7	NOT+ALFOSC	1800	1.19
2018 Sep 18 05:21:58	9.1	P200+DBSP	600	1.720
2018 Sep 18 20:14:35	9.7	LT+SPRAT	1000	1.143
2018 Sep 21 11:15:10	12.3	XLT+BFOSC	3000	1.181
2018 Sep 21 20:58:21	12.7	LT+SPRAT	1000	1.293
2018 Sep 25 11:16:43	16.3	XLT+BFOSC	3000	1.225
2018 Sep 26 20:22:54	17.7	LT+SPRAT	1000	1.242
2018 Sep 27 02:42:29	17.9	P60+SEDM	1440	1.172
2018 Oct 02 04:34:35	23.0	P200+DBSP	600	1.780
2018 Nov 09 05:26:17	61.1	Keck1+LRIS	900	3.242

Gratings used: Wasatch600 (LT+SPRAT), Gr4 (NOT+ALFOSC), 600/4000 (P200+DBSP; blue side), 316/7500 (P200+DBSP; red side), 400/8500 (Keck1+LRIS; red side).
Filters used: 400nm (LT+SPRAT), open (NOT+ALFOSC), clear (Keck1+LRIS)
Wavelength range: 4020–7995 Å (LT+SPRAT), 3200–9600 Å (NOT+ALFOSC), 1759–10311 Å (Keck1+LRIS), 3777–9223 Å (P60+SEDM)
Resolution: 20 (LT+SPRAT), 710 (NOT+ALFOSC)

for N, Na, Al, Ar and Ca, at least 100 levels for C, O, Ne, Mg, Si, and S, and at least 300 levels for Sc, Ti, V, Cr, Mn, Fe, Co, and Ni. In addition we updated the C II - C IV and O II - O III ions with specific recombination rates from the online table by S. Nahar[15].

Data for Measuring Host Properties

In this section we provide the data that we used to derive properties of the host galaxy of SN 2018gep: the host-galaxy spectrum (Figure 6.26), line fluxes extracted from this spectrum (Table 6.7), and host-galaxy photometry (Table 6.8).

[15] `http://www.astronomy.ohio-state.edu/~nahar/_naharradiativeatomicdata/`

Table 6.7: Line fluxes from the host galaxy of SN 2018gep extracted from the Keck/LRIS spectrum obtained on 9 November 2018. All measurements are corrected for Galactic reddening.

Transition	$\lambda_{\rm obs}$ (Å)	F $\left(10^{-17}\ {\rm erg\,cm^{-2}\,s^{-1}}\right)$
[O II]$\lambda\lambda$3726,3729	3848.17 ± 0.05	334.5 ± 6.23
[Ne III]λ3869	3993.50 ± 0.16	82.34 ± 6.18
He Iλ3889,H-8	4014.49 ± 0.16	29.01 ± 4.73
[Ne III]λ3968,Hϵ	4096.66 ± 0.26	36.61 ± 3.98
Hδ	4233.87 ± 0.13	44.88 ± 2.59
Hγ	4480.20 ± 0.10	81.95 ± 3.74
[O III]λ4364	4503.68 ± 0.10	15.01 ± 2.69
Hβ	5017.87 ± 0.08	213.41 ± 10.53
[O III]λ4960	5118.61 ± 0.04	352.42 ± 6.50
[O III]λ5008	5168.04 ± 0.04	1066.70 ± 19.50
He Iλ5877	6064.21 ± 0.20	27.04 ± 2.30
O Iλ6302	6502.18 ± 1.08	6.72 ± 2.94
[N II]λ6549	6758.16 ± 0.02	11.15 ± 6.73
Hα	6773.40 ± 0.02	723.85 ± 7.65
[N II]λ6585	6794.67 ± 0.02	19.01 ± 5.76
[He I]λ6678	6890.29 ± 0.14	7.88 ± 2.19
[S II]λ6718	6931.83 ± 0.10	41.76 ± 2.38
[S II]λ6732	6946.68 ± 0.10	28.15 ± 2.19

Table 6.8: Brightness of the host galaxy from UV ot IR wavelenghts. All measurements are reported in the AB system and are not corrected for reddening. For guidance, we report the effective wavelengths of each filter.

Instrument/ Filter	$\lambda_{\rm eff}$ (Å)	Brightness (mag)	Instrument/ Filter	$\lambda_{\rm eff}$ (Å)	Brightness (mag)
GALEX/FUV	1542.3	20.20 ± 0.03	SDSS/i'	7439.5	18.62 ± 0.04
GALEX/NUV	2274.4	20.09 ± 0.03	SDSS/z'	8897.1	18.59 ± 0.12
UVOT/$w2$	2030.5	19.91 ± 0.12	PS1/$g_{\rm PS1}$	4775.6	18.96 ± 0.04
UVOT/$m2$	2228.1	20.00 ± 0.14	PS1/$r_{\rm PS1}$	6129.5	18.82 ± 0.04
UVOT/$w1$	2589.1	20.11 ± 0.16	PS1/$i_{\rm PS1}$	7484.6	18.88 ± 0.04
UVOT/u	3501.2	19.74 ± 0.16	PS1/$z_{\rm PS1}$	8657.8	18.71 ± 0.05
UVOT/b	4328.6	19.45 ± 0.20	WIRCam/J	12481.5	18.99 ± 0.09
UVOT/v	5402.1	18.45 ± 0.21	2MASS/H	16620.0	18.33 ± 0.36
SDSS/u'	3594.9	19.97 ± 0.12	WISE/$W1$	33526.0	19.39 ± 0.08
SDSS/g'	4640.4	18.88 ± 0.02	WISE/$W2$	46028.0	19.85 ± 0.19
SDSS/r'	6122.3	18.76 ± 0.05			

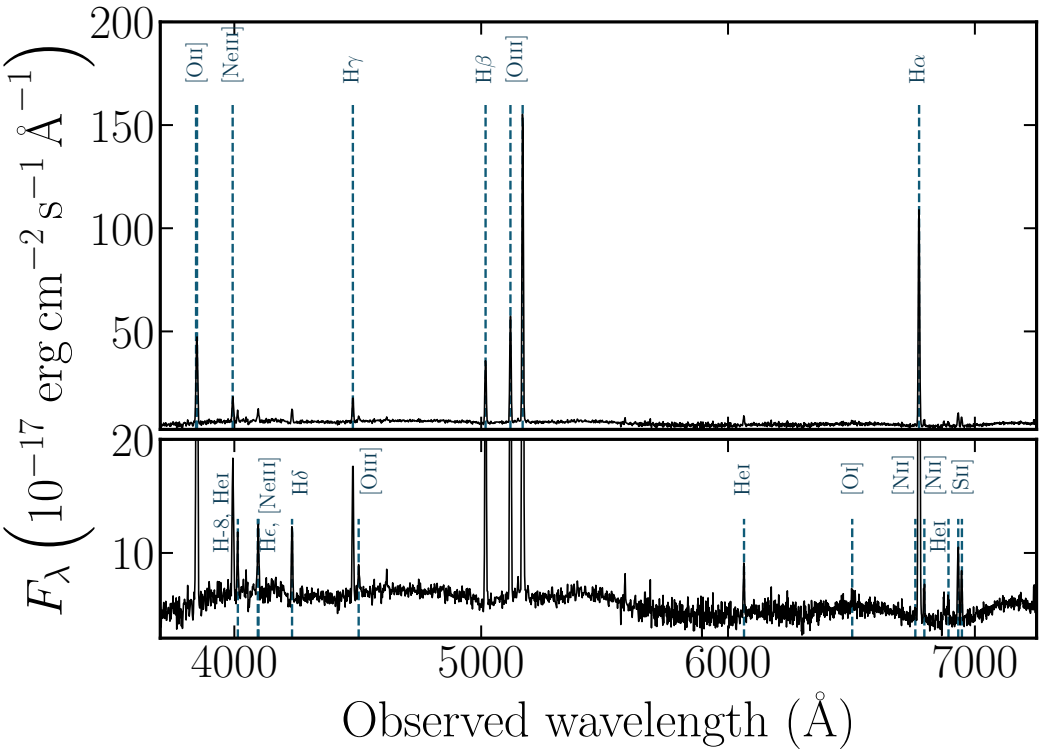

Figure 6.26: Host spectrum of SN 2018gep obtained with Keck/LRIS on 9 November 2018, about two months after explosion. Strong emission lines from the host galaxy are labeled. The low host metallicity of 0.1 solar is reflected by very small N II/Hα flux ratio. The large rest-frame [O III]λ5007 equivalent width of $>$ 160 Å puts the host also in regime of extreme emission-line galaxies. These galaxy class constitute $<$ 2% of all star-forming galaxies at $z < 0.3$ in the SDSS DR15 catalogue. The undulations are due to the supernova. The spectrum is truncated at 7250 Å for presentation purposes, and it is corrected for Galactic reddening.

Part IV. A New Class of Energetic Stellar Explosions in a Dense Medium

...Was wir brauchen, ist ein Schwein,
Das Merinowolle trägt
Und dazu noch Eier legt...

—"DER KAMPF UM DAS EIERLEGENDE WOLLSCHWEIN"
LUDWIG RENN ZUM 70. GEBURTSTAG (1959)

Chapter 7

AT2018COW: A LUMINOUS MILLIMETER TRANSIENT

Ho, A. Y. Q. et al. (2019). "AT2018cow: A Luminous Millimeter Transient". In: *The Astrophysical Journal* 871.1, p. 73. DOI: 10.3847/1538-4357/aaf473. arXiv: 1810.10880 [astro-ph.HE].

Anna Y. Q. Ho[1], E. Sterl Phinney[2], Vikram Ravi[1,3], S. R. Kulkarni[1], Glen Petitpas[3], Bjorn Emonts[4], V. Bhalerao[5], Ray Blundell[3], S. Bradley Cenko[6,7], Dougal Dobie[8,9], Ryan Howie[3], Nikita Kamraj[1], Mansi M. Kasliwal[1], Tara Murphy[8], Daniel A. Perley[10], T. K. Sridharan[3], Ilsang Yoon[4]

[1]Cahill Center for Astronomy and Astrophysics, California Institute of Technology, Pasadena, CA 91125, USA
[2]Theoretical Astrophysics, MC 350-17, California Institute of Technology, Pasadena, CA 91125, USA
[3]Harvard-Smithsonian Center for Astrophysics, 60 Garden Street, Cambridge, MA 02138, USA
[4]National Radio Astronomy Observatory, 520 Edgemont Road, Charlottesville, VA 22903, USA
[5]Department of Physics, Indian Institute of Technology Bombay, Mumbai 400076, India
[6]Astrophysics Science Division, NASA Goddard Space Flight Center, Mail Code 661, Greenbelt, MD 20771, USA
[7]Joint Space-Science Institute, University of Maryland, College Park, MD 20742, USA
[8]Sydney Institute for Astronomy, School of Physics, University of Sydney, Sydney, New South Wales 2006, Australia
[9]ATNF, CSIRO Astronomy and Space Science, PO Box 76, Epping, New South Wales 1710, Australia

Abstract

We present detailed submillimeter- through centimeter-wave observations of the extraordinary extragalactic transient AT2018cow. The apparent characteristics—the high radio luminosity, the rise and long-lived emission plateau at millimeter bands, and the sub-relativistic velocity—have no precedent. A basic interpretation of the data suggests $E_k \gtrsim 4 \times 10^{48}$ erg coupled to a fast but sub-relativistic ($v \approx 0.13$c) shock in a dense ($n_e \approx 3 \times 10^5\,\mathrm{cm}^{-3}$) medium. We find that the X-ray emission is not naturally explained by an extension of the radio–submm synchrotron spectrum, nor by inverse Compton scattering of the dominant blackbody UVOIR photons by energetic electrons within the forward shock. By $\Delta t \approx 20$ d, the X-ray emission shows spectral softening and erratic inter-day variability. Taken together, we are led to invoke an additional source of X-ray emission: the central engine of the event. Regardless of the nature of this central engine, this source heralds a new class of energetic transients shocking a dense medium, which at early times are most readily

observed at millimeter wavelengths.

7.1 Introduction

The Transient Millimeter Sky

Although the sky is regularly monitored across many bands of the electromagnetic spectrum (as well as in gravitational waves and energetic particles) the dynamic sky at millimeter to sub-millimeter wavelengths (0.1–10 mm) remains poorly explored. There has only been one blind transient survey specific to the millimeter band[1] (Whitehorn et al., 2016); millimeter facilities are usually only triggered after an initial discovery at another wavelength. Even when targeting known transients, the success rate for detection is low, and to date only a few extragalactic transients[2] have well-sampled, multifrequency light curves. This sample includes supernovae (SNe; Horesh et al., 2013; Weiler et al., 2007), tidal-disruption events (TDEs; Yuan et al., 2016; Zauderer et al., 2011) and gamma-ray bursts (GRBs; de Ugarte Postigo et al., 2012; Laskar et al., 2013; Perley et al., 2014; Urata et al., 2014). There have also been millimeter detections of galactic transient sources, primarily stellar flares (e.g. Bower et al., 2003, Fender et al., 2015).

The paucity of millimeter transient studies can be attributed in part to costly receiver and electronics systems and the need for excellent weather conditions, but it also reflects challenges intrinsic to millimeter-wave transients themselves: most known classes are either too dim (SNe, most TDEs) to detect unless they are very nearby, or too short-lived (GRBs) to detect without very rapid reaction times (<1 day, and even in these circumstances the emission may only be apparent from low-density environments; Laskar et al., 2013).

An evolving technical landscape, together with rapid follow-up enabled by high-cadence optical surveys, present new opportunities for millimeter transient astronomy. Lower-noise receivers and ultra-wide bandwidth capability have greatly increased the sensitivity of sub-mm facilities (e.g. the Submillimeter Array or SMA; Ho et al., 2004), and the Atacama Large Millimeter Array (ALMA), a flagship facility, recently began operations. Optical surveys are discovering new and unexpected classes of transient events whose millimeter properties are unknown—and possibly different from previously-known types—motivating renewed follow-up efforts.

[1] The authors searched for transient sources at 90 GHz and 150 GHz. They found a single candidate event, which intriguingly showed linear polarization.

[2] Here we use "transient" as distinct from "variable": millimeter observations are used to study variability in protostars (e.g. Herczeg et al., 2017) and more commonly for active galactic nuclei (e.g. Dent et al., 1983)

AT2018cow

AT2018cow was discovered on 2018 June 16 UT as an optical transient (Prentice et al., 2018; Smartt et al., 2018) by the Asteroid Terrestrial-impact Last Alert System (ATLAS; Tonry et al., 2018). It attracted immediate attention because of its fast rise time ($t_{\rm peak} \lesssim 3$ days), which was established by earlier non-detections (Fremling, 2018; Prentice et al., 2018), together with its high optical luminosity ($M_{\rm peak} \sim -20$) and its close proximity ($d = 60\,$Mpc).

UVOIR observations (Perley et al., 2019; Prentice et al., 2018) revealed unprecedented photometric and spectroscopic properties. Long-lived luminous X-ray emission was detected with *Swift*/XRT (Rivera Sandoval and Maccarone, 2018), INTEGRAL (Ferrigno et al., 2018; Savchenko et al., 2018) and NuSTAR (Grefenstette et al., 2018; Margutti et al., 2018). Early radio and sub-millimeter detections were reported by NOEMA (de Ugarte Postigo et al., 2018), JCMT (Smith et al., 2018), AMI (Bright et al., 2018), and by us using the ATCA (Dobie et al., 2018a,b). The source does not appear to be a GRB, as no prompt high-energy emission was detected in searches of *Swift*/BAT (Lien et al., 2018), Fermi/GBM (Dal Canton et al., 2018), Fermi/LAT (Kocevski and Cheung, 2018), and AstroSat CZTI (Sharma et al., 2018).

Perley et al. (2019) suggested that AT2018cow is a new member of the class of rapidly rising ($t_{\rm rise} \lesssim 5$d) and luminous ($M_{\rm peak} < -18$) blue transients, which have typically been found in archival searches of optical surveys (Drout et al., 2014; Pursiainen et al., 2018; Rest et al., 2018). The leading hypothesis for this class was circumstellar interaction of a supernova (Ofek et al., 2010), but this was difficult to test because most of the events were located at cosmological distances, and not discovered in real-time. AT2018cow presented the first opportunity to study a member of this class up close and in real time, but its origin remains mysterious despite the intense ensuing observational campaign. Possibilities include failed supernovae and tidal disruption events, but although AT2018cow shares properties with both of these classes, it is clearly not a typical member of either (Kuin et al., 2019; Perley et al., 2019; Prentice et al., 2018).

Given the unusual nature of the source, we were motivated to undertake high-frequency observations. We began monitoring AT2018cow with the SMA at 230 GHz and 340 GHz and carried out supporting observations with the ATCA from 5 GHz to 34 GHz. To our surprise the source was very bright and still rising at sub-millimeter wavelengths (and optically thick in the centimeter band) days

after the discovery. Our extensive SMA observations represent the first millimeter observation of a transient in its rise phase.

This finding led us to seek Director's discretionary (DD) time with ALMA at even higher frequencies, which enabled us to resolve the peak of the SED. A technical highlight of the ALMA observations was the detection of the source at nearly a terahertz frequency (Band 9). We present the sub-millimeter, radio, and X-ray observations in Section 7.2, and our modeling of the radio-emitting ejecta in Section 7.3. In Section 7.4 we put our velocity and energy measurements in the context of other transients (7.4), attribute the high sub-mm luminosity of AT2018cow to the large density of the surrounding medium (7.4), and discuss some problems with the synchrotron model parameters (7.4). In Section 7.5 we attribute the late-time X-ray emission to a powerful central engine. We look ahead to the future in Section 7.6.

7.2 Observations

All observations are measured Δt (observer-frame) from the zero-point MJD 58285 (following Perley et al., 2019), which lies between the date of discovery (MJD 58285.441) and the last non-detection (58284.13; Prentice et al., 2018). At $\Delta t = 14$ d we find excellent agreement between the SMA and the ALMA data, showing that the flux scales are consistent.

Radio and Submillimeter Observations

The Submillimeter Array (SMA)

AT2018cow was regularly observed with the SMA under its Director Discretionary Time/Target of opportunity program. Observations took place over the period of UT 2018 Jun 21–UT 2018 August 3 ($\Delta t \approx 5$–49 d) in the Compact configuration, with an additional epoch on UT 2018 August 31 ($\Delta t \approx 76$ d). All observations contained 6 to 8 antennas and cover a range of baseline lengths from 16.4 m to 77 m. A majority of these observations were short and were repeated almost nightly by sharing tuning and calibration data with other science tracks. The SMA has two receiver sets each with 8 GHz of bandwidth in each of two sidebands (32 GHz total) covering a range of frequencies from 188–416 GHz. Each receiver can be tuned independently to provide dual-band observations. Additionally, the upper and lower sidebands are separated (center to center) by 16 GHz allowing up to four simultaneous frequency measurements. During some observations, the receivers were tuned to the same local oscillator frequency, allowing the lower and upper

sidebands to be averaged together, thereby improving the signal-to-noise ratio. For all observations, the quasars 1635+381 and 3C 345 were used as primary phase and amplitude gain calibrators, respectively, with absolute flux calibration performed by nightly comparison to Titan, Neptune, or (maser-free) continuum observations of the emission-line star MWC349a. The quasar 3C 279 and/or the blazar 3C 454.3 was used for bandpass calibration. Data were calibrated in IDL using the MIR package. Additional analysis and imaging were performed using the MIRIAD package. Given that the target was a point source, fluxes were derived directly from the calibrated visibilities, but the results agree well with flux estimates derived from the CLEANed images when the data quality and uv-coverage was adequate.

The Australia Telescope Compact Array (ATCA)

We obtained six epochs of centimeter-wavelength observations with the Australia Telescope Compact Array (ATCA; Frater et al., 1992). During the first three epochs, the six 22-m dishes were arranged in an east-west 1.5A configuration, with baselines ranging from 153 m to 4469 m. During the latter three epochs, five of the six dishes were moved to a compact H75[3] configuration, occupying a cardinally oriented 'T' with baselines ranging from 31 m to 89 m. Full-Stokes data were recorded with the Compact Array Broadband Backend (Wilson et al., 2011) in a standard continuum *CFB 1M* setup, simultaneously providing two 2.048 GHz bands each with 2048 channels. Observations were obtained with center frequencies of 5.5 GHz & 9 GHz, 16.7 GHz & 21.2 GHz, and 33 GHz & 35 GHz, with data in the latter two bands typically being averaged to form a band centered at 34 GHz. The flux density scale was set using observations of the ATCA flux standard PKS 1934−638. For observations below 33 GHz, PKS 1934−638 was also used to calibrate the complex time-independent bandpasses, and regular observations of the compact quasar PKS 1607+268 were used to calibrate the time-variable complex gains. For the higher-frequency observations, a brighter source (3C 279) was used for bandpass calibration (except for epochs 1 and 4), and the compact quasar 4C 10.45 was used for gain calibration. In the H75 configuration, we only report results from observations at 34 GHz, from baselines not subject to antenna shadowing. For all 34 GHz observations, data obtained with the sixth antenna located 4500 m from the center of the array were discarded because of the difficulty of tracking the differential atmospheric phase over the long baselines to this antenna. The weather was good for

[3]https://www.narrabri.atnf.csiro.au/operations/array_configurations/configurations.html

all observations, with negligible wind and $< 500\,\mu$m of rms atmospheric path-length variations (Middelberg et al., 2006).

The data were reduced and calibrated using standard techniques implemented in the MIRIAD software (Sault et al., 1995). To search for unresolved emission at the position of AT2018cow, we made multi-frequency synthesis images with uniform weighting. Single rounds of self-calibration over 5–10 min intervals were found to improve the image quality in all bands. For data at 5.5 GHz and 9 GHz, point-source models of all strong unresolved field sources were used for self-calibration. For data at the higher frequencies, self-calibration was performed using a point-source model for AT2018cow itself, as no other sources were detected within the primary beams, and AT2018cow was detected with a sufficient signal-to-noise ratio. We report flux densities derived by fitting point-source models to the final images using the MIRIAD task *imfit*.

The Atacama Large Millimeter/submillimeter Array (ALMA)

AT2018cow was observed with ALMA as part of DD time during Cycle 5 using Bands 3, 4, 7, 8, and 9. Observations were performed on 30 June 2018 ($\Delta t \approx 14$ d; Bands 7 and 8), 08 July 2018 ($\Delta t \approx 22$ d; Bands 3 and 4) and on 10 July 2018 ($\Delta t \approx 23$ d; Band 9).[4]

The ALMA 12-m antenna array was in its most compact C43-1 configuration, with 46–48 working antennas and baselines ranging from 12–312 m. The on-source integration time was 6–8 min for Bands 3–8, and 40 min for Band 9. The Band 3–8 observations used two-sideband (2SB) receivers with 4 GHz bandwidth each centered on 91.5 and 103.5 GHz (Band 3), 138 and 150 GHz (Band 4), 337.5 and 349.5 GHz (Band 7), 399 and 411 GHz (Band 8). The Band 9 observations used double-sideband (DSB) receivers with 8 GHz bandwidth (2 times larger than that for the Band 3–8 observation, by using 90 degree Walsh phase switching) centered on 663 and 679 GHz. All calibration and imaging was done with the Common Astronomical Software Applications (CASA; McMullin et al., 2007). The data in Bands 3–8 were calibrated with the standard ALMA pipeline, using J1540+1447, J1606+1814 or J1619+2247 to calibrate the complex gains, and using J1337−1257 (Band 7), J1550+0527 (Band 3/4) or J1517−2422 (Band 8) to calibrate the bandpass response and apply an absolute flux scale. Band 9 observations were

[4]Band 9 observations were also performed on 09 July 2018, but these data were of too poor quality to use as a result of weather conditions.

delivered following manual calibration by the North American ALMA Science Center, using J1540+1447 for gain calibration, and J1517−2422 for bandpass- and flux-calibration. We subsequently applied a phase-only self-calibration using the target source (for Bands 3–8), performed a deconvolution, imaged the data, and flux-corrected for the response of the primary beam. AT2018cow is unresolved in our ALMA data, with a synthesized beam that ranges from $3.3'' \times 2.5''$ (PA = 29°) in Band 3 to $0.50'' \times 0.36''$ (PA = −46°) in Band 9. The signal-to-noise ratio in the resulting images ranges from ∼500 in Bands 3 and 4 to ∼80 in Band 9. Details about the ALMA Band 9 data reduction can be found in Appendix 7.7.

Table 7.1: Flux-density measurements for AT2018cow. Time of detection used is mean UT of observation. SMA measurements have formal uncertainties shown, which are appropriate for in-band measurements on a given night. However, for night-to-night comparisons, true errors are dominated by systematics and are roughly 10%–15% unless indicated otherwise. ALMA measurements have roughly 5% uncertainties in Bands 3 and 4, 10% uncertainties in Bands 7 and 8, and a 20% uncertainty in Band 9. ATCA measurements have formal errors listed, but also have systematic uncertainties of roughly 10%. [a] Systematic uncertainty 20% due to uncertain flux calibration

Δt (d)	Facility	Frequency (GHz)	Flux Density (mJy)
5.39	SMA	215.5	15.14 ± 0.56
5.39	SMA	231.5	16.19 ± 0.65
6.31	SMA	215.5	31.17 ± 0.87
6.31	SMA	231.5	31.36 ± 0.97
7.37	SMA	215.5	40.19 ± 0.56
7.37	SMA	231.5	41.92 ± 0.66
7.41	SMA	330.8	36.39 ± 2.25
7.41	SMA	346.8	30.7 ± 1.99
8.37	SMA	215.5	41.19 ± 0.47
8.37	SMA	231.5	41.44 ± 0.56
8.38	SMA	344.8	26.74 ± 1.42
8.38	SMA	360.8	22.79 ± 1.63
9.26	SMA	243.3	35.21 ± 0.75

9.26	SMA	259.3	36.1 ± 1.0
9.28	SMA	341.5	22.85 ± 1.53
9.28	SMA	357.5	25.84 ± 2.5
10.26	SMA	243.3	36.6 ± 0.81
10.26	SMA	259.3	31.21 ± 0.92
10.26	SMA	341.5	19.49 ± 1.47
10.26	SMA	357.5	17.42 ± 2.8
11.26	SMA	243.3	22.14 ± 1.05
11.26	SMA	259.3	20.02 ± 1.28
13.3	SMA	215.5	35.67 ± 0.81
13.3	SMA	231.5	32.94 ± 1.01
14.36	SMA	344.8	26.85 ± 2.22
14.36	SMA	360.8	26.13 ± 2.77
14.37	SMA	215.5	42.05 ± 0.5
14.37	SMA	231.5	38.71 ± 0.58
15.23	SMA	225.0	30.82 ± 2.41
15.23	SMA	233.0	28.64 ± 4.0
15.23	SMA	241.0	27.41 ± 3.21
15.23	SMA	249.0	15.4 ± 4.74
17.29	SMA	234.6	36.57 ± 1.55
17.29	SMA	250.6	34.04 ± 1.81
18.4	SMA	217.5	52.52 ± 0.55
18.4	SMA	233.5	49.32 ± 0.65
19.25	SMA	193.5	59.27 ± 1.49
19.25	SMA	202.0	56.03 ± 1.5
19.25	SMA	209.5	55.09 ± 1.39
19.25	SMA	218.0	54.54 ± 1.33
20.28	SMA	215.5	50.6 ± 1.69
20.28	SMA	231.5	49.16 ± 1.84
20.28	SMA	267.0	41.69 ± 1.62
20.28	SMA	283.0	37.84 ± 1.63
24.39	SMA	215.5	55.57 ± 0.53
24.39	SMA	231.5	53.2 ± 0.6
24.4	SMA	333.0	23.98 ± 1.39
24.4	SMA	349.0	28.46 ± 1.37
26.26	SMA	215.6	38.83 ± 1.2

26.26	SMA	231.6	34.1 ± 1.33
31.2	SMA	230.6	36.76 ± 1.12[a]
31.2	SMA	246.6	31.41 ± 1.42[a]
35.34	SMA	215.5	21.59 ± 0.89
35.34	SMA	231.5	20.63 ± 1.04
36.34	SMA	215.5	24.32 ± 1.19
36.34	SMA	231.5	20.79 ± 1.42
39.25	SMA	217.0	18.34 ± 1.65
39.25	SMA	233.0	19.74 ± 1.76
39.26	SMA	264.0	17.61 ± 2.79
39.26	SMA	280.0	8.27 ± 2.93
41.24	SMA	217.0	12.58 ± 1.5
41.24	SMA	225.0	8.91 ± 1.9
41.24	SMA	233.0	15.08 ± 1.73
41.24	SMA	241.0	9.64 ± 2.13
44.24	SMA	230.6	9.42 ± 1.61
44.24	SMA	234.6	8.04 ± 2.51
44.24	SMA	246.3	10.43 ± 2.13
44.24	SMA	250.6	10.06 ± 3.24
45.23	SMA	217.0	8.28 ± 2.24
45.23	SMA	233.0	10.55 ± 2.39
45.23	SMA	264.0	8.35 ± 3.27
45.23	SMA	280.0	5.7 ± 3.49
47.24	SMA	230.6	11.47 ± 2.81
47.24	SMA	234.6	10.81 ± 4.39
47.24	SMA	246.6	11.65 ± 3.76
47.24	SMA	250.6	5.6 ± 5.37
48.31	SMA	217.5	7.63 ± 1.11
48.31	SMA	233.5	5.73 ± 1.32
76.27	SMA	215.5	1.33 ± 0.55
76.27	SMA	231.5	0.61 ± 0.63
76.27	SMA	335.0	−2.27 ± 1.87
76.27	SMA	351.0	−0.32 ± 1.76
10.48	ATCA	5.5	< 0.15
10.48	ATCA	9.0	0.27 ± 0.06
10.48	ATCA	34.0	5.6 ± 0.16

13.47	ATCA	5.5	0.22 ± 0.05
13.47	ATCA	9.0	0.52 ± 0.04
13.47	ATCA	16.7	1.5 ± 0.1
13.47	ATCA	21.2	2.3 ± 0.3
13.47	ATCA	34.0	7.6 ± 0.5
17.47	ATCA	5.5	0.41 ± 0.04
17.47	ATCA	9.0	0.99 ± 0.03
19.615	ATCA	34.0	14.26 ± 0.21
28.44	ATCA	34.0	30.59 ± 0.2
34.43	ATCA	34.0	42.68 ± 0.19
81.37	ATCA	34.0	6.97 ± 0.09
14.03	ALMA	336.5	29.4 ± 2.94
14.03	ALMA	338.5	29.1 ± 2.91
14.03	ALMA	348.5	28.49 ± 2.85
14.03	ALMA	350.5	28.29 ± 2.83
14.14	ALMA	398.0	26.46 ± 2.65
14.14	ALMA	400.0	26.21 ± 2.62
14.14	ALMA	410.0	25.69 ± 2.57
14.14	ALMA	412.0	25.95 ± 2.6
22.02	ALMA	90.5	91.18 ± 4.6
22.02	ALMA	92.5	92.31 ± 4.6
22.02	ALMA	102.5	93.97 ± 4.7
22.02	ALMA	104.5	93.57 ± 4.7
22.04	ALMA	138.0	85.1 ± 4.3
22.04	ALMA	140.0	84.58 ± 4.2
22.04	ALMA	150.0	80.62 ± 4.0
22.04	ALMA	152.0	79.71 ± 4.0
23.06	ALMA	671.0	31.5 ± 6.3

X-ray Observations

***Swift*/XRT**

The Neil Gehrels Swift Observatory (*Swift*; Gehrels et al., 2004) has been monitoring AT2018cow since June 19, with both the Ultraviolet-Optical Telescope (UVOT; Roming et al. 2005) and the X-ray Telescope (XRT; Burrows et al. 2005). The

transient was well-detected in both instruments (e.g. Rivera Sandoval et al. 2018).

We downloaded the *Swift*/XRT data products (light curves and spectra) using the web-based tools developed by the *Swift*-XRT team (Evans et al., 2009). We used the default values, but binned the data by observation. To convert from count rate to flux, we used the absorbed count-to-flux rate set by the spectrum on the same tool, 4.26×10^{-11} erg cm^{-2} ct^{-1}. This assumes a photon index of $\Gamma = 1.54$ and a Galactic N_H column of 6.57×10^{20} cm^{-2}.

NuSTAR

The *Nuclear Spectroscopic Telescope Array* (*NuSTAR*; Harrison et al., 2013) comprises two co-aligned telescopes, Focal Plane Module A (FPMA) and FPMB. Each is sensitive to X-rays in the 3–79 keV range, with slightly different response functions. *NuSTAR* observed AT2018cow on four epochs, and a log of these observations as well as the best-fit spectral model parameters is presented in Table 7.2.

NuSTAR data were extracted using `nustardas_06Jul17_v1` from HEASOFT 6.24. Source photons were extracted from a circle of 60″ radius, visually centered on the object. We note that such a large region, appropriate for *NuSTAR* data, includes the transient as well as the host galaxy. Background photons were extracted from a non-overlapping circular region with 120″ radius on the same chip. Spectra were grouped to 20 source photons per bin, ignoring energies below 3 keV and above 80 keV.

Spectra were analysed in XSPEC (v12.10.0c), using *NuSTAR* CALDB files dated 2018 August 14. Rivera Sandoval et al. (2018) report a low absorbing column density ($N_H = 7.0 \times 10^{20}$ cm^{-2}), hence we ignore this component in fitting. We opt for a simple phenomenological model to describe the spectrum. We do not fit for a cross-normalisation constant between *NuSTAR* FPMA and FPMB. Epoch 1 (OBSID 90401327002) spectra are not consistent with a simple power law or a broken power law, hence we fit it with the `bkn2pow` model (obtaining spectral breaks at 9.0 ± 0.3 keV and 11.1 ± 0.3 keV). Spectra of the remaining three epochs are well-fit by a simple, unabsorbed power law.

We calculate the flux directly from energies of individual source and background photons detected, converted into flux using the Ancillary Response Files (ARF) generated by the *NuSTAR* pipeline. We use a bootstrap method to estimate the error bars: we draw photons from the data with replacement, and calculate the source

flux from this random sample. By repeating this process 10000 times for each OBSID and each energy range, we calculate the 1-sigma error bars on the fluxes. This method gives answers consistent with `xspec` flux and `cflux` measurements for bright sources (see for instance Kaspi et al., 2014), but has the advantage of giving flux measurements without the need to assume a spectral model for the source. We find that the source is not well-detected in the 40–80 keV band at the third and fourth epochs.

7.3 Basic Properties of the Shock

Light Curve

The radio and X-ray light curves are shown in Figure 7.1. The 230 GHz light curve rises (the first observation of a millimeter transient in its rise phase) and then shows significant variability, presumably from inhomogeneities in the surrounding medium. We have tentative evidence that the rise is at least in part due to a decreasing peak frequency: at Δt = 5–6 d, the flux is marginally higher at 231.5 GHz than at 215.5 GHz, and at Δt = 7–8 d, it seems that the peak may have been within the SMA observing bands. However, the position of the peak is ill-constrained; future early observations would benefit from observations at more frequencies.

By Δt = 50 d, the radio flux has diminished both due to the peak frequency shifting to lower frequencies, *and* to a decay in the peak flux. Specifically, the peak of the 15 GHz light curve is 19 mJy around 47 days (A. Horesh, personal communication), substantially less luminous than the peak of the 230 GHz or the 34 GHz light curve. As we discuss in Section 7.4, this diminishing peak flux suggests that the interaction itself is diminishing, and enables us to constrain the size of the "circum-bubble" of material.

The X-ray light curve seems to have two distinct phases. We call the first phase ($\Delta t \lesssim 20$ days) the *plateau* phase because the X-ray emission is relatively flat. The second phase, which we call the *decline* phase, begins around $\Delta t \approx 20$ days. During this period, the X-ray emission exhibits an overall steep decline, but also exhibits strong variation (by factors of up to 10) on shorter timescales (see also Kuin et al., 2019; Perley et al., 2019; Rivera Sandoval et al., 2018).

We use the shortest timescale of variability in the 230 GHz light curve to infer the size of the radio-emitting region, and do the same for the X-ray emission in Section 7.5. On Days 5–6, the 230 GHz flux changed by order unity in one day, setting a length scale for the source size of $\Delta R = c\Delta t = 2.6 \times 10^{15}$ cm (170 AU).

Table 7.2: *NuSTAR* flux measurements for AT2018cow, and the spectral model parameters

Epoch	OBSID	Exp. time (ks)	Δt (d)	Flux[b] (10^{-12} erg cm^{-2} s^{-1})				Photon Index	χ^2/DOF
				3–10 keV	10–20 keV	20–40 keV	40–80 keV		
1	90401327002[a]	32.4	7.9	4.94 ± 0.04	4.41 ± 0.10	12.21 ± 0.39	21.46 ± 4.29	–	421/443
2	90401327004	30.0	16.8	5.21 ± 0.04	4.99 ± 0.10	7.70 ± 0.33	12.80 ± 4.79	1.39 ± 0.02	424/412
3	90401327006	31.2	28.5	1.58 ± 0.03	1.45 ± 0.06	1.74 ± 0.21	–	1.51 ± 0.04	174/169
4	90401327008	33.0	36.8	1.10 ± 0.02	0.92 ± 0.05	1.02 ± 0.20	–	1.59 ± 0.05	134/135

[a]OBSID 90401327002 is best described by a `bkn2pow` model with parameters $\Gamma_1 = 1.24 \pm 0.05$, $E_1 = 9.0 \pm 0.3$ keV, $\Gamma_2 = 3.6 \pm 0.7$, $E_2 = 11.1 \pm 0.3$ keV, $\Gamma_3 = 0.50 \pm 0.05$. All reported values are for this model.

[b]Fluxes were measured with a model-independent method.

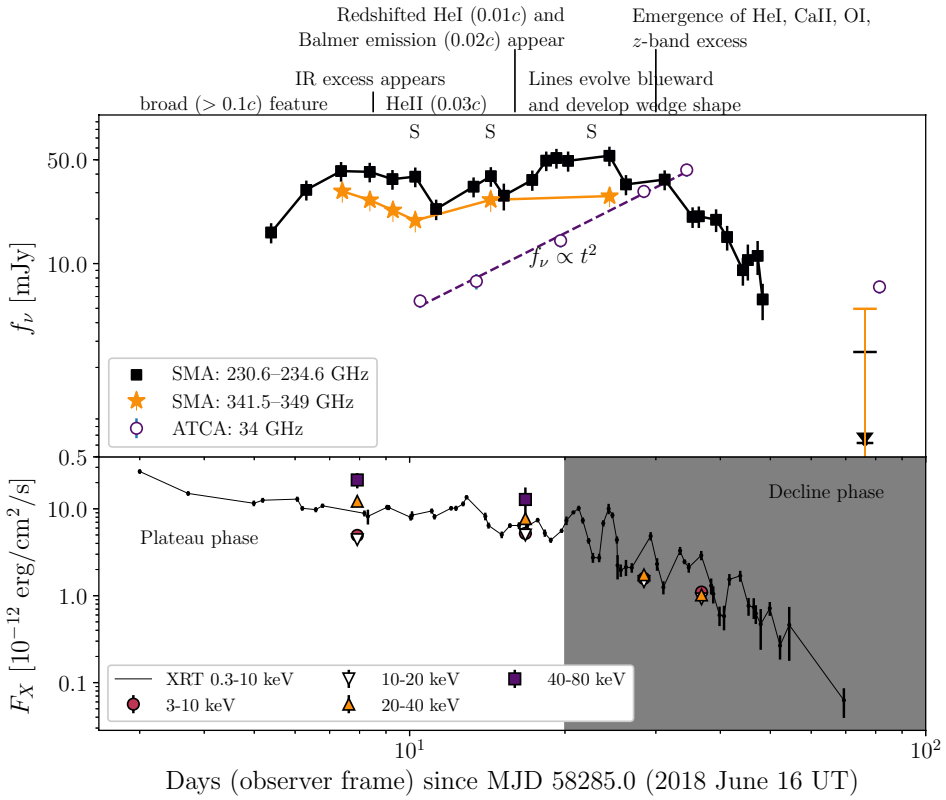

Figure 7.1: (Top panel) Submillimeter (SMA) through radio (ATCA) light curves of AT2018cow, with a timeline of the evolution of the UVOIR spectra (based on Perley et al., 2019) shown above. There were four SMA observations with no frequency tunings in the ranges shown. For these, we took the closest value to 231.5 GHz (243.3 GHz for Days 9, 10, and 11; 218 GHz for Day 19) and scaled them to 231.5 GHz assuming a spectral index $F_\nu \propto \nu^{-1}$. We scaled all SMA fluxes so that the reference quasar 1635+381 would have the value of its mean flux at that frequency. The uncertainties shown on the SMA data represent a combination of formal uncertainties and 15% systematic uncertainties, which is a conservative estimate. Non-detections are represented as a 3-σ upper limit (horizontal bar) and a vertical arrow down to the measurement. The upper limit measurement at 350.1 GHz is -0.32, below the limit of the panel. The error bars shown on the ATCA data are a combination of formal uncertainties and an estimated 10% systematic uncertainty. The ATCA 34 GHz measurements rise as t^2, shown as a dotted line. The full set of SMA light curves for all frequency tunings are shown in Appendix 7.7. The letters 'S' on the top demarcate the epochs with spectra shown in Figure 7.3. (Bottom panel) X-ray light curve from *Swift*/XRT together with four epochs of *NuSTAR* observations. The last two *NuSTAR* epochs have a non-detection in the highest-frequency band (40–80 keV). We denote two distinct phases of the X-ray light curve, the plateau phase and the decline phase, discussed in detail in Section 7.3.

We find no evidence for shorter-timescale variability in our long SMA tracks from the first few days of observations (Figure 7.2).

Together with the 230 GHz flux density ($S_\nu \approx 30$ mJy) and the distance ($d = 60$ Mpc) we infer an angular size of $\theta = 2.8\,\mu$as and a brightness temperature of

$$T_B = \frac{S_\nu c^2}{2k\nu^2 \Delta\Omega} \gtrsim 3 \times 10^{10}\,\mathrm{K}, \tag{7.1}$$

where $\Delta\Omega = \pi\theta^2$. This brightness temperature is close to the typical rest-frame equipartition brightness temperatures of the most compact radio sources, $T_B \sim 5 \times 10^{10}$ K (Readhead, 1994).

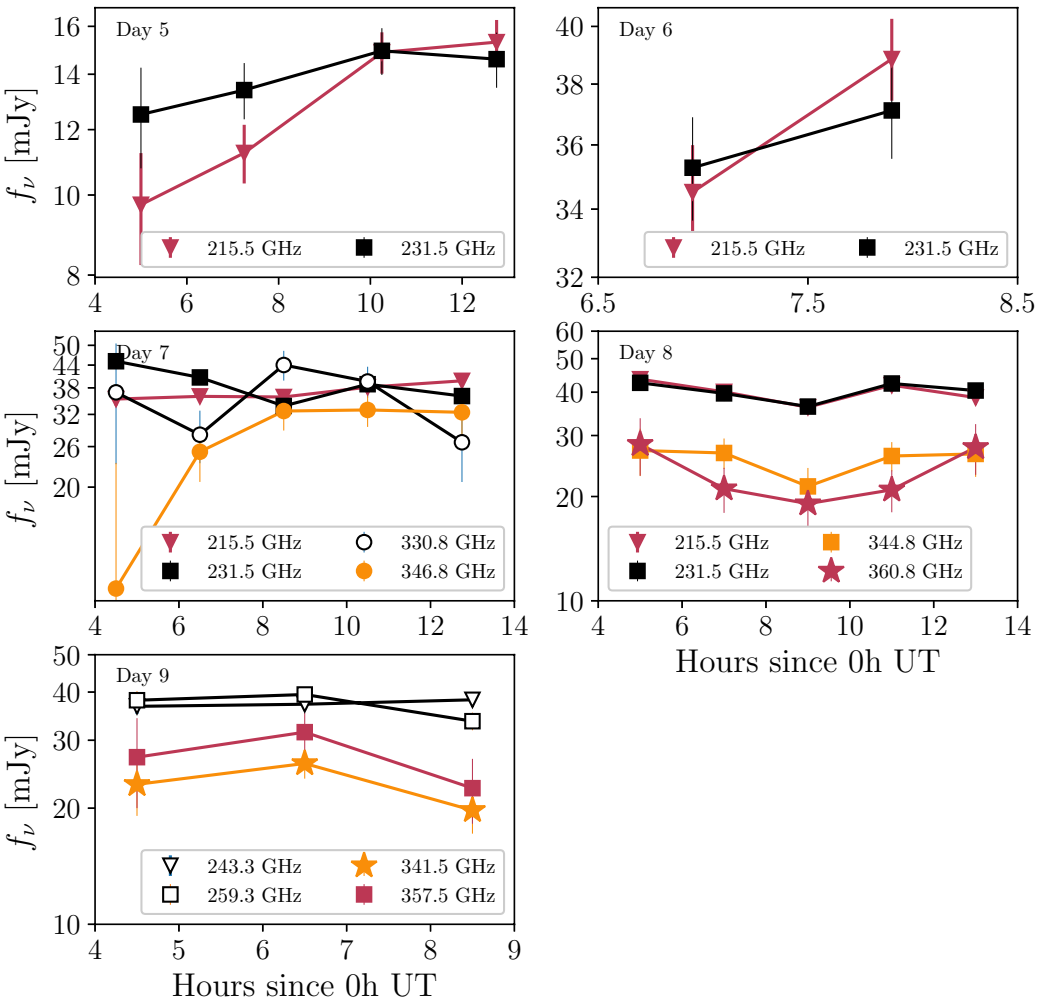

Figure 7.2: Zoomed-in light curves for the first five days of SMA observations. These were the only tracks long enough for binning in time.

Modeling the Radio to Sub-millimeter SED

The shape of the radio to sub-millimeter SED (Figure 7.3), together with the high brightness temperature implied by the luminosity and variability timescale (Section 7.3), can only be explained by non-thermal emission (Readhead, 1994). The observed spectrum is assumed to arise from a population of electrons with a power-law number distribution in Lorentz factor γ_e, with some minimum Lorentz factor γ_m and electron energy power index p:

$$\frac{dN(\gamma_e)}{d\gamma_e} \propto \gamma_e^{-p}, \qquad \gamma_e \geq \gamma_m. \tag{7.2}$$

As argued below, we expect an adiabatic strong shock moving into a weakly magnetized, ionized medium at a non-relativistic speed. First-order Fermi acceleration gives $p = (r+2)/(r-1)$, where r is the compression ratio of the shock. A strong matter-dominated shock has $r = 4$, hence $p = 2$ (Blandford and Eichler, 1987). However the back-reaction of the accelerated particles decelerates the gas flow, weakening the gas dynamic subshock and reducing the compression ratio from the strong shock $r = 3$, so typical $2.5 < p < 3$ are obtained in both simulations and astrophysical data (Jones and Ellison, 1991). Quasi-perpendicular magnetized and relativistic shocks are more subtle, since some particles cannot return along field lines after their first shock crossing, but the limiting value is $p \sim 2.3$ (Pelletier et al., 2017).

Equation 7.3 provides an expression for γ_m. Behind the shock (velocity v) some fraction ϵ_e of the total energy density goes into accelerating electrons. Conserving shock energy flux (using the low-velocity approximation $\gamma \approx 1 + \frac{1}{2}\beta^2$) gives

$$\gamma_m - 1 \approx \epsilon_e \frac{m_p}{m_e} \frac{v^2}{c^2}. \tag{7.3}$$

The value of γ_m is large for relativistic shocks, e.g. in GRBs. But we will see that for this source ($v/c \sim 0.1$, $\epsilon_e \sim 0.1$), the bulk of the electrons are just mildly relativistic ($\gamma_m \sim 2-3$). For ordinary supernova shocks γ_m is always non-relativistic ($\gamma_m - 1 < 1$). Thus in the parameter estimations below, we follow supernova convention and assume that the relativistic electrons follow a power-law distribution down to a fixed γ_m (Chevalier, 1982; Chevalier, 1998; Frail et al., 2000; Kulkarni et al., 1998; Soderberg et al., 2005). We apply ϵ_e *only* to this relativistic power-law, not to the nonrelativistic thermal distribution of shock-heated particles at lower energy.

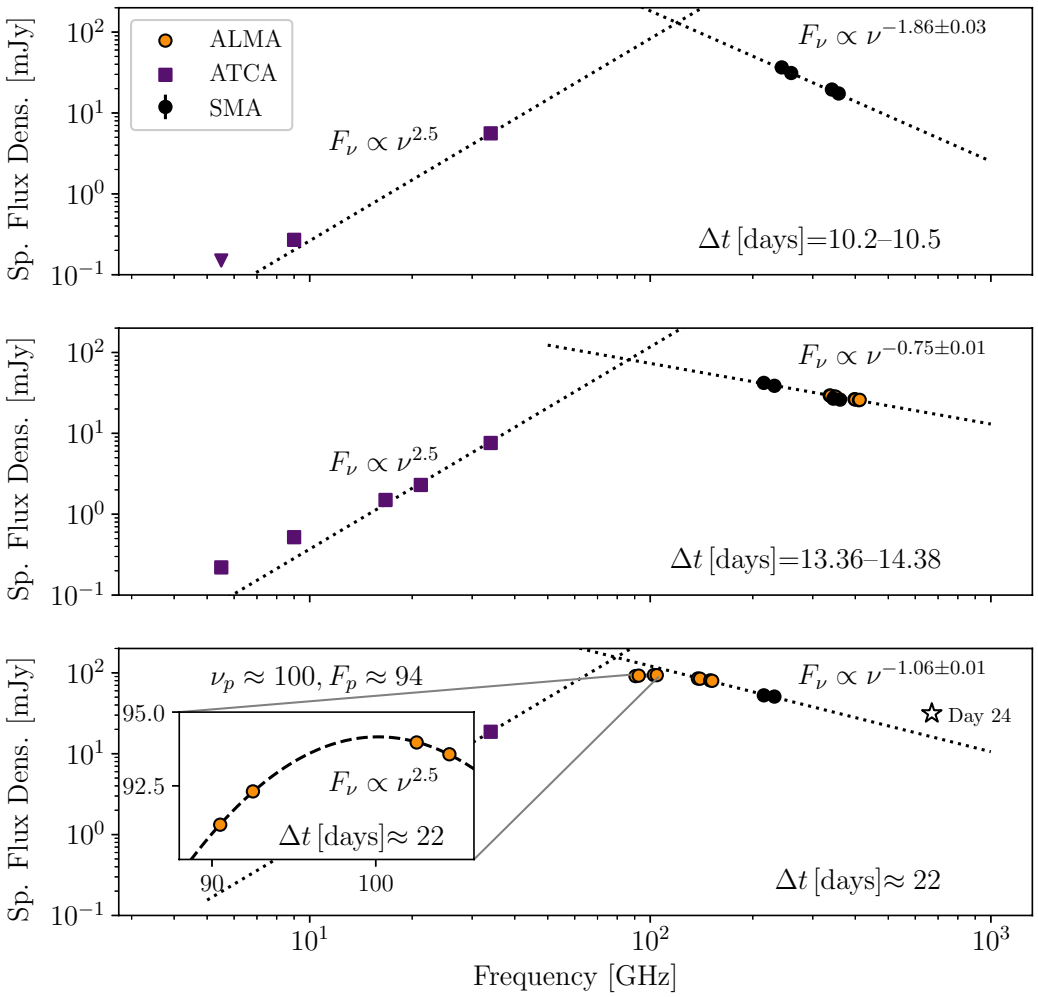

Figure 7.3: Spectrum of AT2018cow at three epochs. In the top panel, we plot the Day 10 data as presented in Table 7.1. In the middle panel, we plot the ATCA data from Day 13 and the SMA and ALMA data from Day 14. In the bottom panel, we plot the ALMA data from Day 22, interpolate the SMA data between Day 20 and Day 24 at 215.5 GHz and 231.5 GHz, and interpolate the ATCA data at 34 GHz (since it varies smoothly; Figure 7.1). We also show the Band 9 measurement from Day 24 as a star. The ATCA data is consistent with a self-absorbed spectral index ($F_\nu \propto \nu^{5/2}$) with an excess at lower frequencies. The peak frequency is resolved on Day 22 with ALMA observations at Band 3 (see inset). To measure the optically thin spectral index, we performed a least squares fit in log space. To estimate the uncertainty on the spectral index, we performed a Monte Carlo analysis, sampling 10^4 times to measure the standard deviation of the resulting spectral index. On Day 10, we used an uncertainty of 15% for each SMA measurement. On Days 14 and 22, we used 10% uncertainty for each ALMA measurement and 20% for each SMA measurement (to take into account the much longer length of the SMA tracks). Uncertainties are too small to be visible on this plot, except for the inset panel, where we do not display them.

We now describe each of the break frequencies that characterize the observed spectrum. First, the characteristic synchrotron frequency ν_m emitted by the minimum energy electrons is

$$\nu_m = \gamma_m^2 \nu_g, \tag{7.4}$$

where ν_g is the gyrofrequency,

$$\nu_g = \frac{q_e B}{2\pi m_e c} \tag{7.5}$$

and q_e is the unit charge, B is the magnetic field strength, m_e is the electron mass, and c is the speed of light.

Next, there is the cooling frequency $\nu_c \equiv \nu(\gamma_c)$, the frequency below which electrons have lost the equivalent of their total energies to radiation via cooling. In general, the timescale for synchrotron cooling depends on the Lorentz factor as $t \propto \gamma_e^{-1}$. Thus, electrons radiating at higher frequencies cool more quickly. Separately, electrons could also lose energy by Compton upscattering of ambient (low energy) photons – the so-called Inverse Compton (IC) scattering. In Section 7.5, we find that IC scattering dominates at early times and that synchrotron losses dominate at later times, and that the transition is at $t \approx 13$ d.

At $\Delta t > 13$ d, electrons with $\gamma_e > \gamma_c$ cool principally by synchrotron radiation to γ_c in a time t, where

$$\gamma_c = \frac{6\pi m_e c}{\sigma_T B^2 t}. \tag{7.6}$$

For $t < 13$ d, Compton cooling on the UVOIR flux exceeds the synchrotron cooling rate by a factor $\sim (t/10\,\mathrm{d})^{-5/2}$, and γ_c is correspondingly lowered. The cooled electrons emit around the characteristic synchrotron frequency

$$\nu_c = \gamma_c^2 \nu_g. \tag{7.7}$$

Next, the self-absorption frequency ν_a is the frequency at which the optical depth to synchrotron self-absorption is unity. The rise at 34 GHz obeys a $f_\nu \propto t^2$ power law (as shown in Figure 7.1), consistent with the optically thick spectral index we measure (Figure 7.3). This indicates that the self-absorption frequency is above the

ATCA bands ($\nu_a > 34\,\mathrm{GHz}$). Figure 7.3 also shows that the emission in the SMA bands is optically thin at $\Delta t \gtrsim 10\,\mathrm{d}$, constraining the self-absorption frequency to be $\nu_a < 230\,\mathrm{GHz}$.

On Day 22, we resolve the peak of the SED with our ALMA data. We denote the peak frequency ν_p and the flux at the peak frequency F_p, and find $\nu_p \approx 100\,\mathrm{GHz}$ and $F_p \approx 94\,\mathrm{mJy}$. Motivated by the observation of optically thick emission at $\nu < \nu_p$, we assume that $\nu_p = \nu_a$, and adopt the framework in Chevalier (1998) (hereafter referred to as C98) to estimate properties of the shock at this epoch. These properties are summarized in Table 7.3, and outlined in detail below.

Following equation (11) and equation (12) in C98, the outer shock radius R_p can be estimated as

$$R_p = \left[\frac{6c_6^{p+5}F_p^{p+6}D^{2p+12}}{(\epsilon_e/\epsilon_B)f(p-2)\pi^{p+5}c_5^{p+6}E_l^{p-2}}\right]^{1/(2p+13)}\left(\frac{\nu_p}{2c_1}\right)^{-1} \tag{7.8}$$

and the magnetic field can be estimated as

$$B_p = \left[\frac{36\pi^3 c_5}{(\epsilon_e/\epsilon_B)^2 f^2 (p-2)^2 c_6^3 E_l^{2(p-2)} F_p D^2}\right]^{2/(2p+13)}\left(\frac{\nu_p}{2c_1}\right), \tag{7.9}$$

where, as in Equation 7.2, p is the electron energy index. Note that C98 use γ for the electron energy power index. We use p instead and γ for the Lorentz factor. The constant $c_1 = 6.27 \times 10^{18}$ in cgs units, and the constants c_5 and c_6 are tabulated as a function of p on page 232 of Pacholczyk (1970). D is the distance to the source, $E_l = 0.51\,\mathrm{MeV}$ is the electron rest mass energy, and ϵ_e/ϵ_B is the ratio of energy density in electrons to energy density in magnetic fields (in C98 this ratio is parameterized as α, but we use α as the optically thin spectral index of the radio SED.) Finally, f is the filling factor: the emitting region is approximated as a planar region with thickness s and area in the sky πR^2, and thus a volume $\pi R^2 s$, which can be characterized as a spherical emitting volume $V = 4\pi f R^3/3 = \pi R^2 s$.

On Day 22, we measure $\alpha = -1.1$ where $F_\nu \propto \nu^\alpha$, which corresponds to $p = 3.2$. Later in this section we show that our sub-millimeter observations lie above the cooling frequency, and therefore that the index of the *source* function of electrons is $p_s = 2.2$. However the C98 prescription considers a distribution as it exists when the electrons are observed, from a combination of the initial acceleration and the energy

losses (to cooling). So, we proceed with $p = 3.2$, and discuss this unusual regime in Section 7.4. The closest value of p in the table in Pacholczyk (1970) is $p = 3$, so we use this value to select the constants (and note that, as stated in C98, the results do not depend strongly on the value of p.) With this, equation 7.8 and equation 7.9 reduce to equation (13) and equation (14) in C98, respectively, reproduced here:

$$R_p = 8.8 \times 10^{15} \left(\frac{\epsilon_e}{\epsilon_B}\right)^{-1/19} \left(\frac{f}{0.5}\right)^{-1/19} \left(\frac{F_p}{\mathrm{Jy}}\right)^{9/19} \left(\frac{D}{\mathrm{Mpc}}\right)^{18/19} \left(\frac{\nu_p}{5\,\mathrm{GHz}}\right)^{-1} \mathrm{cm}, \tag{7.10}$$

$$B_p = 0.58 \left(\frac{\epsilon_e}{\epsilon_B}\right)^{-4/19} \left(\frac{f}{0.5}\right)^{-4/19} \left(\frac{F_p}{\mathrm{Jy}}\right)^{-2/19} \left(\frac{D}{\mathrm{Mpc}}\right)^{-4/19} \left(\frac{\nu_p}{5\,\mathrm{GHz}}\right) \mathrm{G}. \tag{7.11}$$

Next we estimate the total energy U. For $p = 3$, equation 7.10 and equation 7.11 can be combined into the following expression for $U = U_B/\epsilon_B$,

$$\begin{aligned} U &= \frac{1}{\epsilon_B} \frac{4\pi}{3} f R^3 \left(\frac{B^2}{8\pi}\right) \\ &= (1.9 \times 10^{46}\,\mathrm{erg}) \frac{1}{\epsilon_B} \left(\frac{\epsilon_e}{\epsilon_B}\right)^{-11/19} \left(\frac{f}{0.5}\right)^{8/19} \left(\frac{F_p}{\mathrm{Jy}}\right)^{23/19} \left(\frac{D}{\mathrm{Mpc}}\right)^{46/19} \left(\frac{\nu_p}{5\,\mathrm{GHz}}\right)^{-1}. \end{aligned} \tag{7.12}$$

Following C98 we take $f = 0.5$, but the dependence on this parameter is weak. In choosing ϵ_B and ϵ_e there are several normalizations (or assumptions) used in the literature. As a result the inferred energy can vary enormously (see Section 7.4 for further details). For now, we follow Soderberg et al. (2010) in setting $\epsilon_e = \epsilon_B = 1/3$ (in other words, that energy is equally partitioned between electrons, protons, and magnetic fields). With all of these choices, we find that at $\Delta t \approx 22\,\mathrm{d}$, $R_p \approx 7 \times 10^{15}\,\mathrm{cm}$ and $B_p \approx 6\,\mathrm{G}$. We find that the total energy $U \approx 4 \times 10^{48}\,\mathrm{erg}$. Assuming 10% uncertainties in F_p and ν_p and a 50% uncertainty in p, a Monte Carlo with 10,000 samples gives uncertainties of 0.15–0.3 dex in these derived parameters. Our results are robust to departures from equipartition given the large penalty in the required energy (Readhead, 1994).

The mean velocity up to $\Delta t \approx 22\,\mathrm{d}$ is $v = R_p/t_p = 0.13\mathrm{c}$. We can write a general expression for v/c (taking $L_p = 4\pi F_p D^2$, noting that $4\pi\mathrm{Jy\,Mpc}^2 = 1.2 \times 10^{27}\mathrm{erg\ s^{-1}Hz^{-1}}$):

$$v/c \approx \left(\frac{\epsilon_e}{\epsilon_B}\right)^{-1/19} \left(\frac{f}{0.5}\right)^{-1/19} \left(\frac{L_p}{10^{26}\,\mathrm{erg\,s^{-1}\,Hz^{-1}}}\right)^{9/19} \left(\frac{\nu_p}{5\,\mathrm{GHz}}\right)^{-1} \left(\frac{t_p}{1\,\mathrm{d}}\right)^{-1}. \quad (7.13)$$

Furthermore, from the t^2 rise at 34 GHz (Figure 7.1) we can infer that the radius increases as $R \propto t$ and therefore that the velocity $v = dR/dt$ is constant. We put this derived energy and velocity into the context of other energetic transients in Section 7.4.

Next, we estimate the density of the medium into which the forward shock is propagating. The ejecta expands into the medium with velocity v_1, producing a shock front (a discontinuity in pressure, density, and temperature) with shock-heated ejecta immediately behind this front. Conservation of momentum across this (forward) shock front requires that

$$P_1 + \rho_1 v_1^2 = P_2 + \rho_2 v_2^2, \quad (7.14)$$

where P is pressure (not to be confused with p used as the power-law index for the electron energy distribution). The subscript 1 refers to the upstream medium (the ambient CSM) and the subscript 2 refers to the downstream medium (the shocked ejecta). Far upstream, the pressure can be taken to be 0, and in the limit of strong shocks (for a monatomic gas) $\rho_2/\rho_1 = v_1/v_2 = 4$. Thus this can be simplified to

$$\frac{3\rho_1 v_1^2}{4} = P_2. \quad (7.15)$$

If the medium is composed of fully ionized hydrogen, $\mu_p = 1$ and the number densities of protons and electrons are equal ($n_p = n_e$). Using equation 7.15 together with equation 7.11, as well as the relations $P_2 = (1/\epsilon_B)B^2/8\pi$ and $\rho_1 = \mu_p m_p n_e$,

$$n_e \approx (20\,\mathrm{cm^{-3}}) \left(\frac{1}{\epsilon_B}\right) \left(\frac{\epsilon_e}{\epsilon_B}\right)^{-6/19} \left(\frac{f}{0.5}\right)^{-6/19} \left(\frac{L_p}{10^{26}\,\mathrm{erg\,s^{-1}\,Hz^{-1}}}\right)^{-22/19} \times \left(\frac{\nu_p}{5\,\mathrm{GHz}}\right)^{4} \left(\frac{t_p}{1\,\mathrm{d}}\right)^{2}. \quad (7.16)$$

We find that the number density of electrons at $\Delta t \approx 22$ d is $n_e \approx 3 \times 10^5\,\mathrm{cm^{-3}}$. We note that the strong jump conditions used here assume $\gamma = 5/3$, and that there is

Parameter	$\epsilon_e = \epsilon_B = 1/3$	$\epsilon_e = 0.1, \epsilon_B = 0.01$
$\nu_a = \nu_p$ (GHz)	100	100
$F_{\nu,p}$ (mJy)	94	94
r (10^{15} cm)	7	6
v/c	0.13	0.11
B (G)	6	4
$U(10^{48}\,\mathrm{erg})$	4	35
n_e ($10^5\,\mathrm{cm}^{-3}$)	3	41
ν_c (GHz)	2	8

Table 7.3: Quantities derived from Day 22 measurements, using different equipartition assumptions. In the text unless otherwise stated we use $\epsilon_e = \epsilon_B = 1/3$

a correction for the contribution of a relativistic ($\gamma = 4/3$) component. Chevalier (1983) quantify this correction using the factor w, the ratio of the relativistic pressure to the total pressure. In the most extreme case ($w = 1$) the correction is small, only a factor of 1.14 in n_e. This is negligible compared to our uncertainties.

At such a high density, the optical depth to free-free absorption $\tau_{\rm ff}$ might be expected to have a significant effect on the shape of the spectrum at low radio frequencies (Lundqvist and Fransson, 1988). From Lang (1999), we have

$$\tau_{\rm ff} = 8.235 \times 10^{-2} \left(\frac{T_e}{\rm K}\right)^{-1.35} \left(\frac{\nu}{\rm GHz}\right)^{-2.1} \int \left(\frac{N_e}{\rm cm^{-3}}\right)^2 \left(\frac{dl}{\rm pc}\right) \tag{7.17}$$

which, with our measured values of n_e and R on Day 22, gives the characteristic value

$$\tilde{\tau}_{\rm ff} = 68 \left(\frac{T_e}{8000\rm K}\right)^{-1.35} \left(\frac{\nu}{\rm GHz}\right)^{-2.1} . \tag{7.18}$$

However, in AT2018cow the gas through which the shock is propagating is *not* at normal HII-region temperatures of $\sim 10^4$K. The UV and X-ray photons emitted at early times will completely ionize and Compton heat any surrounding gas: for gas at the density and radius given in Table 7.3, the lifetime to photoionization of a neutral hydrogen atom is less than 0.01 s, while the recombination time is years[5]. Compton heating of the electrons increases their temperature at the rate

[5] For much lower temperatures $T \sim 10^4$ K, the Case B (high-density limit) recombination coefficient is $\alpha_B(T = 10^4\,\mathrm{K}) = 2.6 \times 10^{-13}\,\mathrm{cm^3\,s^{-1}}$ (Draine, 2011), and the timescale is $t_{\rm recomb} = 1/(\alpha_B n_e)$. For $n_e = 3 \times 10^5\,\mathrm{cm^{-3}}$, $t_{\rm recomb} \approx 250$ d. This timescale becomes even longer for the expected higher temperatures.

$$\frac{d(3/2)kT_e}{dt} = H = \frac{\sigma_T}{m_e c^2} \int_0^\infty \frac{h\nu L_\nu f_{KN}(h\nu/m_e c^2)}{4\pi R^2} d\nu, \tag{7.19}$$

where the Klein-Nishina correction $f_{KN}(x) \simeq 1 - 21x/5 + O(x^2)$.[6] Even though the blackbody ($T = 30,000$ K) luminosity at $\Delta t = 3$ d is 100 times larger than the coeval X-ray luminosity (Perley et al., 2019), the Compton heating is dominated by the 10–100 keV X-ray flux, and we find, for $3 < \Delta t < 20$ d, gas at the density and radius given in Table 7.3 has

$$T_e(t) \simeq 1.0 \times 10^6 \,\mathrm{K} (t/3\,\mathrm{d})^{0.6}. \tag{7.20}$$

Given the spectral evolution shown in Perley et al. (2019), the Compton temperature (at which Compton heating balances Compton cooling) is $T_c \sim 2.5 \times 10^6$ K on day 3, hardening to $T_c \sim 1.8 \times 10^7$ K on day 20 since the blackbody UV flux drops as $t^{-2.5}$, while the hard X-ray flux drops much more slowly. At these high Compton-heated temperatures $T_e \sim 10^6$ K, the free-free absorption optical depth given by equation 7.18 only rises above unity below frequencies of 300 MHz, accessible to facilities like LOFAR.

Next, we estimate the luminosity from free-free emission of the ionized gas (Lang, 1999):

$$L \approx 1.43 \times 10^{-27} n_e n_i T^{1/2} V Z^2 g \,\mathrm{erg\,s^{-1}}, \tag{7.21}$$

where n_i is the number density of ions, Z is the atomic number, and $g \approx 1$ is the Gaunt factor, a quantum mechanical correction. Assuming that the gas is completely ionized out to the light travel sphere at 22 days ($R = 6 \times 10^{16}$ cm), we have $n_e = n_i$ in the region of interest. We also take $Z = 1$. With the inferred density (Table 7.3) we find $L \approx 9 \times 10^{37}$ erg s^{-1}, so the contribution to the observed X-ray luminosity is negligible.

Finally, we estimate the different break frequencies, beginning with ν_m. Using equation 7.3, taking $\epsilon_e = 1/3$ and using our inferred $\beta = v/c$ from Day 22, $\gamma_m \approx 5$. Next, using equation 7.5 and our measured value of B, $\nu_g \approx 17$ MHz. Equation 7.4 thus gives $\nu_m \approx 0.4$ GHz, substantially below our peak frequency. The spectral

[6] Expressions for f_{KN} for cold electrons are given e.g., in equation (A1) of Sazonov et al. (2004) and equation (5) of Madau and Efstathiou (1999), and for finite temperature electrons in equation (14) of Guilbert (1986).

index at $\nu_m < \nu < \nu_a$ is $\nu^{5/2}$ (Rybicki and Lightman, 1986), which we show as dotted lines in Figure 7.3. Clearly, the lowest frequency fluxes are in excess of $\nu^{5/2}$ extrapolation. This naturally occurs if the source is inhomogeneous (e.g. magnetic field and/or particle energy density decreasing outwards). It can also arise even for a perfectly homogenous source because the energy spectrum of the radiating electrons is not a pure power-law: note that $\nu_a > \nu_c > \nu_m$, so even beyond the Maxwellian-like peak at γ_m, the spectrum is convex, steepening with energy above γ_c. These both produce self-absorbed spectra flatter than $\nu^{5/2}$ (see Section 6.8 in Rybicki and Lightman (1986) and de Kool et al. (1989) for model calculations).

The cooling frequency due to synchrotron radiation is determined by equation 7.6 and equation 7.7. We find $\gamma_c \approx 11$, giving a cooling frequency $\nu_c \approx 2\,\mathrm{GHz}$. The relative contributions to electron cooling from synchrotron radiation and IC scattering are determined by the ratio between the radiation energy density and the magnetic energy density. On Day 22, the bolometric luminosity as measured in the UVOIR is $5 \times 10^{42}\,\mathrm{erg\,s^{-1}}$ (Perley et al., 2019), so the radiation density is $u_{\mathrm{ph}} = 0.26\,\mathrm{erg\,cm^{-3}}$. The magnetic energy density on the same day is $u_B = B^2/8\pi \approx 1.5\,\mathrm{erg\,cm^{-3}}$. Thus synchrotron radiation is the dominant cooling mechanism, with a roughly 10% contribution from IC scattering.

At this epoch, the cooling timescale $t_{\mathrm{cool}} = (\gamma_e m_e c^2)/(\frac{4}{3}\sigma_T u_B \gamma_e^2 c) = 240\,\mathrm{d}/\gamma_e$ for an electron with γ_e, which is roughly 80 for an electron radiating at 100 GHz. So on Day 22 the cooling timescale is shorter than the timescale on which we are observing the source. This means that continuous re-acceleration of the electrons is required, which could be provided by ongoing shock interaction.

As stated in Section 7.3, it seems that ν_p during the rise phase ($\Delta t \approx 5$–$8\,\mathrm{d}$) was above or within the SMA observing bands. Using the peak observed flux and frequency as a lower limit on the peak flux and peak frequency, respectively, we consistently find that $v \approx 0.1c$, albeit with a decreasing n_e ($3\times10^6\,\mathrm{cm^{-3}}$ at $\Delta t \approx 5\,\mathrm{d}$).

7.4 Implications of Shock Properties

AT2018cow in Velocity-Energy Space, and a Discussion of Epsilons

It is challenging to directly compare the energy of AT2018cow to that of other classes of radio-luminous transients, because there are several conventions that produce discrepant results. In particular, the energy partition fractions ϵ_B and ϵ_e are important for determining the total amount of energy in the shock, but are difficult to measure.

In the classical gamma-ray burst (GRB) literature, ϵ_e has been consistently measured to be $\epsilon_e \approx 0.2$, within a factor of 2, while values of ϵ_B have much wider spreads, with a median value of 3×10^{-5} but a distribution spanning four orders of magnitude (Kumar and Zhang, 2015). Kumar and Barniol Duran (2010) constrain $\epsilon_B \sim 10^{-6}$ for a CSM density of $0.1\,\mathrm{cm}^{-3}$, and an even smaller value for higher densities. One of the best-observed GRB afterglows is GRB 130427A, and from modeling the evolving spectrum Perley et al. (2014) find $0.03 < \epsilon_B < 1/3$ and $0.14 < \epsilon_e < 1/3$.

There are different approaches to modeling for the handful of low-luminosity GRBs (LLGRBs) discovered to date. For LLGRB 980425/SN 1998bw, Kulkarni et al. (1998) invoke equipartition ($\epsilon_B = \epsilon_e = 0.5$). For LLGRB 031203/SN2003 lw, Soderberg et al. (2004b) use models from Sari et al. (1998) and Granot et al. (2002) together with the cooling frequency inferred from X-ray observations to estimate $\epsilon_e = 0.4$ and $\epsilon_B = 0.2$. For LLGRB 060218/SN 2006aj, Soderberg et al. (2006b) use the same prescription as was used in SN 1998bw. Finally, for LLGRB 100316D/SN 2010bh, Margutti et al. (2013) set $\epsilon_B = 0.01$ and allow ϵ_e to vary from 0.01–0.1.

For Type II and Type Ibc radio supernovae, approaches range from using the SN 1998bw convention (i.e., $\epsilon_B = \epsilon_e = 0.5$; Horesh et al., 2013; Soderberg et al., 2005) to $\epsilon_B = \epsilon_e = 0.1$ (e.g. Chevalier and Fransson, 2006; Salas et al., 2013; Soderberg et al., 2006b) to $\epsilon_B = \epsilon_e = 1/3$ for the relativistic supernova SN 2009bb (Soderberg et al., 2010).

In this work, we follow the convention in Soderberg et al. (2010) so that we can compare our velocity-energy diagram to the corresponding diagram (Figure 4) in that paper. To put all transients on the same scale, we take the peak frequency, peak luminosity, and peak time for each event, and run them through the same equations that we used to infer the shock properties of AT2018cow. Note that we do not vary the values of c_5, c_6, p, but these are all very small corrections, whereas the effect of ϵ_B and the ratio ϵ_e/ϵ_B in estimating the energy is large. The details of how we selected the peak values for each event are in Appendix 7.7. When possible, we use the peak of the SED at a particular epoch. However, for most events, we use the peak flux density corresponding to a certain frequency, because well-sampled SEDs are rare.

Our rederived velocity-energy diagram is shown in Figure 7.4. AT2018cow has an energy comparable to mildly relativistic outflows (LLGRBs; e.g. SN 1998bw) and energetic supernovae (e.g. SN 2007bg). We display vertical axes for two

different conventions ($\epsilon_B = 1/3$ and $\epsilon_B = 0.01$) to show how this affects the inferred energy. Note that these values are not evaluated for a consistent epoch. However, for AT2018cow, we have reason to believe that the values of velocity and energy do not change significantly over the course of our observations. For other sources, it would be necessary to have a well-sampled SED over multiple epochs in order to trace the evolution of these values, and this is rare in the literature.

A Luminous Millimeter Transient in a Dense Environment

Here we compare the radio luminosity of AT2018cow to that of other transients, as observed at the spectral peak frequency at time Δt. As shown in Figure 7.5, AT2018cow stands out as being several times more luminous than SN 1998bw, and having a late peak at high frequencies. Over time, the peak luminosity diminishes to the value reported in the low-frequency radio observations of Margutti et al. (2019), supporting our inference that the velocity is not changing significantly.

On this diagram we also indicate lines of constant velocity (cf. Figure 3 of Soderberg et al., 2010 and Figure 4 of C98) and lines of constant mass-loss rate scaled by velocity $\dot{M}/v_w$, as a diagnostic of density (cf. Figure 10 of Jencson et al., 2018). Note that these lines assume $\nu_p = \nu_a$.

We now derive relations between the observational coordinates of the diagram in Figure 7.4 and physical quantities: the ordinate, peak radio luminosity L_p, is simply a power of the energy per unit radius U/R. We get an expression for U/R using equation 7.12 and equation 7.10:

$$\frac{U}{R} = (3 \times 10^{29}\,\mathrm{erg\,cm^{-1}}) \left(\frac{1}{\epsilon_B}\right) \left(\frac{\epsilon_e}{\epsilon_B}\right)^{-10/19} \left(\frac{f}{0.5}\right)^{9/19} \left(\frac{L_p}{10^{26}\,\mathrm{erg\,s^{-1}\,Hz^{-1}}}\right)^{14/19}. \tag{7.22}$$

This translation between L_p and U/R is shown on the left and right axis labels of Figure 7.4.

We now show that the abscissa of Figure 7.5, $(\Delta t/1\,\mathrm{d})(\nu_p/5\,\mathrm{GHz})$, is very nearly proportional to the square root of the swept up mass per unit radius M/R, or equivalently, if the surrounding medium was from a pre-explosion steady wind of speed v_w, $\dot{M}/v_w \propto M/R$. A steady spherical wind of ionized hydrogen with velocity v_w has $n_e = \dot{M}/(4\pi m_p r^2 v_w)$, so we can reparameterize the density in terms of the mass-loss rate:

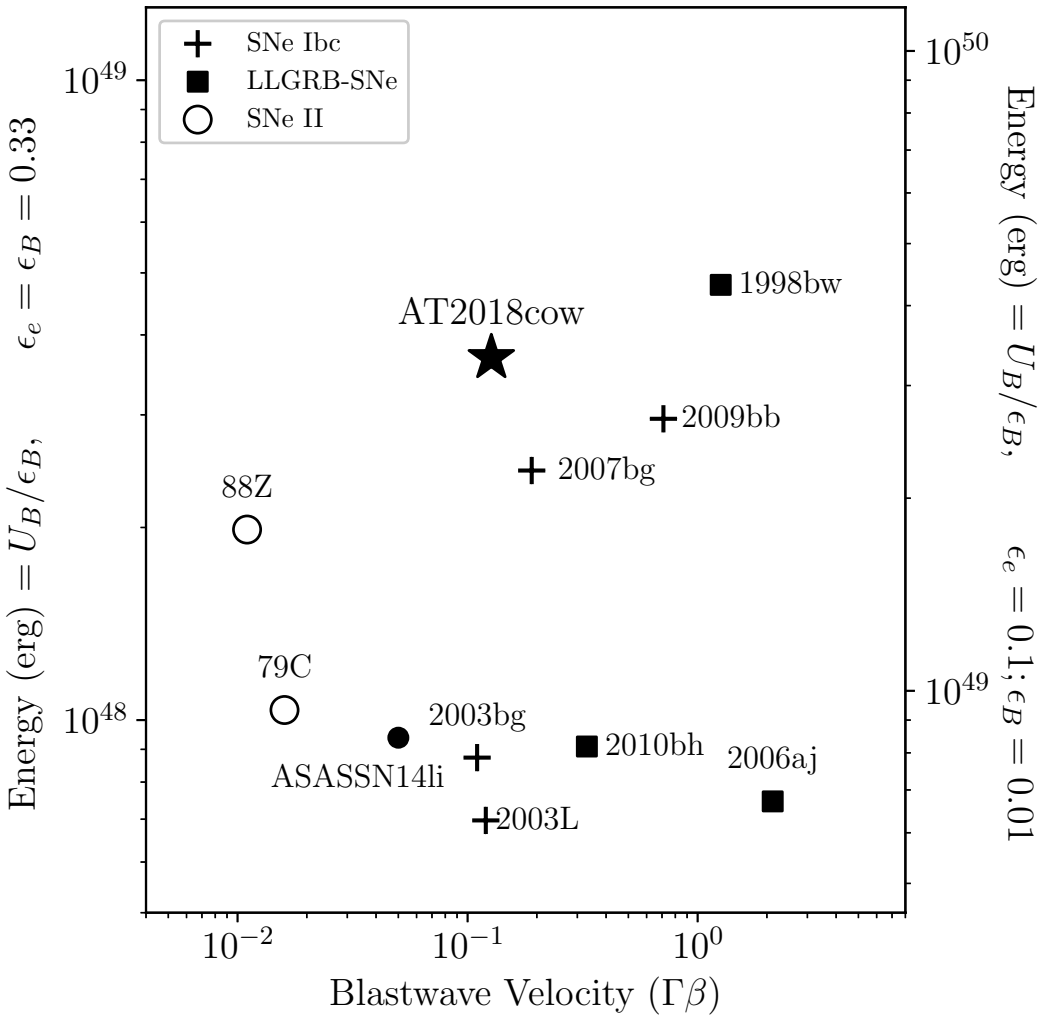

Figure 7.4: AT2018cow in velocity-energy space, compared to other classes of radio-luminous transients: TDEs (filled circles), Ibc supernovae (crosses), SNe associated with LLGRBs (filled squares), and Type II supernovae (open circles). For reference, GRBs lie above the plot at $10^{50}\,\mathrm{erg} < U < 10^{52}\,\mathrm{erg}$, and the relativistic TDE *Swift* J1644 lies at $\approx 10^{51}$ erg in this framework. For all sources, we take values of peak frequency and peak luminosity at some time (described in detail in Appendix 7.7) and estimate velocity and energy using the same prescription that we use for AT2018cow. Estimates of energy are sensitive to the choice of ϵ_B, as illustrated with the secondary axis on the right-hand side.

$$\frac{\dot{M}}{v_w}\left(\frac{1000\,\mathrm{km\,s^{-1}}}{10^{-4}\,M_\odot\,\mathrm{yr^{-1}}}\right) = (0.0005)\left(\frac{1}{\epsilon_B}\right)\left(\frac{\epsilon_e}{\epsilon_B}\right)^{-8/19}\left(\frac{f}{0.5}\right)^{-26/19} \times \left(\frac{L_p}{10^{26}\,\mathrm{erg\,s^{-1}\,Hz^{-1}}}\right)^{-4/19}\left(\frac{\nu_p}{5\,\mathrm{GHz}}\right)^{2}\left(\frac{t_p}{1\,\mathrm{d}}\right)^{2}. \tag{7.23}$$

Notice the weak ($-4/19$ power) dependence on L_p, and the quadratic dependence on $\nu_p t_p$, which means the lines of constant $\dot{M}/v_w$ are nearly vertical in Figure 7.5.

AT2018cow lies along the same velocity line as SN 2003bg and SN 2003L, but n_e is a factor of a few to an order of magnitude larger.[7] Similarly, SN 1998bw lies along a similar velocity line to SN 2006aj, but n_e (using our presscription) is 40 cm^{-3}, while the density inferred for 2006aj using the same prescription is 3 cm^{-3}. For Ibc SNe in general, Chevalier and Fransson (2006) attribute the large spread in radio luminosity to a spread in circumstellar density, with the example that SN 2002ap (not shown in Figure 7.5 due to its relatively low luminosity) is roughly three orders of magnitude less luminous than SN 2003L, and its inferred ambient density is also a factor of three smaller. In SN 2003L and SN 2003bg, the high density was attributed to a stellar wind.

This is not the whole story: as we showed above, high peak radio luminosity just corresponds to high U/R, i.e., high energy and/or small radius. Since U is the *converted* energy, it represents only a lower limit to the actual driving kinetic energy (becoming equal to it as the explosion transitions from free-expansion to the Sedov phase). A higher-density medium more quickly converts the piston's energy to thermal energy than does a low density medium. Thus for a large fixed explosion energy, a denser medium will indeed lead to larger peak radio luminosities. But the direct correlation is with the (thermalized) energy per unit radius, U/R. Similarly, equation 7.11 shows that (except for a very weak $L_p^{-2/19}$ dependence), $\nu_p \propto B_p$. Thus higher peak frequencies are directly indicative of a higher magnetic field, or equivalently, pressures. Thus AT2018cow's high ν_p and high L_p are quite likely mostly a consequence of it being energetic, and observed early, when the high wind density at small radii led to high pressure, and enhanced U/R. As we discuss below, this suggests that many other supernovae could have shown similar bright mm-submm fluxes, had they been observed at those wavelengths in their first week.

On Day 22, the inferred density is $\rho_0 = 4{\times}10^{-19}$ g cm^{-3} at a radius of $r_0 = 7{\times}10^{15}$ cm (Table 3). From this we can infer $\dot{M}/v_{\rm w} = 2.4 \times 10^{14}$ g cm^{-1}. The mass swept up to radius r is $(\dot{M}/v_{\rm w})r$. In Section 7.3 we argue that the blast wave reaches the edge of the surrounding bubble around $\Delta t \approx 50$ d. If so, given our inferred velocity, the

[7] The radial density profile inferred for SN 2003bg is $n_e \approx 2.2 \times 10^5 (r/r_0)^{-2}$ cm^{-3} (Soderberg et al., 2006c) and the radial density profile inferred for SN 2003L is $n_e \approx 6.1 \times 10^4 (r/r_0)^{-2}$ cm^{-3} (Soderberg et al., 2005). In both cases, $r_0 \approx 10^{15}$ cm is the shock radius at $t_0 = 10$ d. For SN 2003L, we infer t_0 using the result that $r = 3{\times}10^{15}$ cm at $t = 28$ d, and that $\alpha_r = 0.96$ in the parameterization $r = r_0(t/t_0)^{\alpha_r}$ (Model 1 in Soderberg et al., 2005).

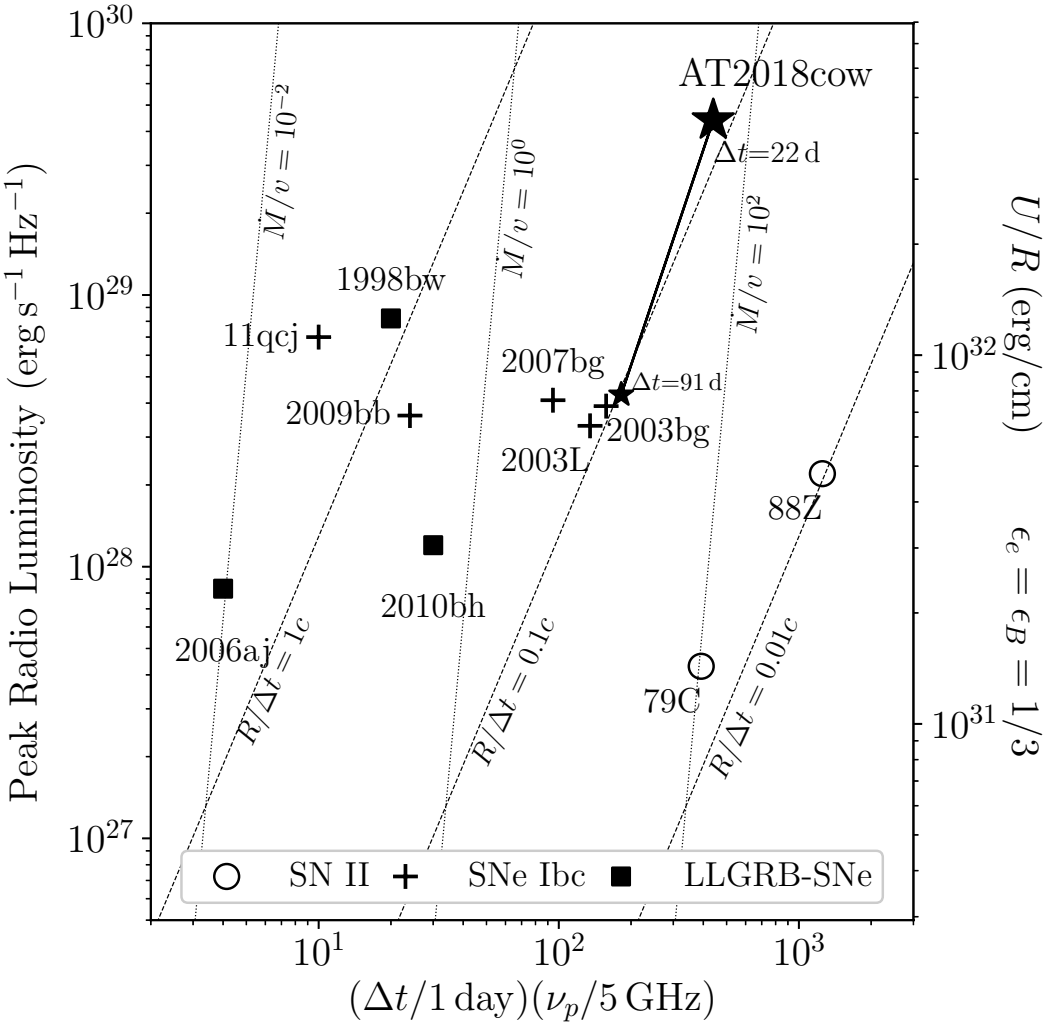

Figure 7.5: The peak luminosity of AT2018cow on two different epochs, compared to classes of energetic transients (cf. Chevalier, 1998; Soderberg et al., 2010). The value at $\Delta t = 22$ d comes from our work. The value at $\Delta t = 91$ d comes from Margutti et al. (2019) and shows that the velocity has not slowed significantly. For other sources, we choose values of peak frequency and peak luminosity as described in Appendix 7.7. AT2018cow is unusual in having a large radio luminosity as well as a high ν_a, and we discuss the physical interpretation of both of these characteristics in the text. Lines of constant mass-loss rate (scaled to wind velocity) are shown in units of $10^{-4}\,M_\odot\,\mathrm{yr}^{-1}/1000\,\mathrm{km\,s}^{-1}$. Note that the dotted lines assume that the radio peak is due to synchrotron self-absorption rather than free-free absorption (FFA), but that FFA has been the preferred fit in some cases, such as for SN 1979C and SN 1980K (Chevalier, 1984)

radius of the "circum-bubble" is 1.7×10^{16} cm, and the mass of the circum-bubble $\approx 2 \times 10^{-3}\, M_\odot$. The mass loss rates for hot stars ($v_w \sim 2,000\,\mathrm{km\,s^{-1}}$, Lamers and Leitherer, 1993) and red supergiants ($v_w \sim 20\,\mathrm{km\,s^{-1}}$, van Loon, 2010) range from 10^{-4}–$10^{-6}\, M_\odot\,\mathrm{yr}^{-1}$ (Smith et al., 2018). Thus r_0/v_w is $\sim$ 1y for a hot star progenitor, and $\sim$ 100y for a red supergiant. Thus the circum-bubble could either have been formed by normal mass loss in a red supergiant, or end-of-life enhanced mass loss from a hot star or red supergiant (see, e.g., Smith et al., 2017 and references therein).

UVOIR observations of AT2018cow place strong constraints on the nature of the surrounding medium (Perley et al., 2019). The high luminosity and fast rise can be interpreted as shock-heating of a dense shell of material at $R = 10^{14}$ cm or 10 AU, qualitatively consistent with the inference of dense material given the properties inferred from the radio shock. On the other hand, early spectra show no narrow emission lines indicative of a shock and the light curve declines steeply after peak, both of which suggest that this dense material must also be quite limited in extent, with little material at larger radii. While the radio observations also suggest a cutoff in the density distribution may exist, the $0.1c$ shock does not reach it for almost 20 days, a quite different timescale than the optical peak (reached in less than 3 days) or early spectroscopy. This might be due to the $0.1c$ shock being produced by breakout from the $R = 10^{14}$cm shell which re-energized the (much slower) supernova shock. Or there could be deviations from spherical asymmetry (for example, with the optical heating a quasi-spherical shell but the radio shock passing through a denser toroidal component or clouds along a bipolar jet).

Thus an energetic shock propagating into a dense environment could produce a radio SED that peaks at sub-millimeter wavelengths at early times. However, as illustrated in the left panel of Figure 7.6 searches at high frequencies at early times have been rare, and primarily limited to transients with relativistic jetted outflows (GRBs, TDEs). We suggest that these searches be expanded to other classes of transients: luminous SNe such as SN 2003L and SN 2007bg, and luminous TDEs such as ASASSN14li, all exploded into dense media and exhibited luminous centimeter-wavelength emission at $t > 10$ d. As time goes on, the SED peak shifts to lower frequencies and diminishes in brightness, so these events could have been bright millimeter transients at $t < 10$ d. This is supported by Figure 7.5, which shows that SN 2007bg, SN 2003bg, and SN 2003L could have appeared similar to AT2018cow had they been observed earlier at higher frequencies.

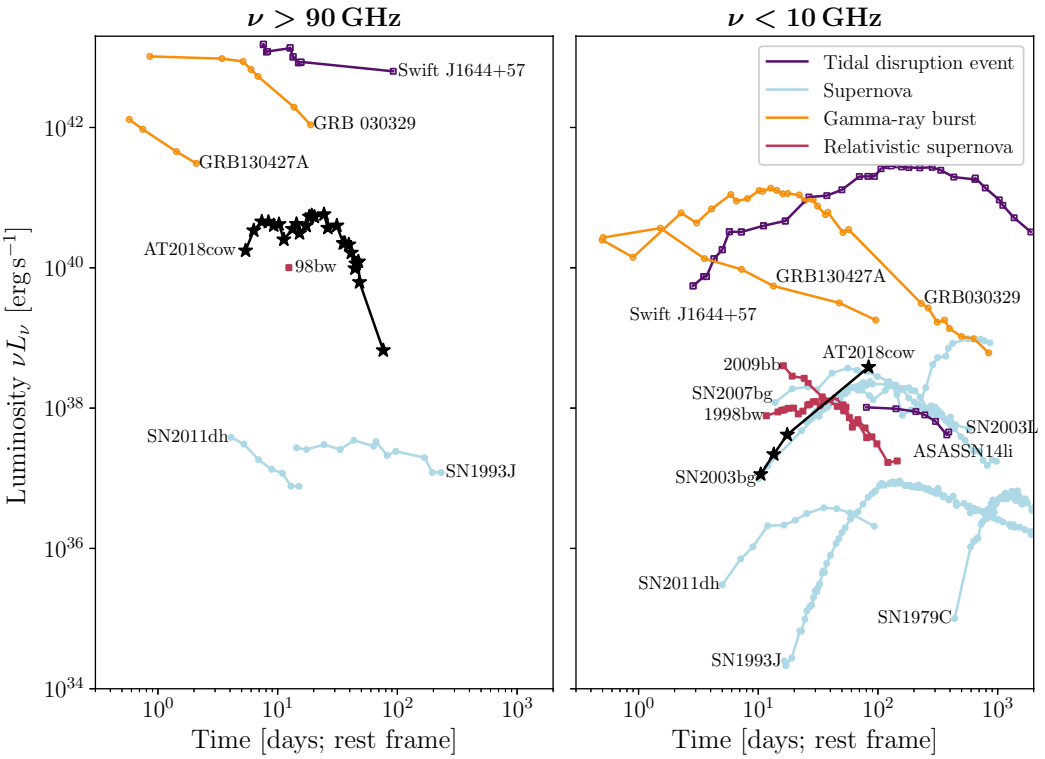

Figure 7.6: Luminosity evolution for different transients, measured at high frequencies ($\nu > 90$ GHz; left panel) and low frequencies ($\nu < 10$ GHz; right panel). Classes are GRBs (orange open circles; Berger et al., 2003; Perley et al., 2014; Sheth et al., 2003), TDEs (purple open squares; Alexander et al., 2016; Berger et al., 2012; Eftekhari et al., 2018; Zauderer et al., 2011, 2013), non-relativistic supernovae (light blue filled circles; Horesh et al., 2013; Krauss et al., 2012; Salas et al., 2013; Soderberg et al., 2005, 2006c; Weiler et al., 1986; Weiler et al., 2007), and relativistic supernovae (red filled squares; Kulkarni et al., 1998; Soderberg et al., 2010). Thus there are a number of transients measured with radio telescopes (relativistic SN 2009bb, energetic supernovae 2003L, 2003bg, and 2007bg) that could have been bright millimeter transients but were not observed at high frequencies. The late-time low-frequency AT2018cow point is from Margutti et al. (2019).

Novel Features of the Synchrotron Model Parameters

The ordering of the break frequencies, $\nu_{\rm ff} < \nu_m < \nu_c < \nu_a$, is an unusual regime for long-wavelength observations. For a relativistic shock (GRBs), the typical orderings are $\nu_a < \nu_c < \nu_m$ (the fast cooling regime) and $\nu_a < \nu_m < \nu_c$ (the slow cooling regime; Sari et al., 1998). For non-relativistic shocks, the ordering in most cases seems to be $\nu_a < \nu_m < \nu_c$ at measured frequencies above 1.4 GHz, but can also be $\nu_m < \nu_a < \nu_c$; ν_c is typically considered unimportant for long-wavelength observations (Nakar and Piran, 2011).

The low cooling frequency is a consequence of a large magnetic field strength, $\nu_c \propto B^{-3}$ (reduced even further for $t < 10$d by Compton cooling on the UVOIR flux, which dominates over synchrotron cooling). This in turn presumably arises from the injection of a large amount of energy into a small volume of material, consistent with the low velocity we measure. From equation 7.11 we see that B_p scales as $(\epsilon_e/\epsilon_B)^{-4/19} L_p^{-2/19} \nu_p$. Changing ϵ_B from 1/3 to 0.01 could increase ν_c by a factor of 8, still much lower than our observed frequencies. This regime is selectively probed by sub-millimeter observations, because a low ν_c (high B_p) gives rise to a ν_a that falls in this wavelength regime. We note that in the same framework, the relativistic TDE *Swift* J1644+57 (whose long-wavelength SED also peaked in the sub-mm for the first few weeks) would also have had a cooling frequency below much of the observed frequency range ($\nu_c \approx 6$ GHz).

Since ν_c is below any of our measured frequencies, the injection spectrum (the spectrum of the electrons prior to cooling) has a shallower power-law index than what we measure, $p_i = p - 1$. This suggests that $p_i \approx 2.2$ on Day 22, when $p \approx 3.2$, This is not unreasonable for Fermi acceleration from a strong shock. Typical young Galactic supernova remnants have $p = p_i = 2.4$ in the radio, flattening to $p \sim 2$ at higher frequencies (Urošević, 2014).

7.5 Origin of the X-ray Emission and Emergence of a Compact Source

During the plateau phase, the fluence in the *Swift*/XRT bands is $\int F_X dt \approx 1.7 \times 10^{-5}$ erg cm^{-2}. Integrating the *Swift*/XRT light curve until $\Delta t = 22$ d, we find 7×10^{48} erg. Using the *NuSTAR* spectra index $\alpha = 0.5$, extrapolating this to 100 keV would increase this energy by a factor of three.

The total X-ray energy emitted in the first three weeks is thus greater than the total energy in the shock inferred from radio observations on Day 22, $U \approx 4 \times 10^{48}$ erg. If a significant proportion of the X-rays are produced by IC emission, then our assumption of $\epsilon_B = \epsilon_e = 1/3$ clearly results in an underestimate of the total energy, and an assumption of $\epsilon_B = 0.01$ would be more appropriate. As shown in Figure 7.4, U would be increased by a factor of 9 with the assumption $\epsilon_B = 0.01$ and $\epsilon_e = 0.1$, just barely comparable to the total energy emitted in X-rays.

The luminosity of the UV/optical/IR (UVOIR) source declines $\propto t^{-\beta}$, where $\beta \approx 2.5$ (Perley et al., 2019). Assuming a constant expansion speed for the shock of $0.13c$ (see Table 7.3 and related discussion in Section 7.3) the photon energy density of the UVOIR source is

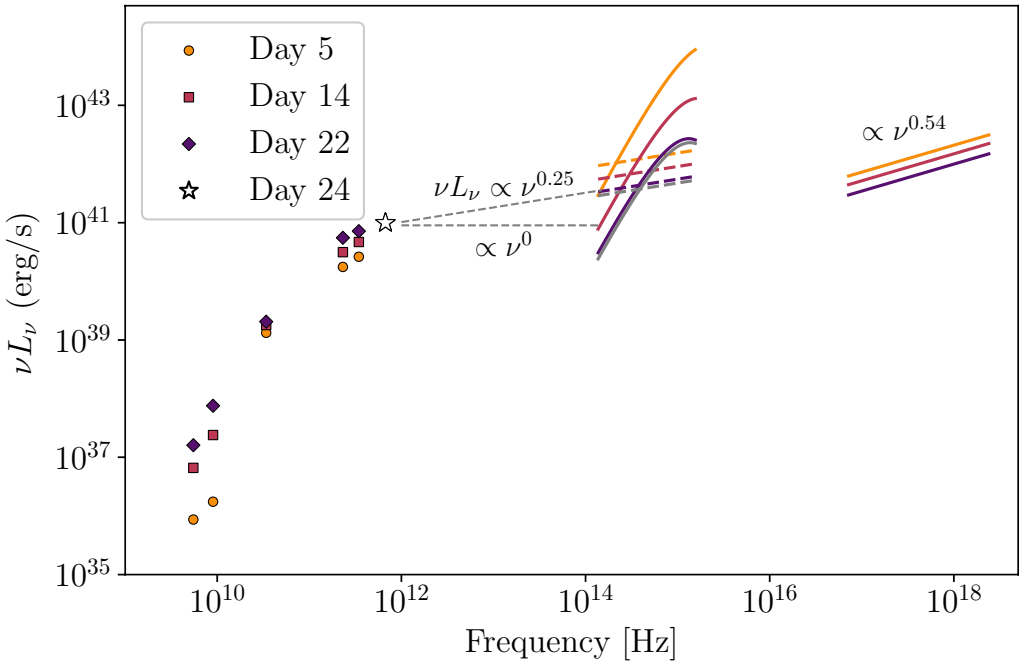

Figure 7.7: The full radio to X-ray SED. Since the ATCA data vary smoothly over the course of our observations, we fit a power law to the existing light curves (see Figure 7.1) and plot the values for the given day at 5.5 GHz, 9 GHz, and 34 GHz. For the SMA data, we interpolate the spectrum for the given day and plot the value at 231.5 GHz and 345 GHz. We plot the ALMA data as measured, including the single Band 9 measurement (white star) which seems to show an excess above the other radio data. We plot the best-fit blackbody and nonthermal component from Perley et al. (2019), and show that the nonthermal component could be an extension of the excess seen in Band 9 on Day 24. We plot the *Swift*/XRT data as follows: we interpolate the light curves to estimate the integrated 0.3–10 keV flux at the given epoch. We use the geometric mean of (0.3 keV, 10 keV) and the spectral index $\nu^{0.54}$ to solve for the normalization coefficient for the spectrum. We display the spectrum across the full XRT range.

$$u_{\rm ph} = \frac{L_{\rm UVOIR}(T)}{c4\pi R(t)^2} = 5.2 \left(\frac{t}{10\,{\rm d}}\right)^{-9/2} \left(\frac{\epsilon_e}{\epsilon_B}\right)^{2/19} {\rm erg\,cm^{-3}}. \tag{7.24}$$

Assuming that the magnetic field pressure scales with the ram pressure of the shock ($\rho_1 v_1^2$) and assuming $\rho \propto r^{-2}$, from equation 7.11, the magnetic energy density $u_B = 7.4(t/10\,{\rm d})^{-2}(\epsilon_B/\epsilon_e)^{8/19}\,{\rm erg\,cm^{-3}}$. For $\epsilon_B = 0.01$ and $\epsilon_e = 0.1$,

$$\frac{u_{\rm ph}}{u_B} = 2\left(\frac{t}{10{\rm d}}\right)^{-2.5}, \tag{7.25}$$

with only a rather weak dependence on the epsilons. This ratio is equal to unity around $t = 13$ d, marking the transition from a regime dominated by Compton cooling to a regime dominated by synchrotron cooling.

This ratio is much lower than the observed ratio $L_X/L_{\rm radio} \gtrsim 30$, and the X-ray spectral index is also substantially flatter than the radio spectral index. We conclude that the X-ray emission during the plateau phase does not naturally arise from IC scattering of the UVOIR source by the electrons in the post-shocked region (which also generate the radio to sub-millimeter emission via synchrotron radiation): IC from the radio-mm emitting region alone underpredicts the X-ray luminosity, predicts an X-ray luminosity declining much more rapidly than observed in the first 20 days, and predicts too steep a spectrum. It also does not naturally arise from an extension of the $\alpha \approx -1.1$ radio-submm synchrotron spectrum: the X-ray emission is some 25 times brighter than that extrapolation (see Figure 7.7), and has a much flatter ($\alpha \approx -0.5$) spectral index. Further speculative modelling of the source of the X-ray emission during the plateau phase is beyond the scope of this paper.

During the decline phase $t > 20$ d, the timescale of these fluctuations is around $0.05t$, while the diameter we infer for the radio-emitting region (see Section 7.3) is $\sim 2 \times 0.13t = 0.26t$. Thus the X-ray emission must arise in a different and more compact source than the radio-emitting shell.

From the plateau phase to the decline phase, the X-ray emission softens, as shown in the bottom panel of Figure 7.1 and reported by Kuin et al. (2019). From the *NuSTAR* data, measuring the flux using `cflux`, we infer a hardness ratio L_X(10–200 keV)/L_X(0.3-10 keV)$\approx$ 26 on Epoch 1, similar to what is inferred by Kuin et al. (2019) using a joint BAT/XRT analysis. From the *NuSTAR* data, we find a hardness ratio of L_X(10–200 keV)/L_X(0.3–10 keV)$\approx$4–5 on Epochs 3 and 4. This is consistent with other studies, which found negligible spectral evolution in the *Swift* 0.3–10 keV band, but significant spectral evolution at higher energies (Kuin et al., 2019; Margutti et al., 2019; Rivera Sandoval et al., 2018).

Thus these two changes, the onset of variability 5 times faster than the light-travel time across the radio-emitting shell, and the striking change in the spectrum, lead us to conclude that the beyond 20 d the X-ray emission arises from a different and more compact source than during the plateau phase—in the decline phase we are, arguably, probing regions closer to the central engine of the event.

The peculiarities of the UVOIR spectrum have led some to propose that AT2018cow

is a tidal disruption event (TDE) of a white dwarf by a $\sim 10^{5-6} M_\odot$ black hole (Kuin et al., 2019; Perley et al., 2019). Given its off-nucleus location (1.7 kpc; Perley et al., 2019) in a star-forming galaxy, and the similarities of the radio-emitting shock to those of other supernovae, it seems more natural to suppose that AT2018cow originated in a stellar cataclysm. Ultimately, however, our radio observations only require a $v \sim 0.1c$ shock wave propagating into a dense medium, which could very plausibly arise in both TDE and supernova models. The radio observations do little to distinguish them. In either picture, the striking late-time change in the X-ray behavior suggests the emergence of a central engine. In the TDE case, this could be an accretion disk around a black hole. In the stellar explosion case, this could be a natal black hole accreting (fall-back) matter from the debris, or a magnetar. The emergence could then be due to a channel between the interior and the surface opened up by a collimated outflow (a "jet" or stifled jet's cocoon breakout; Nakar, 2015), or to gaps in the photosphere opened by Rayleigh-Taylor instabilities.

We now briefly explore the magnetar model, which has been proposed for cosmological long-duration gamma-ray bursts (e.g. Thompson et al., 2004) and superluminous supernovae (e.g. Kasen and Bildsten, 2010). Prentice et al. (2018) invoked a magnetar model to explain the UVOIR observations of AT2018cow and found a best-fit magnetic field strength of 2×10^{15} G and a best-fit spin period of 11 ms. Note that the magnetar itself need not be directly visible: the X-rays we see could be due to the emergence of bubbles of the magnetar-powered wind nebula (Kasen et al., 2016). The spin-down luminosity of a magnetar with period P is $L \propto \omega\dot{\omega}$ where $\omega = 2\pi/P$ is the angular frequency. The spin-down timescale is $\tau_c = P/2\dot{P}$. We set $\tau_c = 20$ d, $L_X = 5 \times 10^{42}$ erg s^{-1} and find $P = 50$ ms and $\dot{P} = 1.4 \times 10^{-8}$ s s^{-1}, assuming that all the spin-down power goes into X-ray production. For a constant spin-down rate, this would correspond to an initial spin period of 26 ms, similar to the result in Prentice et al. (2018) for the model fit to the *griz* light curve.

With P and $\dot{P}$ in hand, using the standard dipole formula, we find a lower limit on the magnetic field strength of 8×10^{14} G, which is consistent with the value found in Prentice et al. (2018). Our modeling of the forward shock led to a lower limit to the energy of $U \approx 10^{49}$ erg, depending on the value of ϵ_B. If this was supplied by a magnetar then the initial period of the magnetar is $\lesssim 10\,\mathrm{ms}\,(U/10^{50}\,\mathrm{erg})^{-1/2}$. We end this discussion by noting that the spin-down luminosity in the dipole model (with constant B-field) is $\propto t^{-2}$, which is roughly consistent with the slope of the decay of the X-ray light curve. This is, however, not easily distinguished from the

$\propto t^{-5/3}$ slope expected from accretion in a TDE (Phinney, 1989) or fallback (Michel, 1988).

If this is a stellar explosion, then the features in the UVOIR spectra and the rise time point to an extended progenitor (10^{14} cm; Perley et al., 2019), comparable in size to the largest red supergiants. This is not consistent with the compact, stripped stars invoked as progenitors for other classes of engine-driven explosions like GRBs and SLSNe (although see Smith et al. (2012) for a possible exception). As discussed in Perley et al. (2019) and Section 7.4, a more likely scenario is that the progenitor experienced a dramatic, abrupt episode of mass loss shortly before the explosion, and the UVOIR photosphere lies within this "brick wall" which the supernova blast wave struck and re-thermalized.

Regardless of the nature of the central engine, we have the following model: the fastest-moving ejecta races ahead at $v_1 = 0.13c$ into a dense "circum-bubble" of radius, R_b. In the post-shocked gas electrons are accelerated into a power-law spectrum and magnetic fields are amplified. We attribute decay of the resulting radio emission at $t_b = 50$ d to the fast-moving ejecta reaching the edge of this circum-bubble and infer a radius $R_b = v_1 t_b \approx 1.7\times10^{16}$ cm, and a mass of $10^{-3}\,M_\odot$. Within the radio-emitting shell is a long-lived engine which may inflate a bubble of plasma and magnetic fields (Bucciantini et al., 2007). There is also slower ejecta heated by a central source (or radioactivity) that expands and emits UVOIR radiation. The photosphere of this component recedes with time, and at early times its large Compton optical depth obscures direct emission from the vicinity of the central engine. At later times, this central region emerges.

7.6 Conclusions and Outlook

Persuasive arguments can and have been made for both supernova and tidal disruption event origins for AT2018cow. Our extensive radio through sub-millimeter observations enable us to draw definitive conclusions about the outer blast wave launched following the event, independent of the origin of the event. The blast wave is sub-relativistic ($v/c = 0.13$) and plows into a dense medium ($n_e = 3\times10^5$ cm^{-3} at $R \sim 7\times10^{15}$cm). The energy contained within this blast wave is $U \approx 10^{49\pm0.3}$ erg. In contrast to the UVOIR luminosity, which declines as $L_{UVOIR} \propto t^{-2.5}$ over the period 3d $< t <$ 20d, the mm-submm and X-ray luminosities are both relatively constant over the same period (with $\sim 50\%$ variations over timescales of a few days, comparable to the light-travel time across the radio-emitting shell, $t_{lc} = 2vt/c = 0.26t$;

see Figure 7.1).

The initially attractive idea of attributing the X-rays to IC scattering of the rapidly declining flux of UVOIR photons by relativistic electrons (which give rise to the radio and sub-millimeter flux) is not naturally consistent with the slow decline of the X-ray and radio-submm flux, the X-ray luminosity, or the X-ray spectral index. Thus we are forced to invoke an additional source of X-ray emission during both the $t < 20$d plateau phase, and during the decline phase after 20 days, when the X-rays begin to fade and show dramatic variations now on timescales several times *shorter* than the light-travel time across the radio-emitting shell. These are suggestive of power from a central engine, which could be consistent with either a stellar explosion or a TDE. Future X-ray monitoring may be useful in differentiating between central engine models; in particular, a power-law decay (t^{-2}) is a distinct signature of the magnetar model, although difficult in practice to distinguish from the $t^{-5/3}$ expected from fall-back or a tidal disruption event.

The radio source is remarkable even on purely observational grounds. The peak radio luminosity (nearly 10^{41} erg s^{-1}) greatly exceeds that of the most radio-luminous supernovae and 'normal' TDEs, and is surpassed only by relativistic jetted transients (GRBs and TDEs). The source remains luminous at sub-millimeter wavelengths for nearly a month, with a self-absorption frequency $\nu_a \sim 100\,\mathrm{GHz}$ at $\Delta t \approx 22\,\mathrm{d}$.

The source is strongly detected at nearly a terahertz (ALMA Band 9; 671 GHz) even three weeks post discovery. We note that the Band 9 flux is higher than the extrapolation based from lower frequency bands (Figure 7.3, middle panel), and intriguingly connects to the NIR non-thermal component suggested by Perley et al. (2019). However, we readily admit that the apparent excess in the Band 9 flux is only 2σ, and also note that the case for the NIR non-thermal component is not secure.

Finally, it is worth re-iterating that AT2018cow is a mere 60 Mpc away. The proximity hints at an extensive population of which AT2018cow is the prototype. The key distinction between AT2018cow and other fast transients is the strong millimeter and sub-millimeter emission. In general, it is apparent from Figure 7.5 that an energetic shock propagating into a dense medium will exhibit strong millimeter emission during the first weeks. Many other supernovae would likely have had bright emission at mm-submm wavelengths, had they been observed early at those wavelengths. Combining velocities measured at very early times at such short wavelengths, with much later observations at low frequencies could reveal the slowing of the shock associated with the transition from free expansion to the Sedov phase, constraining the total

energy in relativistic ejecta. Taken together, these two developments, given that we are now squarely in the era of industrial optical time domain astronomy (e.g. PS-1, PS-2, ASAS-SN, ATLAS, ZTF and soon BlackGEM), argue for a high-frequency facility dedicated to the pursuit of transients.

The code used to produce the results described in this paper was written in Python and is available online in an open-source repository[8].

7.7 Appendix

ALMA Band 9 Calibration

For ALMA Band 9, due to the relatively low signal-to-noise of the data, all eight spectral windows were combined to derive a combined phase solution, which was then mapped to each individual spectral window. As a result, no in-band analysis of the spectral index was done and a single flux value was derived for the Band 9 imaging. When fitting a Gaussian function to the Band 9 image, the source is represented as a point-source, suggesting that the image is of good enough quality to derive a meaningful flux densities. A phase-only self-calibration did not provide good solutions, it decreased the phase coherence, and it resulted in an image that could no longer be fitted with a point-source. Therefore, we did not apply a self-calibration to the Band 9 data. To verify that changing weather conditions did not affect the phase coherence in the data, we split the data in three different time-bins and imaged each time-bin separately. The change in flux density between the different time-bins was within 6%. Similarly, imaging the data from the short, intermediate and long baselines by splitting the data in three bins in uv-range (12−90m, 90−170m and 170−312m) showed a difference in flux density <13%, despite the sparser antenna distribution and poor uv-coverage in the long-baseline bin. Also, the XX and YY polarization images were similar to within 3%. To examine the reliability of the absolute flux calibration of the Band 9 data, we imaged the two secondary calibrators, the quasars J1540+1447 and J1606+1814, using the same flux and bandpass calibrator as for AT2018cow. Figure 7.8 shows that the Band 9 flux densities of these two secondary calibrators are in reasonable agreement with values from the ALMA calibrator catalog in the lower bands if there is no spectral curvature, although uncertainties in absolute flux calibration may have led us to slightly overpredict our derived Band 9 values. In all, our tests are consistent with the ALMA Band 9 flux density being accurate to within a 20% uncertainty, which is standard for high-frequency ALMA observations.

[8] https://github.com/annayqho/AT2018cow

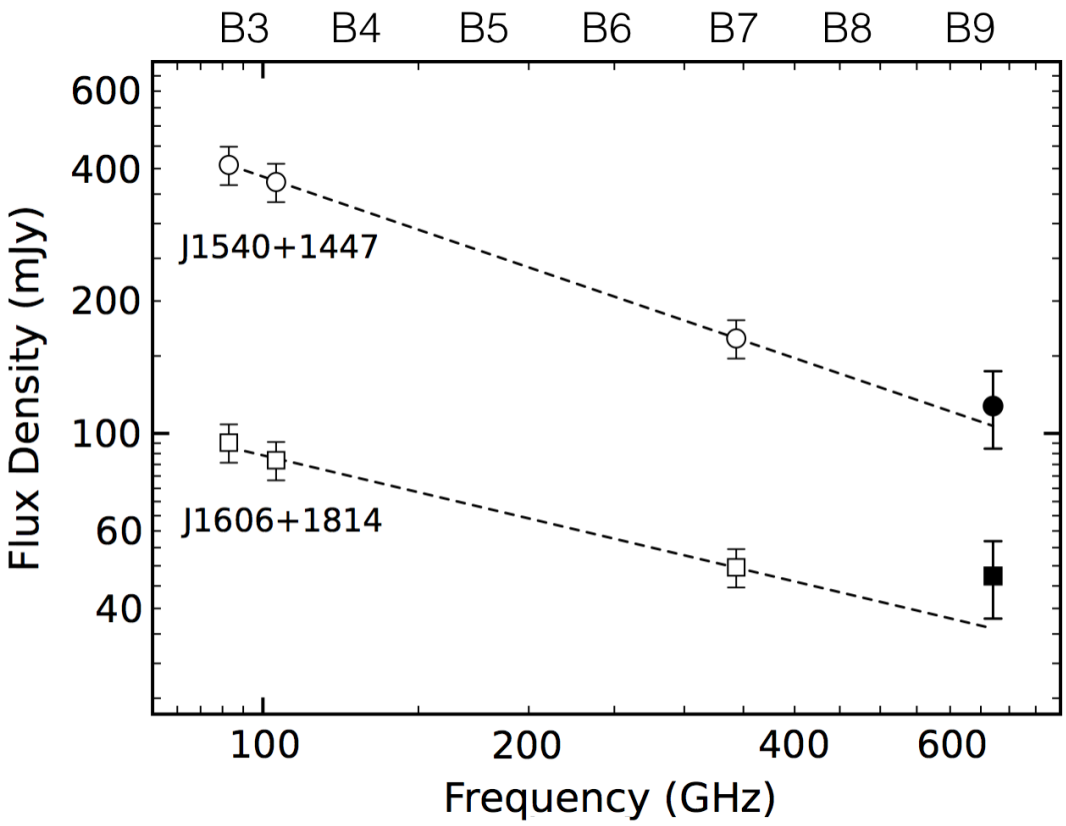

Figure 7.8: ALMA flux measurements of secondary calibrators J1540+1447 and J1606+1814, validating the absolute flux calibration of the Band 9 data. The solid symbol shows our ALMA Band 9 measurement on 10 July 2018. The open symbols represent the estimated flux densities in Bands 3 and 7 on July 10, derived by interpolating between archival values measured by ALMA on 18 May and 9 Aug 2018. Error bars represent 10% uncertainties for the archival data and 20% for our measured Band 9 data. The straight dashed lines have been added for purpose of visualization and do not represent an actual fit to the data. ALMA bands B3–B9 are shown at the top for reference.

Full SMA Light Curves

Figure 7.9 shows the full set of SMA light curves, grouped by frequency.

Selection of Peak Frequency and Peak Luminosity for Other Transients

- **GRB 130427A** (z = 0.340): For Figure 7.6, we use the 93 GHz light curve and 5.1 GHz light curve from Perley et al. (2014).

- **GRB 030329** (z = 0.1686): For Figure 7.6, we use the 250 GHz light curve at high frequencies (Sheth et al., 2003), and at low frequencies the 8.5 GHz and 2.3 GHz light curves from Berger et al. (2003) and van der Horst et al. (2008)

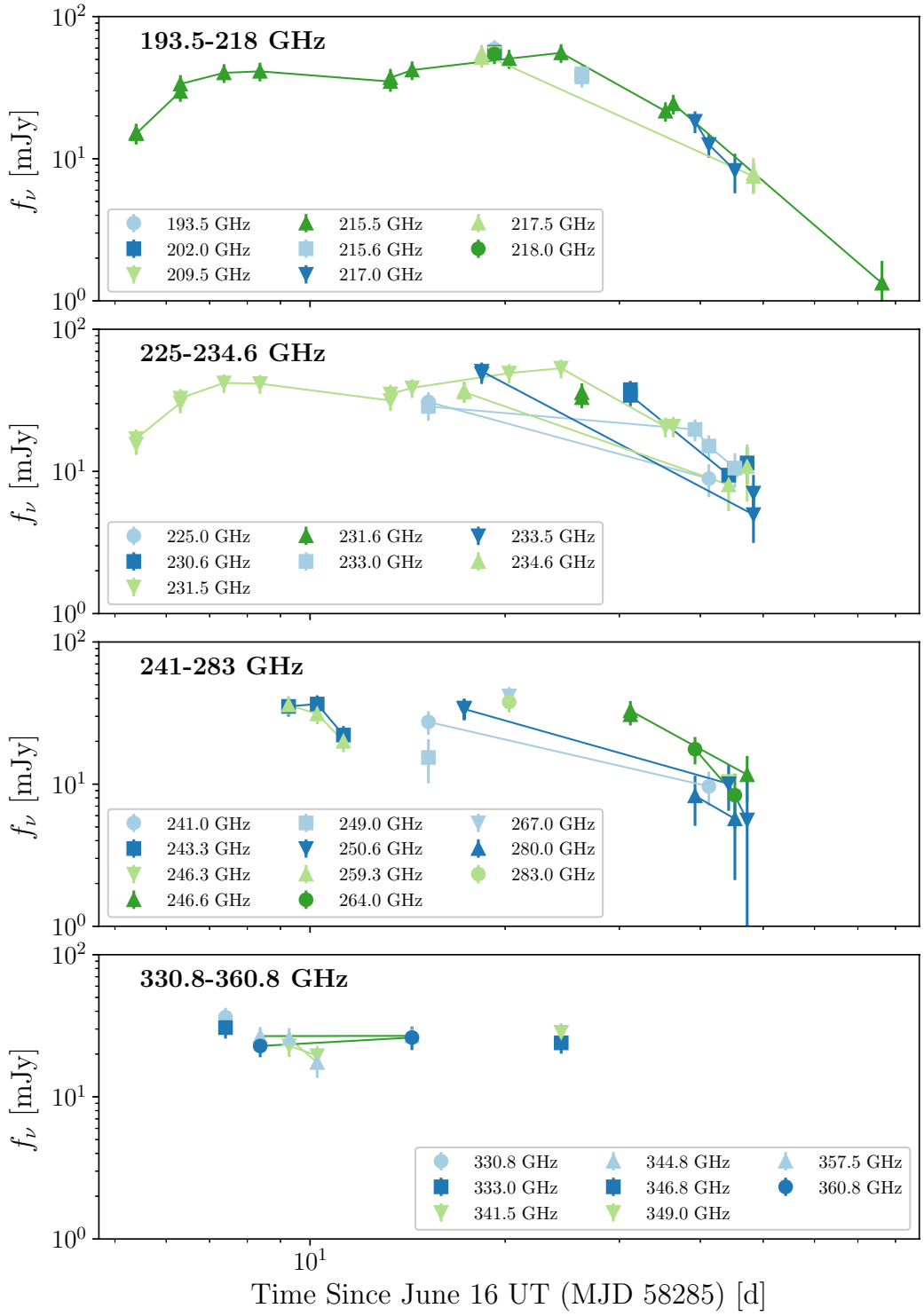

Figure 7.9: Full SMA light curves of AT2018cow for each individual frequency tuning

respectively.

- **SN 2009bb** ($d = 40$ Mpc): For Figures 7.4 and 7.5, we use the report in Soderberg et al. (2010) that from their first spectrum at $\Delta t = 20$ d, they infer $\nu_p = 6$ GHz and $L_p \approx 3.6 \times 10^{28}$ erg s^{-1} Hz^{-1}. For Figure 7.6, we use the 8.5 GHz light curve from Soderberg et al. (2010).

- **SN 1998bw** ($d = 38$ Mpc): For Figures 7.4 and 7.5, we use the report in Kulkarni et al. (1998) that on Day 10 the peak flux is 50 mJy at 10 GHz. For Figure 7.6, we show the single 150 GHz measurement by SCUBA and the 2.3 GHz light curve from Kulkarni et al. (1998).

- **SN 2006aj** ($z = 0.03345$): For Figures 7.4 and 7.5, we use the report in Soderberg et al. (2006b) that at 5 d the radio spectrum peaks near 4 GHz. They do not report the peak luminosity, so we use the reported flux of 4.86 GHz at 5 d, which is 328 μJy.

- **SN 2010bh** ($z = 0.0593$): For Figures 7.4 and 7.5, we use the report in Margutti et al. (2013) that at 30 d, $\nu_a \approx 5$ GHz and $F_{\nu,a} \approx 130\,\mu$Jy.

- **PTF 11qcj** ($z = 0.0287$): For Figures 7.4 and 7.5, we use the report in Corsi et al. (2014) that the peak luminosity at 5 GHz was 7×10^{28} erg s^{-1} Hz^{-1} at 10 d.

- **SN 2011dh** ($d = 8.03$ Mpc): For Figure 7.6, we use the 107 GHz and 93 GHz light curves at high frequencies (Horesh et al., 2013) and the 8.5 GHz and 6.7 GHz light curves at low frequencies (Horesh et al., 2013; Krauss et al., 2012).

- **SN 2007bg** ($d = 152$ Mpc): For Figures 7.4 and 7.5, we use the report in Salas et al. (2013) that in Phase 1 of the explosion, the peak luminosity was 4.1×10^{28} erg s^{-1} Hz^{-1} at 8.46 GHz on Day 55.9. For Figure 7.6, we use the 8.5 GHz light curve from Salas et al. (2013).

- **SN 2003L** ($d = 92$ Mpc): For Figures 7.4 and 7.5, we use the report in Soderberg et al. (2005) that at 30 days, the peak flux density was 3.2 mJy at 22.5 GHz. For Figure 7.6, we use the 8.5 GHz light curve because it is the best-sampled over the largest range of time.

- **SN 2003bg** ($d = 19.6$ Mpc): For Figures 7.4 and 7.5, we use the report in Soderberg et al. (2006c) that the peak flux density is 85 mJy at 22.5 GHz on

Day 35. For Figure 7.6, we use the 8.5 GHz light curve from Soderberg et al. (2006c).

- **SN 1993J** (d = 3.63 Mpc): For Figure 7.6, we use the 5 GHz light curve at low frequencies and the 99.4 GHz light curve at high frequencies (Weiler et al., 2007).

- **SN 1988Z** (z = 0.022): For Figures 7.4 and 7.5, we use the report in van Dyk et al. (1993) that the 6 cm maximum flux density was 1.90 mJy, at 1253 d after the explosion.

- **SN 1979C** (20 Mpc): For Figure 7.6, we use the 1.4 GHz light curve at low frequencies and the 99.4 GHz light curve at high frequencies (Weiler et al., 1986; Weiler et al., 1991). For Figures 7.4 and 7.5, we simply use the peak of the 1.4 GHz light curve, which is roughly 12 mJy at 1400 d.

- ***Swift* J1644+57** (z = 0.354): For Figures 7.4 and 7.5, we use the reported ν_p, F_p on Day 15 (corrected to Day 18 in Eftekhari et al. (2018)). For Figure 7.6, we use the 225 GHz and 230 GHz light curves from the SMA (Berger et al., 2012; Zauderer et al., 2011), adding 3.04 days to the Zauderer et al. (2011) points because (as described in Eftekhari et al., 2018) subsequent analysis of the BAT data revealed emission earlier than had been previously noticed. We use 4.9 GHz data from Berger et al. (2012), Zauderer et al. (2013), and Eftekhari et al. (2018).

The authors are grateful to the staff at the SMA, the CSIRO Astronomy and Space Science (CASS), and ALMA for rapidly scheduling and executing the observations and reducing the data. It is a pleasure to thank John Carpenter for his guidance and his assistance with the ALMA observations. Thank you to Dale Frail, Raffaella Margutti, and Roger Chevalier for providing feedback on the manuscript, and Gregg Hallinan, Dillon Dong, and Jacob Jencson for helpful discussions. Finally, we would like to thank the anonymous referee for thoughtful suggestions that greatly improved the clarity of the paper.

A.Y.Q.H. was supported by a National Science Foundation Graduate Research Fellowship under Grant No. DGE-1144469. This work was supported by the GROWTH project funded by the National Science Foundation under PIRE Grant No 1545949. This research was funded in part by the Gordon and Betty Moore Foundation through

Grant GBMF5076 to ESP, and A.Y.Q.H., E.S.P., and S.R.K. benefited from interactions with Dan Kasen, David Khatami, and Eliot Quataert funded by that grant. TM acknowledges the support of the Australian Research Council through grant FT150100099. DD is supported by an Australian Government Research Training Program Scholarship.

The Submillimeter Array is a joint project between the Smithsonian Astrophysical Observatory and the Academia Sinica Institute of Astronomy and Astrophysics and is funded by the Smithsonian Institution and the Academia Sinica. The Australia Telescope Compact Array is part of the Australia Telescope National Facility which is funded by the Australian Government for operation as a National Facility managed by CSIRO. This paper makes use of the following ALMA data: ADS/JAO.ALMA#2017.A.00047.T. ALMA is a partnership of ESO (representing its member states), NSF (USA) and NINS (Japan), together with NRC (Canada), MOST and ASIAA (Taiwan), and KASI (Republic of Korea), in cooperation with the Republic of Chile. The Joint ALMA Observatory is operated by ESO, AUI/NRAO and NAOJ. The National Radio Astronomy Observatory is a facility of the National Science Foundation operated under cooperative agreement by Associated Universities, Inc. This work made use of data supplied by the UK Swift Science Data Centre at the University of Leicester.

Chapter 8

THE KOALA: A FAST BLUE OPTICAL TRANSIENT WITH LUMINOUS RADIO EMISSION FROM A STARBURST DWARF GALAXY AT $z = 0.27$

Ho, A. Y. Q. et al. (2020). "The Koala: A Fast Blue Optical Transient with Luminous Radio Emission from a Starburst Dwarf Galaxy at z = 0.27". In: *ApJ* 895.1, p. 49. DOI: 10.3847/1538-4357/ab8bcf. arXiv: 2003.01222 [astro-ph.HE].

Anna Y. Q. Ho[1], Daniel A. Perley[2], S. R. Kulkarni[1], Dillon Z. J. Dong[1], Kishalay De[1], Poonam Chandra[3], Igor Andreoni[1], Eric C. Bellm[4], Kevin B. Burdge[1], Michael Coughlin[5], Richard Dekany[6], Michael Feeney[6], Dmitry D. Frederiks[7], Christoffer Fremling[1], V. Zach Golkhou[4,8,9], Matthew J. Graham[1], David Hale[6], George Helou[10], Assaf Horesh[11], Mansi M. Kasliwal[1], Russ R. Laher[10], Frank J. Masci[10], A. A. Miller[12,13], Michael Porter[6], Anna Ridnaia[7], Ben Rusholme[10], David L. Shupe[10], Maayane T. Soumagnac[14,15], Dmitry S. Svinkin[7]

[1]Cahill Center for Astronomy and Astrophysics, California Institute of Technology, Pasadena, CA 91125, USA
[2]Astrophysics Research Institute, Liverpool John Moores University, IC2, Liverpool Science Park, 146 Brownlow Hill, Liverpool L3 5RF, UK
[3]National Centre for Radio Astrophysics, Tata Institute of Fundamental Research, PO Box 3, Pune, 411007, India
[4]DIRAC Institute, Department of Astronomy, University of Washington, 3910 15th Avenue NE, Seattle, WA 98195, USA
[5]School of Physics and Astronomy, University of Minnesota, Minneapolis, Minnesota 55455, USA
[6]Caltech Optical Observatories, California Institute of Technology, Pasadena, CA 91125
[7]Ioffe Institute, Politekhnicheskaya 26, St. Petersburg 194021, Russia
[8]The eScience Institute, University of Washington, Seattle, WA 98195, USA
[9]Moore-Sloan, WRF Innovation in Data Science, and DIRAC Fellow
[10]IPAC, California Institute of Technology, 1200 E. California Blvd, Pasadena, CA 91125, USA
[11]Racah Institute of Physics, The Hebrew University of Jerusalem, Jerusalem 91904, Israel
[12]Center for Interdisciplinary Exploration and Research in Astrophysics and Department of Physics and Astronomy, Northwestern University, 1800 Sherman Ave, Evanston, IL 60201, USA
[13]The Adler Planetarium, Chicago, IL 60605, USA
[14]Lawrence Berkeley National Laboratory, 1 Cyclotron Road, Berkeley, CA 94720, USA
[15]Department of Particle Physics and Astrophysics, Weizmann Institute of Science, Rehovot 76100, Israel

Abstract

We present ZTF18abvkwla (the "Koala"), a fast blue optical transient discovered in the Zwicky Transient Facility (ZTF) One-Day Cadence (1DC) Survey.

ZTF18abvkwla has a number of features in common with the groundbreaking transient AT 2018cow: blue colors at peak ($g - r \approx -0.5$ mag), a short rise time from half-max of under two days, a decay time to half-max of only three days, a high optical luminosity ($M_{g,\mathrm{peak}} \approx -20.6$ mag), a hot ($\gtrsim 40,000$ K) featureless spectrum at peak light, and a luminous radio counterpart. At late times ($\Delta t > 80$ d) the radio luminosity of ZTF18abvkwla ($\nu L_\nu \gtrsim 10^{40}\,\mathrm{erg\,s^{-1}}$ at 10 GHz, observer-frame) is most similar to that of long-duration gamma-ray bursts (GRBs). The host galaxy is a dwarf starburst galaxy ($M \approx 5 \times 10^8\,M_\odot$, SFR $\approx 7\,M_\odot\,\mathrm{yr}^{-1}$) that is moderately metal-enriched ($\log[\mathrm{O/H}] \approx 8.5$), similar to the hosts of GRBs and superluminous supernovae. As in AT2018cow, the radio and optical emission in ZTF18abvkwla likely arise from two separate components: the radio from fast-moving ejecta ($\Gamma\beta c > 0.38c$) and the optical from shock-interaction with confined dense material ($< 0.07\,M_\odot$ in $\sim 10^{15}$ cm). Compiling transients in the literature with $t_{\mathrm{rise}} < 5$ d and $M_{\mathrm{peak}} < -20$ mag, we find that a significant number are engine-powered, and suggest that the high peak optical luminosity is directly related to the presence of this engine. From 18 months of the 1DC survey, we find that transients in this rise-luminosity phase space are at least two to three orders of magnitude less common than CC SNe. Finally, we discuss strategies for identifying such events with future facilities like the Large Synoptic Survey Telescope, and prospects for detecting accompanying X-ray and radio emission.

8.1 Introduction

Historically, the cadence of optical time-domain surveys was tuned to detecting Type Ia supernovae (SNe), whose optical light curves rise from first light to peak in 15–20 days (Miller et al., 2020). Recognizing that this observing strategy resulted in "gaps" in timescale-luminosity phase-space, surveys such as the Palomar Transient Factory (Law et al., 2009; Rau et al., 2009) and the Pan-STARRS1 Medium Deep Survey (Drout et al., 2014) sought to systematically chart the landscape of short-timescale (< 10 day) phenomena. These efforts delineated populations of fast transients spanning many orders of magnitude in peak luminosity, from faint calcium-rich transients (Kasliwal et al., 2012) to luminous relativistic explosions (Cenko et al., 2013).

A population of particular recent interest is "fast evolving luminous transients" (Rest et al., 2018) or "fast blue optical transients" (Margutti et al., 2019). A consistent definition of this "class" does not yet exist; these terms typically refer to transients with rise times and peak luminosities too fast and too luminous, respectively, to be

explained by the radioactive decay of ^{56}Ni. Although they likely arise from a variety of progenitors, fast-luminous transients are primarily found in star-forming galaxies (Drout et al., 2014; Pursiainen et al., 2018) and therefore are thought to represent a variety of poorly understood endpoints of massive-star evolution. As summarized in Kasen (2017), fast and luminous light curves may be powered by shock breakout or shock-cooling emission from material that is closely confined to the progenitor star at the time of explosion, or alternatively by a "central engine": accretion onto a black hole, or the rotational spindown of a magnetar.

Most fast-luminous optical transients have been found in archival searches of optical-survey data, including PS1 (Drout et al., 2014), the Dark Energy Survey (Pursiainen et al., 2018), Kepler (Rest et al., 2018), and the Supernova Legacy Survey (Arcavi et al., 2016). A handful have been discovered while the transient was still active, enabling prompt follow-up observations. For example, spectroscopic monitoring of the fast-luminous transients iPTF16asu and ZTF18abukavn (SN 2018gep) revealed that as the optical emission faded, the spectrum developed features typical of broad-lined Ic SNe (Ho et al., 2019d; Wang et al., 2019; Whitesides et al., 2017).

The discovery of the fast-luminous transient AT2018cow (Prentice et al., 2018) generated considerable excitement because of its proximity (z = 0.0141) and therefore the opportunity for detailed observations. AT2018cow had several remarkable features: (1) near-relativistic ejecta velocities at early times, from optical spectroscopy (Perley et al., 2019); (2) luminous and fast-varying X-ray emission suggesting an exposed central engine (Ho et al., 2019c; Margutti et al., 2019; Rivera Sandoval et al., 2018); (3) high-velocity emission lines of hydrogen and helium emerging at late times (Perley et al., 2019); (4) no second peak that would indicate a significant role for radioactive ejecta in powering the light curve (Perley et al., 2019); and (5) luminous submillimeter emission indicating a large explosion energy injected into a shell of very dense material (Ho et al., 2019c; Huang et al., 2019). Despite extensive observations across the electromagnetic spectrum, the progenitor of AT2018cow is unknown. One suggestion is a massive-star explosion that resulted in the formation of an accreting black hole or magnetar, which drove a mildly relativistic jet or wind (Ho et al., 2019c; Margutti et al., 2019; Perley et al., 2019). Other suggestions include an electron-capture SN (Lyutikov and Toonen, 2019) and a tidal disruption event (TDE; Kuin et al. 2019; Perley et al. 2019; Vinkó et al. 2015). If AT2018cow was a massive-star explosion, the dense confined CSM points to eruptive mass-loss shortly before core-collapse (Ho et al., 2019c), and indeed Fox and Smith (2019)

pointed out the similarity between AT2018cow and interaction-powered Type Ibn SNe.

Here we report the discovery of ZTF18abvkwla[1], a fast-rising luminous optical transient at $z = 0.27$ in Zwicky Transient Facility (ZTF) data.[2] In §8.2 we present the key observational features of ZTF18abvkwla—a rest-frame g-band light curve similar to that of AT2018cow, a luminous radio counterpart similar to gamma-ray burst (GRB) afterglows, and a starburst dwarf host galaxy. In §8.3 we compare ZTF18abvkwla to transients in the literature that have $t_{\rm rise} < 5$ d and $M < -20$ mag, where $t_{\rm rise}$ is defined from 0.75 mag below peak to peak (half-max to max in flux space). We use a cut of $M < -20$ mag to exclude "normal" Type Ibn SNe (Hosseinzadeh et al., 2017) and we exclude the hundreds of optical afterglows discovered in GRB follow-up observations (Kann et al., 2010). The comparison sample is shown in Table 8.1 and Figure 8.1. Note that the Table 8.1 transients have thermal spectra at peak, unlike GRB afterglows which arise from synchrotron radiation.

Table 8.1: Transients in the literature with $t_{\rm rise} < 5$ d and $M < -20$ mag. Timescales are presented in rest-frame and measured using the light curve that most closely matches rest-frame g. Luminosity is corrected for Galactic extinction, assuming zero host-galaxy extinction in all cases except for iPTF15ul and SN 2011kl. SN 2011kl was associated with GRB 111209A, and the afterglow emission has been subtracted.

Name	Redshift	$M_{g,\rm max}$	$t_{\rm rise}$ days	$t_{\rm fade}$ days	Ref
Dougie	0.19	-23.03 ± 0.13	3.92 ± 0.14	9.69 ± 1.19	[1]
SN 2011kl	0.677	-20.31 ± 0.13	4.97 ± 1.20	17.70 ± 5.82	[2,3]
SNLS04D4ec	0.593	-20.26 ± 0.03	< 3.81	8.60 ± 0.43	[4]
SNLS05D2bk	0.699	-20.39 ± 0.02	2.90 ± 0.06	12.75 ± 0.78	[4]
SNLS06D1hc	0.555	-20.28 ± 0.03	4.59 ± 0.06	12.35 ± 0.45	[4]
iPTF15ul	0.066	-21.2 ± 0.3	1.53 ± 0.05	3.72 ± 0.08	[5]
DES16X1eho	0.76	-20.39 ± 0.09	1.28–2.53	1.01 ± 0.27	[6]
iPTF16asu	0.187	-20.3 ± 0.1	1.14 ± 0.13	10.62 ± 0.55	[7]
AT2018cow	0.0141	-20.89 ± 0.06	1.43 ± 0.08	1.95 ± 0.06	[8,9]

[1] Vinkó et al. (2015), [2] Greiner et al. (2015), [3] Kann et al. (2019), [4] Arcavi et al. (2016), [5] Hosseinzadeh et al. (2017), [6] Pursiainen et al. (2018) [7] Whitesides et al. (2017), [8] Prentice et al. (2018) [9] Perley et al. (2019)

[1] nicknamed "Koala" on account of the last four letters of its ZTF ID

[2] After the submission of our paper, Coppejans et al. (2020) published radio and X-ray observations of CSS161010, another transient in a dwarf galaxy with properties similar to AT2018cow.

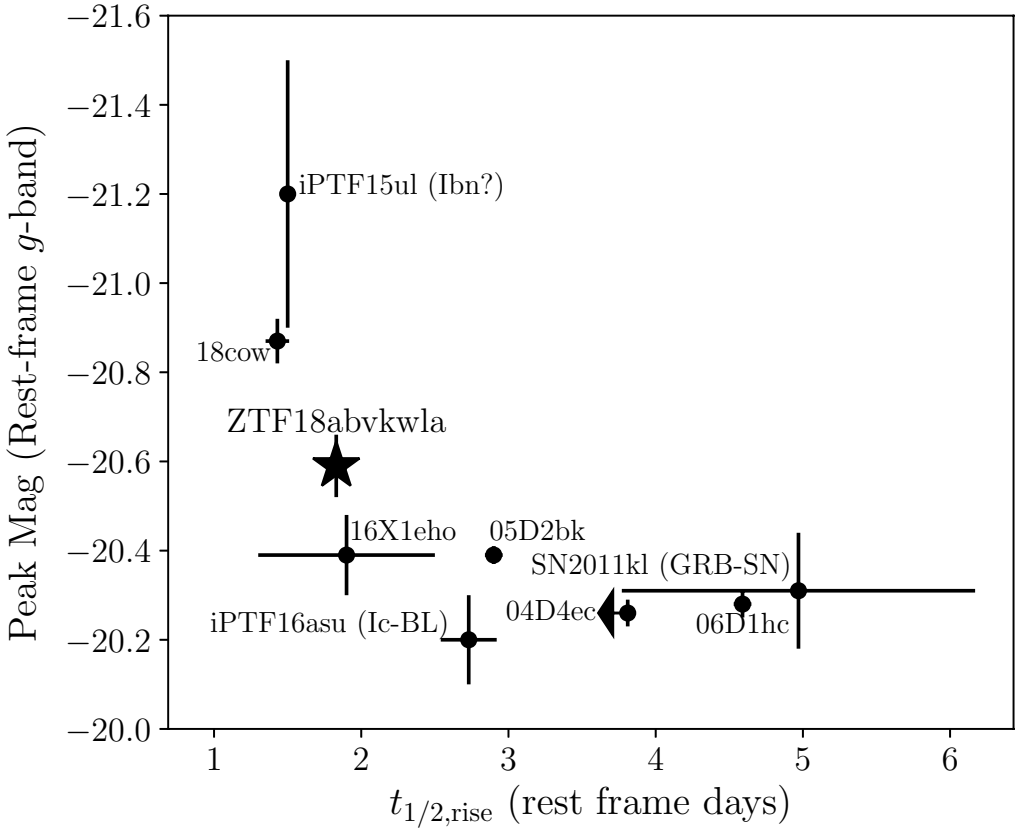

Figure 8.1: Phase-space of luminosity and rise time considered in this paper; see Table 8.1 for data sources. We do not show the transient Dougie (Vinkó et al., 2015), which had a peak absolute magnitude of −23. Note that the peak mag of iPTF15ul includes a large host-galaxy extinction correction, whereas the other sources have zero host extinction correction. Also note that SN 2011kl was associated with an ultra-long duration GRB 111209A (Kann et al., 2018), and the light-curve properties shown here reflect the afterglow-subtracted light curve (Kann et al., 2019).

In §8.4 we model the optical emission from ZTF18abvkwla as thermal emission from shock breakout in dense confined material, and in §8.4 we use the radio emission to estimate properties of the forward shock (velocity, shock energy) and the ambient medium. In §8.4, we discuss possible progenitor systems. Finally, in §8.5 we use 18 months of survey observations to estimate the rate of transients in the phase-space of Figure 8.1, and find that the rate is 2–3 times smaller than the CC SN rate.

Throughout this paper, we use a standard ΛCDM cosmology (Planck Collaboration et al., 2016) and times are reported in UT. Optical magnitudes are reported in the AB system (Oke and Gunn, 1983), and corrected for foreground Galactic extinction using reddening measurements in Schlafly and Finkbeiner (2011) and the extinction

law from Fitzpatrick (1999).

8.2 Discovery and Basic Analysis

Optical

Photometry

Since April 2018, ZTF (Bellm et al., 2019b; Graham et al., 2019) has been conducting a wide-area (2000–3000 deg^2) one-day cadence (1DC) survey in g and r (Bellm et al., 2019a). The sky coverage of the 1DC survey is shown in Figure 8.2 and a histogram of the typical time between exposures is shown in Figure 8.3.

The IPAC ZTF pipeline (Masci et al., 2019) uses the method described in Zackay et al. (2016) to generate difference images using a coadded reference image. Every 5σ point-source detection is assigned a score based on a machine learning real-bogus metric (Duev et al., 2019; Mahabal et al., 2019), and is cross-matched against external catalogs to search for resolved and extended counterparts (Tachibana and Miller, 2018). Alerts are distributed in Avro format (Patterson et al., 2019) and are filtered by the ZTF collaboration using a web-based system called the GROWTH Marshal (Kasliwal et al., 2019).

ZTF18abvkwla was discovered in an image obtained on 12 Sept 2018. The alert passed a filter designed to look for rapidly-evolving transients, and as a result we obtained a follow-up spectrum 24 hours later (§8.2). The discovery magnitude was $g = 19.73 \pm 0.16$ mag and the last non-detection was one day prior, with a limiting magnitude $g > 20.74$.

The source position was measured to be $\alpha = 02^{\mathrm{h}}00^{\mathrm{m}}15.19^{\mathrm{s}}$, $\delta = +16^{\mathrm{d}}47^{\mathrm{m}}57.3^{\mathrm{s}}$ (J2000), which is $0\farcs28 \pm 0\farcs13$ from the nucleus of a blue ($g - r = 0.32$ mag) extended source that has a photometric redshift of 0.11 (68 percentile confidence interval 0.08–0.29) in the eighth data release of LegacySurvey (DR8; Dey et al. 2019). At $z = 0.2714$ (§8.2) this offset corresponds to 1.9 ± 0.9 kpc. The host is approximately $2''$ (14 kpc) across.

The light curve (Figure 8.4; Table 8.2) has a similar timescale and peak luminosity to that of AT2018cow. In rest-frame g-band, the rise time is 1.83 ± 0.05 d, the fade time is 3.12 ± 0.22 d, and the peak magnitude is -20.59 ± 0.07 mag.

We estimate that the onset of the optical emission was around the time of the last non-detection ($t_0 = 2458372.9206$ JD) and use this as a reference epoch for the remainder of the paper.

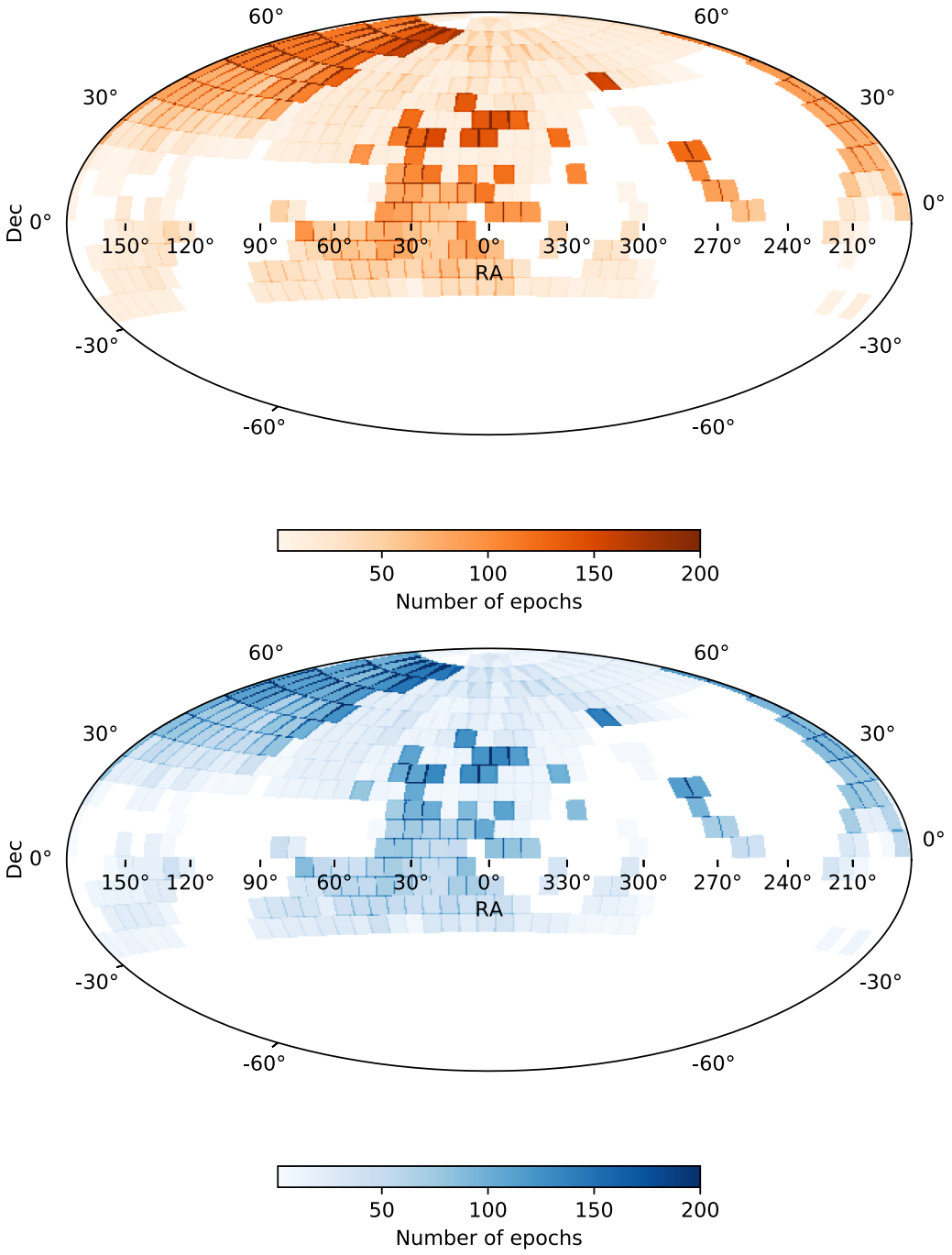

Figure 8.2: Number of epochs obtained by the ZTF one-day cadence survey from 3 April 2018 to 18 October 2019

Spectroscopy and Host Galaxy Properties

One day after discovery, we obtained a spectrum of ZTF18abvkwla using the Double Beam Spectrograph (DBSP; Oke and Gunn 1982) on the 200-inch Hale telescope at

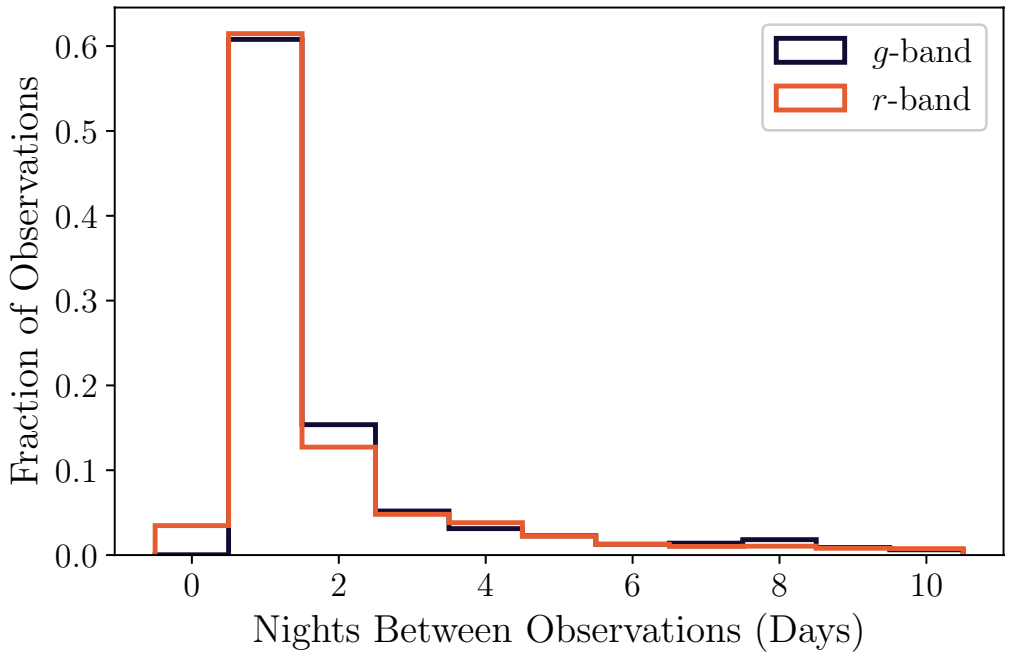

Figure 8.3: Histogram of times between successive observations of a field in the same filter for the ZTF one-day cadence survey. Intervals greater than 10 days are not shown.

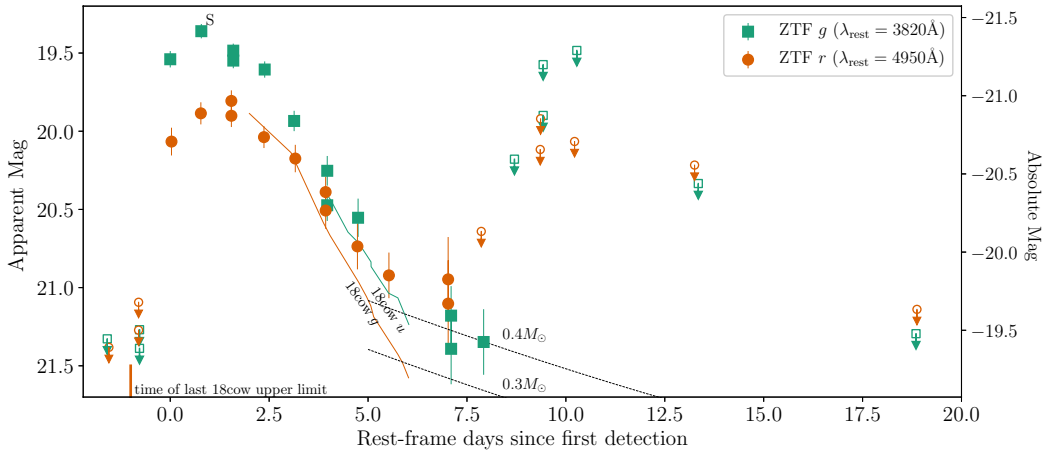

Figure 8.4: Light curve of ZTF18abvkwla in P48 g (filled green squares) and r (open orange circles) with a comparison to AT2018cow at similar rest wavelengths, both corrected for Galactic extinction. The 'S' at the top of the inset indicates the epoch of our DBSP spectrum. Dashed lines show ^{56}Ni-powered light curves for two different nickel masses.

Palomar Observatory. We used the D55 dichroic, a slit width of 1.5 arcseconds, the

Table 8.2: Optical photometry for ZTF18abvkwla from forced photometry on P48 images (Yao et al., 2019). Values have not been corrected for Galactic extinction. Phase Δt is defined from t_0, the last non-detection.

Date (MJD)	Δt	Filter	AB Mag
58372.39	−1.02	r	< 21.39
58372.42	−0.99	g	< 21.56
58373.41	0.00	g	19.71 ± 0.05
58373.45	0.04	r	20.18 ± 0.09
58374.39	0.98	r	20.00 ± 0.07
58374.41	1.00	g	19.53 ± 0.05
58375.37	1.96	r	19.92 ± 0.07
58375.37	1.96	r	20.02 ± 0.07
58375.43	2.03	g	19.65 ± 0.04
58375.43	2.03	g	19.72 ± 0.05
58376.42	3.01	r	20.15 ± 0.07
58376.44	3.04	g	19.77 ± 0.05
58377.39	3.98	g	20.10 ± 0.07
58377.43	4.02	r	20.29 ± 0.09
58378.40	4.99	r	20.50 ± 0.10
58378.40	4.99	r	20.62 ± 0.12
58378.45	5.04	g	20.64 ± 0.10
58378.45	5.05	g	20.42 ± 0.09
58379.42	6.02	r	20.85 ± 0.15
58379.44	6.04	g	20.72 ± 0.12
58380.43	7.03	r	21.04 ± 0.15
58382.34	8.93	r	21.06 ± 0.27
58382.34	8.93	r	21.22 ± 0.28
58382.43	9.03	g	21.35 ± 0.19
58382.43	9.03	g	21.56 ± 0.23
58383.48	10.07	g	21.51 ± 0.21

600/4000 blue grating, and the 316/7500 red grating. The spectrum was reduced using a PyRAF-based pipeline (Bellm and Sesar, 2016). As shown in Figure 8.5, the spectrum shows a hot blue continuum with no broad features in emission or absorption. Superimposed on the spectrum are a variety of narrow emission lines typical of a star-forming galaxy (Hα, Hβ, O III, S II, O II) at a redshift of $z = 0.2714$ plus the Mg II UV doublet in absorption at consistent redshift.

A blackbody fit to the continuum (after subtracting a host-galaxy continuum model, discussed later in this section) indicates an effective temperature $T \gtrsim 40,000$K, although we caution that it could be significantly higher as the bulk of the energy was clearly emitted in the UV (< 2750 Å in the rest frame) and we have no firm constraint

on the host-galaxy extinction. Together with the peak absolute magnitude of the g-band light curve, we derive a bolometric luminosity of $L_{\rm bol} > \nu L_\nu \sim 10^{44}\,{\rm erg\,s^{-1}}$. Assuming $T = 40,000\,{\rm K}$, the photospheric radius is $R > 2 \times 10^{14}\,{\rm cm}$. Since the peak is 2 d after first light, assuming $R(t = t_0) = 0$ gives $V > 0.04c$.

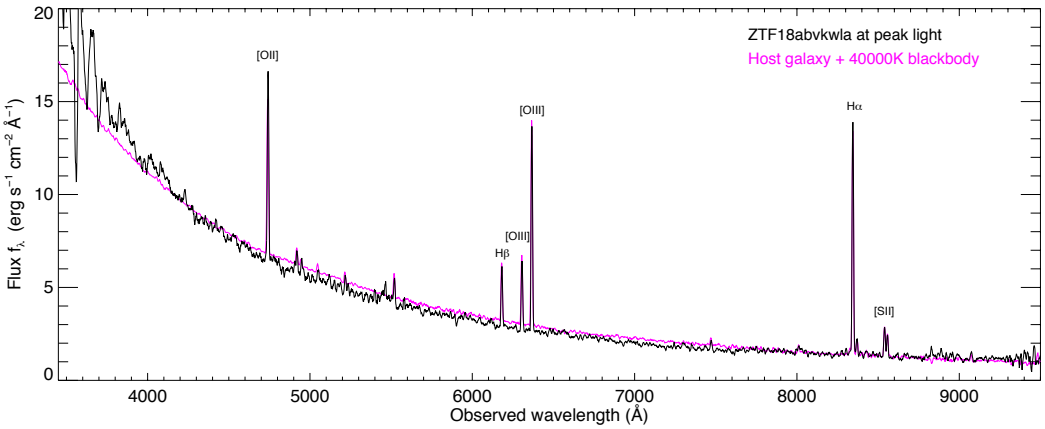

Figure 8.5: The spectrum of ZTF18abvkwla at the peak of the g-band optical light curve (black), which was 1 day after the first detection. The source is extremely hot and blue with no spectral features except those associated with the host galaxy. Overplotted in pink is a rescaled late-time spectrum of the host galaxy with a $40,000$ K blackbody added.

On 4 Jan 2019 (+115 d), we obtained a spectrum of the host galaxy of ZTF18abvkwla using the Low Resolution Imaging Spectrometer (McCarthy et al., 1998; Oke et al., 1995) on the Keck I 10-m telescope, with the 400/3400 grism in the blue camera and the 400/8500 grating in the red camera. Exposure times were 940 and 900 seconds for the blue and red camera respectively. The spectrum was reduced and extracted using `Lpipe` (Perley, 2019). The absolute calibration was established independently for each camera (red vs. blue) by calculating synthetic photometry of the output spectra in the blue and red cameras in the g and r bands, respectively, and rescaling to match the g and r photometry from SDSS DR14 (Abolfathi et al., 2018). The SDSS magnitudes (AB, converted to Pogson) are $u = 21.74 \pm 0.20\,{\rm mag}$, $g = 21.20 \pm 0.04\,{\rm mag}$, $r = 20.81 \pm 0.05\,{\rm mag}$, $i = 20.92 \pm 0.09\,{\rm mag}$, and $z = 20.52 \pm 0.20\,{\rm mag}$.

The host-galaxy spectrum (Figure 8.6) consists of a weak continuum and a series of very strong emission lines. Line fluxes were extracted using an identical procedure as in Perley et al., 2016. We first fit a model to the spectral energy distribution (SED). We used a custom IDL routine based on the templates of Bruzual and Charlot (2003) to fit the SDSS $ugriz$ photometry, including the contribution of nebular lines. As

only SDSS *ugriz* photometry is available to fit the host-galaxy SED it is difficult to constrain the nature of the stellar population of the host galaxy in detail, and we were only able to fit the simplest possible model (a continuous star-formation history). However, the stellar mass is unambiguously low ($\sim 5 \times 10^8\ M_\odot$, comparable to the SMC).

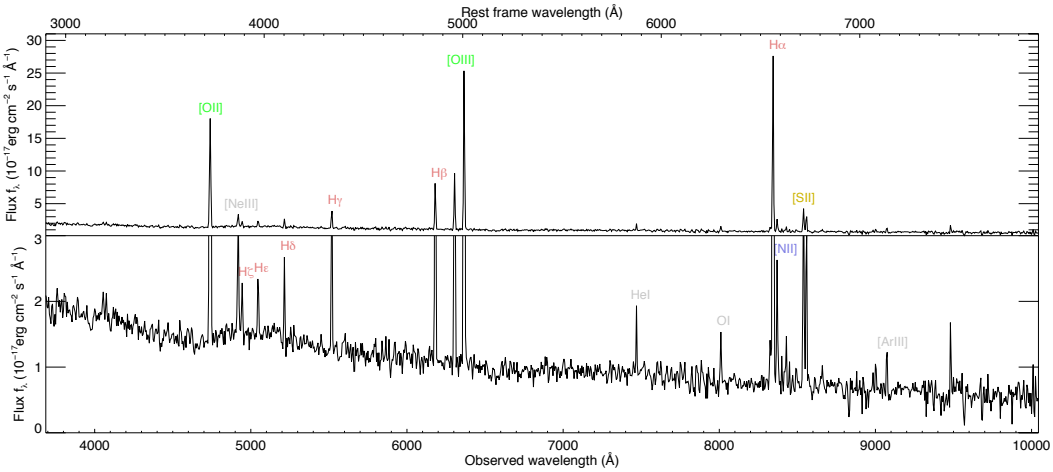

Figure 8.6: Spectrum of the host galaxy of ZTF18abvkwla. The scale on the bottom half has been zoomed in to show the galaxy continuum and weak emission lines. The feature at 9500 Å is a sky-subtraction residual.

This model was then used to produce a synthetic galaxy continuum spectrum, which was subtracted from the observed one (this correction is significant only for higher-order Balmer lines, which overlay strong galaxy absorption features). Emission line fluxes were then measured by fitting a Gaussian function to each emission line (plus a linear baseline to fit any continuum residuals). Lines that were blended or very nearby were fit in groups, and lines whose ratios are fixed from theory were tied together in fitting. A list of all measured line fluxes is given in Table 8.3.

The SED fitting and the emission-line analysis produce consistent estimates of $7\ M_\odot\ \mathrm{yr}^{-1}$ for the star-formation rate, and a very high specific star-formation rate of $\sim 10^{-8}\ \mathrm{yr}^{-1}$. This implies a stellar population dominated by young stars formed in a recent triggered star-formation burst episode.

We used the host galaxy spectrum (Figure 8.6) to calculate standard emission-line diagnostics, including metallicity estimates on a variety of scales using the Monte-Carlo code of Bianco et al. (2016). These metallicity measurements are provided in Table 8.4. The basic properties of the host galaxy are listed in Table 8.5.

Table 8.3: Host emission line fluxes and equivalent widths

Species	Wavelength	Flux	Eq. Width
(Å)	(erg cm^{-2}s^{-1})	(Å)	
Hα	6562.82	214.74 ± 2.71	205.9 ± 7.0
Hβ	4861.33	57.57 ± 1.07	41.3 ± 1.1
Hγ	4340.47	26.98 ± 1.03	17.6 ± 0.8
Hδ	4101.74	13.92 ± 0.91	7.2 ± 0.5
Hϵ	3970.08	11.44 ± 0.86	5.9 ± 0.4
Hζ	3889.06	9.72 ± 0.88	5.0 ± 0.5
[O II]	3727	159.44 ± 1.72	89.0 ± 2.4
[Ne III]	3868.76	16.00 ± 0.94	8.3 ± 0.5
[O III]	4363.21	<3.31	<2.1
[O III]	4958.91	66.35 ± 1.37	47.6 ± 1.4
[O III]	5006.84	196.88 ± 1.60	141.3 ± 3.1
He I	5875.62	6.76 ± 0.72	5.7 ± 0.6
[N II]	6548.06	4.90 ± 0.69	4.7 ± 0.7
[N II]	6583.57	13.91 ± 0.82	13.3 ± 0.9
[S II]	6716.44	27.86 ± 0.95	29.3 ± 1.2
[S II]	6730.82	21.81 ± 0.71	22.9 ± 0.9
O I	6300.30	6.76 ± 0.71	7.2 ± 0.8
[Ar III]	7135.79	5.49 ± 0.53	6.8 ± 0.7

[a]SFR is not from PyMCZ but is calculated directly from the corrected Balmer-line fluxes based on the relation of Kennicutt et al. (1994)

Radio Observations

We obtained four epochs of observations of ZTF18abvkwla using the Karl G. Jansky Very Large Array (VLA; Perley et al. 2011) under the program VLA/18B-242 (PI: D. Perley), listed in Table 8.6. The first epoch was at $\Delta t \approx 81$ d at X-band, while the VLA was in C configuration. We used 3C138 as our flux density and bandpass calibrator, and J0204+1514 as our complex gain calibrator. The next three epochs were at $\Delta t \approx 310$ d, $\Delta t \approx 350$ d, and $\Delta t \approx 400$ d, all while the VLA was in A configuration. We continued to use 3C138 but switched to J0238+1636 as our complex gain calibrator. For each observation, we ran the standard VLA calibration pipeline available in the Common Astronomy Software Applications (CASA; McMullin et al. 2007). After calibration, we inspected the data manually for further flagging. We imaged the data using the CLEAN algorithm (Högbom, 1974) available in CASA, using a cell size that was 1/5 of the synthesized beamwidth. The field size was set to be the smallest magic number (10×2^n) larger than the number of cells needed to cover the primary beam.

Table 8.4: Host galaxy properties (metallicities, mainly) from PyMCZ.

Area	Count
SFR[a]	6.47 ± 1.3
E(B-V)	$0.220^{+0.023}_{-0.022}$
logR23	$0.903^{+0.012}_{-0.012}$
D02	$8.253^{+0.130}_{-0.128}$
Z94	$8.450^{+0.016}_{-0.010}$
M91	$8.219^{+0.026}_{-0.026}$
PP04_N2Ha	$8.200^{+0.010}_{-0.010}$
PP04_O3N2	$8.187^{+0.008}_{-0.009}$
P10_ONS	$8.708^{+0.024}_{-0.024}$
P10_ON	$8.172^{+0.046}_{-0.047}$
M08_N2Ha	$8.361^{+0.020}_{-0.021}$
M08_O3O2	$8.521^{+0.011}_{-0.011}$
M13_O3N2	$8.174^{+0.009}_{-0.009}$
M13_N2	$8.194^{+0.041}_{-0.042}$
KD02_N2O2	$7.567^{+0.722}_{-0.074}$
KK04_N2Ha	$8.381^{+0.028}_{-0.029}$
KK04_R23	$8.390^{+0.021}_{-0.021}$
KD02comb	$8.304^{+0.024}_{-0.024}$

The SFR listed here is derived from the photometry, while the SFR in Table 8.4 was derived from the spectrum. So, there is no expectation of identical values or errors.

Table 8.5: Properties of the host galaxy of ZTF18abvkwla. The stellar mass, star-formation rate, maximum age, and extinction are from a fit to the galaxy SED; the χ^2 refers to that fit. The metallicity [O/H] was measured using the host galaxy spectrum and is provided on the Z94 scale. This value corresponds to 0.6× solar.

Stellar mass	M	$5.1^{+3.4}_{-2.0} \times 10^8\ M_\odot$
Star-formation rate	SFR	$6.8^{+3.7}_{-4.6}\ M_\odot\ \mathrm{yr}^{-1}$
Maximum age	age	$7.5^{+30}_{-4.5} \times 10^7$ yr
Extinction	Av	$0.72^{+0.17}_{-0.54}$ mag
	χ^2/dof	1.6 / 2
Metallicity	12+log[O/H]	8.5

[a]From VLASS

In addition, the position of ZTF18abvkwla was serendipitously covered by the VLA Sky Survey (VLASS; Lacy et al. 2020), which has been mapping the entire sky visible to the VLA at low frequencies (2–4 GHz) in three epochs at a cadence of 32 months. The Quicklook images are now available for the first epoch (17,000 deg^{-2}).

Table 8.6: Radio observations of ZTF18abvkwla with the VLA and the GMRT. Upper limit is reported as 3× the image RMS.

Δt days	Facility	Obs. Date (UT)	Config.	ν (GHz)	Flux Density (mJy)
81	VLA	2018-12-01	C	10	0.364 ± 0.006
188	VLA[a]	2019-03-19	B	3	< 0.134
310	VLA	2019-07-19	BnA	10	0.061 ± 0.003
343	VLA	2019-08-21	A	6	0.089 ± 0.003
346	VLA	2019-08-24	A	3	0.068 ± 0.004
351	VLA	2019-08-29	A	1.5	0.146 ± 0.013
352	VLA	2019-08-30	A	10	0.045 ± 0.003
364	GMRT	2019-09-11	–	0.6	< 0.105
396	VLA	2019-10-13	A	10	0.031 ± 0.003
397	VLA	2019-10-14	A	6	0.033 ± 0.003

We searched the existing Quicklook data using code available on Github[3] that locates the appropriate VLASS tile and subtile for a given RA and Dec and extracts a cutout 12 arcsec on a side. Given a non-detection we estimated an upper limit on the flux density by taking the standard deviation of the pixel values in this cutout, after performing initial 3σ clipping (removing pixels with a value greater than 3× the standard deviation). The VLASS observation of ZTF18abvkwla is also listed in Table 8.6.

We obtained one epoch of observations with the upgraded Giant Metrewave Radio Telescope (GMRT; Gupta et al. 2017; Swarup et al. 1991) under a proposal for Director's Discretionary Time (Proposal # ddtC086; PI: A. Ho). For our GMRT observations, we used 3C147 and 3C48 as our flux density and bandpass calibrators and 0238+166 for our phase calibrator. We calibrated the GMRT data manually using commands in CASA, with 6 rounds of phase-only self-calibration and 2 rounds of amplitude and phase self-calibration.

The radio light curve from the VLA is shown in Figure 8.7. At the time of our first observation, the 10 GHz (rest-frame 12 GHz) luminosity was 10^{30} erg s^{-1} Hz^{-1}, and the in-band spectral index was $\alpha = -0.16 \pm 0.05$ where $F_\nu \propto \nu^{-\alpha}$. At late times ($\Delta t > 300$ d) the decline is very steep: at 6 GHz we find $F_\nu \propto t^{-6.8\pm0.9}$, and at 10 GHz we find $F_\nu \propto t^{-3.2\pm1.4}$.

To estimate the contribution to the radio emission from the host galaxy, we use the relation in Greiner et al. (2016), adapted from Murphy et al. (2011):

[3]https://github.com/annayqho/Query_VLASS

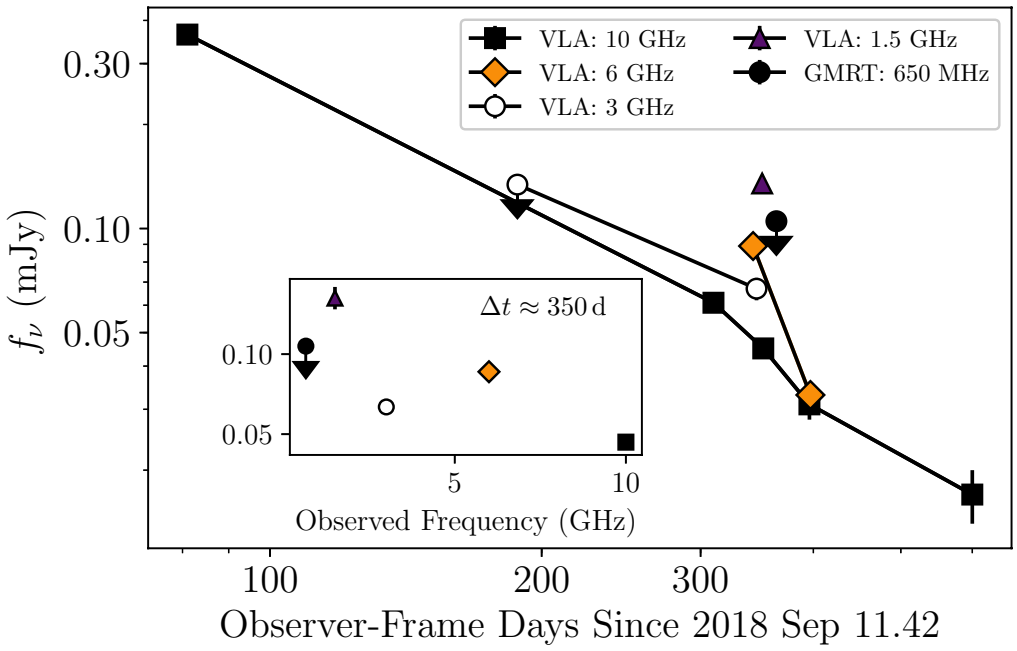

Figure 8.7: The radio light curve of ZTF18abvkwla with the spectral energy distribution at $\Delta t \approx 350$ d (rest-frame $\Delta t \approx 275$ d) shown inset. The upper limit at 3 GHz comes from a serendipitous observation by VLASS.

$$\left(\frac{\mathrm{SFR_{Radio}}}{M_\odot\,\mathrm{yr}^{-1}}\right) = 0.059 \left(\frac{F_\nu}{\mu\mathrm{Jy}}\right) (1+z)^{-(\alpha+1)} \times \left(\frac{D_L}{\mathrm{Gpc}}\right)^2 \left(\frac{\nu}{\mathrm{GHz}}\right)^{-\alpha}. \tag{8.1}$$

In the final epoch of our radio observations, assuming $\alpha = -0.75$ (Condon, 1992) where $F_\nu \propto \nu^\alpha$, the 10 GHz flux density of 0.031 ± 0.003 mJy predicts a SFR of $20\,M_\odot\,\mathrm{yr}^{-1}$. So, we conclude that during the final observation the radio emission is still dominated by the transient, but the host may contribute a non-trivial fraction of the flux.

8.3 Comparison With Extragalactic Explosions

Optical Light Curve and Spectrum

As shown in §8.1, the fast rise time and high peak luminosity of ZTF18abvkwla is shared by only a handful of transients in the literature. In this section we compare the optical properties of ZTF18abvkwla to the transients in Table 8.1. We exclude Dougie because it resided in an old stellar population with no signs of enhanced

star formation (Vinkó et al., 2015); the dominance of absorption features and much lower star-formation rate were confirmed by additional LRIS spectroscopy (Arcavi et al., 2016).

To compare light curves, we selected the light curve in a filter closest to rest-frame g (the same filters used in constructing Figure 8.1). Following Whitesides et al. (2017), we calculated absolute magnitudes using

$$M = m_{\rm obs} - 5\,\log_{10}\left(\frac{D_L}{10\,{\rm pc}}\right) + 2.5\,\log_{10}(1+z). \tag{8.2}$$

We cannot perform a true K-correction because most objects lack sufficient spectroscopic coverage. These equations will introduce systematic errors on the order of 0.1 mag.

In Figure 8.8 we show the rest-frame g-band light curve of ZTF18abvkwla compared to the light curves of transients in Table 8.1. The fast rise time of ZTF18abvkwla is most similar to that of iPTF15ul, AT2018cow, and perhaps iPTF16asu: it is faster than SN 2011kl and the SNLS transients. ZTF18abvkwla fades much more quickly than iPTF16asu (which spectroscopically evolved into a Ic-BL SN) and in this sense is more similar to iPTF15ul and AT2018cow. In terms of peak luminosity, ZTF18abvkwla is close to iPTF15ul, AT2018cow, DES16X1eho, and iPTF16asu, and brighter than SN 2011kl and the SNLS transients. However, we caution that the high peak luminosity of iPTF15ul results from a large host-galaxy extinction inferred in Hosseinzadeh et al. (2017), without which the peak magnitude would be -19.6 mag.

Next we consider color evolution. ZTF18abvkwla showed tentative evidence for reddening over time, from $g-r = -0.47 \pm 0.09$ mag at peak to $g-r = -0.03 \pm 0.21$ mag in the final epoch a week later; however, this is only a 2σ change. AT2018cow, iPTF15ul, and DES16X1eho remained very blue throughout the evolution of their optical light curves, whereas iPTF16asu reddened significantly as the SN became the dominant component.

Finally, we consider the spectral evolution of the transients in Table 8.1. Peak-light spectra were not obtained for DES16X1eho (Pursiainen et al., 2018) or the SNLS transients (Arcavi et al., 2016). The peak-light spectra of iPTF16asu, AT2018cow, and SN 2011kl were featureless (Greiner et al., 2015; Perley et al., 2019; Whitesides

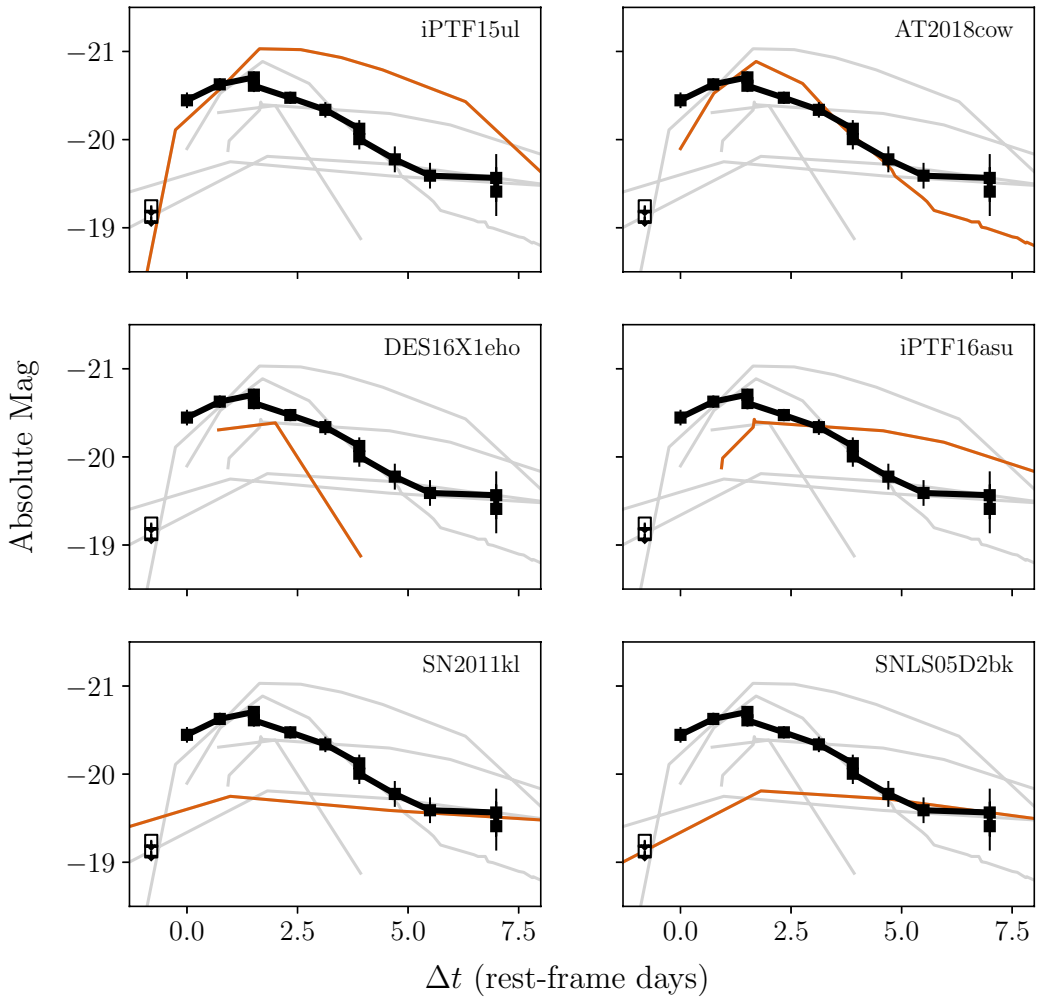

Figure 8.8: The rest-frame g-band (observer-frame r-band) light curve of ZTF18abvkwla (black line), compared to light curves of other transients in the literature in as close to the same rest-frame filter as possible. Each panel shows one transient highlighted in orange for comparison, with the rest shown in grey in the background.

et al., 2017), and iPTF15ul[4] had a weak emission feature attributed to C III (Hosseinzadeh et al., 2017). After peak, iPTF16asu developed features of a Ic-BL SN (Whitesides et al., 2017), and AT2018cow had a complex spectral evolution, with a broad feature ($v > 0.1c$) that appeared and disappeared over several days following peak light and a variety of emission lines that appeared one week later (Perley et al., 2019). Unfortunately we do not have any spectra of ZTF18abvkwla after peak.

[4]iPTF15ul was classified as Type Ibn in Hosseinzadeh et al. (2017), but the lack of distinct He I at peak make this classification uncertain.)

Radio Light Curve

In the previous section (§8.3) we compared the optical properties of ZTF18abvkwla to the transients in Table 8.1: the light curve shape, the color evolution, and the spectrum. In this section we compare the radio properties of ZTF18abvkwla to the same set of transients.

Of the transients in Table 8.1, only AT2018cow and GRB 111209A/SN 2011kl had a detected radio counterpart.[5] Prompt radio follow-up observations were also obtained for iPTF15ul[6] and iPTF16asu, but neither was detected. To our knowledge, Dougie, the SNLS transients, and DES16X1eho did not have deliberate radio follow-up observations; we searched the VLASS archive and found that all except SNLS04D4ec were observed but none were detected. In Figure 8.9 we show the radio measurements of the Table 8.1 transients compared to stellar explosions and tidal disruption events. For completeness, we also searched the positions of all of the transients in the two largest collections of unclassified fast-rising luminous optical transients reported to date, PS1 (Drout et al., 2014) and the Dark Energy Survey (Pursiainen et al., 2018). None were detected, and the limits are listed in Table 8.7.

As shown in Figure 8.9, ZTF18abvkwla is most similar in luminosity to long-duration GRB afterglows (Berger et al., 2003; Perley et al., 2014). The SED is also similar: in §8.2 we found that the SED of ZTF18abvkwla peaked near 10 GHz at $\Delta t = 81$ d, while the SED of GRB 030329 ($z = 0.1685$) peaked at 5 GHz (Berger et al., 2003) at 67 days post-explosion, and the SED of GRB 130427A ($z = 0.340$) peaked at 10 GHz (Perley et al., 2014) at a similar epoch post-explosion.

A Starburst Host Galaxy

In §8.3 and §8.3 we compared the optical and radio properties of ZTF18abvkwla to other transients in the literature. Here we put its host galaxy properties into context.

Galaxies with very high specific star-formation rates (e.g., sSFR $\gtrsim 10^{-8}$ yr^{-1}, our operational definition of a "starburst") contribute a small fraction of star-formation in the low-redshift Universe (Lee et al., 2009), so the appearance of ZTF18abvkwla in such a galaxy (sSFR $\sim 1.4 \times 10^{-8}$ yr^{-1}) is notable. However, their contribution to

[5] In the case of GRB 111209A/SN 2011kl, the radio emission was likely from the GRB afterglow itself (Kann et al., 2018).

[6] Observations of iPTF15ul were obtained within five days of the optical discovery, two observer-frame days after peak optical light, at 6 GHz and 22 GHz with the VLA, at 15 GHz with the Arcminute Microkelvin Imager (Zwart et al., 2008), and at 95 GHz with the Combined Array for Research in Millimeter-wave Astronomy (Bock, 2006). There was no detection at any frequency, with an RMS of 0.235 mJy with CARMA and an RMS of 0.03 mJy with AMI.

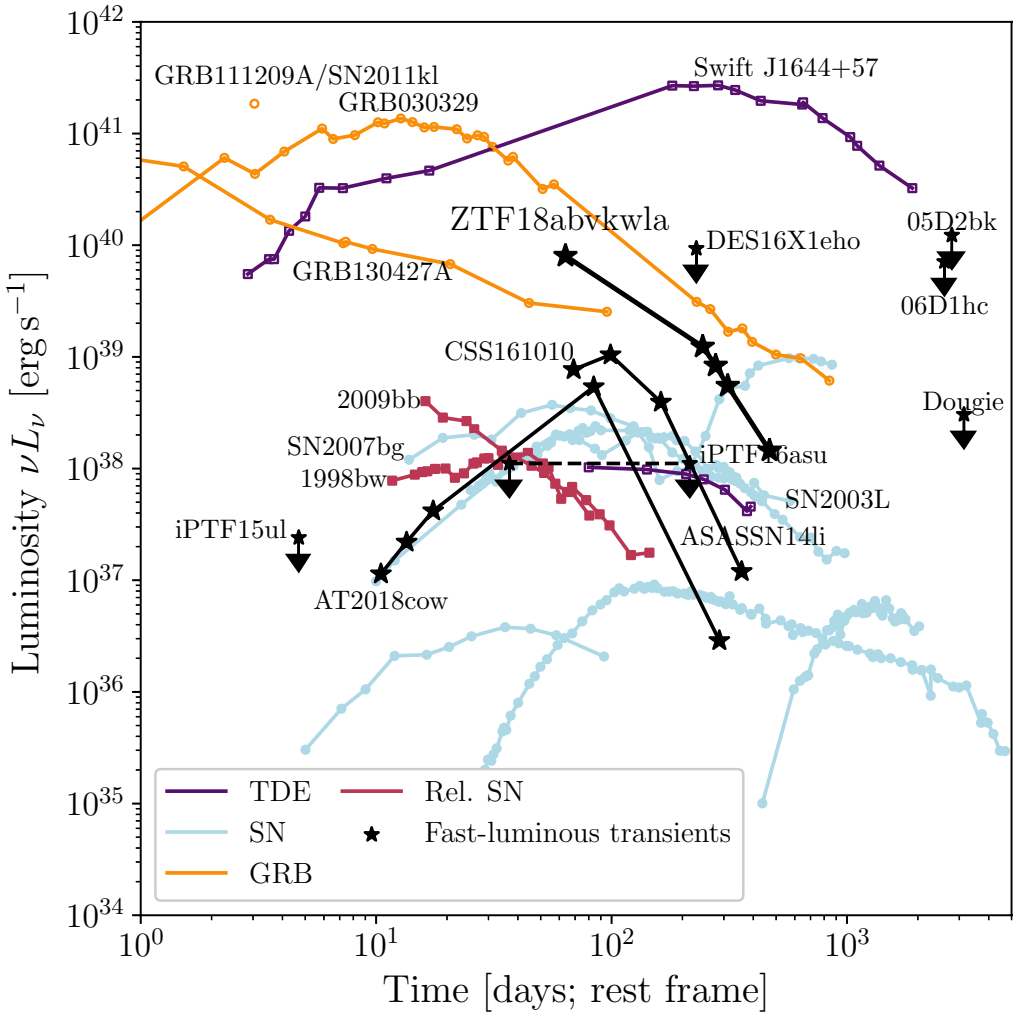

Figure 8.9: The 10 GHz radio light curve of ZTF18abvkwla compared to low-frequency (1–10 GHz) light curves of different classes of energetic explosions: tidal disruption events (purple; Alexander et al. 2016; Berger et al. 2012; Eftekhari et al. 2018; Zauderer et al. 2011, 2013), supernovae exploding in dense CSM (blue lines, $\gtrsim 10^{37}$ erg s^{-1}; Salas et al. 2013; Soderberg et al. 2005, 2006c), relativistic Ic-BL supernovae (red lines; Kulkarni et al. 1998; Soderberg et al. 2010), AT2018cow (black line, small stars), long-duration gamma-ray bursts (orange lines; Berger et al. 2003; Hancock et al. 2012; Perley et al. 2014; van der Horst et al. 2014), and "ordinary" supernovae ($\lesssim 10^{37}$ erg s^{-1}; Horesh et al. 2013; Krauss et al. 2012; Weiler et al. 1986; Weiler et al. 2007). The CSS161010 light curve was taken from Coppejans et al. (2020). The AT2018cow light curve is at 9 GHz with data taken from Ho et al. (2019c), Margutti et al. (2019), and Bietenholz et al. (2020).

Table 8.7: Radio limits for rapidly evolving transients in Drout et al. (2014) and Pursiainen et al. (2018) The Δt is the number of days between the discovery date (Drout et al., 2014) or the time of peak (Pursiainen et al., 2018) and the epoch of the VLASS observation of that field.

ID	z	RA [hh:mm:ss]	Dec [dd:mm:ss]	Δt (days)	Limit (μJy)
PS1-10ah	0.074	10:48:15.784	+57:24:19.48	2836	102
PS1-11qr	0.324	09:56:41.767	+01:53:38.25	2467	130
PS1-12bb	0.101	09:57:23.866	+03:11:04.47	2174	149
PS1-12bv	0.405	12:25:34.602	+46:41:26.97	2642	129
PS1-12brf	0.275	22:16:06.892	-00:58:09.81	1892	124
PS1-11bbq	0.646	08:42:34.733	+42:55:49.61	2731	159
PS1-13duy	0.27	22:21:47.929	-00:14:34.94	1505	127
PS1-13dwm	0.245	22:20:12.081	+00:56:22.35	1422	155
PS1-10iu	–	16:11:34.886	+55:08:47.91	2689	103
PS1-13aea	–	12:18:14.320	+47:20:12.60	2199	88
PS1-13bit	–	16:12:00.765	+54:16:08.16	1618	104
PS1-13cgt	–	16:18:56.245	+54:19:33.71	1552	123
DES15S1fli	0.45	02:52:45.15	-00:53:10.21	826	150
DES13X3gms	0.65	02:23:12.27	-04:29:38.35	1520	139
DES15S1fll	0.23	02:51:09.36	-00:11:48.71	826	139
DES14S2anq	0.05	02:45:06.67	-00:44:42.77	1199	118
DES14X3pkl	0.3	02:28:50.64	-04:48:26.44	1100	105
DES15C3lpq	0.61	03:30:50.89	-28:36:47.08	849	145
DES16S1dxu	0.14	02:50:43.53	-00:42:33.29	385	154
DES15C3mgq	0.23	03:31:04.56	-28:12:31.74	835	99
DES16X1eho	0.76	02:21:22.87	-04:31:32.64	365	152
DES16X3cxn	0.58	02:27:19.32	-04:57:04.27	393	128
DES15C3lzm	0.33	03:28:41.86	-28:13:54.96	839	106
DES13C3bcok	0.35	03:32:06.47	-28:37:29.70	1513	98
DES15C3nat	0.84	03:31:32.44	-28:43:25.06	810	108
DES15C3opk	0.57	03:26:38.76	-28:20:50.12	777	125
DES15C3opp	0.44	03:26:57.53	-28:06:53.61	781	112
DES13X3npb	0.5	02:26:34.11	-04:08:01.96	1411	122
DES16C3axz	0.23	03:31:14.15	-28:40:00.25	523	100
DES16C3gin	0.35	03:31:03.06	-28:17:30.98	391	107
DES14X1bnh	0.83	02:14:59.79	-04:47:33.32	1172	145
DES16X3ega	0.26	02:28:23.71	-04:46:36.18	357	111
DES15C3mfu	–	03:28:36.08	-28:44:20.00	835	187
DES13C3abtt	–	03:30:28.91	-28:09:42.12	1513	107
DES15C3pbi	–	03:28:56.68	-28:00:07.98	772	182
DES15X3atd	–	02:23:21.64	-04:17:28.95	830	146
DES13C3nxi	–	03:27:51.22	-28:21:26.21	1559	75
DES13C3smn	–	03:27:53.08	-28:05:00.93	1564	124
DES13X3aakf	–	02:22:50.84	-04:41:57.01	1441	108
DES13X3afjd	–	02:28:00.31	-04:34:59.39	1411	123
DES13X3kgm	–	02:26:00.92	-04:51:59.29	1508	103
DES16S2fqu	–	02:47:05.94	-00:20:50.40	356	139
DES16X1ddm	–	02:15:18.88	-04:21:52.07	386	111
DES16X3ddi	–	02:21:45.39	-04:41:08.95	393	127
DES16X3erw	–	02:24:49.31	-04:30:51.45	357	117

low-metallicity star-formation is more significant, as they are typically low-mass and therefore low-metallicity (Tremonti et al., 2004). They are also promising candidates to experience a top-heavy IMF (Dabringhausen et al., 2009) and potential sites of enhanced binary or dynamical stellar interactions (van den Heuvel and Portegies Zwart, 2013). Each of these mechanisms have been appealed to in attempts to

interpret the relatively high abundance of exotic transients of other types found in these systems, including superluminous SNe (SLSNe; Leloudas et al. 2015; Lunnan et al. 2014; Perley et al. 2016; Schulze et al. 2018), broad-lined Ic SNe (Modjaz et al., 2020), GRBs (Fruchter et al., 2006; Krühler et al., 2015; Schulze et al., 2015; Vergani et al., 2015), and at least some fast radio bursts (Katz, 2016; Tendulkar et al., 2017).

Based on our measurements in §8.2 we conclude the following about the host of ZTF18abvkwla:

The host is not an AGN — We confirm the lack of any evidence for an optical AGN based on the very weak [NII] emission. The host falls squarely in the star-forming locus of the BPT diagram (Figure 8.10).

The host metallicity is typical for its mass — The host is relatively metal-poor: the precise number is of course scale-dependent, but using the Z94 scale we calculate [O/H] of 8.45, or about 0.6×Solar. This is a lower metallicity than the majority of star-formation in the local Universe, but not an outlier and unexceptional for low-mass galaxies in particular (Figure 8.12).

The star-formation intensity is similar to extreme SLSN and GRB hosts — The most striking nature of the host galaxy is its very high specific star-formation rate, which is evident in Figure 8.13 and 8.11.

The host of AT 2018cow was also a dwarf galaxy, although it was more massive than that of ZTF18abvkwla and not starbursting, with a mass and star-formation rate of $1.4 \times 10^9\,M_\odot$ and $0.22\,M_\odot\,\mathrm{yr}^{-1}$ respectively (Perley et al., 2019). The host galaxy of DES16X1eho had a stellar mass $\log(M/M_\odot) = 9.96^{+0.14}_{-0.51}$ and a specific SFR of $\log(\mathrm{sSFR}/M_\odot\,\mathrm{yr}^{-1}) = -9.25$ (Pursiainen et al., 2018). The host galaxy of iPTF16asu had a stellar mass $M = 4.6^{+2.0}_{-2.3} \times 10^8\,M_\odot$ and an Hα SFR of $0.7\,M_\odot\,\mathrm{yr}^{-1}$, corresponding to a sSFR of $1.4\,\mathrm{Gyr}^{-1}$(Whitesides et al., 2017). Finally, the host galaxies of the SNLS transients harbored relatively evolved stellar populations, and were noted to be markedly different from starburst galaxies (Arcavi et al., 2016).

8.4 Interpretation

Even with the small number of events in the Table 8.1 menagerie, the diversity of optical and radio properties (§8.3, §8.3) suggests that there are several progenitor systems involved. In this section we model the optical and radio light curves of ZTF18abvkwla and discuss the implications for the progenitor.

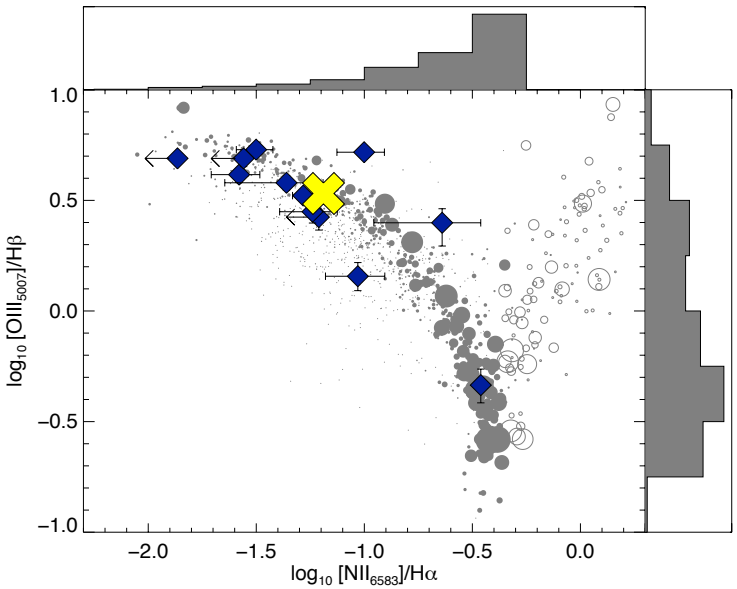

Figure 8.10: BPT diagram comparing the host galaxy of ZTF18abvkwla to <11 Mpc comparison galaxies (grey) and to the host galaxies of nearby hydrogen-poor SLSNe (diamonds), as in Perley et al. 2016. Light diamonds indicate mass-metallicity estimated metallicities. Comparison galaxies are weighted by their SFR; histograms show the SFR-weighted binned totals on each axis. ZTF18abvkwla is indicated by a yellow cross.

Modeling the Optical Light Curve

Shock-interaction with extended low-mass material is an efficient mechanism for producing a fast-peaking luminous optical light curve. Shock breakout occurs when the photon diffusion time drops below the shock crossing time ($\tau < c/v_s$, where τ is the optical depth and v_s is the shock velocity). For normal stellar progenitors, this emission is primarily at X-ray and UV wavelengths and lasts for seconds to a fraction of an hour. In the wake of this shockwave, the outer stellar material is heated to high temperatures, and as it cools it radiates on the timescale of a day ("cooling envelope" emission). See Waxman and Katz (2017) for a review.

Prior to core-collapse, massive stars can undergo mass-loss via steady winds or eruptive episodes (Smith, 2014). As a result, a star can be surrounded by dense, recently-expelled material at the time of explosion. If this material is optically thick, it increases the effective radius of the star and prolongs the light curve from shock breakout. If the light curve of ZTF18abvkwla arises from shock breakout in a shell, we can estimate the radius of this extended material (CSM) assuming a rise to peak bolometric luminosity $t_{\rm rise} < 2$ d, a peak luminosity $L_{\rm bol} > 10^{44}$ erg s^{-1} and a typical

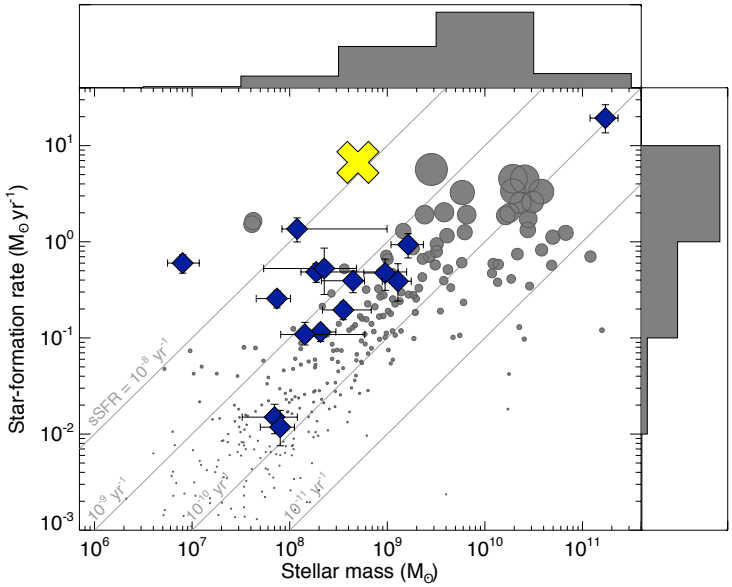

Figure 8.11: Mass–star-formation rate relation comparing the host galaxy of ZTF18abvkwla to <11 Mpc comparison galaxies (grey) and to the host galaxies of nearby hydrogen-poor SLSNe (diamonds), as in Perley et al. 2016. Light diamonds indicate mass-metallicity estimated metallicities. Comparison galaxies are weighted by their SFR; histograms show the SFR-weighted binned totals on each axis. ZTF18abvkwla is indicated by a yellow cross.

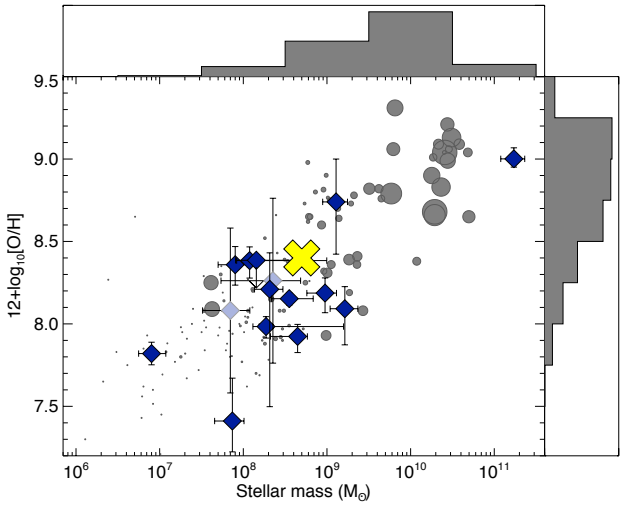

Figure 8.12: Mass-metallicity relation comparing the host galaxy of ZTF18abvkwla to <11 Mpc comparison galaxies (grey) and to the host galaxies of nearby hydrogen-poor SLSNe (diamonds), as in Perley et al. 2016. Light diamonds indicate mass-metallicity estimated metallicities. Comparison galaxies are weighted by their SFR; histograms show the SFR-weighted binned totals on each axis. ZTF18abvkwla is indicated by a yellow cross.

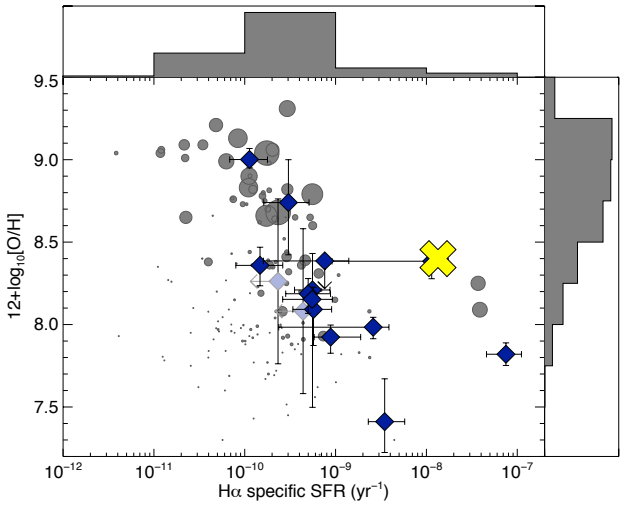

Figure 8.13: Specific star-formation-rate–metallicity relation comparing the host galaxy of ZTF18abvkwla to <11 Mpc comparison galaxies (grey) and to the host galaxies of nearby hydrogen-poor SLSNe (diamonds), as in Perley et al. 2016. Light diamonds indicate mass-metallicity estimated metallicities. Comparison galaxies are weighted by their SFR; histograms show the SFR-weighted binned totals on each axis. ZTF18abvkwla is indicated by a yellow cross. The host is a starbursting galaxy with no evidence of AGN activity, and while it is metal-poor it is not particularly so given its mass.

SN shock velocity of $10^4\,\mathrm{km\,s^{-1}}$. The rise timescale is

$$t_{\rm BO} \sim \frac{R_{\rm CSM}}{v_s} = (1.3\,\mathrm{d})\left(\frac{R_{\rm CSM}}{10^{15}\,\mathrm{cm}}\right)\left(\frac{v_s}{10^4\,\mathrm{km\,s^{-1}}}\right)^{-1}. \tag{8.3}$$

For ZTF18abvkwla, we find $R_{\rm CSM} < 1.5 \times 10^{15}$ cm.

We can also estimate the mass in the shell, assuming that the shock deposits half its kinetic energy $(1/2)\rho v_s^2$ and that this deposited energy is $E_{\rm BO} \sim 4\pi R^2 dR e_s$ where the energy density reflects the amount of thermal energy in the layer. The luminosity scales as

$$L_{\rm BO} \sim \frac{E_{\rm BO}}{t_{\rm cross}} \sim \frac{v_s^3}{4}\frac{dM}{dR} = (2.2\times10^{45}\,\mathrm{erg\,s^{-1}}) \times \left(\frac{v_s}{10^4\,\mathrm{km\,s^{-1}}}\right)^3\left(\frac{dM}{M_\odot}\right)\left(\frac{dR}{10^{15}\,\mathrm{cm}}\right)^{-1}. \tag{8.4}$$

Assuming $dR \sim R$, we find $M_{\rm CSM} < 0.07\,M_\odot$. In this framework, the differences in the light curves of different objects corresponds to differences in the shell mass, shell radius, and shock velocity. The luminosity is most sensitive to the velocity, so it is possible that the transients in Table 8.1 are distinguished by fast velocities, which would naturally explain the inclusion of a Ic-BL SN. For a fixed shock velocity, a fast rise time corresponds to a small shell radius, which in turn requires a large shell mass to produce a high luminosity.

Another possibility is that the light curve is powered not by shock breakout in a shell, but by post-shock envelope-cooling emission. For example, this was the model invoked for iPTF16asu (Whitesides et al., 2017), which led to an inferred shell mass of $0.45\,M_\odot$ and a shell radius of 1.7×10^{12} cm. The light curve of ZTF18abvkwla has a similar rise time but a higher peak luminosity than that of iPTF16asu, and the effective temperature at peak is significantly higher. According to the one-zone analytic formalism in Nakar and Piro (2014) and Piro (2015), a higher peak temperature for a fixed rise time and a fixed opacity arises from a larger shell radius. A larger shell radius can also explain the higher bolometric luminosity, although that could also arise from a larger explosion energy or faster ejecta velocity.

Another mechanism suggested to explain the optical light curve of AT2018cow was reprocessing by dense outer ejecta (Margutti et al., 2019). In this picture, a central source (such as an accretion disk or magnetar) emits high-energy (i.e., X-ray) emission, which is reprocessed by surrounding material to produce lower-energy (i.e., optical) radiation. This is one setup for tidal disruption events, in which case the surrounding material is unbound stellar debris (Strubbe and Quataert, 2009). Indeed, several properties of ZTF18abvkwla and AT2018cow are similar to TDEs in the literature, such as the photospheric radius of 10^{14}–10^{15} cm, the effective temperature of 10^4 K, and high radio luminosities attributed to jets (for reviews of TDE observations, see Gezari (2012) and Komossa (2015)).

Regardless of the power source at peak, we also use the optical light curve to put an upper limit on the mass of ^{56}Ni that could have been synthesized in the explosion. Using Equation (16) in Kasen (2017), the luminosity from the radioactive decay of ^{56}Ni is

$$L(t) = 2 \times 10^{43} \left(\frac{M_{\rm Ni}}{M_\odot}\right) \times \left[3.9 e^{-t/\tau_{\rm Ni}} + 0.678 \left(e^{-t/\tau_{\rm Co}} - e^{-t/\tau_{\rm Ni}}\right)\right] {\rm erg\,s^{-1}}, \tag{8.5}$$

where $\tau_{\rm Ni} = 8.8\,{\rm d}$ and $\tau_{\rm Co} = 113.6\,{\rm d}$. Using the final g-band measurement ($g = 21.51 \pm 0.21$) at $\Delta t = 10\,{\rm d}$ ($\Delta t = 8\,{\rm d}$ rest-frame) $L \approx \lambda F_\lambda \approx 1.4 \times 10^{43}\,{\rm erg\,s^{-1}}$, so the amount of ^{56}Ni that could power the light curve at this epoch is $M_{\rm Ni} \lesssim 0.36\,M_\odot$ (Figure 8.4). From a compilation of CC SNe, Lyman et al. (2016) found nickel masses of $0.11 \pm 0.04\,M_\odot$ for Type IIb SNe, $0.17 \pm 0.16\,M_\odot$ for Type Ib SNe, $0.22 \pm 0.16\,M_\odot$ for Type Ic SNe, and $0.32 \pm 0.15\,M_\odot$ for Type Ic-BL SNe. So, we cannot rule out an underlying nickel-powered light curve for ZTF18abvkwla.

Modeling the Radio Light Curve

The high luminosity and fast variability timescale of the 10 GHz light curve implies a high brightness temperature $T_B \approx 10^{11}\,{\rm K}$, so we conclude that the emission is synchrotron radiation. In the first epoch, the 10 GHz observation is declining and has an in-band (8–12 GHz) spectral index of $\alpha = -0.16 \pm 0.05$ where $F_\nu \propto \nu^{-\alpha}$. This is much shallower than the optically thick ($\alpha = -2.5$) or the optically thin ($\alpha = +0.7$) regimes of a synchrotron self-absorption (SSA) spectrum, which suggests that the peak of the SED is near 10 GHz (observer-frame) at this epoch. In what follows, we assume that the SSA spectrum has a rest-frame peak frequency $\nu_p \lesssim 8\,{\rm GHz}$ (the bottom of the band) and a rest-frame peak flux density $F_p \gtrsim 0.364\,{\rm mJy}$.

When the SSA peak is known, the outer shock radius R_p and magnetic field strength B_p can be derived assuming that energy is equally partitioned into magnetic fields and relativistic electrons (Readhead, 1994; Scott and Readhead, 1977). We use the equations for R_p and B_p for radio SNe in Chevalier (1998) (Equations 11 and 12). Assuming an optically thin spectral index of ν^{-1} and a filling factor $f = 0.5$, we find $R_p \gtrsim 8.0 \times 10^{16}\,{\rm cm}$ and $B_p \lesssim 0.51\,{\rm G}$. So, the mean velocity until $t_{\rm obs} = 81\,{\rm d}$ is $\Gamma\beta c = R_p(1+z)/t_{\rm obs} = 0.38c$. Using Equations 12, 16, and 23 in Ho et al. (2019c), and assuming $\epsilon_e = \epsilon_B = 1/3$, we find that the shock has swept up energy $U = 3.4 \times 10^{49}\,{\rm erg}$ into an ambient medium of density $n_e = 190\,{\rm cm^{-3}}$, corresponding to a mass-loss rate of $\dot{M} = 5.8 \times 10^{-4}\,M_\odot\,{\rm yr^{-1}}$ assuming a wind velocity $v_w = 1000\,{\rm km\,s^{-1}}$. In Figure 8.14 we show these quantities compared to those of other energetic explosions. The peak radio luminosity density is directly proportional to U/R, the energy swept up by the shock divided by the shock radius (right-hand side of Figure 8.14). So, the fact that ZTF18abvkwla, AT2018cow, and CSS161010 are distinguished by high radio luminosities is primarily a consequence of a large explosion energy.

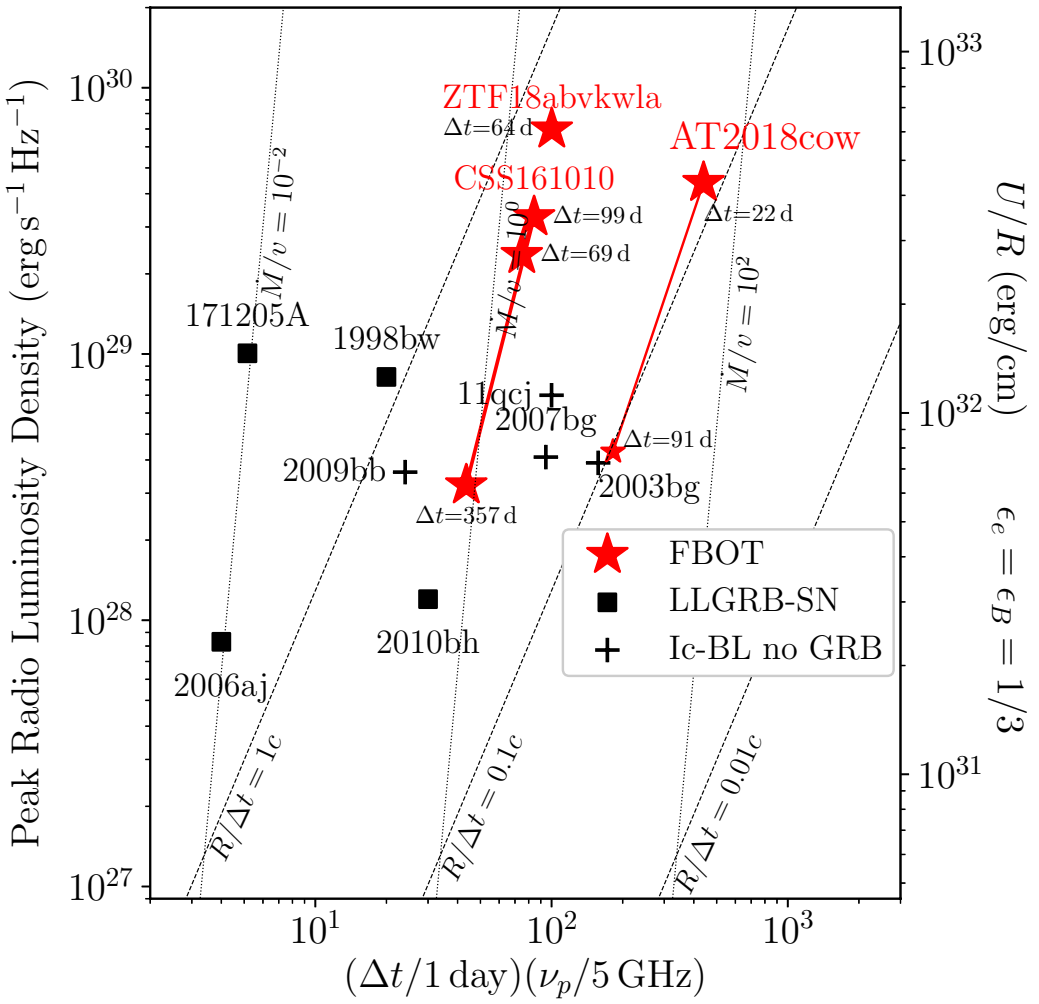

Figure 8.14: Approximate luminosity and frequency of the SSA peak of ZTF18abvkwla at $\Delta t = 81$ d (observer-frame), compared to other energetic explosions in the literature, including AT2018cow (Ho et al., 2019c; Margutti et al., 2019) and CSS161010 (Coppejans et al., 2020). Lines of constant mass-loss rate are shown in units of $10^{-4}\,M_\odot\,\mathrm{yr}^{-1}$ scaled to a wind velocity of 1000 km s^{-1}. The corresponding energy of the explosion (assuming equipartition) is shown on the right-hand side.

Progenitor Systems and a Search for an Associated Gamma-ray Burst

The physical setups outlined in §8.4 — a shock driven through a shell, reprocessing of a high-energy compact source by optically thick material — could arise in a variety of different progenitor systems. An additional clue for ZTF18abvkwla is the host galaxy, which experienced a very recent burst of star-formation activity. In that sense, a massive-star origin seems most natural.

AT2018cow was suggested to have two distinct components: a shock driven through dense equatorial material (producing the optical emission), and a faster polar outflow (producing the radio emission; Margutti et al. 2019). As shown by early millimeter observations (Ho et al., 2019c), later radio observations (Margutti et al., 2019), and Very Long Baseline Interferometry (Bietenholz et al., 2020; Mohan et al., 2020), the fast outflow was subrelativistic with a near-constant velocity of $v = 0.1c$. In ZTF18abvkwla, the radio-emitting ejecta is faster: $> 0.38c$ at the same epochs when the outflow from AT2018cow was $0.1c$. As shown in Figure 8.14, the higher luminosity at late times arises from this faster velocity; the explosion energy of the two events appears to have been similar.

Because the late-time radio light curve is similar of that of GRBs, we searched for potential GRB counterparts to ZTF18abvkwla in the period between the last non-detection (MJD 58372.4206; 2018-09-11 10:05:39.84) and the first detection (MJD 58373.4075; 2018-09-12 09:46:48.00). There were two bursts detected by the interplanetary network (IPN; Hurley et al. 2010, 2016), one by the Gamma-ray Burst Monitor (GBM) aboard the *Fermi* spacecraft (Gruber et al., 2014; Narayana Bhat et al., 2016; von Kienlin, 2014) and one detected by the Konus-*Wind* experiment aboard the *Wind* spacecraft (Aptekar et al., 1995). The positions of both bursts are inconsistent with that of ZTF18abvkwla.

Due to the lack of detected GRB, we can set a limit on the fluence and corresponding isotropic equivalent energy of a prompt burst associated with ZTF18abvkwla. The IPN has essentially a 100% duty cycle across the sky, and detects GRBs with $E_{\rm p} > 20\,{\rm keV}$ down to $6 \times 10^{-7}\,{\rm erg\,cm^{-2}}$ at 50% efficiency (Hurley et al., 2010, 2016). At t_0, the estimated 20–1500 keV limiting peak flux at the position of ZTF18abvkwla was $2 \times 10^{-7}\,{\rm erg\,cm^{-2}\,s^{-1}}$ for a Band model that has $E_{\rm pk}$ in the 50–500 keV range. At the distance of ZTF18abvkwla, this corresponds to a limit on the isotropic peak luminosity of $L_{\rm iso} < 5 \times 10^{49}\,{\rm erg\,s^{-1}}$. Therefore we strongly disfavor an on-axis classical GRB (which is also consistent with the lack of observed optical afterglow emission).

Among GRBs, two events have shown evidence for a luminous optical blackbody component at early times: GRB 060218 ($z = 0.033$; Ferrero et al. 2006; Mirabal et al. 2006; Pian et al. 2006; Soderberg et al. 2006b; Sollerman et al. 2006) and GRB 101225A (Thöne et al. 2011; $z = 0.847$; Levan et al. 2014). GRB 060218 was a very long-duration ($T_{90} \approx 2100\,{\rm s}$) low-luminosity ($L_{\rm iso} = 2.6 \times 10^{46}\,{\rm erg\,s^{-1}}$) GRB associated with the Ic-BL SN 2006aj (Cano et al., 2017b). A GRB with these

properties cannot be ruled out by our limits. GRB 101225A also had a very long duration ($T_{90} > 2000$ sec), and a candidate SN counterpart.

As in the case of AT2018cow, we cannot rule out a TDE origin. In that case, the similarity to the light curve of AT2018cow would suggest a similar kind of system, i.e., an intermediate-mass black hole ($M \sim 10^4\ M_\odot$; Perley et al. 2019) with a white dwarf (Kuin et al., 2019) or a Solar-type (Perley et al., 2019) stellar companion. In the case of AT2018cow, the main argument against a TDE hypothesis was the large ambient density (10^5 cm^{-3}) from millimeter (Ho et al., 2019c) and radio (Margutti et al., 2019) observations. For ZTF18abvkwla, assuming that the flat spectral index indicates a 10 GHz peak at 81 d, we find a much lower density (10^2 cm^{-3}). Among TDEs, the radio light curve of ZTF18abvkwla is most similar to that of the TDE candidate IGR J12580+0134 (Irwin et al., 2015), which had a nearly identical νL_ν (and fade rate) one year post-discovery. The radio emission from IGR J12580+0134 has been attributed to an off-axis relativistic jet (Irwin et al., 2015; Lei et al., 2016) but interpretation is complicated by the coincidence of the source with a known AGN.

8.5 Rate Estimate

An important clue to the progenitor of sources like ZTF18abvkwla is the cosmological rate. Furthermore, three fast-luminous transients—SN 2011kl (associated with GRB 111209A), AT2018cow, and ZTF18abvkwla—have detected luminous radio emission, although the radio emission from SN 2011kl likely arose from the GRB afterglow. Clearly, being able to recognize additional members of this phase-space in optical surveys would be valuable for radio follow-up observations. In this section, we conduct an archival search of 18 months of the 1DC survey (2018 Apr 3 – 2019 Oct 18 UT) to estimate the rate of transients in the phase-space of Figure 8.1 and delineate false positives.

First we selected field-nights in the survey for which the 1-night coverage was approximately maintained. Specifically, we require

- at least one observation the night before ($0.5 < dt < 1.5$ days)
- at least one observation two nights before ($2.5 < dt < 1.5$ days)
- at least three observations in the next five nights ($dt < 5.5$ days)

We find 8064 fields satisfying these criteria. Of these, 6854 fields (85%) have limiting magnitude > 19.75 mag and 4596 fields (57%) have limiting magnitude > 20.5 mag. The dominant effect is lunation, with some night-to-night variations due to weather.

For each of the 8064 field-nights, we searched for fast transients. To detect a fast transient, we require that the peak of the light curve be "resolved:" that is, that there are measurements both before and after peak light that are > 0.75 mag fainter than the peak magnitude. We then measure the time from 0.75 mag below peak to peak by linearly interpolating the light curve. If this rise time is < 5 d, we include the transient in our sample. More specifically, we filtered sources as summarized in Table 8.8. We scanned the remaining 659 sources by eye and removed sources with very noisy light curves or flaring behavior.

Table 8.8: Filtering criteria for sources similar to ZTF18abvkwla in the ZTF 1DC survey

Criteria	# sources remaining
Real[a], bright[b], pos. sub.[c], not star[d]	758,528
Short duration[e] and peak resolved[f]	659

[a] `drb` > 0.99 [b] `magpsf` < 20 [c] `isdiffpos`='t' or '1' [d] not(`sgscore1` > 0.76 and `distpsnr1` < 1) [e] Duration between 1 and 100 days [f] Peak has preceding or subsequent detection/non-detection in a ± 5 d window that is at least 0.75 mag fainter

In Table 8.9 we list all 27 sources with rise times faster than 5 d, including ZTF18abvkwla itself. Five sources are spectroscopically classified SNe: two Type II, two Type Ibn, and one Type IIb. Three sources are classified as CVs, two spectroscopically and one by cross-matching with the AAVSO International Variable Star Index VSX (Watson et al., 2017). Two are very likely flare stars based on previous detections in Pan-STARRS individual-epoch images, and a third is a likely flare star based on a GALEX counterpart. Nine sources are likely extragalactic (based on proximity to a host galaxy). When redshift estimates for these galaxies were not available, we attempted to obtain them using LRIS on 17 Feb 2020. Two sources remain without definitive redshift estimates, so we provide a photometric redshift from LegacySurvey DR8. One source (ZTF18abxxeai) has a very faint host classified as a PSF in LegacySurvey DR8, and the remaining five sources have no clear host counterpart.

Of the sources with a definitive host redshift measurement, ZTF18abvkwla is the only one that is more luminous than $M = -20$ mag. Clearly, the primary interlopers in searches for transients like ZTF18abvkwla are CVs and less luminous SNe. CVs can be ruled out on the basis of repeated flaring, whereas less luminous SNe can only be ruled out if the redshift of the host galaxy is known *a priori*. Aside from ZTF18abvkwla, eight transients in our sample remain as possibly having $M_{\rm g,peak} < -20$, although the lack of an obvious host for six of them suggest that these may be CVs.

We take eight as an upper limit for the number of transients in ZTF that could fall within the phase-space of Figure 8.1. Of these, three peak brighter than 19 mag, and four have a peak between 19 and 19.75 mag. We now calculate two all-sky rates. First we assume that the transient peaks at < 19 mag, in which case we discard field-nights with a limiting magnitude shallower than 19.75 mag. Then we assume that the transient peaks at < 19.75 mag, in which case we discard field-nights with a limiting magnitude shallower than 20.5 mag.

Each ZTF field is 47 deg^2, but there is latitude-dependent overlap that has to be taken into account when converting this to a rate per square degrees in the sky. For the primary grid, a rough estimate of the fill factor is 87.5%. For the 1DC survey, the footprint is 10% smaller than the number of fields multiplied by 47 square degrees. So, taking fill factor and overlap into account, we estimate a typical area-per-field of 37 deg^2. So for transients brighter than 19 mag we have 2.5×10^5 deg^2 d and for transients brighter than 19.75 mag we have 1.7×10^5 deg^2 d. For transients peaking brighter than 19 mag we have a limiting all-sky rate

$$3 \times \frac{41253\,\mathrm{deg}^2}{2.5 \times 10^5\,\mathrm{deg}^2\,\mathrm{d}} \times \frac{365\,\mathrm{d}}{1\,\mathrm{yr}} \approx 180\,\mathrm{yr}^{-1}. \tag{8.6}$$

For transients peaking brighter than 19.5 mag we have a limiting all-sky rate

$$4 \times \frac{41253\,\mathrm{deg}^2}{1.7 \times 10^5\,\mathrm{deg}^2\,\mathrm{d}} \times \frac{365\,\mathrm{d}}{1\,\mathrm{yr}} \approx 350\,\mathrm{yr}^{-1}. \tag{8.7}$$

Now, we use the limiting magnitude to estimate a volumetric rate. Assuming a transient that peaks at $M = -20$ mag, requiring a peak apparent magnitude brighter than 19 mag restricts our sensitivity to 400 Mpc. So, we find a volumetric rate of 7×10^{-7} yr^{-1} Mpc^{-3}. Requiring a peak apparent magnitude brighter than 19.75 mag restricts our sensitivity to 560 Mpc, leading to a volumetric rate

of $4 \times 10^{-7}\,\mathrm{yr}^{-1}\,\mathrm{Mpc}^{-3}$. For reference, we provide rates of core-collapse SNe and GRBs in Table 8.10. The rate of events like ZTF18abvkwla appears to be at least two orders of magnitude smaller than the CC SN rate, and more similar to the rate of GRBs in the local universe.

8.6 Prospects for Detecting X-ray Emission

Clearly, radio observations are an important avenue of follow-up for transients like ZTF18abvkwla. Another valuable avenue is X-ray observations, which were not obtained for ZTF18abvkwla. We can estimate what the predicted X-ray luminosity would be from inverse Compton scattering, using the optical and radio luminosities:

$$\frac{L_X}{L_{\mathrm{radio}}} = \frac{u_{ph}}{u_B}. \tag{8.8}$$

Taking $L_{\mathrm{radio}} = 10^{40}\,\mathrm{erg\,s^{-1}}$, $u_{ph} = 10^{44}\,\mathrm{erg\,s^{-1}}/(4\pi R^3/3)$ where $R = 10^{14}\,\mathrm{cm}$, and $u_B = B^2/8\pi$ where $B = 0.6\,\mathrm{G}$, we find $L_X \approx 10^{43}\,\mathrm{erg\,s^{-1}}$. This is even more luminous than the X-ray emission observed accompanying AT2018cow, which had $L_X \approx 10^{42}\,\mathrm{erg\,s^{-1}}$ (Ho et al., 2019c; Margutti et al., 2019; Rivera Sandoval et al., 2018). To our knowledge there were no X-ray follow-up observations of DES16X1eho, while observations of iPTF16asu resulted in an X-ray upper limit of $10^{43}\,\mathrm{erg\,s^{-1}}$. Hosseinzadeh et al. (2017) report pre-peak UV measurements from *Swift* for iPTF15ul, but to our knowledge X-ray observations have not been reported. We measured an upper limit of $0.005\,\mathrm{ct\,s^{-1}}$ in a single epoch from the publicly available *Swift* data. Assuming $n_H = 1.7 \times 10^{20}\,\mathrm{cm}^{-2}$ and a power-law source model with a photon index $\Gamma = 2$ we obtain an upper limit on the unabsorbed 0.3–10 keV luminosity of $2 \times 10^{42}\,\mathrm{erg\,s^{-1}}$.

8.7 Summary and Conclusions

ZTF18abvkwla is distinguished by two key characteristics: a fast-evolving optical light curve with a hot ($T > 40,000\,\mathrm{K}$) and featureless thermal spectrum at peak, and a long-lived, fast-fading radio light curve similar to those of jet-powered long-duration GRBs. The host galaxy underwent a recent starforming episode and has a very high specific star-formation rate, similar to that of extreme SLSN and GRB hosts. Events like ZTF18abvkwla are rare: from one year of the ZTF 1DC survey, we estimate that the rate is at least 2–3 orders of magnitude smaller than the CC SN rate.

Due to the lack of late-time photometry, we cannot conclude whether the late-

time light curve was powered by the same mechanism as the peak or whether another mechanism such as nickel decay became dominant, and we have only tentative evidence for color evolution (cooling) over time. Furthermore, we cannot determine whether this source developed supernova features and whether it most closely resembles a Ic-BL like iPTF16asu, a continuum with emission lines like the Ibn iPTF15ul or the SN/TDE candidate AT2018cow, or neither.

Among the fast-luminous optical transients in Table 8.1, only AT2018cow and SN 2011kl had detected radio emission. ZTF18abvkwla thus adds to the very small number of events in the literature established to have fast-blue optical light curves, as well as a separate fast ejecta component that produces luminous radio emission. Interestingly, most of the well-studied transients in Table 8.1 are associated with a candidate engine-powered explosion. AT2018cow had a long-lived central engine that powered a fast ($0.1c$) outflow. The Koala likely had a central engine that powered an even faster ($> 0.38c$) outflow, perhaps a relativistic jet. iPTF16asu was a Ic-BL SN, and therefore by definition had faster ejecta velocities than ordinary core-collapse supernovae, although there was no evidence for a jet. SN 2011kl had a burst of high-energy emission (GRB 111209A) and an associated luminous afterglow. Given the sensitivity of the luminosity to the shock speed (Equation 7), perhaps this apparent relationship between engine-driven supernovae and luminous fast-luminous optical transients should not be surprising.

At $z = 0.27$, ZTF18abvkwla was much more distant than AT2018cow ($z = 0.0141$), but the lesson from §8.2 and §8.5 is that we should not be deterred by cosmological distances in pursuing X-ray and radio follow-up observations. The radio emission from ZTF18abvkwla would be easily detecTable by the VLA out to $z = 0.5$ (assuming 5 μJy RMS in half an hour of integration time) or even out to $z = 0.8$ (when it would be 30 μJy). Assuming a *Swift*/XRT sensitivity limit of 4×10^{-14} erg cm^{-2} s^{-1}, the X-ray emission from ZTF18abvkwla may have been on the detection threshold. For a *Chandra* sensitivity limit an order of magnitude deeper, this may be on the detection threshold at $z = 0.7$. At these larger distances ($z = 0.5, z = 0.7$) the optical g-band magnitude would be 21.1 and 22.3 respectively. This is out of reach for current surveys like ZTF, but standard for LSST. The false positives in such a search are lower-luminosity explosions (Type IIb, II, and Ibn SNe) and CVs. These can be ruled out via knowledge of the host redshift (and therefore intrinsic luminosity), so we emphasize the need for extensive and reliable galaxy-redshift catalogs.

The code used to produce the results described in this paper was written in Python

and is available online in an open-source repository[7].

A.Y.Q.H would like to thank the NRAO staff for their help with data calibration and imaging, particularly Steve Myers, Aaron Lawson, Drew Medlin, and Emmanuel Momjian. She is grateful for their support and hospitality during her visit to Socorro. She thanks Gregg Hallinan and Brad Cenko for their advice on reducing the radio and X-ray data, respectively, Jochen Greiner and Iair Arcavi for their assistance in obtaining the afterglow-subtracted light curve of SN 2011kl, Miika Pursiainen for sharing light curves of DES fast-luminous transients, Griffin Hosseinzadeh for useful discussions about iPTF15ul, Jesper Sollerman and Steve Schulze for carefully reading the manuscript, and Tony Piro and Ben Margalit for other productive conversations. This work made use of the IPN master burst list (ssl.berkeley.edu/ipn3/masterli.html) maintained by Kevin Hurley. We would like to thank Raffaella Margutti for pointing out a typo in an earlier version of this paper, and to the anonymous referee for detailed comments that greatly improved the flow and clarity of the paper.

A.Y.Q.H. was supported by a National Science Foundation Graduate Research Fellowship under Grant No. DGE-1144469, by the GROWTH project funded by the National Science Foundation under PIRE Grant No. 1545949, and by the Heising-Simons Foundation. P.C. was supported by the Department of Science and Technology via SwarnaJayanti Fellowship awards (DST/SJF/PSA-01/2014-15). A.H. is grateful for the support by grants from the Israel Science Foundation, the US-Israel Binational Science Foundation, and the I-CORE Program of the Planning and Budgeting Committee and the Israel Science Foundation. This research was funded in part by a grant from the Heising-Simons Foundation and a grant from the Gordon and Betty Moore Foundation through Grant GBMF5076, and benefited from interactions with Daniel Kasen and David Khatami also funded by that grant. A.A.M. is funded by the Large Synoptic Survey Telescope Corporation, the Brinson Foundation, and the Moore Foundation in support of the LSSTC Data Science Fellowship Program; he also receives support as a CIERA Fellow by the CIERA Postdoctoral Fellowship Program (Center for Interdisciplinary Exploration and Research in Astrophysics, Northwestern University).

Based on observations obtained with the Samuel Oschin Telescope 48-inch and the 60-inch Telescope at the Palomar Observatory as part of the Zwicky Transient Facility project. ZTF is supported by the National Science Foundation under Grant

[7] https://github.com/annayqho/Koala

No. AST-1440341 and a collaboration including Caltech, IPAC, the Weizmann Institute for Science, the Oskar Klein Center at Stockholm University, the University of Maryland, the University of Washington, Deutsches Elektronen-Synchrotron and Humboldt University, Los Alamos National Laboratories, the TANGO Consortium of Taiwan, the University of Wisconsin at Milwaukee, and Lawrence Berkeley National Laboratories. Operations are conducted by COO, IPAC, and UW. The National Radio Astronomy Observatory is a facility of the National Science Foundation operated under cooperative agreement by Associated Universities, Inc. We thank the staff of the GMRT that made these observations possible. GMRT is run by the National Centre for Radio Astrophysics of the Tata Institute of Fundamental Research. Some of the data presented herein were obtained at the W. M. Keck Observatory, which is operated as a scientific partnership among the California Institute of Technology, the University of California and the National Aeronautics and Space Administration. The Observatory was made possible by the generous financial support of the W. M. Keck Foundation. The authors wish to recognize and acknowledge the very significant cultural role and reverence that the summit of Maunakea has always had within the indigenous Hawaiian community. We are most fortunate to have the opportunity to conduct observations from this mountain.

8.8 Appendix

Light-curve measurements

To construct Table 8.1, we used observed bands as close as possible to rest-frame g: g-band for $z < 0.15$, r-band for $0.15 < z < 0.45$, i-band for $0.45 < z < 0.78$, and z-band for $0.78 < z < 1.0$. We excluded transients with $z > 1.0$. We measured the rise time from, and fade time to, 0.75 mag below peak by linearly interpolating the single-filter light curve, and measured uncertainties using a Monte Carlo with 1000 realizations of the light curve. Additional notes on each transient are below.

For iPTF15ul ($z = 0.066$; Hosseinzadeh et al. 2017) the uncertainty on the peak magnitude was dominated by the uncertainty from the host-galaxy extinction estimate. For AT2018cow ($z = 0.0141$; Perley et al. 2019; Prentice et al. 2018) we used the time between the last non-detection and the first detection as an upper limit on the rise time, although we note that interpolation would give 0.4 d, much shorter than 3 d. We also corrected for 0.287 mag of Galactic extinction, which was not applied in Table 3 of Perley et al. (2019). For a lower limit, we used the o-band detection before peak (dominated by r-band flux at this epoch), corrected for 0.198 mag of Galactic extinction. We assumed $g - r = -0.4$ mag and $g - i = -0.7$ mag.

For SN 2011kl ($z = 0.677$) we used column M_{4556} in Table 2 of Kann et al. (2019). These values are corrected for rest-frame extinction, and the contributions from the GRB afterglow and host galaxy have been subtracted. For SNLS04D4ec ($z = 0.593$), SNLS05D2bk ($z = 0.699$), and SNLS06D1hc ($z = 0.555$) we used the i-band light curve from Arcavi et al. (2016) and corrected for Milky Way extinction.

For Dougie ($z = 0.19$; Vinkó et al. 2015) we added an additional 0.1 mag in quadrature to account for the zero-point uncertainty, and corrected for 0.031 mag of Milky Way extinction. For iPTF16asu ($z = 0.187$; Whitesides et al. 2017) we could not measure the rise or peak magnitude in rest-frame g because observations in the appropriate filter (r) began only 3 days after peak. We estimated an upper limit to the peak magnitude by assuming that the $g-r$ color at peak was identical to the $g-r$ color during the first r-band measurement. We used the first r-band measurement as a lower limit. For the time from half-max to max, we used the observed g-band light curve instead. We obtained the i-band light curve of DES16X1eho ($z = 0.76$; Pursiainen et al. 2018) from M. Pursiainen (private communication).

Table 8.9: Fast-rising transients in ZTF resulting from our archival search of the one-day cadence survey. In the redshift column, a range refers to the 68 percentile range on the photometric redshift from LegacySurvey DR8 (we provide a corresponding range of absolute magnitude) and a single value corresponds to a spectroscopic redshift. When the distance is known, the peak mag is an absolute magnitude, and when the distance is not known the peak mag is an apparent magnitude. These values correspond to the filter as close to rest-frame g-band as possible, and when the distance is not known they correspond to the observed g-band filter. Magnitudes are corrected for Galactic extinction and timescales are in rest-frame when the redshift is known, and in observer-frame when the redshift is not known.

ZTF Name (IAU Name)	Redshift	Peak Mag	$t_{\rm rise}$	$t_{\rm fade}$	Type	Notes
18abvkwla	0.2714	-20.59 ± 0.07	1.83 ± 0.05	3.12 ± 0.22	FBOT	This paper
19aavbjfp (SN2019fkl)	0.028	-17.4 ± 0.4	3.2 ± 0.9	21.8 ± 6.1	SN II	
19abgbdcp (AT2019lbv)	0.0318	-18.36 ± 0.03	2.32 ± 0.03	14.4 ± 0.9	SN II	
18aalrxas	0.0588	-18.43 ± 0.03	1.86 ± 0.02	2.4 ± 0.3	SN IIb	Fremling et al. (2019b)
19abuvqgw (AT2019php)	0.087	-18.9 ± 0.1	3.6 ± 0.1	4.5 ± 0.3	SN Ibn	
19aapfmki (SN2019deh)	0.05469	-19.90 ± 0.01	4.38 ± 0.03	7.2 ± 0.4	SN Ibn	
18abskrix	Galactic	17.78 ± 0.02	1.26 ± 0.03	2.5 ± 0.2	CV	Spectroscopic classification
18absrffm (AT2018ftw)	Galactic	16.34 ± 0.01	2.60 ± 0.03	5.00 ± 0.03	CV	Spectroscopic classification
18abyzkeq	Galactic	18.32 ± 0.10	1.37 ± 0.04	0.93 ± 0.06	CV	AAVSO Name: CSS 151114:224934+375554
18ablxawt	Galactic	18.31 ± 0.04	2.4 ± 0.3	5.2 ± 0.9	Likely flare star	Previous detection in PS1 DR2 at $i = 19.4$
19abpwygn	-	16.74 ± 0.01	2.03 ± 0.03	1.73 ± 0.03	Likely flare star	Previous detection in PS1 DR2 at $z = 18.75$
18abyjgaa	-	18.39 ± 0.03	0.82 ± 0.03	2.05 ± 0.08	Likely flare star	GALEX source, possible flaring in PS1 DR2
18aasaiyp	0.104	-19.13 ± 0.05	1.9 ± 0.6	17.1 ± 0.6	Unknown	
18abuvqgo	0.155	-19.93 ± 0.05	4.7 ± 0.2	9.9 ± 0.6	Unknown	
18abydmfv (AT2018hkr)	0.042	-18.66 ± 0.03	3.15 ± 0.04	7.7 ± 2.5	Unknown	
18acepuyx (AT2018kxh)	0.0711	-19.1 ± 0.2	1.4 ± 0.3	10.8 ± 1.2	Unknown	
19aatoboa (AT2019esf)	0.0758	-18.90 ± 0.03	2.41 ± 0.03	4.9 ± 0.3	Unknown	
19abgbbpx (AT2019leo)	0.0625	-18.83 ± 0.03	4.2 ± 0.3	> 5	Unknown	
19abiyyhd (AT2019lwj)	0.07	-18.11 ± 0.05	2.5 ± 0.2	4.1 ± 0.3	Unknown	
19aaadfcp	0.08–0.15	19.04 ± 0.04	2.44 ± 0.15	5.86 ± 0.15	Unknown	
19aanvhyc (AT2019coi)	0.056–0.076	18.41 ± 0.04	4.39 ± 0.04	12.1 ± 2.1	Unknown	
18abxxeai		18.55 ± 0.06	1.9 ± 0.1	6.0 ± 0.8	Unknown	'PSF' host in LegacySurvey DR8
18acgnwpo	-	18.90 ± 0.05	0.52 ± 0.03	6.5 ± 0.5	Unknown	No clear host
19aanqqzb	-	16.63 ± 0.04	1.91 ± 0.07	1.2 ± 0.1	Unknown	No clear host
19aaqfdvu	-	19.02 ± 0.06	2.0 ± 0.2	1.6 ± 0.4	Unknown	No clear host
19aaxfqyx	-	18.76 ± 0.03	0.98 ± 0.03	4.68 ± 0.27	Unknown	No clear host
19abfzfbs	-	19.36 ± 0.17	3.7 ± 2.2	13.4 ± 3.2	Unknown	No clear host

Table 8.10: Local ($z = 0$) Rates of core-collapse supernovae and GRBs. Approximately 30% of CC SNe arise from a progenitor stripped of its hydrogen envelope. Among these stripped events, there are roughly equal numbers of IIb, Ib, and Ic events. Of the Ic events, $\sim$ 10% are "broad-lined" with photospheric velocities $\gtrsim$30,000 km/s. The fraction of Ic-BL SNe with associated GRBs has been estimated to be 1/40 (Graham and Schady, 2016) although the rate is highly uncertain. The fraction of Ic-BL SNe with associated LLGRBs remains uncertain. Note that the rate quoted for LLGRBs does not include a beaming correction.

Class	Rate/Fraction	References
SN II	$4.47 \pm 1.39 \times 10^{-5}$ yr^{-1} Mpc^{-3}	[1]
SN Ibc	$2.58 \pm 0.72 \times 10^{-5}$ yr^{-1} Mpc^{-3}	[1]
Frac. of Ibc SN that are Ic	0.69 ± 0.09	[2,3]
Frac. of Ic SN that are Ic-BL	0.21 ± 0.05	[2,3]
LLGRB	$2.3^{+4.9}_{-1.9} \times 10^{-7}$ yr^{-1} Mpc^{-3}	[4]
	$3.3^{+3.5}_{-1.8} \times 10^{-7}$ yr^{-1} Mpc^{-3}	[5]
ℓGRB	$\mathcal{R}_{\rm obs} = 4.2^{+9.0}_{-4.0} \times 10^{-10}$ yr^{-1} Mpc^{-3}	[6]
	$f_b = 0.0019 \pm 0.0003$	[7]
	$f_b = 0.013 \pm 0.004$	[8]

[1] Li et al. (2011), [2] Kelly and Kirshner (2012), [3] Graham and Schady (2016), [4] Soderberg et al. (2006b), [5] Liang et al. (2007), [6] Lien et al. (2014), [7] Frail et al. (2001), [8] Guetta et al. (2005)

Chapter 9

OTHER CONTRIBUTIONS

9.1 ZTF19abvizsw: A Cosmological Afterglow With No Detected Gamma-ray Burst

ZTF19abvizsw is a cosmological ($z = 1.2596$) luminous ($M_{2170} = -24.4$ mag) transient discovered and classified as part of the search for an electromagnetic counterpart to gravitational-wave trigger S190901ap (LIGO Scientific Collaboration and Virgo Collaboration, 2019), a neutron star neutron star merger. ZTF19abvizsw was first detected on 2019 Sept 02 as part of the ZTF partnership survey. Because it had only one detection in r-band and one detection in g-band, it did not pass the fast-transient filter, but was instead flagged by the infant supernova filter. Because the transient was young and in the localization region of S190901ap, ZTF19abvizsw was flagged as a candidate counterpart (Kool et al., 2019) and received a classification spectrum (Burdge et al., 2019b), which showed narrow absorption features consistent with $z = 1.2596$. Immediately after the classification as a cosmological fast transient, I initiated target-of-opportunity observations with *Swift* (Ho et al., 2019b) and searched for an associated GRB counterpart. Since then, detailed radio observations have been obtained, as well as a high-cadence light curve from the Transiting Exoplanet Survey (TESS; Ricker et al. 2015) which was observing this field at the time of the burst. I am contributing the X-ray light curve and limits on a GRB counterpart for a paper led by Dan Perley, which is currently in preparation.

9.2 How Much CSM is Sufficient to Choke a Jet?

Although a significant fraction of Ic-BL SNe appear to be surrounded by dense CSM (resulting in double-peaked optical light curves or luminous radio emission), simulations of jet propagation almost always assume a low-density ISM-like medium. Furthermore, one of the leading "unification schemes" for GRBs, LLGRBs, and Ic-BL SNe rests on the claim that a dense CSM would choke an otherwise ordinary GRB jet (Nakar, 2015), giving rise to an LLGRB. Following discussions at a ZTF-Theory Network meeting, Paul Duffell ran relativistic hydrodynamical simulations to measure how much CSM would be required to choke a GRB jet. My contribution to the paper was a section summarizing the observations of dense CSM surrounding Ic-BL SNe, including typical CSM masses and radii. In the paper that we submit-

ted (currently in press), we argued that the CSM observed surrounding Ic-BL SNe would be insufficient to choke an ordinary GRB jet, but it would slow down the jet to a lower Lorentz factor (Duffell and Ho, 2019). So, if LLGRBs do arise from outflows that are "choked" in CSM, the outflow has to have a lower power than a typical GRB to begin with.

9.3 Radio Observations of Ic-BL SNe Discovered by ZTF

PTF and ZTF enabled a much-increased rate of Ic-BL discoveries: with ZTF we discover and classify approximately one Ic-BL SN per month within $z \lesssim 0.1$. In the PTF era, systematic VLA observations of Ic-BL SNe established that $\lesssim 14\%$ are have radio light curves as luminous as GRB 980425 / SN 1998bw (Corsi et al., 2016). In ZTF, we have had 10 months of ZTF+VLA monitoring, with which we collected a sample of 9 new Ic-BL SNe with radio follow-up observations. Typically, events are ~7–15 d old at the time of classification and $\sim$ 20 d old at the time of the first VLA observation. Our sample included the discovery of ZTF18aaqjovh, a Ic-BL SN with radio emission similar to that of GRB 060218 / SN 2006aj (Ho et al., 2020c)).

Chapter 10

THE FUTURE

In my thesis I elucidated several complications in addressing to what extent GRBs are the tip of the iceberg of a diverse landscape of relativistic stellar explosions: the lack of sensitive continuous all-sky coverage in the soft X-ray band; the delay in radio follow-up observations of Ic-BL SNe imposed by the need for brute-force spectroscopic classification; the difficulty in determining whether a transient's panchromatic properties can be explained solely by CSM interaction or whether an additional mechanism is required; a lack of a dedicated sensitive time-domain facility observing at millimeter wavelengths; and the incompleteness of galaxy redshift catalogs leading to a delay in recognizing luminous explosions.

However, there is reason for hope. The GRB-SN connection comes down to a question of rates. On the horizon are facilities that will measure off-axis afterglows in large numbers. Beginning in October 2022, LSST will conduct a decade-long wide-field survey from northern Chile. The majority of the observing time (90%) will be spent in a "deep-wide-fast" (main) survey mode: 18,000 $\deg^2$ of the sky will be visited 800 times over 10 years. A single visit consists of two 15-second exposures, each in one of six filters, from u to y. At radio frequencies, there is ASKAP and the ngVLA. In particular, since radio afterglows are long-lived, these facilities will provide more robust measurements of the local GRB rate and beaming fraction than what is currently available. In addition, shallow optical surveys like ZTF Phase II will continue to build up volume-complete samples of supernovae, enabling a precise and direct estimate of the local Ic-BL rate. Soon we will be able to directly compare the "true" GRB rate with the rate of Ic-BL SNe.

Then there is the question of LLGRBs. Currently, progress is hampered because LLGRBs are found in small numbers, one every few years. It is difficult to see a path forward without a new all-sky GRB mission sensitive to the soft X-ray band. Such a mission would be capable of finding an enormous number of LLGRBs (not to mention other interesting elusive phenomena, such as shock breakout events) and pin down the low-luminosity end of the GRB log$N$-log$S$ diagram. This would answer the question of whether LLGRBs are truly a completely distinct and more common class than GRBs—and with more routine millimeter and radio follow-up

observations, their ambient CSM densities and how much energy they couple to relativistic ejecta.

Local-volume experiments will be greatly assisted by vastly more complete galaxy redshift catalogs, enabled by massively multiplexed spectroscopic surveys such as DESI. Using Type Ia SNe found as part of BTS, we estimated the the "redshift completeness fraction" as a function of host-galaxy magnitude. As a function of redshift, the RCF is 80% nearby and drops to 20% by $z = 0.1$. DESI's Bright Galaxy Survey will be transformative, performing a magnitude-limited survey of 10 million galaxies brighter than 19.5 (highest priority) and 19.5 < r < 20 (secondary priority). However, the galaxy luminosity function spans over eight orders of magnitude, so it would be useful and timely to develop a strategy for identifying low-mass, faint, nearby galaxies based on known redshifts for bright, massive galaxies. One promising avenue is to take advantage of the fact that galaxies are strongly clustered in the local universe, on length scales as large as 200 Mpc, So, from a given bright galaxy it might be possible to prioritize which nearby galaxies DESI should observe. These redshift catalogs may even assist with the discovery of luminous fast transients such as orphan afterglows; perhaps they can be selected on the basis of luminosity alone, without relying on high-cadence light curves.

Finally, there is great promise for the study of stellar "death omens." At higher redshifts, the question of whether all fast blue optical transients arise from CSM interaction points to a large fraction of massive stars undergoing eruptive mass-loss at the end of their lives. Observationally, we need to characterize a well-defined subset. Theoretically, we need to learn how to determine whether the observational properties can be explained by CSM interaction. In the local universe, LSST will provide deep long-term light curves, years into the past, which can be used to identify pre-explosion eruptions in massive stars. If stars "puff up" and experience a luminosity enhancement days prior to the explosion, perhaps we can even learn to predict when a star will explode.

BIBLIOGRAPHY

Abbott, B. P. et al. (2017). "Gravitational Waves and Gamma-Rays from a Binary Neutron Star Merger: GW170817 and GRB 170817A". In: *ApJL* 848.2, p. L13. DOI: 10.3847/2041-8213/aa920c. arXiv: 1710.05834 [astro-ph.HE].

Abolfathi, B. et al. (2018). "The Fourteenth Data Release of the Sloan Digital Sky Survey: First Spectroscopic Data from the Extended Baryon Oscillation Spectroscopic Survey and from the Second Phase of the Apache Point Observatory Galactic Evolution Experiment". In: *ApJS* 235.2, p. 42. DOI: 10.3847/1538-4365/aa9e8a. arXiv: 1707.09322 [astro-ph.GA].

Ahn, C. P. et al. (2012). "The Ninth Data Release of the Sloan Digital Sky Survey: First Spectroscopic Data from the SDSS-III Baryon Oscillation Spectroscopic Survey". In: *ApJS* 203.2, p. 21. DOI: 10.1088/0067-0049/203/2/21. arXiv: 1207.7137 [astro-ph.IM].

Ahn, C. P. et al. (2014). "The Tenth Data Release of the Sloan Digital Sky Survey: First Spectroscopic Data from the SDSS-III Apache Point Observatory Galactic Evolution Experiment". In: *ApJS* 211.2, p. 17. DOI: 10.1088/0067-0049/211/2/17. arXiv: 1307.7735 [astro-ph.IM].

Alam, S. et al. (2015). "The Eleventh and Twelfth Data Releases of the Sloan Digital Sky Survey: Final Data from SDSS-III". In: *ApJS* 219.1, p. 12. DOI: 10.1088/0067-0049/219/1/12. arXiv: 1501.00963 [astro-ph.IM].

Alard, C. and R. H. Lupton (1998). "A Method for Optimal Image Subtraction". In: *ApJ* 503.1, pp. 325–331. DOI: 10.1086/305984. arXiv: astro-ph/9712287 [astro-ph].

Albareti, F. D. et al. (2017). "The 13th Data Release of the Sloan Digital Sky Survey: First Spectroscopic Data from the SDSS-IV Survey Mapping Nearby Galaxies at Apache Point Observatory". In: *ApJS* 233.2, p. 25. DOI: 10.3847/1538-4365/aa8992. arXiv: 1608.02013 [astro-ph.GA].

Alexander, K. D. et al. (2016). "Discovery of an Outflow from Radio Observations of the Tidal Disruption Event ASASSN-14li". In: *ApJL* 819.2, p. L25. DOI: 10.3847/2041-8205/819/2/L25. arXiv: 1510.01226 [astro-ph.HE].

Alexander, K. D. et al. (2017). "A Reverse Shock and Unusual Radio Properties in GRB 160625B". In: *ApJ* 848.1, p. 69. DOI: 10.3847/1538-4357/aa8a76. arXiv: 1705.08455 [astro-ph.HE].

Alexander, K. D. et al. (2019). "An Unexpectedly Small Emission Region Size Inferred from Strong High-frequency Diffractive Scintillation in GRB 161219B". In: *ApJ* 870.2, p. 67. DOI: 10.3847/1538-4357/aaf19d. arXiv: 1806.08017 [astro-ph.HE].

Almgren, A. S. et al. (2010). "CASTRO: A New Compressible Astrophysical Solver. I. Hydrodynamics and Self-gravity". In: *ApJ* 715.2, pp. 1221–1238. DOI: 10.1088/0004-637X/715/2/1221. arXiv: 1005.0114 [astro-ph.IM].

Amati, L. (2006). "The $E_{p,i}$-E_{iso} correlation in gamma-ray bursts: updated observational status, re-analysis and main implications". In: *MNRAS* 372.1, pp. 233–245. DOI: 10.1111/j.1365-2966.2006.10840.x. arXiv: astro-ph/0601553 [astro-ph].

Aptekar, R. L. et al. (1995). "Konus-W Gamma-Ray Burst Experiment for the GGS Wind Spacecraft". In: *Space Sci. Rev.* 71.1-4, pp. 265–272. DOI: 10.1007/BF00751332.

Arcavi, I. et al. (2011). "SN 2011dh: Discovery of a Type IIb Supernova from a Compact Progenitor in the Nearby Galaxy M51". In: *ApJL* 742.2, p. L18. DOI: 10.1088/2041-8205/742/2/L18. arXiv: 1106.3551 [astro-ph.CO].

Arcavi, I. et al. (2016). "Rapidly Rising Transients in the Supernova—Superluminous Supernova Gap". In: *ApJ* 819.1, p. 35. DOI: 10.3847/0004-637X/819/1/35. arXiv: 1511.00704 [astro-ph.CO].

Arnett, W. D. (1982). "Type I supernovae. I - Analytic solutions for the early part of the light curve". In: *ApJ* 253, pp. 785–797. DOI: 10.1086/159681.

Arnouts, S. et al. (1999). "Measuring and modelling the redshift evolution of clustering: the Hubble Deep Field North". In: *MNRAS* 310.2, pp. 540–556. DOI: 10.1046/j.1365-8711.1999.02978.x. arXiv: astro-ph/9902290 [astro-ph].

Asplund, M. et al. (2009). "The Chemical Composition of the Sun". In: *ARA&A* 47.1, pp. 481–522. DOI: 10.1146/annurev.astro.46.060407.145222. arXiv: 0909.0948 [astro-ph.SR].

Astropy Collaboration et al. (2013). "Astropy: A community Python package for astronomy". In: *A&A* 558, A33. DOI: 10.1051/0004-6361/201322068. arXiv: 1307.6212 [astro-ph.IM].

Band, D. et al. (1993). "BATSE Observations of Gamma-Ray Burst Spectra. I. Spectral Diversity". In: *ApJ* 413, p. 281. DOI: 10.1086/172995.

Barnes, J. et al. (2018). "A GRB and Broad-lined Type Ic Supernova from a Single Central Engine". In: *ApJ* 860.1, p. 38. DOI: 10.3847/1538-4357/aabf84. arXiv: 1708.02630 [astro-ph.HE].

Barnsley, R. M., R. J. Smith, and I. A. Steele (2012). "A fully automated data reduction pipeline for the FRODOSpec integral field spectrograph". In: *Astronomische Nachrichten* 333.2, pp. 101–117. DOI: 10.1002/asna.201111634. arXiv: 1112.2574 [astro-ph.IM].

Barthelmy, S. D. et al. (2005). "The Burst Alert Telescope (BAT) on the SWIFT Midex Mission". In: *Space Sci. Rev.* 120.3-4, pp. 143–164. DOI: 10.1007/s11214-005-5096-3. arXiv: astro-ph/0507410 [astro-ph].

Becker, A. (2015). *HOTPANTS: High Order Transform of PSF ANd Template Subtraction*. ascl: 1504.004.

Bellm, E. C. and B. Sesar (2016). *pyraf-dbsp: Reduction pipeline for the Palomar Double Beam Spectrograph*. ascl: 1602.002.

Bellm, E. C. et al. (2019a). "The Zwicky Transient Facility: Surveys and Scheduler". In: *PASP* 131.1000, p. 068003. DOI: 10.1088/1538-3873/ab0c2a. arXiv: 1905.02209 [astro-ph.IM].

Bellm, E. C. et al. (2019b). "The Zwicky Transient Facility: System Overview, Performance, and First Results". In: *PASP* 131.995, p. 018002. DOI: 10.1088/1538-3873/aaecbe. arXiv: 1902.01932 [astro-ph.IM].

Bellm, E. and S. Kulkarni (2017). "The unblinking eye on the sky". In: *Nature Astronomy* 1, p. 0071. DOI: 10.1038/s41550-017-0071. arXiv: 1705.10052 [astro-ph.IM].

Ben-Ami, S. et al. (2012). "Discovery and Early Multi-wavelength Measurements of the Energetic Type Ic Supernova PTF12gzk: A Massive-star Explosion in a Dwarf Host Galaxy". In: *ApJL* 760.2, p. L33. DOI: 10.1088/2041-8205/760/2/L33. arXiv: 1208.5900 [astro-ph.CO].

Beniamini, P., J. Granot, and R. Gill (2020a). "Afterglow light curves from misaligned structured jets". In: *MNRAS* 493.3, pp. 3521–3534. DOI: 10.1093/mnras/staa538. arXiv: 2001.02239 [astro-ph.HE].

Beniamini, P. and E. Nakar (2019). "Observational constraints on the structure of gamma-ray burst jets". In: *MNRAS* 482.4, pp. 5430–5440. DOI: 10.1093/mnras/sty3110. arXiv: 1808.07493 [astro-ph.HE].

Beniamini, P. and A. J. van der Horst (2017). "Electrons' energy in GRB afterglows implied by radio peaks". In: *MNRAS* 472.3, pp. 3161–3168. DOI: 10.1093/mnras/stx2203. arXiv: 1706.07817 [astro-ph.HE].

Beniamini, P. et al. (2020b). "X-ray plateaus in gamma-ray bursts' light curves from jets viewed slightly off-axis". In: *MNRAS* 492.2, pp. 2847–2857. DOI: 10.1093/mnras/staa070. arXiv: 1907.05899 [astro-ph.HE].

Berger, E. et al. (2003). "A common origin for cosmic explosions inferred from calorimetry of GRB030329". In: *Nature* 426.6963, pp. 154–157. DOI: 10.1038/nature01998. arXiv: astro-ph/0308187 [astro-ph].

Berger, E. et al. (2012). "Radio Monitoring of the Tidal Disruption Event Swift J164449.3+573451. I. Jet Energetics and the Pristine Parsec-scale Environment of a Supermassive Black Hole". In: *ApJ* 748.1, p. 36. DOI: 10.1088/0004-637X/748/1/36. arXiv: 1112.1697 [astro-ph.HE].

Berger, E. et al. (2013). "A Search for Fast Optical Transients in the Pan-STARRS1 Medium-Deep Survey: M-Dwarf Flares, Asteroids, Limits on Extragalactic Rates, and Implications for LSST". In: *ApJ* 779.1, p. 18. DOI: 10.1088/0004-637X/779/1/18. arXiv: 1307.5324 [astro-ph.HE].

Bersier, D. et al. (2006). "Evidence for a Supernova Associated with the X-Ray Flash 020903". In: *ApJ* 643.1, pp. 284–291. DOI: 10.1086/502640. arXiv: astro-ph/0602163 [astro-ph].

Bersten, M. C. et al. (2018). "A surge of light at the birth of a supernova". In: *Nature* 554.7693, pp. 497–499. DOI: 10.1038/nature25151. arXiv: 1802.09360 [astro-ph.HE].

Bersten, M. C. et al. (2012). "The Type IIb Supernova 2011dh from a Supergiant Progenitor". In: *ApJ* 757.1, p. 31. DOI: 10.1088/0004-637X/757/1/31. arXiv: 1207.5975 [astro-ph.HE].

Bertin, E. (2010). *SWarp: Resampling and Co-adding FITS Images Together*. ascl: 1010.068.

Bhalerao, V. et al. (2017). "A Tale of Two Transients: GW 170104 and GRB 170105A". In: *ApJ* 845.2, p. 152. DOI: 10.3847/1538-4357/aa81d2. arXiv: 1706.00024 [astro-ph.HE].

Bianco, F. B. et al. (2014). "Multi-color Optical and Near-infrared Light Curves of 64 Stripped-envelope Core-Collapse Supernovae". In: *ApJS* 213.2, p. 19. DOI: 10.1088/0067-0049/213/2/19. arXiv: 1405.1428 [astro-ph.SR].

Bianco, F. B. et al. (2016). "Monte Carlo method for calculating oxygen abundances and their uncertainties from strong-line flux measurements". In: *Astronomy and Computing* 16, pp. 54–66. DOI: 10.1016/j.ascom.2016.03.002. arXiv: 1505.06213 [astro-ph.IM].

Bietenholz, M. F. et al. (2020). "AT 2018cow VLBI: no long-lived relativistic outflow". In: *MNRAS* 491.4, pp. 4735–4741. DOI: 10.1093/mnras/stz3249. arXiv: 1911.08778 [astro-ph.HE].

Blackburn, J. K. et al. (1999). *FTOOLS: A general package of software to manipulate FITS files*. ascl: 9912.002.

Blackburn, L. et al. (2015). "High-Energy Electromagnetic Offline Follow-Up of Ligo-Virgo Gravitational-Wave Binary Coalescence Candidate Events". In: *ApJS* 217.1, p. 8. DOI: 10.1088/0067-0049/217/1/8. arXiv: 1410.0929 [astro-ph.HE].

Blagorodnova, N. et al. (2018). "The SED Machine: A Robotic Spectrograph for Fast Transient Classification". In: *PASP* 130.985, p. 035003. DOI: 10.1088/1538-3873/aaa53f. arXiv: 1710.02917 [astro-ph.IM].

Blandford, R. and D. Eichler (1987). "Particle acceleration at astrophysical shocks: A theory of cosmic ray origin". In: *Physics Reports* 154.1, pp. 1–75. DOI: 10.1016/0370-1573(87)90134-7.

Blanton, M. R. and S. Roweis (2007). "K-Corrections and Filter Transformations in the Ultraviolet, Optical, and Near-Infrared". In: *AJ* 133.2, pp. 734–754. DOI: 10.1086/510127. arXiv: astro-ph/0606170 [astro-ph].

Blanton, M. R. et al. (2011). "Improved Background Subtraction for the Sloan Digital Sky Survey Images". In: *AJ* 142.1, p. 31. DOI: 10.1088/0004-6256/142/1/31. arXiv: 1105.1960 [astro-ph.IM].

Blaufuss, E. (2018). "ZTF18abukavn/AT2018gep: IceCube neutrino search". In: *The Astronomer's Telegram* 12062, p. 1.

Blondin, S. and J. L. Tonry (2007). "Determining the Type, Redshift, and Age of a Supernova Spectrum". In: *ApJ* 666.2, pp. 1024–1047. DOI: 10.1086/520494. arXiv: 0709.4488 [astro-ph].

Bloom, J. S. et al. (2012). "Automating Discovery and Classification of Transients and Variable Stars in the Synoptic Survey Era". In: *PASP* 124.921, p. 1175. DOI: 10.1086/668468. arXiv: 1106.5491 [astro-ph.IM].

Bochanski, J. J., S. L. Hawley, and A. A. West (2011). "The Sloan Digital Sky Survey Data Release 7 Spectroscopic M Dwarf Catalog. II. Statistical Parallax Analysis". In: *AJ* 141.3, p. 98. DOI: 10.1088/0004-6256/141/3/98. arXiv: 1101.3549 [astro-ph.SR].

Bock, D. C. .-.-J. (2006). "CARMA: Combined Array for Research in Millimeter-Wave Astronomy". In: *Revealing the Molecular Universe: One Antenna is Never Enough*. Ed. by D. C. Backer, J. M. Moran, and J. L. Turner. Vol. 356. Astronomical Society of the Pacific Conference Series, p. 17.

Bourne, N. et al. (2012). "Herschel-ATLAS/GAMA: a census of dust in optically selected galaxies from stacking at submillimetre wavelengths". In: *MNRAS* 421.4, pp. 3027–3059. DOI: 10.1111/j.1365-2966.2012.20528.x. arXiv: 1201.1916 [astro-ph.CO].

Bower, G. C. et al. (2003). "A Giant Outburst at Millimeter Wavelengths in the Orion Nebula". In: *ApJ* 598.2, pp. 1140–1150. DOI: 10.1086/379101. arXiv: astro-ph/0308277 [astro-ph].

Branch, D. et al. (2002). "Direct Analysis of Spectra of Type Ib Supernovae". In: *ApJ* 566.2, pp. 1005–1017. DOI: 10.1086/338127. arXiv: astro-ph/0106367 [astro-ph].

Breeveld, A. A. et al. (2011). "An Updated Ultraviolet Calibration for the Swift/UVOT". In: *American Institute of Physics Conference Series*. Ed. by J. E. McEnery, J. L. Racusin, and N. Gehrels. Vol. 1358. American Institute of Physics Conference Series, pp. 373–376. DOI: 10.1063/1.3621807. arXiv: 1102.4717 [astro-ph.IM].

Bright, J. et al. (2018). "AMI-LA 15.5 GHz observations of AT2018cow". In: *The Astronomer's Telegram* 11774, p. 1.

Brink, H. et al. (2013). "Using machine learning for discovery in synoptic survey imaging data". In: *MNRAS* 435.2, pp. 1047–1060. DOI: 10.1093/mnras/stt1306. arXiv: 1209.3775 [astro-ph.IM].

Bromberg, O., E. Nakar, and T. Piran (2011). "Are Low-luminosity Gamma-Ray Bursts Generated by Relativistic Jets?" In: *ApJL* 739.2, p. L55. DOI: 10.1088/2041-8205/739/2/L55. arXiv: 1107.1346 [astro-ph.HE].

Brown, P. J. et al. (2014). "SOUSA: the Swift Optical/Ultraviolet Supernova Archive". In: *Ap&SS* 354.1, pp. 89–96. DOI: 10.1007/s10509-014-2059-8. arXiv: 1407.3808 [astro-ph.HE].

Brown, T. M. et al. (2013). "Las Cumbres Observatory Global Telescope Network". In: *PASP* 125.931, p. 1031. DOI: 10.1086/673168. arXiv: 1305.2437 [astro-ph.IM].

Bruzual, G. and S. Charlot (2003). "Stellar population synthesis at the resolution of 2003". In: *MNRAS* 344.4, pp. 1000–1028. DOI: 10.1046/j.1365-8711.2003.06897.x. arXiv: astro-ph/0309134 [astro-ph].

Bucciantini, N. et al. (2007). "Magnetar-driven bubbles and the origin of collimated outflows in gamma-ray bursts". In: *MNRAS* 380.4, pp. 1541–1553. DOI: 10.1111/j.1365-2966.2007.12164.x. arXiv: 0705.1742 [astro-ph].

Bufano, F. et al. (2012). "The Highly Energetic Expansion of SN 2010bh Associated with GRB 100316D". In: *ApJ* 753.1, p. 67. DOI: 10.1088/0004-637X/753/1/67. arXiv: 1111.4527 [astro-ph.HE].

Burdge, K. et al. (2019a). "LIGO/Virgo S190901ap: Keck I LRIS spectroscopy of ZTF19abvizsw". In: *GRB Coordinates Network* 25639, p. 1.

Burdge, K. et al. (2019b). "LIGO/Virgo S190901ap: Keck I LRIS spectroscopy of ZTF19abvizsw". In: *GRB Coordinates Network* 25639, p. 1.

Burrows, D. N. et al. (2005). "The Swift X-Ray Telescope". In: *Space Sci. Rev.* 120.3-4, pp. 165–195. DOI: 10.1007/s11214-005-5097-2. arXiv: astro-ph/0508071 [astro-ph].

Calzetti, D. et al. (2000). "The Dust Content and Opacity of Actively Star-forming Galaxies". In: *ApJ* 533.2, pp. 682–695. DOI: 10.1086/308692. arXiv: astro-ph/9911459 [astro-ph].

Campana, S. et al. (2006). "The association of GRB 060218 with a supernova and the evolution of the shock wave". In: *Nature* 442.7106, pp. 1008–1010. DOI: 10.1038/nature04892. arXiv: astro-ph/0603279 [astro-ph].

Cano, Z. et al. (2011). "XRF 100316D/SN 2010bh and the Nature of Gamma-Ray Burst Supernovae". In: *ApJ* 740.1, p. 41. DOI: 10.1088/0004-637X/740/1/41. arXiv: 1104.5141 [astro-ph.SR].

Cano, Z. et al. (2017a). "GRB 161219B/SN 2016jca: A low-redshift gamma-ray burst supernova powered by radioactive heating". In: *A&A* 605, A107. DOI: 10.1051/0004-6361/201731005. arXiv: 1704.05401 [astro-ph.HE].

Cano, Z. (2013). "A new method for estimating the bolometric properties of Ibc supernovae". In: *MNRAS* 434.2, pp. 1098–1116. DOI: 10.1093/mnras/stt1048. arXiv: 1306.1488 [astro-ph.SR].

Cano, Z. et al. (2017b). "The Observer's Guide to the Gamma-Ray Burst Supernova Connection". In: *Advances in Astronomy* 2017, p. 8929054. DOI: 10.1155/2017/8929054. arXiv: 1604.03549 [astro-ph.HE].

Cantiello, M. et al. (2007). "Binary star progenitors of long gamma-ray bursts". In: *A&A* 465.2, pp. L29–L33. DOI: 10.1051/0004-6361:20077115. arXiv: astro-ph/0702540 [astro-ph].

Cao, Y., P. E. Nugent, and M. M. Kasliwal (2016). "Intermediate Palomar Transient Factory: Realtime Image Subtraction Pipeline". In: *PASP* 128.969, p. 114502. DOI: 10.1088/1538-3873/128/969/114502. arXiv: 1608.01006 [astro-ph.IM].

Cenko, S. B. et al. (2009). "Dark Bursts in the Swift Era: The Palomar 60 Inch-Swift Early Optical Afterglow Catalog". In: *ApJ* 693.2, pp. 1484–1493. DOI: 10.1088/0004-637X/693/2/1484. arXiv: 0808.3983 [astro-ph].

Cenko, S. B. et al. (2006). "The Automated Palomar 60 Inch Telescope". In: *PASP* 118.848, pp. 1396–1406. DOI: 10.1086/508366. arXiv: astro-ph/0608323 [astro-ph].

Cenko, S. B. et al. (2013). "Discovery of a Cosmological, Relativistic Outburst via its Rapidly Fading Optical Emission". In: *ApJ* 769.2, p. 130. DOI: 10.1088/0004-637X/769/2/130. arXiv: 1304.4236 [astro-ph.CO].

Cenko, S. B. et al. (2015). "iPTF14yb: The First Discovery of a Gamma-Ray Burst Afterglow Independent of a High-energy Trigger". In: *ApJL* 803.2, p. L24. DOI: 10.1088/2041-8205/803/2/L24. arXiv: 1504.00673 [astro-ph.HE].

Chabrier, G. (2003). "Galactic Stellar and Substellar Initial Mass Function". In: *PASP* 115.809, pp. 763–795. DOI: 10.1086/376392. arXiv: astro-ph/0304382 [astro-ph].

Chakraborti, S. et al. (2015). "A Missing-link in the Supernova-GRB Connection: The Case of SN 2012ap". In: *ApJ* 805.2, p. 187. DOI: 10.1088/0004-637X/805/2/187. arXiv: 1402.6336 [astro-ph.HE].

Chambers, K. C. et al. (2016). "The Pan-STARRS1 Surveys". In: *arXiv e-prints*, arXiv:1612.05560. arXiv: 1612.05560 [astro-ph.IM].

Chand, V. et al. (2020). "Peculiar prompt emission and afterglow in H.E.S.S. detected GRB 190829A". In: *arXiv e-prints*, arXiv:2001.00648. arXiv: 2001.00648 [astro-ph.HE].

Chandra, P. and D. A. Frail (2012). "A Radio-selected Sample of Gamma-Ray Burst Afterglows". In: *ApJ* 746.2, p. 156. DOI: 10.1088/0004-637X/746/2/156. arXiv: 1110.4124 [astro-ph.CO].

Chang, Y.-Y. et al. (2015). "Stellar Masses and Star Formation Rates for 1M Galaxies from SDSS+WISE". In: *ApJS* 219.1, p. 8. DOI: 10.1088/0067-0049/219/1/8. arXiv: 1506.00648 [astro-ph.GA].

Chevalier, R. A. (1982). "The radio and X-ray emission from type II supernovae." In: *ApJ* 259, pp. 302–310. DOI: 10.1086/160167.

Chevalier, R. A. (1983). "Blast waves with cosmic-ray pressure". In: *ApJ* 272, pp. 765–772. DOI: 10.1086/161338.

Chevalier, R. A. (1984). "The interaction of supernovae with a circumstellar medium." In: *Annals of the New York Academy of Sciences* 422, pp. 215–232. DOI: 10.1111/j.1749-6632.1984.tb23355.x.

Chevalier, R. A. (1998). "Synchrotron Self-Absorption in Radio Supernovae". In: *ApJ* 499.2, pp. 810–819. DOI: 10.1086/305676.

Chevalier, R. A. (2012). "Common Envelope Evolution Leading to Supernovae with Dense Interaction". In: *ApJL* 752.1, p. L2. DOI: 10.1088/2041-8205/752/1/L2. arXiv: 1204.3300 [astro-ph.HE].

Chevalier, R. A. and C. Fransson (2006). "Circumstellar Emission from Type Ib and Ic Supernovae". In: *ApJ* 651.1, pp. 381–391. DOI: 10.1086/507606. arXiv: astro-ph/0607196 [astro-ph].

Chevalier, R. A. and C. Fransson (2008). "Shock Breakout Emission from a Type Ib/c Supernova: XRT 080109/SN 2008D". In: *ApJL* 683.2, p. L135. DOI: 10.1086/591522. arXiv: 0806.0371 [astro-ph].

Chevalier, R. A. and C. Fransson (2017). "Thermal and Non-thermal Emission from Circumstellar Interaction". In: *Handbook of Supernovae*. Ed. by A. W. Alsabti and P. Murdin, p. 875. DOI: 10.1007/978-3-319-21846-5_34.

Chevalier, R. A. and C. M. Irwin (2011). "Shock Breakout in Dense Mass Loss: Luminous Supernovae". In: *ApJL* 729.1, p. L6. DOI: 10.1088/2041-8205/729/1/L6. arXiv: 1101.1111 [astro-ph.HE].

Clocchiatti, A. et al. (2011). "The Ultimate Light Curve of SN 1998bw/GRB 980425". In: *AJ* 141.5, p. 163. DOI: 10.1088/0004-6256/141/5/163. arXiv: 1106.1695 [astro-ph.HE].

Condon, J. J. (1992). "Radio emission from normal galaxies." In: *ARA&A* 30, pp. 575–611. DOI: 10.1146/annurev.aa.30.090192.003043.

Cook, D. O. et al. (2019). "Census of the Local Universe (CLU) Narrowband Survey. I. Galaxy Catalogs from Preliminary Fields". In: *ApJ* 880.1, p. 7. DOI: 10.3847/1538-4357/ab2131. arXiv: 1710.05016 [astro-ph.GA].

Coppejans, D. L. et al. (2020). "A mildly relativistic outflow from the energetic, fast-rising blue optical transient CSS161010 in a dwarf galaxy". In: *arXiv e-prints*, arXiv:2003.10503. arXiv: 2003.10503 [astro-ph.HE].

Cordes, J. M. and T. J. W. Lazio (2002). "NE2001.I. A New Model for the Galactic Distribution of Free Electrons and its Fluctuations". In: *arXiv e-prints*, astro–ph/0207156. arXiv: astro-ph/0207156 [astro-ph].

Corsi, A. et al. (2012). "Evidence for a Compact Wolf-Rayet Progenitor for the Type Ic Supernova PTF 10vgv". In: *ApJL* 747.1, p. L5. DOI: 10.1088/2041-8205/747/1/L5. arXiv: 1110.5618 [astro-ph.CO].

Corsi, A. et al. (2014). "A Multi-wavelength Investigation of the Radio-loud Supernova PTF11qcj and its Circumstellar Environment". In: *ApJ* 782.1, p. 42. DOI: 10.1088/0004-637X/782/1/42. arXiv: 1307.2366 [astro-ph.HE].

Corsi, A. et al. (2016). "Radio Observations of a Sample of Broad-line Type IC Supernovae Discovered by PTF/IPTF: A Search for Relativistic Explosions". In: *ApJ* 830.1, p. 42. DOI: 10.3847/0004-637X/830/1/42. arXiv: 1512.01303 [astro-ph.HE].

Corsi, A. et al. (2017). "iPTF17cw: An Engine-driven Supernova Candidate Discovered Independent of a Gamma-Ray Trigger". In: *ApJ* 847.1, p. 54. DOI: 10.3847/1538-4357/aa85e5. arXiv: 1706.00045 [astro-ph.HE].

Costantin, L. et al. (2018). "Asiago classification of a Ic-BL supernova and a symbiotic star". In: *The Astronomer's Telegram* 12047, p. 1.

Curran, P. A., A. J. van der Horst, and R. A. M. J. Wijers (2008). "Are the missing X-ray breaks in gamma-ray burst afterglow light curves merely hidden?" In: *MNRAS* 386.2, pp. 859–863. DOI: 10.1111/j.1365-2966.2008.13043.x. arXiv: 0710.5285 [astro-ph].

Cutri, R. M. et al. (2013). *Explanatory Supplement to the AllWISE Data Release Products*. Explanatory Supplement to the AllWISE Data Release Products.

D'Elia, V. et al. (2018). "GRB 171205A/SN 2017iuk: A local low-luminosity gamma-ray burst". In: *A&A* 619, A66. DOI: 10.1051/0004-6361/201833847. arXiv: 1810.03339 [astro-ph.HE].

Dabringhausen, J., P. Kroupa, and H. Baumgardt (2009). "A top-heavy stellar initial mass function in starbursts as an explanation for the high mass-to-light ratios of ultra-compact dwarf galaxies". In: *MNRAS* 394.3, pp. 1529–1543. DOI: 10.1111/j.1365-2966.2009.14425.x. arXiv: 0901.0915 [astro-ph.GA].

Dai, X. et al. (2008). "Go Long, Go Deep: Finding Optical Jet Breaks for Swift-Era GRBs with the LBT". In: *ApJL* 682.2, p. L77. DOI: 10.1086/591041. arXiv: 0712.2239 [astro-ph].

Dal Canton, T. et al. (2018). "AT2018cow: Fermi/GBM Data Search". In: *The Astronomer's Telegram* 11793, p. 1.

Davenport, J. R. A. (2016). "The Kepler Catalog of Stellar Flares". In: *ApJ* 829.1, p. 23. DOI: 10.3847/0004-637X/829/1/23. arXiv: 1607.03494 [astro-ph.SR].

Davenport, J. R. A. et al. (2012). "Multi-wavelength Characterization of Stellar Flares on Low-mass Stars Using SDSS and 2MASS Time-domain Surveys". In: *ApJ* 748.1, p. 58. DOI: 10.1088/0004-637X/748/1/58. arXiv: 1202.1902 [astro-ph.SR].

de Kool, M., M. C. Begelman, and M. Sikora (1989). "Self-absorbed Synchrotron Sources in Active Galactic Nuclei". In: *ApJ* 337, p. 66. DOI: 10.1086/167087.

de Ugarte Postigo, A. et al. (2012). "Pre-ALMA observations of GRBs in the mm/submm range". In: *A&A* 538, A44. DOI: 10.1051/0004-6361/201117848. arXiv: 1108.1797 [astro-ph.CO].

de Ugarte Postigo, A. et al. (2018). "AT2018cow: NOEMA millimetre detection". In: *The Astronomer's Telegram* 11749, p. 1.

De, K. et al. (2018). "A hot and fast ultra-stripped supernova that likely formed a compact neutron star binary". In: *Science* 362.6411, pp. 201–206. DOI: 10.1126/science.aas8693. arXiv: 1810.05181 [astro-ph.HE].

De, K. et al. (2020). "The Zwicky Transient Facility Census of the Local Universe I: Systematic search for Calcium rich gap transients reveal three related spectroscopic sub-classes". In: *arXiv e-prints*, arXiv:2004.09029. arXiv: 2004.09029 [astro-ph.HE].

Dekany, R. et al. (2016). "The Zwicky Transient Facility Camera". In: *Phys. Rev. Lett.* Vol. 9908. Society of Photo-Optical Instrumentation Engineers (SPIE) Conference Series, p. 99085M. DOI: 10.1117/12.2234558.

Dekany, R. et al. (2020). "The Zwicky Transient Facility: Observing System". In: *PASP* 132.1009, p. 038001. DOI: 10.1088/1538-3873/ab4ca2.

Dent, W. A. et al. (1983). "A rapid millimetre wave outburst in the nucleus of NGC1275". In: *Nature* 306.5938, pp. 41–42. DOI: 10.1038/306041a0.

Dermer, C. D., J. Chiang, and M. Böttcher (1999). "Fireball Loading and the Blast-Wave Model of Gamma-Ray Bursts". In: *ApJ* 513.2, pp. 656–668. DOI: 10.1086/306871. arXiv: astro-ph/9804174 [astro-ph].

Dessart, L. (2019). "Simulations of light curves and spectra for superluminous Type Ic supernovae powered by magnetars". In: *A&A* 621, A141. DOI: 10.1051/0004-6361/201834535. arXiv: 1812.03749 [astro-ph.SR].

Dey, A. et al. (2019). "Overview of the DESI Legacy Imaging Surveys". In: *AJ* 157.5, p. 168. DOI: 10.3847/1538-3881/ab089d. arXiv: 1804.08657 [astro-ph.IM].

Djorgovski, S. G. et al. (2011). "The Catalina Real-Time Transient Survey (CRTS)". In: *arXiv e-prints*, arXiv:1102.5004. arXiv: 1102.5004 [astro-ph.IM].

Djupvik, A. A. and J. Andersen (2010). "The Nordic Optical Telescope". In: *Astrophysics and Space Science Proceedings* 14, p. 211. DOI: 10.1007/978-3-642-11250-8_21. arXiv: 0901.4015 [astro-ph.IM].

Dobie, D. et al. (2018a). "AT2018cow: Further ATCA monitoring". In: *The Astronomer's Telegram* 11818, p. 1.

Dobie, D. et al. (2018b). "ATCA Observations of AT2018cow". In: *The Astronomer's Telegram* 11795, p. 1.

Draine, B. T. (2011). *Physics of the Interstellar and Intergalactic Medium*.

Drake, A. J. et al. (2009). "First Results from the Catalina Real-Time Transient Survey". In: *ApJ* 696.1, pp. 870–884. DOI: 10.1088/0004-637X/696/1/870. arXiv: 0809.1394 [astro-ph].

Drout, M. R. et al. (2014). "Rapidly Evolving and Luminous Transients from Pan-STARRS1". In: *ApJ* 794.1, p. 23. DOI: 10.1088/0004-637X/794/1/23. arXiv: 1405.3668 [astro-ph.HE].

Duev, D. A. et al. (2019). "Real-bogus classification for the Zwicky Transient Facility using deep learning". In: *MNRAS* 489.3, pp. 3582–3590. DOI: 10.1093/mnras/stz2357. arXiv: 1907.11259 [astro-ph.IM].

Duffell, P. C. and A. Y. Q. Ho (2019). "How Dense a CSM is Sufficient to Choke a Jet?" In: *arXiv e-prints*, arXiv:1907.03768. arXiv: 1907.03768 [astro-ph.HE].

Eftekhari, T. et al. (2018). "Radio Monitoring of the Tidal Disruption Event Swift J164449.3+573451. III. Late-time Jet Energetics and a Deviation from Equipartition". In: *ApJ* 854.2, p. 86. DOI: 10.3847/1538-4357/aaa8e0. arXiv: 1710.07289 [astro-ph.HE].

Eichler, D. and J. Granot (2006). "The Case for Anisotropic Afterglow Efficiency within Gamma-Ray Burst Jets". In: *ApJL* 641.1, pp. L5–L8. DOI: 10.1086/503667. arXiv: astro-ph/0509857 [astro-ph].

Eldridge, J. J., N. Langer, and C. A. Tout (2011). "Runaway stars as progenitors of supernovae and gamma-ray bursts". In: *MNRAS* 414.4, pp. 3501–3520. DOI: 10.1111/j.1365-2966.2011.18650.x. arXiv: 1103.1877 [astro-ph.SR].

Ergon, M. et al. (2018). "Monte-Carlo methods for NLTE spectral synthesis of supernovae". In: *A&A* 620, A156. DOI: 10.1051/0004-6361/201833043. arXiv: 1810.07165 [astro-ph.SR].

Evans, P. A. et al. (2007). "An online repository of Swift/XRT light curves of γ-ray bursts". In: *A&A* 469.1, pp. 379–385. DOI: 10.1051/0004-6361:20077530. arXiv: 0704.0128 [astro-ph].

Evans, P. A. et al. (2009). "Methods and results of an automatic analysis of a complete sample of Swift-XRT observations of GRBs". In: *MNRAS* 397.3, pp. 1177–1201. DOI: 10.1111/j.1365-2966.2009.14913.x. arXiv: 0812.3662 [astro-ph].

Fan, Y.-Z., T. Piran, and D. Xu (2006). "The interpretation and implication of the afterglow of GRB 060218". In: *JCAP* 2006.9, p. 013. DOI: 10.1088/1475-7516/2006/09/013. arXiv: astro-ph/0604016 [astro-ph].

Fatkhullin, T. A. et al. (2006). "GRB 060218: emergence of the underlying SN spectrum." In: *GRB Coordinates Network* 4809, p. 1.

Fender, R. P. et al. (2015). "A prompt radio transient associated with a gamma-ray superflare from the young M dwarf binary DG CVn." In: *MNRAS* 446, pp. L66–L70. DOI: 10.1093/mnrasl/slu165. arXiv: 1410.1545 [astro-ph.HE].

Ferrero, P. et al. (2006). "The GRB 060218/SN 2006aj event in the context of other gamma-ray burst supernovae". In: *A&A* 457.3, pp. 857–864. DOI: 10.1051/0004-6361:20065530. arXiv: astro-ph/0605058 [astro-ph].

Ferrigno, C. et al. (2018). "INTEGRAL hard X-ray spectroscopy of AT2018cow: preliminary detection of a cutoff at 40 keV." In: *The Astronomer's Telegram* 11788, p. 1.

Fitzpatrick, E. L. (1999). "Correcting for the Effects of Interstellar Extinction". In: *PASP* 111.755, pp. 63–75. DOI: 10.1086/316293. arXiv: astro-ph/9809387 [astro-ph].

Flewelling, H. A. et al. (2016). "The Pan-STARRS1 Database and Data Products". In: *arXiv e-prints*, arXiv:1612.05243. arXiv: 1612.05243 [astro-ph.IM].

Foley, R. J. et al. (2003). "Optical Photometry and Spectroscopy of the SN 1998bw-like Type Ic Supernova 2002ap". In: *PASP* 115.812, pp. 1220–1235. DOI: 10.1086/378242. arXiv: astro-ph/0307136 [astro-ph].

Fong, W. et al. (2015). "A Decade of Short-duration Gamma-Ray Burst Broadband Afterglows: Energetics, Circumburst Densities, and Jet Opening Angles". In: *ApJ* 815.2, p. 102. DOI: 10.1088/0004-637X/815/2/102. arXiv: 1509.02922 [astro-ph.HE].

Fox, O. D. and N. Smith (2019). "Signatures of circumstellar interaction in the unusual transient AT 2018cow". In: *MNRAS* 488.3, pp. 3772–3782. DOI: 10.1093/mnras/stz1925. arXiv: 1903.01535 [astro-ph.HE].

Frail, D. A., E. Waxman, and S. R. Kulkarni (2000). "A 450 Day Light Curve of the Radio Afterglow of GRB 970508: Fireball Calorimetry". In: *ApJ* 537.1, pp. 191–204. DOI: 10.1086/309024. arXiv: astro-ph/9910319 [astro-ph].

Frail, D. A. et al. (2001). "Beaming in Gamma-Ray Bursts: Evidence for a Standard Energy Reservoir". In: *ApJL* 562.1, pp. L55–L58. DOI: 10.1086/338119. arXiv: astro-ph/0102282 [astro-ph].

Frater, R. H., J. W. Brooks, and J. B. Whiteoak (1992). "The Australia Telescope - Overview". In: *Journal of Electrical and Electronics Engineering Australia* 12.2, pp. 103–112.

Fremling, C. (2018). "Palomar 48-inch observations of the optical transient AT2018cow/ATLAS18qqn". In: *The Astronomer's Telegram* 11738, p. 1.

Fremling, C., A. Dugas, and Y. Sharma (2019a). "ZTF Transient Classification Report for 2019-05-31". In: *Transient Name Server Classification Report* 2019-892, p. 1.

Fremling, C. et al. (2016). "PTF12os and iPTF13bvn. Two stripped-envelope supernovae from low-mass progenitors in NGC 5806". In: *A&A* 593, A68. DOI: 10.1051/0004-6361/201628275. arXiv: 1606.03074 [astro-ph.HE].

Fremling, C. et al. (2019b). "ZTF18aalrxas: A Type IIb Supernova from a Very Extended Low-mass Progenitor". In: *ApJL* 878.1, p. L5. DOI: 10.3847/2041-8213/ab218f. arXiv: 1903.09262 [astro-ph.HE].

Fremling, U. C. et al. (2019c). "The Zwicky Transient Facility Bright Transient Survey I: Spectroscopic Classification and the Redshift Completeness of Local Galaxy Catalogs". In: *arXiv e-prints*, arXiv:1910.12973. arXiv: 1910.12973 [astro-ph.HE].

Fruchter, A. S. et al. (2006). "Long γ-ray bursts and core-collapse supernovae have different environments". In: *Nature* 441.7092, pp. 463–468. DOI: 10.1038/nature04787. arXiv: astro-ph/0603537 [astro-ph].

Fruscione, A. et al. (2006). "CIAO: Chandra's data analysis system". In: *Phys. Rev. Lett.* Vol. 6270. Society of Photo-Optical Instrumentation Engineers (SPIE) Conference Series, p. 62701V. DOI: 10.1117/12.671760.

Fynbo, J. P. U. et al. (2009). "Low-resolution Spectroscopy of Gamma-ray Burst Optical Afterglows: Biases in the Swift Sample and Characterization of the Absorbers". In: *ApJS* 185.2, pp. 526–573. DOI: 10.1088/0067-0049/185/2/526. arXiv: 0907.3449 [astro-ph.CO].

Fynbo, J. P. U. et al. (2006). "No supernovae associated with two long-duration γ-ray bursts". In: *Nature* 444.7122, pp. 1047–1049. DOI: 10.1038/nature05375. arXiv: astro-ph/0608313 [astro-ph].

Gal-Yam, A. (2017). "Observational and Physical Classification of Supernovae". In: *Handbook of Supernovae*. Ed. by A. W. Alsabti and P. Murdin, p. 195. DOI: 10.1007/978-3-319-21846-5_35.

Gal-Yam, A. (2019). "A Simple Analysis of Type I Superluminous Supernova Peak Spectra: Composition, Expansion Velocities, and Dynamics". In: *ApJ* 882.2, p. 102. DOI: 10.3847/1538-4357/ab2f79. arXiv: 1806.08224 [astro-ph.HE].

Gal-Yam, A. et al. (2014). "A Wolf-Rayet-like progenitor of SN 2013cu from spectral observations of a stellar wind". In: *Nature* 509.7501, pp. 471–474. DOI: 10.1038/nature13304. arXiv: 1406.7640 [astro-ph.HE].

Galama, T. J. et al. (1998). "An unusual supernova in the error box of the γ-ray burst of 25 April 1998". In: *Nature* 395.6703, pp. 670–672. DOI: 10.1038/27150. arXiv: astro-ph/9806175 [astro-ph].

Garmire, G. P. et al. (2003). "Advanced CCD imaging spectrometer (ACIS) instrument on the Chandra X-ray Observatory". In: *Phys. Rev. Lett.* Ed. by J. E. Truemper and H. D. Tananbaum. Vol. 4851. Society of Photo-Optical Instrumentation Engineers (SPIE) Conference Series, pp. 28–44. DOI: 10.1117/12.461599.

Gehrels, N., E. Ramirez-Ruiz, and D. B. Fox (2009). "Gamma-Ray Bursts in the Swift Era". In: *ARA&A* 47.1, pp. 567–617. DOI: 10.1146/annurev.astro.46.060407.145147. arXiv: 0909.1531 [astro-ph.HE].

Gehrels, N. et al. (2004). "The Swift Gamma-Ray Burst Mission". In: *ApJ* 611.2, pp. 1005–1020. DOI: 10.1086/422091. arXiv: astro-ph/0405233 [astro-ph].

Gezari, S. (2012). "Ultraviolet and optical observations of tidal disruption events". In: *European Physical Journal Web of Conferences*. Vol. 39. European Physical Journal Web of Conferences, p. 03001. DOI: 10.1051/epjconf/20123903001.

Ghirlanda, G. et al. (2015). "Unveiling the population of orphan γ-ray bursts". In: *A&A* 578, A71. DOI: 10.1051/0004-6361/201526112. arXiv: 1504.02096 [astro-ph.HE].

Goldstein, A. et al. (2016). "Updates to the Fermi-GBM Short GRB Targeted Offline Search in Preparation for LIGO's Second Observing Run". In: *arXiv e-prints*, arXiv:1612.02395. arXiv: 1612.02395 [astro-ph.IM].

Gorosabel, J. et al. (2005). "The GRB 030329 host: a blue low metallicity subluminous galaxy with intense star formation". In: *A&A* 444.3, pp. 711–721. DOI: 10.1051/0004-6361:20052768. arXiv: astro-ph/0507488 [astro-ph].

Graham, J. F. and P. Schady (2016). "The Absolute Rate of LGRB Formation". In: *ApJ* 823.2, p. 154. DOI: 10.3847/0004-637X/823/2/154. arXiv: 1511.01466 [astro-ph.HE].

Graham, M. J. et al. (2019). "The Zwicky Transient Facility: Science Objectives". In: *PASP* 131.1001, p. 078001. DOI: 10.1088/1538-3873/ab006c. arXiv: 1902.01945 [astro-ph.IM].

Granot, J., F. De Colle, and E. Ramirez-Ruiz (2018). "Off-axis afterglow light curves and images from 2D hydrodynamic simulations of double-sided GRB jets in a stratified external medium". In: *MNRAS* 481.2, pp. 2711–2720. DOI: 10.1093/mnras/sty2454. arXiv: 1803.05856 [astro-ph.HE].

Granot, J. and T. Piran (2012). "On the lateral expansion of gamma-ray burst jets". In: *MNRAS* 421.1, pp. 570–587. DOI: 10.1111/j.1365-2966.2011.20335.x. arXiv: 1109.6468 [astro-ph.HE].

Granot, J. et al. (2002). "Off-Axis Afterglow Emission from Jetted Gamma-Ray Bursts". In: *ApJL* 570.2, pp. L61–L64. DOI: 10.1086/340991. arXiv: astro-ph/0201322 [astro-ph].

Grefenstette, B. et al. (2018). "Evidence for fading of the hard X-ray emission from AT2018cow". In: *The Astronomer's Telegram* 11813, p. 1.

Greiner, J. et al. (2011). "The nature of "dark" gamma-ray bursts". In: *A&A* 526, A30. DOI: 10.1051/0004-6361/201015458. arXiv: 1011.0618 [astro-ph.HE].

Greiner, J. et al. (2015). "A very luminous magnetar-powered supernova associated with an ultra-long γ-ray burst". In: *Nature* 523.7559, pp. 189–192. DOI: 10.1038/nature14579. arXiv: 1509.03279 [astro-ph.HE].

Greiner, J. et al. (2016). "Probing dust-obscured star formation in the most massive gamma-ray burst host galaxies". In: *A&A* 593, A17. DOI: 10.1051/0004-6361/201628861. arXiv: 1606.08285 [astro-ph.GA].

Groh, J. H. et al. (2013). "Fundamental properties of core-collapse supernova and GRB progenitors: predicting the look of massive stars before death". In: *A&A* 558, A131. DOI: 10.1051/0004-6361/201321906. arXiv: 1308.4681 [astro-ph.SR].

Gruber, D. et al. (2014). "The Fermi GBM Gamma-Ray Burst Spectral Catalog: Four Years of Data". In: *ApJS* 211.1, p. 12. DOI: 10.1088/0067-0049/211/1/12. arXiv: 1401.5069 [astro-ph.HE].

Gruen, D., S. Seitz, and G. M. Bernstein (2014). "Implementation of Robust Image Artifact Removal in SWarp through Clipped Mean Stacking". In: *PASP* 126.936, p. 158. DOI: 10.1086/675080. arXiv: 1401.4169 [astro-ph.IM].

Guetta, D., T. Piran, and E. Waxman (2005). "The Luminosity and Angular Distributions of Long-Duration Gamma-Ray Bursts". In: *ApJ* 619.1, pp. 412–419. DOI: 10.1086/423125. arXiv: astro-ph/0311488 [astro-ph].

Guilbert, P. W. (1986). "Compton heating and cooling in thermal electron gases". In: *MNRAS* 218, pp. 171–175. DOI: 10.1093/mnras/218.2.171.

Gupta, Y. et al. (2017). "The upgraded GMRT: opening new windows on the radio Universe". In: *Current Science* 113.4, pp. 707–714.

Hamburg, R. and Fermi-GBM Team (2020). "ZTF20aajnksq: Occulted by Earth at the time of GRB 200128A". In: *GRB Coordinates Network* 26970, p. 1.

Hammer, F. et al. (2006). "Detection of Wolf-Rayet stars in host galaxies of gamma-ray bursts (GRBs): are GRBs produced by runaway massive stars ejected from high stellar density regions?" In: *A&A* 454.1, pp. 103–111. DOI: 10.1051/0004-6361:20064823. arXiv: astro-ph/0604461 [astro-ph].

Han, X. H. et al. (2010). "The Wolf-Rayet features and mass-metallicity relation of long-duration gamma-ray burst host galaxies". In: *A&A* 514, A24. DOI: 10.1051/0004-6361/200912475. arXiv: 1001.2476 [astro-ph.GA].

Hancock, P. J. et al. (2012). "GRB111209A: ATCA detection at 5.5, 9, and 18GHz." In: *GRB Coordinates Network* 12804, p. 1.

Harrison, F. A. et al. (2001). "Broadband Observations of the Afterglow of GRB 000926: Observing the Effect of Inverse Compton Scattering and Evidence for a High-Density Environment". In: *arXiv e-prints*, astro–ph/0103377. arXiv: astro-ph/0103377 [astro-ph].

Harrison, F. A. et al. (2013). "The Nuclear Spectroscopic Telescope Array (NuSTAR) High-energy X-Ray Mission". In: *ApJ* 770.2, p. 103. DOI: 10.1088/0004-637X/770/2/103. arXiv: 1301.7307 [astro-ph.IM].

Heger, A. et al. (2003). "How Massive Single Stars End Their Life". In: *ApJ* 591.1, pp. 288–300. DOI: 10.1086/375341. arXiv: astro-ph/0212469 [astro-ph].

Herczeg, G. J. et al. (2017). "How Do Stars Gain Their Mass? A JCMT/SCUBA-2 Transient Survey of Protostars in Nearby Star-forming Regions". In: *ApJ* 849.1, p. 43. DOI: 10.3847/1538-4357/aa8b62. arXiv: 1709.02052 [astro-ph.SR].

HI4PI Collaboration et al. (2016). "HI4PI: A full-sky H I survey based on EBHIS and GASS". In: *A&A* 594, A116. DOI: 10.1051/0004-6361/201629178. arXiv: 1610.06175 [astro-ph.GA].

Hickish, J. et al. (2018). "A digital correlator upgrade for the Arcminute MicroKelvin Imager". In: *MNRAS* 475.4, pp. 5677–5687. DOI: 10.1093/mnras/sty074. arXiv: 1707.04237 [astro-ph.IM].

Hiramatsu, D. et al. (2020). "Global SN Project Transient Classification Report for 2020-02-05". In: *Transient Name Server Classification Report* 2020-403, p. 1.

Hjorth, J. (2013). "The supernova-gamma-ray burst-jet connection". In: *Philosophical Transactions of the Royal Society of London Series A* 371.1992, pp. 20120275–20120275. DOI: 10.1098/rsta.2012.0275. arXiv: 1304.7736 [astro-ph.HE].

Hjorth, J. et al. (2003). "A very energetic supernova associated with the γ-ray burst of 29 March 2003". In: *Nature* 423.6942, pp. 847–850. DOI: 10.1038/nature01750. arXiv: astro-ph/0306347 [astro-ph].

Hjorth, J. et al. (2012). "The Optically Unbiased Gamma-Ray Burst Host (TOUGH) Survey. I. Survey Design and Catalogs". In: *ApJ* 756.2, p. 187. DOI: 10.1088/0004-637X/756/2/187. arXiv: 1205.3162 [astro-ph.CO].

Ho, A. Y. Q. (2020). "VLA X-band Detection of SN2020bvc". In: *Transient Name Server AstroNote* 42, p. 1.

Ho, A. Y. Q. et al. (2017). "Label Transfer from APOGEE to LAMOST: Precise Stellar Parameters for 450,000 LAMOST Giants". In: *ApJ* 836.1, p. 5. DOI: 10.3847/1538-4357/836/1/5. arXiv: 1602.00303 [astro-ph.SR].

Ho, A. Y. Q. et al. (2018a). "VLA 10 GHz observation of AT2018gep (ZTF18abukavn)". In: *The Astronomer's Telegram* 12056, p. 1.

Ho, A. Y. Q. et al. (2018b). "ZTF Discovery of ZTF18abukavn (AT2018gep): a Rapidly Rising, Luminous Blue Transient". In: *The Astronomer's Telegram* 12030, p. 1.

Ho, A. Y. Q. et al. (2019a). "Swift XRT Detection of X-ray Emission from ZTF19abvizsw". In: *GRB Coordinates Network* 25658, p. 1.

Ho, A. Y. Q. et al. (2019b). "Swift XRT Detection of X-ray Emission from ZTF19abvizsw". In: *GRB Coordinates Network* 25658, p. 1.

Ho, A. Y. Q. et al. (2020a). "Chandra Detection of SN2020bvc". In: *Transient Name Server AstroNote* 45, p. 1.

Ho, A. Y. Q. et al. (2020b). "ZTF Discovery of ZTF20abbiixp: The Likely Optical Afterglow to GRB 200524A". In: *GRB Coordinates Network* 25658, p. 1.

Ho, P. T. P., J. M. Moran, and K. Y. Lo (2004). "The Submillimeter Array". In: *ApJL* 616.1, pp. L1–L6. DOI: 10.1086/423245. arXiv: astro-ph/0406352 [astro-ph].

Ho, A. Y. Q. et al. (2018c). "iPTF Archival Search for Fast Optical Transients". In: *ApJL* 854.1, p. L13. DOI: 10.3847/2041-8213/aaaa62. arXiv: 1712.00949 [astro-ph.HE].

Ho, A. Y. Q. et al. (2019c). "AT2018cow: A Luminous Millimeter Transient". In: *The Astrophysical Journal* 871.1, p. 73. DOI: 10.3847/1538-4357/aaf473. arXiv: 1810.10880 [astro-ph.HE].

Ho, A. Y. Q. et al. (2019d). "Evidence for Late-stage Eruptive Mass Loss in the Progenitor to SN2018gep, a Broad-lined Ic Supernova: Pre-explosion Emission and a Rapidly Rising Luminous Transient". In: *ApJ* 887.2, p. 169. DOI: 10.3847/1538-4357/ab55ec. arXiv: 1904.11009 [astro-ph.HE].

Ho, A. Y. Q. et al. (2020c). "The Broad-lined Ic Supernova ZTF18aaqjovh (SN 2018bvw): An Optically Discovered Engine-driven Supernova Candidate with Luminous Radio Emission". In: *ApJ* 893.2, p. 132. DOI: 10.3847/1538-4357/ab7f3b. arXiv: 1912.10354 [astro-ph.HE].

Ho, A. Y. Q. et al. (2020d). "The Koala: A Fast Blue Optical Transient with Luminous Radio Emission from a Starburst Dwarf Galaxy at z = 0.27". In: *ApJ* 895.1, p. 49. DOI: 10.3847/1538-4357/ab8bcf. arXiv: 2003.01222 [astro-ph.HE].

Ho, A. Y. Q. et al. (2020e). "SN2020bvc: a Broad-lined Type Ic Supernova with a Double-peaked Optical Light Curve and a Luminous X-ray and Radio Counterpart". In: *ApJ, accepted*. arXiv: 2004.10406 [astro-ph.HE].

Ho, A. Y. Q. et al. (2020f). "ZTF20aajnksq (AT2020blt): A Fast Optical Transient at $z \approx 2.9$ With No Detected Gamma-Ray Burst Counterpart". In: *ApJ, submitted*. arXiv: 2006.10761 [astro-ph.HE].

Högbom, J. A. (1974). "Aperture Synthesis with a Non-Regular Distribution of Interferometer Baselines". In: *A&AS* 15, p. 417.

Hogg, D. W. et al. (2002). "The K correction". In: *arXiv e-prints*, astro–ph/0210394. arXiv: astro-ph/0210394 [astro-ph].

Hook, I. M. et al. (2004). "The Gemini-North Multi-Object Spectrograph: Performance in Imaging, Long-Slit, and Multi-Object Spectroscopic Modes". In: *PASP* 116.819, pp. 425–440. DOI: 10.1086/383624.

Horesh, A. et al. (2013). "An early and comprehensive millimetre and centimetre wave and X-ray study of SN 2011dh: a non-equipartition blast wave expanding into a massive stellar wind". In: *MNRAS* 436.2, pp. 1258–1267. DOI: 10.1093/mnras/stt1645. arXiv: 1209.1102 [astro-ph.CO].

Hosseinzadeh, G. et al. (2017). "Type Ibn Supernovae Show Photometric Homogeneity and Spectral Diversity at Maximum Light". In: *ApJ* 836.2, p. 158. DOI: 10.3847/1538-4357/836/2/158. arXiv: 1608.01998 [astro-ph.HE].

Howell, D. A. et al. (2013). "Two Superluminous Supernovae from the Early Universe Discovered by the Supernova Legacy Survey". In: *ApJ* 779.2, p. 98. DOI: 10.1088/0004-637X/779/2/98. arXiv: 1310.0470 [astro-ph.CO].

Huang, K. et al. (2019). "ALMA Polarimetry of AT2018cow". In: *ApJL* 878.1, p. L25. DOI: 10.3847/2041-8213/ab23fd. arXiv: 1905.09785 [astro-ph.HE].

Hudelot, P. et al. (2012). "VizieR Online Data Catalog: The CFHTLS Survey (T0007 release) (Hudelot+ 2012)". In: *VizieR Online Data Catalog*, pp. II/317.

Hurley, K. et al. (2010). "The Third Interplanetary Network". In: *American Institute of Physics Conference Series*. Ed. by N. Kawai and S. Nagataki. Vol. 1279. American Institute of Physics Conference Series, pp. 330–333. DOI: 10.1063/1.3509301.

Hurley, K. et al. (2016). "The Interplanetary Network Response to LIGO GW150914". In: *ApJL* 829.1, p. L12. DOI: 10.3847/2041-8205/829/1/L12.

Ilbert, O. et al. (2006). "Accurate photometric redshifts for the CFHT legacy survey calibrated using the VIMOS VLT deep survey". In: *A&A* 457.3, pp. 841–856. DOI: 10.1051/0004-6361:20065138. arXiv: astro-ph/0603217 [astro-ph].

Irwin, C. M. and R. A. Chevalier (2016). "Jet or shock breakout? The low-luminosity GRB 060218". In: *MNRAS* 460.2, pp. 1680–1704. DOI: 10.1093/mnras/stw1058. arXiv: 1511.00336 [astro-ph.HE].

Irwin, J. A. et al. (2015). "CHANG-ES V: Nuclear Outflow in a Virgo Cluster Spiral after a Tidal Disruption Event". In: *ApJ* 809.2, p. 172. DOI: 10.1088/0004-637X/809/2/172. arXiv: 1507.00704 [astro-ph.GA].

Iwamoto, K. et al. (1998). "A hypernova model for the supernova associated with the γ-ray burst of 25 April 1998". In: *Nature* 395.6703, pp. 672–674. DOI: 10.1038/27155. arXiv: astro-ph/9806382 [astro-ph].

Izotov, Y. I. et al. (2006). "The chemical composition of metal-poor emission-line galaxies in the Data Release 3 of the Sloan Digital Sky Survey". In: *A&A* 448.3, pp. 955–970. DOI: 10.1051/0004-6361:20053763. arXiv: astro-ph/0511644 [astro-ph].

Izzo, L. et al. (2017). "The MUSE view of the host galaxy of GRB 100316D". In: *MNRAS* 472.4, pp. 4480–4496. DOI: 10.1093/mnras/stx2244. arXiv: 1704.05509 [astro-ph.GA].

Izzo, L. et al. (2019). "Signatures of a jet cocoon in early spectra of a supernova associated with a γ-ray burst". In: *Nature* 565.7739, pp. 324–327. DOI: 10.1038/s41586-018-0826-3. arXiv: 1901.05500 [astro-ph.HE].

Izzo, L. et al. (2020). "The broad-line type Ic SN 2020bvc: signatures of an off-axis gamma-ray burst afterglow". In: *arXiv e-prints*, arXiv:2004.05941. arXiv: 2004.05941 [astro-ph.HE].

Janka, H.-T. (2012). "Explosion Mechanisms of Core-Collapse Supernovae". In: *Annual Review of Nuclear and Particle Science* 62.1, pp. 407–451. DOI: 10.1146/annurev-nucl-102711-094901. arXiv: 1206.2503 [astro-ph.SR].

Japelj, J. et al. (2018). "Host galaxies of SNe Ic-BL with and without long gamma-ray bursts". In: *A&A* 617, A105. DOI: 10.1051/0004-6361/201833209. arXiv: 1806.10613 [astro-ph.HE].

Jencson, J. E. et al. (2018). "SPIRITS 16tn in NGC 3556: A Heavily Obscured and Low-luminosity Supernova at 8.8 Mpc". In: *ApJ* 863.1, p. 20. DOI: 10.3847/1538-4357/aacf8b. arXiv: 1803.00574 [astro-ph.HE].

Jerkstrand, A. et al. (2015). "Late-time spectral line formation in Type IIb supernovae, with application to SN 1993J, SN 2008ax, and SN 2011dh". In: *A&A* 573, A12. DOI: 10.1051/0004-6361/201423983. arXiv: 1408.0732 [astro-ph.HE].

Jones, F. C. and D. C. Ellison (1991). "The plasma physics of shock acceleration". In: *Space Sci. Rev.* 58.1, pp. 259–346. DOI: 10.1007/BF01206003.

Kann, D. A. et al. (2010). "The Afterglows of Swift-era Gamma-ray Bursts. I. Comparing pre-Swift and Swift-era Long/Soft (Type II) GRB Optical Afterglows". In: *ApJ* 720.2, pp. 1513–1558. DOI: 10.1088/0004-637X/720/2/1513. arXiv: 0712.2186 [astro-ph].

Kann, D. A. et al. (2018). "The optical/NIR afterglow of GRB 111209A: Complex yet not unprecedented". In: *A&A* 617, A122. DOI: 10.1051/0004-6361/201731292. arXiv: 1706.00601 [astro-ph.HE].

Kann, D. A. et al. (2019). "Highly luminous supernovae associated with gamma-ray bursts. I. GRB 111209A/SN 2011kl in the context of stripped-envelope and superluminous supernovae". In: *A&A* 624, A143. DOI: 10.1051/0004-6361/201629162. arXiv: 1606.06791 [astro-ph.HE].

Kasen, D. (2017). "Unusual Supernovae and Alternative Power Sources". In: *Handbook of Supernovae*. Ed. by A. W. Alsabti and P. Murdin, p. 939. DOI: 10.1007/978-3-319-21846-5_32.

Kasen, D. and L. Bildsten (2010). "Supernova Light Curves Powered by Young Magnetars". In: *ApJ* 717.1, pp. 245–249. DOI: 10.1088/0004-637X/717/1/245. arXiv: 0911.0680 [astro-ph.HE].

Kasen, D., B. D. Metzger, and L. Bildsten (2016). "Magnetar-driven Shock Breakout and Double-peaked Supernova Light Curves". In: *ApJ* 821.1, p. 36. DOI: 10.3847/0004-637X/821/1/36. arXiv: 1507.03645 [astro-ph.HE].

Kasliwal, M. M., S. B. Cenko, and L. P. Singer (2014). "Fermi 424934131 / iPTF14cva: Discovery and Redshift of Optical Afterglow." In: *GRB Coordinates Network* 16425, p. 1.

Kasliwal, M. M. et al. (2019). "The GROWTH Marshal: A Dynamic Science Portal for Time-domain Astronomy". In: *PASP* 131.997, p. 038003. DOI: 10.1088/1538-3873/aafbc2. arXiv: 1902.01934 [astro-ph.IM].

Kasliwal, M. M. et al. (2012). "Calcium-rich Gap Transients in the Remote Outskirts of Galaxies". In: *ApJ* 755.2, p. 161. DOI: 10.1088/0004-637X/755/2/161. arXiv: 1111.6109 [astro-ph.HE].

Kaspi, V. M. et al. (2014). "Timing and Flux Evolution of the Galactic Center Magnetar SGR J1745-2900". In: *ApJ* 786.2, p. 84. DOI: 10.1088/0004-637X/786/2/84. arXiv: 1403.5344 [astro-ph.HE].

Katz, B., D. Kushnir, and S. Dong (2013). "An exact integral relation between the Ni56 mass and the bolometric light curve of a type Ia supernova". In: *arXiv e-prints*, arXiv:1301.6766. arXiv: 1301.6766 [astro-ph.HE].

Katz, J. I. (2016). "Fast radio bursts — A brief review: Some questions, fewer answers". In: *Modern Physics Letters A* 31.14, p. 1630013. DOI: 10.1142/S0217732316300135. arXiv: 1604.01799 [astro-ph.HE].

Kauffmann, G. et al. (2003). "The host galaxies of active galactic nuclei". In: *MNRAS* 346.4, pp. 1055–1077. DOI: 10.1111/j.1365-2966.2003.07154.x. arXiv: astro-ph/0304239 [astro-ph].

Kelly, P. L. and R. P. Kirshner (2012). "Core-collapse Supernovae and Host Galaxy Stellar Populations". In: *ApJ* 759.2, p. 107. DOI: 10.1088/0004-637X/759/2/107. arXiv: 1110.1377 [astro-ph.CO].

Kennicutt Robert C., J. (1998). "Star Formation in Galaxies Along the Hubble Sequence". In: *ARA&A* 36, pp. 189–232. DOI: 10.1146/annurev.astro.36.1.189. arXiv: astro-ph/9807187 [astro-ph].

Kennicutt Robert C., J., P. Tamblyn, and C. E. Congdon (1994). "Past and Future Star Formation in Disk Galaxies". In: *ApJ* 435, p. 22. DOI: 10.1086/174790.

Kesseli, A. Y. et al. (2017). "An Empirical Template Library of Stellar Spectra for a Wide Range of Spectral Classes, Luminosity Classes, and Metallicities Using SDSS BOSS Spectra". In: *ApJS* 230.2, p. 16. DOI: 10.3847/1538-4365/aa656d. arXiv: 1702.06957 [astro-ph.SR].

Kewley, L. J. et al. (2001). "Theoretical Modeling of Starburst Galaxies". In: *ApJ* 556.1, pp. 121–140. DOI: 10.1086/321545. arXiv: astro-ph/0106324 [astro-ph].

Klose, S. et al. (2004). "Probing a Gamma-Ray Burst Progenitor at a Redshift of z = 2: A Comprehensive Observing Campaign of the Afterglow of GRB 030226". In: *AJ* 128.5, pp. 1942–1954. DOI: 10.1086/424539. arXiv: astro-ph/0408041 [astro-ph].

Kocevski, D. and C. C. Cheung (2018). "Fermi-LAT Search for Gamma-ray Emission from AT2018cow". In: *The Astronomer's Telegram* 11808, p. 1.

Kocevski, D. and N. Butler (2008). "Gamma-Ray Burst Energetics in the Swift Era". In: *ApJ* 680.1, pp. 531–538. DOI: 10.1086/586693. arXiv: 0707.4478 [astro-ph].

Kocevski, D. et al. (2007). "Multicolor Infrared Observations of SN 2006aj. I. The Supernova Associated with XRF 060218". In: *ApJ* 663.2, pp. 1180–1186. DOI: 10.1086/518159. arXiv: astro-ph/0612621 [astro-ph].

Komossa, S. (2015). "Tidal disruption of stars by supermassive black holes: Status of observations". In: *Journal of High Energy Astrophysics* 7, pp. 148–157. DOI: 10.1016/j.jheap.2015.04.006. arXiv: 1505.01093 [astro-ph.HE].

Kool, E. et al. (2019). "LIGO/Virgo S190901ap: Candidates from the Zwicky Transient Facility". In: *GRB Coordinates Network, Circular Service, No. 25616* 25616.

Kouveliotou, C., R. A. M. J. Wijers, and S. Woosley (2012). *Gamma-ray Bursts*.

Kowalski, A. F. et al. (2009). "M Dwarfs in Sloan Digital Sky Survey Stripe 82: Photometric Light Curves and Flare Rate Analysis". In: *AJ* 138.2, pp. 633–648. DOI: 10.1088/0004-6256/138/2/633. arXiv: 0906.2030 [astro-ph.SR].

Kowalski, A. F. et al. (2013). "Time-resolved Properties and Global Trends in dMe Flares from Simultaneous Photometry and Spectra". In: *ApJS* 207.1, p. 15. DOI: 10.1088/0067-0049/207/1/15. arXiv: 1307.2099 [astro-ph.SR].

Kraft, R. P., D. N. Burrows, and J. A. Nousek (1991). "Determination of Confidence Limits for Experiments with Low Numbers of Counts". In: *ApJ* 374, p. 344. DOI: 10.1086/170124.

Krauss, M. I. et al. (2012). "Expanded Very Large Array Observations of the Radio Evolution of SN 2011dh". In: *ApJL* 750.2, p. L40. DOI: 10.1088/2041-8205/750/2/L40. arXiv: 1201.0770 [astro-ph.HE].

Krühler, T. et al. (2015). "GRB hosts through cosmic time. VLT/X-Shooter emission-line spectroscopy of 96 γ-ray-burst-selected galaxies at 0.1 <z < 3.6". In: *A&A* 581, A125. DOI: 10.1051/0004-6361/201425561. arXiv: 1505.06743 [astro-ph.GA].

Kuin, N. P. M. et al. (2015). "Calibration of the Swift-UVOT ultraviolet and visible grisms". In: *MNRAS* 449.3, pp. 2514–2538. DOI: 10.1093/mnras/stv408. arXiv: 1501.02433 [astro-ph.IM].

Kuin, N. P. M. et al. (2019). "Swift spectra of AT2018cow: a white dwarf tidal disruption event?" In: *MNRAS* 487.2, pp. 2505–2521. DOI: 10.1093/mnras/stz053. arXiv: 1808.08492 [astro-ph.HE].

Kulkarni, S. R. and A. Rau (2006). "The Nature of the Deep Lens Survey Fast Transients". In: *ApJL* 644.1, pp. L63–L66. DOI: 10.1086/505423. arXiv: astro-ph/0604343 [astro-ph].

Kulkarni, S. R. et al. (1998). "Radio emission from the unusual supernova 1998bw and its association with the γ-ray burst of 25 April 1998". In: *Nature* 395.6703, pp. 663–669. DOI: 10.1038/27139.

Kulkarni, S. R. et al. (1999). "The afterglow, redshift and extreme energetics of the γ-ray burst of 23 January 1999". In: *Nature* 398.6726, pp. 389–394. DOI: 10.1038/18821. arXiv: astro-ph/9902272 [astro-ph].

Kumar, P. and R. Barniol Duran (2010). "External forward shock origin of high-energy emission for three gamma-ray bursts detected by Fermi". In: *MNRAS* 409.1, pp. 226–236. DOI: 10.1111/j.1365-2966.2010.17274.x. arXiv: 0910.5726 [astro-ph.HE].

Kumar, P. and B. Zhang (2015). "The physics of gamma-ray bursts & relativistic jets". In: *Physics Reports* 561, pp. 1–109. DOI: 10.1016/j.physrep.2014.09.008. arXiv: 1410.0679 [astro-ph.HE].

Lacy, M. et al. (2020). "The Karl G. Jansky Very Large Array Sky Survey (VLASS). Science Case and Survey Design". In: *PASP* 132.1009, p. 035001. DOI: 10.1088/1538-3873/ab63eb. arXiv: 1907.01981 [astro-ph.IM].

Lamers, H. J. G. L. M. and C. Leitherer (1993). "What are the Mass-Loss Rates of O Stars?" In: *ApJ* 412, p. 771. DOI: 10.1086/172960.

Lang, K. R. (1999). *Astrophysical formulae*.

Laskar, T. et al. (2013). "A Reverse Shock in GRB 130427A". In: *ApJ* 776.2, p. 119. DOI: 10.1088/0004-637X/776/2/119. arXiv: 1305.2453 [astro-ph.HE].

Laskar, T. et al. (2017). "GRB 171205A: VLA detection." In: *GRB Coordinates Network* 22216, p. 1.

Laskar, T. et al. (2016). "A Reverse Shock in GRB 160509A". In: *ApJ* 833.1, p. 88. DOI: 10.3847/1538-4357/833/1/88. arXiv: 1606.08873 [astro-ph.HE].

Laskar, T. et al. (2018). "A VLA Study of High-redshift GRBs. II. The Complex Radio Afterglow of GRB 140304A: Shell Collisions and Two Reverse Shocks". In: *ApJ* 859.2, p. 134. DOI: 10.3847/1538-4357/aabfd8. arXiv: 1707.05784 [astro-ph.HE].

Law, C. J. et al. (2018). "Discovery of the Luminous, Decades-long, Extragalactic Radio Transient FIRST J141918.9+394036". In: *ApJL* 866.2, p. L22. DOI: 10.3847/2041-8213/aae5f3. arXiv: 1808.08964 [astro-ph.HE].

Law, N. M. et al. (2009). "The Palomar Transient Factory: System Overview, Performance, and First Results". In: *PASP* 121.886, p. 1395. DOI: 10.1086/648598. arXiv: 0906.5350 [astro-ph.IM].

Lazzati, D. et al. (2012). "Unifying the Zoo of Jet-driven Stellar Explosions". In: *ApJ* 750.1, p. 68. DOI: 10.1088/0004-637X/750/1/68. arXiv: 1111.0970 [astro-ph.HE].

Lee, J. C. et al. (2009). "Dwarf Galaxy Starburst Statistics in the Local Volume". In: *ApJ* 692.2, pp. 1305–1320. DOI: 10.1088/0004-637X/692/2/1305. arXiv: 0810.5132 [astro-ph].

Lei, W.-H. et al. (2016). "IGR J12580+0134: The First Tidal Disruption Event with an Off-beam Relativistic Jet". In: *ApJ* 816.1, p. 20. DOI: 10.3847/0004-637X/816/1/20. arXiv: 1511.01206 [astro-ph.HE].

Leloudas, G. et al. (2015). "Spectroscopy of superluminous supernova host galaxies. A preference of hydrogen-poor events for extreme emission line galaxies". In: *MNRAS* 449.1, pp. 917–932. DOI: 10.1093/mnras/stv320. arXiv: 1409.8331 [astro-ph.GA].

Levan, A. J. et al. (2014). "A New Population of Ultra-long Duration Gamma-Ray Bursts". In: *ApJ* 781.1, p. 13. DOI: 10.1088/0004-637X/781/1/13. arXiv: 1302.2352 [astro-ph.HE].

Levesque, E. M. et al. (2010). "A High-metallicity Host Environment for the Long-duration GRB 020819". In: *ApJL* 712.1, pp. L26–L30. DOI: 10.1088/2041-8205/712/1/L26. arXiv: 1001.0970 [astro-ph.HE].

Li, W. et al. (2011). "Nearby supernova rates from the Lick Observatory Supernova Search - III. The rate-size relation, and the rates as a function of galaxy Hubble type and colour". In: *MNRAS* 412.3, pp. 1473–1507. DOI: 10.1111/j.1365-2966.2011.18162.x. arXiv: 1006.4613 [astro-ph.SR].

Li, L.-X. (2006). "Correlation between the peak spectral energy of gamma-ray bursts and the peak luminosity of the underlying supernovae: implication for the nature of the gamma-ray burst-supernova connection". In: *MNRAS* 372.3, pp. 1357–1365. DOI: 10.1111/j.1365-2966.2006.10943.x. arXiv: astro-ph/0608315 [astro-ph].

Liang, E. et al. (2007). "Low-Luminosity Gamma-Ray Bursts as a Unique Population: Luminosity Function, Local Rate, and Beaming Factor". In: *ApJ* 662.2, pp. 1111–1118. DOI: 10.1086/517959. arXiv: astro-ph/0605200 [astro-ph].

Liang, E.-W. et al. (2008). "A Comprehensive Analysis of Swift XRT Data. III. Jet Break Candidates in X-Ray and Optical Afterglow Light Curves". In: *ApJ* 675.1, pp. 528–552. DOI: 10.1086/524701. arXiv: 0708.2942 [astro-ph].

Lien, A. Y. et al. (2018). "AT2018cow: Swift/BAT data search". In: *The Astronomer's Telegram* 11782, p. 1.

Lien, A. et al. (2014). "Probing the Cosmic Gamma-Ray Burst Rate with Trigger Simulations of the Swift Burst Alert Telescope". In: *ApJ* 783.1, p. 24. DOI: 10.1088/0004-637X/783/1/24. arXiv: 1311.4567 [astro-ph.HE].

LIGO Scientific Collaboration and Virgo Collaboration (2019). "LIGO/Virgo S190901ap: Identification of a GW compact binary merger candidate". In: *GRB Coordinates Network, Circular Service, No. 25606* 25606.

Lundqvist, P. and C. Fransson (1988). "Circumstellar absorption of UV and radio emission from supernovae." In: *A&A* 192, pp. 221–233.

Lunnan, R. et al. (2014). "Hydrogen-poor Superluminous Supernovae and Long-duration Gamma-Ray Bursts Have Similar Host Galaxies". In: *ApJ* 787.2, p. 138. DOI: 10.1088/0004-637X/787/2/138. arXiv: 1311.0026 [astro-ph.HE].

Lupton, R. et al. (2004). "Preparing Red-Green-Blue Images from CCD Data". In: *PASP* 116.816, pp. 133–137. DOI: 10.1086/382245. arXiv: astro-ph/0312483 [astro-ph].

Luridiana, V., C. Morisset, and R. A. Shaw (2015). "PyNeb: a new tool for analyzing emission lines. I. Code description and validation of results". In: *A&A* 573, A42. DOI: 10.1051/0004-6361/201323152. arXiv: 1410.6662 [astro-ph.IM].

Lyman, J. D. et al. (2016). "Bolometric light curves and explosion parameters of 38 stripped-envelope core-collapse supernovae". In: *MNRAS* 457.1, pp. 328–350. DOI: 10.1093/mnras/stv2983. arXiv: 1406.3667 [astro-ph.SR].

Lyutikov, M. and S. Toonen (2019). "Fast-rising blue optical transients and AT2018cow following electron-capture collapse of merged white dwarfs". In: *MNRAS* 487.4, pp. 5618–5629. DOI: 10.1093/mnras/stz1640. arXiv: 1812.07569 [astro-ph.HE].

MacFadyen, A. I., S. E. Woosley, and A. Heger (2001). "Supernovae, Jets, and Collapsars". In: *ApJ* 550.1, pp. 410–425. DOI: 10.1086/319698. arXiv: astro-ph/9910034 [astro-ph].

Madau, P. and M. Dickinson (2014). "Cosmic Star-Formation History". In: *ARA&A* 52, pp. 415–486. DOI: 10.1146/annurev-astro-081811-125615. arXiv: 1403.0007 [astro-ph.CO].

Madau, P. and G. Efstathiou (1999). "Compton Heating of the Intergalactic Medium by the Hard X-Ray Background". In: *ApJL* 517.1, pp. L9–L12. DOI: 10.1086/312022. arXiv: astro-ph/9902080 [astro-ph].

Mahabal, A. A. et al. (2011). "Discovery, classification, and scientific exploration of transient events from the Catalina Real-time Transient Survey". In: *Bulletin of the Astronomical Society of India* 39.3, pp. 387–408. arXiv: 1111.0313 [astro-ph.IM].

Mahabal, A. et al. (2019). "Machine Learning for the Zwicky Transient Facility". In: *PASP* 131.997, p. 038002. DOI: 10.1088/1538-3873/aaf3fa. arXiv: 1902.01936 [astro-ph.IM].

Malesani, D. et al. (2004). "SN 2003lw and GRB 031203: A Bright Supernova for a Faint Gamma-Ray Burst". In: *ApJL* 609.1, pp. L5–L8. DOI: 10.1086/422684. arXiv: astro-ph/0405449 [astro-ph].

Mannucci, F. et al. (2010). "A fundamental relation between mass, star formation rate and metallicity in local and high-redshift galaxies". In: *MNRAS* 408.4, pp. 2115–2127. DOI: 10.1111/j.1365-2966.2010.17291.x. arXiv: 1005.0006 [astro-ph.CO].

Margutti, R. et al. (2007). "The host galaxy of GRB 031203: a new spectroscopic study". In: *A&A* 474.3, pp. 815–826. DOI: 10.1051/0004-6361:20077698. arXiv: 0709.0198 [astro-ph].

Margutti, R. et al. (2013). "The Signature of the Central Engine in the Weakest Relativistic Explosions: GRB 100316D". In: *ApJ* 778.1, p. 18. DOI: 10.1088/0004-637X/778/1/18. arXiv: 1308.1687 [astro-ph.HE].

Margutti, R. et al. (2014). "Relativistic Supernovae have Shorter-lived Central Engines or More Extended Progenitors: The Case of SN 2012ap". In: *ApJ* 797.2, p. 107. DOI: 10.1088/0004-637X/797/2/107. arXiv: 1402.6344 [astro-ph.HE].

Margutti, R. et al. (2015). "Dust in the Wind: the Role of Recent Mass Loss in Long Gamma-Ray Bursts". In: *ApJ* 805.2, p. 159. DOI: 10.1088/0004-637X/805/2/159. arXiv: 1410.7387 [astro-ph.HE].

Margutti, R. et al. (2018). "NuSTAR observations of AT2018cow reveal a hard X-ray component of emission above 15 keV". In: *The Astronomer's Telegram* 11775, p. 1.

Margutti, R. et al. (2019). "An Embedded X-Ray Source Shines through the Aspherical AT 2018cow: Revealing the Inner Workings of the Most Luminous Fast-evolving Optical Transients". In: *ApJ* 872.1, p. 18. DOI: 10.3847/1538-4357/aafa01. arXiv: 1810.10720 [astro-ph.HE].

Marino, R. A. et al. (2013). "The O3N2 and N2 abundance indicators revisited: improved calibrations based on CALIFA and T_e-based literature data". In: *A&A* 559, A114. DOI: 10.1051/0004-6361/201321956. arXiv: 1307.5316 [astro-ph.CO].

Martin, D. C. et al. (2005). "The Galaxy Evolution Explorer: A Space Ultraviolet Survey Mission". In: *ApJL* 619.1, pp. L1–L6. DOI: 10.1086/426387. arXiv: astro-ph/0411302 [astro-ph].

Masci, F. J. et al. (2017). "The IPAC Image Subtraction and Discovery Pipeline for the Intermediate Palomar Transient Factory". In: *PASP* 129.971, p. 014002. DOI: 10.1088/1538-3873/129/971/014002. arXiv: 1608.01733 [astro-ph.IM].

Masci, F. J. et al. (2019). "The Zwicky Transient Facility: Data Processing, Products, and Archive". In: *PASP* 131.995, p. 018003. DOI: 10.1088/1538-3873/aae8ac. arXiv: 1902.01872 [astro-ph.IM].

Matzner, C. D. and C. F. McKee (1999). "The Expulsion of Stellar Envelopes in Core-Collapse Supernovae". In: *ApJ* 510.1, pp. 379–403. DOI: 10.1086/306571. arXiv: astro-ph/9807046 [astro-ph].

Mazzali, P. A. et al. (2016). "Spectrum formation in superluminous supernovae (Type I)". In: *MNRAS* 458.4, pp. 3455–3465. DOI: 10.1093/mnras/stw512. arXiv: 1603.00388 [astro-ph.HE].

Mazzali, P. A., K. Iwamoto, and K. Nomoto (2000). "A Spectroscopic Analysis of the Energetic Type Ic Hypernova SN 1997EF". In: *ApJ* 545.1, pp. 407–419. DOI: 10.1086/317808. arXiv: astro-ph/0007222 [astro-ph].

Mazzali, P. A. et al. (2008). "The Metamorphosis of Supernova SN 2008D/XRF 080109: A Link Between Supernovae and GRBs/Hypernovae". In: *Science* 321.5893, p. 1185. DOI: 10.1126/science.1158088. arXiv: 0807.1695 [astro-ph].

McCarthy, J. K. et al. (1998). "Blue channel of the Keck low-resolution imaging spectrometer". In: *Phys. Rev. Lett.* Ed. by S. D'Odorico. Vol. 3355. Society of Photo-Optical Instrumentation Engineers (SPIE) Conference Series, pp. 81–92. DOI: 10.1117/12.316831.

McMullin, J. P. et al. (2007). "CASA Architecture and Applications". In: *Astronomical Data Analysis Software and Systems XVI*. Ed. by R. A. Shaw, F. Hill, and D. J. Bell. Vol. 376. Astronomical Society of the Pacific Conference Series, p. 127.

Meegan, C. et al. (2009). "The Fermi Gamma-ray Burst Monitor". In: *ApJ* 702.1, pp. 791–804. DOI: 10.1088/0004-637X/702/1/791. arXiv: 0908.0450 [astro-ph.IM].

Mészáros, P. (2006). "Gamma-ray bursts". In: *Reports on Progress in Physics* 69.8, pp. 2259–2321. DOI: 10.1088/0034-4885/69/8/R01. arXiv: astro-ph/0605208 [astro-ph].

Mészáros, P. and M. J. Rees (1997). "Poynting Jets from Black Holes and Cosmological Gamma-Ray Bursts". In: *ApJL* 482.1, pp. L29–L32. DOI: 10.1086/310692. arXiv: astro-ph/9609065 [astro-ph].

Mészáros, P. and M. J. Rees (1999). "GRB 990123: reverse and internal shock flashes and late afterglow behaviour". In: *MNRAS* 306.3, pp. L39–L43. DOI: 10.1046/j.1365-8711.1999.02800.x. arXiv: astro-ph/9902367 [astro-ph].

Mészáros, P., M. J. Rees, and R. A. M. J. Wijers (1998). "Viewing Angle and Environment Effects in Gamma-Ray Bursts: Sources of Afterglow Diversity". In: *ApJ* 499.1, pp. 301–308. DOI: 10.1086/305635. arXiv: astro-ph/9709273 [astro-ph].

Mészáros, P. and E. Waxman (2001). "TeV Neutrinos from Successful and Choked Gamma-Ray Bursts". In: *Proc. SPIE* 87.17, p. 171102. DOI: 10.1103/PhysRevLett.87.171102. arXiv: astro-ph/0103275 [astro-ph].

Michałowski, M. J. et al. (2009). "The Properties of the Host Galaxy and the Immediate Environment of GRB 980425/SN 1998bw from the Multiwavelength Spectral Energy Distribution". In: *ApJ* 693.1, pp. 347–354. DOI: 10.1088/0004-637X/693/1/347. arXiv: 0809.0508 [astro-ph].

Michel, F. C. (1988). "Neutron star disk formation from supernova fall-back and possible observational consequences". In: *Nature* 333.6174, pp. 644–645. DOI: 10.1038/333644a0.

Middelberg, E., R. J. Sault, and M. J. Kesteven (2006). "The ATCA Seeing Monitor". In: *Pubb Astron. Soc. Australia* 23.4, pp. 147–153. DOI: 10.1071/AS06019. arXiv: astro-ph/0609765 [astro-ph].

Milisavljevic, D. et al. (2015). "The Broad-lined Type Ic SN 2012ap and the Nature of Relativistic Supernovae Lacking a Gamma-Ray Burst Detection". In: *ApJ* 799.1, p. 51. DOI: 10.1088/0004-637X/799/1/51. arXiv: 1408.1606 [astro-ph.HE].

Miller, A. A. et al. (2020). "ZTF Early Observations of Type Ia Supernovae II: First Light, the Initial Rise, and Time to Reach Maximum Brightness". In: *arXiv e-prints*, arXiv:2001.00598. arXiv: 2001.00598 [astro-ph.HE].

Mirabal, N. et al. (2006). "GRB 060218/SN 2006aj: A Gamma-Ray Burst and Prompt Supernova at z = 0.0335". In: *ApJL* 643.2, pp. L99–L102. DOI: 10.1086/505177. arXiv: astro-ph/0603686 [astro-ph].

Modjaz, M. et al. (2006). "Early-Time Photometry and Spectroscopy of the Fast Evolving SN 2006aj Associated with GRB 060218". In: *ApJL* 645.1, pp. L21–L24. DOI: 10.1086/505906. arXiv: astro-ph/0603377 [astro-ph].

Modjaz, M. et al. (2009). "From Shock Breakout to Peak and Beyond: Extensive Panchromatic Observations of the Type Ib Supernova 2008D Associated with Swift X-ray Transient 080109". In: *ApJ* 702.1, pp. 226–248. DOI: 10.1088/0004-637X/702/1/226. arXiv: 0805.2201 [astro-ph].

Modjaz, M. et al. (2016). "The Spectral SN-GRB Connection: Systematic Spectral Comparisons between Type Ic Supernovae and Broad-lined Type Ic Supernovae with and without Gamma-Ray Bursts". In: *ApJ* 832.2, p. 108. DOI: 10.3847/0004-637X/832/2/108. arXiv: 1509.07124 [astro-ph.HE].

Modjaz, M. et al. (2020). "Host Galaxies of Type Ic and Broad-lined Type Ic Supernovae from the Palomar Transient Factory: Implications for Jet Production". In: *ApJ* 892.2, p. 153. DOI: 10.3847/1538-4357/ab4185. arXiv: 1901.00872 [astro-ph.HE].

Mohan, P., T. An, and J. Yang (2020). "The Nearby Luminous Transient AT2018cow: A Magnetar Formed in a Subrelativistically Expanding Nonjetted Explosion". In: *ApJL* 888.2, p. L24. DOI: 10.3847/2041-8213/ab64d1. arXiv: 1911.11912 [astro-ph.HE].

Moriya, T. J., T.-W. Chen, and N. Langer (2017). "Properties of Magnetars Mimicking ^{56}Ni-powered Light Curves in Type IC Superluminous Supernovae". In: *ApJ* 835.2, p. 177. DOI: 10.3847/1538-4357/835/2/177. arXiv: 1612.06917 [astro-ph.HE].

Moriya, T. J., E. I. Sorokina, and R. A. Chevalier (2018). "Superluminous Supernovae". In: *Space Sci. Rev.* 214.2, p. 59. DOI: 10.1007/s11214-018-0493-6. arXiv: 1803.01875 [astro-ph.HE].

Moriya, T. J. and N. Tominaga (2012). "Diversity of Luminous Supernovae from Non-steady Mass Loss". In: *ApJ* 747.2, p. 118. DOI: 10.1088/0004-637X/747/2/118. arXiv: 1110.3807 [astro-ph.HE].

Murphy, E. J. et al. (2011). "Calibrating Extinction-free Star Formation Rate Diagnostics with 33 GHz Free-free Emission in NGC 6946". In: *ApJ* 737.2, p. 67. DOI: 10.1088/0004-637X/737/2/67. arXiv: 1105.4877 [astro-ph.CO].

Nakar, E. (2015). "A Unified Picture for Low-luminosity and Long Gamma-Ray Bursts Based on the Extended Progenitor of llGRB 060218/SN 2006aj". In: *ApJ* 807.2, p. 172. DOI: 10.1088/0004-637X/807/2/172. arXiv: 1503.00441 [astro-ph.HE].

Nakar, E., A. Gal-Yam, and D. B. Fox (2006). "The Local Rate and the Progenitor Lifetimes of Short-Hard Gamma-Ray Bursts: Synthesis and Predictions for the Laser Interferometer Gravitational-Wave Observatory". In: *ApJ* 650.1, pp. 281–290. DOI: 10.1086/505855. arXiv: astro-ph/0511254 [astro-ph].

Nakar, E. and T. Piran (2003). "On-axis orphan afterglows". In: *New Astronomy* 8.2, pp. 141–153. DOI: 10.1016/S1384-1076(02)00202-6. arXiv: astro-ph/0207400 [astro-ph].

Nakar, E. and T. Piran (2011). "Detectable radio flares following gravitational waves from mergers of binary neutron stars". In: *Nature* 478.7367, pp. 82–84. DOI: 10.1038/nature10365. arXiv: 1102.1020 [astro-ph.HE].

Nakar, E., T. Piran, and J. Granot (2002). "The Detectability of Orphan Afterglows". In: *ApJ* 579.2, pp. 699–705. DOI: 10.1086/342791. arXiv: astro-ph/0204203 [astro-ph].

Nakar, E. and A. L. Piro (2014). "Supernovae with Two Peaks in the Optical Light Curve and the Signature of Progenitors with Low-mass Extended Envelopes". In: *ApJ* 788.2, p. 193. DOI: 10.1088/0004-637X/788/2/193. arXiv: 1401.7013 [astro-ph.HE].

Nakar, E. and R. Sari (2010). "Early Supernovae Light Curves Following the Shock Breakout". In: *ApJ* 725.1, pp. 904–921. DOI: 10.1088/0004-637X/725/1/904. arXiv: 1004.2496 [astro-ph.HE].

Narayana Bhat, P. et al. (2016). "The Third Fermi GBM Gamma-Ray Burst Catalog: The First Six Years". In: *ApJS* 223.2, p. 28. DOI: 10.3847/0067-0049/223/2/28. arXiv: 1603.07612 [astro-ph.HE].

Nicholl, M. et al. (2013). "Slowly fading super-luminous supernovae that are not pair-instability explosions". In: *Nature* 502.7471, pp. 346–349. DOI: 10.1038/nature12569. arXiv: 1310.4446 [astro-ph.CO].

Nysewander, M., A. S. Fruchter, and A. Pe'er (2009). "A Comparison of the Afterglows of Short- and Long-duration Gamma-ray Bursts". In: *ApJ* 701.1, pp. 824–836. DOI: 10.1088/0004-637X/701/1/824. arXiv: 0806.3607 [astro-ph].

Ofek, E. O. et al. (2010). "Supernova PTF 09UJ: A Possible Shock Breakout from a Dense Circumstellar Wind". In: *ApJ* 724.2, pp. 1396–1401. DOI: 10.1088/0004-637X/724/2/1396. arXiv: 1009.5378 [astro-ph.HE].

Oke, J. B. and J. E. Gunn (1982). "An Efficient Low Resolution and Moderate Resolution Spectrograph for the Hale Telescope". In: *PASP* 94, p. 586. DOI: 10.1086/131027.

Oke, J. B. and J. E. Gunn (1983). "Secondary standard stars for absolute spectrophotometry." In: *ApJ* 266, pp. 713–717. DOI: 10.1086/160817.

Oke, J. B. et al. (1995). "The Keck Low-Resolution Imaging Spectrometer". In: *PASP* 107, p. 375. DOI: 10.1086/133562.

Osterbrock, D. E. and G. J. Ferland (2006). *Astrophysics of gaseous nebulae and active galactic nuclei*.

Ovaldsen, J. .-.-E. et al. (2007). "A Search for Host Galaxies of 24 Gamma-Ray Bursts". In: *ApJ* 662.1, pp. 294–303. DOI: 10.1086/517962. arXiv: astro-ph/0703388 [astro-ph].

Pacholczyk, A. G. (1970). *Radio astrophysics. Nonthermal processes in galactic and extragalactic sources*.

Panaitescu, A. and P. Kumar (2001). "Fundamental Physical Parameters of Collimated Gamma-Ray Burst Afterglows". In: *ApJL* 560.1, pp. L49–L53. DOI: 10.1086/324061. arXiv: astro-ph/0108045 [astro-ph].

Panaitescu, A. and P. Kumar (2002). "Properties of Relativistic Jets in Gamma-Ray Burst Afterglows". In: *ApJ* 571.2, pp. 779–789. DOI: 10.1086/340094.

Panaitescu, A., P. Mészáros, and M. J. Rees (1998). "Multiwavelength Afterglows in Gamma-Ray Bursts: Refreshed Shock and Jet Effects". In: *ApJ* 503.1, pp. 314–324. DOI: 10.1086/305995. arXiv: astro-ph/9801258 [astro-ph].

Patat, F. et al. (2001). "The Metamorphosis of SN 1998bw". In: *ApJ* 555.2, pp. 900–917. DOI: 10.1086/321526. arXiv: astro-ph/0103111 [astro-ph].

Patterson, M. T. et al. (2019). "The Zwicky Transient Facility Alert Distribution System". In: *PASP* 131.995, p. 018001. DOI: 10.1088/1538-3873/aae904. arXiv: 1902.02227 [astro-ph.IM].

Pelletier, G. et al. (2017). "Towards Understanding the Physics of Collisionless Relativistic Shocks. Relativistic Collisionless Shocks". In: *Space Sci. Rev.* 207.1-4, pp. 319–360. DOI: 10.1007/s11214-017-0364-6. arXiv: 1705.05549 [astro-ph.HE].

Perley, D. A., S. Schulze, and A. de Ugarte Postigo (2017). "GRB 171205A: ALMA observations." In: *GRB Coordinates Network* 22252, p. 1.

Perley, D. A. and K. Taggart (2017). "GRB 171205A: Host galaxy photometric properties." In: *GRB Coordinates Network* 22194, p. 1.

Perley, D. A. et al. (2014). "The Afterglow of GRB 130427A from 1 to 10^{16} GHz". In: *ApJ* 781.1, p. 37. DOI: 10.1088/0004-637X/781/1/37. arXiv: 1307.4401 [astro-ph.HE].

Perley, D. A. et al. (2016). "Host-galaxy Properties of 32 Low-redshift Superluminous Supernovae from the Palomar Transient Factory". In: *ApJ* 830.1, p. 13. DOI: 10.3847/0004-637X/830/1/13. arXiv: 1604.08207 [astro-ph.HE].

Perley, D., S. Schulze, and R. Bruch (2020). "Classification of SN2020bvc (ASASSN-20bs) as a young broad-lined Ic supernova in UGC 9379". In: *Transient Name Server AstroNote* 37, p. 1.

Perley, D. A. (2019). "Fully Automated Reduction of Longslit Spectroscopy with the Low Resolution Imaging Spectrometer at the Keck Observatory". In: *PASP* 131.1002, p. 084503. DOI: 10.1088/1538-3873/ab215d. arXiv: 1903.07629 [astro-ph.IM].

Perley, D. A. et al. (2019). "The fast, luminous ultraviolet transient AT2018cow: extreme supernova, or disruption of a star by an intermediate-mass black hole?" In: *MNRAS* 484.1, pp. 1031–1049. DOI: 10.1093/mnras/sty3420. arXiv: 1808.00969 [astro-ph.HE].

Perley, R. A. et al. (2011). "The Expanded Very Large Array: A New Telescope for New Science". In: *ApJL* 739.1, p. L1. DOI: 10.1088/2041-8205/739/1/L1. arXiv: 1106.0532 [astro-ph.IM].

Perrott, Y. C. et al. (2013). "AMI Galactic Plane Survey at 16 GHz - I. Observing, mapping and source extraction". In: *MNRAS* 429.4, pp. 3330–3340. DOI: 10.1093/mnras/sts589. arXiv: 1208.5343 [astro-ph.GA].

Pettini, M. and B. E. J. Pagel (2004). "[OIII]/[NII] as an abundance indicator at high redshift". In: *MNRAS* 348.3, pp. L59–L63. DOI: 10.1111/j.1365-2966.2004.07591.x. arXiv: astro-ph/0401128 [astro-ph].

Phinney, E. S. (1989). "Manifestations of a Massive Black Hole in the Galactic Center". In: *The Center of the Galaxy*. Ed. by M. Morris. Vol. 136. IAU Symposium, p. 543.

Pian, E. et al. (2006). "An optical supernova associated with the X-ray flash XRF 060218". In: *Nature* 442.7106, pp. 1011–1013. DOI: 10.1038/nature05082. arXiv: astro-ph/0603530 [astro-ph].

Piascik, A. S. et al. (2014). "SPRAT: Spectrograph for the Rapid Acquisition of Transients". In: *Phys. Rev. Lett.* Vol. 9147. Society of Photo-Optical Instrumentation Engineers (SPIE) Conference Series, 91478H. DOI: 10.1117/12.2055117.

Piran, T. (2004). "The physics of gamma-ray bursts". In: *Reviews of Modern Physics* 76.4, pp. 1143–1210. DOI: 10.1103/RevModPhys.76.1143. arXiv: astro-ph/0405503 [astro-ph].

Piro, A. L. (2015). "Using Double-peaked Supernova Light Curves to Study Extended Material". In: *ApJL* 808.2, p. L51. DOI: 10.1088/2041-8205/808/2/L51. arXiv: 1505.07103 [astro-ph.HE].

Planck Collaboration et al. (2016). "Planck 2015 results. XIII. Cosmological parameters". In: *A&A* 594, A13. DOI: 10.1051/0004-6361/201525830. arXiv: 1502.01589 [astro-ph.CO].

Poznanski, D. et al. (2010). "An Unusually Fast-Evolving Supernova". In: *Science* 327.5961, p. 58. DOI: 10.1126/science.1181709. arXiv: 0911.2699 [astro-ph.SR].

Preece, R. D. et al. (2000). "The BATSE Gamma-Ray Burst Spectral Catalog. I. High Time Resolution Spectroscopy of Bright Bursts Using High Energy Resolution Data". In: *ApJS* 126.1, pp. 19–36. DOI: 10.1086/313289. arXiv: astro-ph/9908119 [astro-ph].

Prentice, S. J. et al. (2016). "The bolometric light curves and physical parameters of stripped-envelope supernovae". In: *MNRAS* 458.3, pp. 2973–3002. DOI: 10.1093/mnras/stw299. arXiv: 1602.01736 [astro-ph.HE].

Prentice, S. J. et al. (2018). "The Cow: Discovery of a Luminous, Hot, and Rapidly Evolving Transient". In: *ApJL* 865.1, p. L3. DOI: 10.3847/2041-8213/aadd90. arXiv: 1807.05965 [astro-ph.HE].

Pursiainen, M. et al. (2018). "Rapidly evolving transients in the Dark Energy Survey". In: *MNRAS* 481.1, pp. 894–917. DOI: 10.1093/mnras/sty2309. arXiv: 1803.04869 [astro-ph.HE].

Quataert, E. and J. Shiode (2012). "Wave-driven mass loss in the last year of stellar evolution: setting the stage for the most luminous core-collapse supernovae". In: *MNRAS* 423.1, pp. L92–L96. DOI: 10.1111/j.1745-3933.2012.01264.x. arXiv: 1202.5036 [astro-ph.SR].

Quimby, R. M. et al. (2011). "Hydrogen-poor superluminous stellar explosions". In: *Nature* 474.7352, pp. 487–489. DOI: 10.1038/nature10095. arXiv: 0910.0059 [astro-ph.CO].

Quimby, R. M. et al. (2018). "Spectra of Hydrogen-poor Superluminous Supernovae from the Palomar Transient Factory". In: *ApJ* 855.1, p. 2. DOI: 10.3847/1538-4357/aaac2f. arXiv: 1802.07820 [astro-ph.HE].

Ramirez-Ruiz, E. et al. (2005). "An Off-Axis Model of GRB 031203". In: *ApJL* 625.2, pp. L91–L94. DOI: 10.1086/431237. arXiv: astro-ph/0412145 [astro-ph].

Rau, A. et al. (2008). "A Survey for Fast Transients in the Fornax Cluster of Galaxies". In: *ApJ* 682.2, pp. 1205–1216. DOI: 10.1086/589762. arXiv: 0804.4482 [astro-ph].

Rau, A. et al. (2009). "Exploring the Optical Transient Sky with the Palomar Transient Factory". In: *PASP* 121.886, p. 1334. DOI: 10.1086/605911. arXiv: 0906.5355 [astro-ph.CO].

Readhead, A. C. S. (1994). "Equipartition Brightness Temperature and the Inverse Compton Catastrophe". In: *ApJ* 426, p. 51. DOI: 10.1086/174038.

Rest, A. et al. (2018). "A fast-evolving luminous transient discovered by K2/Kepler". In: *Nature Astronomy* 2, pp. 307–311. DOI: 10.1038/s41550-018-0423-2. arXiv: 1804.04641 [astro-ph.HE].

Rhoads, J. E. (1997). "How to Tell a Jet from a Balloon: A Proposed Test for Beaming in Gamma-Ray Bursts". In: *ApJL* 487.1, pp. L1–L4. DOI: 10.1086/310876. arXiv: astro-ph/9705163 [astro-ph].

Rhoads, J. E. (2003). "Dirty Fireballs and Orphan Afterglows: A Tale of Two Transients". In: *ApJ* 591.2, pp. 1097–1103. DOI: 10.1086/368125. arXiv: astro-ph/0301011 [astro-ph].

Ricker, G. R. et al. (2015). "Transiting Exoplanet Survey Satellite (TESS)". In: *Journal of Astronomical Telescopes, Instruments, and Systems* 1, p. 014003. DOI: 10.1117/1.JATIS.1.1.014003.

Ridnaia, A. et al. (2020). "ZTF20aajnksq: Upper limits from Konus-Wind observations". In: *GRB Coordinates Network* 27039, p. 1.

Rigault, M. et al. (2019). "Fully automated integral field spectrograph pipeline for the SEDMachine: pysedm". In: *A&A* 627, A115. DOI: 10.1051/0004-6361/201935344. arXiv: 1902.08526 [astro-ph.IM].

Rivera Sandoval, L. E. and T. Maccarone (2018). "Swift follow-up observations of the optical transient AT2018cow/ATLAS18qqn". In: *The Astronomer's Telegram* 11737, p. 1.

Rivera Sandoval, L. E. et al. (2018). "X-ray Swift observations of SN 2018cow". In: *MNRAS* 480.1, pp. L146–L150. DOI: 10.1093/mnrasl/sly145. arXiv: 1807.06369 [astro-ph.HE].

Roming, P. W. A. et al. (2005). "The Swift Ultra-Violet/Optical Telescope". In: *Space Sci. Rev.* 120.3-4, pp. 95–142. DOI: 10.1007/s11214-005-5095-4. arXiv: astro-ph/0507413 [astro-ph].

Ryan, G. et al. (2019). "Gamma-Ray Burst Afterglows In The Multi-Messenger Era: Numerical Models and Closure Relations". In: *arXiv e-prints*, arXiv:1909.11691. arXiv: 1909.11691 [astro-ph.HE].

Rybicki, G. B. and A. P. Lightman (1986). *Radiative Processes in Astrophysics*.

Sakamoto, T. et al. (2004). "High Energy Transient Explorer 2 Observations of the Extremely Soft X-Ray Flash XRF 020903". In: *ApJ* 602.2, pp. 875–885. DOI: 10.1086/381232.

Salas, P. et al. (2013). "SN 2007bg: the complex circumstellar medium around one of the most radio-luminous broad-lined Type Ic supernovae". In: *MNRAS* 428.2, pp. 1207–1217. DOI: 10.1093/mnras/sts104. arXiv: 1208.3455 [astro-ph.HE].

Sapir, N. and E. Waxman (2017). "UV/Optical Emission from the Expanding Envelopes of Type II Supernovae". In: *ApJ* 838.2, p. 130. DOI: 10.3847/1538-4357/aa64df. arXiv: 1607.03700 [astro-ph.HE].

Sari, R., T. Piran, and J. P. Halpern (1999). "Jets in Gamma-Ray Bursts". In: *ApJL* 519.1, pp. L17–L20. DOI: 10.1086/312109. arXiv: astro-ph/9903339 [astro-ph].

Sari, R., T. Piran, and R. Narayan (1998). "Spectra and Light Curves of Gamma-Ray Burst Afterglows". In: *ApJL* 497.1, pp. L17–L20. DOI: 10.1086/311269. arXiv: astro-ph/9712005 [astro-ph].

Sault, R. J., P. J. Teuben, and M. C. H. Wright (1995). "A Retrospective View of MIRIAD". In: *Astronomical Data Analysis Software and Systems IV*. Ed. by R. A. Shaw, H. E. Payne, and J. J. E. Hayes. Vol. 77. Astronomical Society of the Pacific Conference Series, p. 433.

Savchenko, V. et al. (2018). "INTEGRAL observations of decaying hard X-ray emission from AT2018cow". In: *The Astronomer's Telegram* 11843, p. 1.

Sazonov, S. Y., J. P. Ostriker, and R. A. Sunyaev (2004). "Quasars: the characteristic spectrum and the induced radiative heating". In: *MNRAS* 347.1, pp. 144–156. DOI: 10.1111/j.1365-2966.2004.07184.x. arXiv: astro-ph/0305233 [astro-ph].

Schlafly, E. F. and D. P. Finkbeiner (2011). "Measuring Reddening with Sloan Digital Sky Survey Stellar Spectra and Recalibrating SFD". In: *ApJ* 737.2, p. 103. DOI: 10.1088/0004-637X/737/2/103. arXiv: 1012.4804 [astro-ph.GA].

Schulze, S. et al. (2014). "GRB 120422A/SN 2012bz: Bridging the gap between low- and high-luminosity gamma-ray bursts". In: *A&A* 566, A102. DOI: 10.1051/0004-6361/201423387. arXiv: 1401.3774 [astro-ph.HE].

Schulze, S. et al. (2015). "The Optically Unbiased GRB Host (TOUGH) Survey. VII. The Host Galaxy Luminosity Function: Probing the Relationship between GRBs and Star Formation to Redshift ~ 6". In: *ApJ* 808.1, p. 73. DOI: 10.1088/0004-637X/808/1/73. arXiv: 1503.04246 [astro-ph.GA].

Schulze, S. et al. (2018). "Cosmic evolution and metal aversion in superluminous supernova host galaxies". In: *MNRAS* 473.1, pp. 1258–1285. DOI: 10.1093/mnras/stx2352. arXiv: 1612.05978 [astro-ph.GA].

Scott, M. A. and A. C. S. Readhead (1977). "The low-frequency structure of powerful radio sources and limits to departures from equipartition." In: *MNRAS* 180, pp. 539–550. DOI: 10.1093/mnras/180.4.539.

Selsing, J. et al. (2019). "The X-shooter GRB afterglow legacy sample (XS-GRB)". In: *A&A* 623, A92. DOI: 10.1051/0004-6361/201832835. arXiv: 1802.07727 [astro-ph.HE].

Shappee, B. J. et al. (2014). "The Man behind the Curtain: X-Rays Drive the UV through NIR Variability in the 2013 Active Galactic Nucleus Outburst in NGC 2617". In: *ApJ* 788.1, p. 48. DOI: 10.1088/0004-637X/788/1/48. arXiv: 1310.2241 [astro-ph.HE].

Sharma, Y. et al. (2018). "AT2018cow - AstroSat CZTI limits on prompt emission". In: *The Astronomer's Telegram* 11809, p. 1.

Sheth, K. et al. (2003). "Millimeter Observations of GRB 030329: Continued Evidence for a Two-Component Jet". In: *ApJL* 595.1, pp. L33–L36. DOI: 10.1086/378933. arXiv: astro-ph/0308188 [astro-ph].

Shivvers, I. et al. (2016). "SN 2015U: a rapidly evolving and luminous Type Ibn supernova". In: *MNRAS* 461.3, pp. 3057–3074. DOI: 10.1093/mnras/stw1528. arXiv: 1603.04866 [astro-ph.HE].

Silverman, J. M. et al. (2012). "Berkeley Supernova Ia Program - I. Observations, data reduction and spectroscopic sample of 582 low-redshift Type Ia supernovae". In: *MNRAS* 425.3, pp. 1789–1818. DOI: 10.1111/j.1365-2966.2012.21270.x. arXiv: 1202.2128 [astro-ph.CO].

Singer, L. P. et al. (2020). "ZTF20aajnksq: Gemini-North r-band photometry". In: *GRB Coordinates Network* 26968, p. 1.

Singer, L. P. et al. (2015). "The Needle in the 100 deg^2 Haystack: Uncovering Afterglows of Fermi GRBs with the Palomar Transient Factory". In: *ApJ* 806.1, p. 52. DOI: 10.1088/0004-637X/806/1/52. arXiv: 1501.00495 [astro-ph.HE].

Skrutskie, M. F. et al. (2006). "The Two Micron All Sky Survey (2MASS)". In: *AJ* 131.2, pp. 1163–1183. DOI: 10.1086/498708.

Smartt, S. J. et al. (2018). "ATLAS18qqn (AT2018cow) - a bright transient spatially coincident with CGCG 137-068 (60 Mpc)". In: *The Astronomer's Telegram* 11727, p. 1.

Smartt, S. J. (2009). "Progenitors of Core-Collapse Supernovae". In: *ARA&A* 47.1, pp. 63–106. DOI: 10.1146/annurev-astro-082708-101737. arXiv: 0908.0700 [astro-ph.SR].

Smith, I. A., N. R. Tanvir, and D. A. Perley (2018). "AT2018cow: JCMT SCUBA-2 sub-mm detection". In: *The Astronomer's Telegram* 11781, p. 1.

Smith, N. (2014). "Mass Loss: Its Effect on the Evolution and Fate of High-Mass Stars". In: *ARA&A* 52, pp. 487–528. DOI: 10.1146/annurev-astro-081913-040025. arXiv: 1402.1237 [astro-ph.SR].

Smith, N. et al. (2012). "SN 2010jp (PTF10aaxi): a jet in a Type II supernova". In: *MNRAS* 420.2, pp. 1135–1144. DOI: 10.1111/j.1365-2966.2011.20104.x. arXiv: 1108.2868 [astro-ph.HE].

Smith, N. et al. (2017). "Endurance of SN 2005ip after a decade: X-rays, radio and Hα like SN 1988Z require long-lived pre-supernova mass-loss". In: *MNRAS* 466.3, pp. 3021–3034. DOI: 10.1093/mnras/stw3204. arXiv: 1612.02011 [astro-ph.HE].

Sobacchi, E. et al. (2017). "A common central engine for long gamma-ray bursts and Type Ib/c supernovae". In: *MNRAS* 472.1, pp. 616–627. DOI: 10.1093/mnras/stx2083. arXiv: 1705.00281 [astro-ph.HE].

Soderberg, A. M. et al. (2004a). "A Redshift Determination for XRF 020903: First Spectroscopic Observations of an X-Ray Flash". In: *ApJ* 606.2, pp. 994–999. DOI: 10.1086/383082. arXiv: astro-ph/0311050 [astro-ph].

Soderberg, A. M. et al. (2004b). "The sub-energetic γ-ray burst GRB 031203 as a cosmic analogue to the nearby GRB 980425". In: *Nature* 430.7000, pp. 648–650. DOI: 10.1038/nature02757. arXiv: astro-ph/0408096 [astro-ph].

Soderberg, A. M. et al. (2005). "The Radio and X-Ray-Luminous Type Ibc Supernova 2003L". In: *ApJ* 621.2, pp. 908–920. DOI: 10.1086/427649. arXiv: astro-ph/0410163 [astro-ph].

Soderberg, A. M. et al. (2006a). "Late-Time Radio Observations of 68 Type Ibc Supernovae: Strong Constraints on Off-Axis Gamma-Ray Bursts". In: *ApJ* 638.2, pp. 930–937. DOI: 10.1086/499121. arXiv: astro-ph/0507147 [astro-ph].

Soderberg, A. M. et al. (2006b). "Relativistic ejecta from X-ray flash XRF 060218 and the rate of cosmic explosions". In: *Nature* 442.7106, pp. 1014–1017. DOI: 10.1038/nature05087. arXiv: astro-ph/0604389 [astro-ph].

Soderberg, A. M. et al. (2006c). "The Radio and X-Ray Luminous SN 2003bg and the Circumstellar Density Variations around Radio Supernovae". In: *ApJ* 651.2, pp. 1005–1018. DOI: 10.1086/507571. arXiv: astro-ph/0512413 [astro-ph].

Soderberg, A. M. et al. (2010). "A relativistic type Ibc supernova without a detected γ-ray burst". In: *Nature* 463.7280, pp. 513–515. DOI: 10.1038/nature08714. arXiv: 0908.2817 [astro-ph.HE].

Sollerman, J. et al. (2002). "Supernova 1998bw - the final phases". In: *A&A* 386, pp. 944–956. DOI: 10.1051/0004-6361:20020326. arXiv: astro-ph/0204498 [astro-ph].

Sollerman, J. et al. (2005). "On the nature of nearby GRB/SN host galaxies". In: *New Astronomy* 11.2, pp. 103–115. DOI: 10.1016/j.newast.2005.06.004. arXiv: astro-ph/0506686 [astro-ph].

Sollerman, J. et al. (2006). "Supernova 2006aj and the associated X-Ray Flash 060218". In: *A&A* 454.2, pp. 503–509. DOI: 10.1051/0004-6361:20065226. arXiv: astro-ph/0603495 [astro-ph].

Stalder, B. et al. (2017). "Observations of the GRB Afterglow ATLAS17aeu and Its Possible Association with GW 170104". In: *ApJ* 850.2, p. 149. DOI: 10.3847/1538-4357/aa95c1. arXiv: 1706.00175 [astro-ph.HE].

Stanek, K. Z. (2020). "ASAS-SN Transient Discovery Report for 2020-02-04". In: *Transient Name Server Discovery Report* 2020-381, p. 1.

Stanek, K. Z. et al. (2003). "Spectroscopic Discovery of the Supernova 2003dh Associated with GRB 030329". In: *ApJL* 591.1, pp. L17–L20. DOI: 10.1086/376976. arXiv: astro-ph/0304173 [astro-ph].

Stanway, E. R. et al. (2015). "GRB 080517: a local, low-luminosity gamma-ray burst in a dusty galaxy at z = 0.09". In: *MNRAS* 446.4, pp. 3911–3925. DOI: 10.1093/mnras/stu2286. arXiv: 1409.5791 [astro-ph.GA].

Starling, R. L. C. et al. (2011). "Discovery of the nearby long, soft GRB 100316D with an associated supernova". In: *MNRAS* 411.4, pp. 2792–2803. DOI: 10.1111/j.1365-2966.2010.17879.x. arXiv: 1004.2919 [astro-ph.CO].

Steele, I. A. et al. (2004). "The Liverpool Telescope: performance and first results". In: *Phys. Rev. Lett.* Ed. by J. Oschmann Jacobus M. Vol. 5489. Society of Photo-Optical Instrumentation Engineers (SPIE) Conference Series, pp. 679–692. DOI: 10.1117/12.551456.

Stephenson, F. R. and D. A. Green (2002). "Historical supernovae and their remnants". In: *Historical supernovae and their remnants* 5.

Strubbe, L. E. and E. Quataert (2009). "Optical flares from the tidal disruption of stars by massive black holes". In: *MNRAS* 400.4, pp. 2070–2084. DOI: 10.1111/j.1365-2966.2009.15599.x. arXiv: 0905.3735 [astro-ph.CO].

Suzuki, A., K. Maeda, and T. Shigeyama (2019). "Relativistic Supernova Ejecta Colliding with a Circumstellar Medium: An Application to the Low-luminosity GRB 171205A". In: *ApJ* 870.1, p. 38. DOI: 10.3847/1538-4357/aaef85. arXiv: 1811.03240 [astro-ph.HE].

Swarup, G. et al. (1991). "The Giant Metre-Wave Radio Telescope". In: *Current Science* 60, p. 95.

Tachibana, Y. and A. A. Miller (2018). "A Morphological Classification Model to Identify Unresolved PanSTARRS1 Sources: Application in the ZTF Real-time Pipeline". In: *PASP* 130.994, p. 128001. DOI: 10.1088/1538-3873/aae3d9. arXiv: 1902.01935 [astro-ph.IM].

Taddia, F. et al. (2016). "iPTF15dtg: a double-peaked Type Ic supernova from a massive progenitor". In: *A&A* 592, A89. DOI: 10.1051/0004-6361/201628703. arXiv: 1605.02491 [astro-ph.HE].

Taddia, F. et al. (2019). "Analysis of broad-lined Type Ic supernovae from the (intermediate) Palomar Transient Factory". In: *A&A* 621, A71. DOI: 10.1051/0004-6361/201834429. arXiv: 1811.09544 [astro-ph.HE].

Taggart, K. and D. Perley (2019). "Core-collapse, superluminous, and gamma-ray burst supernova host galaxy populations at low redshift: the importance of dwarf and starbursting galaxies". In: *arXiv e-prints*, arXiv:1911.09112. arXiv: 1911.09112 [astro-ph.HE].

Tanaka, M. et al. (2016). "Rapidly Rising Transients from the Subaru Hyper Suprime-Cam Transient Survey". In: *ApJ* 819.1, p. 5. DOI: 10.3847/0004-637X/819/1/5. arXiv: 1601.03261 [astro-ph.HE].

Tendulkar, S. P. et al. (2017). "The Host Galaxy and Redshift of the Repeating Fast Radio Burst FRB 121102". In: *ApJL* 834.2, p. L7. DOI: 10.3847/2041-8213/834/2/L7. arXiv: 1701.01100 [astro-ph.HE].

Thompson, T. A., P. Chang, and E. Quataert (2004). "Magnetar Spin-Down, Hyperenergetic Supernovae, and Gamma-Ray Bursts". In: *ApJ* 611.1, pp. 380–393. DOI: 10.1086/421969. arXiv: astro-ph/0401555 [astro-ph].

Thomsen, B. et al. (2004). "The supernova 2003lw associated with X-ray flash 031203". In: *A&A* 419, pp. L21–L25. DOI: 10.1051/0004-6361:20040133. arXiv: astro-ph/0403451 [astro-ph].

Thöne, C. C. et al. (2011). "The unusual γ-ray burst GRB 101225A from a helium star/neutron star merger at redshift 0.33". In: *Nature* 480.7375, pp. 72–74. DOI: 10.1038/nature10611. arXiv: 1105.3015 [astro-ph.HE].

Thöne, C. C. et al. (2014). "The host of the SN-less GRB 060505 in high resolution". In: *MNRAS* 441.3, pp. 2034–2048. DOI: 10.1093/mnras/stu711. arXiv: 1404.0881 [astro-ph.HE].

Thöne, C. C. et al. (2008). "Spatially Resolved Properties of the GRB 060505 Host: Implications for the Nature of the Progenitor". In: *ApJ* 676.2, pp. 1151–1161. DOI: 10.1086/528943. arXiv: astro-ph/0703407 [astro-ph].

Tonry, J. L. et al. (2018). "ATLAS: A High-cadence All-sky Survey System". In: *PASP* 130.988, p. 064505. DOI: 10.1088/1538-3873/aabadf. arXiv: 1802.00879 [astro-ph.IM].

Toy, V. L. et al. (2016). "Optical and Near-infrared Observations of SN 2013dx Associated with GRB 130702A". In: *ApJ* 818.1, p. 79. DOI: 10.3847/0004-637X/818/1/79. arXiv: 1508.00575 [astro-ph.HE].

Tremonti, C. A. et al. (2004). "The Origin of the Mass-Metallicity Relation: Insights from 53,000 Star-forming Galaxies in the Sloan Digital Sky Survey". In: *ApJ* 613.2, pp. 898–913. DOI: 10.1086/423264. arXiv: astro-ph/0405537 [astro-ph].

Urata, Y. et al. (2014). "Synchrotron Self-inverse Compton Radiation from Reverse Shock on GRB 120326A". In: *ApJ* 789.2, p. 146. DOI: 10.1088/0004-637X/789/2/146. arXiv: 1405.4331 [astro-ph.HE].

Urošević, D. (2014). "On the radio spectra of supernova remnants". In: *Ap&SS* 354.2, pp. 541–552. DOI: 10.1007/s10509-014-2095-4. arXiv: 1408.1107 [astro-ph.HE].

Valenti, S. et al. (2008). "The broad-lined Type Ic supernova 2003jd". In: *MNRAS* 383.4, pp. 1485–1500. DOI: 10.1111/j.1365-2966.2007.12647.x. arXiv: 0710.5173 [astro-ph].

van den Heuvel, E. P. J. and S. F. Portegies Zwart (2013). "Are Superluminous Supernovae and Long GRBs the Products of Dynamical Processes in Young Dense Star Clusters?" In: *ApJ* 779.2, p. 114. DOI: 10.1088/0004-637X/779/2/114. arXiv: 1303.6961 [astro-ph.HE].

van der Horst, A. J. et al. (2008). "Detailed study of the GRB 030329 radio afterglow deep into the non-relativistic phase". In: *A&A* 480.1, pp. 35–43. DOI: 10.1051/0004-6361:20078051. arXiv: 0706.1321 [astro-ph].

van der Horst, A. J. et al. (2014). "A comprehensive radio view of the extremely bright gamma-ray burst 130427A". In: *MNRAS* 444.4, pp. 3151–3163. DOI: 10.1093/mnras/stu1664. arXiv: 1404.1945 [astro-ph.HE].

van der Walt, S., A. Crellin-Quick, and J. Bloom (2019). "SkyPortal: An Astronomical Data Platform". In: *The Journal of Open Source Software* 4.37, p. 1247. DOI: 10.21105/joss.01247.

van Dyk, S. D. et al. (1993). "SN 1988Z: The Most Distant Radio Supernova". In: *ApJL* 419, p. L69. DOI: 10.1086/187139.

van Eerten, H. J. et al. (2011). "Jet simulations and gamma-ray burst afterglow jet breaks". In: *MNRAS* 410.3, pp. 2016–2024. DOI: 10.1111/j.1365-2966.2010.17582.x. arXiv: 1005.3966 [astro-ph.HE].

van Loon, J. T. (2010). "The Effects of Red Supergiant Mass Loss on Supernova Ejecta and the Circumburst Medium". In: *Hot and Cool: Bridging Gaps in Massive Star Evolution*. Ed. by C. Leitherer et al. Vol. 425. Astronomical Society of the Pacific Conference Series, p. 279.

van Paradijs, J., C. Kouveliotou, and R. A. M. J. Wijers (2000). "Gamma-Ray Burst Afterglows". In: *ARA&A* 38, pp. 379–425. DOI: 10.1146/annurev.astro.38.1.379.

van Roestel, J. et al. (2019). "The Palomar Transient Factory Sky2Night programme". In: *MNRAS* 484.4, pp. 4507–4528. DOI: 10.1093/mnras/stz241. arXiv: 1902.03768 [astro-ph.HE].

Vergani, S. D. et al. (2015). "Are long gamma-ray bursts biased tracers of star formation? Clues from the host galaxies of the Swift/BAT6 complete sample of LGRBs . I. Stellar mass at z < 1". In: *A&A* 581, A102. DOI: 10.1051/0004-6361/201425013. arXiv: 1409.7064 [astro-ph.HE].

Vinkó, J. et al. (2015). "A Luminous, Fast Rising UV-transient Discovered by ROTSE: A Tidal Disruption Event?" In: *ApJ* 798.1, p. 12. DOI: 10.1088/0004-637X/798/1/12. arXiv: 1410.6014 [astro-ph.HE].

Virtanen, P. et al. (2020). "SciPy 1.0: Fundamental Algorithms for Scientific Computing in Python". In: *Nature Methods* 17, pp. 261–272. DOI: https://doi.org/10.1038/s41592-019-0686-2.

von Kienlin, A. (2014). "GRB 140623A / iPTF14cyb: Fermi GBM detection." In: *GRB Coordinates Network* 16450, p. 1.

Wanderman, D. and T. Piran (2010). "The luminosity function and the rate of Swift's gamma-ray bursts". In: *MNRAS* 406.3, pp. 1944–1958. DOI: 10.1111/j.1365-2966.2010.16787.x. arXiv: 0912.0709 [astro-ph.HE].

Wang, J. et al. (2018). "Spectroscopy of the Type Ic Supernova SN 2017iuk Associated with Low-redshift GRB 171205A". In: *ApJ* 867.2, p. 147. DOI: 10.3847/1538-4357/aae6c3. arXiv: 1810.03250 [astro-ph.HE].

Wang, L. J. et al. (2019). "Broad-lined type Ic supernova iPTF16asu: A challenge to all popular models". In: *MNRAS* 489.1, pp. 1110–1119. DOI: 10.1093/mnras/stz2184. arXiv: 1712.07359 [astro-ph.HE].

Watson, C., A. A. Henden, and A. Price (2017). "VizieR Online Data Catalog: AAVSO International Variable Star Index VSX (Watson+, 2006-2014)". In: *VizieR Online Data Catalog*, B/vsx.

Watson, D. et al. (2004). "A Very Low Luminosity X-Ray Flash: XMM-Newton Observations of GRB 031203". In: *ApJL* 605.2, pp. L101–L104. DOI: 10.1086/420844. arXiv: astro-ph/0401225 [astro-ph].

Waxman, E., P. Mészáros, and S. Campana (2007). "GRB 060218: A Relativistic Supernova Shock Breakout". In: *ApJ* 667.1, pp. 351–357. DOI: 10.1086/520715. arXiv: astro-ph/0702450 [astro-ph].

Waxman, E. and B. Katz (2017). "Shock Breakout Theory". In: *Handbook of Supernovae*. Ed. by A. W. Alsabti and P. Murdin, p. 967. DOI: 10.1007/978-3-319-21846-5_33.

Weiler, K. W. et al. (1986). "Radio Supernovae". In: *ApJ* 301, p. 790. DOI: 10.1086/163944.

Weiler, K. W. et al. (1991). "The 10 Year Radio Light Curves for SN 1979C". In: *ApJ* 380, p. 161. DOI: 10.1086/170571.

Weiler, K. W. et al. (2007). "Long-Term Radio Monitoring of SN 1993J". In: *ApJ* 671.2, pp. 1959–1980. DOI: 10.1086/523258. arXiv: 0709.1136 [astro-ph].

West, A. A. et al. (2011). "The Sloan Digital Sky Survey Data Release 7 Spectroscopic M Dwarf Catalog. I. Data". In: *AJ* 141.3, p. 97. DOI: 10.1088/0004-6256/141/3/97. arXiv: 1101.1082 [astro-ph.SR].

Whitehorn, N. et al. (2016). "Millimeter Transient Point Sources in the SPTpol 100 Square Degree Survey". In: *ApJ* 830.2, p. 143. DOI: 10.3847/0004-637X/830/2/143. arXiv: 1604.03507 [astro-ph.HE].

Whitesides, L. et al. (2017). "iPTF 16asu: A Luminous, Rapidly Evolving, and High-velocity Supernova". In: *ApJ* 851.2, p. 107. DOI: 10.3847/1538-4357/aa99de. arXiv: 1706.05018 [astro-ph.HE].

Wilson, W. E. et al. (2011). "The Australia Telescope Compact Array Broad-band Backend: description and first results". In: *MNRAS* 416.2, pp. 832–856. DOI: 10.1111/j.1365-2966.2011.19054.x. arXiv: 1105.3532 [astro-ph.IM].

Woosley, S. E. (2010). "Bright Supernovae from Magnetar Birth". In: *ApJL* 719.2, pp. L204–L207. DOI: 10.1088/2041-8205/719/2/L204. arXiv: 0911.0698 [astro-ph.HE].

Woosley, S. E. and J. S. Bloom (2006). "The Supernova Gamma-Ray Burst Connection". In: *ARA&A* 44.1, pp. 507–556. DOI: 10.1146/annurev.astro.43.072103.150558. arXiv: astro-ph/0609142 [astro-ph].

Woosley, S. E. and A. Heger (2007). "Nucleosynthesis and remnants in massive stars of solar metallicity". In: *Physics Reports* 442.1-6, pp. 269–283. DOI: 10.1016/j.physrep.2007.02.009. arXiv: astro-ph/0702176 [astro-ph].

Woosley, S. and T. Janka (2005). "The physics of core-collapse supernovae". In: *Nature Physics* 1.3, pp. 147–154. DOI: 10.1038/nphys172. arXiv: astro-ph/0601261 [astro-ph].

Wright, A. H. et al. (2016). "Galaxy And Mass Assembly: accurate panchromatic photometry from optical priors using LAMBDAR". In: *MNRAS* 460.1, pp. 765–801. DOI: 10.1093/mnras/stw832. arXiv: 1604.01923 [astro-ph.GA].

Wright, E. L. et al. (2010). "The Wide-field Infrared Survey Explorer (WISE): Mission Description and Initial On-orbit Performance". In: *AJ* 140.6, pp. 1868–1881. DOI: 10.1088/0004-6256/140/6/1868. arXiv: 1008.0031 [astro-ph.IM].

Wygoda, N., Y. Elbaz, and B. Katz (2019). "Type Ia supernovae have two physical width-luminosity relations and they favour sub-Chandrasekhar and direct collision models - I. Bolometric". In: *MNRAS* 484.3, pp. 3941–3950. DOI: 10.1093/mnras/stz145. arXiv: 1711.00969 [astro-ph.HE].

Yan, L. et al. (2017). "Far-ultraviolet to Near-infrared Spectroscopy of a Nearby Hydrogen-poor Superluminous Supernova Gaia16apd". In: *ApJ* 840.1, p. 57. DOI: 10.3847/1538-4357/aa6b02. arXiv: 1611.02782 [astro-ph.SR].

Yang, S. et al. (2017). "An Empirical Limit on the Kilonova Rate from the DLT40 One Day Cadence Supernova Survey". In: *ApJL* 851.2, p. L48. DOI: 10.3847/2041-8213/aaa07d. arXiv: 1710.05864 [astro-ph.HE].

Yao, Y. et al. (2019). "ZTF Early Observations of Type Ia Supernovae. I. Properties of the 2018 Sample". In: *ApJ* 886.2, p. 152. DOI: 10.3847/1538-4357/ab4cf5. arXiv: 1910.02967 [astro-ph.HE].

Yaron, O. et al. (2017). "Confined dense circumstellar material surrounding a regular type II supernova". In: *Nature Physics* 13.5, pp. 510–517. DOI: 10.1038/nphys4025. arXiv: 1701.02596 [astro-ph.HE].

Yaron, O. and A. Gal-Yam (2012). "WISeREP—An Interactive Supernova Data Repository". In: *PASP* 124.917, p. 668. DOI: 10.1086/666656. arXiv: 1204.1891 [astro-ph.IM].

Yuan, Q. et al. (2016). "Catching jetted tidal disruption events early in millimetre". In: *MNRAS* 461.3, pp. 3375–3384. DOI: 10.1093/mnras/stw1543. arXiv: 1606.06830 [astro-ph.GA].

Zackay, B., E. O. Ofek, and A. Gal-Yam (2016). "Proper Image Subtraction—Optimal Transient Detection, Photometry, and Hypothesis Testing". In: *ApJ* 830.1, p. 27. DOI: 10.3847/0004-637X/830/1/27. arXiv: 1601.02655 [astro-ph.IM].

Zauderer, B. A. et al. (2011). "Birth of a relativistic outflow in the unusual γ-ray transient Swift J164449.3+573451". In: *Nature* 476.7361, pp. 425–428. DOI: 10.1038/nature10366. arXiv: 1106.3568 [astro-ph.HE].

Zauderer, B. A. et al. (2013). "Radio Monitoring of the Tidal Disruption Event Swift J164449.3+573451. II. The Relativistic Jet Shuts Off and a Transition to Forward Shock X-Ray/Radio Emission". In: *ApJ* 767.2, p. 152. DOI: 10.1088/0004-637X/767/2/152. arXiv: 1212.1173 [astro-ph.HE].

Zeh, A., S. Klose, and D. A. Kann (2006). "Gamma-Ray Burst Afterglow Light Curves in the Pre-Swift Era: A Statistical Study". In: *ApJ* 637.2, pp. 889–900. DOI: 10.1086/498442. arXiv: astro-ph/0509299 [astro-ph].

Zhang, B.-B. et al. (2015). "An Analysis of Chandra Deep Follow-up Gamma-Ray Bursts: Implications for Off-axis Jets". In: *ApJ* 806.1, p. 15. DOI: 10.1088/0004-637X/806/1/15. arXiv: 1405.4867 [astro-ph.HE].

Zhang, B. and P. Mészáros (2004). "Gamma-Ray Bursts: progress, problems & prospects". In: *International Journal of Modern Physics A* 19.15, pp. 2385–2472. DOI: 10.1142/S0217751X0401746X. arXiv: astro-ph/0311321 [astro-ph].

Zhang, W. et al. (2011). "CASTRO: A New Compressible Astrophysical Solver. II. Gray Radiation Hydrodynamics". In: *ApJS* 196.2, p. 20. DOI: 10.1088/0067-0049/196/2/20. arXiv: 1105.2466 [astro-ph.IM].

Zwart, J. T. L. et al. (2008). "The Arcminute Microkelvin Imager". In: *MNRAS* 391.4, pp. 1545–1558. DOI: 10.1111/j.1365-2966.2008.13953.x. arXiv: 0807.2469 [astro-ph].